Contract No:

This document was prepared in conjunction with work accomplished under Contract No. 89303321CEM000080 with the U.S. Department of Energy (DOE) Office of Environmental Management (EM).

Disclaimer:

3. ANALYSIS OF PERFORMANCE

This chapter summarizes safety functions and features, events, and processes; conceptual models which apply to all DUs; property data packages; and modeling tools developed and implemented in this PA to analyze ELLWF performance. Conceptual models of GW flow and transport in the VZ, which are specific to type of DU, are presented in Chapter 4.

- **Section 3.1** provides an overview of modeling case development as well as a roadmap of submodel integration in the ELLWF PA.
- **Sections 3.2 and 3.3** summarize the safety functions and features, events, and processes approach implemented in this PA to support development of conceptual models and identification of scenarios to be considered.
- **Section 3.4** presents the conceptual model for the final closure cap, including its expected evolution in performance over time and most likely and influential degradation mechanisms.
- **Section 3.5** describes the historical development, refinement, and implementation of the conceptual model for the GSA aquifer zone, along with aquifer transport modeling.
- **Section 3.6** outlines the implementation of the Atmospheric Release Model for the air and radon pathways analyses.
- **Section 3.7** documents the exposure pathways considered in this PA for the member of the public and the inadvertent human intruder analyses.
- **Section 3.8** presents the radiological; geochemical; material and hydraulic; infiltration; and hydrostratigraphic properties data packages used in the PA model simulations.
- **Section 3.9** briefly describes the primary software tools used in the PA model simulations.

KEY TAKEAWAYS

- ✓ **A blended top-down, safety-functions-based and bottom-up, FEPs-based approach identifies relevant PA scenarios.**
- ✓ **Waste subsidence as a cap degradation mechanism is central to the conceptual design of infiltration, flow, and transport models for all DUs except the NRCDAs.**
- ✓ **The final closure cap is constructed following dynamic compaction of non-crushable waste at end of IC with no active cap maintenance thereafter.**
- ✓ **A recently revised 3-D PORFLOW GSA flow model predicts seepage faces, hydraulic heads, and flow directions that agree with conceptual models and field observations.**
- ✓ **GoldSim® ARM models 1-D flux of gaseous radionuclides as they volatilize from the DU waste zone, diffuse across water-air interface into partially water-saturated, air-filled soil pores, and emanate at land surface.**
- ✓ **A 1-D GoldSim® Trench System Model, calibrated to 2-D and 3-D PORFLOW models, accurately represents ELLWF hydrostratigraphic zones for ST06, ST09, and ET06.**
- ✓ **The primary mechanism for radionuclide transport to MOP is leaching to GW, GW transport to the 100-m POA, and internal or external human exposure. Main IHI transport mechanism is direct intrusion into or excavation near the waste zone.**
- ✓ **Five property data packages are maintained for PA calculations: radiological-dose; geochemical; material and hydraulic; infiltration; and hydrostratigraphic.**
- ✓ **A diverse set of commercial, public-domain, and SRNL computational models and analysis tools is used to demonstrate compliance with POs.**

3.1. OVERVIEW OF ANALYSIS OF PERFORMANCE

As introduced in Section 1.2, this ELLWF PA revision employs an improved, systematic model development approach that builds upon post-2008 ELLWF modeling efforts, LFRG recommendations from PA2008, and the 2016 *Strategic Plan for Next E-Area Low-Level Waste Facility Performance Assessment* (Butcher and Phifer, 2016a; 2016b). A high-level overview of the PA model development process is shown in Figure 1-1. This section provides a more detailed roadmap of this five-step process.

3.1.1. Safety Functions and Features, Events, and Processes Screening

The DOE Technical Standard, "Disposal Authorization Statement and Tank Closure Documentation," (U.S. DOE, 2017) recommends the use of safety functions and features, events, and processes (FEPs) to support development of conceptual models and identification of scenarios to be considered in a PA. The FEPs approach provides a means to describe how a PA considers and addresses the factors that can influence the performance of key barriers. Understanding the roles of barriers in limiting migration highlights how changes in the system can lead to a situation where the roles are not fulfilled, and performance is compromised.

As presented by U.S. DOE (2017), two different approaches are available to identify scenarios for evaluation in the PA: a performance-based, top-down approach and a comprehensive, FEPs-based, bottom-up approach. The top-down approach begins with a new or existing technical understanding of the disposal system and appropriate conceptual models and applies this knowledge to identify the PA scenarios that consider the safety functions and associated FEPs deemed to be most impactful to system and barrier performance. The bottom-up approach, on the other hand, begins by assembling a comprehensive, all-inclusive list of potentially relevant FEPs, and then forms the PA scenarios out of this comprehensive list of factors.

In this PA, a blended top-down, bottom-up approach is employed as described by the Nuclear Energy Agency. The top-down, bottom-up approach (NEA, 2012) "begins with the development of the conceptual model, building an understanding of system behavior, and identifying safety functions associated with different natural and engineered barriers (e.g., roles of different barriers in limiting releases and subsequent migration)." This is followed by the identification of only those FEPs that can negatively impact the safety functions of the key natural and engineered barriers ("rather than comprehensively considering and documenting all possible FEPs, many of which are inconsequential"). As concluded by NEA (2012), the top-down, bottom-up approach utilizes a "recognized FEPs list in a targeted audit role for key aspects of the system rather than being the driver for scenario development."

The FEPs screening and review process was used to identify FEPs that are relevant to the ELLWF and, more specifically, can have a detrimental impact on the effectiveness of a given safety function. For this PA, a default list of FEPs developed by the International Atomic Energy Agency (IAEA, 2004) and an approach implemented for PAs at the Hanford and Idaho sites are employed to identify processes and events that can influence the effectiveness of a given safety function for the ELLWF (e.g., subsidence can impact the safety function of the cover system and lead to increased infiltration through the waste zone). Two of the most recent applications of this approach

are the PA for the INTEC calcined solids storage facility at the Idaho National Laboratory site (DOE-ID, 2019) and the PA for Waste Management Area C at the Hanford site (Mehta et al., 2016). The PA evaluates the potential impacts of changes in performance of different features of the system and demonstrates that the safety functions represent multiple and redundant barriers. Barrier analyses, assuming a safety function is not present, also test the robustness of the system in the event of the loss of one or more safety functions. Such evaluations also support a qualitative illustration of the concept of defense-in-depth.

The safety concept for closure of the ELLWF encompasses a variety of different features (i.e., administrative controls, natural site features, and engineered barriers) that reduce the potential impacts on human health and the environment from the residual waste that will remain after closure. These features can be represented as a collection of safety functions acting independently and as a system to provide for overall safety. In some applications, attempts are made to assign numerical expectations to specific safety functions, but that is not the intent in this case. The concept of safety functions is used more qualitatively in two ways for this PA:

1. To illustrate the robustness of the ELLWF design, operational practices, and closure approach by documenting features that are and are not credited in different modeling cases.
2. To identify the roles of the different features and potential processes and events that can compromise the performance of safety features and need to be considered when developing the modeling approach.

Section 3.1.5 expands on the use of safety functions in PA scenario development, while Section 3.3 provides more detail on the results of FEPs screening in this PA. A complete summary of the blended top-down, bottom-up approach is provided by Seitz (2020).

3.1.2. Conceptual Model Development

FEPs that are relevant to the ELLWF and have a detrimental impact on the effectiveness of a given safety function are chosen to inform conceptual model development for the baseline PA scenario and any alternative scenarios for each type of DU as shown in Figure 3-1. In this PA, a scenario represents a subset of safety functions and associated FEPs that identifies the conditions and processes that may influence the evolution of the disposal units and/or facility. A conceptual model describes the evolution of the system that includes or addresses the safety functions and associated FEPs within a given scenario (subset). Detailed descriptions of the conceptual models developed for this PA are provided in the following report sections:

- **Section 3.4:** Operational, interim, and final cover systems
- **Section 3.5.1:** GW aquifer pathway
- **Section 3.6:** Air and radon pathways
- **Sections 3.7 and 3.8.1:** Exposure and dose pathways (MOP and IHI)
- **Section 4.1:** VZ flow and transport for generic waste in STs and ETs
- **Section 4.2:** VZ flow and transport for simple SWFs in trenches
- **Section 4.3:** VZ flow and transport for complex SWFs in trenches

- **Section 4.4:** VZ and aquifer flow and transport in trenches for GoldSim® stochastics
- **Section 4.5:** VZ flow and transport for generic waste in LAWV
- **Section 4.6:** VZ flow and transport for generic waste and SWFs in ILV
- **Section 4.7:** VZ flow and transport for generic waste and SWFs in NRCDAs

The baseline PA scenario for each type of DU reflects the most likely or expected future evolution of the disposal site (i.e., the most probable and defensible scenario) and is defined along with the baseline conceptual model in the sections listed above. The relevant conceptual models for the baseline PA scenario and any alternative scenarios for each type of DU and waste form are then employed in developing the individual modeling cases as depicted generally in Figure 3-2.

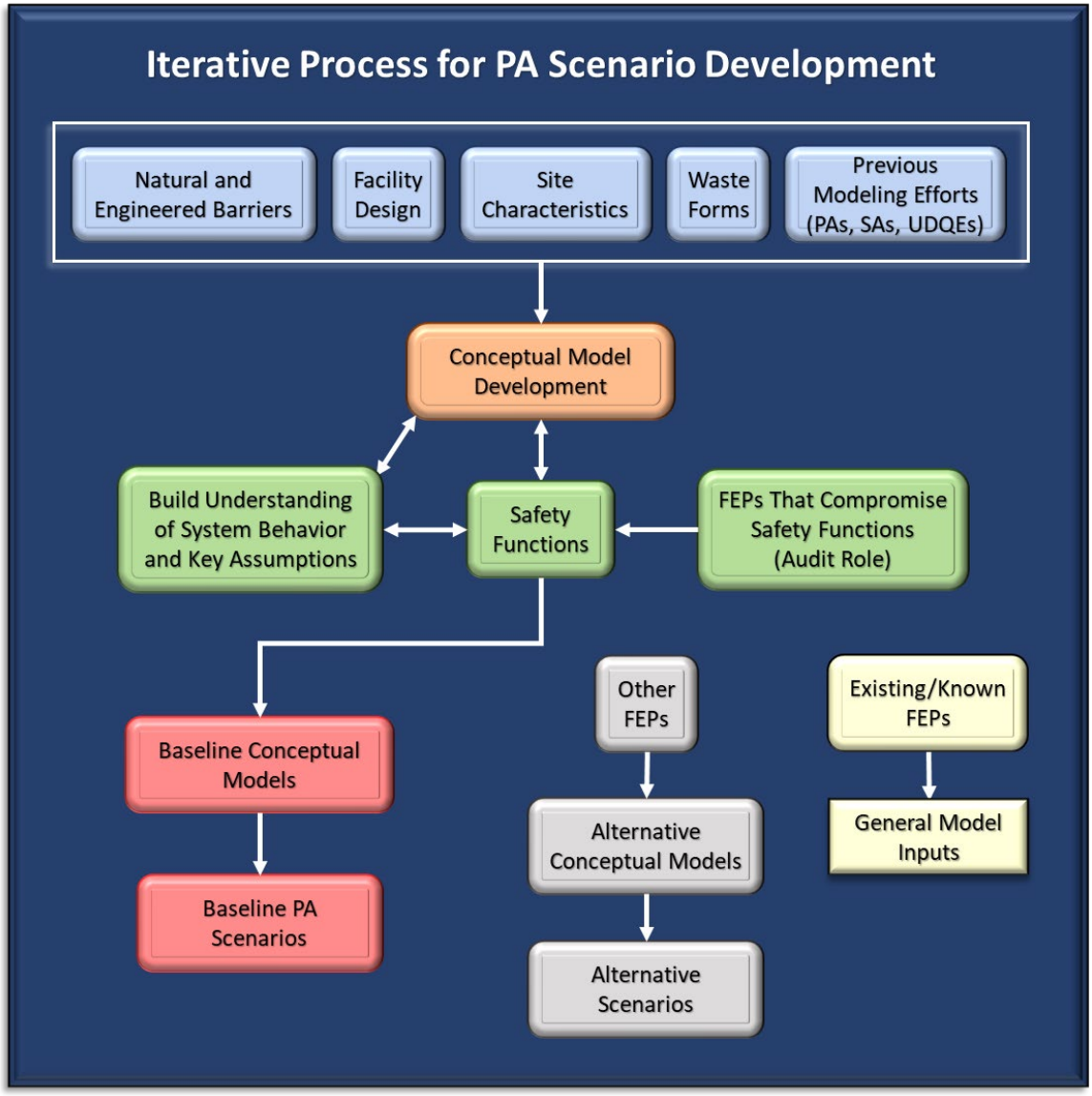

Figure 3-1. Iterative Process for Scenario Development in E-Area Low-Level Waste Facility Performance Assessment

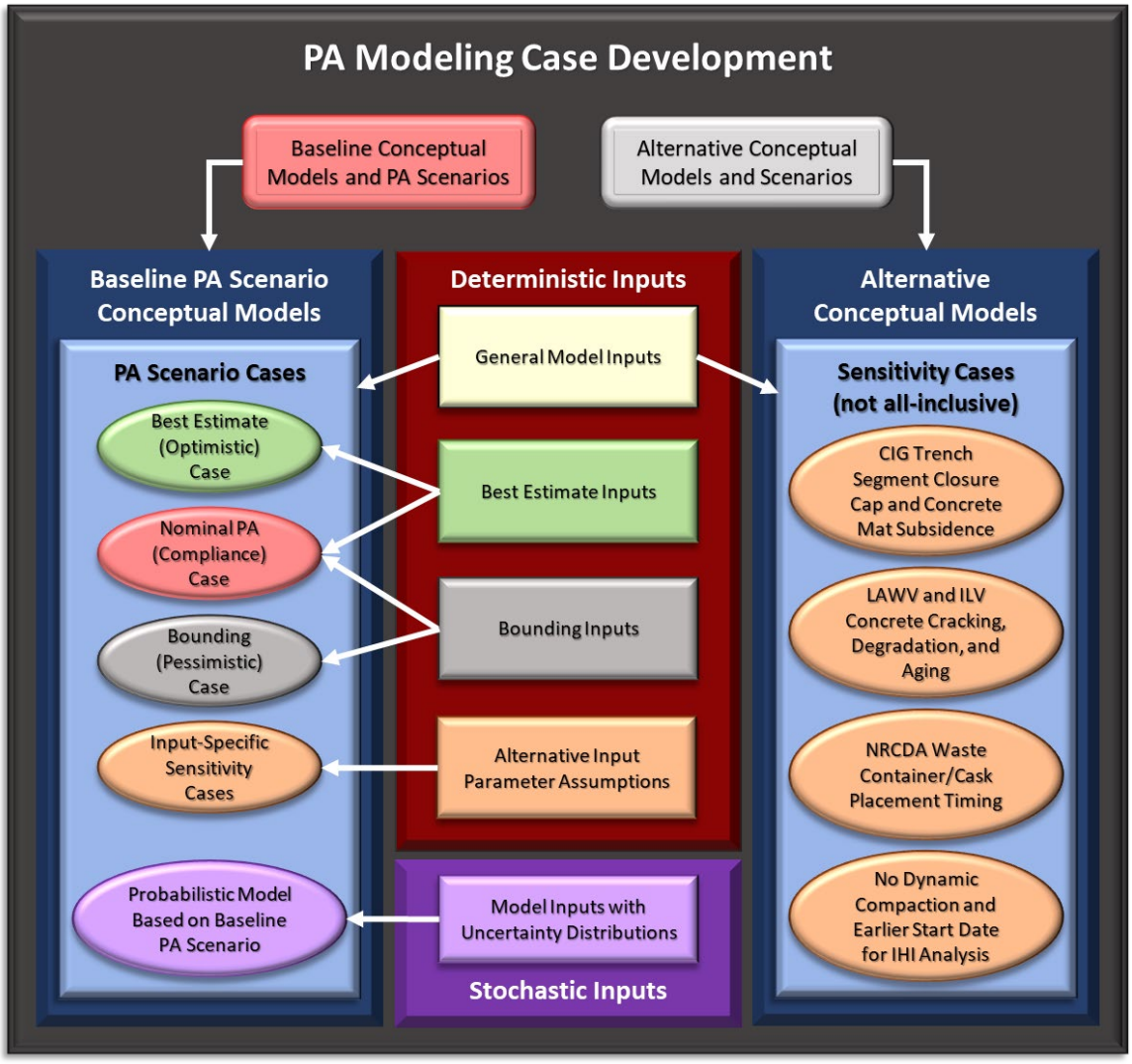

Figure 3-2. Overview of Modeling Case Development in the E-Area Low-Level Waste Facility Performance Assessment

Each type of DU (STs, ETs, LAWV, ILV, and NRCDA) and waste form (generic and special) within each type of DU is treated somewhat differently based on its own unique sets of scenarios (intact closure cap, subsided closure cap, concrete roof collapse, container hydraulic failure, etc.) and associated conceptual models (infiltration; VZ flow and transport; air and radon pathways). For example, the set of conceptual models comprising the baseline PA scenario for generic waste in STs and ETs is generalizable across many individual DUs. Exceptions are special waste forms (SWFs such as CIG trench segments, tall boxes, reactor heat exchangers, etc.) within specific trench DUs that are represented using individual alternative conceptual models of GW flow and transport in the VZ. Conversely, baseline and alternative conceptual models for generic waste and SWFs, respectively, in the LAWV, ILV, and NRCDAs are unique for each type of DU and waste form within each DU.

For the baseline PA scenario for each type of DU, a unique set of modeling cases (as defined below) is developed as outlined in Chapters 4 and 5.

- **Nominal PA (Compliance) Case:** Assumes a combination of the most probable and defensible input parameter values and is used to demonstrate compliance with POs within their compliance periods.
- **Best Estimate (Optimistic) Case:** Assumes best estimate values for input parameters without regard to defensibility.
- **Bounding (Pessimistic) Case:** Assumes input parameter values that are biased toward increasing dose, concentration, or flux to receptors to maximize defensibility.
- **Input Sensitivity Case:** Evaluates the impact of changes in input parameters (K_d, porosity, hydraulic conductivity, infiltration rate, etc.).

Safety functions and associated detrimental FEPs that fall outside the definition of the baseline PA scenario for each type of DU are organized into alternative scenarios that inform the development of alternative conceptual models. In this PA, sensitivity cases based on the alternative conceptual models are developed for the alternative scenarios and associated types of DUs. Examples include:

- For STs and ETs, an alternative conceptual model to the baseline scenario for an intact closure cap is developed that accounts for cap subsidence due to the presence of non-crushable containers.
- For CIG trench segments, an alternative to the intact closure cap conceptual model scenario is included which accounts for concrete mats and closure cap subsidence (pessimistic bounding and best estimate sensitivity cases).
- For the LAWV and ILV, alternative scenarios to the baseline PA scenario for concrete cracking, concrete degradation period, and concrete aging are considered in the sensitivity analysis.
- For NRCDAs, a sensitivity case is included with each of the four nominal PA cases that considers placement of all waste containers at the time of the initial soil cover in calendar years 2005 and 2065 for NR07E and NR26E, respectively, instead of placement of all waste containers at the time of first container disposal in calendar years 1987 and 1997 for NR07E and NR26E, respectively.
- For the IHI analysis, two alternative conceptual model scenarios to the baseline scenario are evaluated: an alternative start to the 1,000-year assessment period and no dynamic compaction of STs and ETs.

3.1.3. Mathematical Model Development

Mathematical models define the governing equations and formulas used to translate the conceptual models from qualitative descriptions into quantifiable calculations. Development of each mathematical model is explicit to respective submodels that represent components of the overall ELLWF system. As such, mathematical model development is discussed along with submodel implementation as outlined in the next section below.

3.1.4. Implementation Via Submodels

Discussions of each submodel are provided in the following PA report sections:

- **Section 3.5.2:** A 3-D aquifer flow and transport model for the GSA using PORFLOW focuses on saturated zone transport and estimates radionuclide concentrations at the 100-meter POA based on GW flow conditions and contaminant fluxes.
- **Section 3.5.3.2.2:** The plume interaction transport modeling generates PIFs for each radionuclide in each DU to account for the contributions of overlapping contaminant plumes from other DUs in the GW flow path to radionuclide concentrations at the 100-meter POA. The PIFs are used to adjust calculated disposal limits.
- **Sections 3.5.4 and 4.4:** A 1-D VZ and aquifer flow and transport model for STs and ETs utilizes the GoldSim® probabilistic software to perform sensitivity analysis and uncertainty quantification of radionuclide concentrations at the 100-meter POA.
- **Section 3.6.2:** The Atmospheric Release Model (ARM) in GoldSim® estimates the gaseous flux of volatile radionuclides at the ground surface as well as the dose to a maximally exposed individual for the air pathway analysis.
- **Section 3.6.3:** The ARM in GoldSim® simulates radon flux at the ground surface for the radon flux analysis.
- **Section 3.8.4:** Infiltration models in HELP estimate water percolation rates through the operational, interim, and final closure cap cover systems to establish the upper boundary condition for flow in the PORFLOW VZ models and the GoldSim® 1-D VZ models.
- **Section 3.9.3:** The SRNL Dose Toolkit calculates GW and IHI disposal limits at POAs for a MOP. The Dose Toolkit consists of four Fortran subroutines (*PreDose* module, *PreDose Maximum Concentration* module, *SRNL PA/CA Limits and Doses Tool*, and *SRNL ELLWF Dose Investigation Tool*).
- **Section 3.9.5**: CAP88-PC estimates the annual dose to human receptors based on atmospheric plume data generated from gas-phase radionuclide diffusion data for each DU simulated in the GoldSim® ARM.
- **Section 3.9.6**: The SRNL Closure Analysis Toolkit performs a stochastically based closure analysis to demonstrate overall compliance with POs for the ELLWF.
- **Section 4.1:** A 3-D flow and transport model in PORFLOW of generic waste in STs and ETs simulates water flow and radionuclide transport through the waste zone, soil backfill, and VZ soil assuming infiltration rates for both intact and subsided closure cap boundary conditions. The transport model calculates radionuclide fluxes to the water table based on water flow, radionuclide release rates, and radionuclide transport properties.
- **Section 4.2:** This section describes the methods used to implement "simple" SWFs in PORFLOW deterministic models for STs and ETs. As defined in this PA, simple SWF models include CIG trench segment; effective K_d; delayed release; solubility-controlled and diffusion-controlled release; and tall boxes.
- **Section 4.3:** Three complex SWFs are included in the VZ flow and transport models in PORFLOW for STs and ETs: Heavy Water Components Test Reactor (HWCTR in ST14), Reactor Process Heat Exchangers (HXs in ST09), and tritiated concrete rubble (232-F in ST01). Complex SWF model implementation in PA2022 makes use of earlier models deployed for each waste form in SAs performed by Hamm and Smith (2010), Hamm et al.

(2012), and Flach et al. (2005) for the HWCTR, HXs, and 232-F concrete rubble, respectively.

- **Section 4.4:** The 1-D VZ and aquifer flow and transport probabilistic model in GoldSim® represents three ELLWF trench DUs: ST06, ST09, and ET06. The GoldSim® model is calibrated to the respective PORFLOW model for each DU. Contaminant transport includes the following advective processes: infiltration from the ground surface, downward migration through the VZ, recharge of the aquifer at the water table, and lateral transport in the saturated zone to the 100-meter POA.
- **Section 4.5.3:** A 2-D flow model of the LAWV VZ in PORFLOW for the generic waste form simulates water flow through the vault concrete, waste zone, soil backfill, and VZ soil based on infiltration rates and concrete degradation rates. A 2-D VZ transport model in PORFLOW calculates radionuclide fluxes in GW from the LAWV to the water table based on water flow, radionuclide release rates, and radionuclide transport properties.
- **Section 4.5.3.6:** A concrete degradation model for the LAWV and ILV implemented in PORFLOW simulates the gradual degradation of concrete hydraulic properties over a period of 500 years.
- **Section 4.6.3:** 2-D PORFLOW models simulate VZ flow and transport in the ILV for generic waste and SWFs as described above for the LAWV.
- **Section 4.7.8:** A 3-D model of the VZ in PORFLOW for the NRCDAs simulates flow and transport for both generic waste (bolted containers) and SWFs (welded steel casks). The flow model estimates water movement through the waste zone (nonleaking and leaking container scenarios), soil backfill, and VZ soil using infiltration rates for the intact final closure cap. The transport model calculates radionuclide fluxes in GW from the NRCDAs to the water table based on water flow, radionuclide release rates (instantaneous for generic waste and corrosion-limited for SWFs), and radionuclide transport properties.
- **Section 4.7.8.5.3:** A PORFLOW model calculates corrosion-limited release rates for activated waste Inconel and Zircaloy metal components disposed in NRCDA casks, which are treated as a SWF for PA GW modeling.

3.1.5. Integration of Submodels

Each submodel requires explicit inputs and provides explicit outputs. Many submodels use the same or similar inputs, such that consistent assumptions are necessary. In order to fully integrate these submodels into a comprehensive ELLWF PA Model, these explicit inputs and outputs must be identified. Figure 3-3 provides an overview of the key inputs for and outputs from each submodel for the integrated deterministic model framework. A companion roadmap for the GoldSim® probabilistic Trench System Model used for sensitivity analysis and uncertainty quantification is provided in Figure 3-72 in Section 3.5.4.1.

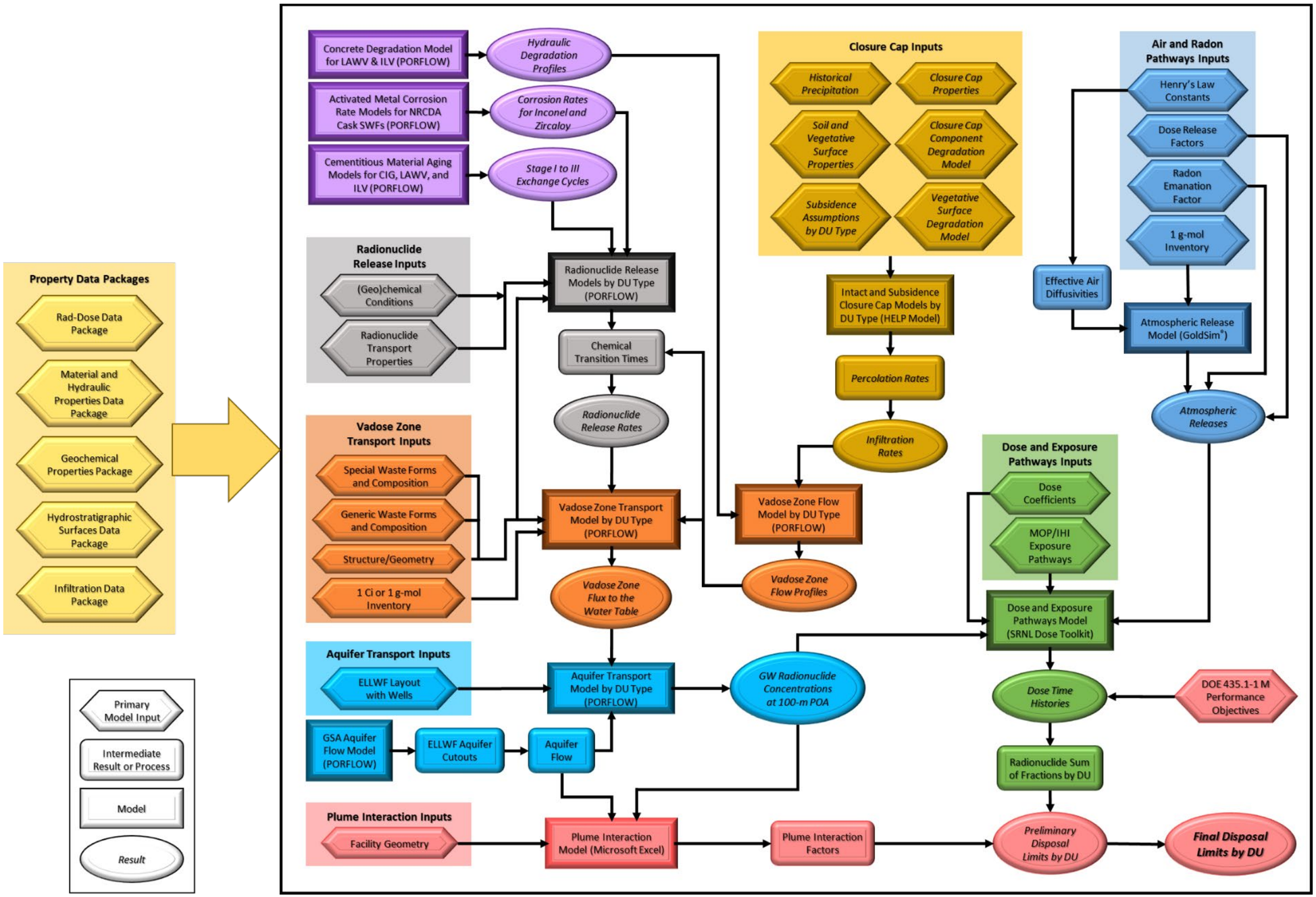

Figure 3-3. Integrated Deterministic Modeling Framework for the E-Area Low-Level Waste Facility Performance Assessment

3.2. SAFETY FUNCTIONS

The first step involved identifying safety functions that are relevant for the ELLWF PA, and the resulting table of safety functions is provided in Table 3-1 (Seitz, 2020). Each safety function includes a general description, a list of FEPs relevant for that function, and those FEPs considered potentially deleterious. The last two columns in the table summarize how the safety function was considered in the ELLWF PA and in any sensitivity and uncertainty analyses. The effectiveness of these safety functions is evaluated as part of the demonstration of a reasonable expectation of meeting the performance objectives and measures. Defense-in-depth is also addressed by considering potential impacts if any of the safety functions are lost or degraded through time or disruptive events. In many cases, the significance of deleterious FEPs relative to the conclusions of the analysis is addressed as more of a bounding approach by ignoring or taking minimal credit for the effectiveness of a given safety function either in the base case or in a barrier analysis. The table helps to highlight these types of deliberate biases.

3.2.1. Contextual Safety Functions

Although there is often a focus on technical safety functions, it is important to recognize safety functions that are provided by administrative or contextual requirements. These are not quantitatively addressed in this PA. For example, the all-pathways dose performance objective (25 mrem/year) is set at a fraction of the overall public dose limit (factor of four less than 100 mrem/year). Furthermore, the performance objective is well below the average annual dose in the United States (roughly a factor of 25 less than 630 mrem/year). Thus, significant safety margins are already built into the overall performance requirements.

A second key aspect of the safety concept for E-Area is associated with the administrative requirement in DOE O 458.1, Chg. 3 (U.S. DOE, 2020b) for continuing land ownership by the U.S. DOE. It is noteworthy that all technical calculations presented in this PA are predicated on the loss of Safety Functions IC1 (institutional control) and IC2 (societal memory) in Table 3-1. That is, loss of institutional control and loss of societal memory of the activities at SRS are both assumed to occur 100 years after facility closure. In the likely case that either one or both of these safety functions remain effective, any exposure scenarios considered at 100 years are not credible.

DOE M 435.1-1, Chg. 3 (U.S. DOE, 2021b) also introduces an administrative safety function related to the assumed location of a receptor (i.e., the point of compliance or point of assessment) and the habits of the receptor (i.e., a more highly exposed individual). Assuming the first two safety functions (institutional control and societal memory) are lost, DOE M 435.1-1, Chg. 3 (U.S. DOE, 2021b) generically expects that a GW well will be installed 100 meters (328 feet) from the disposed waste specifically in the location and at the time of peak concentration. This assumption limits the safety functions provided by the natural environment (i.e., further delays and dilution of contaminants in an aquifer). It is also assumed that a more highly exposed individual with habits intended to increase doses will be the receptor (i.e., a subsistence farmer). People upgradient or further downgradient or people not using GW and growing their own food would receive lower exposures and doses due to disposed waste in E-Area. If memory of SRS is lost, history suggests that people will potentially establish a residence and use untreated GW as their water source.

However, given the widespread knowledge of the site, it is highly unlikely that people would unknowingly establish a residence in E-Area 100 years after facility closure. DOE M 435.1-1, Chg. 3 (U.S. DOE, 2021b), therefore, provides an added layer of safety to the results of the analyses via this safety function where such exposures are assumed to occur at the time and location of the peak concentration very near the facility. Such defense-in-depth adds substantial margins of safety for radionuclides that are short lived or that migrate rather quickly to a 100-meter POA.

3.2.2. Engineered and Natural Safety Functions

The remaining parts of the safety concept involve use of engineered features and the natural setting to provide multiple and redundant barriers to the release and migration of residual wastes from ELLWF DUs. The engineered barriers are divided into one of four categories of safety functions:

- Hydrological
- Intrusion
- Structural
- Chemical

The hydrological safety functions limit the contact of water with the residual wastes, limit the rate at which contamination will migrate out of the units through the unsaturated zone to the compliance point in the aquifer, and provide dilution of contamination through dispersion and mixing with clean surrounding water. The chemical safety functions are intended to decrease the solubility or increase the sorption of key contaminants and to provide a stable and passive chemical environment for the engineered barriers.

The safety concept for the ELLWF relies on a graded approach for disposal where lower-risk wastes are disposed in STs or ETs with limited engineered controls, except for the cover. Higher-risk waste is disposed in the LAWV or ILV which provide additional layers of protection during operations and post closure. Containerized ST and ET waste is expected to result in subsidence of the closure cap as the containers degrade, which will lead to the potential for increased infiltration through the cover. Plans for dynamic compaction before final closure will help limit the extent of subsidence. The vaults provide a longer-term stable support structure for the cover, delaying potential subsidence until the loss of the physical integrity of the vault roof.

As discussed above, this PA serves to evaluate the safety concept and to provide a reasonable expectation of meeting the performance objectives and measures. Confidence in the overall safety concept is enhanced if adequate performance can be achieved even if any of the safety functions are lost or degraded in time (e.g., via subsidence). The safety functions in Table 3-1 describe how different barriers are expected to contribute to the ELLWF's ability to meet the POs. Potential deleterious FEPs are also identified to flag key factors that can lead to reduced performance. Finally, Table 3-1 includes how safety functions are considered in both the PA base case and the additional analysis cases included to address uncertainty associated with potentially deleterious FEPs.

Table 3-1. List of Safety Functions, Associated FEPs, Potentially Deleterious FEPs, and the Analyses Intended to Explore the Deleterious FEPs (Seitz, 2020)

ID	Safety Function	Description	Associated FEPs (Deleterious FEPs bolded)	Nominal PA Case Assumption	Associated Analyses
Administrative Controls					
AR1	Performance objectives and measures	The annual POs for public exposure (25 mrem all pathways, 10 mrem air) in DOE M 435.1-1 Chg. 3 (U.S. DOE, 2021b) are established at a fraction of the ICRP and IAEA dose limits for public exposures (100 mrem) and a substantial fraction of the average annual dose in the United States (630 mrem). The ICRP and IAEA dose limits can be exceeded, but an average dose over 5 years should not exceed 100 mrem. 1,000-year compliance period. Dose response assumptions are specified by DOE technical standards.	0.01 0.02 0.07 0.09	POs include safety margins compared to typical exposures. Calculations are conducted beyond 1,000 years to address potential later peaks.	Considered reasonably bounding.*
AR2	Exposure pathways	Assumptions about how humans are exposed to radioactivity must be made to calculate the dose. The types of potential exposures depend on the activities and conditions typical for the site. There were residents present on the Savannah River Site prior to establishment of the site boundaries, thus there is potential for exposures if institutional controls were to fail and memory of the site was lost. These exposures can include residential, hunter/fisherman, recreational, etc. DOE-SR, EPA and SCDHEC signed a Memorandum of Agreement to establish the *Land Use Control Assurance Plan* (LUCAP) (SRNS 2011). The LUCAP establishes and implements procedures to ensure the long-term effectiveness of Land Use Controls consistent with regulatory cleanup in the *Federal Facility Agreement* (FFA) for the SRS (SRNS 1993). At SRS, long-term stewardship begins at the completion of the Environmental Management mission. The current EM Program Management Plan (DOE-SR 2017) indicates the SRS cleanup program will continue to FY2065. The future use for the SRS is non-residential and will be maintained as such using institutional controls in accordance with the current *SRS Comprehensive Plan/Ten Year Site Plan FY 2016-2025* (SRNS 2015) and the *Land Use Control Assurance Plan for the Savannah River Site* LUCAP, individual RODs, facility specific Land Use Controls Implementation Plans (LUCIPs) and the DOE-SR RCRA Permit.	0.03 1.4.01 2.4.05 **0.04** 1.4.03 2.4.06 0.05 **1.4.06** 2.4.07 0.06 1.4.07 2.4.08 1.1.01 1.4.08 2.4.09 1.1.02 1.4.11 3.2.11 1.1.03 1.4.14 3.2.12 1.1.04 2.2.13 3.2.13 1.1.05 2.3.08 3.3.01 1.1.06 2.3.09 3.3.02 1.1.08 2.3.13 3.3.04 1.1.10 2.4.01 3.3.05 1.1.11 2.4.02 3.3.06 1.1.12 2.4.03 3.3.08 1.3.09 2.4.04	Upon loss of institutional control (see IC1), a more highly exposed individual located 100 meters (328 feet) from the disposed waste at the time of peak concentration is assumed, ignoring the limited likelihood of such exposure.	Considered reasonably bounding.*
IC1	Institutional control	Institutional controls essentially remove the possibility of significant public exposures near the E-Area. DOE O 458.1 Chg. 4 (U.S. DOE, 2020b) requires that DOE maintain control until the site can be released for unrestricted use. DOE P 454.1 Chg. 1 (DOE 2015) and the CERCLA process under the FFA identify how that stewardship is to be carried out. The CERCLA process includes specific land use restrictions to complement DOE requirements. The description under AR2, Administrative Controls Safety Function, summarizes the current planning and implementing documents.	1.1.06 1.4.07 1.1.10 1.4.08 1.4.01 **1.4.11** **1.4.03** 1.4.14 **1.4.06**	100 years of active IC is assumed to end in 2165. Institutional controls are assumed to be ineffective after that time, although CERCLA agreements will be in place and DOE is required to maintain active controls in accordance with DOE O 458.1 (U.S. DOE, 2020b).	Considered reasonably bounding.*
IC2	Societal memory	Societal memory of E-Area can be preserved using records, deed restrictions, local memory of the site, education, and other passive controls that would warn someone of the potential hazards in the area. In order for a member of the public to unknowingly conduct activities in the vicinity of E-Area, all memory of the activities at the Savannah River Site would have to be lost, and any records would have to be forgotten or ignored. DOE O 458.1 Chg. 4 (U.S. DOE, 2020b) requires recordkeeping that would lessen the likelihood of this occurrence. DOE P 454.1 Chg. 1 (DOE 2015) and the *Land Use Control Assurance Plan for the Savannah River Site* LUCAP (SRNS 2011), individual RODs, facility-specific Land Use Controls Implementation Plans (LUCIP) will assure the reliability of land use assumptions. DOE Legacy Management also engages in a number of activities to prolong memory of the site (e.g., visitor centers, active engagement at schools and with the community).	1.1.06 1.4.07 1.1.10 **1.4.08** 1.4.01 **1.4.11** **1.4.03** 1.4.14 **1.4.06**	Complete loss of memory and ineffectiveness of records and passive controls after 100 years of IC is assumed, ignoring widespread knowledge of the site and requirements for land use controls and recordkeeping.	Considered reasonably bounding.*
Natural Site Features					
SC1	Site characteristics	Conditions at the site determine infiltration and groundwater migration rates, geochemical conditions, and factors influencing atmospheric releases. E-Area is located in a humid, temperate climate, resulting in moderate infiltration rates under natural conditions. The water table is relatively shallow and surface water is available in the vicinity making access to water relatively easy.	**1.1.01 2.3.01 2.3.10** **1.3.02 2.3.02 2.3.11** **1.3.06 2.3.07 2.3.12** **1.3.07 2.3.08 2.3.13** **1.3.10 2.3.09 2.3.14** **1.4.01** **2.2.01** **2.2.02** **2.2.03** **2.2.07**	Table A-1 in SRNL-STI-2019-00363 (Dyer, 2019b) provides monthly average precipitation rates yielding an average of roughly 49 inches of precipitation in a year. After accounting for evaporation, transpiration, and runoff, it is assumed that natural infiltration is about 16 inches per year.	Sensitivity and uncertainty analyses considering ranges or variation in annual average precipitation rates.

Table 3-1 (cont'd). List of Safety Functions, Associated FEPs, Potentially Deleterious FEPs, and the Analyses Intended to Explore the Deleterious FEPs (Seitz, 2020)

ID	Safety Function	Description	Associated FEPs (Deleterious FEPs bolded)	Nominal PA Case Assumption	Associated Analyses
VZ1	Water flow in unsaturated zone	The unsaturated zone ranges from roughly 45 to 80 feet thick in E-Area with moderate infiltration as a driving force. Some dispersion is expected to occur as water moves through the unsaturated zone. In the closed disposal system, it would be expected that higher fluxes of water would be directed around the covered areas, which would tend to provide some dilution for releases occurring slowly beneath the cover. South Carolina Well Standards, Regulation 61-71 (SCDHEC 2016) provides requirements for properly sealing abandoned wells and boreholes.	**0.04** **1.1.01** **1.1.02** **1.3.02** **1.3.06** **1.3.07** **1.3.10** **1.4.01** **2.2.01** **2.2.02** **2.2.03** **2.2.07** **2.3.01** **2.3.02** **2.3.08** **2.3.09** **2.3.10** **2.3.11** **2.3.12** **2.3.13** **2.3.14** 3.1.01 3.2.09	Nominal assumptions and values for unsaturated zone hydraulic properties are described in SRNL-STI-2019-00355 (Nichols and Butcher, 2020). Nominal or "best estimate" hydraulic property values are generally assumed in deterministic modeling for establishing disposal limits.	Planned sensitivity and uncertainty analyses will be based on hydraulic property value uncertainty distributions provided in SRNL-STI-2019-0355 (Nichols and Butcher, 2020).
VZ2	Sorption in unsaturated zone	Unsaturated zone soils comprise a mix of clay and sand and will sorb some of the contaminants of potential concern, reducing concentrations in pore water and delaying their arrival at the water table. There is variability in the amounts of clay and sand above the water table in different parts of E-Area, which is addressed in the conceptual model. Sorption is generally expected to be higher in clayey soils than sands.	**1.1.01** **1.4.07** **2.1.09** **2.2.03** **2.2.07** **2.2.08** **2.2.09** **3.2.01** **3.2.02** **3.2.03** **3.2.04** 3.2.05 3.2.06 **3.2.07**	"Best", "minimum" and "maximum" estimates of sorption coefficient or K_d values for unsaturated zone geochemical properties are described in SRNL-STI-2009-00473, Rev. 1 (Kaplan, 2016b). "Best estimate" values are considered central values derived from experimental data, the literature, or, where no sorption data are available, based on chemical analogue. Best estimate geochemical values are assumed in deterministic modeling for establishing disposal limits. Sorption tends to be higher in clayey soils rather than sandy soils. Except where noted otherwise, soil backfill in the trenches is treated as clayey soil. The average clay thickness beneath each disposal unit was provided in SRNL-STI-2017-00301, Rev. 1 (Bagwell and Bennett, 2017). Trench units stretch across the full extent of the E-Area footprint. Trench units were collected into 7 unique hydrostratigraphic groupings and the minimum clay thickness selected as representative of each grouping in SRNL-STI-2019-00193, Rev. 0 (Danielson, 2019c).	Planned sensitivity and uncertainty analyses will be based on geochemical value uncertainty distributions provided in SRNL-STI-2009-00473 (Kaplan, 2016b).
VZ3	Dispersion in unsaturated zone	Spreading of contaminants in the unsaturated zone disperses them and decreases concentrations.	**2.2.01** **2.2.02** **2.2.03** **2.2.07** **2.2.12**	The ELLWF PA will conservatively assume that the process of mechanical dispersion can be neglected at the scale considered in the VZ flow model because dispersion associated with downward flow is expected to be relatively low within native soils.	The nominal PA case assumption is considered reasonably bounding.*
SZ1	Water flow in saturated zone	Mixing of slowly released contaminants from the vadose zone into advective flow in the saturated zone leads to some dilution of the concentrations. Covers over the disposal facility will further reduce flow rates in the vadose zone, which should lead to further decreases in concentrations expected in the saturated zone. There is substantial experience modeling flow in the saturated zone in the GSA.	**0.04** **1.1.01** **1.1.02** **1.3.02** **1.3.06** **1.3.07** **1.3.10** 1.4.01 **1.4.10** **2.2.03** **2.2.07** **2.3.01** **2.3.02** **2.3.08** **2.3.09** **2.3.10** **2.3.11** **2.3.12** **2.3.13** **2.3.14** 3.1.01 3.2.07	The GSA flow model was recently updated to account for current understanding in SRNL-STI-2018-00643, Rev. 0 (Flach, 2019). This report documents further refinement of the GSA_2016 model in 2018 to incorporate, among other things, construction of E-Area ST operational covers. Refined grid spacing specifically for the ELLWF was recently adopted in SRNL-STI-2019-00736 (Hang, 2019a). Modeling is intended to represent expected conditions. Depth to water and thickness of clay were selected at minimum values to bias migration rates on the high end. The range of depths to the water table beneath trenches required use of multiple models to adequately represent hydrostratigraphic features while maintaining a reasonable level of conservatism. Trench units were collected into 7 unique hydrostratigraphic groupings and the minimum depth to water table selected as representative of each grouping in SRNL-STI-2019-00193, Rev. 0 (Danielson, 2019c).	Sensitivity and uncertainty analyses considering alternative aquifer models to be determined.

Table 3-1 (cont'd). List of Safety Functions, Associated FEPs, Potentially Deleterious FEPs, and the Analyses Intended to Explore the Deleterious FEPs (Seitz, 2020)

ID	Safety Function	Description	Associated FEPs (Deleterious FEPs bolded)	Nominal PA Case Assumption	Associated Analyses
SZ2	Sorption on saturated zone soils	Saturated zone soils sorb some of the contaminants of potential concern, delaying their arrival at the point of compliance. The assumed fractions of clay and sand can influence the sorption of some key radionuclides. A number of key contaminants are not believed to sorb significantly.	**1.1.01** **3.2.03** **3.2.07** **2.2.03** **3.2.04** **2.2.08** 3.2.05 **2.2.09** 3.2.06 **3.2.01** **3.2.02**	"Best", "minimum" and "maximum" estimates of K_d values for unsaturated zone geochemical properties are described in SRNL-STI-2009-00473, Rev. 1, (Kaplan, 2016b). "Best estimate" values are considered central values derived from experimental data, the literature, or, where no sorption data are available, based on chemical analogue. Best estimate geochemical values are assumed in deterministic modeling for establishing disposal limits. Sorption tends to be higher in clayey soils rather than sandy soils. Except where noted otherwise, soil backfill in the trenches is treated as clayey soil. The average clay thickness beneath each disposal unit was provided in SRNL-STI-2017-00301, Rev. 1 (Bagwell and Bennett, 2017). Trench units stretch across the full extent of the E-Area footprint. Trench units were collected into 7 unique hydrostratigraphic groupings and the minimum clay thickness selected as representative of each grouping in SRNL-STI-2019-00193, Rev. 0 (Danielson, 2019c).	Planned sensitivity and uncertainty analyses will be based on geochemical value uncertainty distributions provided in SRNL-STI-2009-00473 (Kaplan, 2016b).
SZ3	Dispersion in saturated zone	Mixing and spreading of the plume in the aquifer reduces downstream concentrations. The effects are somewhat limited at a point only 100 meters downstream of the waste zone, but do still contribute to reducing impacts.	**2.2.03** **2.2.07**	Four refined PIF aquifer cutouts for the ELLWF were implemented in the GSA flow model to allow better representation of dispersion as reported in SRNL-STI-2019-00736 (Hang, 2019a). For baseline limits calculations in this PA, the average value for longitudinal dispersivity will be computed using Eq. (3-14) assuming a minimum travel distance of 100 meters for all DUs. Smaller discretization of the aquifer transport model cutouts (i.e., horizontal and vertical grid sizes of 20 feet and 3 feet, respectively) is employed to reduce effects of numerical dispersion as described in SRNL-STI-2019-00736 (Hang, 2019a).	Sensitivity and uncertainty analyses considering alternative saturated zone dispersion parameter settings.
SZ4	Dilution in well	Dilution is caused by drawing a mixture of water with different levels of contamination into the screened section of a well, where it is pumped to the surface, where it is useable and accessible by a member of the public. The vertical and horizontal size of grids used in the model can serve to represent averaging over a well's zone of influence to some extent.	2.2.13 3.2.12 3.3.02 3.2.07 3.3.01 3.3.04	The calculated peak concentration at the 100-meter GW POA is based on the mesh size element used in the model. Thus, dose impacts from groundwater are calculated without directly accounting for potential dilution from pumping a domestic well at the 100-meter POA. As described in SRNL-STI-2019-00736 (Hang, 2019a), the grid size used in the latest GSA aquifer cutout models is 20 feet horizontal and 3 feet vertical. This mesh size is small relative to the zone of plume capture from a typical domestic well down gradient of a trench sized source term and groundwater plume.	The model construct described for obtaining the maximum concentration at the 100-meter POA for the nominal PA case is considered to be reasonably bounding.*
Engineered Barriers					
Hydrological Safety Functions					
EB1	Engineered cover	Engineered covers are used to promote runoff, evapotranspiration and lateral drainage, in order to control the amount of infiltration that can percolate to the waste. The final E-Area multi-layer soil-geomembrane cover is designed to limit infiltration to the disposed waste. Waste layer subsidence is expected in E-Area trenches due to the presence of containerized compactible waste. To address this issue, dynamic compaction will be used over STs and ETs to largely eliminate void volume in crushable containers prior to final closure reducing the extent of subsidence expected. The E-Area Vaults, LAWV and ILV, and wastes within them, as well as the robust waste forms on the NRCDAs, are also assumed to eventually fail structurally, which will also lead to additional subsidence of the cover in the far future well beyond the end of the 1,000-year compliance period.	**1.1.02** **1.3.08** **2.1.09** **1.1.03** **1.3.10** **2.1.10** **1.1.04** **1.3.06** **2.3.01** **1.1.05** **1.3.07** **2.3.02** **1.1.07** **1.3.08** 2.3.07 **1.1.08** **1.3.10** **2.3.08** **1.1.09** **1.4.01** **2.3.09** **1.1.12** **1.4.07** **2.3.10** **1.2.08** **1.4.08** **2.3.11** **1.2.10** **2.1.02** **2.3.12** **1.3.02** **2.1.03** **2.3.13** **1.3.06** **2.1.04** **2.3.14** **1.3.07** **2.1.05** **2.1.06** **2.1.07** **2.1.08**	SRNL-STI-2019-00363 (Dyer, 2019b) includes a description of the cover performance assumptions for each of the disposal concepts in E-Area (i.e., STs, ETs, CIG trench segments, ILV, LAWV, and NRCDAs). Each concept is assigned specific assumptions regarding the timing and extent of subsidence based on the nature of the waste disposed. 3-D VZ modeling is being employed for STs and ETs to account for impacts of subsidence cases and closure cap edge effects on trench performance.	A variety of uncertainty and sensitivity cases are being considered to address the projected impact of ranges of closure cap conditions over time (e.g., spatial distribution of subsided regions of the cover) on the projected infiltration rate through the cover.

Table 3-1 (cont'd). List of Safety Functions, Associated FEPs, Potentially Deleterious FEPs, and the Analyses Intended to Explore the Deleterious FEPs (Seitz, 2020)

ID	Safety Function	Description	Associated FEPs (Deleterious FEPs bolded)	Nominal PA Case Assumption	Associated Analyses
EB2	E-Area Vaults (ILV and LAWV)	The reinforced-concrete structures associated with the ILV and LAWV provide enhanced stability to limit potential subsidence of the cover. Voids within the structures will be limited to reduce potential subsidence. The LAWV is assumed to eventually fail structurally, which is anticipated to lead to subsidence in the cover. The vaults in combination with the cover will also serve as a hydraulic barrier to water flow while intact. As the concrete degrades, cracks are expected to form which will lead to increasing flow rates, limited by infiltration through the cover system, and eventually the concrete will no longer serve as a barrier to water flow.	**1.1.02** **1.1.12** **2.1.07** **1.1.03** 1.2.03 **2.1.08** **1.1.04** **2.1.02** **2.1.09** **1.1.05** **2.1.03** **2.1.10** **1.1.07** **2.1.04** 2.1.11 **1.1.08** **2.1.05** 2.1.13 **1.1.09** **2.1.06** **2.2.08** **2.2.09**	The vaults in combination with the cover are assumed to provide hydraulic protection while they remain intact. E-Area vault failure assumptions are based on LAWV and ILV structural degradation calculations in T-CLC-E-00018, Rev. 1 (Carey, 2005) and T-CLC-E-00024, Rev. 0 (Peregoy, 2006b), respectively, performed by SRNS Design Engineering. Structural failure is assumed to occur after a mean time of approximately 2,800 years (LAWV) and 6,700 (ILV) years, leading to subsidence of the cover and greatly increased infiltration into the vaults. The vault structural analyses provided statistical variability estimates for all results including predicted times of collapse of vault roof and side walls. Seismic loads and differential settlement are assumed to lead to separation at joints in the base of the vaults enabling releases to the vadose zone beneath the vaults.	The structural degradation analysis is judged to be conservative based on the bounding seismic loads used, applying both oxic and anoxic rebar corrosion mechanisms, and simplifying loads for ease of calculations, such as dynamic earth pressures, etc. Thus, the nominal PA case is considered to be reasonably bounding.*
EB3	Waste Forms, Containers, & Backfill	A wide variety of waste forms and containers are disposed in E-Area. Low permeability waste forms, such as cementitious materials, can limit water contact with radionuclides and reduce release rates. Containers will delay contact of infiltrating water with the waste while intact and limit water contact as the containers degrade. Robust containers could potentially delay releases for long time frames while they remain intact.	**1.1.02** **1.1.12** **2.1.07** **1.1.03** 1.1.08 **2.1.08** **1.1.04** **2.1.01** **2.1.09** **1.1.05** **2.1.02** **2.1.10** **1.1.07** **2.1.03** 2.1.11 **1.1.08** **2.1.04** 2.1.13 **1.1.09** **2.1.06** **2.2.08** **2.2.09**	The two broad categories of waste forms and containers in terms of modeling are generic and special waste forms. Generic waste forms comprise the largest fraction of LLW, where no credit is taken for the container or waste form in holding up contaminants (e.g., job control waste in B-25 boxes). In effect, contaminants are assumed to be immediately released and available to the surrounding waste zone medium (e.g., backfill soil in trenches). Two general sub-categories of special waste forms are those that rely on sorption properties alone (e.g., ion exchange resins) in controlling release, and those that rely on the hydraulic integrity of the container, or other properties of the waste form, or a combination (e.g., welded NR casks holding activated metal components) to control release. The latter subcategory is generally precluded from receiving waste layer stabilization measures (e.g., dynamic compaction) prior to installation of the final closure cap. Trench backfill consists of soils typically excavated in creating the trench segment. Because the upper vadose zone in E-Area typically exceeds the 20-foot trench depth, assignment of loose, clayey soil hydraulic and geochemical properties to trench backfill is considered reasonable. Hydraulic properties of cementitious materials used as backfills [i.e, CLSM and grouts] have been measured and are therefore well characterized.	Sensitivity and uncertainty analyses of waste forms and containers are not considered necessary. Treatment of generic wastes in ELLWF nominal PA case modeling (i.e., radionuclides immediately available for release) is considered to be reasonably bounding. SWFs relying on sorption properties have had those properties measured in the laboratory and are therefore generally well characterized. Those special waste forms relying on waste container hydraulic integrity or other waste form properties have been evaluated in Special Analyses using overall bounding assumptions and have been generally tested with limited sensitivity analyses to ensure special waste form disposal limits are defensible. Any sensitivity and uncertainty analyses of backfill properties will be based on hydraulic property value uncertainty distributions provided in SRNL-STI-2019-0355 (Nichols and Butcher, 2020).
Intrusion Safety Functions					
EB4	Engineered cover	Potential inadvertent human intrusion scenarios are limited by the cover thickness and depth of waste and could also be limited by design features included in a cover to deter intrusion. Generally, if the waste is expected to remain more than 3 meters (10 feet) below the surface of any cover after erosion, a basement excavation scenario into the waste is excluded. Inadvertent intrusion via basement excavation is also considered highly unlikely as long as obvious barriers remain (e.g., HDPE layer in cover, biotic intrusion barriers, etc. that are distinguishable from soil that would normally be expected). A cover may also include features that make drilling less likely (e.g., relatively large stones), and the general nature of a cover (relatively steep slopes) make it more likely that a well would be constructed beside rather than on top of a cover.	**1.1.02** **1.2.07** **2.3.01** **1.1.03** 1.3.10 **2.3.12** **1.1.04** **1.4.03** 2.4.07 **1.1.05** **1.4.06** **1.1.07** **1.4.08** **1.1.08** **1.4.11** **1.1.09** **2.1.05** **1.1.12**	Intrusion scenarios for E-Area are assumed to result in penetration through the final closure cap and into or near the waste zone. Thus, doses to an inadvertent intruder are directly related to the concentration of contaminants in the waste disposal facility. Potential intruder scenarios and exposure pathways have been screened in SRNL-STI-2020-00007 (Stagich and Jannik, 2020) to determine those needing to be carried forward into the PA for calculating disposal limits. Intruder scenarios, assumptions, and associated model inputs to be used in the ELLWF PA revision are defined in SRNL-STI-2015-00056, Rev. 1 (Smith et al., 2019). Intruder dose calculation methodology and associated inputs have been encoded in the SRNL Dose Toolkit described in SRNL-TR-2019-00337 (Aleman, 2019) for calculating intruder-based dose impacts and disposal limits. Assumptions regarding impact of erosion on the closure cap, effectiveness of the erosion barrier, potential for biotic intrusion, and depth to the waste layer are all addressed in these documents establishing the nominal PA case.	A consistent set of standard intruder scenarios has been established and employed in DOE O 435.1 PAs across the DOE Complex. These highly conceptualized intruder models are generally recognized as hypothetical constructs based on knowledge of current land use practices and therefore not the subject of sensitivity and uncertainty evaluations. Inputs to these calculations are typically well known (e.g., radionuclide decay data), mandated (e.g., dose coefficients) or assumed based on typical or reference human behavior (e.g., consumption rates) or regional practices (e.g., well drilling, basement construction).

Table 3-1 (cont'd). List of Safety Functions, Associated FEPs, Potentially Deleterious FEPs, and the Analyses Intended to Explore the Deleterious FEPs (Seitz, 2020)

ID	Safety Function	Description	Associated FEPs (Deleterious FEPs bolded)	Nominal PA Case Assumption	Associated Analyses
EB5	E-Area Vaults (LAWV and ILV)	The reinforced concrete vaults provide a significant barrier to intrusion, especially in an environment where drilling and excavation activities will be directed to working in clay and sandy soils. While the reinforced concrete remains intact, it will be an effective physical barrier against inadvertent excavation and drilling. Furthermore, concrete structures would be obviously distinguishable from soil for a very long time and an intruder would be expected to recognize that something was wrong. As long as the concrete and steel maintained some integrity (thousands of years), an inadvertent intruder would not proceed to excavate a basement and drill cuttings would be distinctly different from soil. The disposed waste will also be deeper than 3 meters (10 feet).	**1.1.02** **1.1.09** **1.4.11** **1.1.03** **1.1.12** 2.1.05 **1.1.04** **1.2.03** **2.1.06** **1.1.05** **1.4.03** **2.2.13** **1.1.07** **1.4.06** **1.1.08** **1.4.08**	As described in SRNL-STI-2015-00056, Rev. 1 (Smith et al., 2019), both the LAWV and ILV reinforced concrete roofs are considered to be effective barriers to acute well drilling and basement construction intruder scenarios throughout the 1,000 year compliance period and are therefore screened out from consideration for E-Area vault units in the PA revision. Structural degradation analyses performed for the LAWV in T-CLC-E-00018, Rev. 1 (Carey, 2005) and for the ILV in T-CLC-E-00024 Rev. 0 (Peregoy, 2006b), demonstrated that vaults will maintain their structural integrity well past the 1,000-year compliance period. Once sufficient erosion has occurred, as limited by the closure cap erosion barrier, an intruder is assumed to reach or come near the waste zone with basement construction. Thus, the chronic residential scenario assumes an intruder lives in a home with a basement located directly above the disposal facility. The resident is shielded from external exposure to radionuclides in the waste by the concrete floor slab and the soil remaining between the basement and the vault, trench or pad.	Vault structural failure for both the ILV and LAWV is predicted to occur well past the end of the post-closure 1,000 year compliance period with a high degree of confidence. Thus, the nominal PA case is considered reasonably bounding.*
EB6	Enhanced Waste Forms and Containers	Numerous special waste forms rely on the hydraulic integrity of the container, or other properties of the waste form, or a combination to control contaminant release to the waste zone. Examples, include welded, carbon steel casks containing NR components, HWCTR, Reactor Process HXs, etc.	**1.1.02** **1.1.09** **1.4.14** **1.1.03** **1.1.12** **2.1.03** **1.1.04** **1.4.03** 2.1.04 **1.1.05** **1.4.06** **2.2.13** **1.1.07** **1.4.08** **1.1.08** **1.4.11**	Historically, intruder pathway dose impacts have been relatively insignificant compared to the groundwater pathway. Thus, if special waste form treatment is unnecessary to produce acceptable intruder dose impacts then no further analysis is needed, and intruder-based disposal limits are established without taking waste form credit. If waste form credit is needed to produce acceptable limits, then the intruder analysis can consider the long-term integrity of the outer container and the waste form itself to arrive at special waste form limits for the inadvertent intruder based on the specific intrusion scenario. A potential example of this case is the welded, carbon steel cask containing naval reactor components on the NRCDAs. These robust, welded casks are assumed to be structurally stable for thousands of years after placement on the pads based on estimated corrosion rates discussed in SRNL-STI-2018-00633 (Wohlwend and Butcher, 2018). However, at 750 years, the casks are assumed to hydraulically fail, allowing radionuclides from inside the cask to be released to the surrounding waste zone. Release of contaminants from the cask is controlled by the surface corrosion rate of the activated metal components within the cask. These aspects would be considered in establishing special waste form intruder limits.	For the generic waste category, the PA disposal unit model assumes no barriers to intrusion following loss of IC. Exceptions for certain special waste forms as described under the nominal PA case are based on conservative assumptions of container integrity and barrier performance and, therefore, are considered reasonably bounding.*

Table 3-1 (cont'd). List of Safety Functions, Associated FEPs, Potentially Deleterious FEPs, and the Analyses Intended to Explore the Deleterious FEPs (Seitz, 2020)

ID	Safety Function	Description	Associated FEPs (Deleterious FEPs bolded)	Nominal PA Case Assumption	Associated Analyses
Structural Safety Functions					
EB7	Containers (STs and ETs)	Structural considerations are a critical assumption for long-term evolution of the cover and estimates of the infiltration rates through the cover. Containers used for the STs and ETs generally provide structural stability for safe operations and interim covers. However, the largest category of waste is considered "crushable" consisting of low-density, compactible waste that will eventually lead to extensive subsidence when containers, such as B-25 boxes and SeaLand containers, structurally fail. In recognition of the eventual structural failure of containers, waste stabilization measures are planned to consolidate the waste layer and mitigate non-uniform subsidence of the overlying closure cap. Dynamic compaction is proposed near the end of the 100-year IC period (prior to final closure) to allow time for metal (painted, carbon-steel) disposal containers to substantially corrode in order to optimize the effectiveness of dynamic compaction. Corrosion studies have indicated that this timeframe will be sufficient for a significant amount of degradation of containers leading to a more uniform failure of the closure cap. This condition is known as the "intact" case. A smaller category of waste disposed in STs and ETs, known as "non-crushable" waste, is not expected to be greatly impacted by dynamic compaction measures. Non-crushable waste typically consists of a robust waste form (e.g., vessels with large internal voids) or robust disposal container (e.g., thick-gauge steel boxes fabricated for tank farm equipment) with a higher degree of structural stability than containers typically used for crushable waste (e.g., B-25 boxes). The PA conservatively assumes that non-crushable wastes survive dynamic compaction largely structurally intact, but then fail simultaneously and catastrophically shortly after installation of the final closure cap. This assumption results in localized failure of those portions of the closure cap directly overlying the waste resulting in increased infiltration through the waste zone. This condition is known as the "subsided" case. Historically, the most restrictive radionuclide disposal limits for STs and ETs are based on the subsided case. Such containers are the primary focus because they would fail after the final cover is in place. A final general category consists of robust containers and waste forms that will maintain structural integrity for very long times (e.g., heat exchangers with substantial internal structural elements) and bulk wastes (e.g., concrete rubble) which are not expected to be a subsidence concern.	**1.1.02** **1.2.08** **2.1.09** **1.1.03** **1.2.10** **2.1.10** **1.1.04** **2.1.02** 2.1.11 **1.1.05** **2.1.03** 2.1.13 **1.1.07** **2.1.04** **1.1.08** **2.1.05** **1.1.09** **2.1.06** **1.1.12** **2.1.07** **2.1.08**	The conceptual model includes assumptions about the fraction of non-crushable packages in a given trench disposal unit and uses this to establish the extent of subsidence over the cap from localized failures of non-crushable containers. The current operational restriction on the trench area that can be occupied by non-crushable waste varies between 2 and 10% depending on the trench unit location. Four specific subsidence scenarios (i.e., 0.54%, 2%, 3.6%, and 4.9%) were determined from reviewing historical ST and ET inventory data for non-crushable packages. To incorporate the effect of localized cap subsidence, a weighted blending of radionuclide fluxes to the water table was employed in PORFLOW vadose zone simulations representative of these specific subsidence scenarios.	HELP model results from sensitivity studies of the intact infiltration case were fit to a log-logistic function to generate infiltration profiles over a 10,000-year period for most-optimistic, more-optimistic, best-estimate, more-pessimistic, and most-pessimistic cases, for both the intact and four subsidence scenarios. These discrete cases take into account uncertainty in infiltration due to uncertainties in slope, slope length, surface vegetation, evapotranspiration and geomembrane degradation rate.
EB8	E-Area Vaults (LAWV and ILV)	The primary role for stability is the influence on the cover performance when the concrete vault roof eventually fails. The concrete vaults will delay subsidence while intact, which would be expected to be very long times for reinforced concrete. Structural calculations discussed in EB5, Engineered Barriers Safety Function, were conducted and estimated collapse of the LAWV roof at a mean time of 2,800 years and ILV roof at a mean time of 6,700 years after closure. There will be some void space at the roof of the LAWVs and containers will be subject to compaction under the weight of the roof and overlying soils. Thus, although delayed, the impact of subsidence of the LAWV on infiltration will be significant. Structural considerations also will impact the assumptions for degraded hydraulic functions for the concrete roof, walls and floor.	**1.1.02** **1.1.12** **2.1.07** **1.1.03** **1.2.03** **2.1.08** **1.1.04** **2.1.02** **2.1.09** **1.1.05** **2.1.03** **2.1.10** **1.1.07** **2.1.04** 2.1.11 **1.1.08** **2.1.05** **1.1.09** **2.1.06**	For the E-Area vaults, LAWV and ILV, infiltration rate profiles for a 10,000-year period were developed for both an on-vault (above the concrete vault roof) and an off-vault (10-foot soil zone adjacent to vault walls) scenario. The actual compliance period for the PA is 1,000 years following final closure; however, infiltration estimates were extended to 10,000 years to capture roof collapse. The purpose of the off-vault simulations was to confirm that subsurface runoff from the concrete vault roof will adequately drain through the lowermost backfill layers adjacent to the vault walls. Upon structural failure of the ILV and LAWV roof, the conservative assumption is that the roof collapses into the vault over all waste cells simultaneously (i.e., nine ILV waste cells and 12 LAWV waste cells) and the overlying closure cap subsides. Closure cap subsidence results in the cap losing its runoff and drainage layer functionality together with a decrease in evapotranspiration in the subsided area. Increased infiltration will occur through the portion of the closure cap overlying the collapsed vault. Subsidence potential was estimated to be approximately 21 feet for the LAWV in WSRC-TR-2005-00405 (Jones and Phifer, 2007) and 17 feet for the ILV in WSRC-TR-2007-00306 (WSRC, 2008). This assumes that the waste in the two vaults has the same density as generic containerized waste in STs and ETs. The hydraulic properties assumed for the collapsed roof, walls and floor reflect the results of the structural analysis.	Vault structural failure for both the ILV and LAWV is predicted to occur well past the end of the post-closure 1,000-year compliance period with a high degree of confidence. Thus, the nominal PA case is considered reasonably bounding.*

Table 3-1 (cont'd). List of Safety Functions, Associated FEPs, Potentially Deleterious FEPs, and the Analyses Intended to Explore the Deleterious FEPs (Seitz, 2020)

ID	Safety Function	Description	Associated FEPs (Deleterious FEPs bolded)	Nominal PA Case Assumption	Associated Analyses
EB9	High-Density or Stabilized Waste Forms, High-Integrity Containers	Waste forms and containers may also be considerations for structural stability (beyond the general assumptions for the STs and ETs). Wastes that are considered non-crushable are assumed to remain relatively stable and not significantly contribute to subsidence and impacts on infiltration rates through the cover. CIG disposal would be expected to provide some enhanced stability over normal disposal containers.	**1.1.02** **1.2.03** **2.1.07** **1.1.03** **2.1.01** **2.1.08** **1.1.04** **2.1.02** **2.1.09** **1.1.05** **2.1.03** **2.1.10** **1.1.07** **2.1.04** 2.1.11 **1.1.08** **2.1.06** 2.1.13 **1.1.09** **1.1.12**	In general, high-density waste forms and high-integrity containers will have no long-term impact on final closure cap performance during the 1,000-year compliance period. A structural evaluation of each category of CIG disposals was performed in T-CLC-E-00026 (Peregoy, 2006a). Fully grouted containers (i.e., containers grouted internally and encapsulated externally) were estimated to provide structural stability for the overlying closure cap throughout the entire 1,000-year compliance period. CIG trench segments containing low-density waste will require a reinforced concrete mat similar to the existing mat over CIG01 segment 8 to provide sufficient long-term structural support to the final cover. CIG trench segments protected by the prescribed reinforced concrete mat designs are estimated to provide a minimum of 300 years of structural support to the closure cap.	The assumptions of the nominal PA case are considered reasonably bounding.*
Chemical Safety Functions					
EB10	Waste Forms, Containers, and Backfill	Waste forms and containers can serve to condition the water prior to contact with the radionuclides and also bind radionuclides to limit the fraction available for transport. In a number of cases, the waste forms result from processes that are designed to retain specific radionuclides (e.g., carbon vessels, ion exchange). There are also cases, such as activated metals, where the radionuclides are bound in the matrix of a metal (e.g., NRCDA). In these cases, the radionuclides would be expected to be strongly retained in the waste form. In other cases, a waste form may be designed to isolate specific radionuclides to limit releases in a disposal environment (e.g., CIG, other grouted waste). The retention capability for such designed waste forms needs to be confirmed and justified.	**1.1.02** **2.1.04** **3.2.01** **1.1.03** **2.1.06** **3.2.02** **1.1.04** **2.1.07** **3.2.03** **1.1.08** **2.1.08** **3.2.04** **2.1.01** **2.1.09** 3.2.05 **2.1.02** **2.1.10** 3.2.06 **2.1.03** 2.1.11 **3.2.07**	The container itself or backfill surrounding containers is generally assumed to control the chemistry in the waste zone. For example, iron-oxide content resulting from the surrounding clayey soil and rusted metal containers are expected to control waste zone chemistry in the STs and ETs. In the LAWV, cementitious leachate from infiltrating water migrating through the cracks in the vault roof and walls is expected to alter the tendency of radionuclides to bind to the iron-oxide phases present, i.e., the K_d values will change. In the ILV and CIG trench segments, waste is encapsulated by grout or CLSM, as such, oxidizing grout K_d values are used. Some special waste forms include adjusted K_ds or special release models (e.g., solubility limits) based on the known properties and the process from which the waste is generated. Releases from special waste forms with activated metals are addressed using a corrosion-based release rate. The effectiveness and duration of such chemical barriers are specifically defended and justified.	Planned sensitivity and uncertainty analyses will be based on geochemical value uncertainty distributions provided in SRNL-STI-2009-00473 (Kaplan, 2016b).
EB11	E-Area Vaults (LAWV and ILV)	The concrete of the vaults is designed to initially provide for reducing redox conditions and will age over long times to eventually approach natural pH and redox conditions in the groundwater. The vaults are assumed to maintain structural stability for more than 1000 years, which controls the rate of water flow through the vaults and serves to allow only slow changes in the assumed chemistry for the vault concrete.	**1.1.02** 2.1.05 **3.2.01** **1.1.03** **2.1.06** **3.2.02** **1.1.04** **2.1.07** **3.2.03** **1.1.08** **2.1.08** **3.2.04** **2.1.02** **2.1.09** 3.2.05 **2.1.03** **2.1.10** 3.2.06 **2.1.04** 2.1.11 **3.2.07**	As described in SRNL-STI-2009-00473, Rev. 1 (Kaplan, 2016b), the concrete in the vaults is assumed to evolve in three phases from high to a relatively neutral pH. The K_ds for key radionuclides are modified based on the assumed conditions.	Planned sensitivity and uncertainty analyses will be based on geochemical value uncertainty distributions provided in SRNL-STI-2009-00473 (Kaplan, 2016b).
Air Pathway					
AP1	Engineered Cover	The engineered cover will provide a robust barrier against gaseous releases. An HDPE geomembrane and GCL are expected to essentially block any gas-phase migration due to the low air permeability of both and the expected high-moisture content in the clay layer. The remaining layers of the cover will provide additional distance over which gas-phase diffusion has to occur. Upward gas-phase diffusion will also compete against advective water flow downward and laterally through the upper layers of the cover.	**1.1.02** **1.2.07** 2.1.05 **1.1.03** **1.2.08** 2.1.12 **1.1.04** **1.2.10** **2.3.07** **1.1.05** 1.3.10 **2.3.08** **1.1.07** **1.4.03** **2.3.09** **1.1.08** **1.4.06** **2.3.10** **1.1.09** **1.4.08** **2.3.12** **1.1.12** **1.4.11** 3.1.01 **1.2.03** **1.4.14** 3.1.04 3.2.09 3.2.10	Nominal diffusion properties were assumed for the cover layers, ignoring any advective downward water flow. Layers above the erosion barrier were ignored. Boundary conditions were set to maximize upwards diffusion. No HDPE liner or GCL were included in the model (these two barriers would likely preclude any significant upward diffusion).	Considered reasonably bounding.*

Table 3-1 (cont'd). List of Safety Functions, Associated FEPs, Potentially Deleterious FEPs, and the Analyses Intended to Explore the Deleterious FEPs (Seitz, 2020)

ID	Safety Function	Description	Associated FEPs (Deleterious FEPs bolded)	Nominal PA Case Assumption	Associated Analyses
AP2	E-Area Vaults (LAWV and ILV)	The vaults provide a robust barrier against gas-phase migration to the surface. Diffusion rates through the grout fill and the vault roof are expected to be very low.	**1.1.02** **1.2.03** 2.1.12 **1.1.03** **1.2.07** 2.3.07 **1.1.04** 1.3.10 **2.3.10** **1.1.05** **1.4.03** **2.3.12** **1.1.07** **1.4.06** 3.1.04 **1.1.08** **1.4.08** 3.2.09 **1.1.09** **1.4.11** 3.2.10 **1.1.12** **1.4.14**	High moisture content for relatively intact concrete located underground was not included. Instead, a lower moisture content representative of rubble exposed to the atmosphere was used. The CLSM layer was included for the ILV, but saturation was biased low based on a pessimistic value for suction.	Considered reasonably bounding.*
AP3	Waste Forms, Containers and Backfill	Most radionuclides are not expected to be present in a gaseous form at the conditions in the vault. Thus, the general potential for gas-phase releases is expected to be very low.	**1.1.02** **1.2.03** 2.1.12 **1.1.03** **1.2.07** 2.3.07 **1.1.04** 1.3.10 **2.3.10** **1.1.05** **1.4.03** **2.3.12** **1.1.07** **1.4.06** 3.1.01 **1.1.08** **1.4.08** 3.1.04 **1.1.09** **1.4.11** 3.2.09 **1.1.12** **1.4.14** 3.2.10	Containers and waste forms were generally ignored. However, in the case of the NRCDAs, both the container (welded carbon steel cask) and the waste form (activated metal components) were credited in holding up and controlling the rate of release of volatile radionuclides.	Considered reasonably bounding.*

Notes:

* "Considered reasonably bounding" is used to describe cases where pessimistic assumptions in the PA are considered to reasonably address or bound any uncertainties. Thus, no additional sensitivity or uncertainty analyses are necessary.

3.3. FEATURES, EVENTS, AND PROCESSES

To test the safety functions for the ELLWF, it is necessary to consider potential FEPs with an emphasis on identifying FEPs that can potentially compromise the effectiveness of a given safety function. In this second step, a process was implemented to screen and review FEPs to identify those that need to be considered for the ELLWF PA. Special emphasis was placed on identifying FEPs that may have deleterious effects on any of the safety functions.

The results of the screening and review of FEPs for the safety functions identified for the ELLWF are documented by Seitz (2020). The review was conducted in a working meeting with the ELLWF PA team and key site personnel using a graded approach based on similar work performed for the Waste Management Area C Tank Closure PA at the Hanford Site (Mehta et al., 2016) and the Calcine PA at the Idaho Site (DOE-ID, 2019). The process began with identification of a representative list of FEPs as the basis for the screening exercise.

A FEPs list should be comprehensive enough that it captures FEPs that may need to be accounted for in a PA. The list includes FEPs that are merely associated with a specific safety function and those that may be deleterious to a safety function. For instance, FEP 3.2.07, "Water-mediated transport of contaminants," [see Seitz (2020; Appendix B)] is associated with all safety functions related to the GW pathway but is not necessarily deleterious to that pathway. By contrast, FEP 2.1.05, "EBS characteristics and degradation processes," includes degradation processes that will eventually lead to increased infiltration through a cover or to the creation of pathways for migration out of a concrete vault. It therefore may be a deleterious FEP for safety functions related to cover infiltration or engineered structure permeability.

The safety functions approach described in Section 3.1.5 helps to highlight important processes to include in conceptual models for individual components of the disposal system. The approach also provides a logical means to identify a set of sensitivity analyses that can be used to explore the implications of the loss of safety functions, while at the same time exploring the implications of aggregated FEPs that might affect the safety function in similar ways. The structure of the ELLWF PA includes identifying sensitivity cases and alternative models for the safety functions shown in Table 3-1, developing distributions for key input parameters for an uncertainty analysis, and examining what happens in the PA model when a safety function behaves differently than expected, is degraded compared to a base case, or is lost entirely. The process also addresses FEPs that may affect multiple safety functions simultaneously.

The choice of sensitivity analysis cases associated with deleterious FEPs also included barrier analyses. Barrier analyses are provided to investigate the robustness of the system in the face of complete loss of safety functions. The barrier analyses are not intended to represent realistic behavior of the system but instead to explore the importance of various parts of the system to the overall performance.

3.3.1. Review Process

A list of FEPs developed for the IAEA Improvement of Safety Assessment Methodologies (ISAM) project (IAEA, 2004) was used as the starting point for the screening process. The IAEA list is a

reasonably comprehensive collection for the purposes of the ELLWF PA. The list was developed with the participation of representatives from many countries actively involved in LLW disposal around the globe. The DOE review process also provides redundant confirmation of the intent of the FEPs process as reviewers will also challenge whether key FEPs may have been missed.

A record was created for each FEP, with each record containing (1) a title and definition; (2) record number (e.g., 1.1.02, 3.2.10, etc.); (3) comments on the assessment context; (4) key concepts, examples, and related FEPs; and (5) application to the disposal facility and potentially deleterious effects of a failed FEP. The table of FEP records from the report by IAEA (2004) (including the associated FEPs record numbers listed in Column 4 of Table 3-1) is reproduced by Seitz (2020; Appendix B). The emphasis of the review process described here was to document the information requested in the last (bottom) section for each FEP record. Namely, the applicability to the ELLWF PA and whether each FEP posed any potential deleterious impacts that need to be considered in the PA.

A team of subject matter experts was assembled for the review. The team comprised experts in the PA process, numerical modeling, facility and equipment design, ELLWF operations, and facility closure. The FEPs review process involved two key activities. First, each team member independently reviewed the FEPs list beforehand and then participated in a working meeting to review the complete list and to develop consensus input for applicability and potentially deleterious effects. Second, following the initial review and screening, the results were summarized in a draft table that was then reviewed by each team member and finalized.

3.3.2. Results of Review and Screening

The effort focused on populating the last rows of each FEP record by identifying applicability to the ELLWF PA and potentially deleterious effects. The description and example entries for each FEP record were not modified but were preserved to use as context for understanding the relevance. The team determined whether each FEP is relevant for the ELLWF PA and whether it is also potentially deleterious to the safety functions for E-Area. The result of this review of each FEP is provided by Seitz (2020). When a FEP was deemed relevant, each entry also includes brief explanatory information. At the end of the process, the results of the FEPs screening were integrated into Safety Functions Table 3-1 to provide a cross-reference between the two efforts.

The number of FEPs that are both relevant to and potentially deleterious to the safety functions for the ELLWF is quite high. The sections below highlight those FEPs that are relevant to and potentially deleterious to 50% or more of the safety functions within one (or more) of the three broad categories of safety functions: administrative controls, natural site features, and engineered barriers.

3.3.2.1. Administrative Controls

Three FEPs (1.4.03, 1.4.06, and 1.4.11) were deemed relevant and potentially deleterious to the majority of the four administrative control safety functions (performance objectives and measures, exposure pathways, institutional control, and societal memory).

3.3.2.1.1. Drilling Activities (Inadvertent Human Intrusion)

Definition: FEPs related to any type of drilling activity near the repository.

Intrusion via well drilling can result in waste being brought to the surface, potentially leading to exposures.

3.3.2.1.2. Surface Excavations

Definition: FEPs related to any type of human activities during surface excavations that can potentially affect the performance of the engineered and/or natural (geological) barriers or affect the exposure pathways.

Surface excavation FEPs are relevant and potentially deleterious to the ELLWF for PA intrusion scenarios if the waste is located within 3 meters of the surface of the cover. This evaluation will be excluded for most waste based on the depth of waste disposal (>3 meters) and the presence of intrusion barriers. Reinforced concrete is considered a substantial barrier to an excavation scenario while recognizable and relatively intact.

3.3.2.1.3. Social and Institutional Developments

Definition: FEPs related to changes in social patterns and degree of local government, planning, and regulation.

Loss of memory of the site and institutional controls is assumed at 100 years after closure which leads to possible drilling intrusion, basement intrusion, and resident farmer scenarios.

3.3.2.2. Natural Site Features

Three FEPs (1.1.01, 2.2.03, and 2.2.07) were deemed relevant and potentially deleterious to the majority of the eight natural site feature safety functions (site characteristics; water flow, sorption, and dispersion in the unsaturated zone; water flow, sorption, and dispersion in the saturated zone; and dilution in well).

3.3.2.2.1. Site Investigation

Definition: FEPs related to the investigations that are carried out at a potential repository site to characterize the site both before repository excavation and during construction and operation.

Backfill materials obtained during trench excavation may vary chemically and hydraulically (e.g., horizontal and vertical conductivities of the UVZ versus LVZ differ by an order of magnitude) depending on the location in E-Area. Variability in data will be addressed using sensitivity and uncertainty analyses.

3.3.2.2.2. Other Lithological Units

Definition: FEPs related to the properties and characteristics of the lithology other than the host lithology as they may evolve both before and after repository closure.

Uncertainties in the lithology and its properties can impact water flow and chemical safety functions in the unsaturated zone and are addressed in the sensitivity and uncertainty analyses.

3.3.2.2.3. Hydraulic and Hydrogeological Processes and Conditions in the Geosphere

Definition: FEPs related to the hydraulic and hydrogeological processes that affect the saturated and unsaturated zones, and the overall evolution of conditions with time. This includes the effects of changes in condition (e.g., change in hydraulic head due to the excavation, construction, and long-term presence of the repository).

Excavations and addition of covers can have an influence on flow and contaminant migration in the unsaturated zone and aquifer. Uncertainty regarding their influence on infiltration, aquifer flow, and contaminant migration rates is considered in the base case and sensitivity and uncertainty analyses.

3.3.2.3. Engineered Barriers

Seventeen FEPs (1.1.02 thru 1.1.05, 1.1.07 thru 1.1.09, 1.1.12, and 2.1.02 thru 2.1.10) were deemed relevant and potentially deleterious to the majority of the 14 engineered barrier safety functions, which include three hydrological (engineered covers, concrete vaults, and waste forms/containers), three intrusion (engineered covers, concrete vaults, and waste forms/containers), three structural (containers, concrete vaults, and stabilized waste forms/high-integrity containers), two chemical (concrete vaults and waste forms/containers), and three atmospheric pathway (engineered covers, concrete vaults, and waste forms/containers) safety functions.

3.3.2.3.1. Repository Design

Definition: FEPs related to the design of the repository, including both the safety concept (i.e., the general features of design and how they are expected to lead to a satisfactory performance) and the more detailed engineering specifications for excavation, construction, and operation.

Changes in the planned areal footprint and/or orientation of future trenches (e.g., rotation by 90 degrees), waste forms, operations, and waste placement will potentially result in different contaminant transport, plume interaction, and peak concentrations at the points of assessment. Any changes to waste forms, design, operation, waste placement, etc. are evaluated through the PA Maintenance process prior to implementation to provide a reasonable expectation of continued compliance.

3.3.2.3.2. Repository Construction

Definition: FEPs related to the construction (e.g., excavation) of shafts, tunnels, disposal galleries, silos, trenches, and vaults of a repository, as well as the stabilization of these openings and the installation and assembly of structural elements according to the design criteria.

For E-area, repository construction FEPs relate to disposal unit (DU) construction, operation, and closure assumptions (i.e., excavation, trench and vault construction, soil backfill and grout emplacement, and operational, interim and final cover installation). Potential degradation of safety functions associated with the engineered components of the system may result from quality control failure. Poor placement quality and introduction of an abnormally high number of defects in the geomembrane/GCL composite barrier during installation could lead to increased leakage rate into

the waste zone. Significant deviations from design specs on trench geometries, dimensions, and orientations could occur. Any deviations from planned construction must be addressed through the PA maintenance process.

3.3.2.3.3. Emplacement of Wastes and Backfilling

Definition: FEPs related to placing wastes (usually in containers) at their final position within the repository and then placing buffer and/or backfill materials in the disposal zone to fill voids.

For the ELLWF PA, the relevance applies to placement of containers, grout, and/or backfill, as well as to the number and assumed placement of non-crushable containers, including their impact on subsidence assumptions. This is particularly important for E-Area due to the wide variety of waste forms, packaging, and placement approaches across DUs. Any changes from assumed operations as described in the PA must be addressed via the PA maintenance process.

Safety functions associated with the grout, containers, and cover may be degraded by incorrect emplacement of the materials. Emplacement of grout must take due account of the heat of hydration and potential shrinkage. Non-crushable packages offer the potential for enhanced subsidence of the closure cap, leading to increased infiltration. Improper backfilling could also lead to increased closure cap subsidence. Backfill materials obtained during trench excavation may vary chemically and hydraulically (e.g., horizontal and vertical conductivities of upper vs. lower vadose zone soils differ by an order of magnitude) depending on the location in E-Area). Conceptual models will address potential variability in emplacement assumptions. Non-crushable containers are specifically defined; however, there could be a deleterious impact if different than assumed.

3.3.2.3.4. Repository Closure

Definition: FEPs related to the cessation of waste disposal operations at the site, the backfilling and sealing of borehole-type facilities, and the capping and covering of trenches, vaults, etc.

The repository closure FEPs are relevant to the ELLWF PA for grout, backfill, and cover emplacement. Incremental closure using dynamic compaction must also be considered. Safety functions associated with the grout and cover may be degraded by incorrect closure. Emplacement of fill grout must take due account of the heat of hydration and shrinkage. Dynamic compaction is assumed to be implemented consistent with assumptions in the PA; however, there could be a deleterious impact on system performance if different than assumed.

3.3.2.3.5. Waste Allocation

Definition: FEPs related to the allocation of wastes to the repository, including waste type(s) and amount(s).

For E-Area, there is a general tendency to bias radionuclide inventories pessimistically high to account for difficulties in measuring key radionuclides. The potential deleterious impact of the waste allocation FEPs is to underestimate the projected inventories in future trenches because of changes in waste delivery or generation.

3.3.2.3.6. Quality Control

Definition: FEPs related to quality assurance and control procedures and tests during the design, construction, and operation of the repository, as well as the manufacture of the waste forms, containers, and engineered features.

Relevant to the ELLWF PA for waste characterization, packaging, waste placement, vault and trench construction, and grout/fill and cover emplacement. Site quality programs are in place that are applied to all activities. Safety functions associated with waste release (inventory and waste form), construction, operation and closure may be degraded if there is a failure of quality control. Poor placement quality and the introduction of an abnormally high number of defects in the geomembrane/GCL composite barrier during installation will lead to increased leakage into waste zone.

3.3.2.3.7. Schedule and Planning

Definition: FEPs related to the sequence of events and activities occurring during repository excavation, construction, waste emplacement, and sealing.

The PA includes assumptions for the timing and sequence of operations and closure that have some flexibility. Changes to the sequence of events assumed for the ELLWF PA could impact the projected results. Changes in operating and closure assumptions for each trench and vault can also influence the timing of peaks, etc. The timing of the placement of interim stormwater runoff covers over Slit Trenches had some impact on the projected doses during the compliance period. Any changes in plans from the envelope of assumptions in the PA will be addressed using the PA Maintenance process before a change is implemented.

3.3.2.3.8. Accidents and Unplanned Events

Definition: FEPs related to accidents and unplanned events during construction, waste emplacement, and closure which might have an impact on long-term performance or safety.

The SWM facility Documented Safety Analysis (DSA) is in place and covers operation of the ELLWF (SWM, 2021). From a long-term performance perspective, subsidence of trench covers is assumed to occur immediately following the end of the IC period and longer-term degradation of the vaults and covers is also addressed. Operational accidents are addressed in the DSA. There is the potential for early degradation of the engineered cover caused by surface events as well as early degradation of hydraulic safety functions in the engineered system due to a geological event. Non-crushable packages and concrete roof collapse over vaults will result in subsidence of the closure cap, leading to increased infiltration.

3.3.2.3.9. Waste Form Materials, Characteristics, and Degradation Processes

Definition: FEPs related to the physical, chemical, and biological characteristics of the waste form at the time of disposal and as they may evolve in the repository, including FEPs that are specifically relevant as waste degradation processes.

In general, no added credit is taken in the ELLWF PA for limitation of releases from a given waste form. Generic limits assuming no release limitations are primarily applied. However, some special

waste forms have been identified and specific credit for enhanced performance is included in the PA and in the limits applied to those wastes (e.g., activated metals, ion exchange resins, or specific waste streams). Potentially deleterious impacts include uncertainty regarding waste forms; this is generally resolved by assuming instantaneous release. Justification is required for special case waste forms.

3.3.2.3.10. Container Materials, Characteristics, and Degradation/Failure Processes

Definition: FEPs related to the physical, chemical, and biological characteristics of the container at the time of disposal and as they may evolve in the repository, including FEPs that are specifically relevant as container degradation/failure processes.

Degradation (corrosion) of B-25 boxes, SeaLand containers, and non-crushable packages influences closure cap performance. In general, no credit is taken for the hydraulic performance of most containers. Some special containers, such as a TPBAR cask and heat exchangers, are credited as hydraulic barriers. Changes from PA assumptions could be a concern for calculated infiltration rates and projected doses. An increase in the assumed number of non-crushable packages remaining after dynamic compaction will lead to increased cap subsidence and infiltration. Containers that are assumed to provide some isolation capability must be justified.

3.3.2.3.11. Buffer and Backfill Materials, Characteristics, and Degradation Processes

Definition: FEPs related to the physical, chemical, and biological characteristics of the buffer and/or backfill at the time of disposal and as they may evolve in the repository, including FEPs that are specifically relevant as buffer/backfill degradation processes (effect on hydrology/flow).

Properties for backfill are based on the source of the soil. Generally, backfill is assumed to be obtained from the soil excavated to create a trench. Grout properties are assigned based on the specific design of the grout mix. Changes from PA assumptions could be a concern for projected doses. There will be uncertainty in the properties and performance of backfills or grout. If different soils or grout are used, different properties may need to be assumed.

3.3.2.3.12. Engineered Barrier System Characteristics and Degradation Processes

Definition: FEPs related to the design, physical, chemical, and hydraulic characteristics of the cavern/tunnel/shaft seals at the time of sealing and closure and also as they may evolve in the repository, including FEPs that are specifically relevant as cavern/tunnel/shaft seal and cap degradation processes (effect on hydrology/flow and change over time).

FEPs relevant to ELLWF PA engineered barriers (e.g., CIG, cover system) are included. As-built properties are controlled using site quality assurance procedures. Long-term degradation is addressed for key engineered features. Changes from PA assumptions could be a concern for projected doses. Uncertainties in the current state and long-term performance of the cover system are addressed in the PA using uncertainty distributions or ranges for intact and degraded material properties, bounding assumptions, stochastic models for failure of containers in STs and ETs, and Monte Carlo simulations of structural degradation of the LAWV and ILV concrete.

3.3.2.3.13. Other Engineered Features Materials, Characteristics, and Degradation Processes

Definition: FEPs related to the physical, chemical, and biological characteristics of the engineered features (other than containers, buffer/backfill, closure caps, and seals) at the time of disposal and also as they may evolve in the repository, including FEPs that are relevant specifically as degradation processes acting on the engineered features.

FEPs relevant to the safety functions for concrete vault walls and roofs. As-built properties are controlled using site quality assurance procedures. Long-term degradation is addressed for key engineered features. Changes from PA assumptions could be a concern for projected doses. Potential degradation in the current state and future evolution of the safety functions of the engineered barriers (intrusion, water flow, and chemical) is considered in the PA as well as the sensitivity and uncertainty analyses. Degradation of the membrane layer on ILV and LAWV roofs and the formation of cracks in vault roofs will lead to increased infiltration during the post-closure period before roof collapse.

3.3.2.3.14. Mechanical Processes and Conditions in Wastes and Engineered Barrier Systems

Definition: FEPs related to the mechanical processes that affect the wastes, containers, seals, and other engineered features, and the overall mechanical evolution of the near field with time. This includes the effects of hydraulic and mechanical loads imposed on wastes, containers, and repository components by the surrounding geology.

FEPs are included that are relevant to the hydraulic performance of LAWV and ILV concrete walls and roofs as cracks form and as the final closure cap changes due to subsidence. Structural loads in the design of engineered barriers are also considered. Potential degradation in the current state and future evolution of the E-Area hydraulic safety function are considered in the PA. Formation of cracks in vault roofs can lead to increased infiltration during the time before roof collapse. Subsidence of the final closure cap after roof collapse will lead to increased infiltration through the waste zone.

3.3.2.3.15. Hydraulic/Hydrogeological Processes and Conditions in Wastes and Engineered Barrier Systems

Definition: FEPs related to the hydraulic/hydrogeological processes that affect the wastes, containers, seals and other engineered features, and the overall hydraulic/hydrogeological evolution of the near field with time. This includes the effects of hydraulic/hydrogeological influences on wastes, containers, and repository components by the surrounding geology.

FEPs are included that are relevant to the release and transport of radionuclides from the different ELLWF structures and disposal concepts. Potential degradation in the current state and future evolution of the water flow safety functions of the engineered barriers are considered in the base case and sensitivity and uncertainty analyses.

3.3.2.3.16. (Geo)Chemical Processes and Conditions in Wastes and Engineered Barrier Systems

Definition: FEPs related to the chemical/geochemical processes that affect the wastes, containers, seals, and other engineered features, and the overall chemical/geochemical evolution of the near

field with time. This includes the effects of chemical/geochemical influences on wastes, containers, and repository components by the surrounding geology.

FEPs are included that are relevant to the influence of the assumed geochemical properties of engineered features on the release and transport of radionuclides. For example, K_d values for the LAWV are influenced by container corrosion products; therefore, variability in K_d needs to be addressed. Cementitious materials will also influence the migration of radionuclides. If the assumed geochemistry is overly optimistic, releases can be underestimated. Intentional pessimistic bias and sensitivity and uncertainty analyses are used to address potential variability.

3.3.2.3.17. Biological/Biochemical Processes and Conditions in Wastes and Engineered Barrier Systems

Definition: FEPs related to the biological/biochemical processes that affect the wastes, containers, seals and other engineered features, and the overall biological/biochemical evolution of the near field with time. This includes the effects of biological/biochemical influences on wastes, containers, and repository components by the surrounding geology.

Assumptions dealing with biological processes are relevant to the ELLWF PA because of their influence on the release and transport of radionuclides. The potential deleterious influence of cellulosic materials on radionuclide release and transport has been considered, and it has been determined that the impact is not significant.

3.4. COVER SYSTEM CONCEPTUAL MODEL

Key design features, engineered barrier safety functions, key assumptions, and evolution of performance of the intact final closure cap for the ELLWF are presented in Section 2.2.2. Aspects of the conceptual models for the operational, interim, and final covers for the ELLWF that are specific to the type of DU (including scope and timing assumptions and failure of the final closure cap due to waste-layer subsidence or concrete roof collapse) are introduced in Sections 2.2.3, 2.2.4, 2.2.5, 2.2.6, and 2.2.7 for STs, ETs, LAWV, ILV, and NRCDAs, respectively. Implementation of the cover system conceptual models in the infiltration models for each type of DU is described in detail in Section 3.8.4. In this section, the conceptual model for the degradation of the final closure cap will be more fully described.

3.4.1. Closure Cap Evolution of Performance

Potential degradation mechanisms for the ELLWF final cover system are discussed below assuming a base-case land use scenario: Bahia grass vegetative cover; current climate conditions which remain unchanged throughout the 1,000-year compliance period; a 100-year period of IC following interim closure in 2065 with active maintenance of the interim cover; final closure cap installation in 2165 at final facility closure with no active cap maintenance; pine forest succession of the original Bahia grass cover beginning 160 years after the final closure cap is installed. Table 3-2 outlines potential degradation mechanisms for the major layers comprising the ELLWF final cover system.

Table 3-2. Final Cover System Potential Degradation Mechanisms

Affected Cap Layer[1]	Potential Degradation Mechanism[2]
All	Static loading induced settlement Seismic-induced liquefaction and subsequent settlement Seismic-induced slope instability Seismic-induced lateral spread Seismic-induced direct rupture due to faulting **Waste zone subsidence**
Vegetative Cover	**Succession** Stressors (droughts, disease, fire, and biological)
Soil above the Erosion Barrier	**Erosion and gully formation** Loss of compaction Desiccation (wet-dry cycles)
Erosion Barrier	Weathering (dissolution) **Biological (root penetration**, burrowing animals) Chemical (waste leachate)
LDL	**Silting-in** **Biological (root penetration**, burrowing animals) Mineral precipitation and microbial growth
HDPE Geomembrane	Ultraviolet (UV) radiation **Antioxidant depletion** **Thermal oxidation** High-energy irradiation **Tensile stress cracking** **Biological (root penetration**, burrowing animals, microbial) Chemical (waste leachate)
GCL	Slope stability Freeze-thaw cycles Dissolution **Divalent cations (such as Ca^{+2}, Mg^{+2})** Desiccation (wet-dry cycles) **Biological (root penetration**, burrowing animals) Chemical (waste leachate)

Notes:

1 Foundation layers were excluded from degradation considerations.

2 **Bolded** mechanisms are considered further in the infiltration and/or flow and transport models.

3.4.1.1. Static Loading and Seismic-Induced Degradation

Of the five potential static loading and seismic-induced degradation mechanisms listed in Table 3-2, only three – static loading induced settlement, seismic-induced liquefaction and subsequent settlement, and seismic-induced slope instability – require attention at SRS during closure cap design. Seismic-induced lateral spread and seismic-induced direct rupture due to faulting are not relevant because conditions at SRS are not conducive to lateral spreading (at least not at the locations of the proposed cover systems) and surface faulting is nonexistent in the Southeast U.S.

The current ELLWF closure cap conceptual design indicates that the maximum thickness of the cover system will be 30 feet above the DUs. According to Phifer et al. (2007), settlement due to this static load (~3,600 lb_f/ft^2) will be approximately 2 to 3 inches based on previous analyses for the nearby FTF. This amount of settlement is expected to occur uniformly across the entire cap

area; therefore, differential settlement will be negligible assuming subsurface conditions are relatively uniform.

Settlement due to liquefaction or partial liquefaction is a result of the dissipation of excess porewater pressures that have been elevated due to a seismic event. Previous studies in F-Area (for PC-3 seismic events, return period of 2,500 years, peak ground acceleration of 0.16 g, and a repeat of the 1886 Charleston, SC event) indicate that these settlements should be on the order of a few inches, and they too should be rather uniform (Phifer et al., 2007).

The stability of the closure caps depends on the final geometry of the system and strength of the materials used. Given the types of soils used for constructing these systems, global slope stability is not expected to be an issue (Phifer et al., 2007). Side slopes will be set at 3:1 horizontal to vertical. Interface stability can control the system design, particularly under seismic conditions. Interface stability refers to the stability between interfaces of various geosynthetic materials and between geosynthetic materials and soil. This can be a key issue and depends heavily on environmental conditions. In both cases, it is fully expected that a stable design will be achieved with reasonable slopes and grades given the known subsurface conditions in E-Area and the types of fill materials that will be utilized.

The final design of the ELLWF closure cap will appropriately address (design out) the three relevant static loading and seismic-induced degradation mechanisms discussed above, thereby removing them from further consideration as degradation mechanisms for infiltration, flow, and transport modeling purposes.

3.4.1.2. Waste Zone Subsidence

Waste zone subsidence as a closure cap degradation mechanism is central to the conceptual designs of the infiltration, flow, and transport models (both deterministic and stochastic) for all ELLWF DUs except the NRCDAs. For STs, ETs, and the CIG trench segments, waste zone subsidence will impact DU performance during the 1,000-year compliance period. For the LAWV and ILV, subsidence of the closure cap due to structural collapse of the concrete vault covers will occur during the extended 10,000-year simulation period. Because of its central importance to long-term closure cap performance, as well as its unique treatment in the PA models for each type of DU, subsidence will be addressed in Section 3.8.4.3.3 for the infiltration models and individually by type of DU in Sections 4.1.3.6, 4.2.1.2, 4.5.3.5, and 4.6.3.4 for STs and ETs, CIG trench segments, LAWV, and ILV, respectively.

3.4.1.3. Vegetative Cover Degradation Mechanisms

A vegetative cover will be established on the final closure cap to promote runoff, control soil erosion, prevent the initiation of gullying, and promote evapotranspiration. The initial vegetative cover will be a persistent turf grass consisting predominately of Bahia (*Paspalum notatum*). After installation of the interim cover in 2065, a 600-foot-wide treeless Bahia grass buffer zone will be actively maintained on all sides of the interim cover. For PA modeling purposes, it is assumed that at the end of IC in 2165, mature pine trees will exist at the outer edge of the 600-foot buffer zone; however, no pine trees will have become established within the ELLWF active maintenance area.

This means that the nearest mature pine tree stand is at least 600 feet from the ELLWF closure cap upon its installation in 2165. Once dynamic compaction of trenches is complete and the final closure cap is installed, the 1,000-year post-closure compliance period will begin, during which time no active ELLWF facility maintenance will be performed.

Phifer et al. (2007) present a detailed analysis of five potential succession and stressor (drought, disease, fire, and biological) degradation mechanisms for the vegetative cover, based on typical events occurring in the SRS region, that are likely to occur after active ELLWF facility maintenance has ceased. The vegetative transition is basically one from an old field community into an upland pine community. Only the conclusions of the analysis, particularly as they pertain to development of the infiltration models, are presented here.

Bahia is a very hardy species in the SRS region, and will continue to be a dominant ground cover for many years after active maintenance has ceased; however, over time there will likely be some deterioration of the Bahia grass cover from multiple disturbances. For infiltration modeling purposes, vegetation succession from a Bahia grass field to a pine forest is considered as an ELLWF closure cap degradation mechanism. This will primarily result in the deep tap roots of the pine tree penetrating various closure cap layers resulting in degradation of the composite geomembrane/GCL hydraulic barrier. Vegetative stressors (drought, disease, fire, and biological) primarily influence the rate of pine tree succession rather than serving as long-term degradation mechanisms on their own. For this reason, these four vegetative stressors will not be considered as ELLWF closure cap degradation mechanisms for infiltration, flow, and transport modeling purposes.

3.4.1.4. Soil Above the Erosion Barrier Degradation Mechanisms

Three possible degradation mechanisms are discussed below but only erosion is explicitly addressed in the infiltration model.

3.4.1.4.1. Erosion

As described in Section 2.2.2.4, the ELLWF erosion barrier, side slope, and toe of the side slope have been designed with sufficient engineering controls (e.g., large riprap) to be physically stable relative to erosion and gully formation from an SRS-specific PMP event (Abt and Johnson, 1991; Johnson, 2002). Conversely, the six-inch topsoil and 30-inch upper backfill layers emplaced over the erosion barrier, while designed for physical stability, are not designed for the PMP event. As stated in Section 2.2.2.4, Phifer et al. (2007) determined that a Bahia grass soil cover with a two-percent slope over a 585-foot slope length will ensure physical stability as well as prevent the initiation of gullying during a PMP event. However, after factoring in all engineering design constraints and considerations as outlined in Section 2.2.2, the proposed Bahia grass soil cover (Figure 2-36 through Figure 2-44) for the ELLWF final closure cap has a slope ranging from a minimum of 2% to a maximum of 5%. While slope lengths were adjusted accordingly to ensure physical stability at the higher percent slopes, this will not completely protect against gully initiation during a PMP event in localized areas of the final closure cap. Cap layers positioned below the erosion barrier are not subject to erosion.

Erosion of the topsoil and upper backfill layers due to non-PMP rainfall events and shallow animal burrowing is included as a closure-cap-wide degradation mechanism in the infiltration model for both a Bahia grass and pine forest vegetative cover as quantified in Section 3.4.4 for this PA. While limited erosion is expected to occur over the 10,000-year period considered in this PA, it is not expected to significantly impact the infiltration estimates. Acute erosion of the closure cap, caused by deep animal burrowing (e.g., feral hogs) or a PMP event that initiates gully formation, is expected to be localized such that the overall impact to closure cap performance is minimal. Regardless, a sensitivity case is included in the infiltration calculations for the intact closure cap case that considers the complete loss of the 36-inch-thick combined topsoil/upper backfill layer above the erosion barrier.

In the 2019 PA for the Saltstone Disposal Facility (SDF) at SRS (Savannah River Remediation, 2020), the SDF PA team used the Revised Universal Soil Loss Equation (RUSLE) from the USDA's *Handbook: Predicting Soil Erosion by Water: A Guide to Conservation Planning with the Revised Universal Soil Loss Equation (RUSLE)* (Rengard et al., 1997) to estimate the potential erosion rate of the soil layers above the erosion barrier for a 10,000-year period. The SDF PA calculations considered three vegetative covers: pinewood forest, Bahia grass, and unmanaged undergrowth. Total soil loss estimates for the three vegetative covers ranged from 0.3 inches (pinewood forest) to 1.8 inches (unmanaged undergrowth) after 1,000 years and 2.6 inches (pinewood forest) to 18.3 inches (unmanaged undergrowth) after 10,000 years. At worst, the RUSLE model predicts that only 50% of the 36-inch-thick combined topsoil/upper backfill layer above the erosion barrier will have eroded after 10,000 years. The sensitivity case described above (i.e., complete loss of the 36-inch-thick combined topsoil/upper backfill layer) will therefore represent an upper bound on the impact of erosion on infiltration rates for the intact (non-subsided) closure cap case.

It is also important to note that the conceptual models of infiltration for subsidence assume localized failure of the final closure cap. For STs and ETs, this occurs upon the catastrophic collapse of non-crushable packages immediately after installation of the final closure cap, For the LAWV and ILV, the localized failure occurs upon the long-range structural failure of the concrete vault roofs. Functionally, these subsided areas or "holes" in the closure cap result in localized infiltration into the waste zone that dwarfs the globally cap-averaged infiltration rates for the intact closure cap case as will be presented in Section 3.8.4.3.3. Flow and radionuclide transport simulations for the subsidence cases, therefore, will, in essence, account for the impact of acute erosion (e.g., gully formation and deep animal burrowing) as well.

3.4.1.4.2. Loss of Compaction

The upper backfill layer will be controlled compacted backfill (CCB) and is assumed to maintain compaction throughout the lifecycle of the closure cap. Sensitivity analysis by Shipmon and Dyer (2017) showed that changes in the hydraulic conductivity of the upper backfill layer will have a minor impact on predicted infiltration rates compared to the more impactful degradation mechanisms such as subsidence, geomembrane degradation, and pine tree root penetration. For this reason, loss of compaction will also not be considered a closure cap degradation mechanism in the infiltration model.

3.4.1.4.3. Desiccation (Wet-Dry Cycles)

SRS topsoil consists predominately of sand with a very small clay fraction and would be classified as loamy sand or sandy loam. Typical SRS backfill consists predominately of sand with a smaller fraction of clay and would be classified as clayey sand or sandy clay loam (Phifer et al., 2007). The predominant clay mineral in SRS topsoil and backfill is kaolinite, which is characterized as a low plasticity clay with a low shrink/swell capacity, low cation exchange capacity (3 to 15 meq/100g) and a low specific surface area (10 to 20 m^2 g^{-1}). In addition, SRS soils are highly leached, meaning that the likelihood of a significant loading of monovalent exchangeable ions such as sodium is low. For all the above reasons, significant shrinkage and subsequent cracking of SRS topsoil and backfill upon drying is highly unlikely and will therefore not be considered as an ELLWF closure cap degradation mechanism in the infiltration model.

3.4.1.5. Erosion Barrier Degradation Mechanisms

Erosion barrier degradation mechanisms are not explicitly addressed in the infiltration model. Brief discussions of the two primary mechanisms are provided below.

3.4.1.5.1. Weathering (Dissolution)

Phifer et al. (2007) outlines important design considerations related to weathering (dissolution) of the rock selected for the below-grade erosion barrier and the above-grade side slopes and the toe of the side slopes. In humid environments, silicate rocks, particularly those containing higher percentages of quartz such as granite and quartzite, are desirable for their resistance to chemical weathering. A likely material to be used for both the erosion barrier and the side slopes and toe is granite from nearby Georgia quarries. Another option is mylonitic quartzite from a nearby Georgia quarry. Both below-grade and above-grade weathering will be considered in the final closure cap design as detailed by Phifer et al. (2007).

The size of the emplaced stone and the thickness of the stone layer will be increased, if necessary, during final closure cap design to accommodate anticipated weathering to ensure closure cap physical stability relative to erosion for 10,000 years. Additionally, the voids within the erosion barrier rock mass will be filled with a material to prevent loss of the overlying upper backfill into the erosion barrier. Among other considerations, the infill material will be selected based upon its impact on below-grade weathering of the erosion barrier stone. An infill material that favors a decreased weathering rate will be favored. Based upon appropriate consideration of weathering during the final design phase for the ELLWF closure cap, rock weathering will not be considered as an ELLWF closure cap degradation mechanism in the infiltration model.

3.4.1.5.2. Biological Degradation of Erosion Barrier

Potential biological degradation mechanisms include tree root penetration and burrowing animals. As discussed in detail by Phifer et al. (2007) and assuming a Bahia grass cover versus bamboo, it is anticipated that a pine forest will eventually replace the initial Bahia grass vegetative cover with the pine trees growing 6-foot to 12-foot deep tap roots that will eventually penetrate hard layers such as the erosion barrier. One criterion to be used in selecting the material to fill the void space of the erosion barrier stone mass will be its ability to help hinder root penetration. However, for the infiltration model, pine tree roots are allowed to freely penetrate the erosion barrier stone (upper

bounding assumption). As such, root penetration is considered a viable closure cap degradation mechanism in the infiltration model for the erosion barrier as well as for the underlying LDL and GCL as described in more detail by Dyer (2019b) and Phifer et al. (2007).

At SRS, burrowing animals include oldfield mouse (*Peromyscus polionotus*), short tail shrew (*Blarine brevicauda*), eastern mole (*Scalopus aquiticus*), harvester ant (*Pogonomyrmex badius*), pyramid ant (*Dorymyrmex pyramicus*), imported red fire ant (*Solenopsis invicta*), and earthworms (McDowell-Boyer et al., 2000). Feral hogs, an invasive species present in large numbers at SRS, can also cause extensive damage to vegetative covers while rooting for food. As discussed above for tree roots, the erosion barrier will be designed to act also as a barrier to burrowing animals and feral hogs, which includes selection of the material used to fill the void space of the erosion barrier stone. For this reason, animals burrowing/rooting into and below the erosion barrier is not considered a viable closure cap degradation mechanism for the infiltration model.

3.4.1.6. Lateral Drainage Layer Degradation Mechanisms

The silting-in degradation mechanism is explicitly addressed in the infiltration model. Brief discussions of the two primary mechanisms are provided below.

3.4.1.6.1. Silting-In

As discussed in detail by Phifer et al. (2007), the LDL will be overlain with a geotextile filter fabric to help prevent silting-in of the sand drainage layer caused by fines migration from above. Sufficient data is not currently available to estimate the service life of the filter fabric; however, it will degrade due to oxidation and root penetration, both of which will increase its already high through-plane saturated hydraulic conductivity. The geotextile filter fabric itself is unlikely to clog because there is very little organic matter in SRS soils to promote the formation of a biofilm and SRS soils consist predominately of quartz and non-swelling kaolinite clay. Any potential clogging of the filter fabric will be more than compensated for by the formation of root penetrations over time. Therefore, for infiltration modeling purposes, the presence of the geotextile filter fabric is ignored.

Because pine tree roots are allowed to freely penetrate the erosion barrier and the presence of the geotextile filter fabric is ignored (upper bounding assumptions), the LDL is assumed to progressively silt-in with colloidal clay that migrates from the overlying upper backfill layer, thereby steadily reducing its saturated hydraulic conductivity over time. Silting-in of the LDL is included as a closure cap degradation mechanism in the infiltration model.

3.4.1.6.2. Mineral Precipitation and Microbial Growth

Mineral precipitation and microbial growth in sand layers are primarily degradation mechanisms associated with leachate collection systems (Phifer et al., 2007). LDLs in closure caps receive only uncontaminated water from precipitation infiltration. At SRS, the infiltrating water is very low in Ca/Mg hardness and total organic carbon. For this reason, mineral precipitation and microbial growth will not be considered a closure cap degradation mechanism in the infiltration model.

3.4.1.7. Geomembrane Degradation Mechanisms

For the ELLWF final closure cap, a 60-mil HDPE geomembrane will be utilized in conjunction with a 200-mil GCL to form a composite hydraulic barrier to infiltration. A detailed analysis of the seven potential degradation mechanisms for HDPE geomembranes listed in Table 3-2 is provided by Benson and Benavides (2018), Phifer et al. (2007), and Savannah River Remediation (2020). Brief discussions of the degradation mechanisms are provided below (see Section 3.4.1.9 for chemical degradation by waste leachate).

3.4.1.7.1. Ultraviolet Degradation

Current HDPE geomembrane formulations typically contain 2% to 3% carbon black and may contain other UV chemical stabilizers to minimize UV degradation. Due to carbon black usage, UV radiation is not considered a significant degradation mechanism for short-term exposures associated with construction, where the geomembrane is covered in a timely manner [i.e., two to four weeks as determined by Bonaparte et al. (2002)]. UV degradation is not autocatalytic and, therefore, does not continue to occur after burial (Bonaparte et al., 2002). Even a thin, 150-mm-thick layer of soil is adequate to eliminate the potential for UV degradation. UV degradation is not considered a closure cap degradation mechanism in the infiltration model.

3.4.1.7.2. Antioxidant Depletion

Antioxidants are added to HDPE geomembranes primarily to prevent thermal oxidative degradation. As long as significant antioxidants are present, thermal oxidative degradation of the polymer will be prevented and mechanical properties of the geomembrane will remain essentially unchanged. However, once the antioxidants have been depleted, thermal oxidation of the geomembrane can occur. Phifer et al. (2007) extensively reviewed three major antioxidant depletion studies (Hsuan and Koerner, 1998; Mueller and Jakob, 2003; Sangam and Rowe, 2002) in developing the original basis for the ELLWF and FTF PA infiltration models. Based upon these studies, Phifer et al. (2007) estimated that antioxidant depletion times will be less than 100 years at 33-40ºC. Needham et al. (2004) also performed an extensive review of these same studies and developed his own methodology for estimating the antioxidant depletion time. He concluded that antioxidant depletion times may be significantly longer than those estimated by Hsuan and Koerner (1998) and Sangam and Rowe (2002) based on the two-stage depletion observed by Mueller and Jakob (2003). More recent studies by Tian et al. (2017) suggest that antioxidant depletion of a 2-mm-thick HDPE geomembrane in a composite liner in contact with LLW leachate will take approximately 730 years.[1]

Antioxidant depletion of the HDPE geomembrane will therefore be treated as a relevant closure cap degradation mechanism in the infiltration model using the methodology developed by Needham et al. (2004).

[1] Antioxidant depletion represents Stage I in a three-stage chemical aging model for HDPE proposed by Hsuan and Koerner (1998). Stage I will be followed by an induction period (Stage II) of approximately 25 years, after which HDPE oxidative degradation (Stage III) begins as described in Section 3.4.1.7.3.

3.4.1.7.3. Thermal Oxidative Degradation

Thermal oxidative degradation is the principal degradation mechanism for HDPE geomembranes in landfills; it can begin only after the antioxidants have been depleted and if oxygen is available (Koerner, 1998; Mueller and Jakob, 2003; Needham et al., 2004). Thermal oxidative degradation is initiated with the production of free radicals ($R^{\bullet}$) within the polymer structure due to elevated temperatures, high-energy irradiation, etc. (Koerner, 1998; Needham et al., 2004). If oxygen is available, the free radicals rapidly combine with oxygen producing peroxide free radicals ($ROO^{\bullet}$), which can then react with intact portions of the polymer to form additional free radicals and hydroperoxides [i.e., oxidized polymer chains (ROOH)]. The hydroperoxides can then decompose to produce even more free radicals. This free radical progression accelerates polymer chain reactions that ultimately result in polymer main-chain scission (Koerner, 1998; Koerner and Hsuan, 2003; Needham et al., 2004). Main-chain scission causes embrittlement of the HDPE geomembrane, which degrades its mechanical properties (Koerner and Hsuan, 2003; Mueller and Jakob, 2003).

Koerner (1998) and Needham et al. (2004) concluded that HDPE geomembranes in landfill service will slowly degrade by thermal oxidation, with oxidation usually limited by oxygen availability in the subsurface. Based on the recent study by Tian et al. (2017), if the geomembrane is assumed to no longer perform as designed once the stress crack resistance (Section 3.4.1.7.4) of the HDPE reaches 50%, the duration of Stage III oxidative degradation will be approximately 1,220 years. When added to the Stage I antioxidant depletion period (730 years) and Stage II induction period (25 years), the total estimated service life of the HDPE geomembrane is at least 1,975 years. Using a more optimistic set of assumptions, Tian et al. (2017) report that the total service life could be as long as 3,550 years. Slow oxidative degradation, therefore, will not result in the disintegration or disappearance of the geomembrane during the 1,000-year compliance period.

Thermal oxidative degradation, being closely tied to antioxidant depletion, will therefore be included as a closure cap degradation mechanism in the infiltration model using the methodology developed by Needham et al. (2004).

3.4.1.7.4. Tensile Stress Cracking Degradation

After antioxidants in the HDPE geomembrane have been depleted, thermal oxidation of the geomembrane commences if oxygen is present, causing embrittlement and degradation of mechanical properties over time. However, the geomembrane will remain an effective hydraulic barrier unless it is physically damaged or develops holes or cracks. Holes or cracks can develop in an HDPE geomembrane from two types of tensile stress cracking (Needham et al., 2004):

- Ductile tensile failure where the applied tensile stress exceeds the geomembrane's short-term tensile break strength.
- Brittle stress cracking where the applied long-term tensile stress is less than the geomembrane's short-term tensile break strength.

HDPE geomembrane installations should be planned and performed in a way that the geomembrane's short-term tensile break strength is not exceeded. However, subgrade settlement

and geomembrane downdrag caused by waste settlement on the side slopes can occur and cause exceedance of the geomembrane's tensile break strength (Needham et al., 2004). Brittle stress cracking, on the other hand, can occur over the longer term as oxidation of the HDPE geomembrane proceeds and causes increased embrittlement and degradation of its mechanical properties over time. Brittle stress cracking occurs at locations where the geomembrane is under stress, and as the extent of thermal oxidative degradation increases with aging, the stress level necessary to cause cracking decreases. Conversely, stresses are relieved as cracking occurs, thereby decreasing the likelihood of further cracking.

The extent of brittle stress cracking depends upon the geomembrane's stress crack resistance, the local and global stress over the geomembrane, the geomembrane temperature, the fluid in contact with the geomembrane, and the extent of thermal oxidative degradation. However, as long as the geomembrane is not subjected to tensile or shear stresses, it should not fragment and disintegrate but should remain, for practical considerations, intact indefinitely (Needham et al., 2004).

Tensile stress cracking degradation of the HDPE geomembrane, coupled with antioxidant depletion (Section 3.4.1.7.2) and thermal oxidative degradation (Section 3.4.1.7.3), is considered a closure cap degradation mechanism in the infiltration model using the methodology developed by Needham et al. (2004).

3.4.1.7.5. High-Energy Irradiation Degradation

According to Koerner (1998) and Needham et al. (2004), high-energy irradiation of HDPE at a total dose greater than 1 to 10 Mrad will begin to change the basic mechanical properties of the polymer as the result of main-chain scission. Based upon an extensive literature review and an evaluation of the proposed FTF closure cap geomembrane (Rosenberger, 2007), Phifer et al. (2007) concluded that high-energy irradiation of the HDPE geomembrane will be an insignificant degradation mechanism; therefore, it will not be included in the infiltration model.

3.4.1.7.6. Biological Degradation of the Geomembrane

Based upon a review of the literature and SRS field experience, Phifer et al. (2007) concluded that roots reaching intact portions of the HDPE geomembrane will be unable to penetrate it. Instead, the roots will turn and continue to grow laterally along the top of the geomembrane in a downslope direction. Roots will be able to penetrate the geomembrane only at locations where holes have already formed due to HDPE degradation. Root penetration through existing holes in the HDPE geomembrane, coupled with subsequent penetration though the underlying GCL (see Section 3.4.1.8.6), is considered a closure cap degradation mechanism in the infiltration model.

While burrowing animals can potentially damage unprotected HDPE geomembranes in general, damage of the ELLWF closure cap HDPE geomembrane is considered unlikely because of the presence of the overlying erosion barrier, which will be designed to preclude burrowing animals from reaching the HDPE geomembrane (Section 3.4.1.5.2). For this reason, burrowing animals are not considered a closure cap degradation mechanism for the HDPE geomembrane in the infiltration model.

Limited investigations of the microbial degradation of HDPE geomembranes have been performed. Koerner (1998) states that the high-molecular-weight polymers used for geomembranes are judged insensitive to microbial (i.e., fungal or bacterial) biodegradation.

3.4.1.8. Geosynthetic Clay Liner Degradation Mechanisms

For the ELLWF final closure cap, a 200-mil GCL will be utilized in conjunction with a 60-mil HDPE geomembrane to form a composite hydraulic barrier to infiltration. A detailed analysis of the seven potential degradation mechanisms listed in Table 3-2 for GCLs is provided by Benson and Benavides (2018), Phifer et al. (2007), and Savannah River Remediation (2020). Brief discussions of the degradation mechanisms are provided below (see Section 3.4.1.9 for chemical degradation by waste leachate).

3.4.1.8.1. Slope Stability

In general, GCLs can be safely placed on slopes of 10% (i.e., 10:1 horizontal to vertical) or less without the need for internal reinforcement or slope stability analysis (Bonaparte et al., 2002). On the other hand, internally reinforced GCLs can be safely placed on slopes as steep as 33% (i.e., 3:1 horizontal to vertical). Based on the conceptual design for the ELLWF final closure cap (Section 2.2.2.6; Figure 2-36 through Figure 2-44), slope failure due to the GCL will be designed out and not be considered as a closure cap degradation mechanism in the infiltration model.

3.4.1.8.2. Freeze-Thaw Cycles

The maximum frost depth at SRS is only about 5 inches according to Phifer et al. (2007), which is much shallower than the 5-foot burial depth of the GCL. In addition, field studies have found that GCLs are resistant to damage from freezing temperatures, are undamaged by freeze-thaw cycling, and do not need to be protected from frost (Benson, 1999; Bonaparte et al., 2002) because the hydrated bentonite is soft and readily consolidates around ice lenses and other defects during thawing (Benson, 1999). For these reasons, freeze-thaw cycling will not be considered as a closure cap degradation mechanism in the infiltration model.

3.4.1.8.3. Dissolution

Phifer et al. (2007) calculated worst-case sodium montmorillonite clay dissolution rates for a sodium bentonite GCL. Assuming complete closure cap failure and a worst-case infiltration rate of 16.45 inches per year, Phifer et al. (2007) estimated that it would take approximately 1,200 years to completely convert the sodium montmorillonite to kaolinite and quartz. Under slowly degrading closure cap conditions, it would take significantly longer for this conversion to occur. In addition, while montmorillonite can weather directly to kaolinite and quartz, it more commonly weathers through a series of predominately clay minerals. Based on these lines of evidence, Phifer et al. (2007) concluded that sodium bentonite dissolution is not likely to be a dominant degradation mechanism for the ELLWF closure cap over 10,000 years. Therefore, dissolution of sodium bentonite clay in the GCL will not be included as a degradation mechanism in the infiltration model.

3.4.1.8.4. Divalent Cations

The bentonite used in GCLs is typically sodium or calcium bentonite. Sodium bentonite is more commonly used because of its superior swelling capacity and lower initial permeability (Witt and Siegmund, 2001). However, within closure caps, sodium bentonite GCLs that are not protected by an overlying geomembrane (this is not the case for the ELLWF closure cap which will use a composite barrier) are susceptible to exchange of sodium with divalent cations such as calcium and magnesium, particularly when calcium- and magnesium-rich soils overlie the GCL (Benson, 1999; Bonaparte et al., 2002; Egloffstein, 2001). The conversion of hydrated sodium bentonite to calcium bentonite results in a decrease in the swell potential or potential volume of water bound to the mineral surface (i.e., immobile water) and a subsequent increase in the saturated hydraulic conductivity of the GCL particularly under conditions of low confining or overburden stress such as found in closure caps (Bonaparte et al., 2002; Egloffstein, 2001; Jo et al., 2005).

Based upon a review of the literature concerning the impact of the exchangeable cations on the saturated hydraulic conductivity of sodium bentonite and geochemical modeling using the Geochemist's Workbench® Ver. 6.0 (Bethke, 2005), Phifer et al. (2007) concluded that degradation of the bentonite GCL by divalent cation exchange should be considered as a closure cap degradation mechanism for the FTF PA infiltration model. Even though the ELLWF final closure cap conceptual design includes a composite barrier (HDPE geomembrane above a GCL), this degradation mechanism is included in the infiltration model by assigning a degraded saturated hydraulic conductivity of 5.0E-08 cm s^{-1} regardless of whether a sodium- or calcium bentonite GCL is initially employed. Because it is difficult to assign a timeline for the conversion of sodium bentonite to calcium or magnesium bentonite, the infiltration model will assume a saturated hydraulic conductivity for the GCL of 5.0E-09 cm s^{-1} for the first 100 years and 5.0E-08 cm s^{-1} thereafter.

3.4.1.8.5. Desiccation (Wet-Dry Cycles)

Phifer et al. (2007) analyzed the important factors that will preclude or reduce the negative impact of GCL desiccation and desiccation coupled with divalent cation exchange (Section 3.4.1.8.4) on the saturated hydraulic conductivity of the GCL and, hence, potential infiltration through the composite barrier. The proposed ELLWF closure cap, being located in a humid, wet environment with relatively uniform annual precipitation and having a 60-mil HDPE geomembrane with a sufficient soil thickness overlying the GCL, conforms to the requirements laid out by Benson (1999), Benson (2018), Egloffstein (2001), Lin and Benson (2000), and Witt and Siegmund (2001) for closure cap systems that preclude desiccation damage of the GCL. Additionally, if a sodium bentonite GCL is selected for the closure cap final design, the choice of material utilized to fill the voids within the erosion barrier stone layer will consider its impact upon the sodium bentonite GCL. In particular, materials with significant calcium content would likely not be utilized. Use of a calcium bentonite GCL will also be considered. For these reasons, GCL desiccation damage will not be considered as a closure cap degradation mechanism for the infiltration model.

3.4.1.8.6. Biological Degradation of the Geosynthetic Clay Liner

Plant roots can freely penetrate unprotected GCLs, which results in increases in the hydraulic conductivity of the GCL (Bonaparte et al., 2002; Witt and Siegmund, 2001). On the other hand,

plant roots will not penetrate intact HDPE geomembranes except at locations of existing cracks (holes) within the polymer sheet (Section 3.4.1.7.6). For purposes of the infiltration model, root penetration of the GCL is assumed to occur at existing holes within the HDPE geomembrane and is considered as a closure cap degradation mechanism.

While burrowing animals can potentially damage unprotected GCLs, damage to the ELLWF closure cap GCL is not considered a threat because of the presence of the overlying erosion barrier (Section 3.4.1.5.2). For this reason, burrowing animals will not be considered as a closure cap degradation mechanism for the infiltration model.

3.4.1.9. Chemical Degradation by Waste Leachate

Chemical degradation of the closure cap (GCL and layers above) by waste leachate is not considered feasible because the closure cap sits well above the waste zone with buffers/barriers in between. For trenches, the waste zone is located at least 6 feet below the GCL (4-foot-thick operational soil cover plus 12-inch-thick blended soil-bentonite layer plus minimum 12-inch-thick CCB foundation layer). In addition, for trench segments containing CIG SWFs, the waste zone is encapsulated in grout and, if needed, reinforced-concrete mats are placed over each trench segment before the operational stormwater runoff cover is installed. For vaults, a concrete roof and concrete walls isolate containerized (and grouted for the ILV) waste from the cap layers above. For NRCDAs, the waste is contained in welded steel casks or bolted containers. Chemical degradation will not be considered a closure cap degradation mechanism in the infiltration model.

3.4.1.10. Closure Cap Degradation Mechanism Summary

Table 3-3 summarizes the applicability of the potential closure cap degradation mechanisms listed in Table 3-2 to the ELLWF conceptual closure cap design (Section 2.2.2; Figure 2-36 through Figure 2-44). The summary of applicability categorizes the degradation mechanisms as follows:

- **Not Applicable**: For the reason(s) provided in the table, the potential degradation mechanism has been deemed not applicable to the ELLWF final closure cap design and will not be considered in the PA infiltration and/or fate and transport models.
- **Not Significant**: For the reason(s) provided in the table, the potential degradation mechanism has not been deemed a significant degradation mechanism for the ELLWF final closure cap design and will not be considered in the PA infiltration and/or fate and transport models.
- **Incorporate in System Design**: Sufficient design measures exist, and will be taken as necessary, to preclude the mechanism from contributing to the degradation of the closure cap. The mechanism, therefore, will not be considered in the infiltration and/or fate and transport models.
- **Applicable**: The mechanism is considered a potentially significant closure cap degradation mechanism and is accounted for in the infiltration and/or fate and transport models.

3.4.2. Closure Cap Degradation Mechanisms Applicable to the Infiltration Model

Section 3.4.1 discusses in detail potential degradation mechanisms for the final closure cap assuming a base-case land use scenario. Table 3-2 provides a complete listing of these potential degradation mechanisms for the major layers comprising the final cover system, while Table 3-3 summarizes the applicability of the potential closure cap degradation mechanisms listed in Table 3-2 to the conceptual closure cap design.

The closure cap degradation model is based largely on the conceptual model development work for the FTF final closure cap concept by Phifer et al. (2007). The development of the closure cap degradation model is quite extensive and will not be repeated in its entirety in this report. Instead, degradation model assumptions that impact infiltration through specific layers of the ELLWF final closure cap are summarized in Table 3-4. The operational and interim HDPE covers placed over closed STs and ETs are excluded from the degradation model because they will be actively maintained during the operational and IC periods.

Table 3-3. Applicability of Potential Degradation Mechanisms to Final Closure Cap Conceptual Design

Affected Cap Layer	Potential Degradation Mechanism	Summary of Applicability to the ELLWF Closure Cap Conceptual Design
All Layers	Static loading induced settlement	Not Significant: Settlement due to static loading is anticipated to be a few inches and is expected to occur uniformly over the entire cap area. Differential settlement is also anticipated to be negligible.
	Seismic-induced liquefaction and subsequent settlement	Not Significant: Settlement due to seismic loading and the resulting liquefaction is anticipated to be only a few inches and is expected to occur uniformly over the entire cap area. Differential settlement is also anticipated to be negligible.
	Seismic-induced slope instability	Incorporate in System Design: The side slopes will be designed for seismic stability.
	Seismic-induced lateral spread	Not Applicable: Conditions at SRS are not conducive to lateral spreading.
	Seismic-induced direct rupture due to faulting	Not Applicable: Surface faulting is nonexistent in the U.S. Southeast.
	Waste zone subsidence	**Applicable**: Waste zone subsidence as a closure cap degradation mechanism is central to the conceptual designs of the infiltration, flow, and transport models (both deterministic and stochastic) for all ELLWF DUs except the NRCDAs. For STs, ETs, and the CIG trench segments, waste zone subsidence will impact DU performance during the 1,000-year compliance period. For the LAWV and ILV, subsidence of the closure cap due to structural collapse of the concrete vault covers will occur during the extended 10,000-year simulation period.
Vegetative Cover	**Succession**	**Applicable**: Vegetation succession from a Bahia grass field to a pine forest is considered a closure cap degradation mechanism, resulting in an assumption that deep pine tree roots penetrate various closure cap layers leading to degradation of the composite hydraulic barrier in particular.
	Stressors (droughts, disease, fire, and biological)	Not Significant: Vegetative stressors (drought, disease, fire, and biological) primarily impact the closure cap in terms of the rate of succession rather than as any long-term degradation mechanism on their own.
Soil above the Erosion Barrier	**Erosion and gully formation**	**Applicable**: Chronic erosion of soil above the erosion barrier (six-inch topsoil and 30-inch upper backfill layers) over a 10,000-year period is considered a closure cap degradation mechanism and is included in the infiltration model. The impact of localized gully formation is addressed via sensitivity analysis.
	Loss of compaction	Not Significant: The upper backfill layer will be CCB and is assumed to maintain compaction throughout the lifecycle of the closure cap.
	Desiccation (wet-dry cycles)	Not Significant: Significant cracking of SRS topsoil and backfill upon drying is highly unlikely because the soils consist predominately of quartz sand, the clay content is predominately kaolinite, SRS soils are highly leached, and the backfill is compacted.
Erosion Barrier	Weathering (dissolution)	Incorporate in System Design: The erosion barrier stone size will be designed considering the applicable weathering rate over 10,000 years. Materials used to infill the stone voids will be selected so that it has either no impact on weathering or, preferably, lowers the weathering rate of the stone.
	Biological (root penetration)	**Applicable**: Deep pine tree roots are assumed to penetrate the erosion barrier.
	Biological (burrowing animals)	Incorporate in System Design: The erosion barrier will be designed to act as a barrier to burrowing animals.
	Chemical (waste leachate)	Not Applicable: Chemical degradation of the erosion barrier from leachate associated with the waste is not considered applicable because the erosion barrier will be located well above the waste zone.
LDL	**Silting-in**	**Applicable**: Over time, the LDL is assumed to silt-in with colloidal clay that migrates from the overlying upper backfill layer through the erosion barrier voids.
	Biological (root penetration)	**Applicable**: Deep pine tree roots are assumed to penetrate the LDL.
	Biological (burrowing animals)	Not Applicable: The erosion barrier located above the LDL will be designed to act as a barrier to burrowing animals.
	Mineral precipitation and microbial growth	Not Significant: LDLs in closure caps receive only uncontaminated water from precipitation infiltration. At SRS, the infiltrating water is very low in Ca/Mg hardness and total organic carbon.
HDPE Geomembrane	Ultraviolet (UV) radiation	Incorporate in System Design: The HDPE geomembrane will contain carbon black which acts as a UV stabilizer and HDPE geomembrane exposure to sunlight during closure cap construction will be limited in duration.
	Antioxidant depletion	**Applicable**: Antioxidant depletion of the HDPE geomembrane will occur via oxidation of the antioxidants and diffusion out of the geomembrane.
	Thermal oxidation	**Applicable**: Thermal oxidation of the HDPE geomembrane will occur after depletion of the antioxidants and is assumed to occur in conjunction with tensile stress cracking, which will cause degradation of the geomembrane.
	High-energy irradiation	Not Significant: High-energy irradiation of the HDPE geomembrane is considered an insignificant degradation mechanism over 10,000 years.
	Tensile stress cracking	**Applicable**: Tensile stress cracking of the HDPE geomembrane will occur after depletion of the antioxidants and is assumed to occur in conjunction with thermal oxidation.
	Biological (root penetration)	**Applicable**: Intact HDPE geomembranes preclude root penetration and cause the roots to follow laterally atop the geomembrane surface; however, it is assumed that roots can penetrate the geomembrane in locations where holes have already formed due to other degradation mechanisms.
	Biological (burrowing animals)	Not Applicable: The erosion barrier will be designed to act as a barrier to burrowing animals and preclude their ability to reach the geomembrane.
	Biological (microbial)	Not Significant: The high-molecular-weight polymers used for geomembranes appear to be insensitive to microbial biodegradation.
	Chemical (waste leachate)	Not Applicable: Chemical degradation of the erosion barrier from leachate associated with the waste is not considered applicable because the erosion barrier will be located well above the waste zone.
GCL	Slope stability	Incorporate in System Design: The GCL will be placed at a 2%-5% slope, which is well below the 10% stability limit for nonreinforced GCLs. The GCL for the side slopes will be reinforced and will therefore be stable on the 3:1 slope.
	Freeze-thaw cycles	Incorporate in System Design: GCLs are resistant to damage from freeze-thaw cycling and the closure cap GCL will be positioned well below the SRS maximum frost depth of approximately 5 inches.
	Dissolution	Not Significant: Sodium montmorillonite has a low solubility; therefore, a large volume of water and extended time are required to weather it through a series of clay minerals.
	Divalent cations (Ca^{+2}, Mg^{+2})	**Applicable**: It is assumed that sodium bentonite is converted to calcium and magnesium bentonite, resulting in an order of magnitude increase in saturated hydraulic conductivity.
	Desiccation (wet-dry cycles)	Incorporate in System Design: The GCL will be located beneath a 60-mil HDPE geomembrane as well as 6 feet of soil materials to preclude desiccation damage. In addition, the material utilized to fill the voids of the erosion barrier stone will be selected so that it does not negatively impact the underlying GCL by leaching Ca^{2+} and Mg^{2+}.
	Biological (root penetration)	**Applicable**: The GCL will be overlain by a HDPE geomembrane. Intact HDPE geomembranes preclude root penetration; however, it is assumed that roots can penetrate the GCL at locations where holes have already formed in the geomembrane due to other degradation mechanisms.
	Biological (burrowing animals)	Not Applicable: The erosion barrier will be designed to act as a barrier to burrowing animals and preclude their ability to reach the GCL.
	Chemical (waste leachate)	Not Applicable: Chemical degradation of the erosion barrier from leachate associated with the waste is not considered applicable because the erosion barrier will be located well above the waste zone.

Notes:

Bolded mechanisms are considered further in the infiltration and/or flow and transport models.

Table 3-4. Final Closure Cap Degradation Mechanisms Applicable to Infiltration Modeling (after Phifer et al., 2007, Table 52)

Affected	Applicable Degradation Mechanism	Modeling Approach
Vegetative Cover	Succession	Vegetation succession from a Bahia grass field to a pine forest is assumed to begin at the end of the 100-year IC period as outlined in Section 3.4.1.3.
Soil above Erosion Barrier	Erosion	Erosion of soil layers above the erosion barrier is assumed to begin immediately following closure cap construction as outlined in Section 3.4.1.4.1.
Erosion Barrier	Root Penetration	Pine tree roots are assumed to freely penetrate the erosion barrier consistent with the rate of root production outlined in Section 3.4.3 below; however, such penetration is assumed to have no impact on the hydraulic properties of the erosion barrier as outlined in Section 3.4.1.5.2.
Lateral Drainage Layer (LDL)	Silting-In	Upon closure cap construction, accumulation of colloidal clay, which migrates from the upper backfill into the underlying LDL, is assumed to begin to reduce the saturated hydraulic conductivity of the LDL over time as outlined in Section 3.4.1.6.1.
	Root Penetration	Pine tree roots are assumed to freely penetrate the erosion barrier into the LDL consistent with the rate of root production outlined in Section 3.4.3 and to reduce the saturated hydraulic conductivity of the layer (impermeable volume) until they decay.
HDPE Geomembrane	Antioxidant Depletion, Thermal Oxidation, & Tensile Stress Cracking	The number of holes in the geomembrane over time is calculated based on methodologies developed by Mueller and Jakob (2003) for antioxidant depletion and by Needham et al. (2004) for turning the combined set of three degradation mechanisms into a defect (hole) generation rate. K_{sat} for intact HDPE geomembrane = 2.0E-13 cm s^{-1}.
	Root Penetration	Once a significant number of deep tap roots have developed, it is assumed that every HDPE geomembrane hole generated over time is penetrated by a tap root that subsequently penetrates the GCL.
Geosynthetic Clay Liner (GCL)	Divalent Cations (Ca^{2+}, Mg^{2+})	The GCL is assumed to consist of Na-bentonite (K_{sat} = 5.0E-09 cm s^{-1}) during the first 100 years of closure cap life and Ca-bentonite (K_{sat} = 5.0E-08 cm s^{-1}) thereafter.
	Root Penetration	Once a significant number of deep tap roots have developed, it is assumed that every HDPE geomembrane hole generated over time is penetrated by a tap root that subsequently penetrates the GCL.

3.4.3. Pine Tree Root Production Conceptual Model

As a pessimistic, bounding assumption, vegetation succession from a Bahia grass field to a pine forest will result in the deep roots of pine trees penetrating multiple layers of the ELLWF closure cap, resulting in degradation of the composite hydraulic barrier. The following assumptions are made in the conceptual infiltration model for the ELLWF PA (Phifer et al., 2007, pg. 118):

- Upon installation of the interim cover in 2065 at interim closure, a 100-year IC period begins during which the Bahia grass is maintained and pine trees are excluded.
- At the end of IC and upon final closure, the final cover system is installed and immediately begins to degrade.
- 160 years after the end of IC, the establishment of pine seedlings on top of the final closure cap is assumed to begin.
- Pine trees are considered mature once they reach 40 years of age.
- Approximately three cycles of "pine seedlings to mature pine trees" (i.e., approximately 40 years per cycle) are needed to establish a mature pine forest over the entire closure cap.
- The entire closure cap is assumed to be dominated by mature loblolly pine approximately 280 years after the end of IC.
- Complete turnover of 400 mature trees per acre is assumed to occur every 100 years (i.e., 400 mature trees per acre die every 100 years in a staggered manner).[2]
- It will take approximately 30 years for the tap roots to reach a 6-foot depth and the remainder of the tree's life (i.e., 70 years) for the root to go its full depth.
- Each mature tree has four tap roots to 6 feet and one tap root to 12 feet. The roots are 3 inches in diameter at a depth of one foot and 0.25 inches in diameter at either six or 12 feet, whichever is applicable.
- Deep roots are assumed to freely penetrate the erosion barrier (Section 3.4.1.5.2) and the GCL (Section 3.4.1.8.6).
- Deep roots will be unable to penetrate the intact HDPE geomembrane; roots that reach the HDPE geomembrane will only penetrate at locations where holes in the geomembrane have already formed due to HDPE degradation (Section 3.4.1.7).

Table 3-5 summarizes the pine tree succession timeline.

[2] Tree density is anticipated to remain fairly constant. For a natural regeneration stand over 100 years, tree density is assumed to be about 550 dominant and co-dominant trees per acre with about 400 mature (40 to 125 years old) trees per acre per Phifer et al. (2007). Complete turnover of the 400 mature trees per acre is assumed to occur every 100 years (400 mature trees per acre die every 100 years in a staggered manner). Smaller trees are assumed to be suppressed and die.

Table 3-5. Vegetative Cover Pine Tree Succession Timeline (Phifer et al., 2007; Table 53)

Relative Year	Occurrence
0	Start of IC / Interim cover
100	End of IC / Installation of the final closure cap
260	Pine tree seedlings begin to become established on the ELLWF closure cap
290	Pine tree roots first begin to reach the HDPE geomembrane
300	Mature pine trees are established over one-third of the ELLWF closure cap
340	Mature pine trees established over two-thirds and pine tree seedlings established over the entire ELLWF closure cap
380	Mature pine trees established over the entire ELLWF closure cap
380 and beyond	Complete turnover of mature trees occurs every 100 years

3.4.4. Erosion of Soil Above the Erosion Barrier

The projected erosion rates for the topsoil and upper backfill layers are estimated by Phifer et al. (2007; Appendix I) for the FTF closure cap utilizing the Universal Soil Loss Equation (Goldman et al., 1986) for both Bahia grass and pine forest vegetative covers. Table 3-6 lists the calculated vegetative cover soil loss rates from erosion for the topsoil and upper backfill layers, which are assumed to apply for the ELLWF cap design. To maximize erosion for the bounding infiltration model, the Bahia grass erosion rate is used until relative Year 380 when mature pine trees are assumed to cover the entire closure cap (Table 3-5). Using erosion rates listed in Table 3-6, Phifer et al. (2007; Table 55 and Appendix I) calculated the thickness of the topsoil and upper backfill layers for the FTF closure cap design and timeline. Table 3-7 reports layer thicknesses used in the infiltration model, which were interpolated to account for the different ELLWF timeline.

Table 3-6. Estimated Final Closure Cap Vegetative Soil Cover Soil Losses

Soil-Vegetation Condition	Estimated Soil Loss (ton/acre/year)	Estimated Soil Loss (inches/year)
Topsoil with a Bahia grass vegetative cover	0.099	5.2E-04
Topsoil with a pine forest	0.025	1.3E-04
Backfill with a Bahia grass vegetative cover	0.071	3.7E-04
Backfill with a pine forest	0.018	9.3E-05

Table 3-7. Topsoil and Upper Backfill Layer Thicknesses over Time

Relative Year	Topsoil Thickness (inches)	Upper Backfill Thickness (inches)
100	6.0	30
180	5.96	30
290	5.90	30
300	5.90	30
340	5.88	30
380	5.85	30
480	5.84	30
660	5.82	30
1,100	5.76	30
1,900	5.66	30
2,723	5.55	30
3,300	5.47	30
5,700	5.16	30
10,100	4.59	30

3.4.5. Silting-In of Lateral Drainage Layer

Because pine tree roots are allowed to freely penetrate the erosion barrier and the presence of the geotextile filter fabric is ignored (bounding assumptions), the LDL is assumed to progressively silt-in with colloidal clay that migrates from the overlying upper backfill layer, thereby steadily reducing its saturated hydraulic conductivity over time. Phifer et al. (2007; Appendix I) calculated values of saturated hydraulic conductivity, porosity, field capacity, and wilting point for the FTF Closure Cap LDL based upon the following silting-in assumptions:

- Over time, colloidal clay migrates with the water flux from the 12-inch-thick middle backfill to the underlying 12-inch -thick LDL at a concentration of 63 mg of colloidal clay per liter of water flux.
- Once half the clay content of the backfill has migrated to the drainage layer, the two layers essentially become the same material and material property changes cease with an endpoint saturated hydraulic conductivity equal to that of the log mid-point between the initial backfill and drainage layer conditions.
- The saturated hydraulic conductivity of the middle backfill layer is assumed to increase log-linearly with time. Conversely, the saturated hydraulic conductivity of the LDL is assumed to decrease log-linearly with time.
- The endpoint porosity, field capacity, and wilting point are assumed to equal the arithmetic average of the middle backfill layer and LDL.

Even though the middle backfill layer is no longer included in the proposed ELLWF closure cap design (Figure 2-35) to ensure that the average cap thickness above the LAWV and ILV satisfies differential settlement and maximum seismic load considerations, the infiltration model assumes that the degradation of LDL performance still happens as described above.[3] With the current cap design, the fines would instead have to originate from the 30-inch-thick upper backfill layer.[4]

As noted in Table 3-4, pine tree roots are assumed to freely penetrate the erosion barrier into the LDL and to reduce the saturated hydraulic conductivity of the layer (impermeable volume) until they decay. Phifer et al. (2007; Appendix I) calculated that the roots within the LDL will represent an impermeable volume that ranges from only 0.032% to 0.17% at any time, depending upon the extent of erosion above the erosion barrier. To compensate for the presence of the roots within the LDL, Phifer et al. (2007) reduced the saturated hydraulic conductivity of the LDL by 0.2%

[3] Even though the 12-inch-thick middle backfill layer is not included in the HELP model simulations, deterioration of the 12-inch-thick LDL's hydraulic properties is calculated to occur as if the middle backfill was still present as the source of the fines.

[4] In reality, silting-in of the LDL in the ELLWF closure cap design is less likely to occur than in the FTF design because the upper backfill layer is not immediately adjacent to the LDL but is instead separated from the LDL by the 12-inch-thick erosion barrier. The voids within the erosion barrier rock mass will be filled with a yet-to-be determined material to prevent loss of the overlying upper backfill into the erosion barrier. Among other considerations, the infill material will be selected based upon its impact on below-grade weathering of the erosion barrier stone. An infill material that favors a decreased weathering rate will be favored. For this reason, it is assumed that degradation of the upper backfill layer's hydraulic properties does not occur.

beginning in relative Year 300 when a third of the closure cap is anticipated to be covered in mature pine trees.

Table 3-8 lists the degraded hydraulic properties for the LDL assumed in the infiltration model simulations for the intact closure cap case.

Table 3-8. Lateral Drainage Layer Saturated Hydraulic Conductivity, Porosity, Field Capacity, and Wilting Point Assumptions for E-Area Low-Level Waste Facility Infiltration Model

Relative Year	Saturated Hydraulic Conductivity (cm s^{-1})	Porosity (cm^3 cm^{-3})	Field Capacity (cm^3 cm^{-3})	Wilting Point (cm^3 cm^{-3})
100	5.0E-02	0.417	0.045	0.018
180	4.48E-02	0.416	0.048	0.021
290	3.86E-02	0.414	0.052	0.024
300	3.81E-02	0.414	0.053	0.024
340	3.60E-02	0.414	0.054	0.026
380	3.41E-02	0.413	0.056	0.027
480	2.98E-02	0.412	0.060	0.030
660	2.33E-02	0.409	0.067	0.036
1,100	1.28E-02	0.403	0.084	0.049
1,900	4.30E-03	0.392	0.116	0.074
2,723	1.40E-03	0.380	0.148	0.100
3,300	1.40E-03	0.380	0.148	0.100
5,700	1.40E-03	0.380	0.148	0.100
10,100	1.40E-03	0.380	0.148	0.100

3.4.6. Degradation of the Geomembrane

As listed in Table 3-4 and as outlined in detail by Phifer et al. (2007; Sections 7.6.2.3 and 7.6.7), the cumulative defect area (expressed as the equivalent number of 1-cm^2 holes) in the HDPE geomembrane over time is calculated based on methodologies developed by Mueller and Jakob (2003) for antioxidant depletion and by Needham et al. (2004) for turning the combined impact of the three relevant degradation mechanisms (antioxidant depletion, thermal oxidation, and tensile stress cracking) into a defect (hole) generation rate. Phifer et al. (2007; Appendix I) calculated the hole generation rate for the FTF closure cap design based on these three degradation mechanisms, which was applied to the ELLWF closure cap design adjusting for differences in the cap installation timelines. Table 3-9 provides a schedule for the equivalent number of 1-cm^2 geomembrane holes assumed in the infiltration model simulations for the ELLWF final closure cap.

Table 3-9. Number of Geomembrane Holes Assumed in the E-Area Low-Level Waste Facility Infiltration Model

Relative Year	Equivalent Number of 1-cm^2 Holes per Acre
100	4
180	40
290	96
300	101
340	121
380	141
480	479
660	1,115
1,100	2,669
1,900	5,496
2,723	8,403
3,300	10,442
5,700	18,921
10,100	34,466

3.4.7. Root Penetration of Composite Hydraulic Barrier

As stated in Table 3-4, once a significant number of deep tap roots have developed, it is assumed that every HDPE geomembrane hole generated over time is penetrated by a tap root that subsequently penetrates the GCL. As with the LDL, it is assumed that significant roots are available for penetration at relative Year 300 and beyond. Phifer et al. (2007; Section 8.7) determined that the number of pine tree roots will far exceed the number of geomembrane holes; therefore, the assumption of one tap root per geomembrane hole is numerically feasible and bounding, if not probable.[5]

Because the HELP model code does not allow for the presence of holes in a barrier soil liner, the GCL must either be excluded or combined with the HDPE geomembrane for all simulation cases at relative Year 300 and beyond. For this reason, the infiltration model employs the following equivalent representation of the composite hydraulic barrier (i.e., combined HDPE geomembrane and GCL) as originally developed by Phifer et al. (2007; Appendix I):

- For relative year ≤ 200 (≤ 100 years after cap is installed, where relative Year 0 is the start of IC), the HDPE geomembrane (K_{sat} = 2.0E-13 cm s^{-1}) and GCL (K_{sat} = 5.0E-09 cm s^{-1}) are modeled as separate layers with holes in the HDPE geomembrane and an intact GCL.
- For 200 ≤ relative year ≤ 300, the HDPE geomembrane and GCL are again modeled as separate layers with holes in the HDPE geomembrane and an intact GCL; however, K_{sat}

[5] Shine (2007) developed a probability-based root penetration model to estimate the probability of pine tree roots penetrating cracks in the HDPE geomembrane and subsequently producing a hole in the underlying GCL. The probability model affirmed that infiltration estimates produced under the assumption that every HDPE geomembrane hole generated over time is penetrated by a root that subsequently penetrates the GCL are clearly bounding. In fact, Shine (2007) calculated that a mean of only 2% and 20% of the geomembrane holes were occupied by a live or dead tap root after 1,000 years and 10,000 years, respectively.

for the GCL is increased by an order of magnitude to 5.0E-08 cm s^{-1} to account for divalent cation degradation (Table 3-4).

- For relative year > 300, the HDPE geomembrane and GCL are modeled as a single, combined, 0.26-inch-thick composite barrier layer with holes. The equivalent K_{sat} for flow perpendicular to layering (Freeze and Cherry, 1979) is 8.7E-13 cm s^{-1} for the intact portion of the combined layer as calculated by Phifer et al. (2007; Appendix I).

3.5. GROUNDWATER AQUIFER PATHWAY CONCEPTUAL MODEL

Section 2.1.7 provides a detailed description of the hydrostratigraphic units that will impact the subsurface distribution of contaminants potentially released from ELLWF DUs. In the GSA at SRS, where the ELLWF is located, the surrounding surface streams influence GW flow as illustrated in Figure 2-4 and Figure 2-22. Three streams (Upper Three Runs to the north; McQueen Branch, a tributary of Upper Three Runs, to the northeast; Fourmile Branch to the south) are natural boundaries to GW flow in the UTRA Unit. All creeks cut into this unit, and thus GW is either intercepted by the creeks or recharges the underlying Gordon Aquifer Unit (GAU). In addition, a GW divide (see Figure 2-22) exists in the UTRA Unit because of the influence of these streams. Figure 2-23 further illustrates the influence of creeks on GW flow directions local to the ELLWF.

As justified in Section 2.1.7, a discussion of GW hydrology for the ELLWF PA is restricted to hydrostratigraphic units located above the Meyers Branch Confining System because units below the Meyers Branch Confining System are considered protected from contamination. As illustrated in Figure 3-4, the hydrostratigraphic units of concern comprising the local aquifer system include the UAZ (subdivided into the AAA and Transmissive Zones), TCCZ, LAZ, Gordon Confining Unit (GCU), and GAU. Beneath these units is the Crouch Branch Confining Unit, a laterally continuous, dense unit of low permeability.

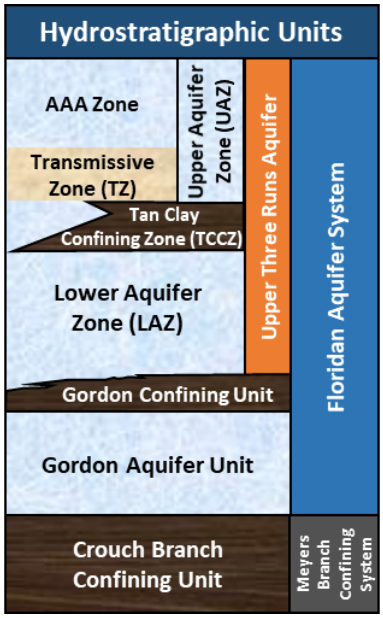

Figure 3-4. Hydrostratigraphic Units Relevant to ELLWF Aquifer Zone Simulations (after Jones et al., 2010, Figure 2; modified from Savannah River Remediation, 2020)

Following is a brief description of the hydrostratigraphic units shown in Figure 3-4 (after Flach and Harris, 1999; Flach et al., 1999; Savannah River Remediation, 2020):

- The UAZ includes the Upland Unit, Tobacco Road Sand, and a portion of the Dry Branch Formation. It is characterized by sand and clayey sand with minor intercalated clay layers. The sediment within the Upland Unit is commonly very dense and clayey and contains gravelly sand. To be consistent with the hydrostratigraphic units included in the most recent GSA GW flow models (Flach, 2019; Flach et al., 2017), the UAZ is subdivided into a Transmissive Zone (TZ) and an overlying, combined A and AA zone (AAA).
- The TCCZ includes sediment of the Dry Branch Formation and is characterized by light yellowish to orange clay and sandy clay, interbedded with clayey sand and sand. The clay layers of the TCCZ are not laterally continuous over distances greater than 100 to 200 feet. As a result, the water table in E-Area can be located above or below the TCCZ depending on location relative to recharge zones.
- The LAZ consists predominantly of the fine-grained, well-sorted sand and clayey sand of the Santee Limestone and parts of the Dry Branch Formation beneath the TCCZ, and includes carbonate sediments and various calcareous components (calcarenaceous sand, micritic sand, shelly sand, and some sandy calcarenite and shelly limestone).
- The GCU separates the GAU from the Upper Three Runs Aquifer (Water Table Aquifer), which is located locally within the UAZ. The GCU is also known as the "green clay" and comprises layers of interbedded silty and clayey sand, sandy clay, and clay. Glauconite is a common constituent that imparts a distinctive greenish cast to the sediment. Beneath the GSA, the GCU includes some calcareous sediment and limestone, primarily calcarenaceous sand and clayey sand with subordinate calcarenaceous and micritic clay, and sandy micrite and limestone.
- The GAU is the lowermost unit considered for the ELLWF PA; it is bounded by the Crouch Branch Confining Unit. Beneath the GSA, the GAU predominantly comprises the loose sand and clayey sand of the Congaree Formation. The sand is yellowish to grayish orange in color and is medium- to coarse-grained. Pebbly layers and zones of iron and silica cement are common.

3.5.1. Conceptual Model for Aquifer Transport

As conceptualized by Savannah River Remediation (2020), once radionuclides released from the ELLWF DU waste zones have been transported through the VZ by infiltrating precipitation, they will breach the water table and enter the saturated (aquifer) zone. GW flowing within the saturated zone will then transport the radionuclides downgradient and away from the ELLWF DUs. Radionuclides within the GW will form contaminant plumes; plumes that intercept GW wells or seepage faces may contribute to contaminant exposures.

Figure 3-5 provides a conceptual model of GW flow beneath the 15-mi^2 GSA, including the hydrostratigraphic units through which radionuclide contaminants will be transported to the points of compliance. The light blue dashed line in the figure identifies the water table surface. The water table in the GSA is generally located in the UAZ. Near the ELLWF, the water table ranges from

approximately 45 feet below the ground surface in the eastern sector of the ELLWF to approximately 80 feet below ground surface in the western sector of the ELLWF (Bagwell and Bennett, 2017). The ELLWF is located on a topographically elevated interfluvial plateau bounded by two tributaries to the Savannah River: Upper Three Runs to the north and Fourmile Branch to the south. At each tributary, the distance from the ground surface to the water table reaches zero, terminating at a seepage face (Savannah River Remediation, 2020). Radionuclide contaminants will enter the saturated zone beneath the DU waste zones from which they were released. Based on predicted aquifer zone flow rates from the GSA_2018 PORFLOW GW Flow Model (Flach, 2019), together with transport properties for the aquifer zone soils, the radionuclide contaminants will be transported toward the seepage faces.

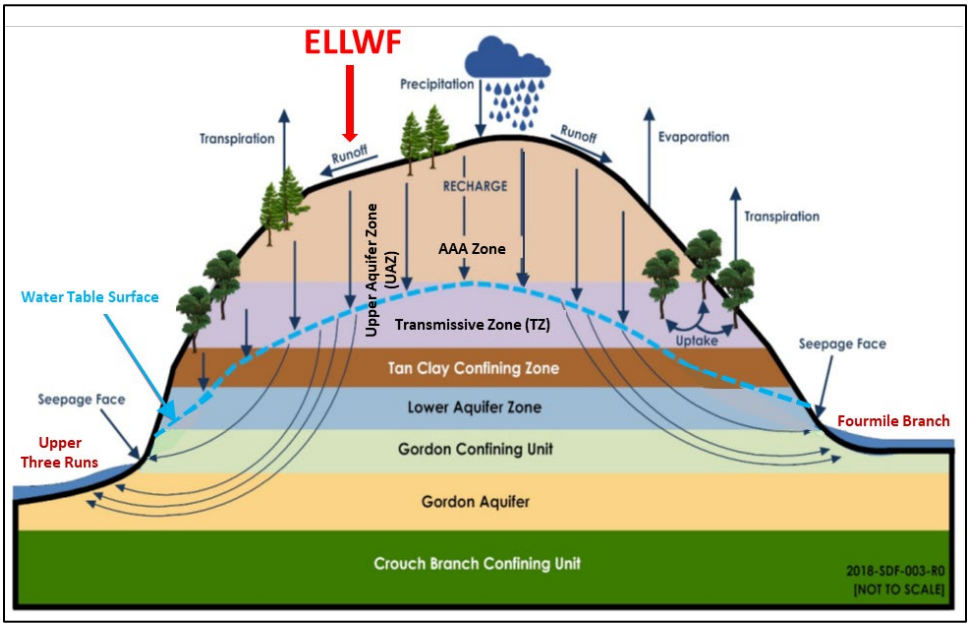

Figure 3-5. Conceptual Model of Groundwater Flow Beneath General Separations Area Near E-Area (modified from Savannah River Remediation, 2020)

The overall aquifer transport model computes transient contaminant plumes for parent radionuclides and their short-chain progeny with the following incorporated features:

- Transient fluxes at the water table just beneath a single DU are handled as distributed source terms (in a tabulated form) where these fluxes result from VZ migration of a single parent radionuclide buried in the DU's waste zone (along with the ingrowth and migration of the short-chain progeny).
- The aquifer flow field is input to the transient transport model where a small series of steady-state flow fields have been previously generated. The slow evolution of the aquifer flow field is represented by these state-state flow fields which address the slow degradation of covers.

Implementation of the ELLWF PA aquifer transport model consists of two steps (Savannah River Remediation, 2020):

- Aquifer flow field refinement, which involves refinement of the baseline GSA_2021 flow model[6] to generate localized flow fields for E-Area (Section 3.5.3.2.3). These aquifer domain cutouts have (1) refined meshes to accommodate numerical dispersion issues and (2) extended footprints to ensure that the at and beyond 100-meter POA is captured (while operating under a 3 million node limit for PORFLOW applications).
- Aquifer transport model implementation as discussed in Section 3.5.3)

The GSA_2021 flow model extends vertically from the ground surface down to the top of the Crouch Branch Confining Unit. The aquifer cutouts also extend over this same vertical range, while the horizontal model domain is significantly reduced and altered to accommodate the two features listed above. PORFLOW has a variably-saturated porous media formulation and both the VZ and aquifer zone are included within the computational domains. During aquifer transport simulations, negligible back-diffusion from the water table is observed.

The discussion below describes the development and calibration of the baseline GSA flow model upon which the aquifer transport model simulations are based.

3.5.2. General Separations Area Flow Model in PORFLOW

The horizontal extent of the GSA flow model is established based on natural boundaries such as creeks and their tributaries. These surface water features are shown in Figure 3-6 along with several of the key processing areas (e.g., E-Area, F-Area, H-Area, S-Area, and Z-Area).

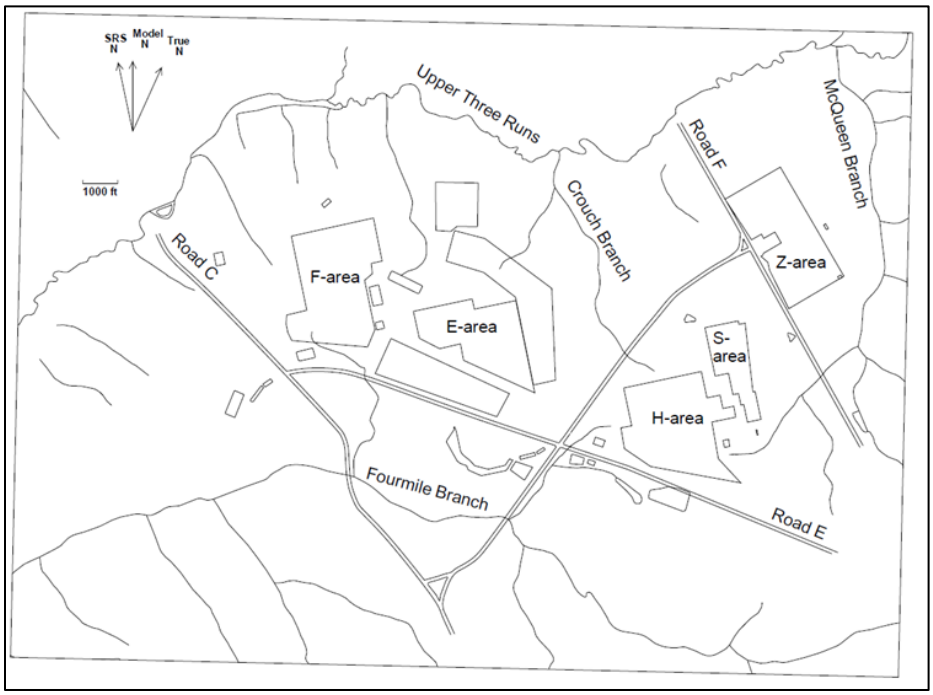

Figure 3-6. General Separations Area of the Savannah River Site

[6] A revised version of the GSA_2018 flow model (Flach, 2019) where emphasis is placed on calibration targets in the vicinity of E-Area.

As originally described by Flach and Harris (1999), the GSA flow model simulates GW flow under steady-state conditions from the ground surface to the bottom of the GAU within a 15-square-mile area bounded by Fourmile Branch to the south, Upper Three Runs (UTR) to the north, marshes beyond F-Area to the west, and McQueen Branch to the east (see Figure 2-22 and Figure 3-7). GW from the UTR Aquifer is assumed to discharge equally from each side of UTR, Fourmile Branch, and McQueen Branch. As a result, these three streams provide natural, no-flow boundary conditions for most of the UTRA unit. The GSA flow model boundary conditions are displayed graphically in Figure 3-7. The seepage faces associated with UTR result in a fairly broad wetland area both north and south of the actual creek. The aerial extent of the PORFLOW active grid is expanded north of this creek to coincide with the estimated centroid of this wetland region where a no-flow boundary condition is applied.

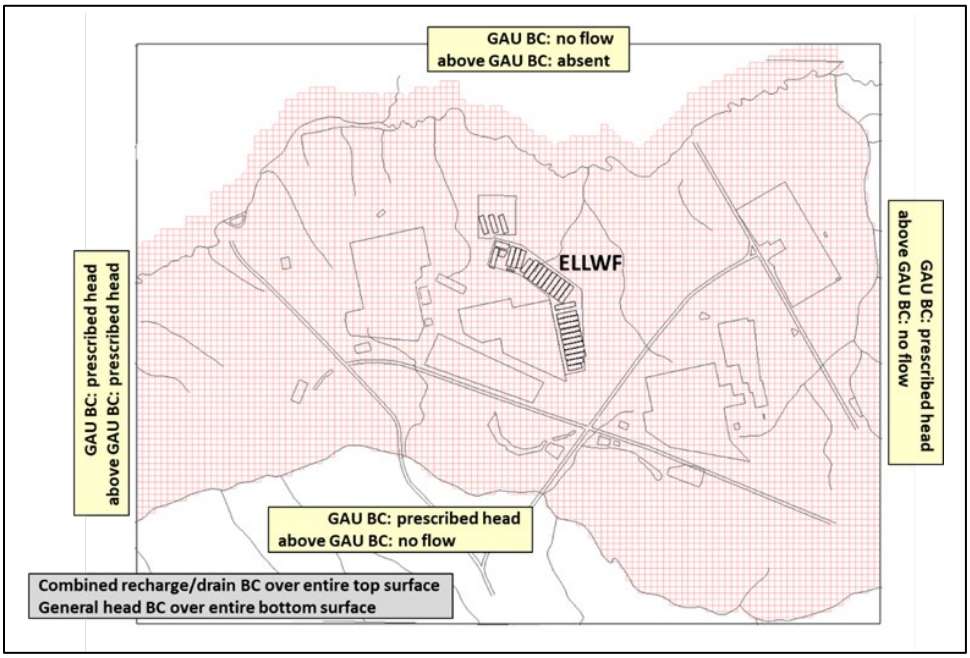

Figure 3-7. General Separations Area Flow Model Active Mesh and Boundary Conditions (BCs)

On the west side of the UTRA unit, hydraulic head values from a contour map of measured water elevations are prescribed. The GAU is assumed to discharge equally from both sides of UTR and, therefore, a no-flow boundary condition is specified over the entire north face of the GSA flow model (i.e., because the ground surface coincides with the elevation of UTR, the units above the GAU do not exist along the north face). Lacking natural boundary conditions, hydraulic heads are specified over the west, south, and east faces of the GSA flow model within the GAU. Areas of GW recharge and discharge consistent with computed hydraulic head at the ground surface are computed as part of the model solution using a combined recharge/drain boundary condition applied over the entire top (ground) surface of the model. GW discharges to surface water in regions where the computed head is above ground elevation.

The GSA flow model has grid coordinates that are both rotated and translated from the reference coordinate system. Because the majority of the data available is in SRS coordinates (i.e., SRS

easting and northing), this system is chosen the reference system for this PA. Model coordinates are translated by (Δx,Δy) and rotated counterclockwise by an angle θ relative to site coordinates. The transformation from model to site coordinates is:

$$E = \Delta x + \left(x \cos\theta - y \sin\theta \right)$$
$$N = \Delta y + \left(x \sin\theta + y \cos\theta \right) \qquad \text{Eq. (3-1)}$$

where:

Δx Translation from easting (ft)
Δy Translation from northing (ft)
θ Rotation from site to model (degree)

The above boundary conditions are imposed during calibration activities as well as for every steady-state time period of interest. The numerical settings for the combined recharge/drain boundary condition along the top (ground) surface are altered for each time period considered. For example, its settings are changed to reflect uncovered versus covered conditions.

3.5.2.1. Developmental History of the Baseline General Separations Area Flow Model

GSA/FACT Flow Model

The GSA GW flow model was originally developed for environmental restoration applications at SRS by Flach and Harris (1999) using the FACT code (Aleman et al., 1999; Hamm and Aleman, 2000).[7] The original GSA/FACT model—consistent with detailed characterization and monitoring data through 1996—was modified slightly for use in the 2000 ELLWF PA (McDowell-Boyer et al., 2000) to perform steady-state simulations of GW flow in the GSA as a prerequisite for the saturated-zone contaminant transport analyses executed for source-zone radionuclides and their progeny in PORFLOW, Ver. 4.00 (ACRi, 2000).

2004 GSA/PORFLOW Flow Model

Prior to PA2008, Flach (2004) converted the GSA GW flow model into PORFLOW (Ver. 5.95.0) using the former GSA/FACT model as the basis. The original GSA/FACT characterization and monitoring datasets, pre-processing algorithms, and model calibration strategies were largely preserved. No updates were made to the characterization and monitoring datasets used to develop the 1999 GSA/FACT model. Differences in flow results between the two models, due to mesh and code differences,[8] were minimized to the extent practical. Flach (2004) concluded that the 2004

[7] FACT is a transient, 3-D, finite element code designed to simulate isothermal GW flow, moisture movement, and solute transport in variably saturated and fully saturated subsurface porous media. The SRS-developed code was designed specifically to handle complex multilayer and/or heterogeneous aquifer systems in an efficient manner and to accommodate a wide range of boundary conditions. FACT utilizes deformed brick elements. Material properties are defined at element centers, and state variables such as hydraulic head are located at element vertices (Hamm and Aleman, 2000).

[8] PORFLOW utilizes control volume discretization and the nodal point integration method, with all properties and state variables being defined at the center of an interior grid cell. This introduced two issues when using both codes for aquifer contaminant transport modeling. First, the Darcy velocity field computed by FACT had to be translated into a form compatible for input to PORFLOW. The FACT velocity field is defined at element vertices, whereas PORFLOW requires flux across cell faces. For the 2000 ELLWF PA, PORFLOW cell face flux was computed in a

GSA/PORFLOW model was an equally valid representation of GW flow in the GSA compared to GSA/FACT as well as a suitable new baseline for future PAs.

The 2004 GSA/PORFLOW model supported PA2008 (WSRC, 2008) and related SAs and was reviewed by the DOE LFRG in 2008. Considering the significant amount of field data acquired since the mid-1990s and maturation of optimization software available for model calibration, the LFRG "recommended that the model be reevaluated with more current data and recalibrated using automated inverse procedures" (Bagwell and Flach, 2016; DOE LFRG, 2008). In response to these reviews and in preparation for the current ELLWF PA revision, Bagwell and Flach (2016) developed a program and execution plan for GSA GW flow modeling with the following objectives:

- Reevaluate the GSA flow model with selected new data acquired since 1997.
- Recalibrate the GSA flow model using automated inverse modeling procedures.
- Estimate uncertainty in model input and output parameters.

Under the program plan, PORFLOW (ACRi, 2018) was retained as the GW flow simulation code of choice, and the PEST code (http://www.pesthomepage.org) was adopted for model calibration/optimization/inverse modeling (Flach, 2015a). At the request of SRNL, PORFLOW Ver. 6.42.3 was upgraded to incorporate a combined recharge/drain boundary condition option [originally developed by Hamm and Aleman (2000)] as well as a velocity correction option for nonorthogonal computational meshes (Flach, 2015a; 2015b). PORFLOW Ver. 6.42.3 and PEST Ver. 13.6 were placed under Software QA control (Whiteside, 2016a; 2016b). PORFLOW 6.42.4 was subsequently used during the GSA/PORFLOW flow model update and was similarly placed under QA control (Whiteside, 2017b).

GSA_2016 Flow Model

During 2016 and 2017, the 2004 GSA/PORFLOW model was substantially revised to incorporate new hydrostratigraphic surfaces and updated well-water level calibration targets current through late 2014 (Bagwell et al., 2017; Bagwell and Flach, 2016). The revised model, referred to as GSA_2016, is documented in detail by Flach et al. (2017). In addition, GSA_2016 switched to semi-automated model calibration using the PEST mathematical optimization code (Flach, 2015a). Earlier versions of the GSA flow model had been manually calibrated to field data using an ad hoc approach, which was commonplace during that GW modeling era. GSA_2016 also addressed issues raised by the DOE LFRG in 2008 as described above. The recommended version of GSA_2016[9] exhibited good agreement with well-water level, stream baseflow, and seepline data, but was not comprehensively validated against contaminant plume data in the GSA. Flach et al. (2017) also discuss model uncertainty and presents 95% confidence limits for the GSA_2016

two-step process. An initial face flux was computed from FACT as an average of the normal components of Darcy velocity at the four corners. The derived flux field was subsequently perturbed to force rigorous mass conservation on a cell-by-cell basis. The undocumented process was non-unique and could introduce significant artifacts into the final flux field. Second, the different mesh numbering systems used by the two codes led to errors in defining source zones (Flach, 2004).

[9] The recommended version of GSA_2016 was the optimization case identified by Flach et al. (2017) as PEST.51/GSA_2016.LW (layer-cake *K* field and weighted calibration targets).

model input parameters optimized by PEST. Additional details on the revisions and updates to the GSA/PORFLOW model are described below.

- **Calibration Targets:** Hiergesell et al. (2015) developed new well-water level targets for GSA GW flow model calibration and provided information to enable nonuniform weighting of these targets in the PEST optimization function using statistical uncertainty and spatial de-clustering concepts. The calibration targets were developed using data from 2004 through August 2014, a period of relatively stable hydrologic conditions that followed major remediation activities such as pump-treat-reinjection at the F- and H-Area Seepage Basins. Average water levels were defined in 283 UAZ, 275 LAZ, and 81 GAU wells, for a total of 639 calibration targets. The standard error of the mean was computed for each target as a potential weighting factor in optimization software to be used for model calibration. Similarly, a polygonal de-clustering method was used to generate an additional weighting factor inversely proportional to spatial data density.
- **Computational Grid:** Hydrostratigraphic surfaces were updated based on the work by Bagwell et al. (2017). Flach et al. (2017; Appendix A) provide plots of the topographic and hydrostratigraphic surfaces used to build the PORFLOW computational grid.
- **Hydraulic Conductivity Field:** The vertical hydraulic conductivity of the GCU was increased from 1.0E-05 to 7.5E-05 (0.75E-04) ft d^{-1} to achieve better agreement with hydraulic head targets and to honor characterization data (Flach and Harris, 1999) and regional GW flow modeling (Flach et al., 1999) that indicate $K_v \cong$ 1.0E-04 ft d^{-1} for the GCU (note that the vertical hydraulic conductivity of the GCU was subsequently changed back to 1.0E-05 ft d^{-1} in GSA_2018 as described in Section 3.5.2.8). The UAZ was subdivided into the TZ and a combined A and AA zone (AAA) using terminology by Flach et al. (1999). Figure 3-8 is an example cross-section running north-south through E-Area showing GSA_2016 hydrostratigraphy. Separate calibration adjustments were applied independently to the TZ and AAA zones. As defined, the TZ coincides with the first three UAZ grid layers above the TCCZ, while the AAA occupies the remainder of the UAZ. Calibration of the hydraulic conductivity field was aided by the PEST code using updated hydraulic head targets reported by Hiergesell et al. (2015).
- **Boundary Conditions:** A combined recharge/drain condition was applied to the top boundary using a new option in PORFLOW Ver. 6.42.3 described by Flach (2015a). The equivalent condition was applied in the 2004 GSA/PORFLOW model in an indirect, less computationally efficient, manner. The local recharge rate was set to 15 inches per year based on the recharge estimates cited by Flach et al. (1999). The general head boundary that was applied to the bottom of the 2004 GSA/PORFLOW model used an unintended reference head around 195 feet. GSA_2016 uses the intended 180 feet. Side boundary conditions were not altered (see Section 3.5.2 and Figure 3-7).
- **Velocity Field:** Velocity components are computed using a new PORFLOW option described by Flach (2015b) which corrects for non-orthogonality in the computational mesh.

- **Vadose Zone:** Although the focus of the model simulation is saturated GW flow, the GSA flow model domain continues to include the VZ to enable varying seepline locations and recharge between and within optimization case iterations. The pseudo-soil characteristic curves used in the GSA_2016 model are listed below. Relative permeability is assumed to equal one for the purpose of transmitting water from the ground surface to the water table.

```
MULTiphase properties: (S,P) from TABLe with 4 sets:
0.4          10
0.7          5
0.9          2
1            0
MULTIphase properties: (S,COND) from TABLe with 4 sets:
0.4          1
0.6          1
0.8          1
1            1
```

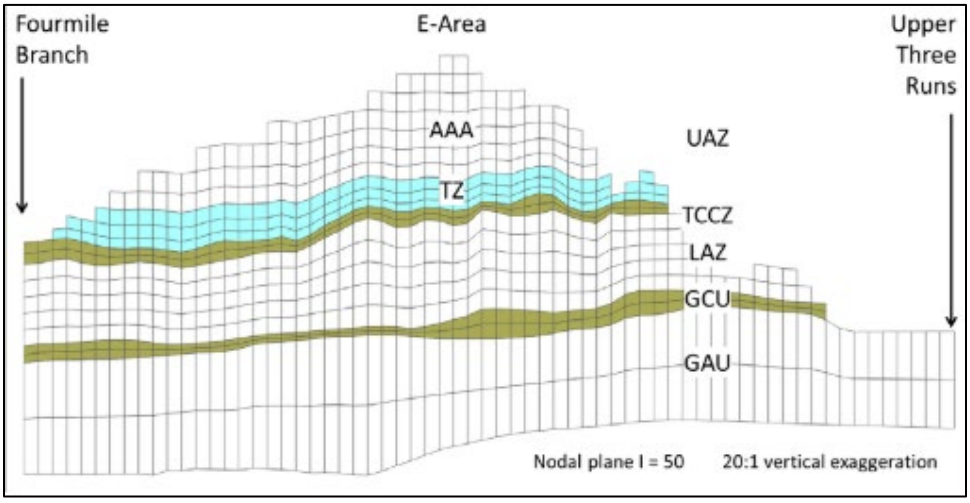

Figure 3-8. Stratigraphy and Permeability Zones in GSA_2016 Computational Grid (Flach et al., 2017)

GSA_2018 Flow Model

Hydraulic head residuals (simulated hydraulic head minus measured head) were observed to be biased low around the F- and H-Area seepage basins in the GSA_2016 flow model (Flach et al., 2017; see Figure 7-6). To address this, in 2018, Flach (2019) added another calibration zone (FHbasins2; see Figure 3-9) to the GSA_2016 flow model to help decrease hydraulic head residuals. In addition, the GSA_2016 flow model was further refined by Flach (2019) to incorporate updates to model calibration targets, the closure of H-Area Ash Basin, the construction of ELLWF ST operational stormwater runoff covers, and plume information from the MWMF and LLRWDF.

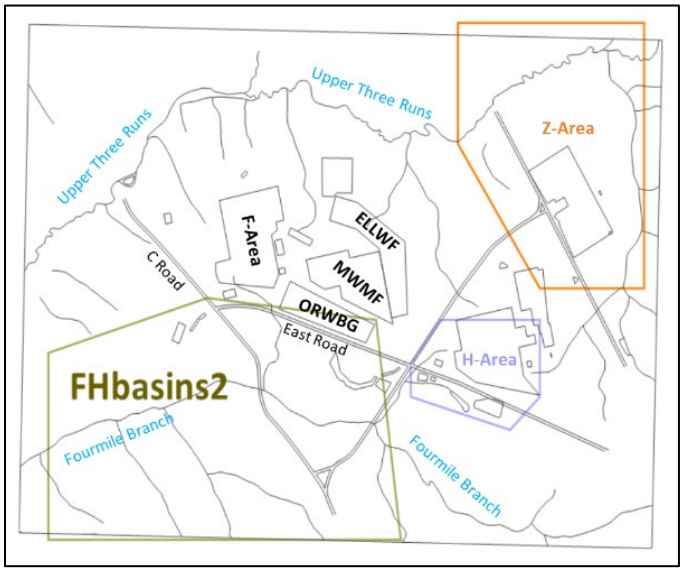

Figure 3-9. Conductivity Zone "FHbasins2" added to GSA_2018 Calibration

Updates to the GSA_2016 flow model (Flach, 2019) included the following:

- Wohlwend (2018) extended the data averaging period for well water levels from 2004-August 2014 to 2004-March 2018, thereby increasing the number of model calibration targets from 639 to 711. Near Z-Area, the number of target well locations increased from 3 in the UAZ and 7 in the LAZ to 6 and 11, respectively, to the benefit of the Saltstone Disposal Facility PA (Savannah River Remediation, 2020).
- As shown in Figure 3-10, the H-Area Ash Basin is no longer in service, and thus is no longer a source of enhanced infiltration in the GW flow model. Conversely, operational covers over closed STs in the ELLWF reduce local infiltration. These changes in the field correspond to boundary condition changes in the GSA flow model.

Figure 3-10. Annotated Aerial Photo Showing the Former H-Area Ash Basin and E-Area Slit Trench Operational Stormwater Runoff Covers (Flach, 2019)

- Multiple-depth Cone Penetration Testing (CPT) at 10 locations near ELLWF (Figure 3-11) also delineated tritium (H-3) and volatile organic compound (VOC) plumes presumed to emanate from MWMF/LLRWDF and ELLWF (Kubilius and Joyce, 2018). Figure 3-12 lists species concentrations as a function of depth and elevation. Intervals of elevated concentration are highlighted with darker shading. The conceptual model (Figure 3-12) is that deeper, mixed H-3 and VOC, plumes originate from the MWMF while shallower, H-3 only, plumes are associated with the ELLWF. This enabled simulated GW path lines to be compared to the MWMF plume information to calibrate and/or validate the flow model.

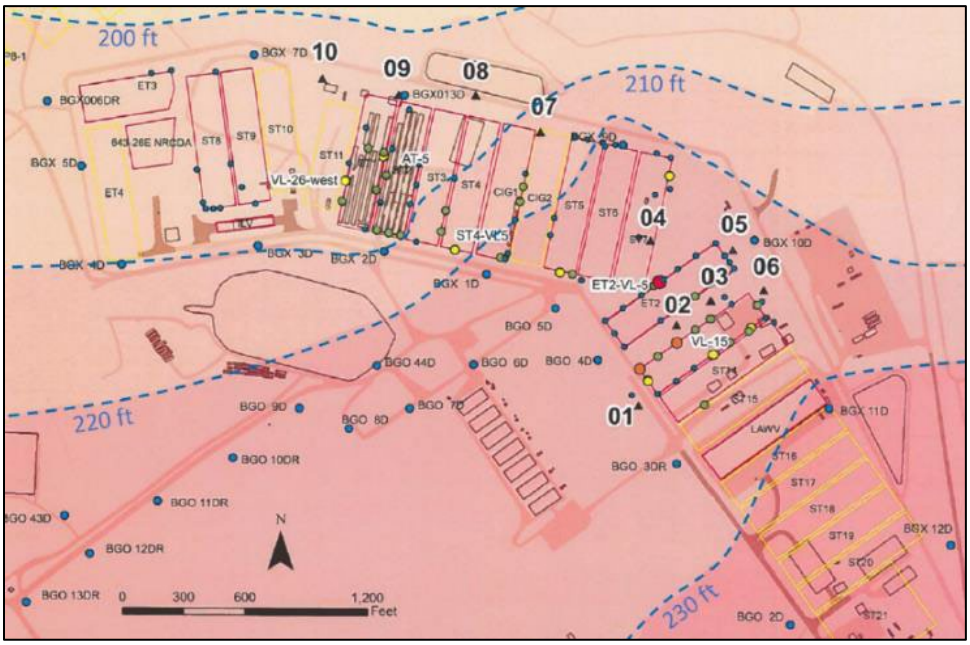

Figure 3-11. Cone Penetration Testing Locations 01 to 10 and Water Table Contours (Flach, 2019)

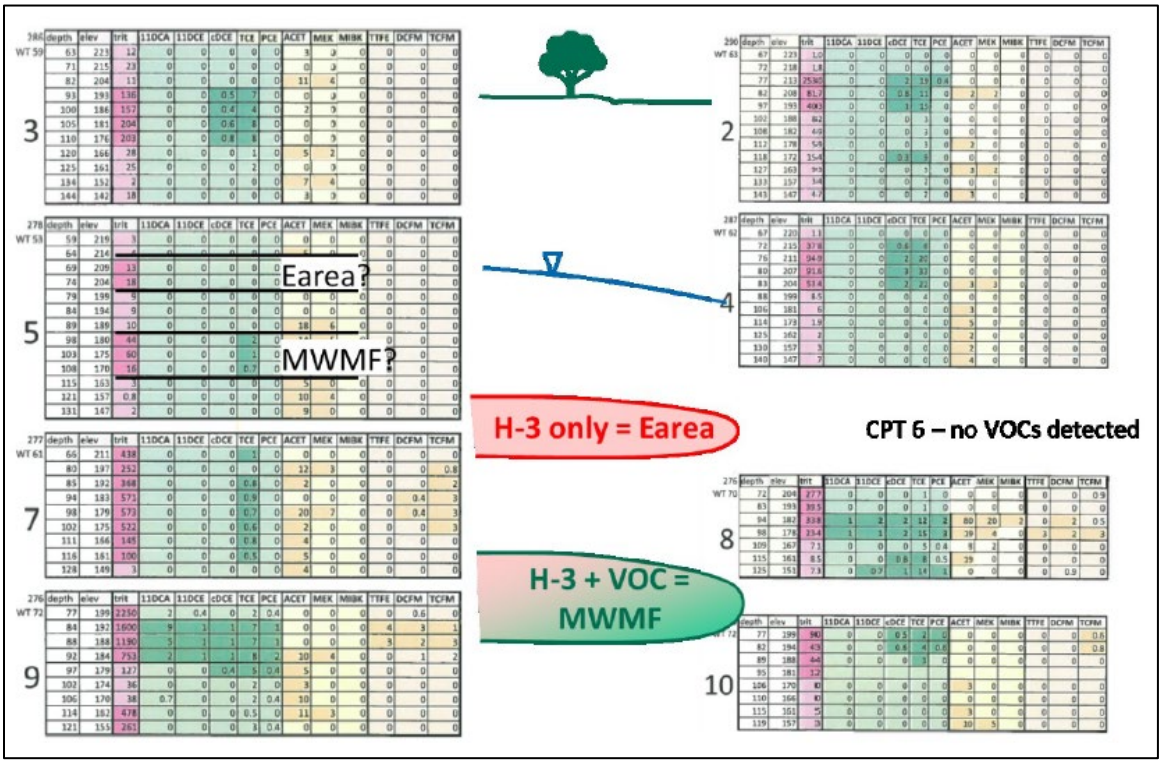

Figure 3-12. E-Area Cone Penetration Testing Data and Plumes Conceptual Model (Flach, 2019)

GSA_2021 Flow Model

During model implementation in this PA, several upgrades to the GSA_2018 model were found to be needed. The updated features include: (1) improved vertical flow within the VZ; (2) sharper focus on optimization within E-Area via increased weighting of E-Area head targets; (3) improved moisture retention curves to address the vertical flow field in the VZ; and (4) reduction in the vertical-to-horizontal hydraulic anisotropic ratios. This updated version is referred to as the GSA_2021 flow model and is used in this PA.

3.5.2.2. GSA_2016 Flow Model Initial Condition Simulations

To generate initial conditions for PEST optimization, Flach et al. (2017) crudely calibrated the GSA_2016 flow model framework to the updated water-level observations for two conceptual models of the hydraulic conductivity (*K*) field: a traditional "Layer-cake" concept and a "Heterogeneous" concept. The traditional Layer-cake concept views hydraulic conductivity as uniform within hydrostratigraphic units (e.g., LAZ, TCCZ, GAU, etc.). The Heterogeneous concept, which was adopted for the GSA/FACT and 2004 GSA/PORFLOW flow models, views hydraulic conductivity as heterogeneous within hydrostratigraphic units, as defined by mud fraction and permeability data using the methods described by Flach and Harris (1999). Flach et al. (2017) denoted these simulation cases as PEST.0L (Layer-cake) and PEST.0H (Heterogeneous). The purpose of this 2016-2017 analysis was to choose a preferred *K* field conceptual model for GSA_2016 and subsequent versions that minimized hydraulic head residuals.

The hydraulic conductivity field for the PEST.0L Layer-cake model was defined through direct specification of the horizontal (K_h) and vertical hydraulic conductivity (K_v) in each hydrostratigraphic zone as indicated by Table 3-10. K_h for the GAU (38 ft d^{-1}) was based on multiple well pumping test data and earlier GSA models (Flach and Harris, 1999). K_v for the GCU (1.0E-4 ft d^{-1}) was based on multiple well-pumping-test and laboratory permeability data summarized by Flach and Harris (1999) and well-supported by the CKLP reactor regional GW flow model (Flach et al., 1999). Selection of K_h in the remaining aquifer zones (LAZ, TZ, AAA) and K_v in the TCCZ was guided by the earlier GSA models, preliminary application of the PEST code, and visual observation of residuals between simulated hydraulic head and measured well water level targets. The remaining conductivities were defined based on assumed anisotropy ratios of 100, 10, and 30 in the GAU, GCU, and remaining zones, respectively. GW flow simulations are mildly sensitive to these values. Anisotropy is typically assumed to lie within the range $1 = 10^0$ to $1000 = 10^3$ (Anderson and Woessner, 1992, p. 70) and the geometric midpoint of this range is $10^{1.5} \approx 30$. Nichols and Butcher (2020) indicate that anisotropy ratios for Savannah River sediments are of this order of magnitude. An anisotropy ratio higher than 30 is used in the GAU because of its thicker model layers (such that a greater range of heterogeneity may be encountered). A lower ratio is assumed for the GCU because the unit is believed to be relatively uniform compared to other hydrostratigraphic units (as evidenced by its hydraulic competence).

Table 3-10. Calibration Parameters for GSA_2016 PEST.0L Case

Calibration Parameter	Value (ft d^{-1})
Horizontal hydraulic conductivity of GAU, <GAUkh>	38
Vertical hydraulic conductivity of GAU, <GAUkv>	0.38
Horizontal hydraulic conductivity of GCU, <GCUkh>	1.0E-03
Vertical hydraulic conductivity of GCU, <GCUkv>	1.0E-04
Horizontal hydraulic conductivity of LAZ, <LAZkh>	12
Vertical hydraulic conductivity of LAZ, <LAZkv>	0.4
Horizontal hydraulic conductivity of TCCZ, <TCCZkh>	0.18
Vertical hydraulic conductivity of TCCZ, <TCCZkv>	0.006
Horizontal hydraulic conductivity of TZ, <TZkh>	9
Vertical hydraulic conductivity of TZ, <TZkv>	0.3
Horizontal hydraulic conductivity of AAA, <AAAkh>	9
Vertical hydraulic conductivity of AAA, <AAAkv>	0.3

Simulation results for the PEST.0L case are summarized by Figure 3-13, where a positive residual value indicates the simulated head is above the measured head. Although not fully calibrated, the PEST.0L case generally produced good agreement with monitoring data. However, the model underpredicted hydraulic conductivity significantly in H-Area and moderately in Z-Area, indicating consideration of further calibration.

The hydraulic conductivity field for the PEST.0H Heterogeneous model was defined through direct specification in the GAU and GCU, and multiplication factors to the baseline heterogeneous K field in the overlying hydrostratigraphic units (Table 3-11). The baseline K field was adopted from the GSA/FACT and 2004 GSA/PORFLOW models (Flach, 2004; Flach and Harris, 1999). A multiplication factor of 1.4 was selected based on visual inspection of hydraulic head residuals. Minimum and maximum value limits were also placed on K to avoid extreme values from

small-scale characterization data that are not likely to reflect conditions over larger scales (Table 3-12). The chosen limits generally create a one-order of magnitude range around the nominal values in Table 3-10. One notable exception is the AAA zone. Simulation results (not shown) were similar to the PEST.0L case (Flach et al., 2017; Figure 4-2). Again, simulated head was biased low in H-Area and Z-Area, motivating further optimization of the *K* field. Flach et al. (2017) provides X-Y plots of the 21 vertical grid layers comprising the PEST.0H conductivity field.

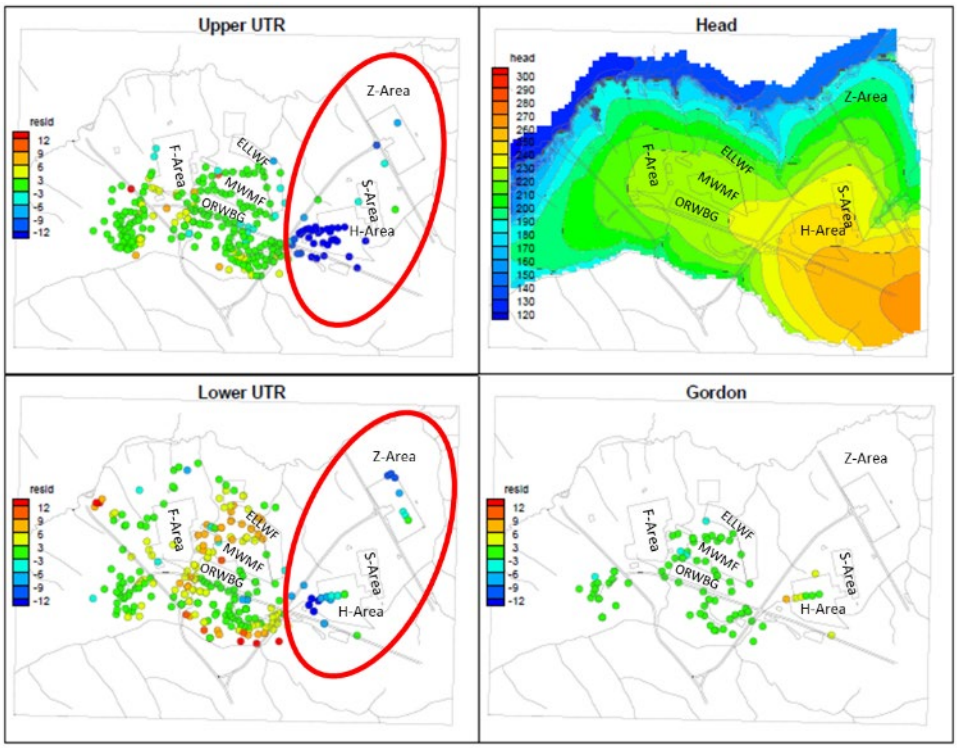

Figure 3-13. Hydraulic Head Residuals and Water Table Surface for Layer-Cake *K* Field (PEST.0L Case)

Table 3-11. Calibration Parameters for GSA_2016 PEST.0H Case

Calibration Parameter	Value
Horizontal hydraulic conductivity of GAU, <GAUkh>	38 ft d^{-1}
Vertical hydraulic conductivity of GAU, <GAUkv>	0.38 ft d^{-1}
Horizontal hydraulic conductivity of GCU, <GCUkh>	1.0E-03 ft d^{-1}
Vertical hydraulic conductivity of GCU, <GCUkv>	1.0E-04 ft d^{-1}
Horizontal hydraulic conductivity multiplier for LAZ, <LAZkhf>	1.4
Vertical hydraulic conductivity multiplier for LAZ, <LAZkvf>	1.4
Horizontal hydraulic conductivity multiplier for TCCZ, <TCCZkhf>	1.4
Vertical hydraulic conductivity multiplier for TCCZ, <TCCZkvf>	1.4
Horizontal hydraulic conductivity multiplier for TZ, <TZkhf>	1.4
Vertical hydraulic conductivity multiplier for TZ, <TZkvf>	1.4
Horizontal hydraulic conductivity multiplier for AAA, <AAAkhf>	1.4
Vertical hydraulic conductivity multiplier for AAA, <AAAkvf>	1.4

Table 3-12. Hydraulic Conductivity Limits for Heterogeneous *K* field

Limits (ft d^{-1})	K_h min	K_h max	K_v min	K_v max
LAZ	3.8	38	0.13	1.3
TCCZ	0.057	1.8	0.0019	0.06
TZ	3.2	32	0.11	1.1
AAA	0.1	3.2	0.0033	0.11

A few examples are displayed in Figure 3-14. Similarly, Figure 3-15 and Figure 3-16 are representative north-south vertical cross sections of the final calibrated *K* field employed in the 2004 GSA/PORFLOW model, which further illustrate the horizontal and vertical hydraulic conductivity fields, respectively, for the Heterogeneous concept.

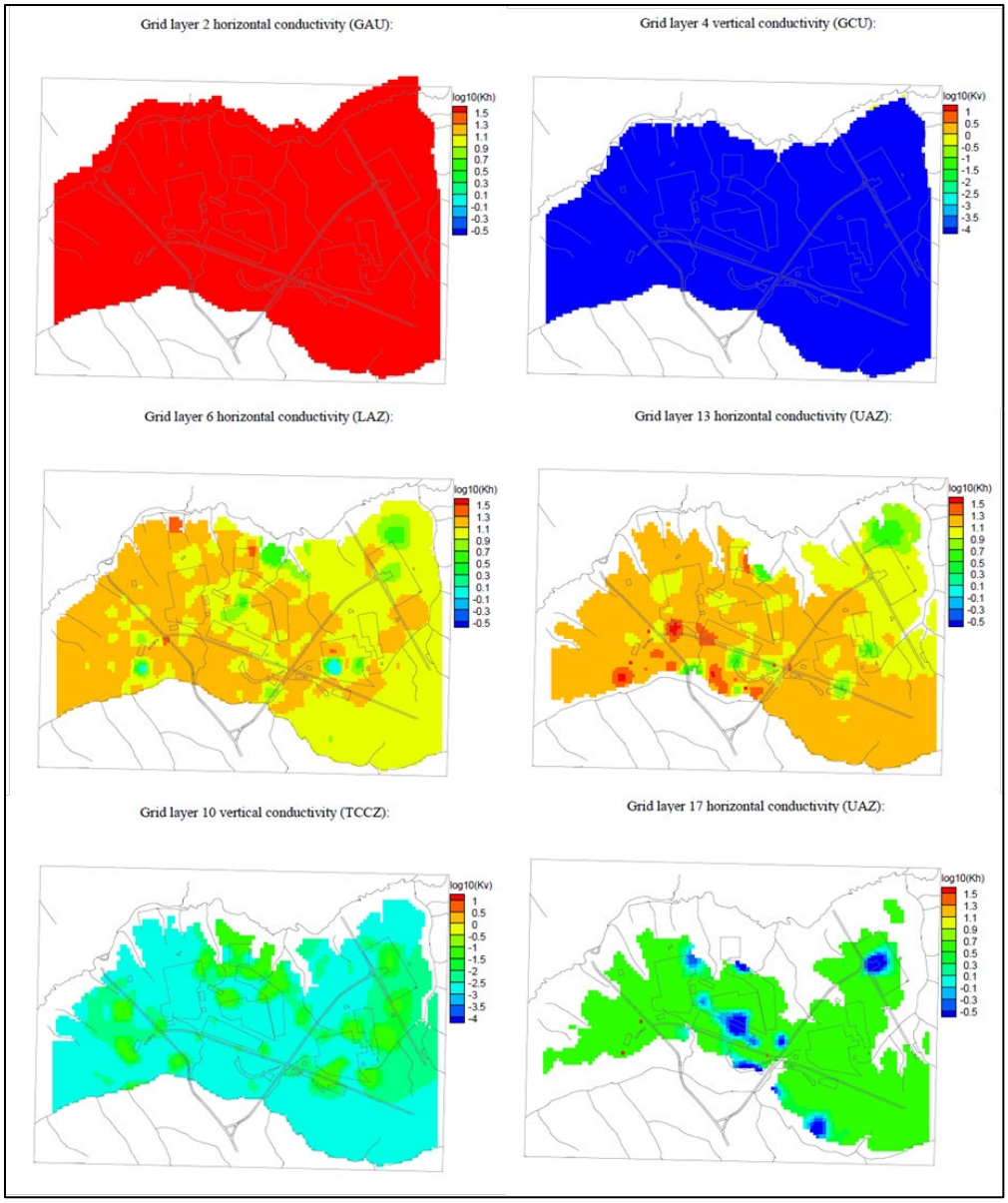

Figure 3-14. Example Heterogeneous Hydraulic Conductivity Fields (X-Y) for Various Vertical Grid Layers in the GSA_2016 Model (PEST.0H Case)

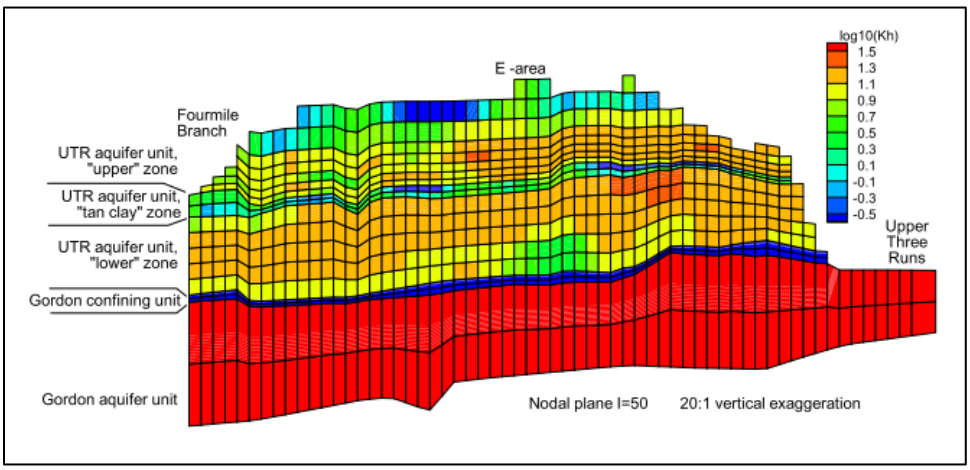

Figure 3-15. North-South Cross-Sectional View of Horizontal Hydraulic Conductivity Field Near E-Area in 2004 GSA/PORFLOW Model (Flach, 2004)

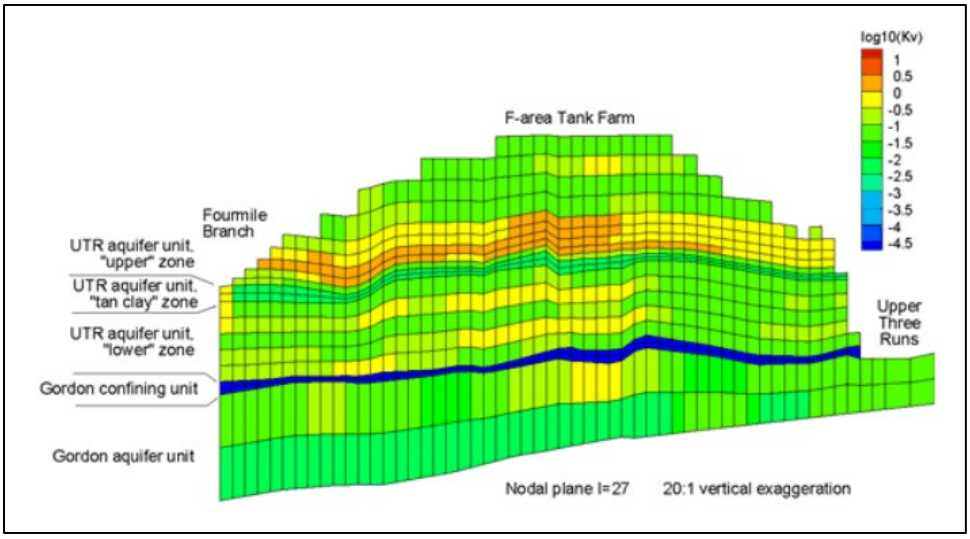

Figure 3-16. North-South Cross-Sectional View of Vertical Hydraulic Conductivity Field Near F-Area Tank Farm in 2004 GSA/PORFLOW Model (Savannah River Remediation, 2009)

3.5.2.3. GSA_2016 Flow Model Calibration Approach

PEST offers four modes of operation: "estimation," "predictive analysis," "regularization," and "pareto." The basic "estimation" mode was chosen for GSA_2016 calibration.[10] The "estimation" mode uses the Gauss-Marquardt-Levenberg method to iteratively adjust model parameters in a manner that ultimately minimizes a user-defined "objective function" (Watermark Numerical

[10] Use of the "regularization" mode to conduct "highly parameterized inversion" (Watermark Numerical Computing, 2016, Section 3.3.3) was considered, but rejected because of PORFLOW license and computing resource limitations. "Highly parameterized inversion" using the "regularization" mode would have involved many more parameters and required days if not weeks of wall-clock time for each PEST run (Flach et al., 2017). The "predictive analysis" mode is designed to be used after a successful "estimation" or "regularization" run to quantify uncertainty in a user-designated model output or "prediction" (Watermark Numerical Computing, 2016, Section 3.3.4). The "pareto" mode is an advanced estimation mode involving multiple, competing, optimization functions (Watermark Numerical Computing, 2016, Section 3.3.5).

Computing, 2016, Section 3.3.2 and 3.7). Estimation of these optimal parameter values, parameter estimation in short, is also known as inverse modeling. Because no Tikhonov regularization (or similar scheme) is applied in the "estimation" mode, PEST requires a mathematically well-posed inverse problem. In layman's terms, the number and type of model output targets (e.g., measured well-water levels) must be sufficient such that a unique set of parameter values minimizes the objective function. For example, the number of calibration targets (knowns) must equal or exceed the number of parameters to be estimated (unknowns).

PEST Objective Function and Weights

The basic form of the objective (cost) function Φ minimized using the PEST "estimation" mode is:

$$\Phi = \sum_i \left(w_i r_i \right)^2 \qquad \text{Eq. (3-2)}$$

where:

r_i i^{th} model - target residual
w_i Weight given to i^{th} residual

Thus, PEST "estimation" constitutes a weighted least-squares optimization. "Unweighted" optimization refers to the special case of uniform weights, or equivalently:

$$w_i = 1 \qquad \text{Eq. (3-3)}$$

for all i. Otherwise, the optimization is "Weighted." Weighting is used to give more or less emphasis to an individual target compared to its peers, and is generally recommended in parameter estimation practice (Doherty and Hunt, 2010, p. 14). Residuals are commonly given weights that are inversely proportional to their uncertainty, for example:

$$w_i^u = \frac{1}{\left(s_e \right)_i} = \frac{\sqrt{n}}{s_i} \qquad \text{Eq. (3-4)}$$

where:

s_e Standard error of the mean for a sample mean
n Number of measurements
s Standard deviation of the population (transient well record)
i Indicates a particular calibration target

The presence of s_i in the denominator gives less weight to targets exhibiting more variability, and the presence of $\sqrt{n}$ in the numerator gives more weight to targets with more measurements (longer record). Hiergesell et al. (2015; Appendix C) provide values of s_e for the GSA_2016 flow model updated targets.

Weights can also be used to deal with data clustering/sparsity within and between hydrostratigraphic units (HSUs). "Geographic" weights, w_i^g, are proposed by Hiergesell et al.

(2015; Appendix D). These weighting factors account for differences in data density across the GSA footprint. Another consideration is the data density between HSUs. Equal weight can be given to each unit by defining weighting factors that are the inverses of the fractions of targets within each HSU:

$$w^{GAU} = \frac{639}{81} = 7.9 \quad \text{Eq. (3-5)}$$

$$w^{LAZ} = \frac{639}{275} = 2.3 \quad \text{Eq. (3-6)}$$

$$w^{UAZ} = \frac{639}{283} = 2.3 \quad \text{Eq. (3-7)}$$

For GSA_2016 flow model calibration using weighted PEST "estimation," the effects of data uncertainty (w_i^u) and spatial density (w_i^g) are combined by defining residual weights as:

$$w_i = w_i^u w_i^g w^{HSU} \quad \text{Eq. (3-8)}$$

where HSU = GAU, LAZ, or UAZ (TZ + AAA) depending on the location of the target. Weights were also limited to a maximum value of 100, approximately 10 times the median value, to avoid excessive emphasis on isolated locations that may occur using the polygonal de-clustering algorithm developed by Hiergesell et al. (2015). Flach et al. (2017; Appendix C) list hydraulic head targets provided by Hiergesell et al. (2015) and associated weights computed by Eq. (3-8).[11] One well, "ZBG 1A," is suspected to reflect perched water, or water held up in the well sump, and was ignored during PEST "estimation" through an assigned weight of zero.

The objective function Φ differs by orders of magnitude for unweighted [Eq. (3-3)] and weighted [Eq. (3-8)] optimization, and relative goodness-of-fit cannot be directly assessed by comparing Φ for calibration runs using different weighting schemes. However, a more meaningful comparison can be achieved by normalizing the objective function for weighted optimization by the sum of the squared weights:

$$\Phi_{normalized} = \frac{\sum_i \left(w_i r_i\right)^2}{\sum_i \left(w_i\right)^2} \quad \text{Eq. (3-9)}$$

[11] Targets values are taken as the "Mean" values reported by Hiergesell et al. (2015). The optimization function weights are defined by Eq. (3-8) subject to a maximum value of 100, with the exception of target "o281" (Well ZBG 1A). This well is suspected to reflect perched water, or water held up in the well sump, and was effectively removed from the PEST objective function by setting its weight to zero.

This normalized metric is similar in magnitude regardless of weighting, enabling approximate comparisons of unweighted versus weighted optimization results. For the weights listed by Flach et al. (2017; Appendix C), $1/\sum_i (w_i)^2$ = 6.89E-4.

PEST Parameterization Strategy

The hydraulic properties of the GAU and GCU are moderately certain based on data and previous modeling studies. Therefore, these two HSUs were not subjected to PEST optimization to improve how well-posed they were mathematically and to reduce wall-clock time (PEST computational load is roughly proportional to the number of parameters to be estimated). However, the UAZ was subdivided into TZ and AAA zones as noted in Section 3.5.2.1, based on the work by Flach et al. (1999) and preliminary model calibration. The TZ zone is approximately 30 feet thick. The additional TZ and AAA HSUs increase the number of conductivity parameters that are candidates for PEST estimation.

Recharge was not estimated to limit calibration targets to well-water levels and to avoid mathematical non-uniqueness. Recharge and hydraulic conductivity cannot be independently estimated unless stream baseflow measurements are introduced to the set of calibration targets, because the former parameters are correlated with respect to hydraulic head. Figure 3-17 illustrates this general concept using two simple GW flow problems as examples; also indicated in Figure 3-17 are the corresponding analytic solutions. Note that the flow rate (Q) and conductivity (K) parameters appear as the quotient Q/K. Therefore, only the quotient can be estimated using hydraulic head (h) data alone as calibration targets. In this study, recharge is fixed so that conductivity can be estimated from head targets through the quotient. Omitting stream baseflows from the model calibration process also has the advantage of making these data available for post-calibration model validation. Furthermore, limiting the number of parameters to be estimated significantly reduces PEST runtime, enabling consideration of more parameter sets.

Flach et al. (2017; Table 5-1) provide a complete listing of the two initial condition PEST cases (PEST.0L and PEST.0H; Section 3.5.2.2) and a progression of 53 optimization/calibration PEST cases. Each round of PEST optimization generally considered a two-by-two matrix of four cases: Layer-cake vs. Heterogeneous K field and Unweighted vs. Weighted targets. Although four cases were defined for most rounds, some optimization cases were not run. Every optimization case (PEST.1 through PEST.53) included global multipliers to the LAZ, TCCZ, TZ, and AAA baseline K_h and K_v fields, whether Layer-cake or Heterogeneous. These four global multipliers were denoted g01 (LAZ), g02 (TCCZ), g03 (TZ) and g04 (AAA) and were effectively unconstrained during optimization. For baseline optimization cases PEST.1 through PEST.4, only the four global, zonal multipliers (g01, g02, g03, and g04) were allowed to change from the global specification. For optimization cases PEST.5 through PEST.53 on the other hand, in addition to optimization of the four global multipliers, hydraulic conductivities for the LAZ, TCCZ, TZ, and AAA were also allowed to deviate from the global specification locally (e.g., H-Area, S-Area, and/or Z-Area) within an elliptical or polygonal region having variable location, orientation, size, and shape.

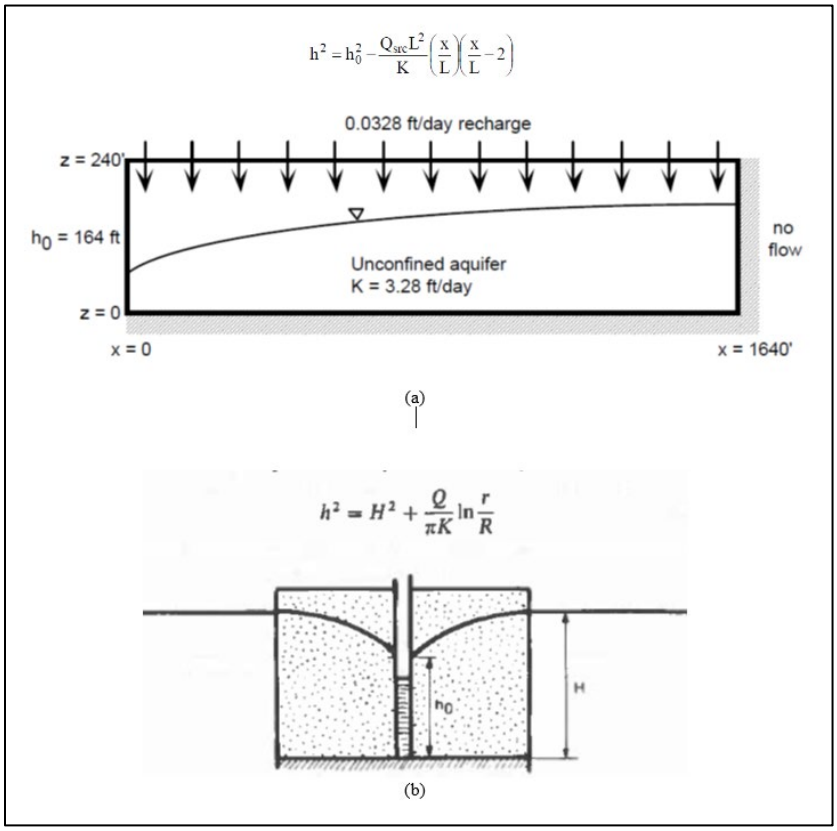

Figure 3-17. Groundwater Flow Examples Highlighting Correlation between Flow Rate and Hydraulic Conductivity Parameters: (a) Unconfined Two-Dimensional (2-D) Flow in Unconfined Aquifer with Recharge (Aleman, 2007; Figure 4.2.2); (b) Steady-State Flow to Well in Unconfined Aquifer (de Marsily, 1986; Figure 7.5)

PEST optimization for all cases was conducted using the parallel version of PEST ("ppest") with seven CPUs running up to seven simultaneous model simulations. Table 3-13 provides a truncated listing of the initial condition and optimization/calibration PEST cases. Included in the truncated listing are the four baseline optimization cases (PEST.1 through PEST.4) and the preferred GSA_2016 optimization case: PEST.51/GSA_2016.LW (Layer-cake *K* Field and Weighted calibration targets).

Table 3-13. Truncated Listing of PEST Initial Condition and Optimization and Calibration Cases for GSA_2016 Flow Model (Flach et al., 2017; Table 5-1)

PEST Case	Base *K* Field	Zonal *K* Adjustments	Zonal *K* Layers	Constraints [1]	Targets
0L	Layer cake	None	N/A	N/A	N/A
0H	Heterogeneous	None	N/A	N/A	N/A
1	Layer cake	None	N/A	N/A	Unweighted
2	Heterogeneous	None	N/A	N/A	Unweighted
3	Layer cake	None	N/A	N/A	Weighted
4	Heterogeneous	None	N/A	N/A	Weighted
47	Layer cake	HS&Zarea.ply	LAZ,TCCZ, TZ, AAA	kGCU = 0.75e-4 + vadoseFlag off + one order of magnitude + 4 iterations	Unweighted
51	Layer cake	HS&Zarea.ply	LAZ,TCCZ, TZ, AAA	kGCU = 0.75e-4 + vadoseFlag off + one order of magnitude + 4 iterations	Weighted
52	Heterogeneous	HS&Zarea.ply	LAZ,TCCZ, TZ, AAA	kGCU = 0.75e-4 + vadoseFlag off + one order of magnitude + 4 iterations	Unweighted
53	Heterogeneous	HS&Zarea.ply	LAZ,TCCZ, TZ, AAA	kGCU = 0.75e-4 + vadoseFlag off + one order of magnitude + 4 iterations	Weighted

Notes:

PEST Case 51 is highlighted in orange to indicate that it is the baseline case GSA_2016.

[1] The units of hydraulic conductivity (kGCU) are ft d^{-1}.

3.5.2.4. GSA_2016 Flow Model Calibration Results

Optimization results for PEST.3 (Layer-cake *K* Field and Weighted calibration targets) are summarized by Figure 3-18 and Table 3-14. In Table 3-14, "Net Kh" and "Net Kv" for the Layer-cake case denote net conductivities after multiplying the "Base Kh" and "Base Kv" values by the global multipliers (*g*01 to *g*04) indicated in the "PEST.3a" column. The four rightmost columns represent an independent calculation of average conductivity, where "Kv avg" is computed from the average "log10" value (geometric averaging). "Ratio" is the ratio of "Kh avg" to "Kv avg". Although the local anisotropy ratio is nominally 30X in the Upper Three Runs aquifer, the average ratio can deviate from 30 because of maximum and/or minimum conductivity cutoffs and spatial averaging.

Above the capillary fringe adjoining the water table, the hydraulic head gradient tends to be close to 1.0 (e.g., Nimmo et al., 2002, Figure 15; Wilson, 1980, Figure 2), in which case Darcy velocity, *U*, and hydraulic conductivity, *K*, are approximately equal according to Darcy's Law. Therefore:

$$K = U = 15\frac{in}{yr} = 0.00342\frac{ft}{d} = 1.2\times10^{-6}\frac{cm}{s} \qquad \text{Eq. (3-10)}$$

is approximately the minimum saturated conductivity value that will allow the AAA zone to accept 15 inches/year of surface infiltration.

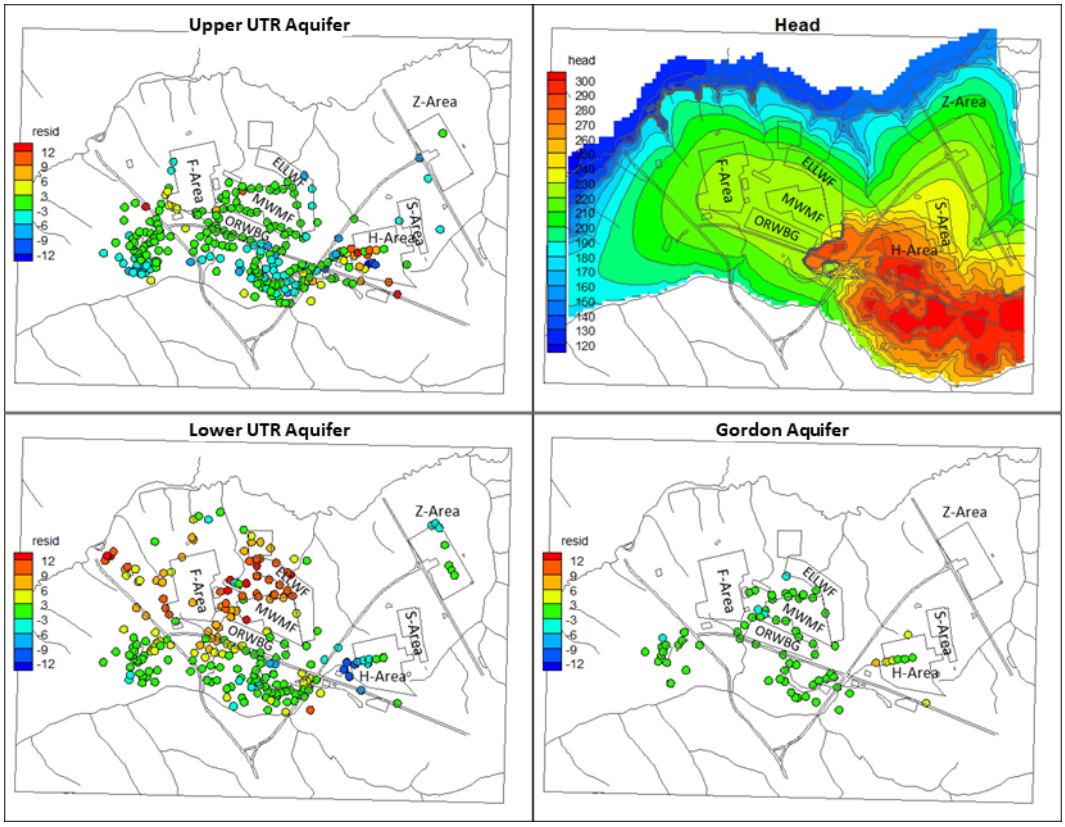

Note: A positive residual value indicates the simulated head is above the measured head.

Figure 3-18. Hydraulic Head Residuals and Water Table Surface for the PEST.3 Case

Table 3-14. Hydraulic Conductivity Summary for PEST.3 Case (Flach et al., 2017)

Param.	Unit	Region	Base K_h (ft d^{-1})	Base K_v (ft d^{-1})	PEST.3a	Net K_h (ft d^{-1})	Net K_v (ft d^{-1})	K_h (cm s^{-1})	K_v (cm s^{-1})	K_h avg (ft d^{-1})	K_v avg (ft d^{-1})	log10 K_v	K_h/K_v Ratio
Phi	--	--	--	--	1.17E+07	--	--	--	--	--	--	--	--
g01	LAZ	Global	12	0.4	0.723788	8.7	0.29	3.1E-03	1.0E-04	**8.7**	0.290	-0.5383	30x
g02	TCCZ	Global	0.18	0.006	17.6766	3.2	0.11	1.1E-03	3.7E-05	3.2	**0.106**	-0.9744	30x
g03	TZ	Global	9	0.3	1.06805	9.6	0.32	3.4E-03	1.1E-04	**9.6**	0.320	-0.4943	30x
g04	AAA	Global	9	0.3	1.08E-02	0.10	0.0032	3.4E-05	1.1E-06	**0.10**	0.0033	-2.488	30x
h01	TCCZ	Local	--	--	1	3.2	0.11	1.1E-03	3.7E-05	--	--	--	--
h02	TZ	Local	--	--	1	9.6	0.32	3.4E-03	1.1E-04	--	--	--	--
h03	AAA	Local	--	--	1	0.10	0.0032	3.4E-05	1.1E-06	--	--	--	--

Note: Highlighting is used within a parameter grouping (Column 1) to separate out hydrostratigraphic units (Column 2).

In all four cases, the optimized vertical conductivity of the AAA is very low, approaching 0.00342 ft d^{-1}. Around H-Area, where the water table resides in the AAA, K near 0.003 ft d^{-1} has the effect of raising the water table significantly compared to lower values of K. However, K approaching 1.0E-06 cm s^{-1} [Eq. (3-10)] is unrealistically low compared to average soil properties compiled by Nichols and Butcher (2020; Table 5-18), which range from approximately 1.0E-05 to 1.0E-04 cm s^{-1} for vertical conductivity. Furthermore, the water table east of H-Area is at or just below the ground surface, which would create wetland conditions inconsistent with casual field observations. The results for PEST.3 (and likewise for PEST.1, 2, and 4; not shown) suggest the need for perturbations to global K settings near H-Area. Alternatively, recharge could be increased near H-Area to achieve higher hydraulic heads. Because H-Area rainfall and topography are like

other areas of the GSA, the hypothesis of higher recharge was deemed less likely than a conductivity perturbation and was not pursued further.

After working through a progression of 53 optimization/calibration cases, PEST.47 (Layer-cake *K* field, unweighted calibration targets), PEST.51 (Layer-cake *K* field, weighted calibration targets), PEST.52 (Heterogeneous *K* field, unweighted calibration targets), and PEST.53 (Heterogeneous *K* field, weighted calibration targets) were accepted as the final round of model calibration. PEST.51 (alternately referred to as GSA_2016.LW, where the suffix LW is shorthand for Layer-cake *K* Field and Weighted calibration targets) resulted in the lowest hydraulic head residuals and was identified by Flach et al. (2017) as the preferred GSA_2016 flow model moving forward (i.e., defined as the Baseline GSA Flow Model at that time). As listed in Table 3-13, PEST.47, 51, 52, and 53 included the following specifications:

- The HSZ-Area polygon was divided into the HS-Area and Z-Area polygons.
- Lower bounds were imposed on the AAA HSU: K_h > 3.0E-04 cm s^{-1} (0.85 ft d^{-1}) and K_v > 1.0E-05 cm s^{-1} (0.028 ft d^{-1}).
- K_v for the GCU (*kGCU*) was varied between 1.0E-05 and 1.0E-04 ft d^{-1} for cases PEST.41-53, rather than being held fixed at 1.0E-04 ft d^{-1} as in prior cases. The optimal *kGCU* was determined to be ~0.75E-04 ft d^{-1}, which was the *kGCU* setting for PERST.51.
- The option to set the VZ hydraulic conductivity (vadoseFlag) to 0.1 ft d^{-1} (Flach, 2004), employed in optimization cases through PEST.40, was determined to be unnecessary following implementation of the implicit recharge/drain boundary condition in PORFLOW Ver. 6.42.3 (and later versions). This option was turned off for PEST.47, 51, 52, and 53 (vadoseFlag off).
- The half-order-of-magnitude constraint 0.3162 < h0# < 3.162 (where # is 1 through 4) was replaced with a one-order-of-magnitude constraint 0.1 < h0# < 10 to allow further adaptation of the hydraulic conductivity field around the H-Area Tank Farm (designated as “one order of magnitude” in Table 3-13).
- Beginning with PEST.21, large positive hydraulic head residuals were observed along Fourmile Branch (FMB), apparently due to an excessively low TCCZ conductivity along FMB. The preferred remedy beginning with PEST.33 was to introduce a new optimization parameter, *j*01, as a lower-bound multiplier applied to conductivity along FMB within 15 feet of the ground surface: $K = max\left[j01, K_{reference} \right]$ for $z_{grd} - z < 15$ feet within `./Polygons/FMBrev2.ply`. The underlying conceptual model is that pine tree tap-root penetration and/or other phenomena limit the competency of the TCCZ along FMB where it crops out or is very shallow depending on location.
- Material property averaging at computational cell interfaces within PORFLOW was changed from geometric averaging weighted by proximity to adjoining nodes (PROP GEOM) to harmonic averaging weighted by node to interface distance (PROP HARM TRAV). The latter option was a new feature available in PORFLOW Ver. 6.42.4 that more accurately simulates flow perpendicular to layers, notably the GCU (PORFLOW Ver. 6.42.4 was subsequently used instead of Ver. 6.42.3 for PEST.41-53).

- PEST.47-50 determined that 400 PORFLOW steady-state iterations (4 outer and 100 inner loop iterations) will produce an adequately converged solution (designated as "4 iterations" in Table 3-13).

Calibration results for PEST.51 are presented in Table 3-15 and Figure 3-19.

Table 3-15. Hydraulic Conductivity Summary for PEST.51 Case (Flach et al., 2017)

Param.	Unit	Region	Base K_h (ft d^{-1})	Base K_v (ft d^{-1})	PEST.51a	Net K_h (ft d^{-1})	Net K_v (ft d^{-1})	K_h (cm s^{-1})	K_v (cm s^{-1})	K_h avg (ft d^{-1})	K_v avg (ft d^{-1})	log10 K_v	K_h/K_v Ratio
Phi	--	--	--	--	1.02E+07	--	--	--	--	--	--	--	--
g01	LAZ	Global	12	0.4	0.661616	7.9	0.26	2.8E-03	9.3E-05	**7.4**	0.242	-0.6161	31x
g02	TCCZ	Global	0.18	0.006	0.623232	0.11	0.0037	4.0E-05	1.3E-06	0.1304	**0.004**	-2.417	34x
g03	TZ	Global	9	0.3	1.44508	13.0	0.43	4.6E-03	1.5E-04	**12.2**	0.419	-0.3777	29x
g04	AAA	Global	9	0.3	1.01E-01	0.91	0.030	3.2E-04	1.1E-05	**1.0**	0.057	-1.241	17x
h01	LAZ	Harea	--	--	0.120234	1.3	0.042	4.5E-04	1.5E-05	--	--	--	--
h02	TCCZ	Harea	--	--	0.100547	0.017	0.0006	5.9E-06	2.0E-07	--	--	--	--
h03	TZ	Harea	--	--	0.1	0.62	0.021	2.2E-04	7.3E-06	--	--	--	--
h04	AAA	Harea	--	--	2.34E-01	0.42	0.014	1.5E-04	5.0E-06	--	--	--	--
i01	LAZ	Zarea	--	--	0.768128	8.1	0.27	2.9E-03	9.6E-05	--	--	--	--
i02	TCCZ	Zarea	--	--	0.692103	0.11	0.0038	4.0E-05	1.3E-06	--	--	--	--
i03	TZ	Zarea	--	--	0.794679	4.9	0.16	1.7E-03	5.8E-05	--	--	--	--
i04	AAA	Zarea	--	--	0.742783	1.3	0.044	4.7E-04	1.6E-05	--	--	--	--
j01	FMB	--	--	--	1.67E+00	--	--	--	--	--	--	--	--

Note: Highlighting is used within a parameter grouping (Column 1) to separate out hydrostratigraphic units (Column 2).

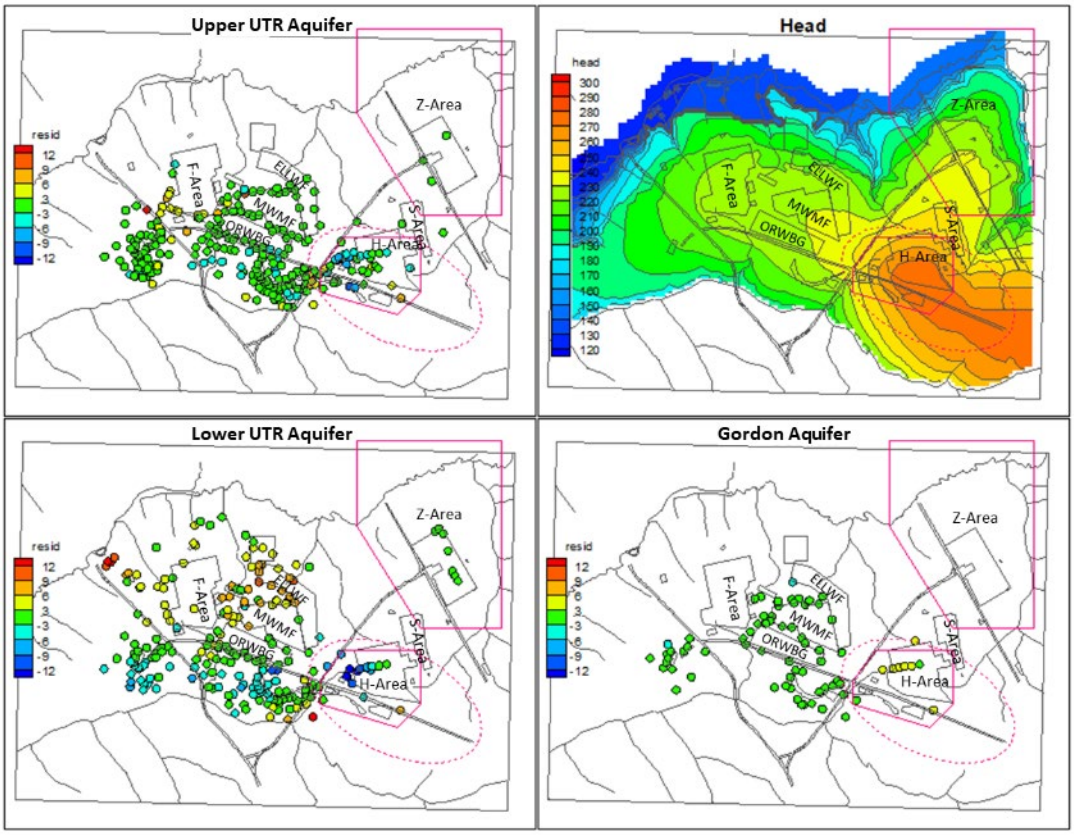

Note: A positive residual value indicates the simulated head is above the measured head.

Figure 3-19. Hydraulic Head Residuals and Water Table Surface for the PEST.51 Case

In addition to optimization of the four global multipliers (*g*01 to *g*04), hydraulic conductivities for the LAZ, TCCZ, TZ, and AAA were also allowed to deviate from the global specifications locally within the red-outlined HS-Area (*h*01 to *h*04) and Z-Area (*i*01 to *i*04) polygonal regions, as shown in Figure 3-19. Table 3-16 and Table 3-17 provide a comparison to stream baseflow validation targets and hydraulic head residual statistics, respectively, for PEST.47, 51, 52, and 53, where the Baseline Model is highlighted in light orange.

Table 3-16. Stream Baseflow Validation Targets for PEST.47, .51, .52, and .53

Flow Parameter	Target	PEST.47 (GSA_2016.LU)[2]	PEST.51 (GSA_2016.LW)[2]	PEST.52 (GSA_2016.HU)[2]	PEST.53 (GSA_2016.HW)[2]
Avg. Recharge (inches/year) [1]	N/A	12.0	12.1	11.9	12.0
Stream Baseflow (ft^3/sec)					
UTR and tribs. less McQueen Branch	18.2	10.6	10.4	10.4	10.3
FMB and tribs.	2.6	2.4	2.8	2.5	2.8
McQueen Branch	1.5	1.6	1.6	1.6	1.6
Crouch Branch	1.8	1.2	1.2	1.2	1.2

Notes:

1 Surface infiltration divided by total surface area including seepage faces. The recharge estimate of 15 inches/year for the GSA is not a model calibration target.

2 "L" = Layer-cake *K* field; "H" = Heterogeneous *K* field; "U" = Unweighted calibration targets; "W" = Weighted calibration targets.

Table 3-17. Hydraulic Head Residual Statistics for PEST.47, .51, .52, and .53

Case	Number	Median	Average	Root-Mean-Square	Minimum	Maximum
PEST.47 (GSA_2016.LU)[1]						
GAU	79	0.3578	0.2164	1.9996	-5.1905	5.4197
LAZ	271	0.2628	0.463	4.1961	-9.4724	19.0612
UAZ	278	0.1209	0.0866	2.9947	-12.005	11.3281
PEST.51 (GSA_2016.LW)[1]						
GAU	79	0.3836	0.2036	1.9593	-5.1606	5.3118
LAZ	271	-0.272	0.0029	5.2508	-14.5862	19.4421
UAZ	278	0.3143	0.0404	3.2295	-13.6501	14.7023
PEST.52 (GSA_2016.HU)[1]						
GAU	79	0.3639	0.2208	2.0068	-5.1829	5.4701
LAZ	271	0.5704	0.5361	4.4711	-9.1071	19.6796
UAZ	278	1.1217	0.7551	3.7462	-12.512	12.8674
PEST.53 (GSA_2016.HW)[1]						
GAU	79	0.358	0.174	1.9722	-5.1878	5.3123
LAZ	271	-1.1656	-0.6728	5.0052	-12.2174	19.7422
UAZ	278	0.674	-0.0051	4.3273	-16.2931	16.5871

Notes:

1 "L" = Layer-cake *K* field; "H" = Heterogeneous *K* field; "U" = Unweighted calibration targets; "W" = Weighted calibration targets.

3.5.2.5. GSA_2016 Flow Model Simulation Validation

Flach et al. (2017; Table 7-1) list inflows and outflows for boundary face normal vectors grouped by coordinate direction for PEST.47, 51, 52, and 53. Cumulative inflow and outflow differed by only a few tenths of one percent, indicating that the models conserved mass on a global basis. Flach et al. (2017; Table 7-2 thru Table 7-5) provide the same information for various subregions

of each model. Flach et al. (2017; Table 7-6) provide mass balance information broken out by boundary condition type. In all cases, the flow discrepancy was no more than a few tenths of a percent, which is an indication that mass was conserved throughout the model domain. Flach et al. (2017; Table 7-7) summarize an independent calculation to confirm that PORFLOW results satisfied Darcy's Law in the saturated zone. The calculation was performed by systematically searching the grid for saturated cells and computing Darcy velocity for each cell face that adjoined another saturated cell. Flach et al. (2017; Figure 7-1 thru Figure 7-4) compare simulated seepage faces to surveyed seeplines, where available. Again, good agreement was observed.

Flach et al. (2017; Appendix D) provide a listing of hydraulic head targets, simulated head, and residuals. Flach et al. (2017; Figure 7-5 thru Figure 7-8) plot hydraulic head residuals for the original set of Flach and Harris (1999) calibration targets. Residuals were biased toward negative values (simulated head biased low) in these figures because the water-table targets from the 1990s were about 3.5 feet higher compared to those from the 2004-2014 period used to calibrate the current GSA_2016 model. Flach et al. (2017; Figure 7-9 thru Figure 7-12) show residuals for the 2004-2014 timeframe, including any wells culled by Hiergesell et al. (2015) because of fewer than four records or other reason. Flach et al. (2017; Figure 7-13 thru Figure 7-16) show crossplots of simulated hydraulic head versus hydraulic head targets for the UAZ, LAZ, and GAU HSUs. Also shown are coefficient of determination (R^2) values, which ranged from 0.85 to 0.97. R^2 is the fraction of the observed hydraulic head variability that was captured by the model simulation.

Local recharge could potentially vary significantly with elevation, slope, and vegetation, whereas model simulations assumed uniform recharge over areas above the seeplines. Smaller-scale spatial perturbations would average-out and have little impact on the GW flow field. Of greater concern are potential variations at or approaching the scale of the model. For example, higher elevations in the center of the model tend to have shallower slopes, less tree cover, and more man-made features compared to outlying areas approaching the model boundaries. This large-scale variation in topography could increase recharge in the center of the model and decrease recharge elsewhere. Hydraulic head residual plots were examined for spatial biases that might indicate nonuniform recharge. Figure 3-19 for GSA_2016.LW (PEST.51) and Flach et al. (2017; Figure 6-27, 6-31, and 6-32) for GSA_2016.LU (PEST.47), GSA_2016.HU (PEST.52), and GSA_2016.HW (PEST.53), respectively, do not provide compelling evidence for significant large-scale variations in recharge. Thus, the model assumption of uniform recharge is deemed an adequate approximation of physical reality.

3.5.2.6. GSA_2016 Flow Model Simulation Results

Results and discussion of the four final-round GSA_2016 model optimization cases are reported by Flach et al. (2017; Section 7.2). Simulated water tables for the final-round GSA_2016 model optimization cases (Flach et al., 2017; Figure 7-17 thru Figure 7-20) were compared to a kriging interpolation of measured water table elevations (Flach et al., 2017; Figure 7-21). In addition, vertically-averaged simulated hydraulic heads for each aquifer zone (Flach et al., 2017; Figure 7-22 thru Figure 7-33) were compared against a kriging interpolation of measured hydraulic head in the GAU (Flach et al., 2017; Figure 7-34). Finally, plots of simulated surface flux (Flach et al., 2017; Figure 7-35 thru Figure 7-38) were compared to the surveyed seeplines (Flach et al., 2017;

Figure 7-1 thru Figure 7-4). Rather than presenting the graphical and tabular output for the GSA_2016 model here, a similar set of results will be presented in the next section for GSA_2018.

Among the four final-round optimization cases, the PEST.51/GSA_2016.LW model was recommended as the baseline case for PAs and similar analyses for the following reasons:

- The layer-cake conductivity field produced a better fit to data than the heterogeneous *K* field, for both unweighted and weighted optimization.
- The layer-cake *K* field is more parsimonious; that is, it involves fewer assumptions and inputs while reproducing field observations to a degree similar to the alternative.
- Weighted optimization approximately accounts for data spatial density and uncertainty.
- Outside of the H-Area and Z-Area calibration zones, weighted optimization produced a TZ conductivity that is larger than those in the adjoining aquifer zones, consistent with hydrogeologic conceptual models associated with the F-Area seepage basins, Old Burial Ground, and H-Area seepage basins (e.g., SAIC, 2000; SRNS, 2017a; WSRC, 2000). The TZ corresponds to the Irwinton Sand member of the Dry Branch formation and is "believed to be the primary pathway for contaminant travel in the UAZ" (WSRC, 2000).
- Weighted optimization produced particle tracks (Flach et al., 2017; Figure 7-41 and Figure 7-43) emanating from the Old Burial Ground in the south-central GSA that discharge to Fourmile Branch, consistent with tritium plume observations at that site (Flach et al., 1996; Flach and Harris, 1997).

Together these observations supported selection of the GSA_2016.LW model with a layer-cake *K* field, calibrated using weighted targets.[12]

3.5.2.7. Updated General Separations Area Groundwater Model Calibration Targets

In support of the SRS SDF and ELLWF PAs, Wohlwend (2018) updated the GSA regional GW flow calibration targets to incorporate additional well data. A total of 45,667 depth-to-water measurements obtained from a total of 731 wells were evaluated and used to generate new base-period target-well hydrographs using a modified version of the Excel-based Well Hydrograph Analysis Tool (WHAT) developed by Hiergesell and Taylor (2015) and Hiergesell et al. (2015). The original version of WHAT did not correctly compute the median well-water level and, occasionally, the minimum and maximum values. An exercise was conducted to identify and remove any spurious measurements from the hydrographs; water level statistical quantities were then computed for each well. Hydrographs are reported by Wohlwend (2018; see Appendix A) for 65 newly evaluated wells added to the original 666 wells analyzed by Hiergesell et al. (2015). Each well's mean water level is the "target" water level used in recalibrating the GSA GW flow model.

[12] Although PEST.51/GSA_2016.LW was the recommended best-estimate/baseline/base case model, each of the remaining three GSA_2016 models was a generally credible alternative and suitable for sensitivity analysis, out-performing GSA_2016.LW in specific areas. For example, within the H- and Z-Area calibration zones, the calibrated conductivity of the TZ (K_{TZ}) was lower than in the LAZ (K_{LAZ}) in the GSA_2016.LW model (the reason for this was not clear at the time but was subsequently addressed in GSA_2018). On the contrary, the GSA_2016.LU model (layer-cake, unweighted), provided better agreement in H- and Z-Areas because calibrated $K_{TZ} > K_{LAZ}$.

In addition, Wohlwend (2018) conducted an analysis of the selected target wells, by location, to determine an appropriate weighting factor to associate with each target well. Two different de-clustering methods were considered: a "polygonal de-clustering" method (Hiergesell et al., 2015) and an inverse-distance weighting approach. A listing of target wells, sorted by HSU, together with well coordinates, target water level, and weighting factors, is reported by Wohlwend (2018; see Appendix D).

3.5.2.8. GSA_2018 Groundwater Flow Model Recalibration Approach

In 2018, Flach (2019) further refined the GSA_2016 flow model to incorporate updates to model calibration targets, closure of the H-Area Ash Basin, construction of ELLWF ST operational covers, and plume information from the MWMF and LLRWDF. Another objective was to lower hydraulic head residuals around the F-Area and H-Area seepage basins by adding a third calibration zone ("FHbasins2"; Figure 3-9) to the existing "Harea" and "Zarea2" conductivity zones included in GSA_2016. Section 3.5.2.1 describes these updates in more detail. The resulting model is referred to as "GSA_2018," and only the previously recommended GSA_2016.LW baseline model was recalibrated in 2018.

The areal resolution of the baseline GSA_2018 flow model is 200 feet square except in peripheral areas. There are 108 grid blocks along the east-west axis, and 77 blocks along the north-south axis. The vertical resolution varies depending on hydrogeologic unit and terrain/hydrostratigraphic surface variations as depicted in Figure 3-8. The UAZ of the UTRA unit (Figure 3-4) is represented with up to 10 finite elements in the vertical direction (the VZ is included in the model). The LAZ of the UTRA unit (Figure 3-4) contains five elements, while the TCCZ separating the aquifer zones is modeled with two vertical elements. The GCU and GAU (Figure 3-4) each contain two elements, leading to a total of 21 vertical elements from ground surface to the bottom of the Gordon Aquifer. The 3-D grid comprises 102,294 active cells as depicted in Figure 3-20.

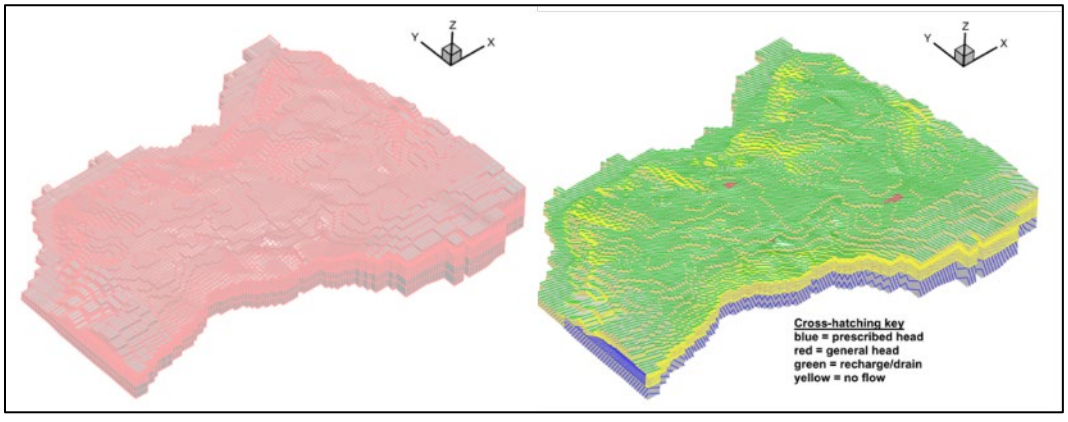

Figure 3-20. GSA/PORFLOW Flow Model 3-D Computational Mesh (left) with Boundary Conditions Applied (right) (Flach, 2004)

Each hydrostratigraphic surface is defined by control points (or stratigraphic "picks") using the elevation data provided in the *Hydrostratigraphic Surfaces Data Package* (SRNL, 2017) and accompanying reports (Bagwell and Bennett, 2017; Bagwell et al., 2017). CPT over the past two

decades has enabled delineation of hydrostratigraphic elevations at many more locations than available through the mid-1990s. As noted for the GSA_2016 flow model, Bagwell et al. (2017) revised hydrostratigraphic "picks" and generated detailed hydrostratigraphic surfaces for the GSA per the *General Separations Area (GSA) Groundwater Flow Model Update: Program and Execution Plan* (Bagwell and Flach, 2016). The new hydrostratigraphic surfaces were adopted as-is for grid generation in the GSA_2018 flow model update. The total number of controls points employed in GSA_2018 for the three hydrostratigraphic surfaces of interest defined by Bagwell and Bennett (2017) in Figure 3-21 is 716 (LAZ = 218; TCCZ = 233; Tobacco Road Sand = 265).

Characterization data in the form of large- and small-scale pumping tests, slug tests, laboratory permeability measurements, and visual descriptions of recovered sediment core were used to develop the GSA/FACT model (Flach and Harris, 1999) and 2004 GSA/PORFLOW model (Flach, 2004) hydraulic conductivity fields. The comprehensive characterization data set is documented in "Integrated Hydrogeological Model of the General Separations Area, Volume 1: Hydrogeologic Framework" by Smits et al. (1997) and "Integrated Hydrogeological Model of the General Separations Area, Volume 2: Groundwater Flow Model" by Flach and Harris (1999). More than two decades ago, CPT largely supplanted drilling in GSA field characterization efforts. As a result, relatively little borehole-based hydraulic conductivity characterization data have appeared since then. Recognizing that monitoring data play a more significant role in defining the calibrated model hydraulic conductivity field, no attempt was made to update the existing datasets related to permeability for the GSA_2016 and GSA_2018 flow models (Flach et al., 2017).

As shown in the vertical slice provided in Figure 3-21, the surface of the water table crosses over the TCCZ beneath the ELLWF. The crossover point is in the center section of ELLWF.

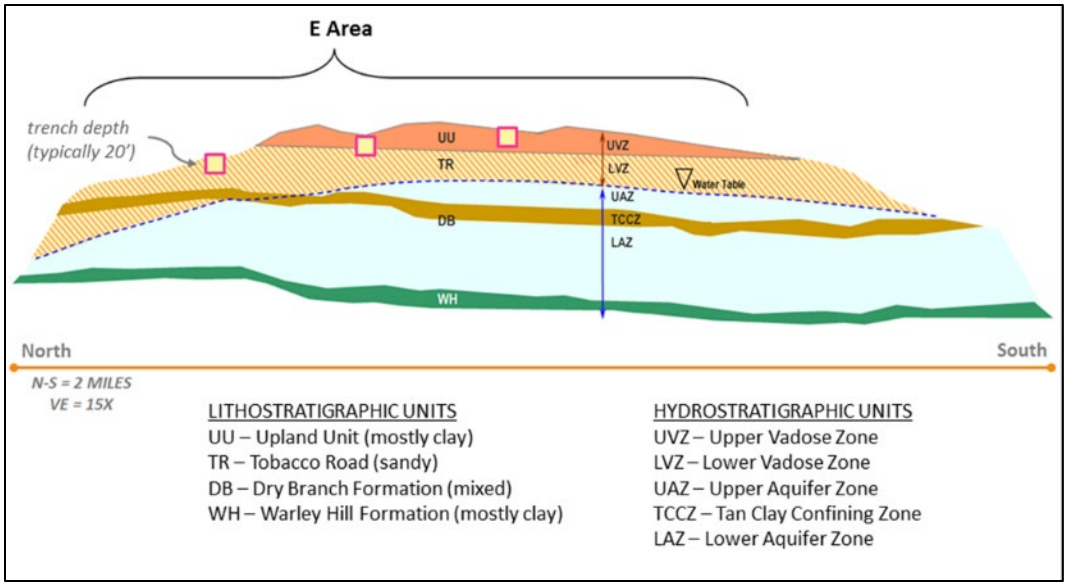

Figure 3-21. Generalized Schematic Cross-Section Through E-Area Showing Underlying Stratigraphic Units and Typical Excavation Depth of Slit and Engineered Trenches (Bagwell and Bennett, 2017)

In the layer-cake concept, the hydraulic conductivity field is uniform within hydrostratigraphic units (e.g., LAZ, TCCZ, GAU, etc.). As in previous calibration efforts, variations in GCU conductivity (<GCUkv>) were handled outside the PEST code through parametric study, while conductivities in higher hydrostratigraphic units were adjusted within PEST. The recommended GSA_2016.LW model settled on <GCUkv> equal to 0.75E-04 ft d^{-1}. The GSA_2018 model, however, lowers <GCUkv> to 1.0E-05 ft d^{-1} to achieve a better match to GW pathlines inferred from MWMF plume data. The average "global" horizontal conductivities in the saturated UAZ, LAZ, and GAU are approximately 14.8, 9.5, and 38.0 ft d^{-1}, respectively, as reported in Table 2-9. The average "global" vertical conductivities for the TCCZ and the GCU are roughly 3.0E-3 ft d^{-1} and 1.0E-5 ft d^{-1}, respectively, also as reported in Table 2-9.

The total number of calibration targets for GSA_2018 is 711 (Flach, 2019). Model calibration targets included hydraulic head, GW recharge, and stream baseflow measurements. The GSA_2018 flow model was calibrated and validated using measured well water levels from the period 2004 through March 2018 (Wohlwend, 2018). Estimates of GW recharge and discharge rates, which are critical to boundary condition specification and model calibration, are based on historical data and estimates described by Flach and Harris (1999).[13] The average natural recharge over the entire model domain is 15 inches per year (Flach et al., 2017),[14] which compares well with the median (14.5 inches per year) and range (9.1 to 16 inches per year) of ten historical field and modeling studies summarized in Table 3-18 (Dyer, 2019c). Various man-made features (e.g., basins) provide additional recharge in localized areas. Away from seepage faces, recharge is assumed to be uniform; the adequacy of this assumption is discussed post-calibration. The stream baseflow validation targets for UTR (and tributaries excluding McQueen Branch) and Fourmile Branch within the model domain are 18.2 and 2.6 cubic feet per second, respectively (Flach, 2019; Table 4-2).

Table 3-19 summarizes the GW flow information adopted for the GSA_2018 flow model. The range of uncertainty in recharge is 10 to 16 inches/year according to Flach et al. (1999). Uncertainties in the stream baseflow estimates have not been quantified. However, stream baseflows may be biased high relative to the head calibration targets, because rainfall and water levels were higher on average during the 1973-1995 period compared to 2004-2014 (Hiergesell et al., 2015; see Figure 3-1 or 3-2).

[13] As explained by Flach et al. (2017), USGS monitoring of GSA streams generally ended in 2002, providing no more than seven years of additional data beyond the 1973 to 1995 historical record used by Flach and Harris (1999). The baseflow estimates were also based on hydrologic budget studies conducted by Parizek and Root (1986) and baseflow measurements reported by Cook and Hunt (1994); WSRC (1992). No further studies of this nature have been identified. Therefore, no attempt was made to revise the stream baseflow estimates from 1997, which were judged to be adequate for validating an updated GSA GW flow model.

[14] Lacking any substantive new information for the 2004 to 2014 period associated with well targets, the previous recharge estimate of 15 inches/year by Flach and Harris (1999) was retained in GSA_2016 and GSA_2018.

Table 3-18. Summary of Historical Water Balance, Infiltration, and Groundwater Recharge Field and Modeling Studies Relevant to Savannah River Site (Dyer, 2019c)

Source	Annual-Average Rate (inches per year) [a]			
	Precipitation	Runoff	Evapotranspiration	Net Infiltration/ Recharge
Cahill (1982)	46.62	0	31.62	15
Stricker (1983)	--	--	--	14
Hubbard and Emslie (1984)	47	2	30	15
Hubbard (1986)	48	2	30	16
Parizek and Root (1986)	47.78	2	30.78	15
Hubbard and Englehardt (1987)	48.51	1.21	32.6	14.7
Dennehy and McMahon (1989)	47.8	0	33.5	14.3
Clarke and West (1998)	--	--	--	15.6 (New Ellenton) 14.3 (above Road C) [c] 10.6 (at Road A)
Young and Pohlmann (2001)	10 years Augusta, GA data from 1977 to 1987	--	Determined but not reported in the document [b]	9.1
Young and Pohlmann (2003)	10 years Augusta, GA data from 1977 to 1987	--	Determined but not reported in the document [b]	11.7
Median of the ten studies [d]	**47.79**	**1.6**	**31.2**	**14.5**

Notes:

[a] All studies assumed that the change in water storage was a negligible component in the overall water budget.

[b] Based on the magnitude of the infiltration rate, the associated evapotranspiration rate will be relatively high (> 30 inches/year).

[c] Station closest to E-Area.

[d] The median of the ten studies does not include precipitation, runoff, and evapotranspiration rates from Young and Pohlmann (2001; 2003), Stricker (1983), and Clarke and West (1998).

Table 3-19. Recharge and Stream Baseflow Validation Targets for GSA_2018.LW Model

Flow Parameter	Target	PEST.51 (GSA_2016.LW)[2]	PEST.102 (GSA_2018.LW)[2]
Avg. Recharge (inches/year) [1]	N/A	12.1	12.1
Stream Baseflow (ft^3/sec)			
UTR and tributaries less McQueen Branch	18.2	10.4	10.7
FMB and tributaries	2.6	2.8	3.0
McQueen Branch	1.5	1.6	1.8
Crouch Branch	1.8	1.2	1.4

Notes:

[1] Surface infiltration divided by total surface area including seepage faces. The recharge estimate of 15 inches/year for the GSA is not a model calibration target.

[2] "L" = Layer-cake *K* field; "W" = Weighted calibration targets

Hiergesell et al. (2015; Appendix E) describe "GSA operations potentially enhancing or reducing infiltration adjacent to the ELLWF." The authors remark that "studies indicate that kaolin caps return to background infiltration within two to four years if they are not overlain by a geomembrane and at least 6 feet of soil in humid environments," which means that the MWMF,

F-Area Seepage Basin, and H-Area Seepage Basin caps do not represent a low-infiltration region during the 2004 to 2014 period and beyond. However, the LLRWDF and ORWBG/GSA Consolidation Unit caps incorporate a geomembrane and significantly reduce infiltration. Considering cap degradation over time, cap infiltration for these units is set to 1.5 inches/year (10% of 15 inches/year).

3.5.2.9. GSA_2018 PEST Recalibration Results

Table 3-20 summarizes the level of agreement between simulated and measured hydraulic heads for PEST Optimization Run 102 (PEST.102) corresponding to GSA_2018.LW. Compared to PEST.51/GSA_2016.LW, the GSA_2018.LW model exhibits a higher root-mean-square (r.m.s.) residual for the GAU, a similar r.m.s. head difference for the LAZ, and a slightly lower r.m.s. residual in the UAZ. Stream baseflows for GSA_2018.LW are larger than for GSA_2016.LW (Flach et al., 2017; Table 6-35) as shown in Table 3-19 because GCU leakance is lower causing higher GW discharges to nearby streams.

Table 3-20. Hydraulic Head Residual Statistics for GSA_2018.LW Model

HSU	Number	Median	Average	Root-mean-square	Minimum	Maximum
GAU	80	-1.1743	-1.6126	2.6939	-8.3457	2.7495
LAZ	285	1.9143	1.4866	5.2524	-15.2519	15.9644
UAZ	334	-0.1907	-0.1204	3.4494	-12.3604	13.5146

Figure 3-22 shows individual hydraulic head residuals for the three aquifer zones, in addition to the simulated water table.

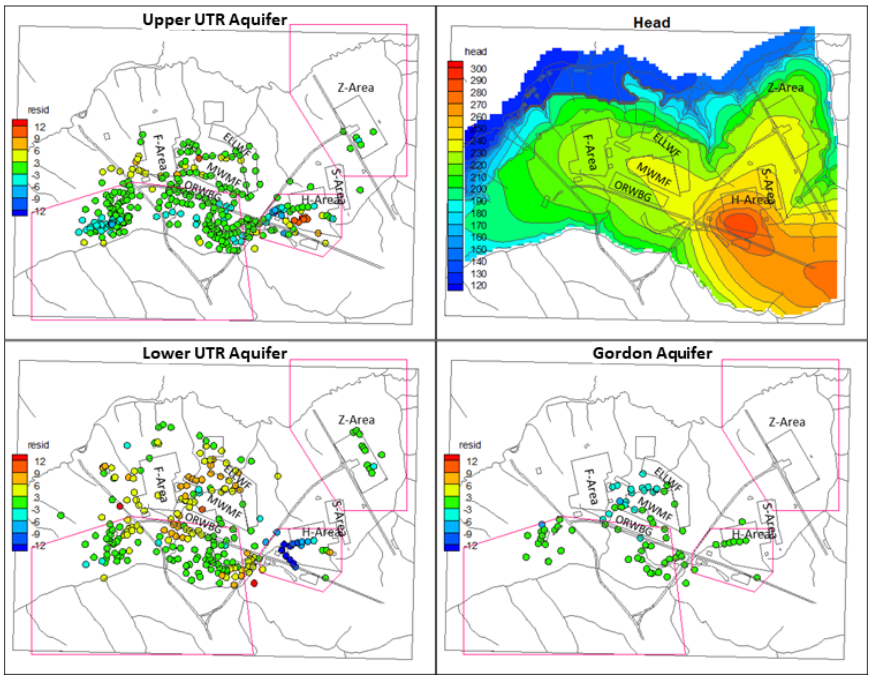

Note: A positive residual value indicates the simulated head is above the measured head.

Figure 3-22. Hydraulic Head Residuals and Water Table Surface for the GSA_2018.LW Model (Flach, 2019; Figure 4-1)

Table 3-21 summarizes the calibrated conductivity field. These results can be compared to Figure 3-19 and Table 3-15 for the PEST.51/GSA_2016.LW model case. In the GSA_2016.LW model, calibrated horizontal conductivity of the TZ within the Z-Area calibration did not agree with the general conceptual model of the TZ having a higher hydraulic conductivity than other aquifer zones within the UTRA. In the recalibrated GSA_2018.LW model, on the other hand, the horizontal conductivity of the TZ in Z-Area is 14.8 ft d^{-1}, which is identical to that for the Global TZ zone and higher than that for the LAZ. Thus, GSA_2018.LW model recalibration to updated targets, coupled with assuming <GCUkv> equal to 1.0E-05 ft d^{-1}, improved agreement with the hydrogeologic conceptual model in Z-Area.

Flach (2019; see Table 4-4 through Table 4-6) demonstrates that the GSA_2018.LW model conserves mass. Flach (2019; see Table 4-4) lists flowrates across the six faces of the overall model domain. Total inflow and outflow differed by only 0.22%. Flach (2019; see Table 4-5) presents mass balance results for each aquifer unit and zone. Again, inflows and outflows were observed to differ by less than 0.3%. Finally, Flach (2019; see Table 4-6) provides a global mass balance analogous to Flach (2019; see Table 4-4), but broken out by boundary condition type (i.e., RECH## = recharge zone ##, GENH## = general head zone ##, and HEAD## = prescribed head zone ##).

Table 3-21. Hydraulic Conductivity Summary for the GSA_2018.LW Model (Flach, 2019; Table 4-3)

Parameter	Unit	Region	Base Kh (ft/d)	Base Kv (ft/d)	PEST.102c	Net Kh (ft/d)	Net Kv (ft/d)	Kh (cm/s)	Kv (cm/s)	Kh avg (ft/d)	Kv avg (ft/d)	log10 Kv	Kh,v ratio
Phi					79713								
N/A	GAU	Global	38	0.38									
N/A	GCU	Global	1.e-4	1.0e-5									
g01	LAZ	Global	8	0.267	1.18752	9.5	0.3	3.4E-03	1.1E-04	**7.2**	0.220	-6.58E-01	33x
g02	TCCZ	Global	0.18	0.006	0.444638	0.08	0.003	2.8E-05	9.4E-07	1.63E-01	**0.004**	-2.38E+00	39x
g03	TZ	Global	16	0.533	0.927212	14.8	0.49	5.2E-03	1.7E-04	**15.9**	0.513	-2.90E-01	31x
g04	AAA	Global	1	0.033	2.06358	2.06	0.068	7.3E-04	2.4E-05	**2.8**	0.123	-9.09E-01	23x
h01	LAZ	Harea			0.621258	5.9	0.2	2.1E-03	6.9E-05				
h02	TCCZ	Harea			0.01226666	0.001	3.3E-05	3.5E-07	1.2E-08				
h03	TZ	Harea			0.01453753	0.2	0.01	7.6E-05	2.5E-06				
h04	AAA	Harea			0.10151	0.21	0.007	7.4E-05	2.4E-06				
i01	LAZ	Zarea			0.572989	5.4	0.2	1.9E-03	6.4E-05				
i02	TCCZ	Zarea			0.744731	0.06	0.002	2.1E-05	7.0E-07				
i03	TZ	Zarea			0.994785	14.8	0.49	5.2E-03	1.7E-04				
i04	AAA	Zarea			2	4.13	0.136	1.5E-03	4.8E-05				
j01	LAZ	FHbasins			0.3	2.9	0.1	1.0E-03	3.4E-05				
j02	TCCZ	FHbasins			5	0.40	0.013	1.4E-04	4.7E-06				
j03	TZ	FHbasins			1.45352	21.6	0.72	7.6E-03	2.5E-04				
j04	AAA	FHbasins			2	4.13	0.136	1.5E-03	4.8E-05				

Notes:
Highlighting indicates the unique parameter variables for the four different hydrostratigraphic units.

Figure 3-23 compares simulated seepage faces (blue shading) to surveyed seeplines (white lines). Predicted seepage faces are consistent with field observations. Figure 3-24 compares simulated hydraulic heads to measured well water levels in the form of cross plots. Also shown are R^2 values, which ranged from 0.84 to 0.97. R^2 is the fraction of the observed hydraulic head variability that was captured by the model simulation.

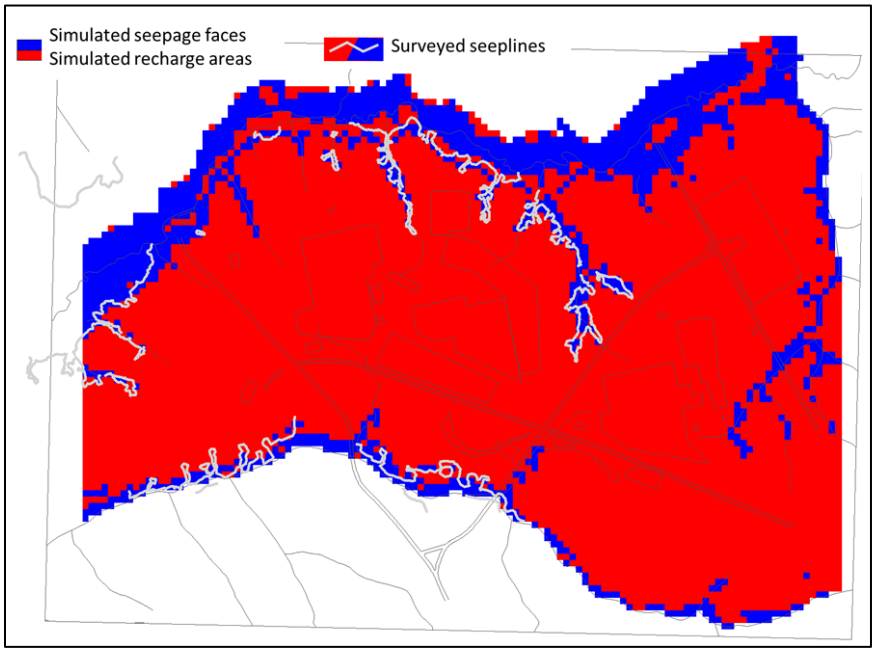

Figure 3-23. Simulated Seepage Faces Compared to Surveyed Seeplines for GSA_2018.LW Model (Flach, 2019; Figure 4-2)

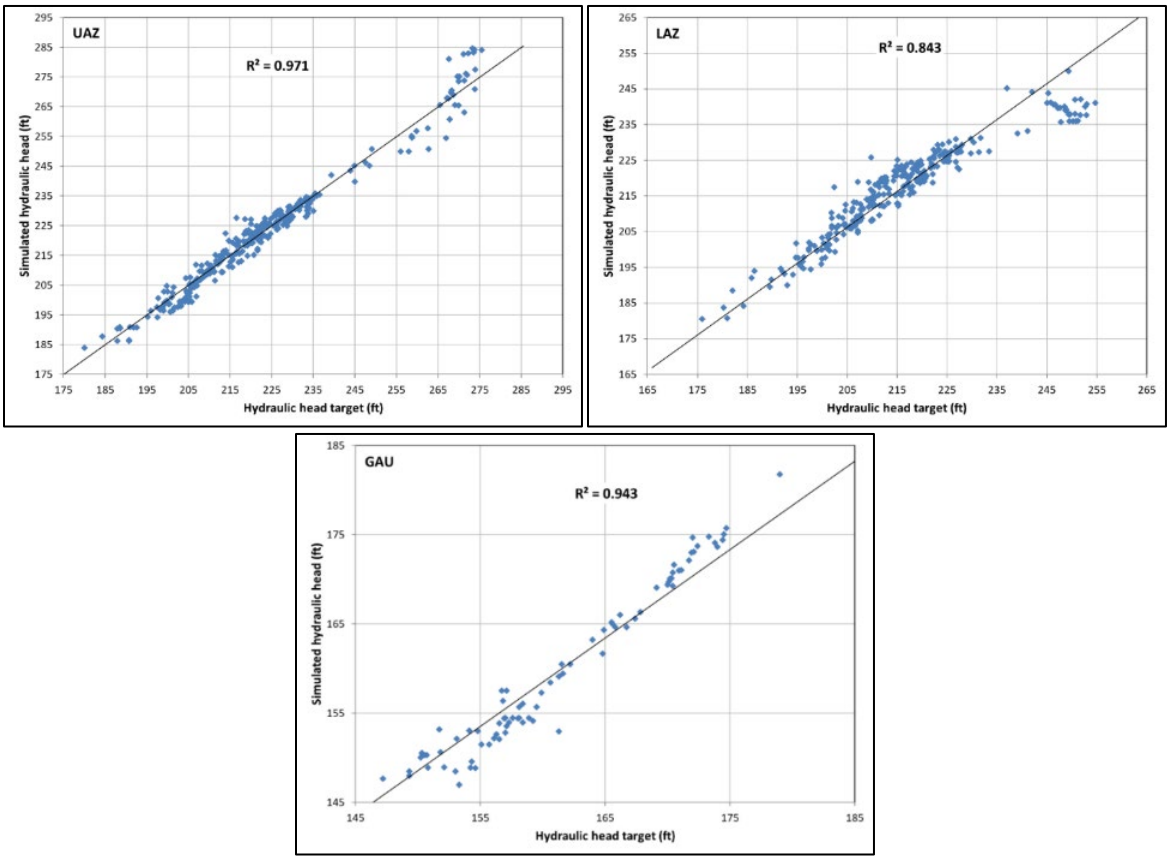

Figure 3-24. Hydraulic Head Crossplots for GSA_2018.LW Model Recalibration (Flach, 2019; Figure 4-3)

3.5.2.10. GSA_2018 Simulation Results

Figure 3-25 through Figure 3-31 display simulated hydraulic heads, measured hydraulic heads (in feet above MSL), and simulated ground surface fluxes (recharge). The corresponding figures for GSA_2016.LW are reported by Flach et al. (2017; Section 7.2). Predicted seepage faces are consistent with field observations. Simulated hydraulic heads, vertically averaged over the entire thickness of the UAZ, LAZ, and GAU, agree with potentiometric maps based on measured heads. Simulated flow directions vertically averaged over the entire thickness of the aquifer zones agree with conceptual models of GW flow.

The GSA flow model simulates GW flow under steady-state conditions representing current topography and climate. The influence of closure caps on the ELLWF and other surrounding facilities is addressed in the modeling upgrades discussed for the GSA_2021 flow model (see Sections 3.5.2.11 through 3.5.2.16). The presence of the closure cap is expected to slightly lower the water table beneath E-Area, thereby increasing the VZ transport distance.

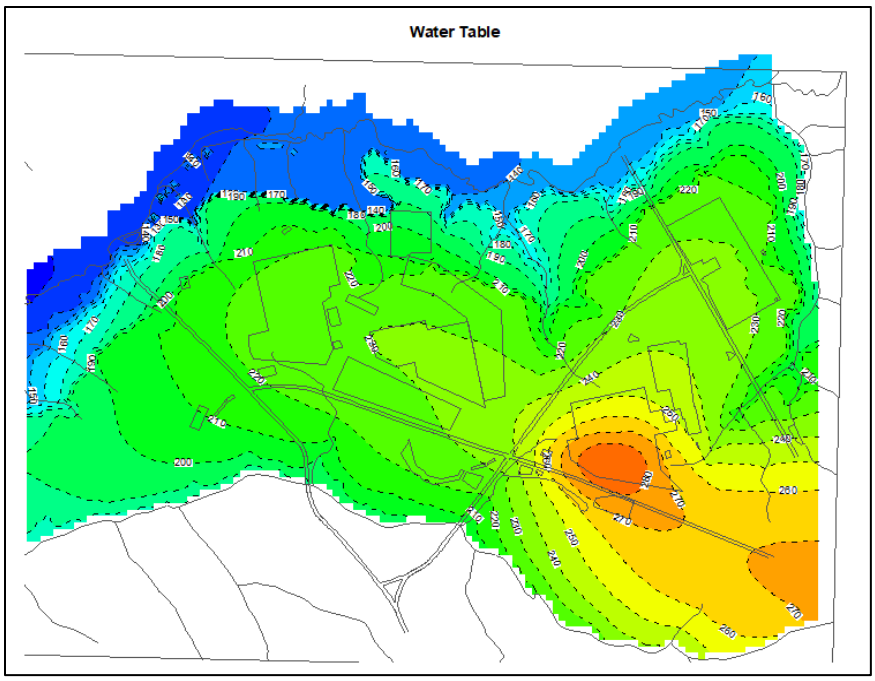

Figure 3-25. Simulated Water Table in Feet from GSA_2018.LW Model (Flach, 2019; Figure 4-4)

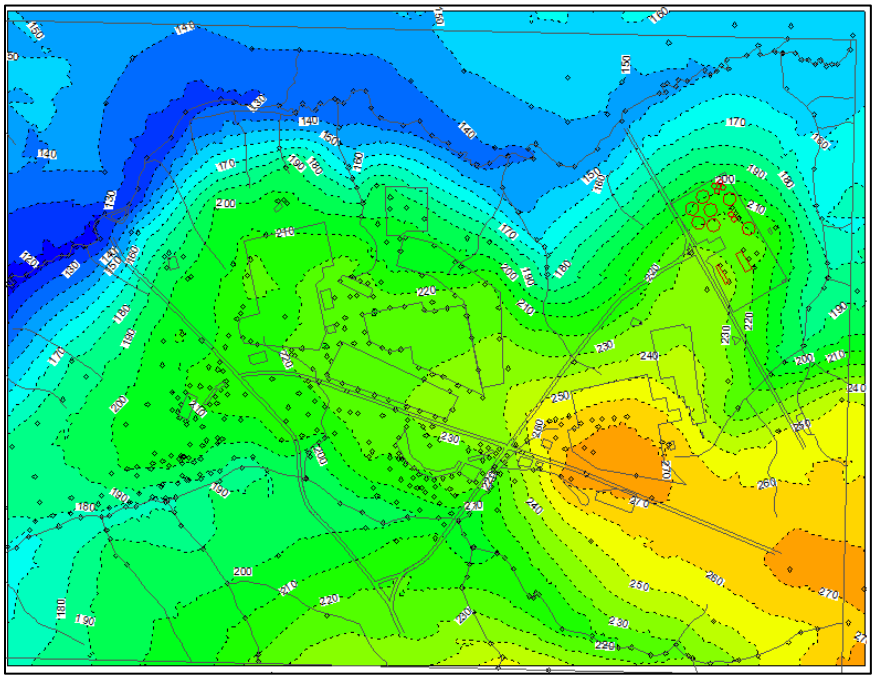

Figure 3-26. Kriging Interpolation Representation of Measured Water Table in Feet (Flach, 2019; Figure 4-5)

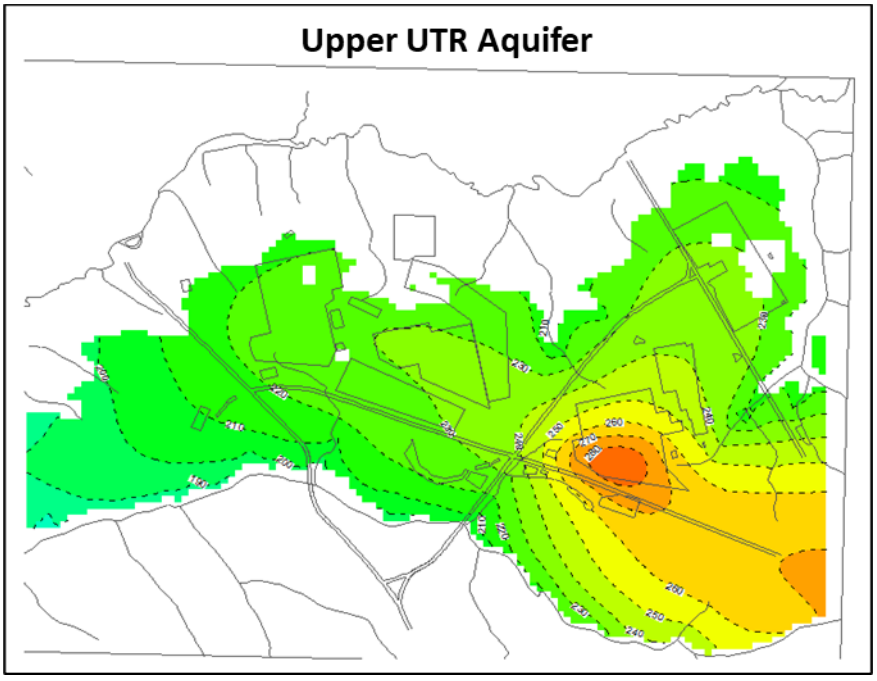

Figure 3-27. Simulated Hydraulic Head (Feet) in Upper Aquifer Zone from GSA_2018.LW Model (Flach, 2019; Figure 4-6)

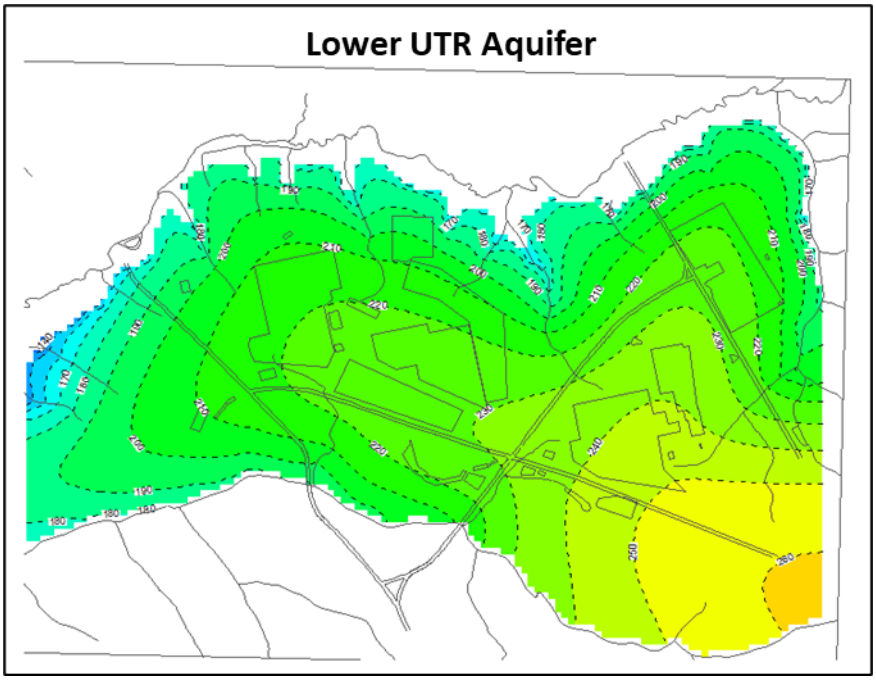

Figure 3-28. Simulated Hydraulic Head (Feet) in Lower Aquifer Zone from GSA_2018.LW Model (Flach, 2019; Figure 4-7)

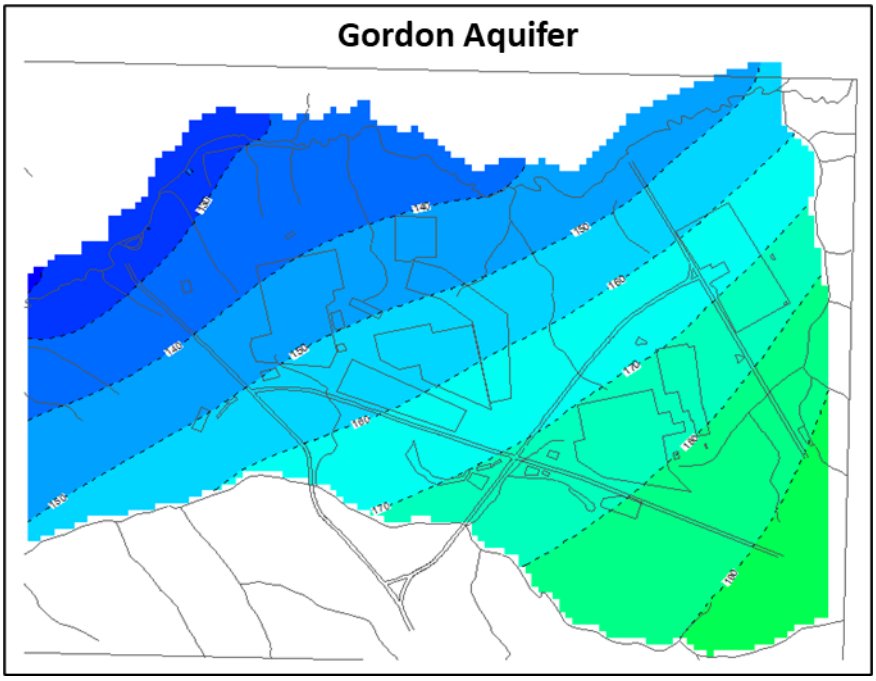

Figure 3-29. Simulated Hydraulic Head (Feet) in Gordon Aquifer Unit from GSA_2018.LW Model (Flach, 2019; Figure 4-8)

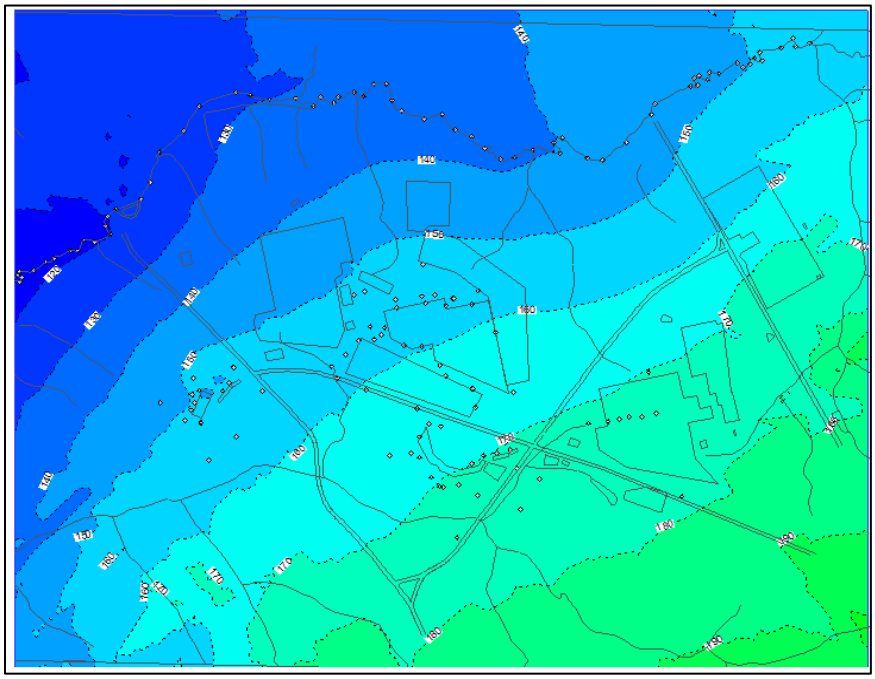

Figure 3-30. Kriging Interpolation Representation of Gordon Aquifer Unit Measurements in Feet (Flach, 2019; Figure 4-9)

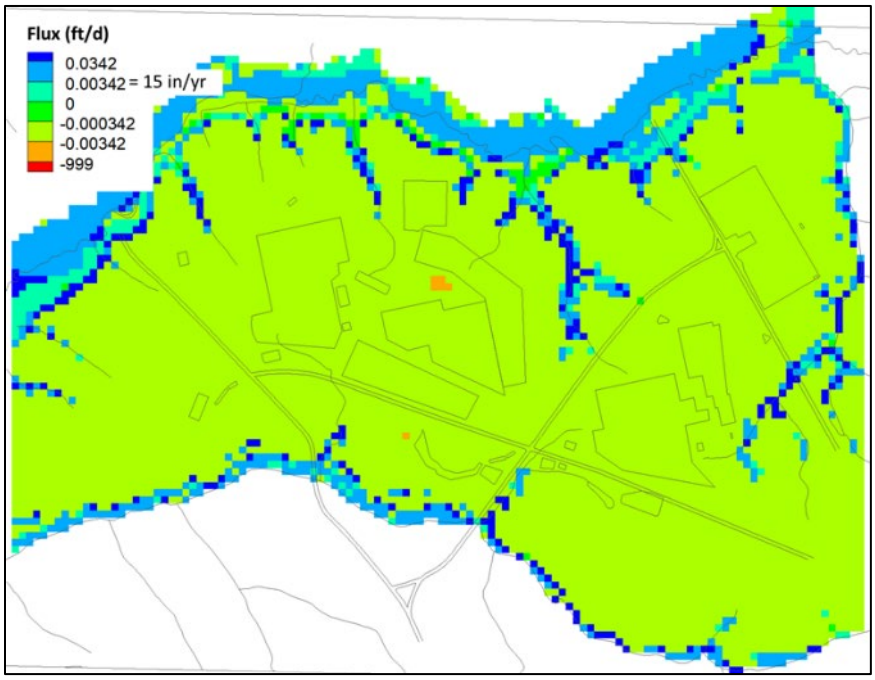

Figure 3-31. Simulated Surface Flux in Feet per Day from GSA_2018.LW Model (Flach, 2019; Figure 4-10)

The 95% confidence limits for GSA_2018.LW model parameters are summarized in Table 3-22 for use in sensitivity and uncertainty analyses. For additional information on aquifer flow modeling for the ELLWF, refer to *Updated Groundwater Flow Simulations of the Savannah River Site General Separations Area* by Flach (2019).

Table 3-22. GSA_2018.LW Flow Model Parameter Confidence Limits for Uncertainty Analysis (Flach, 2019; Table 4-7)

Parameter Description	Parameter ID	Estimated Value	95% Percent Confidence Limits	
			Lower Limit	Upper Limit
Global multiplier to LAZ	g01	1.18752	1.09265	1.29063
Global multiplier to TCCZ	g02	0.444638	0.376461	0.525161
Global multiplier to TZ	g03	0.927212	0.714795	1.20275
Global multiplier to AAA	g04	2.06358	0.637252	6.68235
HS-Area multiplier to LAZ	h01	0.621258	0.191975	2.01048
HS-Area multiplier to TCCZ	h02	1.226666E-02	1.458471E-04	1.03170
HS-Area multiplier to TZ	h03	1.453753E-02	5.662121E-06	37.3252
HS-Area multiplier to AAA	h04	0.101510	7.833978E-07	13153.3
Z-Area multiplier to LAZ	i01	0.572989	0.409960	0.800849
Z-Area multiplier to TCCZ	i02	0.744731	0.270276	2.05206
Z-Area multiplier to TZ	i03	0.994785	0.231014	4.28370
Z-Area multiplier to AAA	i04	2.00000	1.314937E-02	304.197
FH-Basins multiplier to LAZ	j01	0.300000	0.120565	0.746483
FH-Basins multiplier to TCCZ	j02	5.00000	2.35770	10.6035
FH-Basins multiplier to TZ	j03	1.45352	0.906665	2.33023
FH-Basins multiplier to AAA	j04	2.00000	0.299779	13.3431

3.5.2.11. GSA_2021 Flow Model Recalibration Approach

During model implementation in this PA, several upgrades to the GSA_2018.LW model were needed. The updated features include: (1) improved vertical flow within the VZ; (2) sharper focus on optimization within E-Area via increased weighting of E-Area head targets; (3) improved moisture retention curves to address the vertical flow field in the VZ; and (4) changes in the horizontal-to-vertical hydraulic anisotropy ratios and base hydraulic conductivities. This updated version is referred to as the PEST.109/GSA_2021 baseline flow model for PA2022.

The GSA_2018 flow calibration targets are used in the recalibration of the GSA_2021 flow model. Twenty water table wells (UAZ and LAZ) of the observation head targets are in the vicinity of the ELLWF as shown in Figure 3-32. Within the ELLWF, the water table is below and above the tan clay, north and south of the transition region (delineation of LAZ and UAZ), respectively.

The 20 selected water table wells are assigned weighting factors that are ten times the values assigned by Wohlwend (2018). The increased weighting factors are assigned to reduce the head residuals in the vicinity of the ELLWF during the PEST optimization. The well ID, HSU, well data statistics, well screen heights, and PEST ID are shown in Table 3-23. All elevations in the table are in feet above MSL.

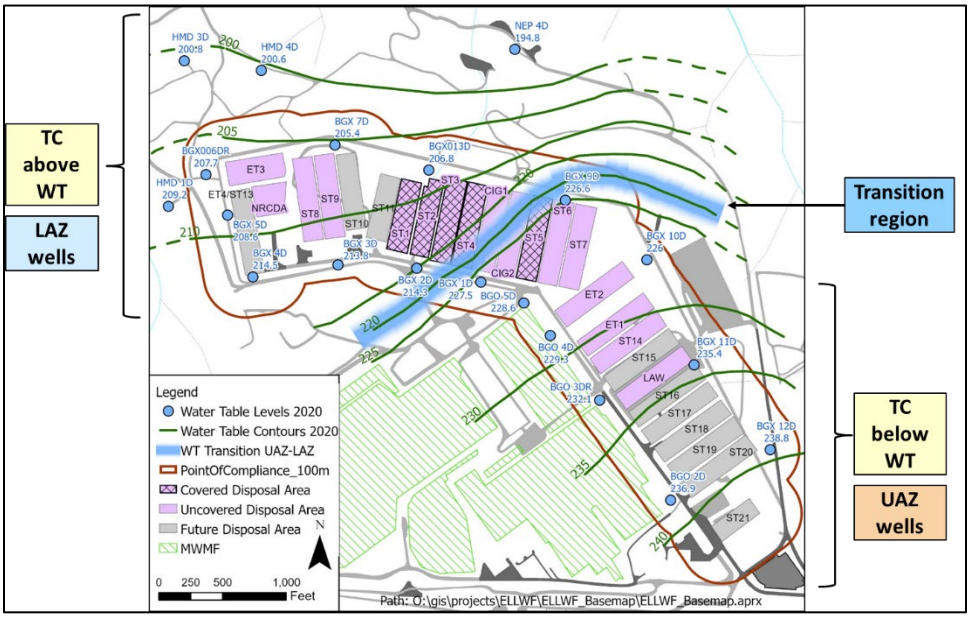

Figure 3-32 E-Area Well Locations: Measurements from Summer 2020

Table 3-23 Water Table Observation Wells for E-Area Low-Level Waste Facility

Well ID	HSU	Head (Feet above MSL)					PEST ID
		Max	Min	Mean	Screen Top	Screen Bot	
BGO 2D	UAZ	235.80	228.00	232.00	241.7	221.7	o2
BGO 3DR		231.03	226.44	229.00	237.6	217.5	o3
BGO 4D		228.53	224.33	226.50	240.2	220.2	o4
BGO 5D		227.94	223.84	226.00	238.8	218.8	o5
BGX 1D		227.10	223.20	225.30	234.7	214.7	o47
BGX 9D		225.60	221.86	224.00	232.4	212.4	o48
BGX 10D		224.90	221.40	223.50	236.2	216.2	o49
BGX 11D		234.30	228.42	231.70	236.7	216.7	o50
BGX 12D		238.58	231.00	234.90	243.7	223.7	o51
BGX 2D	LAZ	214.00	207.70	210.30	191.1	181.1	o382
BGX 3D		212.60	208.00	210.60	221.6	201.6	o383
BGX 5D		206.80	202.10	204.70	215.0	195.0	o385
BGX 7D		203.70	198.40	201.90	214.1	194.1	o387
BGX006DR		205.65	201.13	204.10	203.4	183.4	o390
BGX013D		205.48	200.80	203.30	202.7	182.6	o391
HMD 1D		207.40	203.97	206.10	219.7	199.7	o537
HMD 2D		200.90	195.00	197.70	210.8	190.8	o538
HMD 3D		200.10	194.70	197.30	207.7	187.7	o539
HMD 4D		199.20	195.30	197.40	208.9	188.9	o541
NEP 4D		194.02	189.67	192.00	196.7	186.7	o607

An improved water retention curve is derived from the van Genuchten WRC for UVZ soil reported by Nichols and Butcher (2020). The new WRC is altered by increasing the pore-size distribution parameter (n) from 1.154 to 1.7 [$m = (1\text{-}1/n)$ and increased from 0.133 to 0.412] and decreasing the inverse of the air entry suction parameter (α) from 0.030177 to 0.001 cm^{-1}. These alterations improve and accelerate convergence of the flow solution in PORFLOW® with a reduction of mass balance disparities. A plot of pressure head and relative hydraulic conductivity as a function of

water saturation is shown in Figure 3-33 along with the van Genuchten parameters. Implementation of the WRC in PORFLOW® utilizes a table of truncated pressure heads and relative hydraulic permeabilities above a water saturation of 0.8178 (vertical black line in Figure 3-33) which corresponds to a maximum pressure head of 32.81 ft (1,000 cm). Pressure suction heads greater than 32.81 ft are not anticipated to occur in the VZ of the converged flow solution.

Changes have been made to the initial global base hydraulic conductivities and anisotropy ratios used in the calibration of the GSA_2018 flow model. The large changes are in the reduction of the anisotropy ratio from 30 to 10 in HSUs TCCZ, TZ, and AAA during the GSA_2021 flow model calibration. An increase in the vertical hydraulic conductivities in the LAZ, TCCZ and TZ along with the new WRC is instrumental in creating a vertically dominated downflow in the VZ to the water table. Table 3-24 shows the changes in these values.

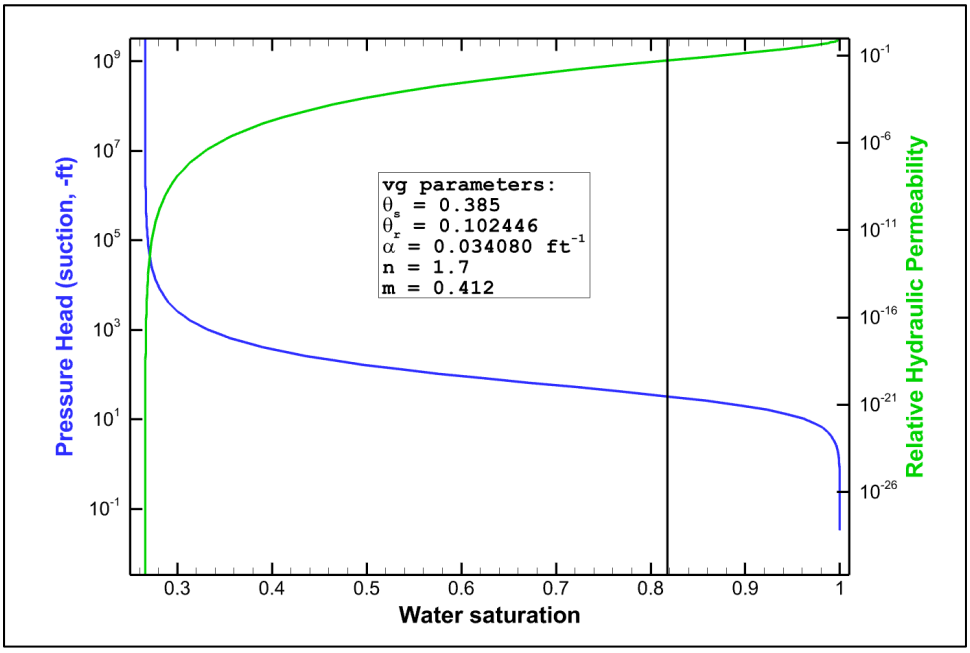

Figure 3-33 GSA_2021 Water Retention Curve

Table 3-24 Initial Global Base Hydraulic Conductivities in GSA_2018 and GSA_2021

HSU	PEST.102/GSA_2018			PEST.109/GSA_2021		
	Base K_h (ft d^{-1})	Base K_v (ft d^{-1})	Ratio K_h/K_v	Base K_h (ft d^{-1})	Base K_v (ft d^{-1})	Ratio K_h/K_v
LAZ	8	0.267	30	11	0.37	30
TCCZ	0.18	0.006	30	0.11	0.011	10
TZ	16	0.533	30	15	1.5	10
AAA	1	0.033	30	0.18	0.018	10

The GSA_2021 flow model is recalibrated using the PEST code. The model recalibration accounts for areas of the GSA where installed surface covers reduce assumed infiltration rates and other areas where sedimentation and seepage basins increase assumed infiltration rates. Flach et al. (2017) and Flach (2019) provide details on GSA flow model recalibration. These alterations to the baseline recharge/drain boundary conditions are assumed to be appropriate because their existence

corresponds reasonably well with the monitoring well head data employed as targets in the optimization efforts.

For recalibration purposes the primary application of covers in the ELLWF is operational covers for stormwater runoff, which are placed over STs once they are closed (a four-year delay is assumed). Operational covers have limited extent with overhangs of approximately 10 feet and a reduced infiltration rate of 0.1 in yr^{-1}.

The recalibration efforts are based on surface conditions during the ELLWF operational period (Years 0 – 71), consistent with the target heads employed, and represents the "uncovered" time period TP0. Table 3-25 lists the surface boundary conditions used in the recalibration effort. Both surface recharge/drain (seepage) and general head boundary conditions are employed, which is consistent with the boundary conditions utilized in the GSA_2018 flow model.

Table 3-25 Time-Averaged Intact Recharge Rates for Baseline GSA_2021 Flow Model

Material Type	Surface Region ID	TP0 [Yr 0–71] (in yr^{-1})	TP1 [Yr 71–451] (in yr^{-1})	TP2 [Yr 451–731] (in yr^{-1})	TP3 [Yr 731–1,171] (in yr^{-1})	TP4 [Yr 1,171–10,171] (in yr^{-1})
None	Top (Global)	15.0	15.0	15.0	15.0	15.0
Kaolin Clay Caps	MWMF_Cap_East	15.0	15.0	15.0	15.0	15.0
	MWMF_Cap_West					
	F_Seep_12					
	F_Seep_3					
	H_Seep_12					
	H_Seep_3					
	H_Seep_4					
Geosynthetic Caps	OBG_Cap	1.50	0.1109	1.7138	4.7775	1.7138
	LLRWDF					
	ST1to4_Cover					
	ST5_Cover					
	Group1_40ft	N/A				
	Group2_40ft					
	Group3_40ft					
	Group4_40ft					
	Group5_40ft					

As highlighted in Figure 3-34, the following surface features have imposed boundary conditions:

- **Recharge/Drain:** A uniform value of 15.0 in yr^{-1} is applied to the entire domain including regions with kaolin caps: the MWMF, F-Area Seepage Basin, and the H-Area Seepage Basin. However, the LLRWDF, ORWBG/GSA Consolidation Unit caps, and ST01-ST05 operational stormwater runoff covers incorporate a geomembrane that significantly reduces infiltration. Considering cap degradation over time, cap infiltration for these units is set to 1.5 in yr^{-1} (10% of 15.0 in yr^{-1}).
- **General Head:** Influx of water from the following sedimentation basins where varying heads are specified: (1) SWMF North and (2) Southern.

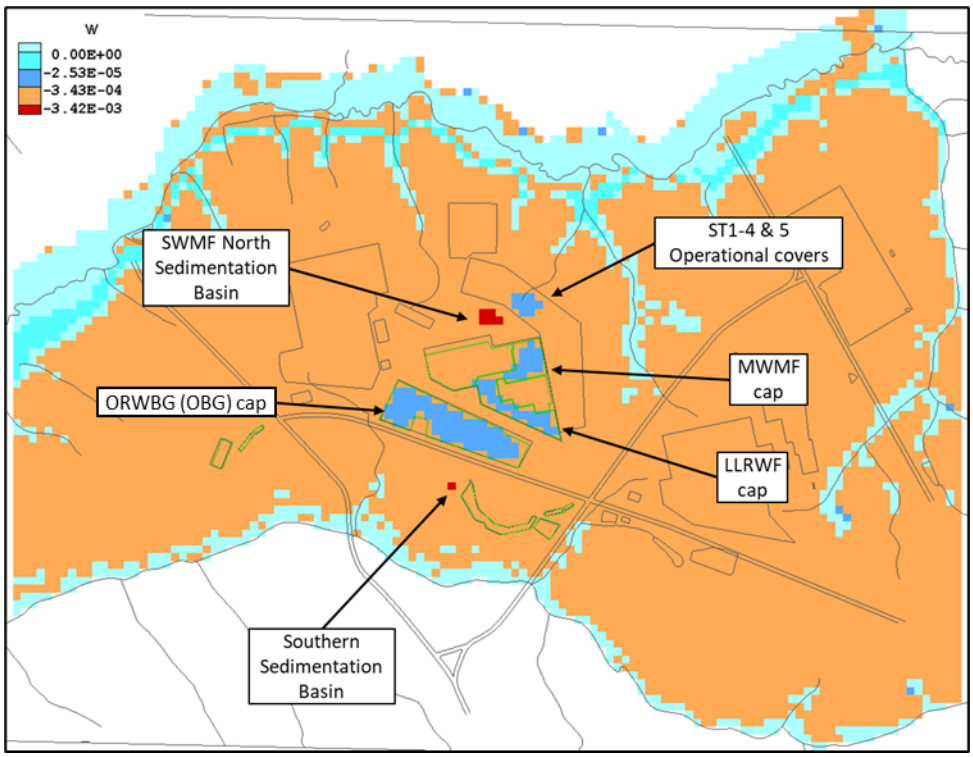

Figure 3-34 Surface Infiltration Rate Boundary Conditions Imposed for Uncovered Calibration Case

These features are shown at the top surface of the flow model in Figure 3-34. The color coding employed is based on: (1) background recharge of 15 in yr^{-1} in orange; (2) recharge above background in red; (3) recharge below background in blue; (4) seepage/drainage in light cyan.

The recharge/drain boundary condition is implemented as seepage boundary conditions (Mode 6 of the BOUNdary command) for the PORFLOW® software tool. This boundary condition combines recharge and drainage into a single boundary condition that is dependent on the pressure head. The use of a combined boundary condition requires the variably saturated formulation that PORFLOW® provides to users as an option. A negative pressure head (water table below the ground surface) results in infiltration and a positive pressure head results in a discharge, with a continuous transition (based on a cubic polynomial fit) between these two conditions.

3.5.2.12. GSA_2021 Flow Model Recalibration Results

Table 3-26 summarizes the level of agreement between simulated and measured hydraulic heads for PEST Optimization Run 109 (PEST.109) corresponding to GSA_2021.LW. Compared to PEST.102/GSA_2018.LW, the GSA_2021.LW model exhibits minor changes in residuals for the GAU because hydraulic conductivities are not updated. The median and average residuals for the LAZ decrease from 1.9 and 1.6, to -0.6 and -0.7 feet, respectively. The median and average residuals for the UAZ increase from -0.19 and -0.12, to -2.2 and -2.3 feet, respectively. These statistics represent all well targets in each HSU within the GSA domain.

Table 3-26. Hydraulic Head Residual Statistics (in feet) for GSA_2021.LW Model

HSU	Number	Median	Average	Root-mean-square	Minimum	Maximum
GAU	80	-1.1839	-1.6232	2.7029	-8.3623	2.7434
LAZ	285	-0.5890	-0.6854	4.7034	-15.3636	17.4392
UAZ	334	-2.1566	-2.3396	4.1696	-13.2575	8.3699

Focusing on the 20 ELLWF water table targets described in Section 3.5.2.11, the residuals for wells in the UAZ and LAZ are lower for GSA_2021.LW (Figure 3-35). Well Nos. 1 through 9 represent UAZ wells, and Well Nos. 10 through 20 are LAZ wells. The well residuals are greatly improved for the LAZ wells. These wells are located northwest of the blue transition line shown in Figure 3-32.

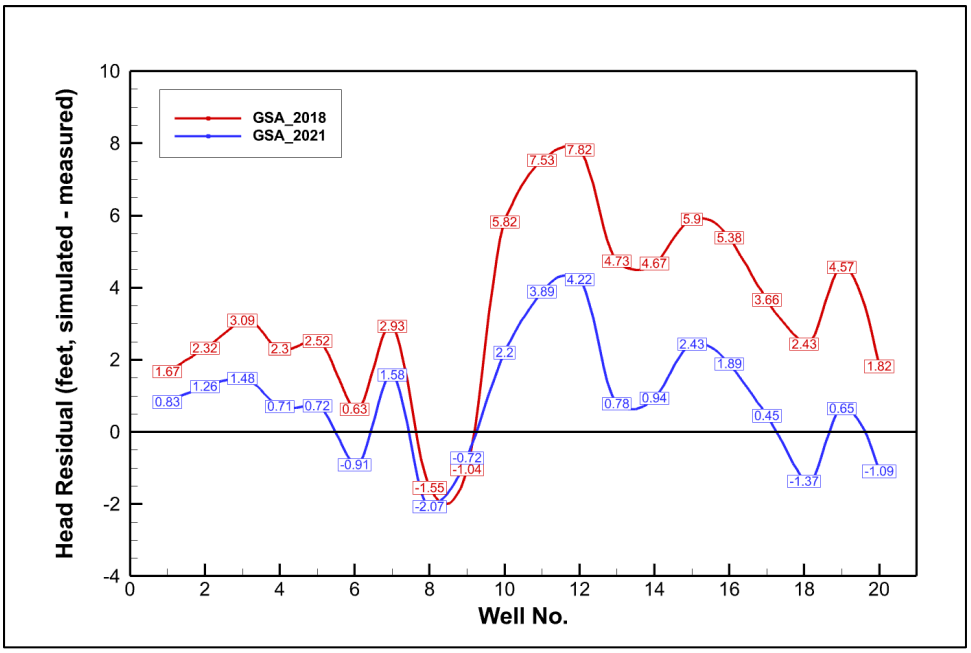

Figure 3-35 ELLWF Water Table Observation Well Residuals for GSA_2018 and GSA_2021

Table 3-27 provides a comparison of recharge and stream baseflows for the PEST.102/GSA_2018.LW and PEST.109/GSA_2021.LW calibrations. The stream baseflows for UTR and its tributaries, FMB and its tributaries, and the Crouch Branch are closer to the targeted values in GSA_2021.LW. There is a 0.1-inch increase in recharge and no change in the stream baseflow for the McQueen Branch in GSA_2021.LW.

Table 3-27. Recharge and Stream Baseflow Validation Targets for GSA_2021.LW Model

Flow Parameter	Target	PEST.102 (GSA_2018.LW)[2]	PEST.109 (GSA_2021.LW)[2]
Avg. Recharge (inches per year)[1]	N/A	12.1	12.2
Stream or Tributary	**Stream Baseflow (ft^3/sec)**		
UTR and tributaries less McQueen Branch	18.2	10.7	11.1
FMB and tributaries	2.6	3.0	2.8
McQueen Branch	1.5	1.8	1.8
Crouch Branch	1.8	1.4	1.5

Notes:

1 Surface infiltration divided by total surface area including seepage faces. The recharge estimate of 15 in yr^{-1} for the GSA is not a model calibration target.

2 "L" = Layer-cake *K* field; "W" = Weighted calibration targets

Figure 3-36 shows individual hydraulic head residuals for the three aquifer zones, in addition to the simulated water table. A similar set of plots is shown in Figure 3-22 for the GSA_2018 flow model calibration results. Overall, both sets of results are similar.

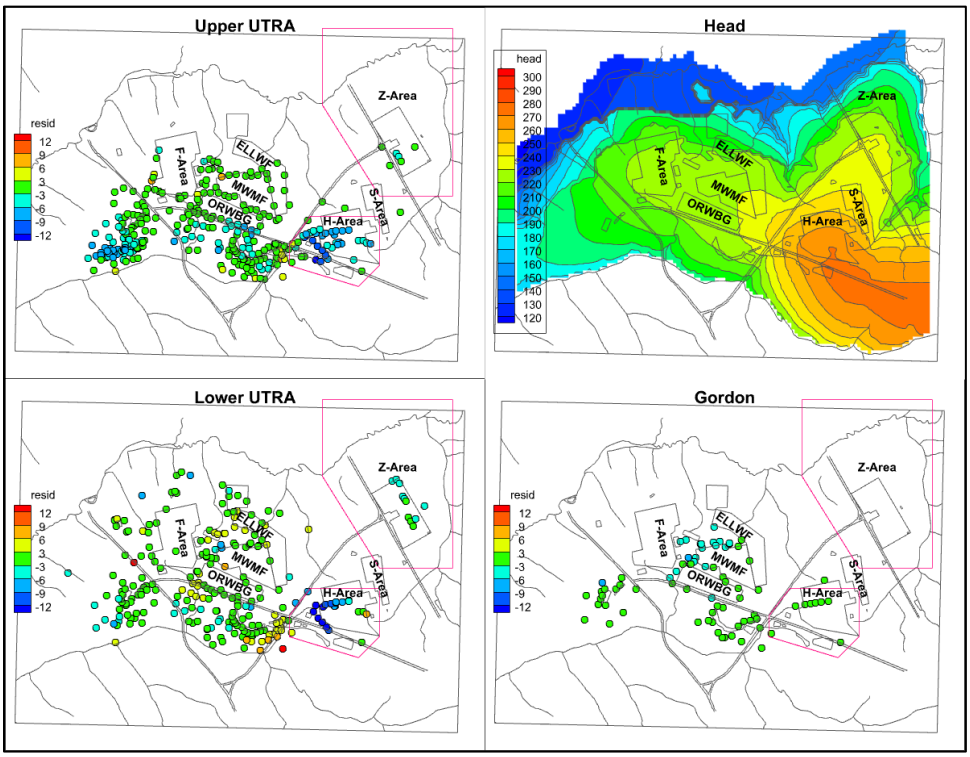

Note: A positive residual value indicates the simulated head is above the measured head.

Figure 3-36. Hydraulic Head Residuals and Water Table Surface for GSA_2021 Flow Model

Table 3-28 summarizes the calibrated conductivity field. These results can be compared to Table 3-21 for the PEST.102/GSA_2018.LW model case. Base and net hydraulic conductivities are color highlighted by HSU. Base conductivities are initial values for the start of the calibration process, and net values are the final estimate of the conductivities. The numbers highlighted in cyan are final estimates of the parameters in the first column. The global parameters are multipliers used to compute the net values from base values for each HSU. The region parameters for Harea,

Zarea, and FHbasins2 are multiplied by the global net values for each HSU to produce net values for the region. The global horizonal and vertical hydraulic conductivities are spatially averaged using appropriate techniques.

Hydraulic conductivities for the GAU and GCU remain unchanged from the GSA_2018 flow model. The net horizonal hydraulic conductivities of the LAZ, TCCZ, TZ, and AAA are 155%, 38%, 75%, and 1% of the global values in the GSA_2018 calibration, respectively. The net vertical hydraulic conductivities of the LAZ, TCCZ, TZ, and AAA are 156%, 114%, 224%, and 3% of the global values in the GSA_2018 calibration, respectively. Anisotropic ratios (K_h/K_v) of averaged hydraulic conductivities for the LAZ, TCCZ, TZ, and AAA are 32x, 14x, 10x, 17x, compared to 33x, 39x, 31x, and 23x in the GSA_2018 calibration, respectively. Changes in the net hydraulic conductivities for regions other than the global are reported but are not the focus of this calibration effort.

Table 3-28. Hydraulic Conductivity Summary for GSA_2021 Flow Model

Parameter	HSU	Region	Base K_h (ft d^{-1})	Base K_v (ft d^{-1})	PEST.109b	Net K_h (ft d^{-1})	Net K_v (ft d^{-1})	K_h (cm s^{-1})	K_v (cm s^{-1})	K_h avg (ft d^{-1})	K_v avg (ft d^{-1})	K_h/K_v ratio
Phi	--	--	--	--	1.75E+05	--	--	--	--	--	--	--
N/A	GAU	Global	38	0.38	--	--	--	--	--	--	--	--
N/A	GCU	Global	1.E-04	1.E-05	--	--	--	--	--	--	--	--
g01	LAZ	Global	11	0.37	1.336490	14.7	0.49	5.2E-03	1.7E-04	11.2	0.344	32x
g02	TCCZ	Global	0.11	0.011	0.276227	0.03	0.0030	1.1E-05	1.1E-06	7.44E-02	0.005	14x
g03	TZ	Global	15	1.5	0.736844	11.1	1.11	3.9E-03	3.9E-04	12.9	1.255	10x
g04	AAA	Global	0.18	0.018	0.131725	0.02	0.0024	8.4E-06	8.4E-07	0.9	0.051	17x
h01	LAZ	Harea	--	--	1.031590	15.2	0.5	5.4E-03	1.8E-04	--	--	--
h02	TCCZ	Harea	--	--	0.136371	0.004	4.1E-04	1.5E-06	1.5E-07	--	--	--
h03	TZ	Harea	--	--	0.668378	7.4	0.739	2.6E-03	2.6E-04	--	--	--
h04	AAA	Harea	--	--	1.334080	0.03	0.003	1.1E-05	1.1E-06	--	--	--
i01	LAZ	Zarea	--	--	0.514223	7.6	0.3	2.7E-03	9.0E-05	--	--	--
i02	TCCZ	Zarea	--	--	1.093040	0.03	0.003	1.2E-05	1.2E-06	--	--	--
i03	TZ	Zarea	--	--	0.720571	8.0	0.80	2.8E-03	2.8E-04	--	--	--
i04	AAA	Zarea	--	--	0.664096	0.02	0.002	5.6E-06	5.6E-07	--	--	--
j01	LAZ	FHbasins2	--	--	0.3	4.4	0.1	1.6E-03	5.2E-05	--	--	--
j02	TCCZ	FHbasins2	--	--	5.0	0.15	0.015	5.4E-05	5.4E-06	--	--	--
j03	TZ	FHbasins2	--	--	1.878110	20.8	2.08	7.3E-03	7.3E-04	--	--	--
j04	AAA	FHbasins2	--	--	0.693473	0.02	0.002	5.8E-06	5.8E-07	--	--	--

Notes:
Highlighting indicates the unique parameter variables for the different hydrostratigraphic units.

One of the goals of the GSA_2021 flow model calibration is to produce a flow field that predominantly downflows vertically in the VZ to the water table. Figure 3-37 shows stream traces for the GSA_2021 flow model, in addition to the location of a vertical slice through the north-south center of the ELLWF. GSA_2021 flow model velocity and pressure head profiles on the vertical

slice are also displayed in Figure 3-38. The velocities in the vertical slice above the water table are predominantly downward except near the ends where seepage faces occur at FMB and UTR.

A flow divide is evident within the aquifer region in Figure 3-38. The velocity vectors represented in Figure 3-38 do not show the actual relative magnitude of the flow field; instead, they have been normalized and show only the flow direction. The vertical flows through the GCU (i.e., the 3rd and 4th cells from the bottom) are very small because this confining unit is very competent. To a large degree, the GCU disconnects the UTRA from the Gordan Aquifer as can be seen in the pressure and flow fields shown in Figure 3-38. For example, the GAU essentially does not hydraulically "feel" the presence of FMB while it discharges to UTR. This disconnect also shows up in aquifer transport runs where stream traces and contaminant plumes show a distinct directional shift as contaminant leaves the UTRA and begins to enter the GAU (e.g., see Appendix C).

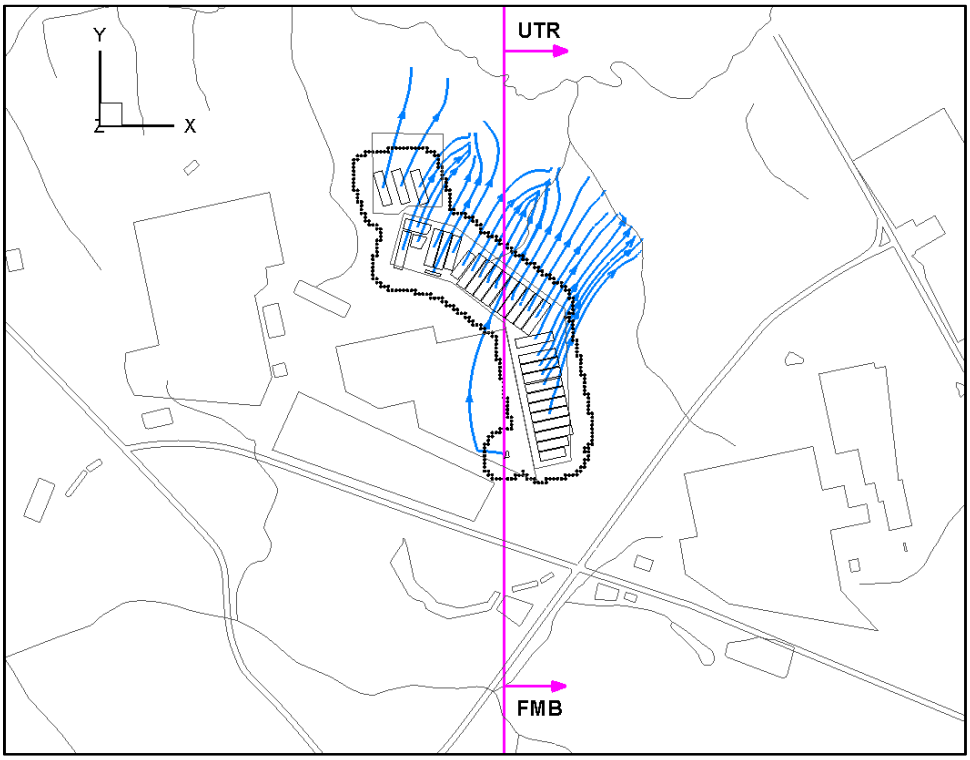

Figure 3-37. Location of a Vertical Slice and Stream Traces for the GSA_2021 Flow Model

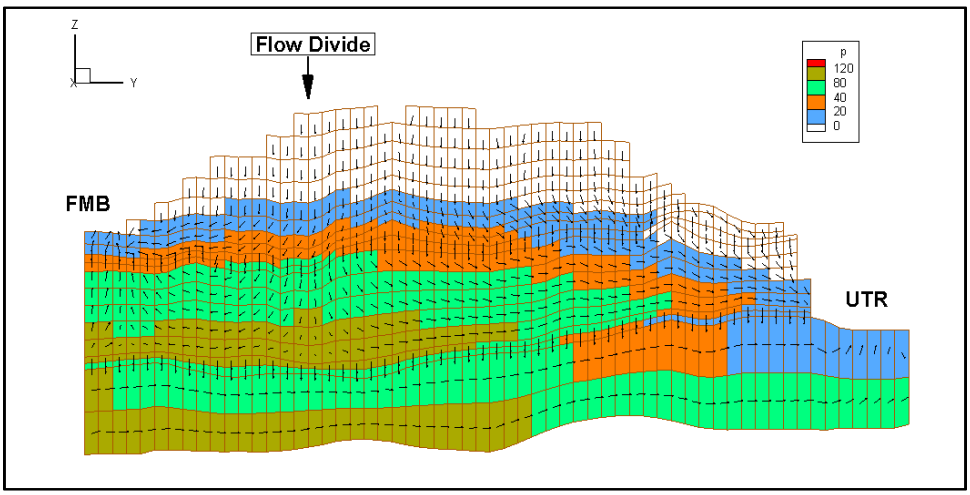

Figure 3-38. GSA_2021 Flow Model Velocity and Pressure Head Profiles on the Vertical Slice

Table 3-29 through Table 3-31 demonstrate that the GSA_2021 flow model conserves mass. Table 3-29 lists flowrates across the six faces of the overall model domain. Total inflow and outflow differ by only 0.15%. Table 3-30 presents mass balance results for each aquifer unit and zone. Again, inflows and outflows are observed to differ by less than 0.22%. Finally, Table 3-31 provides a global mass balance analogous to Table 3-29 but broken out by boundary condition type (i.e., RECH## = recharge zone ##, GENH## = general head zone ##, and HEAD## = prescribed head zone ##).

Table 3-29. Global Mass Balance (ft^3/s)

BOUNDARY:	IN	OUT	NET	FLOW
ALL x-	1.854E-01	7.821E-01	-5.968E-01	
ALL x+	2.233E+00	0.000E+00	2.233E+00	
ALL y-	1.977E+00	0.000E+00	1.977E+00	
ALL y+	0.000E+00	1.777E-01	-1.777E-01	
ALL z-	3.022E-01	1.578E-02	2.865E-01	
ALL z+	1.010E+01	1.385E+01	-3.745E+00	
TOTALS	1.480E+01	1.482E+01	-2.291E-02	**-0.15%**

Table 3-30. Aquifer Zone Mass Balances (ft^3/s)

BOUNDARY:	IN	OUT	NET	FLOW
GAU x-	1.055E-01	5.103E-01	-4.048E-01	
GAU x+	2.233E+00	0.000E+00	2.233E+00	
GAU y-	1.977E+00	0.000E+00	1.977E+00	
GAU y+	0.000E+00	1.777E-01	-1.777E-01	
GAU z-	3.022E-01	1.578E-02	2.865E-01	
GAU z+	4.627E-01	4.378E+00	-3.915E+00	
TOTALS	5.080E+00	5.081E+00	-8.639E-04	**-0.02%**

BOUNDARY:	IN	OUT	NET	FLOW
UTR x-	7.986E-02	2.718E-01	-1.920E-01	
UTR x+	0.000E+00	0.000E+00	0.000E+00	
UTR y-	0.000E+00	0.000E+00	0.000E+00	

UTR y+	0.000E+00	0.000E+00	0.000E+00	
UTR z-	8.433E-06	1.744E-01	-1.744E-01	
UTR z+	9.814E+00	9.470E+00	3.443E-01	
TOTALS	9.894E+00	9.916E+00	-2.205E-02	**-0.22%**

BOUNDARY:	IN	OUT	NET	FLOW
LAZ x-	7.480E-02	2.691E-01	-1.943E-01	
LAZ x+	0.000E+00	0.000E+00	0.000E+00	
LAZ y-	0.000E+00	0.000E+00	0.000E+00	
LAZ y+	0.000E+00	0.000E+00	0.000E+00	
LAZ z-	8.433E-06	1.744E-01	-1.744E-01	
LAZ z+	7.281E+00	6.920E+00	3.607E-01	
TOTALS	7.356E+00	7.364E+00	-8.038E-03	**-0.11%**

BOUNDARY:	IN	OUT	NET	FLOW
UAZ x-	5.064E-03	2.761E-03	2.303E-03	
UAZ x+	0.000E+00	0.000E+00	0.000E+00	
UAZ y-	0.000E+00	0.000E+00	0.000E+00	
UAZ y+	0.000E+00	0.000E+00	0.000E+00	
UAZ z-	5.556E-01	6.482E+00	-5.926E+00	
UAZ z+	9.016E+00	3.106E+00	5.910E+00	
TOTALS	9.576E+00	9.590E+00	-1.401E-02	**-0.15%**

Table 3-31. Boundary Condition Mass Balances (ft³/s)

BOUNDARY:	IN	OUT	NET	FLOW	IN	OUT	NET	FLUX
RECH01:	9.956E+00	1.385E+01	-3.891E+00		1.217E+01	1.693E+01	-4.756E+00	
RECH02:	1.124E-01	0.000E+00	1.124E-01		1.498E+01	0.000E+00	1.498E+01	
RECH03:	1.678E-02	0.000E+00	1.678E-02		1.498E+00	0.000E+00	1.498E+00	
GENH01:	2.544E-01	1.299E-02	2.414E-01		3.060E-01	1.562E-02	2.904E-01	
GENH02:	6.164E-03	0.000E+00	6.164E-03		5.831E+01	0.000E+00	5.831E+01	
GENH04:	1.090E-02	0.000E+00	1.090E-02		2.063E+01	0.000E+00	2.063E+01	
HEAD01:	7.986E-02	2.719E-01	-1.920E-01		9.861E+01	3.357E+02	-2.371E+02	
HEAD02:	4.363E+00	6.908E-01	3.673E+00		2.558E+02	4.050E+01	2.153E+02	
TOTALS:	1.480E+01	1.482E+01	-2.312E-02	**-0.16%**				

Figure 3-39 shows the flow rates entering the top surface of the GSA_2021 flow model (i.e., incoming recharge) versus the flow rates exiting the top surface (i.e., outgoing drainage). Figure 3-39 also compares simulated seepage faces (blue shading) to surveyed seeplines (white lines). The predicted seepage faces are consistent with field observations.

Figure 3-40 compares simulated hydraulic heads to measured well water levels in the form of crossplots. The solid-black lines represent linear fits to the data. A linear fit to a perfect calibration would have an intercept of 0 feet and an angle of 45 degrees. Also shown are R^2 values, which range from 0.91 to 0.97. R^2 is the fraction of the observed hydraulic head variability that is captured by the model simulation. The linear fit to the UAZ data has an intercept of 8.116 feet and an angle of 43.6 degrees (arctan of 0.953). The linear fit to the LAZ data has an intercept of 34.26 feet and an angle of 40.0 degrees. The linear fit to the GAU data has an intercept of -23.47 feet and an angle of 48.6 degrees.

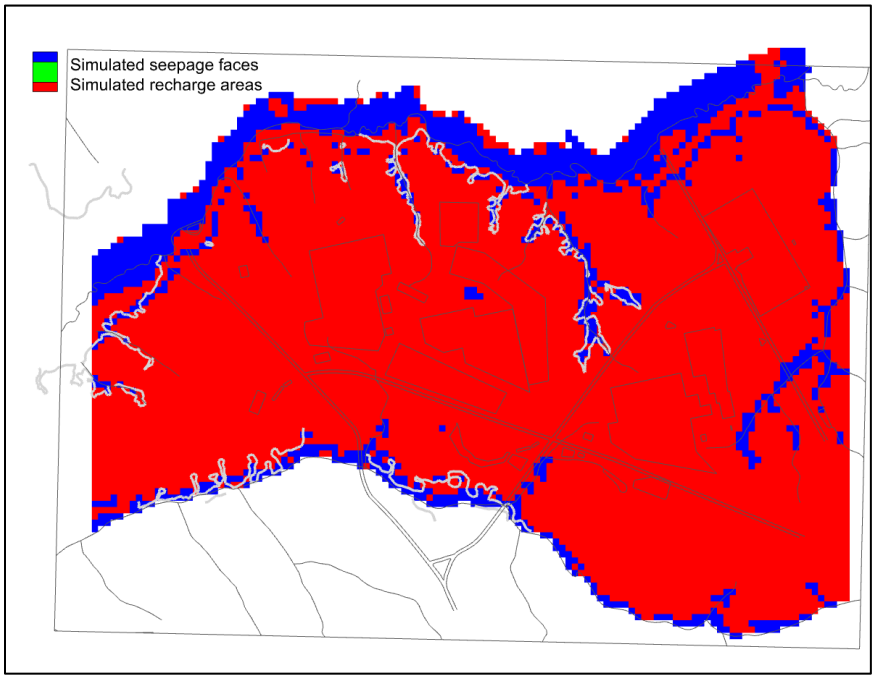

Figure 3-39. Simulated Seepage Faces Compared to Surveyed Seeplines for GSA_2021 Flow Model

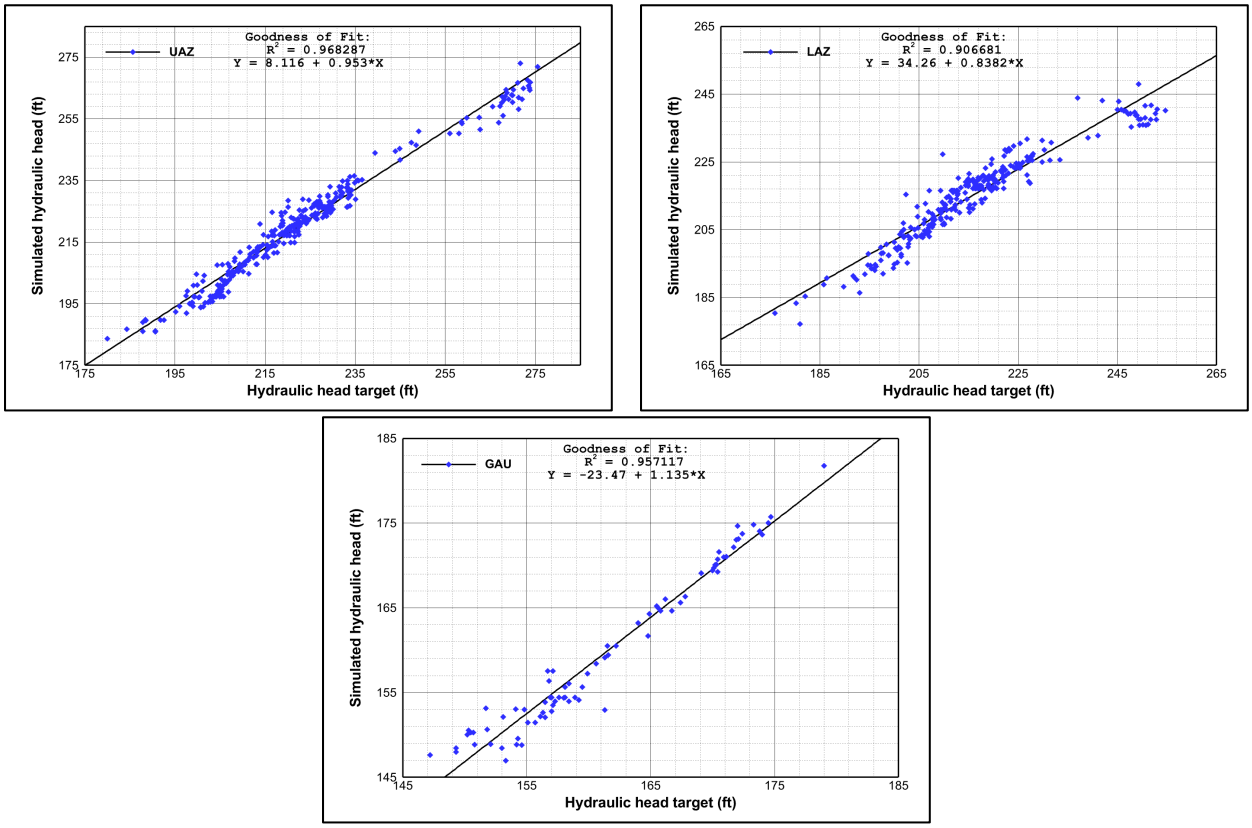

Figure 3-40. Hydraulic Head Crossplots for GSA_2021 Flow Model Recalibration

The PEST optimization case PEST.109 is chosen as the baseline GSA flow model for PA2022. The top surface of the baseline GSA flow model corresponds to the local ground surface as shown

in the left image of Figure 3-41. Ground surface in the GSA varies from ~80 feet to over 300 feet MSL. For the ELLWF, the general aquifer flow travels toward the UTR and its tributaries, outcropping at various locations along the seepage faces. 3-D stream traces (shown in orange) are displayed for ET07, ET09, ST09, ST05, ET02, and ST17 in the right image of Figure 3-41.

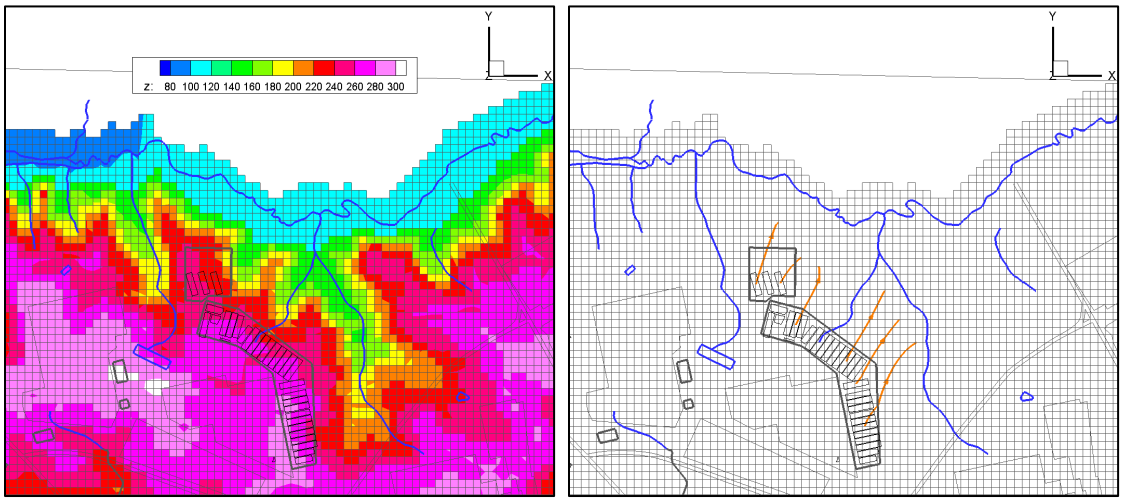

Figure 3-41 Ground Elevation and Stream Traces in Baseline GSA Flow Model

Figure 3-42 displays the resulting surface pressures where, for positive pressure head values, water is leaving the ground surface at seepage faces.

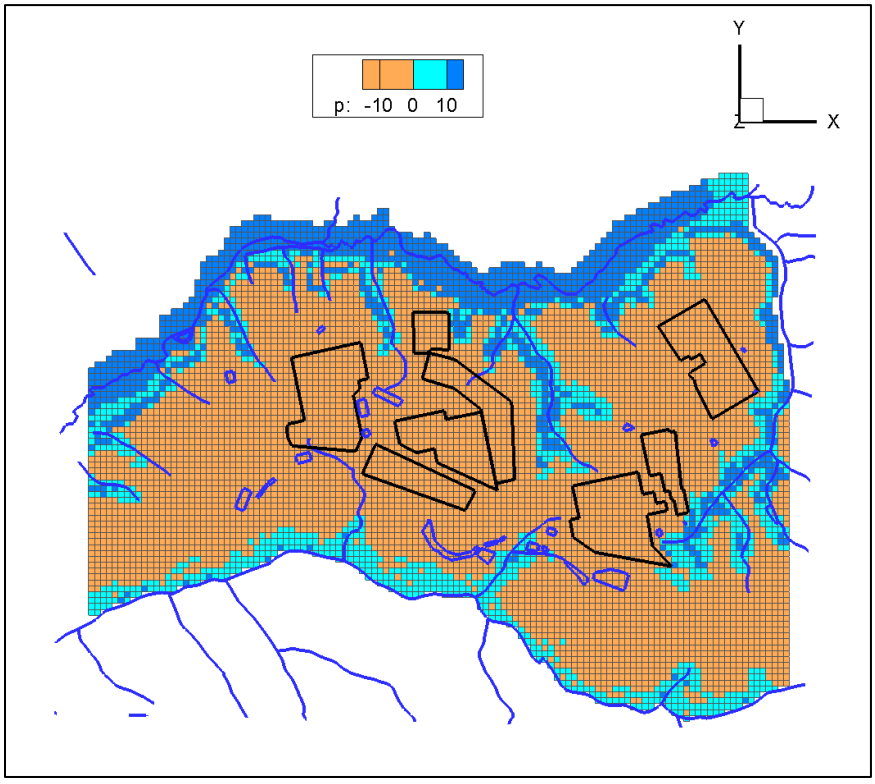

Figure 3-42 Predicted Surface Pressure Head for Baseline GSA Flow Model

3.5.2.13. GSA_2021 Flow Model Simulation Results (Uncovered, Years 0 to 71)

Figure 3-43 through Figure 3-49 display simulated hydraulic heads, measured hydraulic heads (in feet above MSL), and simulated ground surface fluxes (recharge). The corresponding figures for GSA_2018.LW are reported by Flach (2019; Section 4.0). The predicted seepage faces are consistent with field observations. Simulated hydraulic heads, vertically averaged over the entire thickness of the UAZ, LAZ, and GAU, agree with potentiometric maps based on measured heads. Simulated flow directions vertically averaged over the entire thickness of the aquifer zones agree with conceptual models of GW flow.

The GSA flow model simulates GW flow under steady-state conditions representing current topography and climate. Potential climate changes affecting infiltration are addressed through sensitivity cases (Chapters 5 and 6). The influence of the future ELLWF closure cap on GW flow rates and directions in the aquifers is explicitly considered in the aquifer transport model simulations. The influence of caps over other surrounding facilities is also addressed in the modeling upgrades (see Sections 3.5.2.11 and 3.5.2.14). The presence of the final closure cap is expected to slightly lower the water table beneath E-Area, thereby increasing the VZ transport distance.

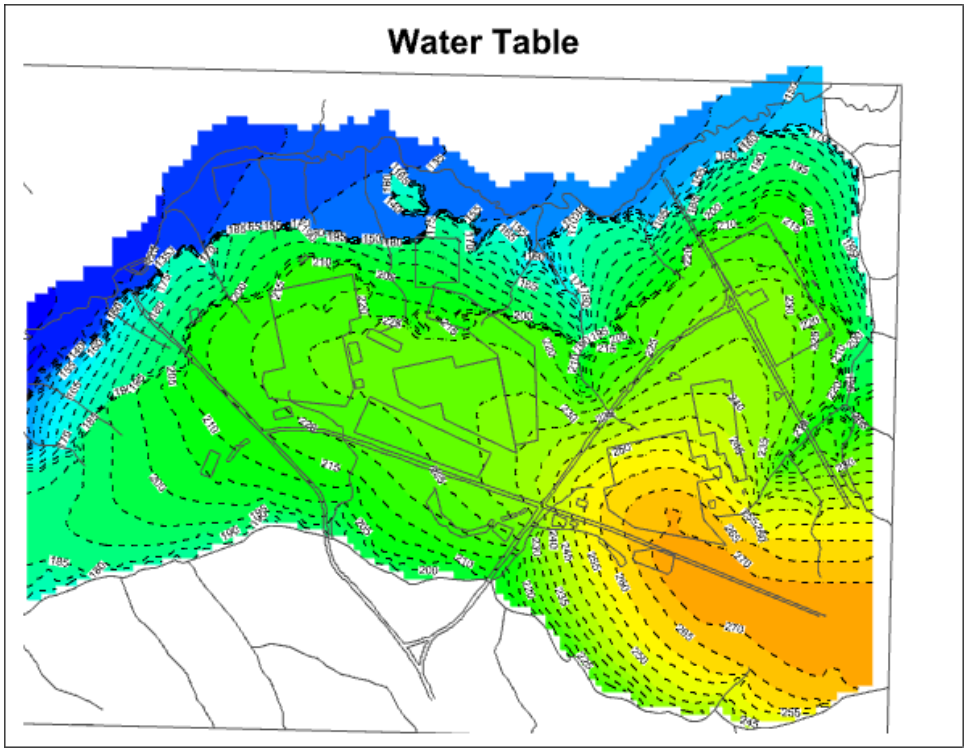

Figure 3-43. Simulated Water Table for GSA_2021 Flow Model (Feet)

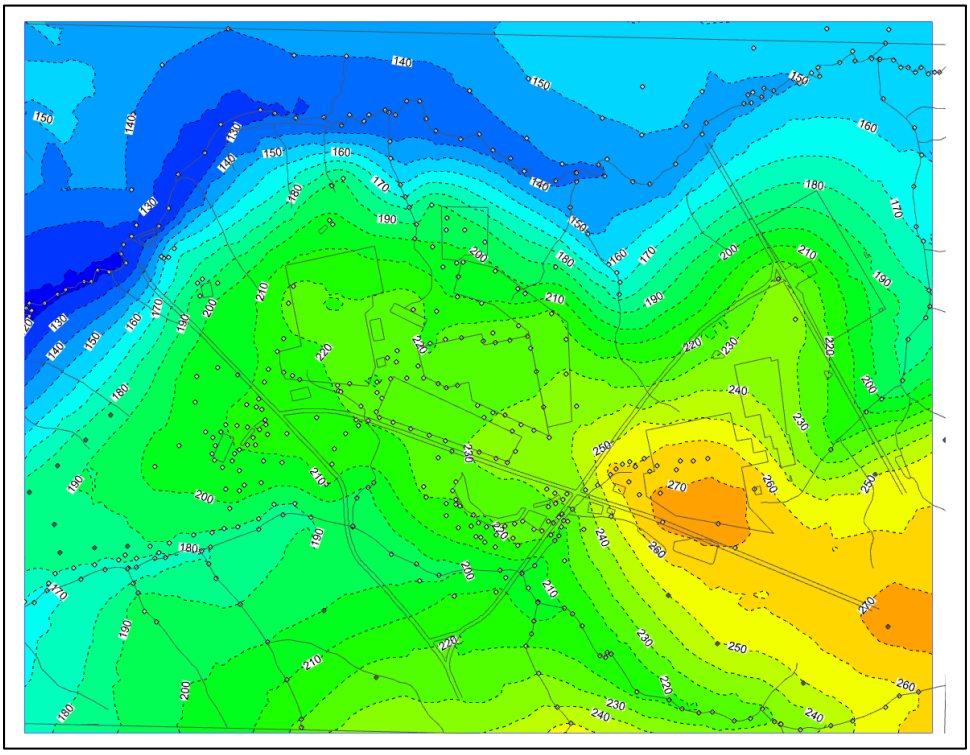

Figure 3-44. Kriging Interpolation Representation of Measured Water Table (Feet)

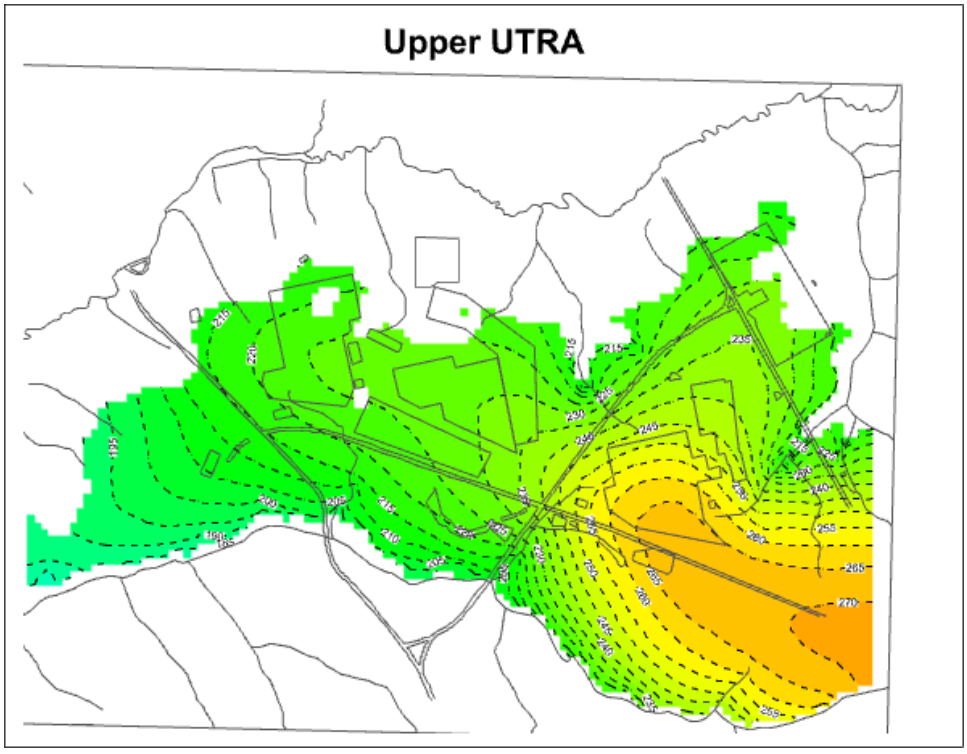

Figure 3-45. Simulated Hydraulic Head (Feet) in Upper Aquifer Zone for GSA_2021 Flow Model

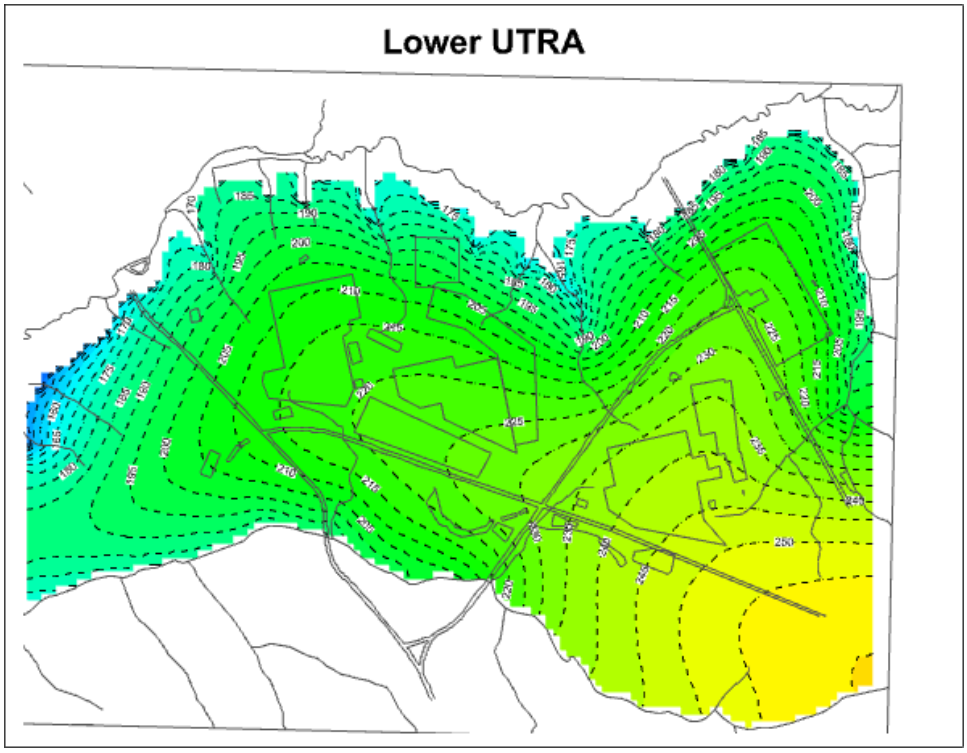

Figure 3-46. Simulated Hydraulic Head (Feet) in Lower Aquifer Zone for GSA_2021 Flow Model

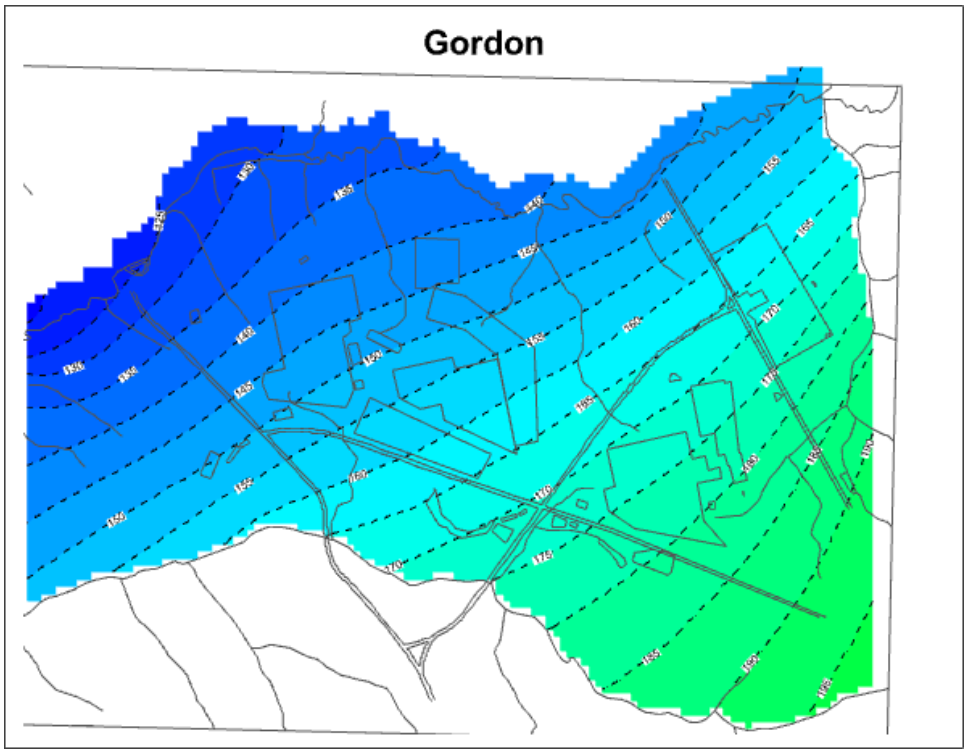

Figure 3-47. Simulated Hydraulic Head (Feet) in Gordon Aquifer Unit for GSA_2021 Flow Model

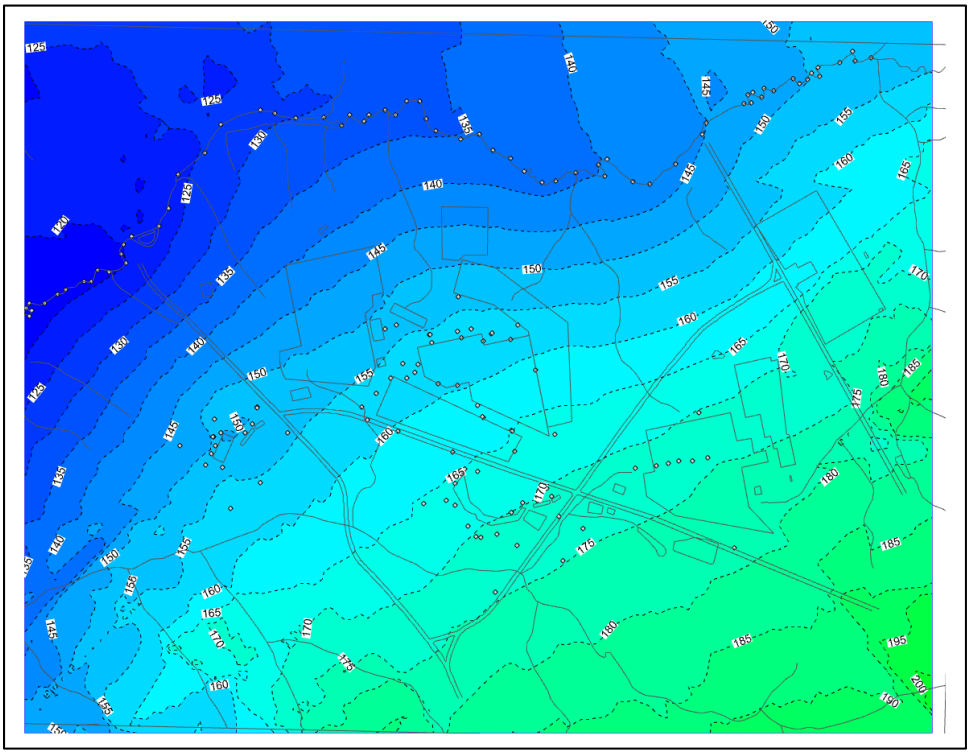

Figure 3-48. Kriging Interpolation Representation of Gordon Aquifer Unit Measurements (Feet)

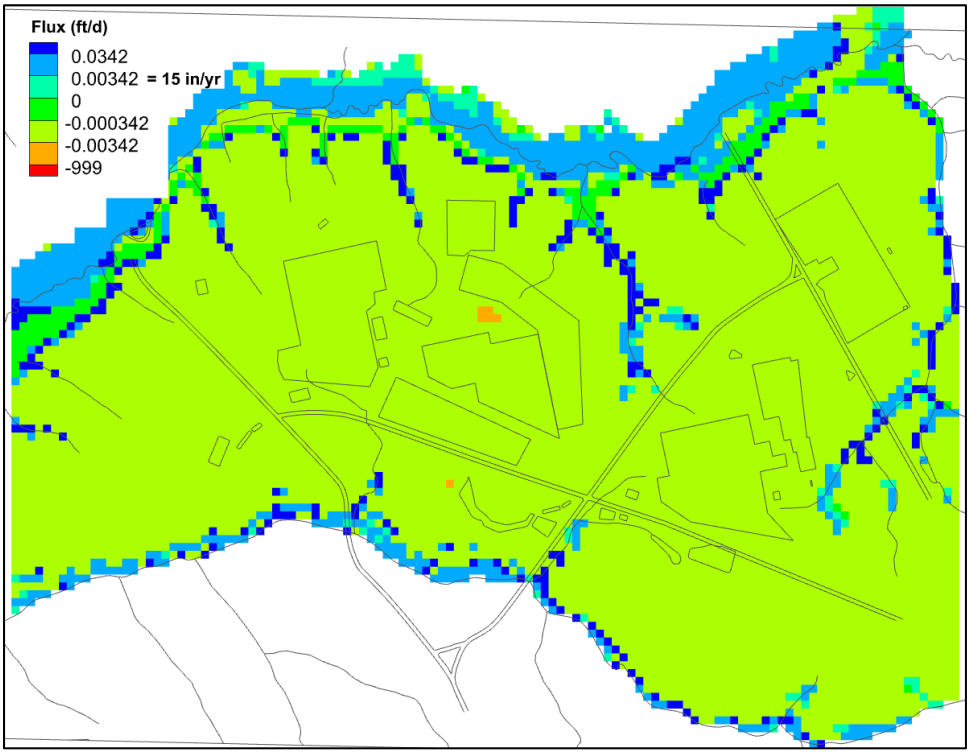

Figure 3-49. Simulated Surface Flux in Feet per Day for GSA_2021 Flow Model

3.5.2.14. GSA_2021 Flow Model Infiltration Rates for Uncovered and Intact Covers

The following flow fields are considered for transient aquifer transport:

- **Operational Time Period:** From the start of facility operations (September 28, 1994) until the start of IC (September 30, 2065), the ELLWF is assumed to be essentially uncovered (i.e., relative Years 0 to 71).
- **Compliance Period:** From the start of IC until the end of the period of performance, a series of time segments are employed during which incremental degradation of the final intact closure cap is accounted for in the model.
- **Beyond the Period of Performance:** From the end of the period of performance until dose peaks at the 100-meter POA are observed, the aquifer flow model is conservatively set to uncovered conditions.

Due to environmental degradation of the final closure cap, intact infiltration rates for STs and ETs vary with time after the end of IC. Section 3.8.4 and Dyer (2019b) document the infiltration data package for this PA. The intact infiltration rates for STs and ETs are provided in Table 3-32. As Table 3-32 indicates, the final cover's effectiveness degrades over time; uncovered conditions will eventually return well beyond Year 10,171.

Table 3-32 Intact Infiltration Rates for Slit and Engineered Trenches

Relative Year [a]	Surface Condition	Infiltration Rate		Cover Effectiveness Factor (%)
		in yr^{-1}	cm yr^{-1}	
0	Uncovered (Year 0 – 71)	15.78	40.0812	100.000%
71	Interim cover (Year 71 – 171)	0.1	0.254	0.634%
170.99		0.1	0.254	0.634%
171	Final cover (Year 171 and beyond)	0.0008	0.002032	0.005%
251		0.007	0.01778	0.044%
361		0.16	0.4064	1.014%
371		0.18	0.4572	1.141%
411		0.3	0.762	1.901%
451		0.38	0.9652	2.408%
551		1.39	3.5306	8.809%
731		3.23	8.2042	20.469%
1,171		6.82	17.3228	43.219%
1,971		10.24	26.0096	64.892%
2,794		11.1	28.194	70.342%
3,371		11.18	28.3972	70.849%
5,771		11.3	28.702	71.610%
10,171		11.35	28.829	71.926%

Notes:

[a] Relative time from the start of operations on September 28, 1994.

Mass-balance-averaged infiltration rates over specific time periods are computed by:

$$\langle I \rangle_i = \frac{1}{(t_{i+1} - t_i)} \int_{t_i}^{t_{i+1}} I(t')dt' \qquad \text{Eq. (3-11)}$$

where:

$\langle I \rangle_i$ time-averaged infiltration rate for i^{th} time period (in)

t_i i^{th} time (yr)

$I(t)$ infiltration rate at time t (in yr^{-1})

Average effectiveness factors are computed by:

$$\langle E \rangle_i = \frac{\langle I \rangle_i}{I_0} \qquad \text{Eq. (3-12)}$$

where:

$\langle E \rangle_i$ average effectiveness factor for i^{th} time period (unitless)

I_0 infiltration rate for uncovered conditions (15.78 in yr^{-1})

The results of applying Eq. (3-11) and Eq. (3-12) for selected time periods are listed in Table 3-33.

Table 3-33 Time-Averaged Intact Infiltration Rates for Slit and Engineered Trench Disposal Units

Zone ID	Time Period (TP)	Start Time (yr)	End Time (yr)	<I> (in yr^{-1})	<E> (-)
0	TP0	0	71	15.780	100.00%
1	TP1	71	451	0.117	0.74%
2	TP2	451	731	1.801	11.41%
3	TP3	731	1,171	5.025	31.84%
4	TP4	1,171	10,171	10.982	69.60%
5	--	71	1,171	2.509	15.90%

Zone 0 represents the uncovered case, while Zone 1 through Zone 5 represent averaged cover behaviors for varying periods. The results listed in Table 3-33 are also plotted in Figure 3-50.

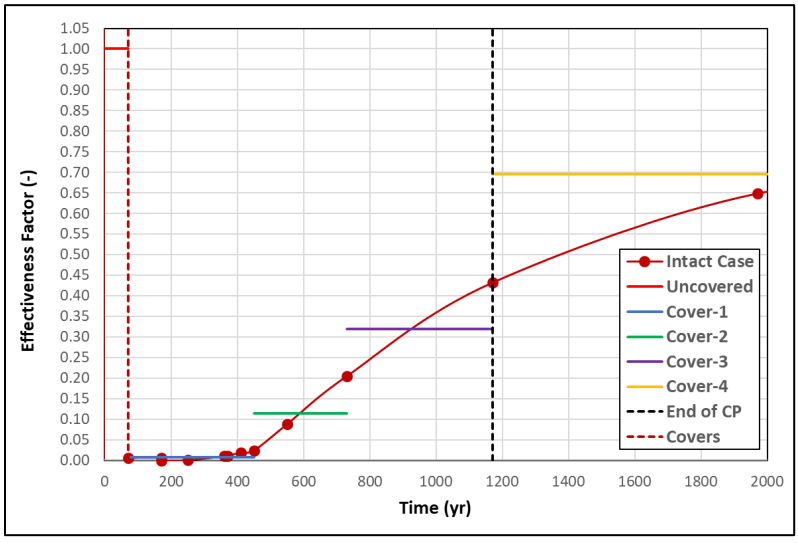

Figure 3-50 Comparison of Effectiveness Factors Across Varying Time Periods

Based on the effectiveness factor curve (i.e., red bulleted line in Figure 3-50), Zone 1 is defined as Years 71 to 451 to match its early behavior. Zones 2 and 3 represent simple stair steps to the end of the compliance period. Zone 4 represents the average behavior beyond the compliance period to Year 10,171, which is representative of the NRC's 10,000-year compliance period. The impact of employing Zone 4 instead of Zone 0 after Year 1,171 (i.e., the end of the compliance period) is highlighted in Figure 3-51. The effectiveness curve will eventually return to the uncovered case; however, HELP model simulations are performed for a 10,000-year compliance period only based on NRC-related guidance.

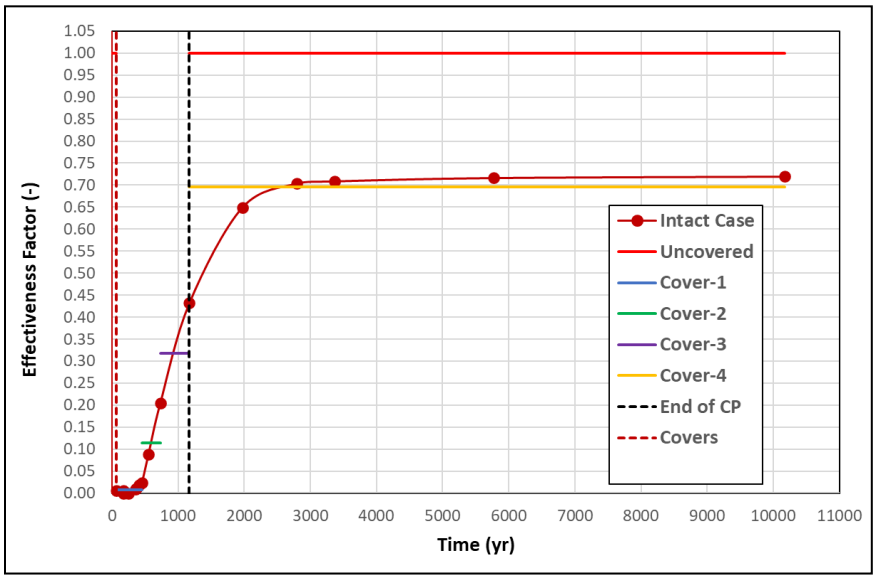

Figure 3-51 Comparison of Effectiveness Factors Over 10,171 Years

The infiltration rates discussed above and presented in Table 3-33 are based on a recharge rate of 15.78 in yr^{-1} for uncovered trenches (with 4-foot soil cover sloped away from trench) residing within the ELLWF footprint. This infiltration rate is based on HELP model simulations focused locally on STs and ETs within the ELLWF only. The model parameters employed in these HELP model simulations are not necessarily representative of recharge rates across the entire GSA footprint. For example, the average ground surface slope, which impacts rainfall runoff, is greater for the GSA on average than for the ELLWF on average. Based on other sources of information (see Section 3.5.2.8 and Table 3-18), it is estimated that an average value ~15 in yr^{-1} is more appropriate for use in the baseline GSA flow model.

The time-averaged infiltration rates in Table 3-33 are scaled down by a factor of 0.95 (i.e., 15.0/15.78) to account for GSA versus ELLWF geometrical differences. The effectiveness factor is assumed to be unchanged. Table 3-25 shows the results of this scaling process.

Table 3-25 lists the local recharge rates for all regions within the GSA model domain. The Top (Global) surface region represents the entire GSA footprint and sets the entire top surface to the stated values (15.0 in yr^{-1}). For each subsequent surface region (descending each column), the listed recharge rates supersede the prior region's values. Because the kaolin clay caps only last a few years, they are assumed to have nearly the original uncovered recharge rates.

Two sedimentation basins (SWMF North and Southern Sedimentation Basins) are also addressed as general head boundary conditions (i.e., a type-3 boundary condition) and their locations are highlighted in Figure 3-34 and Figure 3-52. Table 3-34 lists the parameter settings employed for all time periods.

Table 3-34 Sedimentation Basin General Head Boundary Conditions for Baseline GSA_2021 Flow Model

SWMF Sedimentation Basin	Reference Head (ft)	Leakance Coefficient (in yr^{-1})
North	275.0	0.0002
Southern	253.0	0.002

3.5.2.15. GSA_2021 Flow Model Simulation Results

The PEST recalibration is based on surface boundary conditions present during the uncovered operational period for the ELLWF (i.e., Years 0 to 71) as discussed in Section 3.5.2.11 and shown schematically in Figure 3-34. The surface boundary conditions chosen are consistent with the prevailing surface conditions within that time period. Table 3-35 summarizes the resulting best estimate parameter settings for the GSA_2021 flow model.

Table 3-35. GSA_2021 Flow Model Best Estimate Parameter Values and Their Confidence Limits

Parameter Description	Parameter ID	Best Estimate Value	95% Percent Confidence Limits	
			Lower Limit	Upper Limit
Global multiplier to LAZ	g01	1.3365E+00	1.2733E+00	1.4029E+00
Global multiplier to TCCZ	g02	2.7623E-01	2.6179E-01	2.9146E-01
Global multiplier to TZ	g03	7.3684E-01	6.2944E-01	8.6258E-01
Global multiplier to AAA	g04	1.3173E-01	9.3945E-02	1.8470E-01
HS-Area multiplier to LAZ	h01	1.0316E+00	2.5067E-01	4.2454E+00
HS-Area multiplier to TCCZ	h02	1.3637E-01	1.3332E-02	1.3949E+00
HS-Area multiplier to TZ	h03	6.6838E-01	3.7897E-02	1.1788E+01
HS-Area multiplier to AAA	h04	1.3341E+00	7.7294E-02	2.3026E+01
Z-Area multiplier to LAZ	i01	5.1422E-01	3.7322E-01	7.0850E-01
Z-Area multiplier to TCCZ	i02	1.0930E+00	3.6771E-01	3.2491E+00
Z-Area multiplier to TZ	i03	7.2057E-01	5.2490E-02	9.8918E+00
Z-Area multiplier to AAA	i04	6.6410E-01	4.5867E-04	9.6152E+02
FH-Basins multiplier to LAZ	j01	3.0000E-01	1.3058E-01	6.8924E-01
FH-Basins multiplier to TCCZ	j02	5.0000E+00	2.4160E+00	1.0348E+01
FH-Basins multiplier to TZ	j03	1.8781E+00	9.9322E-01	3.5514E+00
FH-Basins multiplier to AAA	j04	6.9347E-01	5.1145E-81	9.4028E+79

Notes:
Parameters highlighted in green are used in the lower-bound and upper-bound estimates of the GSA_2021 flow fields.

For the application of future covers and consideration of the impacts of cover degradation, the best estimate parameter settings remain fixed and, instead, steady-state PORFLOW GSA_2021 flow model simulations are completed for a series of forward time periods consistent with TP1 through TP4 listed in Table 3-33. The impact of installed covers is explicitly considered in the PA fate and transport model simulations.

The flow field for the initial uncovered time period (TP0) corresponds to the flow field obtained during the PEST recalibration process (Sections 3.5.2.11 and 3.5.2.12) and addresses operational (stormwater runoff) covers. To address future ELLWF surface conditions, the following applications of ELLWF covers are modeled:

- **Interim Cover:** Placed over the entire ELLWF at the start of IC and is maintained for the entire 100-year IC period. The interim cover extends globally about 40 feet beyond the DU footprint boundaries and has a reduced infiltration rate of 0.1 in yr^{-1}.
- **Final Cover:** A soil-geomembrane multilayer closure cap is installed over the entire ELLWF at the end of IC. Like the interim cover, the final closure cap extends globally about 40 feet beyond the DU footprint boundaries and includes a composite GCL-geomembrane barrier where intact, undegraded infiltration rates are initially as low as 0.0008 in yr^{-1}.

Subsidence is a local phenomenon caused by the collapse of non-crushable containers and results in a significant increase in local infiltration rates. The areal footprint of non-crushable containers is limited in each ST and ET (e.g., 2% or less in all future STs and ETs). Given the local aspects of subsidence and the limited number of non-crushable containers within a given trench, the impact of subsidence on aquifer flow is assumed to be minor and infiltration rates are assumed to follow the degradation behavior of an intact final cover.

Based on the computational strategy employed, transient transport calculations are performed using steady-state aquifer flow fields extracted from the calibrated GSA_2021 flow model. Time-average flow fields are assumed because aquifer flow fields are generally slowly varying over seasonal periods. The primary factor leading to changes in the aquifer flow field is ground-surface condition alterations, such as the placement of covers with significant footprints. The local STs' operational covers, which will be placed throughout the operational period of the ELLWF, are assumed to not significantly alter the aquifer flow fields beneath the ELLWF, downstream to the 100-meter POA.

Both surface recharge/drain and general head boundary conditions are employed, which is consistent with the boundary conditions utilized in the GSA_2021 flow model recalibration. As highlighted in Figure 3-52, the following surface features have imposed boundary conditions:

- **Recharge/Drain:** A uniform value of 15.0 in yr^{-1} is applied except at the following locations where recharge is uniquely specified: (1) MWMF cap; (2) LLRWDF cap; (3) ORWBG cap; and (4) ELLWF cap where their infiltration performance is degraded over time using four non-overlapping time periods (TP1, TP2, TP3, and TP4).
- **General Head:** Influx of water from the following sedimentation basins where varying heads are specified: (1) SWMF North; (2) Southern.

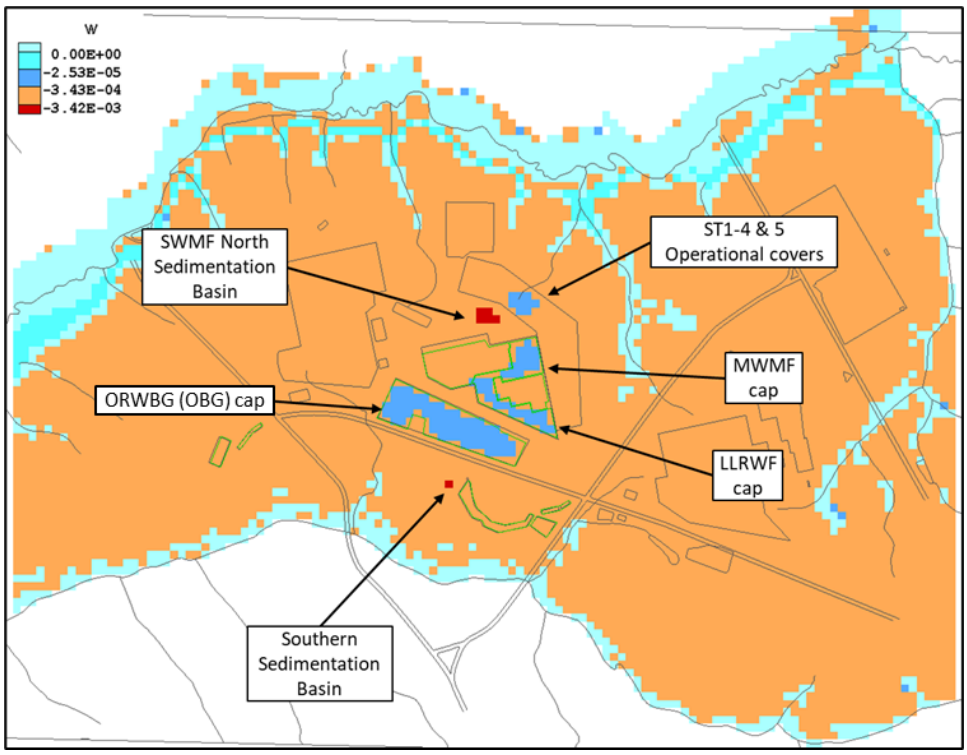

Figure 3-52 Cover and Basin Infiltration Rate Boundary Conditions Imposed for Covered Time Periods (TP1, TP2, TP3, and TP4)

Steady-state flow fields are computed for each time period based on the best estimate parameter settings and each time period's appropriate boundary conditions. 3-D stream traces are generated where seed values are placed at the footprint centroid of each of the 27 DUs. In Figure 3-53 through Figure 3-56, the left image displays the stream traces associated with each time period (TP1 through TP4), while the right image provides a comparison to the uncovered time period (TP0). The left image includes 5-year marker particles (soli-red circles) based on pore velocities and the 100-meter POA (solid-black circles). The right image illustrates the net impact of the degraded covers with respect to the uncovered case. Application of a cover creates a counterclockwise rotation of the flow field in the eastern portion of the ELLWF.

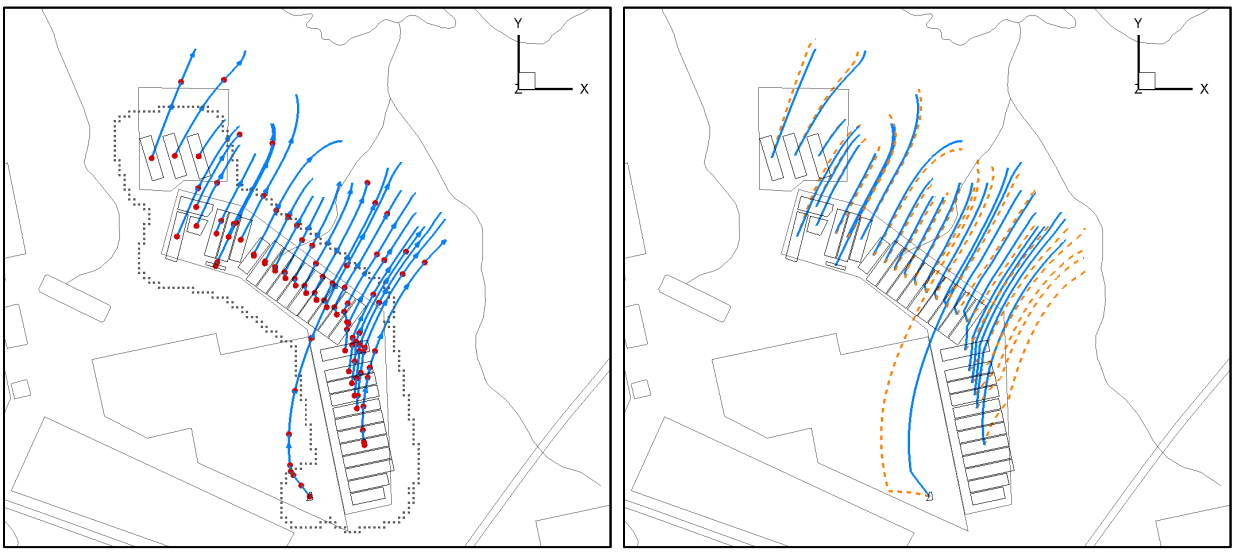

Legend: TP0 (dashed orange); TP1 (solid blue)

Figure 3-53 GSA_2021 Stream Traces from each DU for TP1 only (left) and TP0 plus TP1 (right)

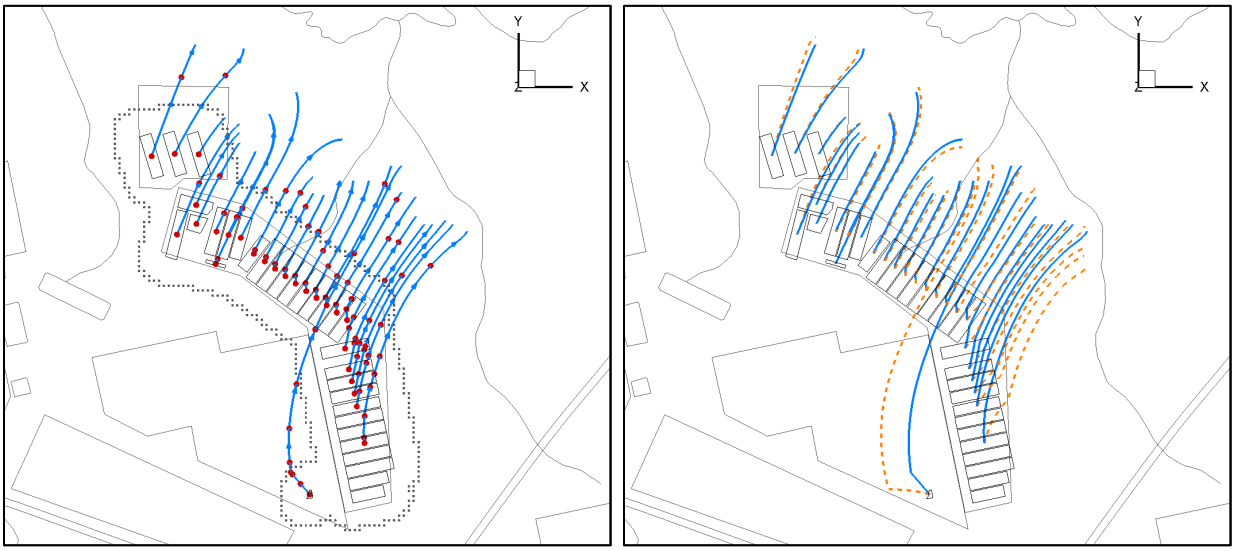

Legend: TP0 (dashed orange); TP2 (solid blue)

Figure 3-54 GSA_2021 Stream Traces from each DU for TP2 only (left) and TP0 plus TP2 (right)

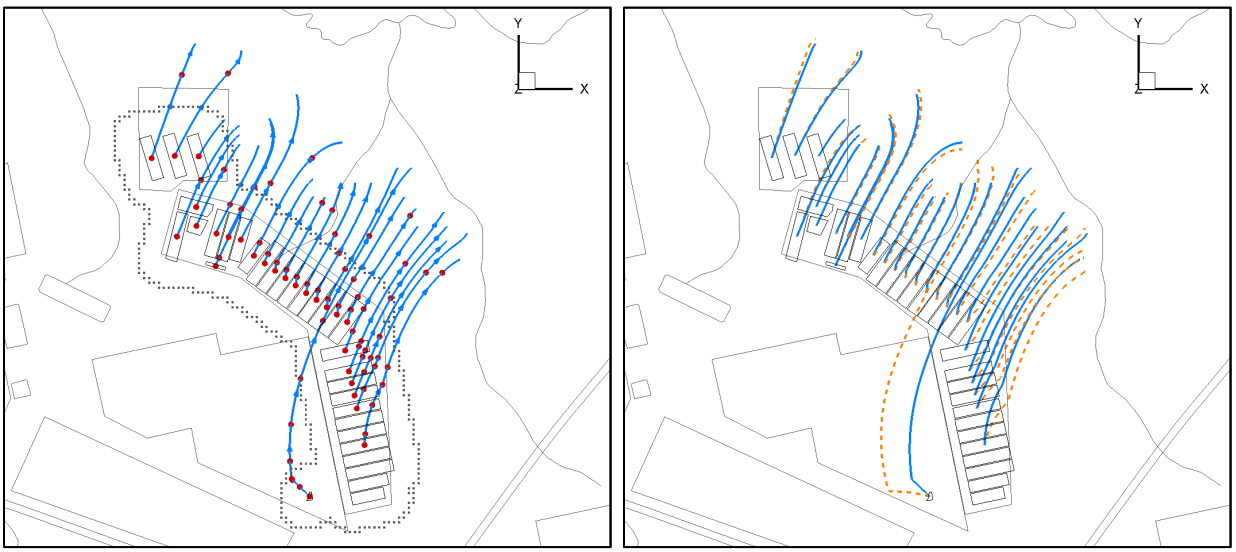

Legend: TP0 (dashed orange); TP3 (solid blue)

Figure 3-55 GSA_2021 Stream Traces from each DU for TP3 only (left) and TP0 plus TP3 (right)

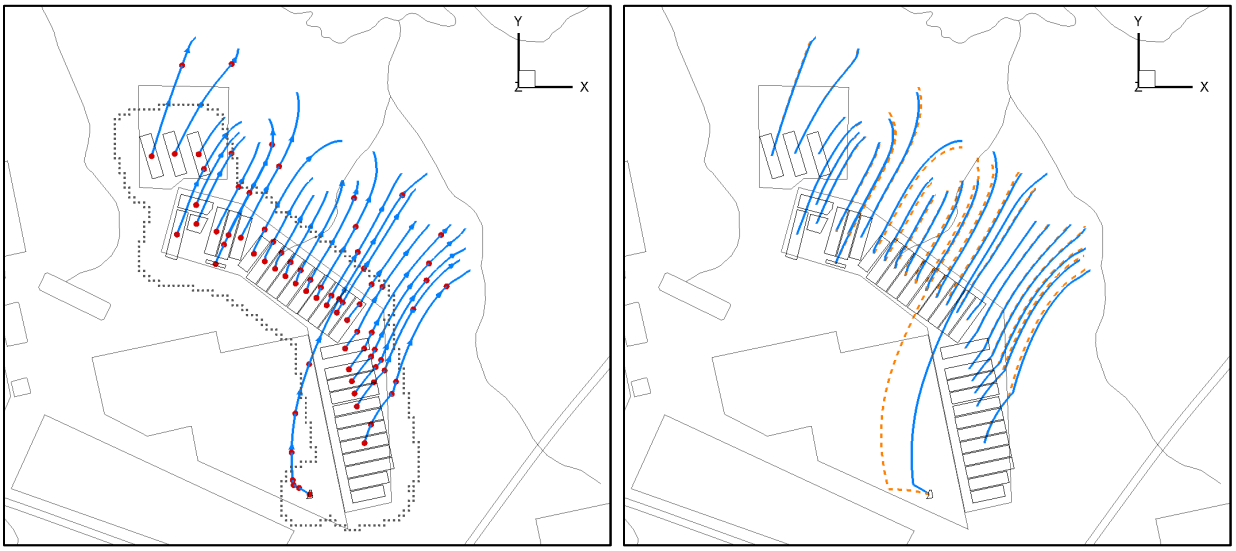

Legend: TP0 (dashed orange); TP4 (solid blue)

Figure 3-56 GSA_2021 Stream Traces from each DU for TP4 only (left) and TP0 plus TP4 (right)

To more clearly highlight the impact associated with degraded covers, Figure 3-57 shows stream traces for the four time periods (TP1, TP2, TP3, and TP4) for select DUs within the eastern sector of the ELLWF.

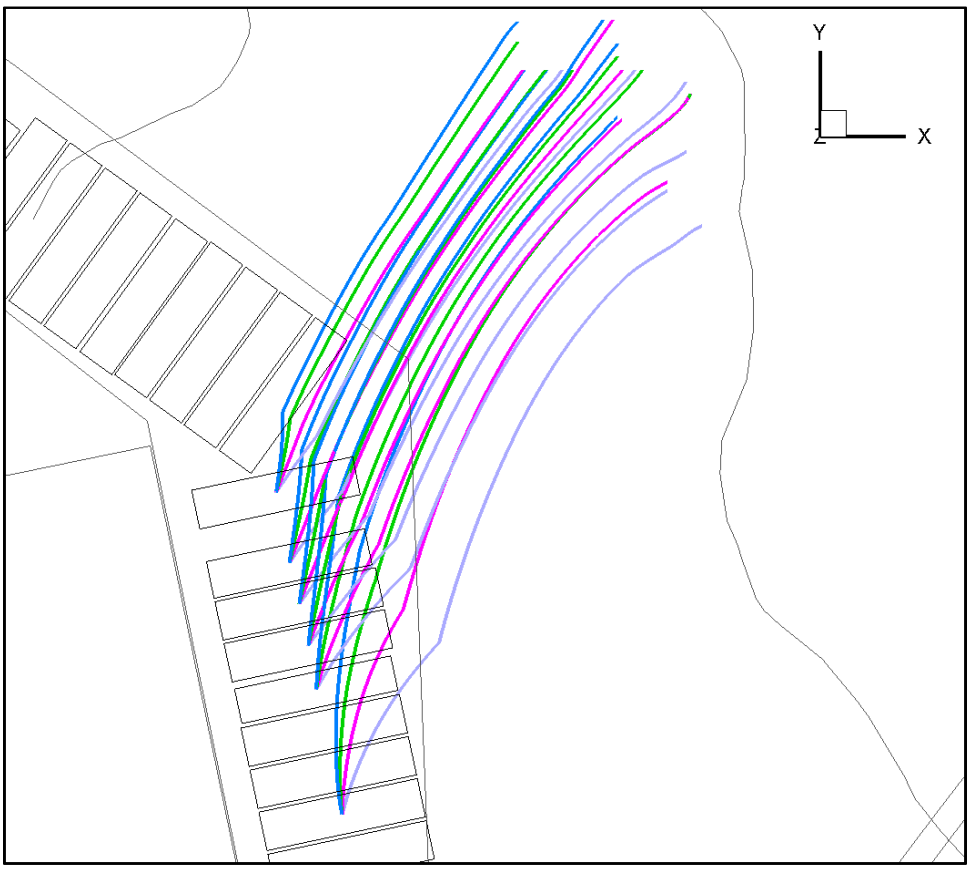

Legend: TP1 (blue); TP2 (green); TP3 (magenta); TP4 (purple)

Figure 3-57 GSA_2021 Stream Traces from Selected DUs in Eastern Sector

3.5.2.16. GSA_2021 Flow Model Uncertainty

The best estimate and 95% confidence limits for GSA_2021 flow model parameters are summarized in Table 3-35 for use in sensitivity and uncertainty analyses. Lower-bound and upper-bound estimates of the GSA_2021 flow fields are generated using the parameter values highlighted in green in Table 3-35; the remaining parameters are unchanged. Flach (2019) provides more detail on aquifer flow modeling for the ELLWF.

Table 3-36 displays the parameter covariance matrix for the GSA_2021 flow model. The parameter correlation coefficient matrix for the GSA_2021 flow model is shown in Table 3-37.

To understand the overall impact associated with the GSA Flow Model parameter settings, forward runs are made employing the PEST parameter values for the best estimate (BE), lower bound (LB), and upper bound (UB) scenarios. Figure 3-58 displays stream traces for the uncovered (TP0) time period for the 27 ELLWF DUs for which CWTS inventory limits are provided in Chapter 8. For each DU, seed values are placed on the water table surface at each DU's footprint centroid. The stream traces terminate once they reached the ground surface where a seepage face exists.

Table 3-36. GSA_2021 Flow Model Parameter Covariance Matrix

	g01 i01	g02 i02	g03 i03	g04 i04	h01 j01	h02 j02	h03 j03	h04 j04
g01	1.1536E-04	3.6572E-06	-1.8202E-05	-4.2635E-05	5.5883E-04	7.7062E-04	-1.5384E-03	7.9841E-04
	-2.3171E-04	-3.0919E-04	8.5826E-04	-2.0950E-04	1.2043E-04	8.4331E-04	-6.4754E-04	-6.6031E-03
g02	3.6572E-06	1.4140E-04	-5.0532E-05	-4.6901E-05	1.4137E-03	9.5979E-04	-8.3123E-04	-2.1686E-04
	9.9418E-05	5.4200E-04	-1.4378E-03	-3.7835E-03	-5.1815E-04	3.3425E-04	2.4680E-04	3.5781E-03
g03	-1.8202E-05	-5.0532E-05	1.2187E-03	-1.0872E-03	5.3838E-03	-2.0597E-03	-9.9386E-03	7.5849E-03
	1.3394E-04	1.8257E-03	-5.1275E-03	1.8055E-02	1.5937E-03	-7.8729E-04	-2.4278E-03	1.3629E-03
g04	-4.2635E-05	-4.6901E-05	-1.0872E-03	5.6093E-03	-5.6186E-03	-3.6984E-03	4.2506E-03	-5.7560E-03
	3.1579E-05	-1.6698E-03	4.4668E-03	-1.9000E-02	-2.9757E-04	-1.7495E-05	1.9197E-03	1.3190E-02
h01	5.5883E-04	1.4137E-03	5.3838E-03	-5.6186E-03	9.8266E-02	4.0543E-02	-0.1238	5.7635E-02
	2.0385E-03	9.5232E-03	-3.5519E-02	4.5973E-02	2.2700E-03	3.4419E-03	-4.5679E-03	0.3662
h02	7.7062E-04	9.5979E-04	-2.0597E-03	-3.6984E-03	4.0543E-02	0.2654	-1.4105E-03	-0.1545
	3.7986E-03	1.4329E-02	-3.9629E-02	-5.4427E-02	5.3420E-04	1.0049E-02	2.2954E-03	-3.8420E-02
h03	-1.5384E-03	-8.3123E-04	-9.9386E-03	4.2506E-03	-0.1238	-1.4105E-03	0.4044	-0.3298
	1.8517E-03	1.1239E-02	-8.8027E-03	-0.3380	-2.6491E-02	3.6471E-04	2.9865E-02	-1.058
h04	7.9841E-04	-2.1686E-04	7.5849E-03	-5.7560E-03	5.7635E-02	-0.1545	-0.3298	0.3983
	-4.5437E-03	-2.3134E-02	4.7079E-02	0.3686	2.1445E-02	-7.7330E-03	-2.3834E-02	0.9032
i01	-2.3171E-04	9.9418E-05	1.3394E-04	3.1579E-05	2.0385E-03	3.7986E-03	1.8517E-03	-4.5437E-03
	5.0432E-03	6.9417E-03	-3.2381E-02	-1.4584E-02	-2.6882E-04	-2.5208E-03	1.4496E-03	-2.6600E-02
i02	-3.0919E-04	5.4200E-04	1.8257E-03	-1.6698E-03	9.5232E-03	1.4329E-02	1.1239E-02	-2.3134E-02
	6.9417E-03	5.8269E-02	-0.1112	-7.9852E-02	1.2967E-03	-8.5725E-03	6.3418E-04	-0.1766
i03	8.5826E-04	-1.4378E-03	-5.1275E-03	4.4668E-03	-3.5519E-02	-3.9629E-02	-8.8027E-03	4.7079E-02
	-3.2381E-02	-0.1112	0.3369	0.2092	-3.5386E-03	2.0215E-02	2.8995E-04	0.4734
i04	-2.0950E-04	-3.7835E-03	1.8055E-02	-1.9000E-02	4.5973E-02	-5.4427E-02	-0.3380	0.3686
	-1.4584E-02	-7.9852E-02	0.2092	2.601	-2.9642E-02	-6.9951E-03	-7.0457E-03	1.955
j01	1.2043E-04	-5.1815E-04	1.5937E-03	-2.9757E-04	2.2700E-03	5.3420E-04	-2.6491E-02	2.1445E-02
	-2.6882E-04	1.2967E-03	-3.5386E-03	-2.9642E-02	3.3970E-02	7.4714E-03	-2.0916E-02	-0.3002
j02	8.4331E-04	3.3425E-04	-7.8729E-04	-1.7495E-05	3.4419E-03	1.0049E-02	3.6471E-04	-7.7330E-03
	-2.5208E-03	-8.5725E-03	2.0215E-02	-6.9951E-03	7.4714E-03	2.5974E-02	-9.9394E-03	-0.1415
j03	-6.4754E-04	2.4680E-04	-2.4278E-03	1.9197E-03	-4.5679E-03	2.2954E-03	2.9865E-02	-2.3834E-02
	1.4496E-03	6.3418E-04	2.8995E-04	-7.0457E-03	-2.0916E-02	-9.9394E-03	1.9926E-02	0.2436
j04	-6.6031E-03	3.5781E-03	1.3629E-03	1.3190E-02	0.3662	-3.8420E-02	-1.058	0.9032
	-2.6600E-02	-0.1766	0.4734	1.955	-0.3002	-0.1415	0.2436	1671.

Table 3-37. GSA_2021 Flow Model Parameter Correlation Coefficient Matrix

	g01 i01 g01 i01	g02 i02 g02 i02	g03 i03 g03 i03	g04 i04 g04 i04	h01 j01 h01 j01	h02 j02 h02 j02	h03 j03 h03 j03	h04 j04 h04 j04
g01	1.000	2.8636E-02	-4.8546E-02	-5.3002E-02	0.1660	0.1393	-0.2252	0.1178
	-0.3038	-0.1193	0.1377	-1.2096E-02	6.0835E-02	0.4872	-0.4271	-1.5038E-02
g02	2.8636E-02	1.000	-0.1217	-5.2663E-02	0.3793	0.1567	-0.1099	-2.8896E-02
	0.1177	0.1888	-0.2083	-0.1973	-0.2364	0.1744	0.1470	7.3601E-03
g03	-4.8546E-02	-0.1217	1.000	-0.4158	0.4920	-0.1145	-0.4477	0.3443
	5.4027E-02	0.2167	-0.2531	0.3207	0.2477	-0.1399	-0.4927	9.5494E-04
g04	-5.3002E-02	-5.2663E-02	-0.4158	1.000	-0.2393	-9.5844E-02	8.9246E-02	-0.1218
	5.9374E-03	-9.2361E-02	0.1028	-0.1573	-2.1557E-02	-1.4494E-03	0.1816	4.3077E-03
h01	0.1660	0.3793	0.4920	-0.2393	1.000	0.2510	-0.6211	0.2913
	9.1569E-02	0.1259	-0.1952	9.0943E-02	3.9289E-02	6.8128E-02	-0.1032	2.8575E-02
h02	0.1393	0.1567	-0.1145	-9.5844E-02	0.2510	1.000	-4.3049E-03	-0.4750
	0.1038	0.1152	-0.1325	-6.5508E-02	5.6255E-03	0.1210	3.1561E-02	-1.8240E-03
h03	-0.2252	-0.1099	-0.4477	8.9246E-02	-0.6211	-4.3049E-03	1.000	-0.8218
	4.1003E-02	7.3216E-02	-2.3849E-02	-0.3296	-0.2260	3.5585E-03	0.3327	-4.0710E-02
h04	0.1178	-2.8896E-02	0.3443	-0.1218	0.2913	-0.4750	-0.8218	1.000
	-0.1014	-0.1518	0.1285	0.3622	0.1844	-7.6025E-02	-0.2675	3.5002E-02
i01	-0.3038	0.1177	5.4027E-02	5.9374E-03	9.1569E-02	0.1038	4.1003E-02	-0.1014
	1.000	0.4049	-0.7856	-0.1273	-2.0539E-02	-0.2202	0.1446	-9.1619E-03
i02	-0.1193	0.1888	0.2167	-9.2361E-02	0.1259	0.1152	7.3216E-02	-0.1518
	0.4049	1.000	-0.7936	-0.2051	2.9146E-02	-0.2204	1.8611E-02	-1.7896E-02
i03	0.1377	-0.2083	-0.2531	0.1028	-0.1952	-0.1325	-2.3849E-02	0.1285
	-0.7856	-0.7936	1.000	0.2235	-3.3079E-02	0.2161	3.5390E-03	1.9950E-02
i04	-1.2096E-02	-0.1973	0.3207	-0.1573	9.0943E-02	-6.5508E-02	-0.3296	0.3622
	-0.1273	-0.2051	0.2235	1.000	-9.9731E-02	-2.6915E-02	-3.0951E-02	2.9654E-02
j01	6.0835E-02	-0.2364	0.2477	-2.1557E-02	3.9289E-02	5.6255E-03	-0.2260	0.1844
	-2.0539E-02	2.9146E-02	-3.3079E-02	-9.9731E-02	1.000	0.2515	-0.8039	-3.9842E-02
j02	0.4872	0.1744	-0.1399	-1.4494E-03	6.8128E-02	0.1210	3.5585E-03	-7.6025E-02
	-0.2202	-0.2204	0.2161	-2.6915E-02	0.2515	1.000	-0.4369	-2.1470E-02
j03	-0.4271	0.1470	-0.4927	0.1816	-0.1032	3.1561E-02	0.3327	-0.2675
	0.1446	1.8611E-02	3.5390E-03	-3.0951E-02	-0.8039	-0.4369	1.000	4.2210E-02
j04	-1.5038E-02	7.3601E-03	9.5494E-04	4.3077E-03	2.8575E-02	-1.8240E-03	-4.0710E-02	3.5002E-02
	-9.1619E-03	-1.7896E-02	1.9950E-02	2.9654E-02	-3.9842E-02	-2.1470E-02	4.2210E-02	1.000

Legend: Best Estimate (solid blue); Lower Bound (dashed orange); Upper Bound (dashed green)

Figure 3-58. Best-Estimate, Lower-Bound, and Upper-Bound Stream Traces for GSA_2021 Flow Model During Uncovered (TP0) Time Period

As Figure 3-58 illustrates, the 95% lower- and upper-bound parameter sets do not result in significant variations in the stream traces for the majority of the DUs. As such, when generating the CWTS inventory limits in Chapter 5, only the best-estimate PEST parameter settings are employed in the PORFLOW® aquifer transport model simulations of the nominal PA and sensitivity cases.

3.5.3. Aquifer Transport Model Implementation in PORFLOW

As mentioned above, the output from the baseline GSA aquifer flow model is a precursor to the aquifer transport model simulations. Specifically, five steady-state GSA flow fields are developed (i.e., one uncovered and four degraded cover conditions) for transport modeling purposes. Because of mesh size and node number limitations, multiple aquifer cutouts are generated with each DU residing in one of these cutouts. Sections 3.5.3.1 and 3.5.3.2 address these limitations.

3.5.3.1. Aquifer Dispersion

In PA2008, dispersion was included in the aquifer transport models of STs and ETs only; however, in this PA, aquifer dispersion is considered for all types of DUs including STs, ETs, LAWV, ILV, and NRCDAs. Mechanical dispersion is a physical aspect that is explicitly included within every aquifer transport simulation. For inventory limit calculations, best-estimate dispersion parameter

settings are included as input into the baseline limits tool. To keep numerical dispersion at reasonable levels, adequate meshing of the aquifer transport model is employed. Details associated with the choice of dispersion model and its parameter settings are provided by Hamm et al. (2019).

3.5.3.1.1. Four-Parameter Dispersion Model

A four-parameter dispersion model is used to perform all aquifer transport simulations. This model was extracted from the FACT code (Hamm and Aleman, 2000) and incorporated into the version of PORFLOW (Ver. 6.43.0) used in this PA. The following four parameter values are required inputs:

$$\begin{aligned} \alpha_{LH} &= \alpha_L = [a_L] \times [L_{dist}] \\ \alpha_{TH} &= [10\% \times a_L] \times \alpha_L \\ \alpha_{LV} &= [10\% \times a_L] \times \alpha_L \\ \alpha_{TV} &= [1\% \times a_L] \times \alpha_L \end{aligned} \qquad \text{Eq. (3-13)}$$

where:

L_{dist} Travel distance along plume from source to 100-meter POA curtain (m)

α_{LH} Longitudinal-horizontal dispersivity (m)

α_{TH} Transverse-horizontal dispersivity (m)

α_{LV} Longitudinal-vertical dispersivity (m)

α_{TV} Transverse-vertical dispersivity (m)

α_L Longitudinal dispersivity [traditional parameter] (m)

a_L Fraction of travel length associated with mechanical dispersion (unitless)

The implementation of the four-parameter dispersion model in PORFLOW was verified by Aleman and Flach (2010) through execution of a variety of test cases. The PORFLOW results were compared against results from the FACT code, COMSOL, and multi-dimensional analytical transport solutions.

A critical review of available in-the-field longitudinal dispersivity data was made by Gelhar et al. (1992). The altered data reported by Gelhar et al. (1992; Figure 3) was digitized and extracted into Microsoft Excel[15] and plotted as shown in Figure 3-59. Two models recommended by Flach (2018) are also shown in Figure 3-59 as follows:

- The general 10% of travel distance rule-of-thumb shown as a solid black line.
- A 3.2% of travel distance adjustment to account for the reliability of the data by weighting [shown as a red dashed line created by Flach (2018) from visual observation].

[15] Microsoft, Excel, and Word are trademarks of the Microsoft group of companies.

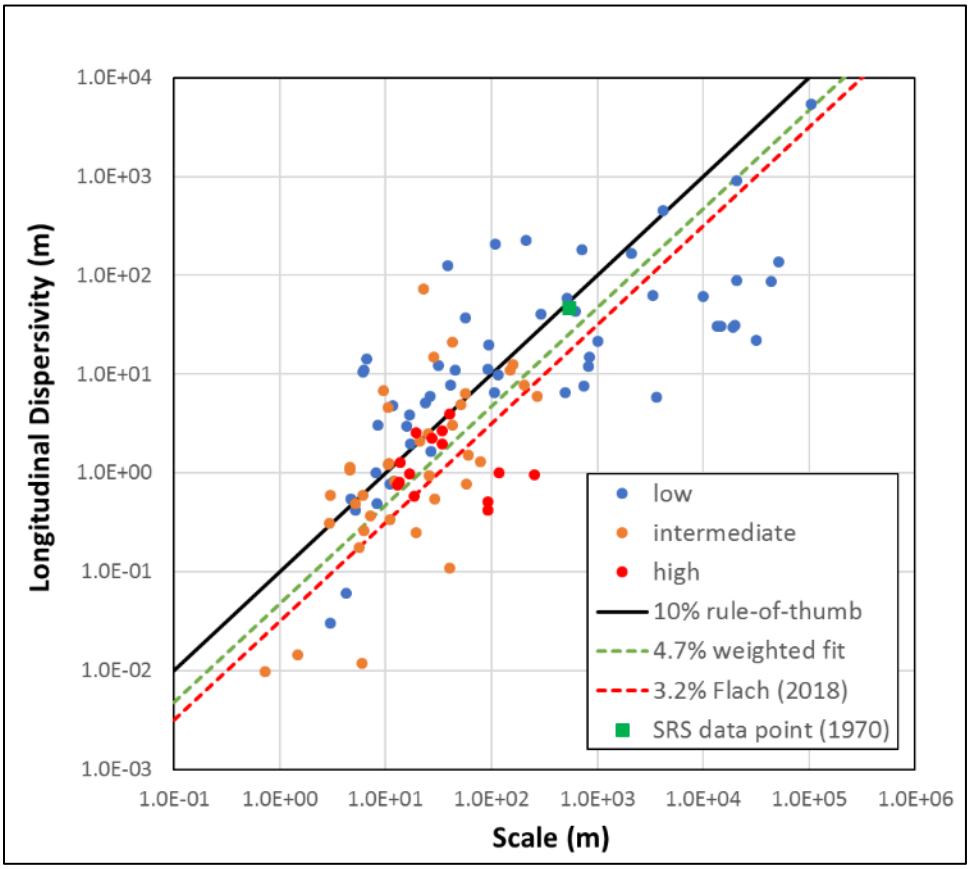

Figure 3-59. Data of Longitudinal Dispersivity versus Scale Extracted from Figure 3 by Gelhar et al. (1992)

Gelhar et al. (1992) altered several data points to improve their accuracy and upgraded them with respect to reliability classification. Also provided in Figure 3-59 is a computed least-squares fit to the altered digital data where the following weightings are applied:

- W=1 for low-reliability data
- W=4 for intermediate-reliability data
- W=16 for high-reliability data

The weighting factors are estimated from confidence ranges provided by Gelhar et al. (1992) where geometric mean values were computed (i.e., the weights provided are relative weightings normalized to the low-reliability classification). Gelhar et al. (1992) also noted that, in general, the reported data values are higher than they should be (i.e., they are biased slightly high).

Using the above weighting factors and altered data set, the result of the least-squares fitting yields:

$$\alpha_L = [4.7\%] \times [L_{dist}] \qquad \text{Eq. (3-14)}$$

As indicated in Eq. (3-13), a 10% factor is applied to transverse dispersion, and an additional 10% factor is applied to vertical dispersion. Gelhar et al. (1992) continued to support these other factors as well.

Variations in travel distance between each DU and the 100-meter POA occur because of streamline variations and distributed sources across each DU footprint (i.e., a typical trench footprint being on the order of 157-foot wide by 656-foot long).

Streamlines emanating from the centroids of each DU within the eastern ELLWF cutout of the 2018 GSA flow model (Flach, 2019) are shown in Figure 3-60. For each DU, estimated travel distances are computed for a seed placed (1) at the DU centroid and (2) along the outer edge of each DU closest to the 100-meter POA curtain.

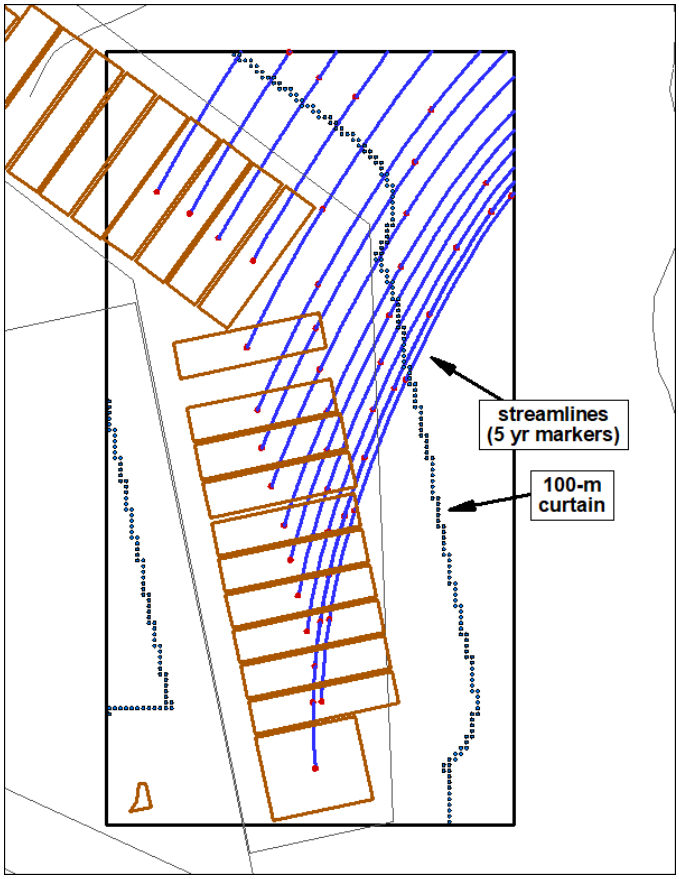

Figure 3-60. Streamlines from Centroid of Each Disposal Unit Out Beyond the 100-meter POA Curtain Based on Most Current Model Aquifer Cutout from 2018 GSA Flow Model

The computed travel distances are listed in Table 3-38 where a wide range of values is observed. As expected, a minimum travel distance of 100 meters is computed for several of the DUs. Values as high as 600 meters are also observed. The DU listing is rank ordered with respect to travel distance.

Table 3-38. Estimated Average and Minimum Travel Distances for Each Disposal Unit Within Eastern Model Aquifer Cutout to 100-meter POA Curtain Based on Most Recent 2018 GSA Flow Model

Disposal Unit (from west to east)	Average Travel Distance (m)	Minimum Travel Distance (m)
ST24	200	100
ST05	200	100
ST06	200	100
ST07	200	100
ET02	300	200
ET01	350	150
ST14	380	160
ET05	330	170
LAWV	360	180
ET06	380	200
ST17	380	210
ST18	400	220
ST19	420	240
ST20	500	250
ST21/ST22	600	380

Based on the information provided above, an assessment study by Flach (2018) recommended the following nominal parameter settings (i.e., the use of the 10% rule-of-thumb and the 100-meter POA travel distance):

$$\begin{aligned}
\alpha_{LH} &= \alpha_L = [10\%] \times [L_{dist}] = [10\%] \times [100\ m] = 10\ m = 32.8\ ft \\
\alpha_{TH} &= [10\%] \times \alpha_L = 1.0\ m = 3.28\ ft \\
\alpha_{LV} &= [10\%] \times \alpha_L = 1.0\ m = 3.28\ ft \\
\alpha_{TV} &= [1\%] \times \alpha_L = 0.1\ m = 0.328\ ft
\end{aligned} \qquad \text{Eq. (3-15)}$$

Flach (2018) also recommended the following settings as lower-bound values:

$$\begin{aligned}
\alpha_{LH} &= \alpha_L = [3.2\%] \times [L_{dist}] = [3.2\%] \times [100\ m] = 3.2\ m = 10.5\ ft \\
\alpha_{TH} &= [10\%] \times \alpha_L = 0.32\ m = 1.05\ ft \\
\alpha_{LV} &= [10\%] \times \alpha_L = 0.32\ m = 1.05\ ft \\
\alpha_{TV} &= [1\%] \times \alpha_L = 0.032\ m = 0.105\ ft
\end{aligned} \qquad \text{Eq. (3-16)}$$

From these two sets of parameter settings, Flach (2018) investigated the level of mesh refinement required to maintain numerical dispersion acceptably low in baseline PA deterministic models as well as models for uncertainty quantification and sensitivity analysis (UQSA). In addition, mesh refinement increases the computational demand; therefore, the goal is to refine the mesh only to the degree necessary. Flach (2018) provided the following mesh guidance:

- 25-foot by 25-foot horizontal grid
- 3-foot or less vertical grid

For baseline limits calculations in this PA, the averaged value for longitudinal dispersivity will be computed using Eq. (3-14) assuming a minimum travel distance of 100 meters for all DUs. The baseline dispersivity settings for all DUs are as follows:

$$\begin{aligned}
\alpha_{LH} &= \alpha_L = [4.7\%] \times [L_{dist}] = [4.7\%] \times [100\ m] = 4.7\ m = 15.4\ ft \\
\alpha_{TH} &= [10\%] \times \alpha_L = 0.47\ m = 1.54\ ft \\
\alpha_{LV} &= [10\%] \times \alpha_L = 0.47\ m = 1.54\ ft \\
\alpha_{TV} &= [1\%] \times \alpha_L = 0.047\ m = 0.154\ ft
\end{aligned} \qquad \text{Eq. (3-17)}$$

For UQSA studies, a_L will be statistically varied about its mean value of 4.7%.

3.5.3.1.2. Impact of Dispersion Model on Maximum Sum-of-Fractions

Aquifer dispersion will impact the maximum SOF values along the 100-meter POA curtain by altering the shape of a concentration plume emanating from a given DU. In the baseline PA limits strategy, this will impact:

- PORFLOW-generated preliminary inventory limits that are generated for each DU in isolation (i.e., no plume interaction considerations included).
- PORFLOW-generated PIFs calculated based on steady-state tracer runs for each DU.

Impacts associated with plume interaction are discussed below.

To evaluate the sensitivity of plume interaction to the four-parameter dispersion model, a series of steady-state tracer runs was completed for ST05 (closed unit) in 2019 wherein a_L was varied from 0.1% to 15% as shown in Table 3-39. This sensitivity range for a_L is wider than the range (3.2% to 10%) recommended by Flach (2018). For each simulation run in the series, an equal mass of tracer was uniformly distributed throughout ST05.

The results of the simulations are displayed in Figure 3-61. As is generally observed, an increase in dispersion leads to a reduction in tracer concentrations along the 100-meter curtain. The uppermost curves (α_{LH} = 0.3 feet and 0.0 feet) represent essentially zero actual dispersion, even though some degree of numerical dispersion is present because of the finite-size mesh employed. As Figure 3-61 indicates, the peak tracer concentration when mechanical dispersion is turned off (α_{LH} = 0.0 feet; red dashed curve) is 50% higher when compared to the α_{LH} = 32.8 feet case (solid black curve). Conversely, a reduction of about 50% in peak tracer concentration is observed relative to the α_{LH} = 32.8 feet case (solid black curve) when the PA2008 dispersion model is applied [α_{LH} = 32.8 feet (stratOFF); dashed blue curve at bottom]. As this sensitivity analysis indicates, aquifer dispersion can impact peak concentrations (and therefore dose and SOF values) significantly and thus warrants special consideration in the PA limits methodology.

Table 3-39. Four-Parameter Dispersion Model Parameter Settings Considered in Sum-of-Fractions Sensitivity Study for ST05

a_L [1]	Based on 100-meter Travel Distance (L_{dist} [2] = 100 m)				
	α_L [3]	α_{LH} [4]	α_{TH} [5]	α_{LV} [6]	α_{TV} [7]
%	(m)	(ft)			
0.1	0.1	0.3	0.03	0.03	0.003
5	5.0	16.4	1.64	1.64	0.164
7.5	7.5	24.6	2.46	2.46	0.246
10	10.0	32.8	3.28	3.28	0.328
12.5	12.5	41.0	4.10	4.10	0.410
15	15.0	49.2	4.92	4.92	0.492

Notes:

1 Fraction of travel length associated with mechanical dispersion

2 Travel distance along plume from source to 100-meter POA curtain

3 Longitudinal dispersivity [traditional parameter]

4 Longitudinal-horizontal dispersivity

5 Transverse-horizontal dispersivity

6 Longitudinal-vertical dispersivity

7 Transverse-vertical dispersivity

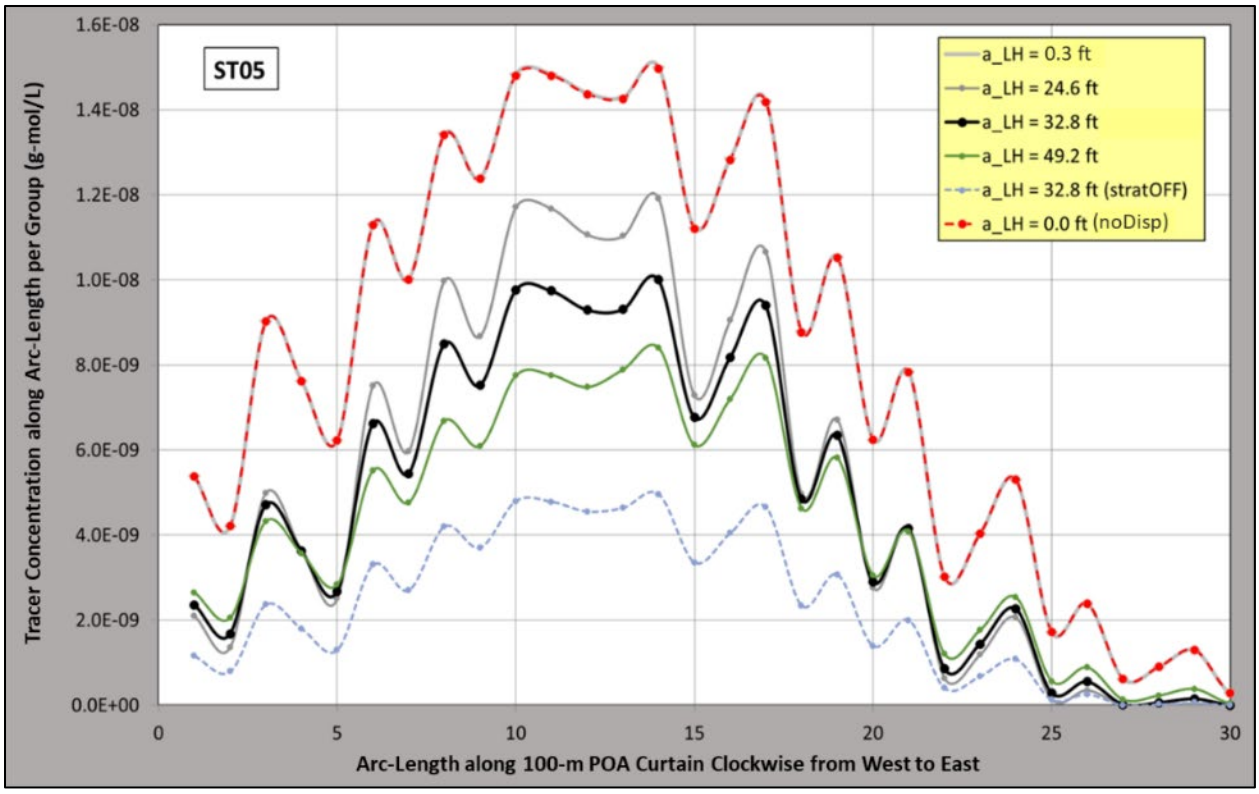

Figure 3-61. Maximum Tracer Concentration along 100-meter POA Curtain for ST05 Based on a Range of Four-Parameter Dispersion Model Settings

The baseline (nominal) case subsequently chosen for this PA (a_L = 4.7% and α_{LH} = 15.4 feet) for all DUs was not included in the 2019 sensitivity analysis; however, its tracer concentration profile would lie between the curves for α_{LH} = 0.3 feet and α_{LH} = 24.6 feet.

It is important to note that the waves observed in Figure 3-61 are an artifact of the discrete approximation to the actual 100-meter POA curtain. The 100-meter curtain is approximated in PORFLOW by a series of areal nodes whose cell footprints are near the 100-meter distance outside of the ELLWF DUs. If a node's areal footprint contains this 100-meter distance, then it is selected as part of the discrete approximation to the actual smooth 100-meter POA curtain.

To confirm that the waves observed are simply an artifact of the discrete approximation to the actual 100-meter curtain, the Tecplot software (Tecplot, 2021) was employed to interpolate tracer concentrations across a vertical slice taken along the 100-meter curtain positioned downstream of ST05 (Figure 3-62). The tracer concentration on this vertical slice is displayed in Figure 3-63. As Figure 3-63 indicates, concentration waves do not actually occur along a smooth 100-meter surface. Therefore, PORFLOW tracer simulations are acceptable for addressing plume interaction among neighboring DUs.

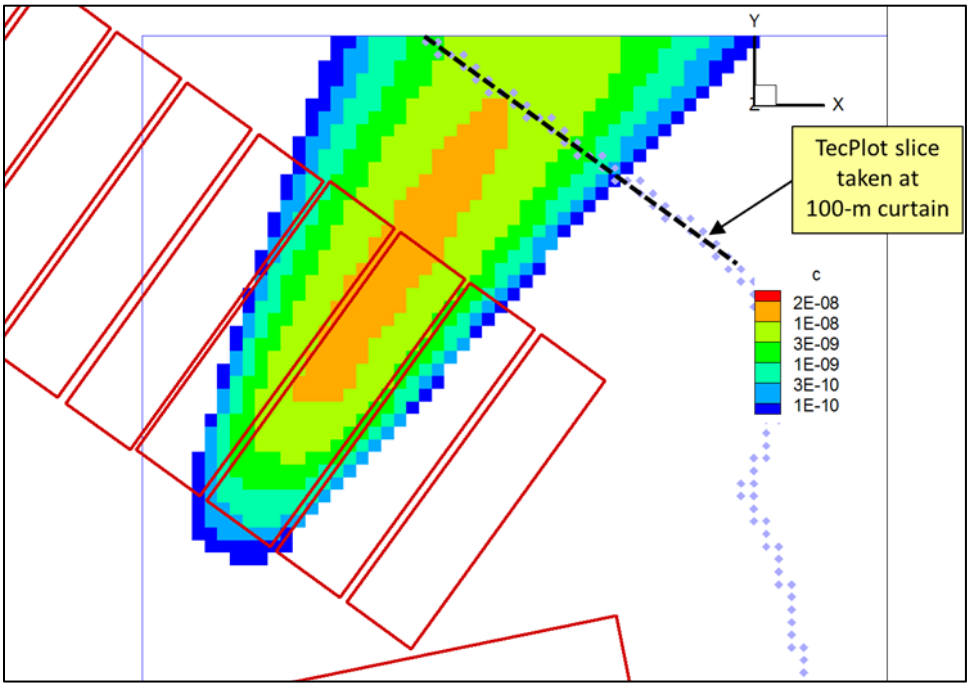

Figure 3-62. Steady-State Tracer Concentration X-Y Contour for ST05 Assuming a Longitudinal Dispersivity of 32.8 Feet (a_L = 10%) Showing Location of Vertical Slice Along the 100-meter POA Curtain

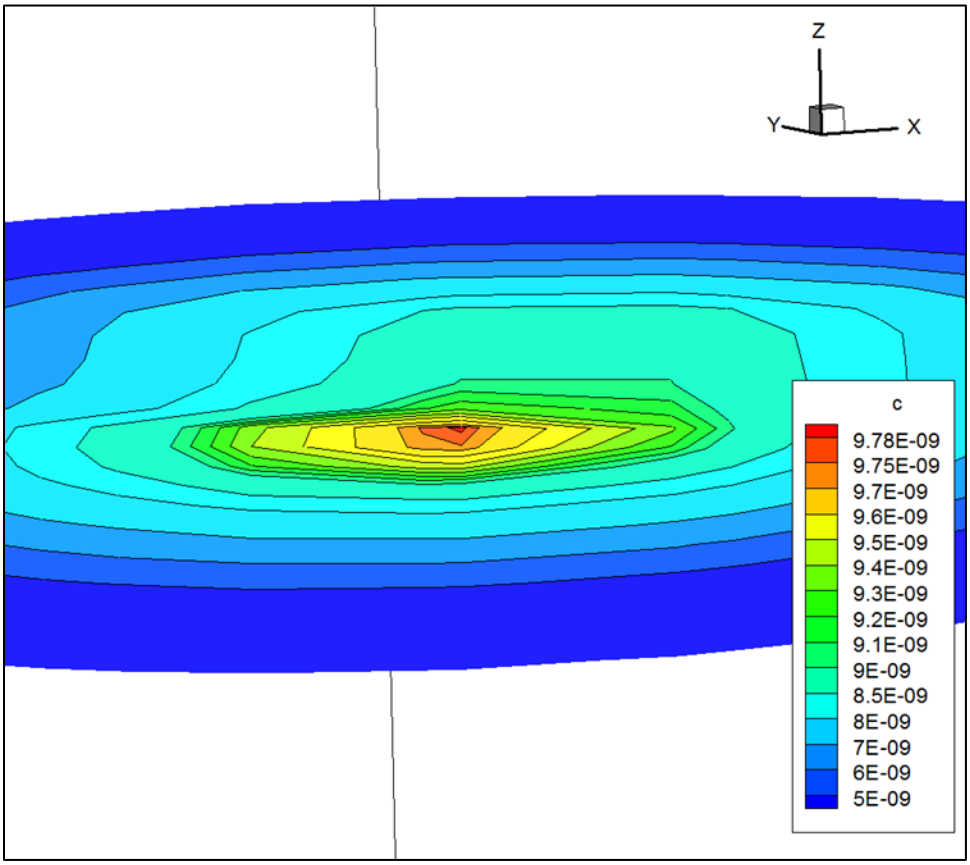

Figure 3-63. Steady-State Tracer Concentration Z-X/Y Contour for ST05 Assuming a Longitudinal Dispersivity of 32.8 Feet (a_L = 10%) Along 100-meter POA Curtain

3.5.3.2. Aquifer Cutouts

If unlimited computational resources are available, a single aquifer flow and transport model would be utilized in the PA. However, to meet mesh demands associated with numerical dispersion, regulatory guidance on the points of compliance, and finite PORFLOW nodal and computational storage and runtime limitations, several aquifer cutouts are employed instead.

Specifically, the following two sets of aquifer cutouts are required to compute concentrations at and beyond the 100-meter POA:

- **PIF Aquifer Cutouts**. These cutouts are employed to establish DU-specific plume interaction profiles (PIPs) that are used, in turn, to compute PIFs, which account for the commingling of contaminant plumes from neighboring DUs at the 100-meter POA. For a system of two DUs, two extremes are possible: (1) the plumes emanating from the DUs are completely isolated, yielding a PIF equal to 1.0 for each; (2) an upstream DU's plume completely encompasses a downstream DU's plume, yielding a PIF equal to 2.0.
- **Limits Aquifer Cutouts.** These cutouts are employed during the transient transport simulations where (1) maximum concentrations are computed for a parent and its progeny at and beyond the 100-meter POA (PORFLOW STATistic file) and (2) concentrations for a parent and its progeny are computed along a vertical curtain at the 100-meter POA

(PORFLOW HISTory file). The calculations are performed for specific parent radionuclides that are uniformly distributed within a single DU for generic waste form radionuclides, while for some SWFs, the areal footprints reflect their actual physical footprints. Here, contributions from neighboring DUs are not explicitly addressed. The maximum concentrations computed in this case are referred to as preliminary concentrations.

To arrive at final, predicted parent-radionuclide and progeny concentrations, the preliminary concentrations and corresponding PIFs are combined. The key aspects associated with each set of aquifer cutouts are discussed next.

3.5.3.2.1. 100-Meter Point of Assessment

The same strategy employed in PA2008 to determine the 100-meter POA is used in this PA. The only difference is that the three additional Plot 8 DUs (i.e., ET07, ET08, and ET09) are added to the overall footprint.

A 100-meter POA is computed using a rubber-band algorithm that is applied to the 33 DUs currently comprising the ELLWF. The resulting boundary (i.e., a vertical curtain surrounding the ELLWF) is divided into two separate sections as follows (see Figure 3-64):

- North curtain extending along the north-east regions
- South curtain extending along the south-west regions

Each 2-D curtain connects with the other at the red and blue circles shown in Figure 3-64. The small, solid, gray dots mark the 100-meter POA.

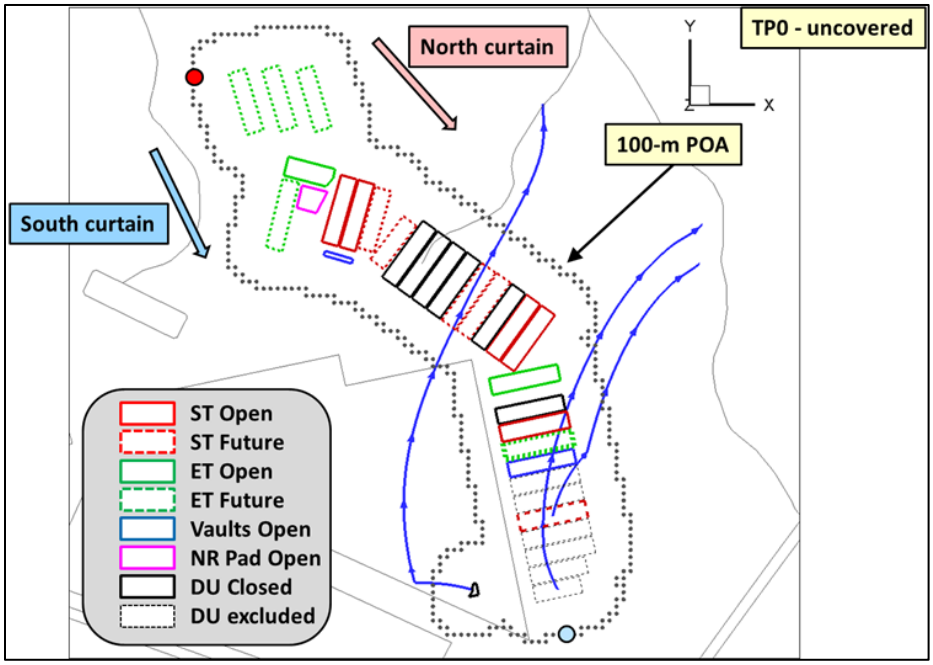

Figure 3-64 100-meter POA Surrounding 33 Disposal Units Comprising the E-Area Low-Level Waste Facility

All PIP and PIF analyses are performed for the 100-meter POA displayed in Figure 3-64. During the assignment of PIFs, six of the 33 DUs are excluded from future deployment as discussed in Chapter 8 and Appendix H. An updated 100-meter POA for the ELLWF is computed using a rubber-band algorithm that is applied to just the remaining 27 DUs. This updated 100-meter POA is shown alongside the original one in Figure 3-65. The 100-meter POA is only altered along the southeast portion of the boundary as highlighted in Figure 3-65. 3-D stream traces emanating from ST18, ST22, and NR07E are also shown. Maximum doses along the 100-meter POA for all DUs occur along the original POA (i.e., see blue stream traces crossing the North curtain marked by solid red line). The region where the updated POA differs from its original is located upstream of all DUs, resulting in negligible dose impacts in that region.

Because there will be no impact on CWTS inventory limits, the original 100-meter POA is recommended for use in this PA. No change is needed to alter the 100-meter POA if future analyses are required to bring excluded units into operation.

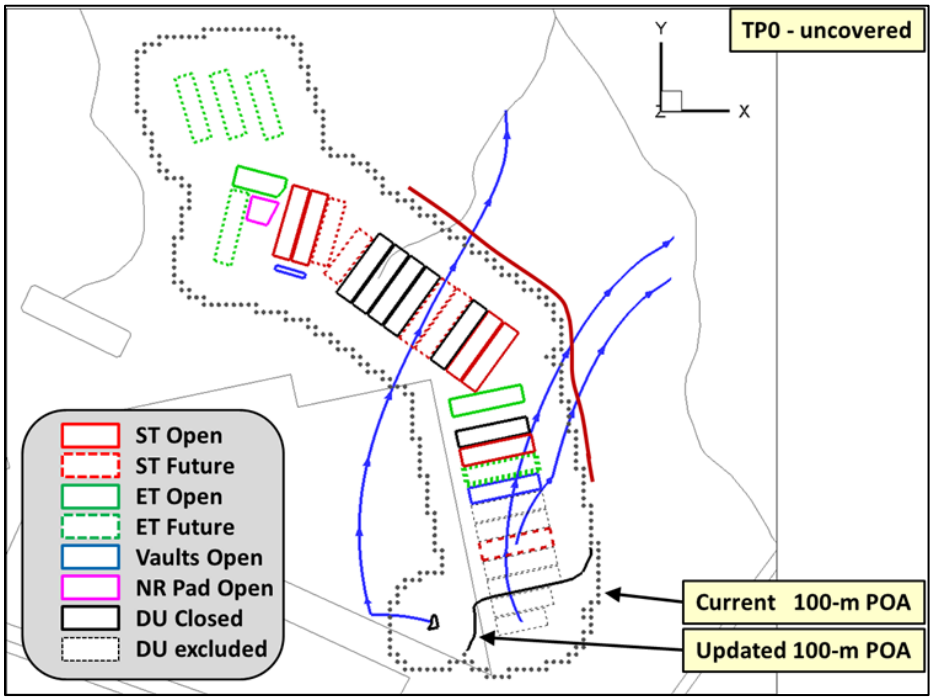

Figure 3-65 Updated 100-meter POA Surrounding 27 Disposal Units Comprising the E-Area Low-Level Waste Facility

3.5.3.2.2. Aquifer Cutouts for Plume Interaction Factor Analyses

The following set of criteria and assumptions is employed in the process of obtaining acceptable PIF aquifer cutouts:

- Steady-state parent radionuclide and tracer (for comparison and checking purposes) source terms are applied uniformly within each DU footprint at the surface of the water table; a constant source (gmol yr^{-1}) is applied.

- Aquifer cutouts must accommodate all flow time periods (TPs), where the uncovered (TP0) and undegraded, intact cover (TP1) bound the five possible time periods.
- Tracer concentrations of greater than 0.1% of the maximum value along the 100-meter POA curtain must be present for every DU within a given aquifer cutout to ensure that the majority of plume overlap potential is captured.
- Minimal mass loss at vertical boundaries of the domain is achieved before the plume reaches the 100-meter POA (or POAs when the flow field crosses the POA more than once).
- The baseline GSA_2021 flow model is employed, where the best-estimate parameter settings, obtained via PEST optimization, are chosen.

Transport results are provided for both the uncovered (TP0) and first covered time period (TP1) flow fields. Scoping results indicate that these surface boundary conditions bound the entire range of conditions modeled to Year 10,171; therefore, results for the intermediate flow fields are not shown.

3.5.3.2.2.1. Overview

For PIF analyses, four aquifer cutouts are established, each containing a subset of the 33 total DUs comprising the ELLWF. A breakdown of the four PIF aquifer cutouts, including DUs residing within each, is as follows:

- **West (11 DUs):** ET07, ET08, ET09, ET03, ET04, NR26E, ST08, ST09, ST10, ILV, ST11
- **Center (9 DUs):** ST01, ST02, ST03, ST04, ST23, ST24, ST05, ST06, ST07
- **East1 (12 DUs):** ET02, ET01, ST14, ET05, LAWV, ET06, ST17, ST18, ST19, ST20, ST21, ST22
- **East2 (1 DU):** NR07E

In general, the DU listings begin from the west and move in the southeastern direction. Note that the NRCDA DU naming convention is shortened to better handle formatting issues within file structures:

- **NR07E:** NRCDA7E (sometimes referred to as NR0 and 643-7E)
- **NR26E:** NRCDA26E (sometimes referred to as NR1 and 643-26E)

An overview of the footprints for each of these PIF aquifer cutouts is presented in Figure 3-66, which is annotated to highlight key features associated with each aquifer cutout. The intent of the figure is to show how the four PIF aquifer cutouts relate to the North and South 100-meter POA curtains as described below. As illustrated in Figure 3-66 there is partial overlap among these four PIF aquifer cutouts resulting from mesh requirements to meet desired 100-meter POA coverage. During post-processing, these overlap regions are addressed such that continuous North and South curtains are established.

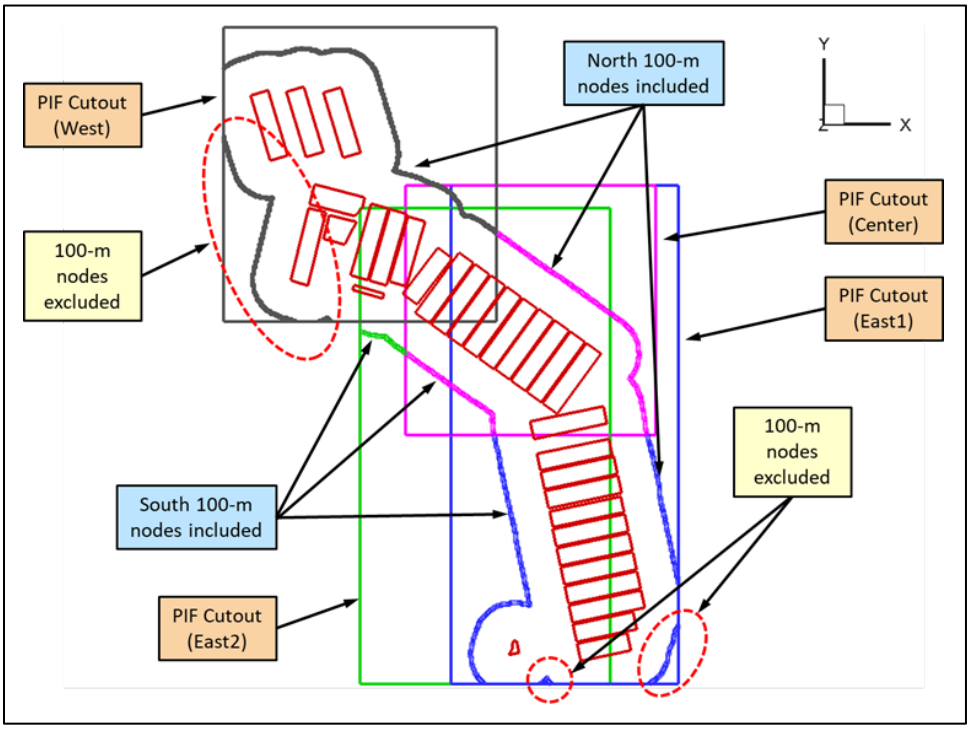

Figure 3-66 North and South 100-meter Curtains Used in Plume Interaction Factor Analyses

The 100-meter POA surrounding the ELLWF is separated into segments. Given the known, general aquifer flow direction, some segments will never experience contaminant concentrations of any significance because they are situated upstream of the DUs. These segments (contained within red dashed circles) are omitted from further plume interaction analyses; however, for actual limits analyses, the entire 100-meter POA boundary is retained. As shown in Figure 3-66, the following two composite boundaries are considered for PIF analyses:

- **North Curtain:** Represents100-meter POA passing through West, Center, East1, and East2 PIF aquifer cutouts.
- **South Curtain:** Represents 100-meter POA passing through East2, Center, and East1 PIF aquifer cutouts.

Specific details on the PIF aquifer cutouts that contribute to the North and South curtains, as well as the curtains themselves, are reported in Appendix C, Section C.1.1.

Conservative (pessimistically leaning) steady-state tracer concentration profiles for individual DUs in each of the four PIF aquifer cutouts for the two bounding flow fields are presented in Appendix C, Sections C.1.2.1 through C.1.2.4. The TP0 flow field (i.e., uncovered case) is compared with the TP1 flow field (i.e., intact case with minimal degradation). Only best-estimate flow fields are shown. Because these two cases bound the behavior, no plots are shown for the TP2, TP3, and TP4 periods.

3.5.3.2.2.2. West Footprint

Flow field comparisons for the West PIF aquifer cutout footprint (DUs ET07, ET08, ET09, ET03, ET04, NR26E, ST08, ST09, ST10, ILV, and ST11) are provided in Appendix C, Section C.1.2.1. For all cases shown, the West footprint meets the criteria chosen (Section 3.5.3.2.2) in establishing this footprint.

3.5.3.2.2.3. Center Footprint

Flow field comparisons for the Center PIF aquifer cutout footprint (DUs ST01, ST02, ST03, ST04, ST23, ST24, ST05, ST06, and ST07) are provided in Appendix C, Section C.1.2.2. For all cases shown, the Center footprint meets the criteria chosen (Section 3.5.3.2.2) in establishing this footprint.

3.5.3.2.2.4. East1 Footprint

Flow field comparisons for the East1 PIF aquifer cutout footprint (DUs ET02, ET01, ST14, ET05, LAWV, ET06, ST17, ST18, ST19, ST20, ST21, and ST22) are provided in Appendix C, Section C.1.2.3. For all cases shown, the East1 footprint meets the criteria chosen (Section 3.5.3.2.2) in establishing this footprint.

3.5.3.2.2.5. East2 Footprint

Flow field comparisons for the East2 PIF aquifer cutout footprint (DU NR07E) are provided in Appendix C, Section C.1.2.4. For the case shown, the East2 footprint meets the criteria chosen (Section 3.5.3.2.2) in establishing this footprint.

3.5.3.2.3. Aquifer Cutouts for Inventory Limits Analyses

Per DOE M 435.1-1, Chg. 3(U.S. DOE, 2021b), the point of compliance (i.e., POA) "shall correspond to the point of highest projected dose or concentration beyond a 100-meter buffer zone surrounding the disposed waste." To provide coverage "at and beyond" the 100-meter POA, the PIF cutouts discussed above had to be extended. Due to computational demands, DUs within these PIF cutouts are divided into subgroups. A PORFLOW node limit of three million is imposed, where up to a seven-member chain can be handled. PORFLOW Ver. 6.43.0 (Whiteside, 2020) is employed for all flow and transport analyses presented in this PA.

The following set of criteria and assumptions is added to the earlier set of PIF criteria (Section 3.5.3.2.2) to obtain acceptable limits aquifer cutouts:

- PIF aquifer cutouts are expanded toward UTR and its tributaries to address the "at and beyond" regulatory guidance.
- Expansion is limited by either reaching the seepage faces near tributaries, capturing more than 90% of the contaminant plume, or reaching the nodal limits for the current version of PORFLOW.

Based on transport considerations, horizontal and vertical mesh refinement is performed up to the 3-million-node limit. The horizontal gridding details for the transport models used in the limits analyses are provided in Table 3-40.

Table 3-40 Grid Details of PORFLOW Aquifer Transport Models Used in Inventory Limits Analyses

Aquifer Cutout		Indices				Number of Elements			Total Elements	Total Nodes [a]
PIF	Limits	i_{min}	j_{min}	i_{max}	j_{max}	X	Y	Z	NE	NN
West	West_A	55	63	67	78	192	240	40	1,843,200	1,971,816
	West_B	57	57	72	74	240	272	40	2,611,200	2,784,936
Center	Center_A	63	54	74	69	176	240	40	1,689,600	1,809,192
	Center_B	66	52	78	69	192	272	40	2,088,960	2,232,552
East1	East1_A	68	47	79	67	176	320	40	2,252,800	2,407,272
	East1_B	68	43	80	64	192	336	40	2,580,480	2,754,024
	East1_C	65	41	78	62	208	336	40	2,795,520	2,981,160
East2	East2_A	59	41	72	62	208	336	40	2,795,520	2,981,160

Notes:

[a] Total number of PORFLOW nodes limited to 3 x 10^6 for Ver. 6.43.0.

The horizontal grid spacing is uniform in both the X and Y directions, where a 12.5-foot spacing provides an acceptable level of numerical dispersion.

The vertical resolution of elements is constrained such that each of the eight limits analysis models have the same vertical placement. This ensures that results along the curtain from one transport model will align with its neighboring transport models. The overall vertical assignments of elements are shown in Figure 3-67, along with the corresponding hydrostratigraphic units.

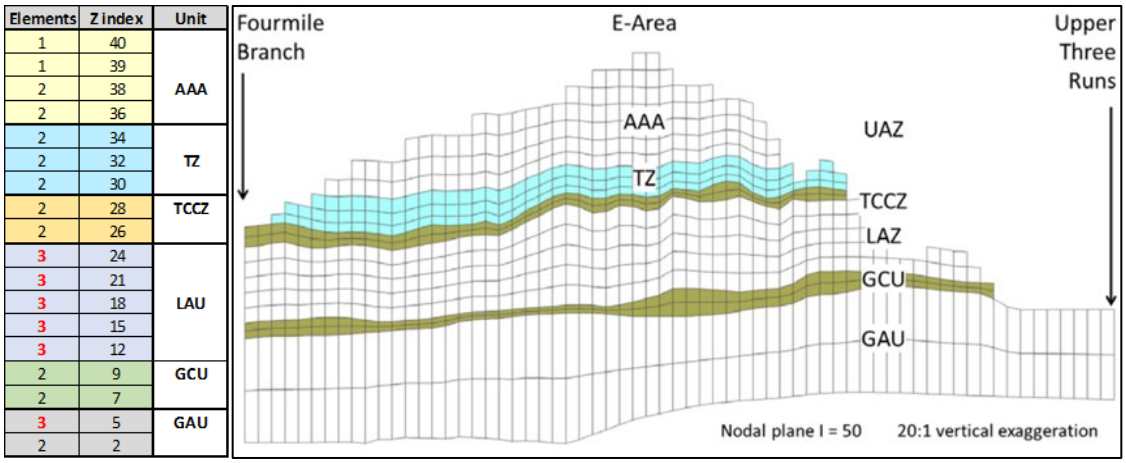

Figure 3-67 Vertical Grid Assignments for PORFLOW Transport Models Used in Limits Analyses

A total of 40 nonuniform vertical elements are employed, where mesh refinement is performed in those areas of most importance.

Transport results for both the uncovered (TP0) and first covered time period (TP1) flow fields are provided. Scoping results indicate that these surface boundary conditions bound the entire range of conditions modeled.

Every computational node within the PORFLOW aquifer transport model that resides on or beyond the 100-meter POA is queried for every radionuclide in the short chain and at every point in time. The maximum node concentration for every chain member and point in time is stored for later post-processing. Note that, at any given point in time, the location of maximum concentrations

among the chain members will most likely differ (i.e., an embedded conservatism in the follow-on dose conversion calculations).

Figure 3-68 through Figure 3-71 illustrate which nodes are monitored during a simulation (i.e., the observation nodes), where plots on the left are "at" the 100-meter POA (i.e., black solid curve surrounding the ELLWF) and plots on the right show "beyond" the 100-meter POA (i.e., gray shaded region). All vertically stacked nodes are included in these regions (i.e., a 2-D curtain for the "at" condition and a 3-D domain for the "beyond" condition).

Figure 3-68 through Figure 3-71 are steady-state 3-D concentration plumes that have been projected onto a 2-D *z* plane. The local (*x*,*y*) concentrations shown represent the maximum vertical concentration values. Contours varying by one order in magnitude were chosen, where the key values are:

- 1.0E-08 gmol L^{-1} – located at the orange-yellow interface where the DU source strength is set such that it touches the 100-meter POA curtain (referred to as the concentration limit) and used to calibrate DUs for comparison purposes.
- 1.0E-09 gmol L^{-1} – located at the yellow-green interface representing the 10% value of the concentration limit and used for processing Limits aquifer cutouts.
- 1.0E-11 gmol L^{-1} – located at the cyan-purple interface representing the 0.1% value of the concentration limit and used for processing PIF aquifer cutouts.

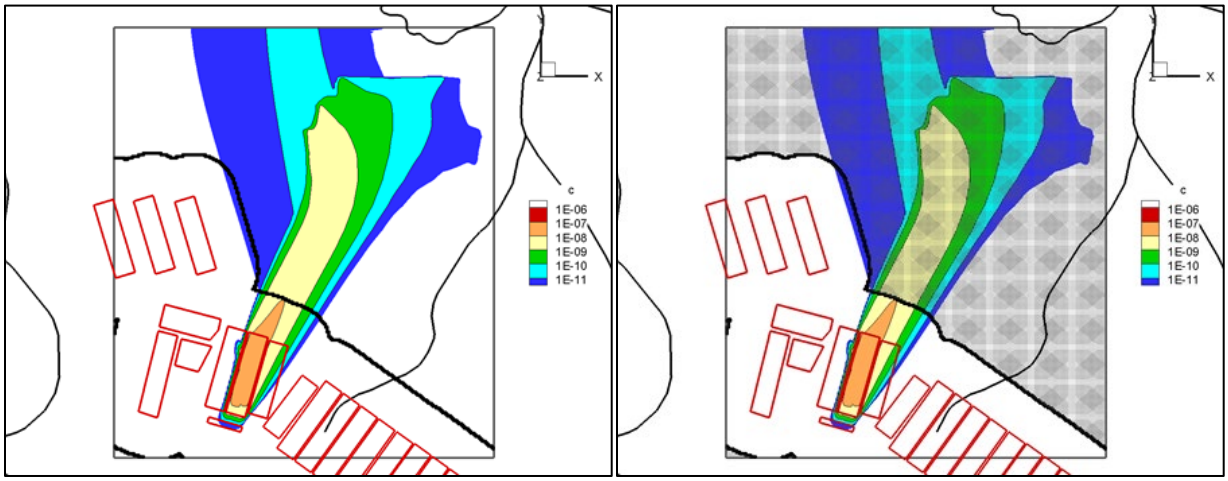

Figure 3-68 Steady-State Tracer Concentration Profiles for TP0 Showing "At" and "Beyond" Compliance Regions for West_B (ST09)

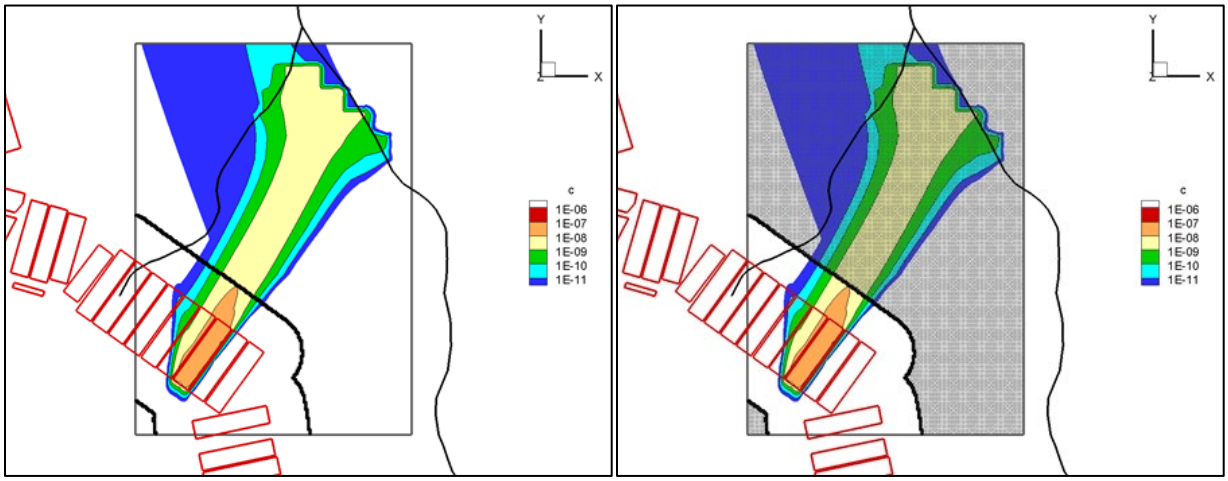

Figure 3-69 Steady-State Tracer Concentration Profiles for TP0 Showing "At" and "Beyond" Compliance Regions for Center_B (ST05)

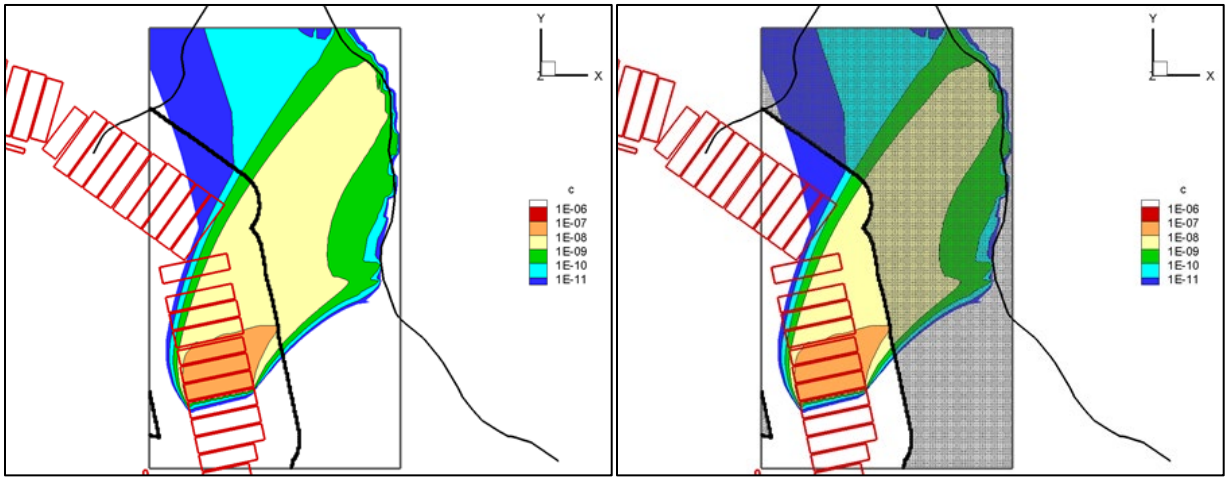

Figure 3-70 Steady-State Tracer Concentration Profiles for TP0 Showing "At" and "Beyond" Compliance Regions for East1_B (ST17)

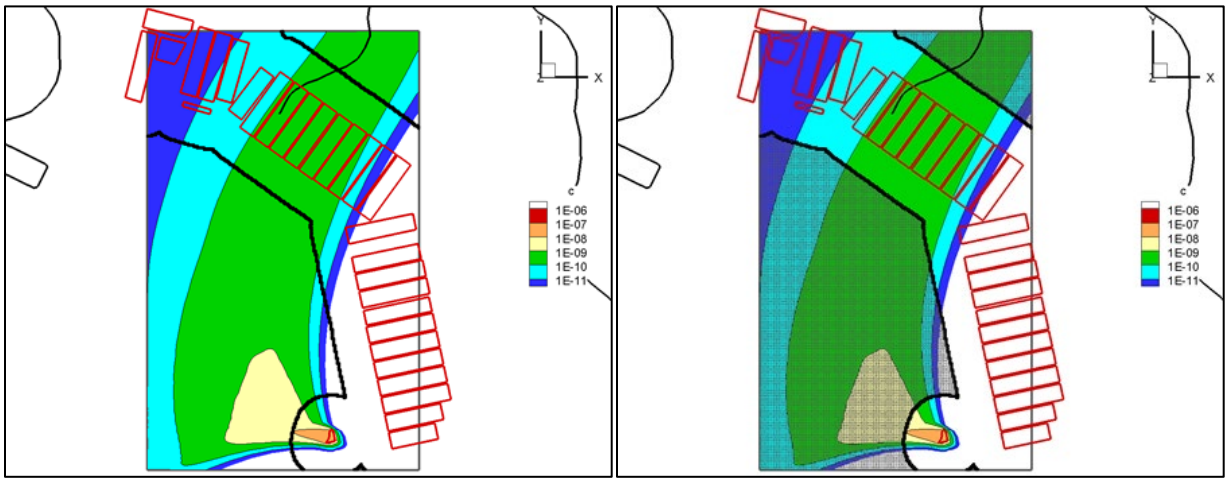

Figure 3-71 Steady-State Tracer Concentration Profiles for TP0 Showing "At" and "Beyond" Compliance Regions for East2_A (NR07E)

Transport results for both the uncovered (TP0) and the first covered time period (TP1) flow fields are provided in Appendix C, Section C.1.3.

3.5.3.2.3.1. West Footprint

The DUs residing within the West PIF aquifer cutout footprint are separated into two subgroups:

- **West_A:** ET07, ET08, ET09
- **West_B:** ET03, ET04, NR26E, ST08, ST09, ST10, ILV, ST11

PORFLOW steady-state tracer runs are made to assess the adequacy of the chosen footprint domains. The results are presented in Appendix C, Section C.1.3.1. For all cases shown, the West_A and West_B footprints meet the criteria chosen (Sections 3.5.3.2.2 and 3.5.3.2.3) in establishing this footprint.

3.5.3.2.3.2. Center Footprint

The DUs residing within the Center PIF aquifer cutout footprint are separated into two subgroups:

- **Center_A:** ST01, ST02, ST03, ST04, ST23
- **Center_B:** ST24, ST05, ST06, ST07

PORFLOW steady-state tracer runs are made to assess the adequacy of the chosen footprint domains. The results are presented in Appendix C, Section C.1.3.2. For all the cases shown, the Center_A and Center_B footprints meet the criteria chosen (Sections 3.5.3.2.2 and 3.5.3.2.3) in establishing this footprint.

3.5.3.2.3.3. East1 Footprint

The DUs residing within the East1 PIF aquifer cutout footprint are separated into three subgroups:

- **East1_A:** ET02, ET01, ST14, ET05, LAWV
- **East1_B:** ET06, ST17, ST18, ST19, ST20
- **East1_C:** ST21, ST22

PORFLOW steady-state tracer runs are made to assess the adequacy of the chosen footprint domains. The results are presented in Appendix C, Section C.1.3.3. For all the cases shown, the East1_A, East1_B, and East1_C footprints meet the criteria chosen (Sections 3.5.3.2.2 and 3.5.3.2.3) in establishing this footprint.

3.5.3.2.3.4. East2 Footprint

The only DU residing within the East2 PIF aquifer cutout footprint is addressed as:

- **East2_A:** NR07E

PORFLOW steady-state tracer runs are made to assess the adequacy of the chosen footprint domain. The results are presented in Appendix C, Section C.1.3.4. For the case shown, the East2_A footprint meets the criteria chosen (Sections 3.5.3.2.2 and 3.5.3.2.3) in establishing this footprint.

3.5.4. General Separations Area E-Area Low-Level Waste Facility GoldSim® System Model

The GSA ELLWF System Model (hereafter referred to as the System Model) has been developed by Wohlwend (2020) to address specific recommendations from the 2015 ELLWF PA strategic plan (Butcher and Phifer, 2016a) for including UQSA in the next revision of the PA. UQSA is a required component of the PA that provides a reasonable expectation that POs will be met.

The System Model, whose primary purpose is to generate a distribution of reasonable, potential dose exposures to an individual via the GW exposure pathway, performs both deterministic and stochastic (probabilistic) simulations. The probability distribution in dose exposure is a measure of the overall uncertainty arising from uncertainties embedded in input parameters throughout the model. To capture this uncertainty, the "stochastic element" within the GoldSim® Monte Carlo simulation software (GoldSim Technology Group, 2018a) is utilized. The stochastic element provides the user a means to explicitly account for the uncertainty associated with each input parameter. During the probabilistic simulations, GoldSim® employs the Monte Carlo simulation technique across the set of stochastic elements within the model. Each probabilistic simulation, which comprises thousands of realizations, generates a distribution of uncertainty that represents the potential dose exposure to a receptor. The model results are then reviewed against the POs to determine if risk is properly managed.

Sensitivity analysis provides insight into the uncertainty inherent in the PA calculations and gives context to decision makers. One goal of sensitivity analysis is to identify which variables exert the greatest influence on the variability in dose. Stochastic parameters will have different sensitivities at different times because the major contributing radionuclide can be different. Quantitative assessment of the importance of inputs is necessary when the level of uncertainty in the concentration (and therefore dose) exceeds the acceptable threshold (or PO). Sensitivity and uncertainty results are useful in determining which parameters associated with the disposal facility should be the focus of future PA maintenance activities. These activities may include development of more rigorous analytical techniques or enhanced efforts to quantify more accurately environmental and other physical parameters.

Interpretation of UQSA is focused on the performance of key safety functions of the engineered and natural features of the disposal facility that influence the magnitude and timing of the predicted peak dose. This is accomplished by identifying the structural, hydraulic, and chemical inputs and assumptions that have a significant influence on the source-term release from the disposal facility, the flux to the water table, and the concentrations at the 100-meter POA. The results of UQSA simulations are used to identify features, events, and processes that are components of one or more key safety functions and can significantly influence the magnitude of the releases. From sensitivity analysis, the factors influencing timing can be understood as well as the effect of key assumptions.

In this PA, the System Model addresses UQSA for STs and ETs only. Because they contain concrete barriers, the vaults and CIG trench segments are better represented by 2-D PORFLOW models. A sub-model for NRCDA DUs has been developed for the System Model by Wohlwend (2020); however, it is not implemented in this PA. Instead, UQSA for the NRCDAs as well as the LAWV, ILV, and CIG trench segments is performed using PORFLOW.

3.5.4.1. System Model Description

The overall structure and flow diagram of the System Model is shown in Figure 3-72. The five main configuration-controlled PA data sources shown on the left side of the diagram serve to standardize key inputs to all the models to ensure consistency throughout the PA calculations. Four separate "sub-models" comprise the overall System Model: HELP, PORFLOW, GoldSim®, and the SRNL Dose ToolKit. The HELP model provides infiltration data to PORFLOW. PORFLOW generates the subsurface flow fields, water saturations, and flow velocities that are used to calibrate the GoldSim® model to ensure confidence in the stochastic results. Lastly, the concentrations from the GoldSim® transport simulations are input to the SRNL Dose Toolkit to calculate dose impacts. The sub-model components and interfaces are described in more detail below.

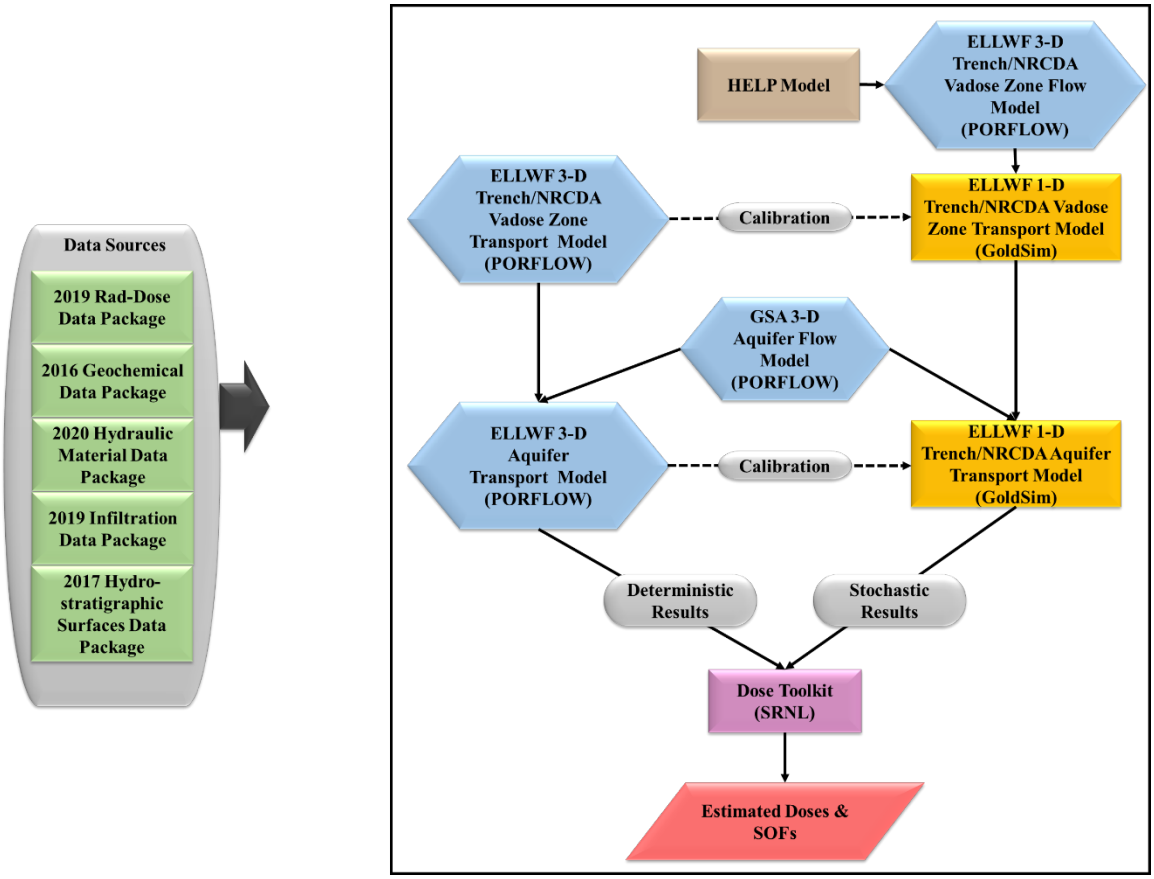

Figure 3-72. Flow Diagram of the System Model

3.5.4.2. System Model Components and Interfaces

As shown in Figure 3-72, four key components comprise the overall flow analyses. Each of the key components is addressed below in Sections 3.5.4.2.1 through 3.5.4.2.4.

3.5.4.2.1. Data Sources

A significant body of hydrostratigraphic information and hydraulic properties data exists for the GSA, and several of the major facilities within the GSA have undertaken PA or closure analyses in prior years. As will be discussed in Section 3.8 the key input data sources for PA models are maintained by SRNL and are referred to as "Data Packages" (i.e., databases that are routinely

updated as new, approved, critically reviewed data becomes available and are maintained under the ELLWF PA maintenance program). As shown in Figure 3-72, the key up-to-date data sources highlighted in green include:

- **2019 Rad-Dose Data Package** (Smith et al., 2019; SRNL, 2019b): Radiological information, including parameters such as half-life, decay modes, dose conversion factors for internal and external exposure, MCLs, and human consumption factors, for 1,252 radionuclides based on ICRP Publication 107 (ICRP, 2008).
- **2016 Geochemical Data Package** (Kaplan, 2016b; SRNL, 2018): Geochemical data, including sorption coefficients (K_d values), liquid-phase solubilities, and chemical leach factors, for various materials typically considered in fate and transport analyses of SRS facilities.
- **2020 Hydraulic Properties Data Package** (Nichols and Butcher, 2020; SRNL, 2020): Estimates of material and hydraulic properties, including porosity, dry bulk density, particle density, saturated hydraulic conductivity, characteristics curves, and effective diffusion coefficients, for soils, cementitious materials, and waste zones associated with the ELLWF engineered and natural disposal systems.
- **2019 Infiltration Data Package** (Dyer, 2019b; SRNL, 2019a): Closure cap design and material properties assumptions as well as infiltration data for intact and subsidence cases used to establish the upper boundary conditions for PORFLOW VZ flow model simulations of the five ELLWF types of DUs.
- **2017 Hydrostratigraphic Surfaces Data Package** (Bagwell and Bennett, 2017; SRNL, 2017): Subsurface elevations and depths to the water table, the Lower Aquifer Zone of the Upper Three Runs Aquifer, the Tan Clay Confining Zone, and the Tobacco Road Sand for ELLWF DUs.

All data are imported into the GoldSim® sub-models of the System Model as either GoldSim® Data Elements or Time Series Elements. Data Elements contain radionuclide data as well as hydraulic and geochemical data organized by material type. Tables of infiltration data are contained in Time Series Elements.

3.5.4.2.2. HELP Sub-Model

Infiltration data from the HELP model (highlighted in tan in Figure 3-72) simulations establish the upper boundary conditions for the VZ flow model simulations of STs, ETs, LAWV, ILV, and CIG trench segments in PORFLOW (Dyer, 2019b). For STs and ETs, infiltration rates were generated over a 10,100-year timeline for both intact and subsidence cases. For worst-case subsidence scenarios, localized catastrophic failures of the final cover system are assumed for sections of closure cap underlain by "non-crushable" containers. These containers are assumed to simultaneously fail immediately upon installation of the final cover system at the end of the 100-year IC period. Estimates of infiltration rate through the closure cap are calculated based on the maximum areal extent occupied by non-crushable containers in the various STs and ETs.

For the NRCDAs, HELP model infiltration rate estimates were generated for an intact case only. NR components and auxiliary equipment are packaged in thick-walled, welded, carbon-steel casks and bolted, gasket-sealed, steel containers which are assumed to remain structurally intact well beyond the end of the 1,000-year post-closure period.

Infiltration data for the different types of DUs (STs, ETs, and NRCDAs) and infiltration scenarios are provided in the *Infiltration Data Package* (Dyer, 2019b)and are utilized by the GoldSim® VZ sub-model as described above in Section 3.5.4.2.1.

3.5.4.2.3. PORFLOW Sub-Models

Figure 3-72 highlights in blue how the various PORFLOW sub-models fit into the overall System Model. The recently updated 3-D PORFLOW aquifer flow model (centered in Figure 3-72), referred to as the GSA_2018 flow model (Flach, 2019), was used to define the aquifer flow path for all 1-D GoldSim® DU models. Although the GSA flow field can be used directly in PORFLOW aquifer transport simulations, SRNL chose to instead use flow information defined on a localized grid of smaller extent but higher resolution. To that end, a subregion of the GSA_2018 flow model underlying the ELLWF was subdivided into four refined "PIF aquifer cutouts" for performing aquifer transport simulations for the ELLWF PA (Hang, 2019a). The estimated flow field provided by the PORFLOW 3-D aquifer model cutouts was entered into a GoldSim® data element by specifying an initial estimate of the aquifer Darcy velocity and geometric parameters.

Deterministic transport simulation results from the detailed PORFLOW 3-D VZ models and 3-D aquifer model (left middle in Figure 3-72) were employed to calibrate the 1-D GoldSim® sub-models. Accounting for differences in infiltration boundary conditions, eighteen unique ST and ET VZ PORFLOW models, defined by seven hydrostratigraphic groupings, were developed for the current ELLWF PA (Danielson, 2019c). Trench DUs were sorted into the seven groupings based on similar depth to water table and clay thickness. The Trench System Model locations were selected and developed from three of the seven hydrostratigraphic groupings to benchmark with the respective PORFLOW trench model at each location. Trench units are considered "earthen" DUs due to the absence of engineered barriers between the waste form and soil. System Model calibration utilizes PORFLOW fluxes to the water table and concentrations at the 100-meter POA for the radionuclides that were simulated.

PORFLOW deterministic analyses were used instead to quantify uncertainty in the release and transport of radionuclides from concrete DUs (i.e., LAWV and ILV) and the NRCDAs. These two different approaches (deterministic PORFLOW analysis and probabilistic GoldSim® analysis), form a hybrid approach for evaluating total disposal system uncertainty.

3.5.4.2.4. SRNL Dose Model Simulations

The SRNL Dose Model Toolkit (Aleman, 2019) performs a series of calculations using six separate software codes. Its position within the System Model is highlighted in purple in Figure 3-72.

- First, concentration time series output for each parent and short-chain progeny radionuclide at the 100-meter POA boundary are taken from *GoldSim*® and *PORFLOW* GW simulations and used as input to the *SRNL PreDose Module*. The *SRNL PreDose Module* expands the

short-chain radionuclide decay chain results in the time series output files to produce full decay chain results using the assumption of secular equilibrium.

- The expanded concentration time series files for each existing/future inventory scenario analyzed are next input to the *SRNL PreDose Maximum Concentration Module* to generate composite 'worst case' full-chain concentration history profiles.
- The 'worst case' concentration history profiles are then input to the *SRNL PA/CA Limits and Doses Tool*. The output of this tool is a series of concentration and dose files for each GW pathway where contributions from each full-chain progeny have been rolled up to the parent nuclide on a "per Ci of parent buried" basis. The concentration and dose files serve as input to the *SRNL ELLWF Dose Investigation Tool*.
- The *SRNL ELLWF Dose Investigation Tool* quantifies the dose impact to GW protection and all-pathways human dose receptors at the 100-meter POA boundary surrounding the ELLWF. This POA boundary comprises a 'curtain' of PORFLOW aquifer model computational cells where concentrations of select parent radionuclides and short-chain radioactive progeny are calculated and recorded at a specified time frequency. The total time history of the calculation encompasses the period-of-performance for GW protection and all-pathways.

For GoldSim® simulations, the maximum concentration time series for each parent radionuclide and short-chain progeny at the 100-meter POA are exported into a Microsoft Excel workbook. The workbook is then transferred to the SRNL Dose Toolkit directory where it is read into the initial PreDose Module as a list-directed input file.

3.5.4.3. GoldSim® Trench System Model

The functions of the GoldSim® sub-models in the overall GSA ELLWF System Model are highlighted in gold in Figure 3-72. GoldSim® sub-models have been developed for ST and ET DUs using GoldSim® Ver. 12.1.4 #235 (October 22, 2019). The sub-models for STs and ETs are hereafter referred to as the GoldSim® Trench System Model (Wohlwend, 2020). A schematic of the conceptual model for the GoldSim® Trench System Model is illustrated in Figure 3-73.

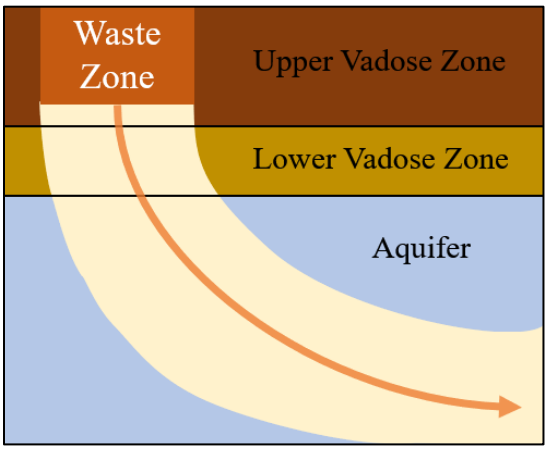

Figure 3-73. Conceptual Model Schematic for GoldSim® Trench System Model (Wohlwend, 2020; Figure 2-2)

Trench units representing five of the seven unique hydrostratigraphic zones defined by Danielson (2019c) are selected as locations for the GoldSim® Trench System Model and included ST06, ST09, and ET06. More detailed development and calibration of the GoldSim® Trench System Model are discussed in Section 4.4. Contaminant transport in the aqueous phase of the porous medium includes the following advective processes: infiltration of precipitation from the ground surface, downward migration through the VZ, recharge of the aquifer at the water table (from the base of the LVZ), and lateral transport in the aquifer saturated zone to the 100-meter POA. To simplify the initial model calibration, the ST06 model utilized the PORFLOW ET geometry and waste properties. Ultimately, the three trenches noted above are modeled and calibrated within the GoldSim® Trench System Model.

3.5.4.4. GoldSim® Vadose Zone Transport Model Development

This section introduces the methodology employed by Wohlwend and Aleman (2020) to develop the simplified 1-D GoldSim® VZ flow and transport models for STs and ETs. The application of this methodology in benchmarking the VZ component of the GoldSim® System Model for ETs and STs is discussed in Sections 4.4.8 and 4.4.9, respectively. The GoldSim®-based VZ models are generic models capable of being benchmarked to any of the other trench locations within the ELLWF. Wohlwend and Aleman (2020) benchmarked GoldSim® transport simulations for ST06 executed in a deterministic mode (using nominal best-estimate parameter settings) against the results of best-estimate deterministic simulations using the PORFLOW 3-D VZ Model for STs and ETs. Subsequent development work to couple the GoldSim®-based 1-D VZ models to the GoldSim® 1-D Aquifer Transport Model for purposes of performing stochastic analyses that couple all pertinent fate and transport processes from the ground surface to the 100-meter POA is presented in Section 4.4.11. This is a key component of the effort to include uncertainty quantification and sensitivity analysis in this revision of the ELLWF PA.

3.5.4.4.1. Overview of Vadose Zone Models

PORFLOW 3-D VZ models of a centrally located ST and ET were developed by Danielson (2019c) using the depth to water table and hydrostratigraphic surfaces beneath ST06 (Bagwell and Bennett, 2017). The upper boundary condition of the PORFLOW models is defined by time-dependent infiltration rates to account for the operational (uncovered), IC (interim cover), and post-closure (final closure cap – intact case, subsided cases, and long-term degradation) periods. The final closure cap extends beyond the trench footprint by 40 feet while the interim cover overhangs the trench by 10 feet. An operational stormwater runoff (geomembrane) cover is installed over a closed ST four years after the placement of the last waste package but was not implemented in this study because the timing of each operational cover installation is unique. The design specifications for the stormwater runoff cover assume the same overhang (10 feet) and infiltration rate as the interim cover.

The ST and ET trench models include both intact and subsidence cases (Case01 and Case11b, respectively, using PA2008 nomenclature). Subsidence refers specifically to non-crushable containers and vessels that do not collapse during dynamic compaction. Instead, they are assumed to fail catastrophically immediately upon installation of the final closure cap, resulting in localized subsidence (holes) in the cap. Subsidence cases are investigated using only a single discrete hole

with a specific dimension and location as discussed in Sections 4.4.9.2 and 4.4.9.3.2 for STs and Section 4.4.8.1 for ETs. The intact and subsidence cases both include dynamic compaction of the waste zone. Dynamic compaction of the waste zone and subsidence are assumed to occur at the end of IC.

The VZ model represents three porous media zones comprising the disposal system including: the waste zone (WZ), UVZ, and LVZ. The hydraulic properties for the three zones employ the following six material types defined by Nichols and Butcher (2020): STETboxesBC, STETboxesAC, SThybridBC, SThybridAC, ClayeySoil (UVZ), and SandySoil (LVZ).

GoldSim® VZ models of the ELLWF trenches are built using the Contaminant Transport Module in GoldSim® Ver. 12.1.4 #235 (October 22, 2019). GoldSim®'s cell pathway element was used to build a column and network of cells for modeling the advective and diffusive transport of radionuclides below the operational soil cover to the water table in the ST and ET, respectively. The cell pathway allows inventory transfer within the WZ during dynamic compaction. The cell pathway accommodates back diffusion which can occur after dynamic compaction of the waste zone. The GoldSim® ET Trench Model includes intact and subsidence cell pathway elements. The GoldSim® ST Trench Model includes intact, between-segment, and subsidence cell pathway elements.

Vertical Darcy velocities and water saturations from the PORFLOW VZ flow simulations are extracted for each steady-state simulation (time period) and averaged within user-specified material zones for the GoldSim® VZ model. Volume-averaged vertical Darcy velocities are computed for the porous media zones (WZ, UVZ, and LVZ) in each cell pathway column for input to the GoldSim® VZ model. Transport properties for ET boxed and ST hybrid waste (pre- and post-dynamic compaction), the UVZ, and the LVZ are extracted from the PORFLOW VZ model and included in the GoldSim® VZ model.

Seven parent radionuclides and their progeny (half-lives greater than one year) are modeled in the PORFLOW and GoldSim® VZ models. The parent radionuclides include C-14, H-3, I-129, Np-237, Sr-90, Tc-99 and U-238. A tracer was also modeled for assessing mass balance of fluxes from the waste zone and to the water table. The radionuclide data for the species modeled are obtained from the SRNL Radionuclide-Dose Data Package (Smith et al., 2019; SRNL, 2019b) and are given in Table 3-41.

Best-estimate soil/water partition coefficients (K_d values) for the various solid materials are defined for each chemical element in the model (i.e., not for each radionuclide species; for example, a single K_d value was assigned to all isotopes of uranium). Clayey and Sandy Sediment K_d values are assigned to radionuclides in the different material zones in the VZ model (i.e., WZ, UVZ, and LVZ) based on the chemical characteristics of the material types.

Table 3-41. Radionuclide Data for Species Included in GoldSim® Trench System Model (Wohlwend and Aleman, 2020; Table 2-1)

Species ID	Atomic Weight (g/mol)	Half-life (years)	Sp. Act. (Ci/gmol)	Daughter
C-14	14	5.70E+03	6.2719E+01	
H-3	3	1.23E+01	2.9018E+04	
I-129	129	1.57E+07	2.2770E-02	
Np-237	237	2.14E+06	1.6674E-01	U-233
U-233	233	1.59E+05	2.2456E+00	Th-229
Th-229	229	7.34E+03	4.8705E+01	
Sr-90	90	2.88E+01	1.2417E+04	
Tc-99	99	2.11E+05	5.2100E+08	
U-238	238	4.47E+09	8.0012E-05	U-234
U-234	234	2.46E+05	1.4562E+00	Th-230
Th-230	230	7.54E+04	4.7426E+00	Ra-226
Ra-226	226	1.60E+03	2.2343E+02	Pb-210
Pb-210	210	2.22E+01	1.6103E+04	

Notes:
Radionuclide parents are bolded and progeny are indented.

Clayey Sediment K_d values are assigned to radionuclides in the WZ (i.e., waste cells in the model) because the geochemistry of clayey sediment is assumed to approximate that of the rusted metal waste containers. Best-estimate K_d values are given in Table 3-42. In the VZ model, uncertainty distributions for these best-estimate K_d values are based on recommendations by Kaplan (2016b) as described in Section 3.8.2.6.

Table 3-42. Mean Soil/Water Partition Coefficients for GoldSim® Trench System Model (Wohlwend, 2020; Table 2-3)

Element	Best Sand K_d (mL g^{-1})	Best Clay K_d (mL g^{-1})
C	1.0E+00	3.0E+01
H	0.0E+00	0.0E+00
I	1.0E+00	3.0E+00
Np	3.0E+00	9.0E+00
Pb	2.0E+03	5.0E+03
Ra	2.5E+01	1.8E+02
Sr	5.0E+00	1.7E+01
Tc	6.0E-01	1.8E+00
Th	9.0E+02	2.0E+03
U	3.0E+02	4.0E+02

3.5.4.5. GoldSim® Aquifer Transport Model Development

This section introduces the development methodology for the GoldSim® 1-D aquifer transport model described in detail by Wohlwend and Hamm (2020). The application of this methodology to calibrate the aquifer zone component of the System Model for trenches (STs and ETs) is discussed in Section 4.4.11. The calibration focuses on the maximum (peak) concentration and timing for a nonsorbing, nondecaying tracer and seven parent radionuclides: C-14, H-3, I-129, Np-237, Sr-90, Tc-99, and U-238. Because Np-237 and U-238 have progeny, their short-chain progeny are included in the calibration analysis. The results of benchmarking the GoldSim®

aquifer transport model to best-estimate PORFLOW simulation data are also presented in Section 4.4.11.

3.5.4.5.1. Introduction

As indicated in Figure 3-72, the aquifer transport model is a sub-model of the System Model described above and by Wohlwend (2020). GoldSim® does not explicitly solve porous-media flow equations. Instead, it solves the transport equation typically expressed as a 1-D model representation. When considering the ELLWF, several aspects of the fate and transport of contaminants from the water table beneath a DU to the 100-meter POA well are multidimensional in nature. Typically, stream traces emanating into the aquifer at the water table surface are nonlinear as they progress toward the downstream 100-meter POA. Additional distortion among these stream traces occurs because of the potential presence of underlying clay layers. Therefore, the results of the GoldSim® flow and transport simulations require calibration to the more-realistic results of the 3-D PORFLOW aquifer zone deterministic model simulations. This calibration process provides a level of confidence that the GoldSim®-based stochastic results are reliable.

Capturing 3-D flow effects in a 1-D model usually requires some adjustment to nominal model settings. In this case, better agreement between the two models is obtained by adjusting the nominal volumetric flow rate and the flow area of the aquifer.

ST06 resides within the center set of STs (Figure 2-32) and contains the underlying TCCZ within the aquifer unit. The vertical location of this clay layer places it in the direct transport path for many of the PORFLOW stream traces before they reach the 100-meter POA. The TCCZ ranges in thickness from ~6 feet to ~22 feet (averages 12-15 feet) within E-Area and the future Plot 8. Figure 3-74 displays the distance in feet from the top of the water table to the top of the TCCZ. The red-dashed line in Figure 3-74 shows where these two surfaces cross.

Negative numbers represent where the TCCZ surface resides within the VZ above the water table and positive numbers where the TCCZ resides within the aquifer zone. For footprints in the western sector of the ELLWF, the TCCZ resides completely within the VZ, while in the eastern sector of the ELLWF, the TCCZ resides deep enough into the aquifer zone to minimize its impact on streamline behavior. As such, the more challenging location within the center sector was chosen for model development. The 1-D aquifer zone model developed and presented below is therefore general enough to handle the other ELLWF footprint conditions, where geometric parameter adjustments will be required but no additional modelling components (e.g., no additional flow paths) are envisioned. Figure 1-2 and Figure 2-30 show the location of ST06 relative to the overall ELLWF facility layout and the 100-meter POA.

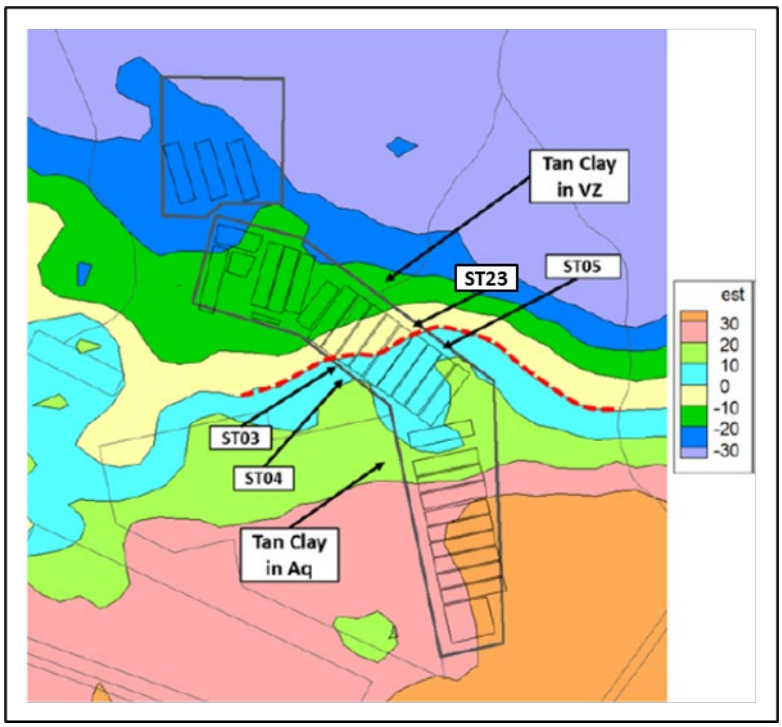

Figure 3-74. Position of Tan Clay Confining Zone Relative to Water Table (Wohlwend and Hamm, 2020; Figure 1-2)

3.5.4.5.2. Aquifer Zone Model Description

The conceptual model of the aquifer zone is shown schematically in Figure 3-73. After transport through the UVZ and LVZ, the radionuclides enter the aquifer zone at the top surface of the water table. Contaminant flux from the VZ is transferred to an aquifer pathway that represents the footprint below the VZ DU. Multiple aquifer pathways are then utilized to model radionuclide transport through the aquifer, ending at the 100-meter POA.

To better understand GW through the aquifer zone beneath the ELLWF DUs, flow fields summarized in Section 3.5.2.10 from the GSA_2018 aquifer flow model (Flach, 2019) were investigated. The flow fields beneath the DUs are complex due to the presence of multiple hydrostratigraphic layers as shown in Figure 3-75. The blue lines in the figure represent flow through the aquifer (i.e., 3-D stream traces extracted from the 3-D flow field). The stream traces first enter an upper sandy layer where flow is almost horizontal. Next, they pass through the TCCZ, where flow is almost vertical, followed by a second sandy layer where flow is again almost horizontal. Finally, the stream traces pass through the green clay layer where flow is almost vertical. The ultimate discharge points for the stream traces are seepage faces associated with UTR.

Flow through the aquifer zone can be represented by a GoldSim® streamtube (Figure 3-76), where Segment 1 represents flow through the initial sandy layer with flow area, A_1, Segment 2 represents flow through the TCCZ with flow area, A_2, and Segment 3 represents flow through a second sandy layer with flow area, A_3. Note that flow directly beneath the ST06 footprint does not pass through the green clay layer before reaching the POA.

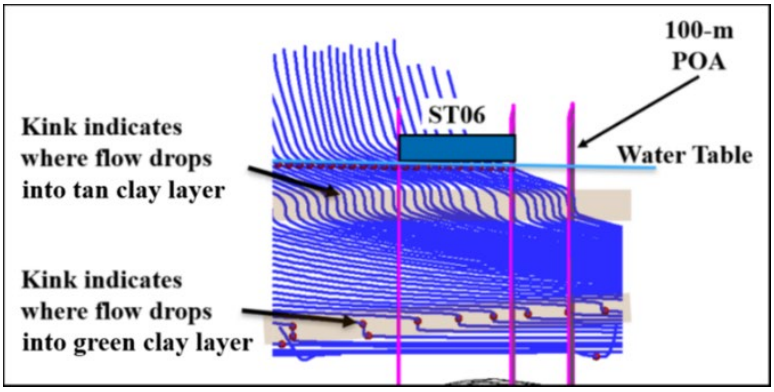

Figure 3-75. Flow Fields Beneath ST06 from the GSA_2018 Aquifer Flow Model (Wohlwend and Hamm, 2020; Figure 2-2)

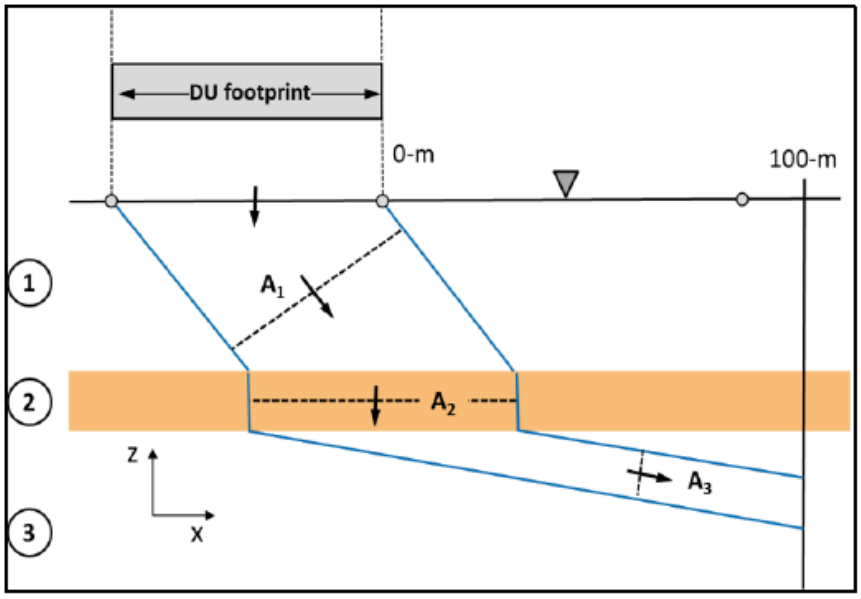

Figure 3-76. Streamtube Representation of Flow Through Aquifer Zone (Wohlwend and Hamm, 2020; Figure 2-3)

Within a streamtube at steady-state flow:

$$Q = Q_1 = Q_2 = Q_3 \qquad \text{Eq. (3-18)}$$

where:

Q_i Volumetric flowrate of water through segment i ($ft^3\ yr^{-1}$)

The flowrates can be further defined as follows:

$$Q_i = A_i U_i = A_i \phi_i v_i \qquad \text{Eq. (3-19)}$$

where:

A_i Cross-sectional area of segment *i* (ft^2)

U_i Darcy velocity of segment *i* ($ft\ yr^{-1}$)

ϕ_i Effective porosity of segment *i* ($ft^3\ ft^{-3}$)

v_i Phasic velocity of segment *i* ($ft\ yr^{-1}$)

For GoldSim® modeling purposes, a simple 1-D model (aligned with respect to the flow direction) is shown in Figure 3-77.

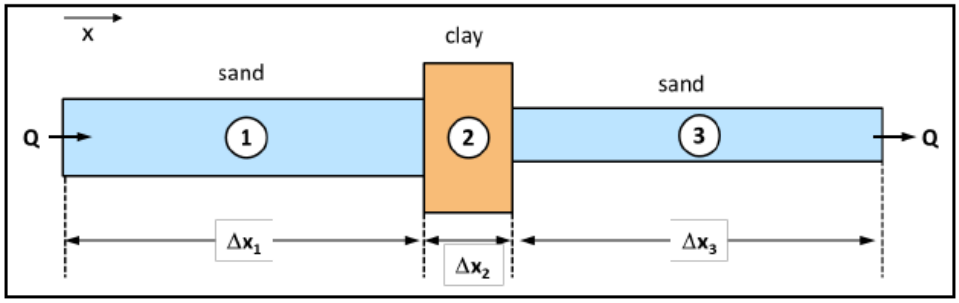

Figure 3-77. One-Dimensional Model of Streamtube in GoldSim® (Wohlwend and Hamm, 2020; Figure 2-4)

The PORFLOW aquifer transport model employs transverse dispersion which allows the contaminants to disperse laterally as well as in the longitudinal direction of flow (along a streamtube). As the contaminants disperse laterally, they can migrate into neighboring streamtubes, which changes their flow paths. For some contaminants (specifically those with high K_d values in clay), this can lead to a substantial portion of the radionuclide mass to bypass the clayey layer and travel along the sandy layer just above the clay layer to the POA (i.e., short-circuiting the more highly retarded flow path). This is evident in the PORFLOW concentration profiles shown in Figure 3-78. As time progresses, contaminants begin to arrive at the 100-meter POA at successively greater depths.

This effect is also seen in Figure 3-79 for Tc-99 where the maximum concentration (solid black line labeled "Max") at the 100-meter POA at any point in time is represented by the peak concentration of the six nodal concentration profiles (i.e., Nodes 1 through 6). Nodes 1 through 6 identify locations of increasing depth at the 100-meter POA. The peak of the peaks occurs at Node 2, which is located above the clayey layer. At Nodes 3 through 6 of increasing depth, the peak Tc-99 concentration moves from the upper sandy layer (Nodes 1 and 2) into the tan clay layer (i.e., the TCCZ) and then into the lower sandy layer. This effect is significantly dampened after the GoldSim® VZ model is connected to the GoldSim® aquifer zone model, when the inventory is placed at the waste zone instead of at the water table. The contaminant transport complexity this behavior indicates is one example of the difficulty in matching the 1-D GoldSim® model to the 3-D PORFLOW model results.

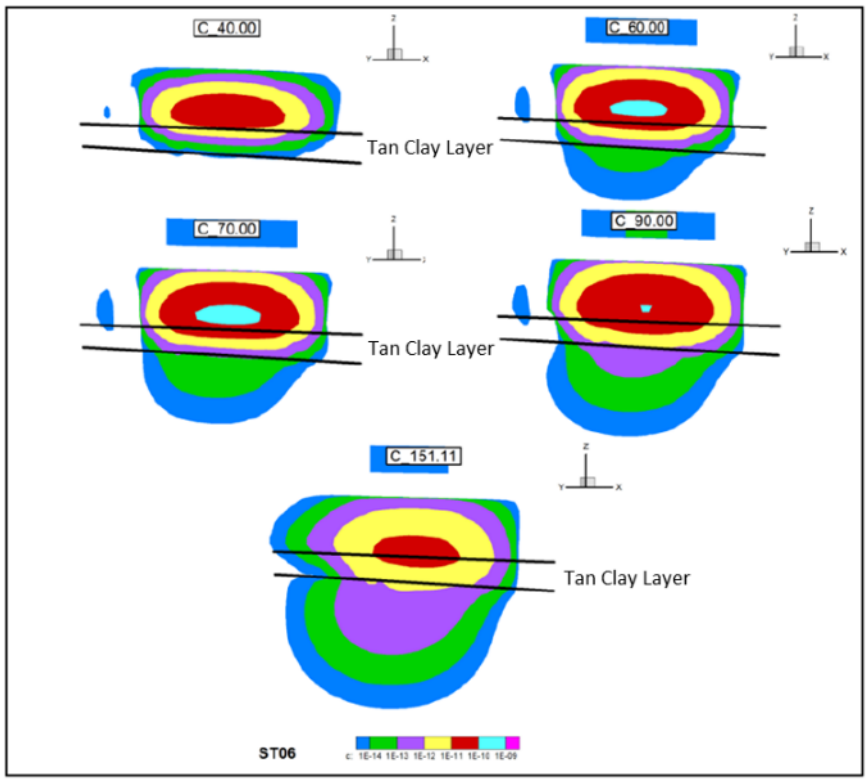

Figure 3-78. Sr-90 Concentration Profiles for ST06 at 100-meter POA Through Time from PORFLOW Aquifer Transport Model (Wohlwend and Hamm, 2020; Figure 2-5)

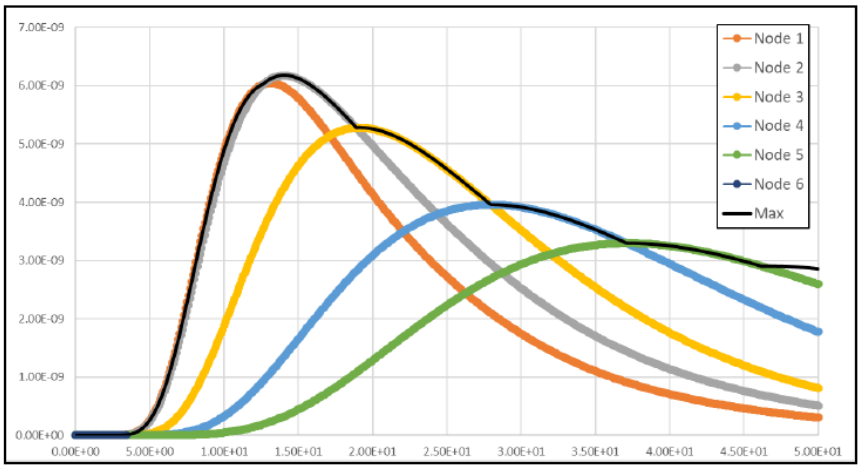

Figure 3-79. Tc-99 Concentration (gmol L^{-1}) Versus Time (year) at 100-meter POA from PORFLOW Aquifer Transport Model (Wohlwend and Hamm, 2020; Figure 2-6)

In GoldSim®, aquifer pathway elements representing the different material zones comprise each flow path (Figure 3-80). The conceptual model implemented within the aquifer pathway element is a row of linked computational cells having no-flow boundaries on the top, bottom, and sides, which allows 1-D transport solely in the aquifer flow direction. The Footprint_Sand element (Figure 3-80) represents the area directly beneath the DU footprint and the sandy portion above the clayey layer (first streamtube segment), while the AquiferWell_Clay and AquiferWell_Sand_below elements represent the segments of the aquifer pathway that are

comprised of clayey and sandy (below the clayey layer) soils, respectively. Each aquifer element contains several transport and geometric parameters to simulate the entire aquifer zone. The Footprint_Sand element also contains a source region where the inventory is uniformly placed. An example of the aquifer pathway and associated transport and geometric parameters is shown in Figure 3-81. The initial volumetric flow rate is estimated based on the phasic velocity, area, and porosity (0.25) calculated in the clayey region by the GSA_2018 aquifer flow model. To calibrate to PORFLOW targets, the volumetric flow rate and aquifer flow area of the streamtubes are modified.

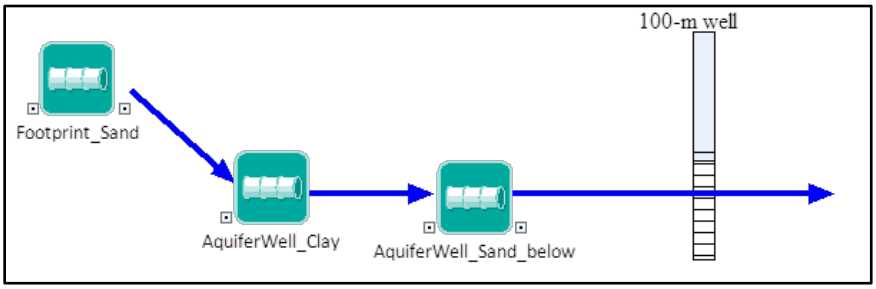

Figure 3-80. GoldSim® Representation of Aquifer Zone

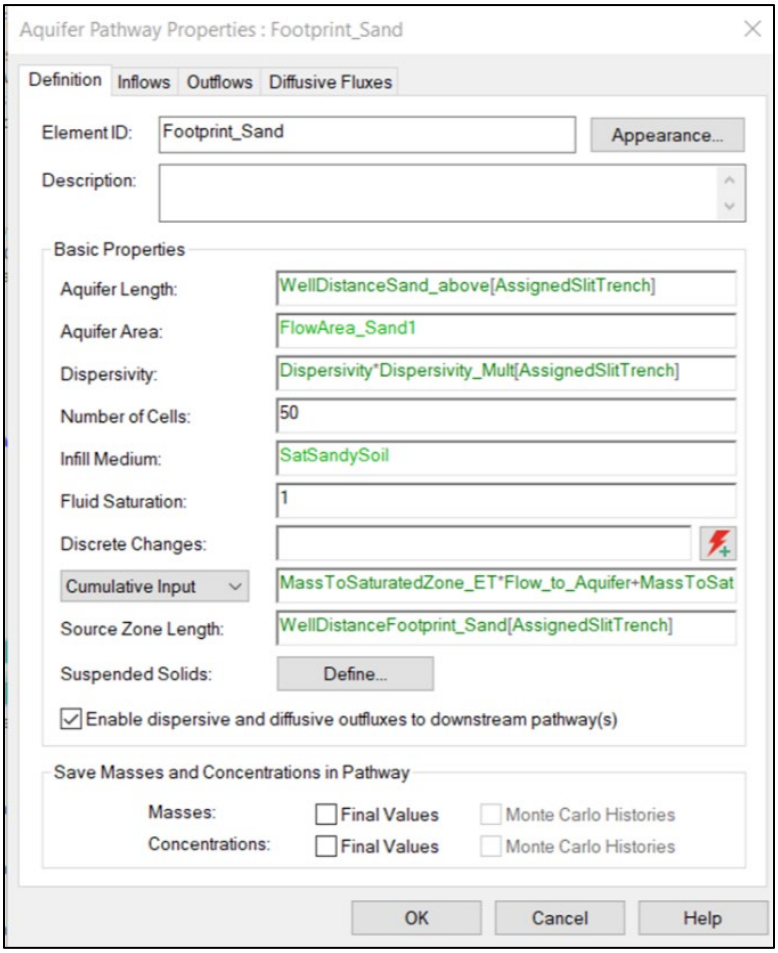

Figure 3-81. Footprint Region Aquifer Pathway Dialog Box Showing Transport and Geometric Parameters

Each aquifer pathway element defines the length, area, dispersivity, number of cells, the infill medium, saturation, and inventory (if applicable) of the pathway. The infill medium sets the porosity and density of the medium as well as the K_d of each element. The aquifer length, flow area, and Darcy velocity of each pathway are calibrated to PORFLOW aquifer model results and are reported in Section 4.4.11.

3.6. AIR AND RADON PATHWAYS CONCEPTUAL MODELS

The ARM utilizes the GoldSim® Ver. 12.1.4 #235 (October 22, 2019) Monte Carlo simulation software (GoldSim Technology Group, 2018a) to evaluate the flux of gaseous radionuclides as they volatilize from ELLWF DU waste zones, diffuse across the water-air interface into the partially water-saturated, air-filled soil pores surrounding the waste, and emanate at the land surface. The ARM is used in both the air pathway and radon flux analyses.

The ARM was originally developed by Hiergesell and Taylor (2011) for the 2011 ELLWF SA to analyze an LFRG concern regarding the potential for atmospheric plume overlap at the SRS boundary during the IC period. The model represents the physical features and properties of each DU facility, honoring the configuration of the waste zones, engineered features, and overlying closure cap layers. Input and design parameters are built into the ARM using the GoldSim® software's probabilistic input elements, which allow for both deterministic (central value) and probabilistic realizations. The ARM is executed in a deterministic mode for the air pathway and radon flux analyses in this PA. More importantly, the ARM incorporates a mechanism to equilibrate radionuclide concentrations across the air-water interface according to Henry's Law, providing a more accurate simulation of contaminant flux at the land surface. During each simulation, the ARM automatically computes effective diffusion coefficients for all radionuclide species for each cell material. This feature enables the user to investigate the impact of varying selected model parameter values (e.g., porosity and residual saturation) on contaminant flux. Lastly, the ARM combines the individual transport models constructed for each ELLWF DU into a single model to facilitate evaluation of the combined impact of multiple DUs on a single receptor to address the impact of plume overlap.

The ARM is a 1-D vertical stack of computational cells ranging from the bottom of the waste zone up to ground surface. The following conservative (pessimistically leaning) assumptions are employed: (1) lateral gaseous diffusion is assumed to be zero and (2) GW leaching of radionuclides from the waste zone is assumed to be zero. Thus, the only migration paths to remove or add contaminants is (1) radioactive decay or ingrowth and (2) vertical diffusion to the ground surface. The advective migration associated with atmospheric pumping is also assumed to be negligible.

Numerous modifications to the original 2011 ARM were made in preparation for the current ELLWF PA, much of which are described below or in Chapter 5. ARM features and modifications specific to each type of DU are presented in Section 5.1.5 (STs, ETs, and CIG trench segments), Section 5.2.3 (LAWV), Section 5.3.3 (ILV), and Section 5.4.3 (NRCDAs). Seldom used, the ARM is treated as an "engineering calculation." In lieu of a SQAP, model results are design checked on a project-by-project basis.

3.6.1. Atmospheric Release Model Implementation

The conceptual model implemented in the ARM is a 1-D column of computational elements or cells having no-flow boundaries on the sides and bottom. This serves to divert all contaminant fluxes upward to the land surface. The no-flow boundary conditions are pessimistically biased because diffusion will also proceed laterally and downward in the subsurface. The materials contained within the computational elements represent those of the waste zone, engineered barriers, sand backfill, and final closure cap for each of the individual disposal facilities. The configurations conform to the anticipated closure designs for each facility type (e.g., dimensions of waste zones and engineered barriers), as do the general occurrence and timeline of events encompassed in the loading and closure of the ELLWF facilities. Material properties associated with each DU, including porosity, particle density, residual water saturations, etc., are obtained from multiple sources as described below.

The radionuclides evaluated in the ARM exist in the gaseous state (i.e., they are volatile species). Consequently, air is assumed to represent the dominant medium through which mass transport occurs. While some fraction of the gaseous elements and compounds solubilizes in residual porewater, the diffusion rate of the aqueous species through the porewater is negligible compared to the rate of diffusion of gaseous species through the vapor-filled fraction of the partially water-saturated pore space. In fact, diffusion coefficients are approximately four orders of magnitude greater in air than water. In light of this difference, plus the fact that water is pessimistically assumed to be stationary in the model (when in fact it is migrating downward), diffusion in the aqueous (porewater) phase is ignored in the ARM (Hiergesell and Taylor, 2011).

The flow field is assumed to be isobaric and isothermal. The impact of naturally occurring fluctuations in atmospheric pressure at the land surface, which could induce pulses of air movement into and out of the shallow soil profile over relatively short periods of time (barometric soil venting), was considered to have a small impact. However, because the operational period is excluded from this analysis, the effect of barometric venting on atmospheric releases is assumed to have zero net effect when averaged over long periods (Hiergesell and Taylor, 2011). The geomembrane cover(s) present after the operational period will result in minimal barometric pressure variance below the surface (Li et al., 2012; Lowry et al., 1996). Further, the prepared, homogenous soil present at the ELLWF is not expected to facilitate significant transport through fractures (Lowry et al., 1996; Neeper, 2002).

In summary, for the 1,000-year compliance period evaluated in this PA, vertical air diffusion is the only mass transport mechanism modeled in the ARM; advective transport is assumed to be negligible.

3.6.1.1. Key Inputs and Assumptions

The following key inputs and assumptions are employed in the ARM. Listed beside each input or assumption is a determination of whether it represents a pessimistically biased, best estimate, or potentially optimistic factor. Inputs and assumptions apply to a specific pathway only (i.e., air vs. radon) are addressed separately.

- Zero-flux boundaries are assumed on the sides and base of the 1-D stack of GoldSim® computational elements. Vapor-phase diffusion is assumed to only occur vertically to the ground surface while in actuality, some diffusion will also occur laterally and vertically downward (pessimistically biased).
- The HDPE geomembrane, which is part of the final closure cap design, is not included in the 1-D stack of GoldSim® computational elements (pessimistically biased).
- The flow field is assumed to be isobaric and isothermal. Short-term oscillations in temperature and pressure are thought to have a long-term net-zero effect (slightly optimistic).
- Air is the medium through which all diffusion is assumed to occur. Diffusion in the aqueous phase is ignored because the diffusion rates in water are negligible compared to rates in air (pessimistically biased).
- The water phase is assumed to be stationary, when in fact it is infiltrating slowly downward (pessimistically biased).
- The erosion barrier is assumed to be the top layer of the closure cap in the flux calculations. The 6-inch topsoil and 30-inch upper compacted backfill layers are assumed to have eroded away, thereby reducing the diffusive length by 36 inches (pessimistically biased).
- Releases from the waste zone do not occur until operational closure. Radioactive, diffusive air releases that occur during operations are not accounted for in the simulations; therefore, the initial source term is slightly larger than actual (pessimistically biased).
- Operational closure occurs on the same date for all DUs. Peaks in surface flux tend to occur simultaneously, which has a negative impact on plume overlap (pessimistically biased).

Based on the inputs, and assumptions employed in the ARM, the calculated fluxes are considered pessimistically biased values.

3.6.1.2. Atmospheric Release Model Configuration in GoldSim®

The configuration of each DU in GoldSim® consists of a 1-D stack of model cells representing the waste emplacement zone, engineered barriers, and closure cap. The extent of the vertical stack of cells is from the base of the waste zone to the top of the erosion barrier within the overlying closure cap. The erosion barrier is assumed to be the ground surface from which contaminant fluxes emanate during the post-closure period (i.e., the 6-inch topsoil and 30-inch upper compacted backfill layers have eroded away). The opening and closing of diffusive links between various cells are synchronized to conform to the operation and closure sequences for each DU. The 1-D stack is assigned a 1-m^2 unit area to represent a point source.

3.6.1.3. Radionuclide Species

Radionuclide atomic weights and half-lives are updated to comply with ICRP (2008) radionuclide data as reported by Smith et al. (2019). Table 3-43 displays the updated ARM radionuclide species list where radionuclides that can exist as a volatile compound in the disposal environment are shown with the molecular formula in parentheses. For the air pathway, only those radionuclides that have already been screened in are shown in Table 3-43. This is because the air pathway

screening is conducted in a separate step using dose release factors (DRFs) before employing the ARM. Conversely, for the radon pathway, Table 3-43 includes the entire prescreening list of volatile radionuclides and their progeny (limited to daughters down to Rn-222). Radionuclide screening for the radon pathway is performed internally within the ARM.

Table 3-43. Atmospheric Release Model Radionuclide Species List

Radionuclide [a,b]	Atomic Weight (g/mol)	Half-life	Pathway
C-14 ($^{14}CO_2$)	46.0012	5.7000E+03 year	Air
H-3 (^{3}HOH)	20.015	1.2320E+01 year	Air
Kr-85	84.9125	1.0756E+01 year	Air
Am-242	242.060	1.6020E+01 hour	Radon
Am-242m	242.060	1.4100E+02 year	Radon
Am-246m	246.070	2.5000E+01 min	Radon
Bk-250	250.078	3.2120E+00 hour	Radon
Cf-246	246.069	3.5700E+01 hour	Radon
Cf-250	250.780	1.3080E+01 year	Radon
Cm-242	242.059	1.6280E+02 day	Radon
Cm-246	246.067	4.7600E+03 year	Radon
Cm-250	250.078	8.3000E+03 year	Radon
Np-234	234.043	4.4000E+00 day	Radon
Np-238	238.051	2.1170E+00 day	Radon
Pa-230	230.035	1.7400E+01 day	Radon
Pa-234	234.043	6.7000E+00 hour	Radon
Pa-234m	234.043	1.1700E+00 min	Radon
Pu-238	238.050	8.7700E+01 year	Radon
Pu-242	242.059	3.7500E+05 year	Radon
Pu-246	246.070	1.08400E+01 day	Radon
Ra-226 ($^{226}RaCl_2$)	296.931	1.6000E+03 year	Radon
Rn-222	222.018	3.8235E+00 day	Radon
Th-230	230.033	7.5380E+04 year	Radon
Th-234	234.044	2.4100E+01 day	Radon
U-234	234.041	2.4550E+05 year	Radon
U-238	238.051	4.4680E+09 year	Radon

Notes:

[a] For the air pathway, only the three parent radionuclides requiring CWTS inventory limits are listed. Other radionuclides included in the ARM database are not listed because they have zero mass.

[b] For the radon pathway, progeny of parent radionuclides are included in the species list because decay is explicitly modeled in the ARM.

3.6.1.4. Material Properties Database

A Microsoft Access database stores all material properties (i.e., porosity, water saturation, and bulk density) utilized in the ARM. The database also records the origin of each property value in the "Description" column (sources include: Hiergesell and Taylor, 2011; Nichols and Butcher, 2020; Phifer, 2003a; Phifer et al., 2006; WSRC, 2008). Material properties for the closure cap as well as the waste emplacement zone and engineered barriers for each ARM DU are defined in the following report sections: Section 3.4 (final closure cap), Section 5.1.5 (STs, ETs, and CIG trench segments), Section 5.2.3 (LAWV), Section 5.3.3 (ILV), and Section 5.4.3 (NRCDAs).

3.6.1.5. Solubility in Cementitious Materials

For systems involving cementitious materials, the ARM imposes a constant $^{14}CO_2$ concentration in the vapor-filled pore space of the cementitious medium. Kaplan (2005) provides the thermodynamic basis for this model boundary condition by evaluating the thermodynamic equations governing the equilibration of a C-14 waste source with high-pH water. From Kaplan's analysis, Hiergesell and Taylor (2011) concluded that the C-14 equilibrium vapor-phase concentration will not exceed 1.9E-07 Ci m^{-3}. This is exercised in the ARM by defining C-14 solubility limits in the CIG trench segment and ILV waste columns and the LAWV concrete roof.

3.6.1.6. Accounting for Air Diffusion in GoldSim®

Graham's Law describes diffusion through air, where the effective diffusion coefficient, D_e, is given as the effective diffusion coefficient for Rn-222 times the square root of the molecular weight ratio between Rn-222 and the radionuclide of interest, *s*:

$$D_e = D_e^{Rn-222}\sqrt{\frac{MW_{Rn-222}}{MW_s}} \qquad \text{Eq. (3-20)}$$

where:

D_e Effective diffusion coefficient for radionuclide of interest, *s* ($m^2\ s^{-1}$)
D_e^{Rn-222} Effective diffusion coefficient for Rn-222 ($m^2\ s^{-1}$)
MW_{Rn-222} Molecular weight of Rn-222 (g mol^{-1})
MW_s Molecular weight of radionuclide of interest, *s* (g mol^{-1})

Two equations are provided to calculate D_e^{Rn-222}. The first is given by Rogers and Nielson (1991):

$$D = D_o A_o \eta_a^{b_o} \qquad \text{Eq. (3-21)}$$

where:

D D_e^{Rn-222} ($m^2\ s^{-1}$)
D_o Diffusion coefficient for Rn-222 in air ($m^2\ s^{-1}$)
A_o, b_o Empirical functions of porosity or dimensionless constants (0.74 and 2.2, respectively)
η_a Air-filled porosity ($m^3\ m^{-3}$) which equals [$\eta(1 - S)$]
S Volume fraction of water saturation ($m^3\ m^{-3}$)

The second equation is an updated diffusion correlation based upon a larger database (see Rogers and Nielson, 1991; Equation 9):

$$D_c = D_o\eta \times \exp\left(-6S\eta - 6S^{14\eta}\right) \qquad \text{Eq. (3-22)}$$

where:

D_c D_e^{Rn-222} ($m^2\ s^{-1}$)
η Total porosity [in contrast to air-filled porosity, η_a, used in Eq. (3-21)] ($m^3\ m^{-3}$)

Both Eq. (3-21) and Eq. (3-22) are incorporated in the ARM; however, because Eq. (3-22) is based upon a larger database, it is used in the ARM simulations for this PA.

As presented by Flach et al. (2016), the 1-D form of Fick's law in a saturated porous medium is given by:

$$j = -D_i \frac{\partial c}{\partial x} \qquad \text{Eq. (3-23)}$$

where:

j Diffusive flux per unit area (g m^{-2} s^{-1})
D_i Intrinsic diffusion coefficient (m^2 s^{-1})
c Gas-phase concentration (g m^{-3})

D_i is significantly less than D_m, the molecular diffusion coefficient, because of multiple porous medium effects (i.e., porosity, tortuosity, and water saturation). Accounting for these multiple effects, D_i in unsaturated media is given by:

$$D_i \equiv \eta \; S \tau \, D_m \qquad \text{Eq. (3-24)}$$

where:

τ Tortuosity (m m^{-1})
D_m Molecular diffusion coefficient (m^2 s^{-1})

Combining Eq. (3-23) and Eq. (3-24), and multiplying by the cross-sectional area of the diffusive mass flux link, A, yields:

$$J = A\eta S\tau D_m \frac{\Delta c}{L} \qquad \text{Eq. (3-25)}$$

where:

J Diffusive flux (g s^{-1})
A Cross-sectional area of the diffusive mass flux link (m^2)
L Diffusive length (m)
Δc Gas-phase concentration difference across L (g m^{-3})

As recognized by Wohlwend (2017), the built-in diffusive flux equation in GoldSim® does not account for partial saturation (S) of the porous medium. Specifically, the diffusive flux from cell i to cell j is calculated in GoldSim® using Eq. (3-26):

$$f_{s,i\to j} = D_s \left(c_{ias} - \frac{c_{jws}}{K_{was}} \right) \qquad \text{Eq. (3-26)}$$

where:

$$D_s = \frac{A}{\frac{L_i}{d_{as}\tau_i\eta_i} + \frac{L_j}{d_{ws}\tau_j\eta_j}} \quad \text{Eq. (3-27)}$$

and

$f_{s,i\to j}$ Flux of species, *s*, from cell *i* to cell *j* (g s^{-1})
D_s Diffusive conductance for species *s* (i.e., C-14) in the mass flux link (m^3 s^{-1})
c_{ias} Dissolved concentration of species *s* in medium *a* (air) within cell *i* (g m^{-3})
c_{jws} Dissolved concentration of species *s* in medium *w* (water) within cell *j* (g m^{-3})
K_{was} Partition coefficient (unitless Henry's Law constant for diffusion through air) between fluid medium *w* (water, in cell *j*) and fluid medium *a* (air, in cell *i*) for species $\left(\text{gmol L}^{-1}\text{ Air}/\text{gmol L}^{-1}\text{ Water}\right)$
A Area of the diffusive mass flux link (m^2)
L_i Diffusive length for the diffusive mass flux link in cell *i* (m)
L_j Diffusive length for the diffusive mass flux link in cell *j* (m)
d_{as} Diffusivity for species *s* in fluid *a* (air, in cell *i*) (m^2 s^{-1})
d_{ws} Diffusivity for species *s* in fluid *w* (water, in cell *j*) (m^2 s^{-1})
η_i Porosity for porous medium defined for diffusive mass flux link in cell *i* (m^3 m^{-3})
η_j Porosity for porous medium defined for diffusive mass flux link in cell *j* (m^3 m^{-3})
τ_i Tortuosity for porous medium defined for diffusive mass flux link in cell *i* (m^3 m^{-3})
τ_j Tortuosity for porous medium defined for diffusive mass flux link in cell *j* (m^3 m^{-3})

As a workaround in GoldSim®, the ARM includes the effect of saturation by dividing the diffusive flux length, *L*, in Eq. (3-27) by the air saturation, S_a, of the cell for all diffusive flux links.

$$D_s = \frac{A}{\frac{\left(L_i / S_{ai}\right)}{d_{as}\tau_i\eta_i} + \frac{\left(L_j / S_{aj}\right)}{d_{ws}\tau_j\eta_j}} \quad \text{Eq. (3-28)}$$

where:

S_{ai} Air saturation within cell *I* (m^3 m^{-3})
S_{aj} Air saturation within cell *j* (m^3 m^{-3})

Eq. (3-28) reconciles the inconsistency between Eq. (3-25) and Eq. (3-27) due to unsaturation. The flux calculation by the GoldSim® ARM is consistent with the analytical solution in Eq. (3-25).

3.6.1.7. Henry's Law Constants

Henry's Law describes equilibrium partitioning of species between the aqueous and gas phases. Henry's Law constants used in Eq. (3-26) to calculate solute fluxes at the air-water interface were calculated by Dyer (2017d) for the volatile radionuclides included in the current version of the ARM. GoldSim® uses a dimensionless form of the Henry's Law constant (molar vapor/molar liquid) as given by:

$$H_i = \frac{C_{i\,Vapor}}{C_{i\,Liquid}} \qquad \text{Eq. (3-29)}$$

where:

C_i Concentration of species i (gmol m^{-3})

At pH 5.4, Hg-194 can exist as $HgCl_2$, Hg(0), or both depending on redox conditions. To be bounding, the dimensionless Henry's Law constant for the more volatile Hg(0) species is used. The calculated Henry's Law constants for soil at pH 5.4 are used for soil element cells in GoldSim® while the values for soil at pH 8.23 are used for cells having cementitious materials (Table 3-44).

Table 3-44. Dimensionless Henry's Law Constants used in Atmospheric Release Model

Radionuclide	Dimensionless H_i	
	pH 5.4	pH 8.23
C-14	1.1	0.015
H-3	1.90E-05	1.90E-05
Kr-81	17	17
Kr-85	17	17
Hg-194	0.32	8.60E-11
Ra-226	1.00E-30	1.00E-30
Rn-222	4.5	4.5

3.6.1.8. Sorption Coefficients

Sorption coefficients (K_d) are used to describe linear equilibrium partitioning of species between the aqueous and solid phases. Of the species in the ARM, only C-14 and Ra-226 are affected by the application of sorption coefficients. H-3, Kr-85, and Rn-222 are not expected to sorb to solids while other radionuclides do not volatilize and are assumed stationary. Sorption coefficients are defined for sandy soils, clayey soils, and cementitious material. All cementitious material is conservatively assigned sorption coefficients of degraded concrete. Sorption coefficients align with the values used in the GW pathway analyses and are listed in Table 3-45.

Table 3-45. Sorption Coefficients (mL g^{-1}) used in Atmospheric Release Model

Radionuclide	Sorption Coefficient (mL g^{-1})		
	Sandy Soil	Clayey Soil	Degraded Concrete
C-14	1	30	50
H-3	0	0	0
Kr-85	0	0	0
Ra-226	25	180	180
Rn-222	0	0	0

3.6.1.9. Closure Cap Representation

A standardized closure cap model that conforms to the design of the proposed ELLWF final closure cap is implemented in the ARM for each type of DU. Features of the final closure cap are described in Section 2.2.2.

Figure 3-82 depicts the closure cap mixing cell arrangement within the model. The arrows in the figure indicate the diffusive links existing between adjacent cells. Table 3-46 lists the specific layer thicknesses, bulk densities, porosities and expected long-term residual saturations associated with each layer. Within each cell, Porosity (η) and DryBulkDensity (ρ_d) are used to calculate the mass/volume quantities for the three media as given by:

$$VM_{soil} = V_{cell} \times \rho_d \quad \text{Eq. (3-30)}$$

$$VM_{water} = V_{cell} \times \eta \times S_w \quad \text{Eq. (3-31)}$$

$$VM_{air} = V_{cell} \times \eta \times S_a \quad \text{Eq. (3-32)}$$

where:

VM_{soil} Mass quantity of soil (g)

VM_{water} Volume of water (m^3)

VM_{air} Volume of air (m^3)

V_{cell} Volume of cell (m^3)

S_w Water saturation ($m^3\ m^{-3}$)

S_a Air saturation ($m^3\ m^{-3}$)

η Porosity of erosion barrier ($m^3\ m^{-3}$)

ρ_d Dry bulk density of erosion barrier ($g\ m^{-3}$)

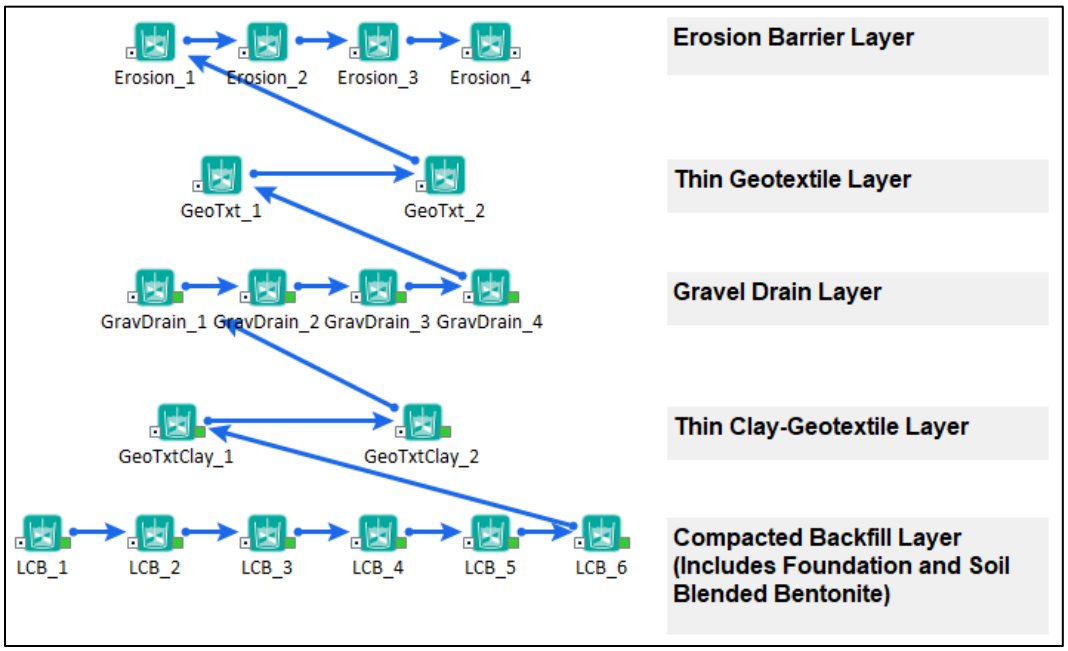

Figure 3-82. Closure Cap Cells in GoldSim® Atmospheric Release Model

Table 3-46. Closure Cap Layer Properties

Layer (Modeled Material)	Thickness (inches)	Bulk Dry Density (g cm^{-3})	Porosity	Residual Water Saturation
Erosion Barrier	12	2.4168[a]	0.088[a]	0.825[a]
Geotextile[b]	0.2	1.82	0.3	0.5
Gravel Drain	12	1.82[c]	0.3[c]	0.5[d]
Clay-Geotextile[b]	0.2	1.71	0.355	0.675
Lower Compacted Backfill	24	1.71[c]	0.355[c]	0.675[c]

Notes:

[a] Phifer (2003a)

[b] Assigned properties of layer below

[c] Nichols and Butcher (2020)

[d] Phifer et al. (2006)

3.6.2. Air Pathway Analysis

DOE M 435.1-1, Chg. 3 (U.S. DOE, 2021b) prescribes a PO (10 mrem yr^{-1}) for evaluating atmospheric releases of radionuclides from DOE LLW disposal facilities. The potential dose to an individual resulting from exposure to radionuclides released into the atmosphere from LLW disposals is estimated by applying radionuclide-specific DRFs in mrem per curie released at the ground surface (mrem Ci_{Air}^{-1}) to estimated gaseous flux rates (Ci_{Air} yr^{-1}) at a particular time and location. The analysis of performance approach described below for the air pathway is based upon model development efforts by Dixon and Minter (2017) for calculating DRFs and Wohlwend (2017) for simulating peak gaseous flux rates at the ground surface from the DU waste zones.

The overall conceptual model for evaluating atmospheric dose to a MOP from the ELLWF is depicted in Figure 3-83. First, subsurface mass transport simulations are performed for volatile radionuclides released from the DU waste zones through the overlying engineered cover system to determine a gaseous flux rate at the ground surface (middle portion of Figure 3-83). Second, atmospheric dispersion of the gaseous radionuclide flux is simulated using an atmospheric transport model to compute air concentrations near a hypothetically exposed individual at the POA. The computed air concentrations are then input to a dose model to calculate a DRF, which represents the dose impact per curie of an individual radionuclide *released* (mrem Ci_{Air}^{-1}) to the receptor from various exposure pathways related to atmospheric transport (upper portion of Figure 3-83). Third, the overall PO (10 mrem yr^{-1}) is divided between all radionuclides released from all ELLWF DUs after accounting for temporal release differences (lower portion of Figure 3-83). Disposal limits for each unit are then calculated from this division of dose to ensure spatial plume overlap does not result in an exceedance of the PO.

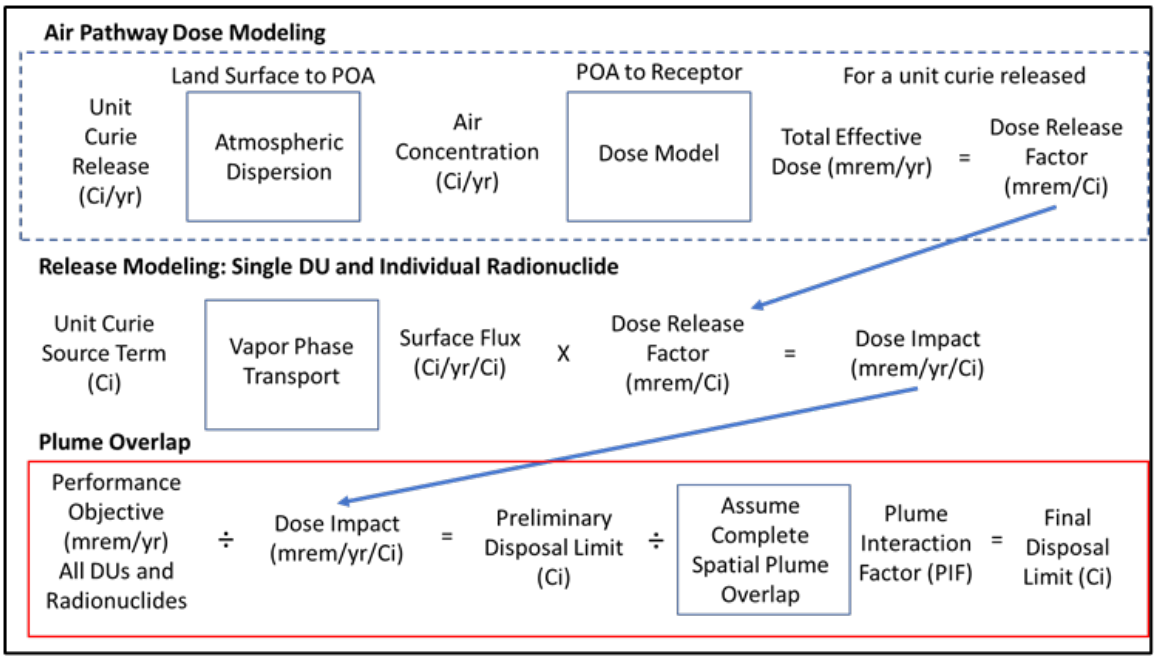

Figure 3-83. Air Pathway Performance Assessment Schematic

3.6.2.1. Radionuclide Screening

The current air pathway screening approach used to reduce the number of radionuclide DRFs is described in Section 2.3.8. The radionuclides, summarized in Table 2-31, include Ar-37, Ar-39, C-14, H-3, Hg-194 (with Au-194 in secular equilibrium), Hg-206, Kr-81, Kr-83m, and Kr-85.

3.6.2.2. Dose Model

Lee (2006) calculated DRFs for potential atmospheric releases of 15 volatile radionuclides from seven ELLWF DUs in support of PA2008 (WSRC, 2008). Numerous parameter values (i.e., dose coefficients, physical parameters, human usage/uptake factors, and decay data) have been updated and dose methodology improvements have been made since 2008 (Dixon and Minter, 2017). The improvements are incorporated in the current version of the U.S. EPA's dose model CAP88-PC Version 4.1.0.2, which is used in this PA (Jannik and Trimor, 2017).

3.6.2.2.1. Points of Assessment and Disposal Unit Considerations

For DRF calculations, the terrain and grade elevation of E-Area are specified for the atmospheric release of radionuclides from ELLWF DUs (Jannik, 2014). Figure 2-30 displays the layout of DUs within the 100-acre facility. While many individual DUs share a common-sized footprint, other DUs, such as the NRCDAs, ILV, and a few STs and ETs, have unique sizes and shapes. Despite these differences, DUs can be treated reasonably as a point source in atmospheric models when the POA is defined as the SRS boundary, which is 7.09 miles (11,410 meters) from the ELLWF because of the large plume travel distance relative to the size of the DUs. The SRS boundary is adopted as the POA during the 100 years of IC when site access will be controlled.

Following the end of IC, unrestricted site access is assumed and the POA moves to the 100-meter ELLWF DU boundary prescribed by U.S. DOE (2021b). In this scenario when assuming area

sources, DU size and dimensions have a major impact on the air pathway dose received by the now nearby receptor. Notably, as the size of the DU footprint increases, the dose impact to the 100-meter receptor decreases for a unit curie inventory uniformly distributed within the DU. As a result, treating DUs as point sources for the 100-meter POA calculations (i.e., where the point source is located at the minimum distance) results in larger DRFs and hence lower disposal limits.

Despite this, DUs in this PA are treated as point sources for both the 100-meter and SRS boundary POAs. This approach, along with other pessimistically biased assumptions described below, produces a reasonably bounding estimate to ensure no MOP will receive a dose of more than 10 mrem yr^{-1} via the air pathway, excluding the dose from radon and its progeny (U.S. DOE, 2021b) as addressed separately in Section 3.6.3.

3.6.2.2.2. Performance Assessment Analysis Approach

Air pathway dose modeling includes a 1-D Gaussian plume atmospheric model for calculating dispersion of the contaminant release to each POA as well as a dose model for calculating a DRF or dose impact per curie *released* to the receptor from various exposure pathways related to atmospheric transport. The DRF is applied to the peak flux of a volatile radionuclide from the DU to obtain a dose impact per curie *disposed*. The peak flux is obtained by modeling vapor-phase transport from the waste zone to the land surface. The dose impact per curie *disposed* is in turn used to produce air-pathway-based radionuclide disposal limits. Figure 3-83 is a schematic of the overall air pathway analysis for the PA.

The dashed box in Figure 3-83 shows the portion of the overall air pathway model developed by Dixon and Minter (2017). DRFs (mrem Ci^{-1}) are estimated by first modeling atmospheric dispersion to the POA and then calculating the total effective dose (TED) in mrem yr^{-1} assuming an annual atmospheric release of the associated radionuclide unit source term (Ci yr^{-1}). The DRFs are simply the ratio of the TED to the annual release activity. Because the DRFs are determined using a unit curie release, the TED (mrem yr^{-1}) is equal to the DRF (mrem Ci^{-1}). For this PA, TEDs and DRFs are determined using CAP88-PC Version 4.1.0.2 (U.S. EPA, 2020), the latest version of U.S. EPA's National Emission Standards for Hazardous Air Pollutants; Radionuclides (NESHAPs) required dosimetry code.

In compliance with DOE Order 458.1 (U.S. DOE, 2020b), dose may be calculated for the MEI or a representative person. In this PA, DRFs are calculated for the MEI, rather than a representative person, to facilitate use of CAP88-PC. The CAP88-PC software was chosen for this PA because it is necessary to model Hg-194 as a vapor. The use of the MEI is pessimistically biased, resulting in larger DRFs and hence lower disposal limits compared to the representative person.

3.6.2.2.3. Dose Model Method

CAP88-PC is described in Section 3.9.5. The MEI is assumed to live at the specified location the entire year and to eat vegetables, meat, and milk produced at that location. For ELLWF DUs, 1 Ci of each of the volatile radionuclides of concern are assumed to be released from ground level over a one-year period. The 2014-2018 meteorological database for the closest meteorological tower in H-Area (Bell, 2020a) is used to disperse releases from the potential release locations to the MEI

at the site boundary and 100-meter POAs. Site- and pathway-specific parameters used in the CAP88-PC model to estimate the resulting DRFs are reported by Stagich et al. (2021). CAP88-PC, which uses the DC_PAK 3.02 release of FGR13 for dose conversion factors, does not provide an air submersion dose conversion factor for Ar-37 (U.S. EPA, 2020). Therefore, the most recent dose conversion factor for Ar-37, provided by the DOE Derived Concentration Technical Standard (U.S. DOE, 2011a), is used to develop the Ar-37 DRFs.

3.6.2.2.4. Key Inputs and Assumptions

The following key inputs and assumptions are employed in the calculation of DRFs. Listed beside each input or assumption is a determination of whether it represents a pessimistically biased, best estimate, or optimistic factor.

- Use the 2014-2018 database for the closest meteorological tower in H-Area (Bell, 2020a) to disperse the releases to the 100-meter and site boundary POAs (best estimate).
- Employ the MEI for dose calculations using the latest version of U.S. EPA's CAP88-PC dose model (pessimistically biased).
- Utilize updated dose model parameters from Table 3-47 (generally best estimate but selectively pessimistically biased).
- Represent DUs as a point source (pessimistically biased).
- Adopt ground-level release of radionuclides above the DU (best-estimate).
- Assume radionuclide release over a period of one year, which is the standard methodology for dose calculations (potentially optimistic).
- The receptor stands in the plume centerline and receives continuous exposure over the entire year, which is the standard methodology for dose calculations (pessimistically biased).

Based on the methodology, inputs, and assumptions employed in the atmospheric dispersion and dose models, calculated DRFs are considered bounding values from a disposal limits perspective.

Table 3-47. Dose Model Parameter Updates

Data	Updated Reference
Radionuclide half-lives, atomic mass units, specific activities, and decay constants	ICRP Publication 107 (ICRP, 2008)
Internal dose coefficients (air inhalation, water ingestion)	SRNL-STI-2013-00115 (Stone and Jannik, 2013)
External exposure dose coefficients (air immersion, ground shine)	DOE-STD-1196-2011 (U.S. DOE, 2011a) EPA-402-R-93-081 (FGR No. 12) (Eckerman and Ryman, 1993)
Bio-transfer factors, human usage factors, physical parameters	SRNL-STI-2021-00284 (Jannik and Stagich, 2017)

3.6.2.2.5. Dose Release Factors

Table 3-48 lists DRFs for Ar-37, Ar-39, C-14, H-3, Hg-194 (with Au-194 in secular equilibrium), Hg-206, Kr-81, Kr-83m, and Kr-85 at the site boundary and 100-meter POAs. DRFs for C-14 and

H-3 (only radionuclides investigated in PA2008) increased relative to values used in 2008, which lends support to the position that the revised DRFs are bounding values from a disposal limits perspective. Updates have also been made to meteorological data, decay factors, dose conversion factors, usage factors, and other radionuclide-independent parameters, which contribute to increases in the DRFs for H-3 and C-14.

Table 3-48. Dose Release Factors for Radionuclides Included in Air Pathway Analysis

Radionuclide	DRF (mrem Ci^{-1})	
	100-meter POA [a]	Site Boundary [a,b]
Ar-37	2.4E-07	8.0E-11
Ar-39	4.5E-05	1.5E-08
C-14	1.2E+00	4.1E-04
H-3	7.8E-03	2.6E-06
Hg-194	2.7E+00	9.3E-04
Hg-206	2.3E-03	1.0E-08
Kr-81	1.5E-05	5.0E-09
Kr-83m	4.3E-07	1.0E-10
Kr-85	9.4E-05	3.2E-08

Notes:

[a] TED to the MEI is estimated by CAP-88-PC.

[b] Site boundary is 11,410 meters due north of E-Area.

3.6.2.3. Atmospheric Release Model Implementation

To calculate surface fluxes for the air pathway, 1.0 Ci of each air pathway radionuclide is buried in each simulated DU. The diffusion to and subsequent flux from the surface is then projected by the ARM as described in Section 3.6.1. The ARM's role in the air pathway PA analysis is conceptualized in the middle row in Figure 3-83. Specifics related to the implementation of the ARM for the air pathway are discussed below.

3.6.2.3.1. Key Inputs and Assumptions

The following key inputs and assumptions are employed in the implementation of the air pathway analysis in the ARM. Listed beside each input and assumption is a determination of whether it represents a pessimistically biased, best estimate, or optimistic factor.

- For the air pathway analysis, waste is not introduced into the model of each DU until operational closure. Radioactive source decay during operations is therefore not considered, and the source term is slightly larger than actual (pessimistically biased).
- C-14 is saturation-limited in cementitious material. For systems involving cementitious materials, the ARM imposes a constant $^{14}CO_2$ concentration in the vapor-filled pore space of the cementitious medium (best estimate).
- 100% spatial overlap of atmospheric plumes is assumed at the site boundary and 100-meter POAs (pessimistically biased).

3.6.2.3.2. Model Timeline

A data element, Start_Time, in the ARM establishes the time when radionuclides are added to the waste cells. In this PA, the simulation start time is set to zero, which corresponds in calendar

notation to September 30, 2065. This date marks the end of ELLWF disposal operations (Sink, 2016c). A second data element, Hold_Time, establishes the time when flux from the waste zone commences. This allows for radioactive decay and the accumulation of progeny in the waste zone during the operational period. In this PA, the hold time is set at zero, which results in immediate radionuclide release at the start time with no prior decay. As explained above, this is a pessimistically biased assumption that leads to higher fluxes and doses at the POAs.

3.6.3. Radon Flux Analysis

DOE M 435.1-1, Chg. 3 (U.S. DOE, 2021b) prescribes a PO of 20 pCi m^{-2} s^{-1} for radon flux at the surface of DOE LLW disposal facilities. The ARM model is employed to predict radon flux from the radon-producing parents selected for evaluation in this PA.

3.6.3.1. Radionuclide Screening

Past and current radon flux analysis screening approaches used to reduce the number of radioisotopes requiring vapor-phase transport calculations are described in Section 2.3.8.2. The parent radionuclides are U-238, Th-234, Pa-234m, Pu-238, U-234, Th-230, Ra-226, Cf-250, Cm-242, Am-242m, Am-242, Np-238, Cm250, Cm-246, Am-246m, Pu-242, Pu-246, Bk-250, and Pa-234. The PA2008 (WSRC, 2008) and the 2011 ELLWF SA (Hiergesell and Taylor, 2011) included only five parents (U-238, U-234, Th-230, Ra-226, and Pu-238).

3.6.3.2. Atmospheric Release Model Implementation

To establish limits for the Rn-222 producing parents, each parent is run individually within the ARM and a predicted Rn-222 flux per one curie parent buried is calculated. The parent radionuclide is considered stationary and does not migrate downward. Radon diffusion to and the subsequent flux from the surface is calculated by the ARM as described in Section 3.6.1.

3.6.3.2.1. Key Inputs and Assumptions

The following key inputs and assumptions are employed in the implementation of the radon flux analysis in the ARM. Listed beside each input and assumption is a determination of whether it represents a pessimistically biased, best estimate, or optimistic factor.

- Waste is assumed to be uniformly placed in the DUs (best estimate).
- In the radon flux analysis for this PA, waste is introduced 25 years before radon release from the waste zone is assumed to commence. This bake time allows for decay of Rn-222-producing parents as well as the build-up of Rn-222 without accounting for diffusive air releases that will occur during operations (pessimistically biased).
- Radon parents are stationary. In actuality, the parent radionuclides exist in the solid phase and therefore do not migrate upward through the air-filled pore space; however, they can leach and be transported downward from the waste zone by pore water movement. This potential downward migration of the parent radionuclides is neglected in the ARM (pessimistically biased).

3.6.3.2.2. Model Timeline

The data element, Hold_Time, establishes the hold time before radon flux from the waste zone commences at the end of ELLWF operations in 2065. Hold_Time is set at 71 years in this PA. The hold time allows for radioactive decay and the accumulation of progeny in the waste zone during ELLWF operations. This assumption is pessimistically biased because it results in the build-up of radon within the waste zone (larger source term) before release at the end of ELLWF operations.

3.6.3.2.3. Radon Emanation Factor

Only a fraction of Rn-222 generated by the decay of each parent is available for migration away from its source into open pore space. Because Rn-222 parent radionuclides exist as oxides or other crystalline forms, only a fraction of Rn-222 generated by decay of Ra-226 has sufficient energy to migrate away from its original location into adjacent pore space before further decay occurs.

The emanation coefficient is generally defined as the fraction of the total amount of Rn-222 produced by radium decay that escapes from soil particles and enters the pore space of the medium. This is the fraction of the Rn-222 that is available for transport. This coefficient has been shown to vary between 0.02 and 0.7 in soils but is typically 0.25 (Yu et al., 2001). To account for this effect in the model, an effective source term of 0.25 Ci of parent radionuclide is utilized as the source term for each Ci disposed within a DU.

3.7. EXPOSURE PATHWAYS CONCEPTUAL MODEL

The MOP and IHI exposure pathways must be defined to calculate receptor doses. For this PA, exposure pathways and scenarios are outlined in detail by Stagich and Jannik (2020). The primary mechanism for transport of radionuclides from the ELLWF to the MOP is expected to be leaching to GW, GW transport to the well at 100 meters, and subsequent internal or external human exposure. The main transport mechanisms for the IHI are direct intrusion into the waste zone, excavation of areas near the waste zone, or radioactive shine. Leaching to GW and use of contaminated GW are not calculated for the IHI in accordance with the DOE position (U.S. DOE, 2007). Intrusion scenarios are assumed to not occur (and the DOE All-Pathways PO does not apply) until the 100-year IC period ends, after which time it is assumed that no active ELLWF facility maintenance will be conducted. Surface water and recreational pathways were evaluated in the 2010 SRS CA (SRNL, 2010) and are not considered in SRS PA analyses.

A general overview of the potential pathways to human exposure from the undisturbed disposed LLW is provided by Stagich and Jannik (2020) in Figure 3-84. Table 3-49 and Table 3-50 list the individual exposure pathways for the MOP and IHIs, respectively. The last column in both tables identifies whether an individual pathway is assumed to occur and, therefore, whether a quantified dose calculation is required (yes or no). Pathways requiring a quantified dose calculation are highlighted in green. The intake and exposure rate factors are provided by Smith et al. (2019).

3.7.1. Terminology

At SRS, the terms “reference person” and “typical person” are used when values of dose parameters related to human behavior are reported. SRS defines a reference person as a hypothetical aggregation of human (male and female) physical and physiological characteristics

arrived at by international consensus for the purpose of standardizing radiation dose calculations and is at the 95th percentile of national usage and exposure parameter data. SRS defines the concept of a typical person as a hypothetical person who is typical of the entire population group established at the 50th percentile (median) of national usage and exposure parameter data. See Jannik and Stagich (2017) for more information. DOE Order 458.1 (U.S. DOE, 2020b) states that compliance with the DOE annual dose limit of 100 mrem (1 mSv) for a member of the public may be demonstrated by calculating dose to the MEI or a representative person. At SRS, the representative person (who is based on the SRS-specific reference person at the 95th percentile of national usage and exposure data) is now used as a replacement for the MEI in compliance dose calculations. For the air and radon pathways in this PA, DRFs are calculated for the MEI, rather than a representative person, to facilitate use of CAP88-PC. The use of the MEI is pessimistically biased, resulting in larger DRFs and hence lower disposal limits compared to the representative person. On the other hand, for the GW and IHI exposure pathways, usage and exposure parameters for a typical person at the 50th percentile are employed in the best estimate, deterministic, sensitivity, and stochastic calculations of limits and doses in this PA. The usage and exposure parameters are fixed at that their typical person settings for all dose calculations.

3.7.2. Member of the Public Exposure Pathways

Table 3-49 lists the MOP exposure pathways that are considered in this PA, along with the subset of exposure pathways that are recommended for quantitative dose calculations. All scenarios are assumed to occur at the end of the 100-year IC period when active ELLWF facility maintenance is discontinued. The discussion below justifies the recommendations in Table 3-49.

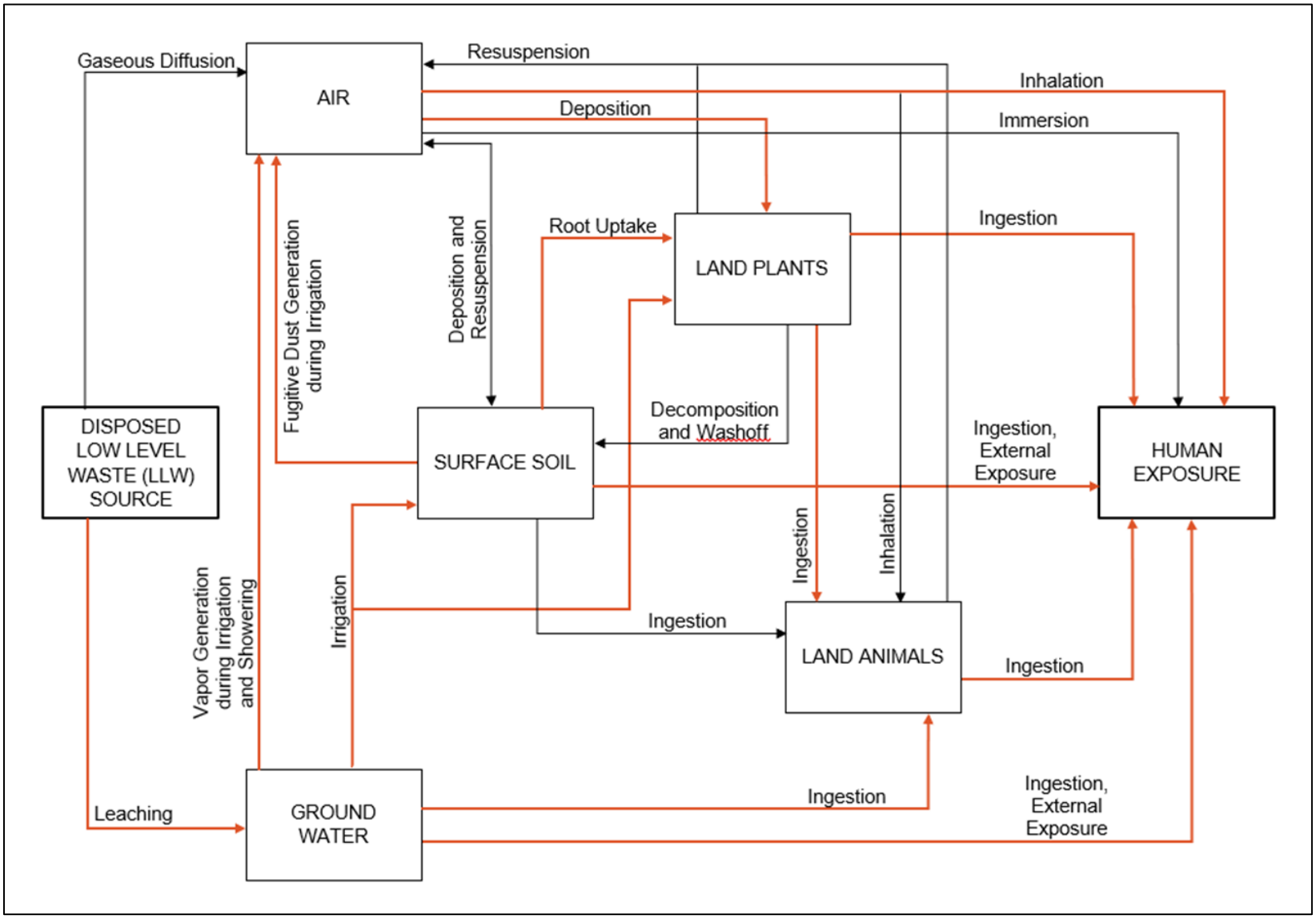

Figure 3-84. Potential Pathways to Human Exposure for Undisturbed Disposed Low-Level Waste (Red Arrows Indicate Pathways Requiring Quantified Dose Calculation for MOP)

Table 3-49. Potential Member of the Public Contaminant Exposure Pathways

Human Receptor	Scenario	Exposure Route	Primary Pathway	Secondary Pathway	Tertiary Pathway	Quantified Dose Calculations Needed?
Member of Public	Resident Farmer (GW 100-meter Well)	Ingestion	Domestic Use of Well Water	Drinking Water	N/A	Yes
				Showering (incidental)	N/A	No
			Well Water to Livestock	Livestock Biotic Uptake	Meat	Yes
					Milk	Yes
			Well Water Irrigation	Garden Vegetables Biotic Uptake	Vegetables	Yes
				Fodder Biotic Uptake	Livestock Biotic Uptake – Meat	Yes
					Livestock Biotic Uptake – Milk	Yes
				Direct Garden Soil Contact	N/A	Yes
					Livestock Biotic Uptake – Meat	No
					Livestock Biotic Uptake – Milk	No
		Inhalation	Domestic Use of Well Water	Showering	N/A	No
			Well Water Irrigation	Fugitive Dust Generation during Irrigation	Ambient Air (particulates)	Yes
				Vapor Generation during Irrigation	Ambient Air (vapors)	Yes
		External Exposure	Domestic Use of Well Water	Showering	N/A	Yes
			Well Water Irrigation	Direct Rad Emission from Soil	N/A	Yes
			Deposition and Resuspension of Garden Soil		N/A	No
			Decomposition and Washoff of Plants		N/A	No

Table 3-50. Potential Inadvertent Human Intruder Contaminant Exposure Pathways

Human Receptor	Scenario	Exposure Route	Primary Pathway	Secondary Pathway	Tertiary Pathway	Quantified Dose Calculations Needed?
Acute IHI	Basement Construction	Ingestion	Exhumed Waste mixed in Clean Soil	Direct Soil Contact	N/A	Yes
		External Exposure		Direct Rad Emissions from Soil	N/A	Yes
		Inhalation	Fugitive Dust Generation during Construction	Ambient Air (particulates)	N/A	Yes
	Well Drilling	Ingestion	Exhumed Waste mixed in Clean Soil	Direct Soil Contact	N/A	Yes
		External Exposure		Direct Rad Emissions from Soil	N/A	Yes
		Inhalation	Fugitive Dust Generation during Drilling activities	Ambient Air (particulates)	N/A	Yes
	Discovery	External Exposure	Exhumed Waste mixed in Clean Soil	Direct Rad Emissions from Soil	N/A	Yes
Chronic IHI	Agriculture	Ingestion	Exhumed Waste mixed in Garden Soil	Garden Vegetables Biotic Uptake	Vegetables	Yes
				Direct Soil Contact	N/A	Yes
		Inhalation		Fugitive Dust Generation while working in Garden	Ambient Air (particulates)	Yes
				Fugitive Dust Generation while residing in Home	Ambient Air (particulates)	Yes
		External Exposure		Direct Rad Emissions from Soil	N/A	Yes
			Residential building built on Soil mixed with Exhumed Waste	Direct Rad Emissions from Soil	N/A	Yes
	Post-Drilling	Ingestion	Exhumed Waste mixed in Garden Soil	Garden Vegetables Biotic Uptake	Vegetables	Yes
				Direct Soil Contact	N/A	Yes
		Inhalation		Fugitive Dust Generation while working in Garden	Ambient Air (particulates)	Yes
				Fugitive Dust Generation while residing in Home	Ambient Air (particulates)	No
		External Exposure		Direct Rad Emissions from Soil	N/A	Yes
			Residential building built on Soil mixed with Exhumed Waste	Direct Rad Emissions from Soil	N/A	No

Table 3-50 (cont'd). Potential Inadvertent Human Intruder Contaminant Exposure Pathways

Human Receptor	Scenario	Exposure Route	Primary Pathway	Secondary Pathway	Tertiary Pathway	Quantified Dose Calculations Needed?
Chronic IHI	Residential	Ingestion	Exhumed Waste mixed in Garden Soil	Garden Vegetables Biotic Uptake	Vegetables	No
				Direct Soil Contact	N/A	No
		Inhalation		Fugitive Dust Generation while working in Garden	Ambient Air (particulates)	No
				Fugitive Dust Generation while residing in Home		No
		External Exposure	Residential building built above Waste	Direct Rad Emissions	N/A	Yes
Acute and Chronic IHI	Bio-Intrusion by Burrowing Animal	Ingestion	Waste is brought to Surface by Burrowing Animal	Exhumed Waste mixed in Soil	Direct Soil Contact	No
					Garden Vegetables Biotic Uptake – Vegetables	No
		Inhalation			Fugitive Dust Generation while working in Garden – Ambient Air (particulates)	No
					Fugitive Dust Generation while residing in Home – Ambient Air (particulates)	No
		External Exposure			Direct Rad Emissions from Soil	No
	Bio-Intrusion by Pine Tree Root Penetration	Ingestion	Decomposition of Fallen Contaminated Pine Needles	Decomposed Needles mixed in Soil	Direct Soil Contact	No
					Garden Vegetables Biotic Uptake – Vegetables	No
		Inhalation			Fugitive Dust Generation while working in Garden – Ambient Air (particulates)	No
					Fugitive Dust Generation while residing in Home – Ambient Air (particulates)	No
		External Exposure			Direct Rad Emissions from Soil	No

3.7.2.1. Scenario with Well Water as Primary Water Source

The primary water source for MOP exposure pathways is a well drilled into aquifers contaminated by the ELLWF. In the GW well-dose analyses, doses are calculated using water from a well for domestic purposes (e.g., drinking water, irrigation). The following exposure pathways involving contaminated well water are assumed to occur as presented in Table 3-49 and Figure 3-84.

- Direct ingestion of well water
- Ingestion of milk and meat from livestock (e.g., dairy and beef cattle, chickens, and hogs) that drink well water
- Ingestion of vegetables grown in garden soil irrigated with well water
- Ingestion of milk and meat from livestock (e.g., dairy and beef cattle, chickens, and hogs) that eat fodder from pasture irrigated with well water
- Ingestion and inhalation of well water while showering
- External exposure to irrigation water and irrigated garden soil

Additional exposure pathways could involve releases of radionuclides into the air from the water taken from the well (i.e., volatile radionuclides such as H-3, C-14, I-129). Exposure from the atmospheric pathway may include:

- Direct plume shine
- Inhalation

There are other secondary and indirect pathways that contribute relatively minor doses to a receptor when compared to direct pathways such as ingestion of milk and meat. These pathways include:

- Inhalation of well water used for irrigation
- Inhalation of dust from the soil that was irrigated with well water
- Ingestion of soil that was irrigated with well water
- Direct radiation exposure from radionuclides deposited on the soil that was irrigated with well water

3.7.2.2. Basis for Public-Release Pathways

Table 3-49 provides a list of ELLWF exposure pathways identified as candidates for detailed analyses. The candidates list was developed based on a review of SRS PA analysis documents by Butcher and Phifer (2016a) and Savannah River Remediation (2009).With an emphasis on local practices, activities at SRS that could bring humans into contact with stabilized contaminants (e.g., water use, hunting, fishing, recreational activities such as swimming and boating, habitation in dwellings, and other unique activities that involve water use or ground disturbance) were considered to ensure that any pathways unique to SRS were taken into account. Surface water and recreational pathways were evaluated for the 2010 SRS CA (SRNL, 2010) and are not considered in SRS PA analyses, which includes the ELLWF PA. *SRS Ecology: Environmental Information Document* by Wike et al. (2006) was used as a reliable source of relevant environmental

information and conditions at SRS. For example, Wike et al. (2006) identifies potential onsite wild game, bio-intrusion candidates (flora and fauna), and fish and/or shellfish present in creeks bordering the ELLWF. Based on this screening analysis, if a pathway has a negligible contribution to human exposure, the pathway may be removed from consideration in the dose analysis (U.S. DOE, 2017).

The following assumptions are made for pathways related to the MOP, Resident Farmer scenario with well water as the primary water source:

- For contaminants in a stabilized system that have not been disturbed through intrusion, the release mechanism to the MOP is leaching of stabilized contaminants to GW. Well drilling is not a release mechanism because any well drilling associated with the MOP scenarios will occur outside the ELLWF buffer zone, and therefore stabilized contaminants will remain undisturbed.
- In the "Well Water as Primary Water Source" scenario, well water will be used as a primary potable water source for a resident near the well (e.g., drinking water, showering) and as a primary water source for agriculture (e.g., irrigation, livestock water).
- Any wild game ingested (e.g., deer, wild pigs) will merely offset ingested livestock, and will result in a lower total dose because livestock raised near the ELLWF will be impacted more by ELLWF-stabilized contaminants than transient wild game.
- A local trend has developed in recent years where farmers and suburban residents are raising free-range chickens and pigs rather than using commercial food. For this reason, the determination of "meat" production and consumption includes all meats (Stone and Jannik, 2013).
- Because a substantial water source is absent at the well site, no consideration was given to pathways connected to water-related commercial activities. Based on the relative proximity of a large, natural water source (i.e., the Savannah River), an assumption is made that a man-made body of water will not be created at the MOP resident site.
- The dose associated with dermal absorption of radionuclides is considered insignificant because, unlike some organic chemicals, the expected radionuclide particulate compounds generally absorb poorly into the body. For tritium oxide (12.3-year half-life), the estimated residual concentrations in GW are relatively small, which renders this pathway an insignificant contributor to dose when considered in combination with the short exposure time during showering (ten minutes per day).
- Water ingested during the relatively short activity of showering is negligible and is not addressed independently. Instead, the impact of showering is addressed with the "Direct Ingestion of Well Water" pathway (i.e., included in the 300 liters of water assumed to be ingested every year) as recommended by Jannik and Stagich (2017).

3.7.3. Inadvertent Human Intruder Exposure Pathway

The stabilized contaminant materials following ELLWF closure will be located beneath a multi-layer, soil-geomembrane closure cap. The higher-activity fraction of the waste will be

contained within concrete vaults or sealed within robust casks or containers that are clearly distinguishable from the surrounding native soil. Regional drilling practices would preclude drilling through the ELLWF reinforced concrete vaults (i.e., the LAWV and ILV), causing drillers to cease operations and move the drilling locations. The IHI drilling scenarios, therefore, are analyzed for slit and engineered trench units only.

Table 3-50 presents the dose pathways for an IHI which, except for the addition of two bio-intrusion scenarios, are based on "Dose Calculation Methodology and Data for Solid Waste Performance Assessment and Composite Analysis at the Savannah River Site" by Smith et al. (2019). Additionally, Table 3-50 indicates whether detailed dose calculations are required. The assumption is that IHI release scenarios will occur after the 100-year IC period ends (i.e., after active ELLWF facility maintenance has concluded). The following release scenarios are considered in the calculation of dose to an IHI:

- Acute IHI – Basement Construction Scenario
- Acute IHI – Discovery Scenario
- Acute IHI – Drilling Scenario
- Chronic IHI – Agriculture Scenario
- Chronic IHI – Resident Scenario
- Chronic IHI – Post-Drilling Scenario
- Bio-Intrusion Scenario

3.7.3.1. Acute Inadvertent Human Intruder – Basement Construction Scenario

In this scenario, it is assumed that after the end of active institutional controls, a construction project begins at the site with associated earthmoving activities. The IHI construction scenario involves an IHI who chooses to excavate or construct a residence on the closure site. The IHI is assumed to excavate a basement to a depth of approximately 10 feet. Due to surface erosion of the cap by the time of intrusion, some portion of the excavation is assumed to reach the waste zone. It is further assumed that the waste material brought to the surface is indistinguishable from native soil, such that the IHI does not recognize the hazardous nature of the excavated material. The exposure pathways for the acute basement construction scenario include:

- Inadvertent ingestion of contaminated soil from the waste zone
- Inhalation of resuspended contaminated soil from the waste zone
- External exposure to contaminated soil from the waste zone

3.7.3.2. Acute Inadvertent Human Intruder – Discovery Scenario

The IHI discovery scenario is a modification of the IHI construction scenario. The basis for the IHI discovery scenario is the same as the IHI construction scenario except that the exposure time is reduced. The scenario involves the IHI excavating a basement to a depth of approximately 10 feet; however, the IHI recognizes that he or she is digging into very unusual soil immediately upon encountering the waste zone and leaves the site. The discovery scenario can occur at any time after loss of IC whereas the basement construction scenario cannot occur until the thickness of the overlying cover material is eroded to a depth less than that of a typical basement.

3.7.3.3. Acute Inadvertent Human Intruder – Drilling Scenario

In this scenario, a well is drilled into the waste DU sometime after the end of active institutional controls with an intended use for domestic water and irrigation. Lacking identification of other natural resources in the ELLWF, additional drilling scenarios are not considered. The person or persons who perform the well installation are the acute IHI in a drilling scenario, and exposure to drill cuttings is anticipated during installation.

The drilling borehole is assumed to penetrate the closure site, and stabilized contaminants are assumed to be disturbed and brought to the surface as drill cuttings. The acute drilling scenario assumes that an IHI drills a well through the trench units, but not through the reinforced concrete vaults. The IHI is exposed to well cuttings containing waste material that have been brought to the surface and mixed with clean soil; therefore, the exposure pathways for the acute drilling scenario are the same as the pathways described for the acute basement construction scenario.

3.7.3.4. Chronic Inadvertent Human Intruder – Agriculture Scenario

The agriculture scenario assumes that the IHI comes onto the site after the end of active institutional controls and establishes a permanent homestead. Waste in the disposal facility is assumed to be accessed when an IHI constructs a home directly on top of a disposal facility and the basement of the home extends into the waste zone. Waste exhumed from the disposal facility is assumed to be mixed with native soil in the IHI's vegetable garden.

The following exposure pathways involving exhumed waste or waste remaining in the exposed disposal facility on which the IHI's home is located are assumed to occur:

- Ingestion of vegetables grown in contaminated garden soil
- Direct ingestion of contaminated soil, primarily in conjunction with the intake of vegetables from the garden
- External exposure to contaminated soil while working in the garden or residing in the home on top of the disposal facility
- Inhalation of radionuclides attached to soil particles resuspended into the air from contaminated soil while working in the garden or residing in the home

3.7.3.5. Chronic Inadvertent Human Intruder – Resident Scenario

In this scenario, it is assumed that after the end of active institutional controls, an IHI lives in a home with a basement located directly above the disposal facility. The resident is shielded from exposure to radionuclides in the waste by the concrete floor slab and the soil remaining between the basement and the top of the waste zone. The exposure pathway for this scenario is therefore external exposure to photon-emitting radionuclides in the disposal facility while residing in a home located on top of the facility. Because the IHI does not excavate into the waste zone, it is assumed that no significant inhalation or ingestion exposure occurs.

3.7.3.6. Chronic Inadvertent Human Intruder – Post-Drilling Scenario

The post-drilling scenario assumes that an IHI residing permanently near the disposal facility drills through the disposal facility while constructing a well for a domestic water supply. Contaminated waste material brought to the surface during drilling operations, which is assumed to be indistinguishable from native soil, is mixed with native soil in the IHI's vegetable garden. The chronic post-drilling scenario assumes that the well is drilled through a trench unit, but not through a reinforced concrete vault.

The exposure pathways involving ingestion of contaminated vegetables, ingestion of contaminated soil, and external and inhalation exposures while working in the garden are the same as the pathways described previously for the agriculture scenario. In the post-drilling scenario, however, external and inhalation exposures are limited to time spent in the garden and do not include pathways for time residing in the home.

3.7.3.7. Bio-Intrusion Scenario

The bio-intrusion scenario assumes that an IHI moves onto the site but does not excavate into the stabilized contaminants. Rather, radioactivity is brought to the surface by plants through root uptake and by burrowing animals. Bio-intrusion is not considered a credible mechanism for significant stabilized contaminant disturbance until the cap has been eroded down to the erosion barrier, based on burrowing species characteristics and the stabilized contaminant depth. Of the likely burrowing animal residents at SRS, two burrowers, the Florida Harvester ant and the gopher tortoise, are expected to burrow only 2 meters. Still, only 5% of the harvester ant's burrows and 10% of the gopher tortoises' burrows are expected to be that deep (McKenzie et al., 1986).

The Florida Harvester ant has a population density of approximately 27 colonies per hectare; the 27 colonies bring an estimated volume of 0.05 m^3/ha of soil to the surface each year (McKenzie et al., 1986). Provided below is the estimated total volume of waste brought to the surface by the Florida Harvester Ant ($V_{Total,Ant}$). This calculation assumes that the area of focus is not 1 hectare, but the area above the trench DUs and includes a dilution factor (1:10) to account for the ratio of waste material to the total volume of soil brought to the surface (f_{Waste}). Because only 5% of the burrows are expected to penetrate the waste zone ($f_{Penetrate\_WZ}$), only 5% of the total volume brought to the surface was used in the calculation. The waste material is considered indistinguishable from the soil. Because only the edges of the closure cap over the closed trench units will erode sufficiently to allow burrowing into the waste zone (i.e., zones close to the toe of the slope on the closure cap), only the last 50 feet on either end of a nominal trench footprint need be considered. Thus, a nominal trench DU is 157 ft wide, resulting in 15,700 ft^2 of surface area available to the burrowing harvester ant as shown below.

$$V_{Total,Ant} = A_{DU} v_{Ant} f_{Penetrate\_WZ} f_{Waste} \qquad \text{Eq. (3-33)}$$

$$V_{Total,Ant} = \left(\frac{0.146\,\text{ha}}{\text{DU}}\right)\left(\frac{0.05\,\text{m}^3}{\text{ha}\cdot\text{yr}}\right)(0.05)\left(\frac{0.10\,\text{m}^3}{\text{m}^3}\right) = \frac{3.65\times10^{-5}\ \text{m}^3}{\text{DU}\cdot\text{yr}} \qquad \text{Eq. (3-34)}$$

where:

$$A_{DU} = \left(50\ \text{ft} \times 157\ \text{ft}\right) \times 2 = \frac{15700\ \text{ft}^2}{\text{DU}} \equiv \frac{0.146\ \text{ha}}{\text{DU}} \qquad \text{Eq. (3-35)}$$

and

$V_{Total,Ant}$ Total volume of waste brought to surface by Florida Harvester ant ($m^3\ DU^{-1} \cdot yr^{-1}$)

$f_{Penetrate\_WZ}$ Fraction of burrows expected to penetrate the waste zone (0.05, unitless)

f_{Waste} Dilution factor (1:10) accounting for ratio of waste material to total volume of soil brought to the surface ($0.1\ m^3\ m^{-3}$)

v_{Ant} Volume of waste brought to surface by Florida Harvester ants assuming a population density of 27 colonies per hectare ($0.05\ m^3\ ha^{-1} \cdot yr^{-1}$)

A_{DU} Surface area available to the burrowing Florida Harvester ant ($ha\ DU^{-1}$)

An estimated seven tortoises reside in a hectare; collectively they bring approximately $1.05\ m^3\ ha^{-1}$ of soil to the surface each year (McKenzie et al., 1986). Using the same trench area ($0.146\ ha\ DU^{-1}$) and waste-to-total soil dilution factor (1:10) as above, the estimated total volume of waste brought to the surface by the gopher tortoise is calculated below. In this case, 10% of the tortoise burrows are expected to penetrate the waste zone ($f_{Penetrate\_WZ}$).

$$V_{Total,Tortoise} = A_{DU} v_{Tortoise} f_{Penetrate\_WZ} f_{Waste} \qquad \text{Eq. (3-36)}$$

$$V_{Total,Ant} = \left(\frac{0.146\ \text{ha}}{\text{DU}}\right)\left(\frac{1.05\ \text{m}^3}{\text{ha} \cdot \text{yr}}\right)(0.10)\left(\frac{0.10\ \text{m}^3}{\text{m}^3}\right) = \frac{1.53 \times 10^{-3}\ \text{m}^3}{\text{DU} \cdot \text{yr}} \qquad \text{Eq. (3-37)}$$

where:

$V_{Total,Tortoise}$ Total volume of waste brought to surface by Florida Harvester ant ($m^3\ DU^{-1} \cdot yr^{-1}$)

$f_{Penetrate\_WZ}$ Fraction of burrows expected to penetrate the waste zone (0.10, unitless)

f_{Waste} Dilution factor (1:10) accounting for ratio of waste material to total volume of soil brought to the surface ($0.1\ m^3\ m^{-3}$)

$v_{Tortoise}$ Volume of waste brought to surface by gopher tortoises assuming a population density of 7 per hectare ($1.05\ m^3\ ha^{-1} \cdot yr^{-1}$)

A_{DU} Surface area available to the burrowing gopher tortoise per Eq. (3-35) ($ha\ DU^{-1}$)

As shown in Table 3-51, the total volume of waste material brought to the surface through bio-intrusion is many orders of magnitude lower than the total volume brought to the surface during construction of a basement.

Table 3-51. Total Volume of Waste Material Brought to Surface Via Bio-Intrusion Versus Basement Construction

	Bio-Intrusion (Florida Harvester Ant)	Bio-Intrusion (Gopher Tortoise)	Acute IHI (Basement Construction)
Total Volume of Waste Material brought to Surface (m^3/DU-yr)	3.65E-05	1.53E-03	1.00E+02

Assuming the ELLWF cover reverts to pine forest in the future, the pine trees could also pose a bio-intrusion risk, with a mature pine having roots from 6-ft to 12-ft deep (Phifer and Nelson, 2003). The final closure cap includes an HDPE geomembrane liner which sheds infiltrating water through a lateral drainage layer before reaching the waste zone, thereby causing water to pool above and flow laterally away from the cap. Roots from vegetation prefer areas where water is readily available and, therefore, will accumulate above the essentially impervious HDPE liner rather than penetrating through it. Field evidence supporting this assertion is provided by Benson and Benavides (2018) from evaluations of similar covers.

3.7.3.8. Basis for Inadvertent Human Intruder Pathways

Table 3-50 provides a list of the ELLWF exposure pathways identified as candidates for detailed analyses. The candidates list was developed based on a review of SRS PA analysis documents by Butcher and Phifer (2016a), Savannah River Remediation (2009), Savannah River Remediation (2012), and Savannah River Remediation (2020). With an emphasis on local practices, activities at SRS that could bring humans into contact with stabilized contaminants (e.g., water use, hunting, fishing, recreational activities such as swimming and boating, habitation in dwellings, and other unique activities that involve water use or ground disturbance) were considered to ensure that any pathways unique to SRS were taken into account. Surface water and recreational pathways were evaluated for the 2010 SRS CA (SRNL, 2010) and are not considered in SRS PA analyses, which includes the ELLWF PA. Pathways that are found to make a negligible contribution to the overall exposure to humans may be removed from consideration (U.S. DOE, 2017).

The following assumptions were made for the IHI release pathways scenario:

- The stabilized contaminant release mechanism for the IHI is inadvertent drilling into trench units. Leaching of stabilized contaminants to GW and use of contaminated GW are credible release mechanisms; however, they are not calculated for the IHI in accordance with the DOE position (U.S. DOE, 2007).
- Once erosion of material occurs above the erosion barrier, the bio-intrusion scenario becomes a credible mechanism for contaminant transport. However, the total volume of waste material brought to the surface via this scenario (3.65E-05 m^3 DU^{-1} yr^{-1} and 1.53E-03 m^3 DU^{-1} yr^{-1}) is estimated to be significantly less than the estimated volume brought to the surface by the acute basement construction scenario (100 m^3 DU^{-1} yr^{-1}).

- The HDPE geomembrane in the final cover system will cause infiltrating water to pool and flow laterally away from the barrier, providing a readily available water supply for roots above the geomembrane. Evaluations of similar covers by Benson and Benavides (2018) have found no evidence of root penetration into the layers situated below the geomembrane.

3.8. PROPERTY DATA PACKAGES

3.8.1. Radionuclide, Element, and Dose Parameters

The *Radionuclide, Element and Dose Parameters Data Package* (SRNL, 2019b) refers specifically to the SRNL-compiled and SRNL-maintained Microsoft Excel database of radiological information for 1,252 radionuclides based on ICRP Publication 107 (ICRP, 2008). The data package (known as the *Rad-Dose Data Package* for short) includes parameters such as half-life, decay modes, dose conversion factors for internal and external exposure, MCLs, and human consumption factors that are used in the ELLWF PA model simulations. Radionuclide data is extracted from ICRP Publication 107 (ICRP, 2008). Internal exposure dose coefficients are obtained from an SRNL compilation of data (Stone and Jannik, 2013). External exposure and soil contamination dose coefficients are obtained from an Oak Ridge National Laboratory compilation of data (Eckerman and Leggett, 2013; DC_PAK 3.02). The technical report detailing the development and content of the *Rad-Dose Data Package* is "Dose Calculation Methodology and Data for Solid Waste Performance Assessment and Composite Analysis at the Savannah River Site" by Smith et al. (2019).

Smith et al. (2019) provides a detailed description of the methodology developed to perform dose calculations for the ELLWF PA and SRS CAs, including the derivation of a complete set of equations to calculate dose for individual exposure pathways. Special dose considerations related to human consumption of meat and dairy as well as the treatment of tritium in dose calculations are also included. Human consumption parameters for the typical and reference persons are also provided.

The methodology builds upon the dose calculation methods used in PA2008 (WSRC, 2008) and SRS CA (SRNL, 2010). The dose calculation methodology is similar to that used by SRR in the Saltstone Disposal Facility PA, H-Area Tank Farm PA, and F-Area Tank Farm PA (Savannah River Remediation, 2014). Although similar in many respects, the SRR dose calculation methodology is designed to accommodate the unique features of these three SRS disposal facilities, in addition to the different regulatory framework under the Ronald W. Reagan National Defense Authorization Act for Fiscal Year 2005, Section 3116 (NDAA, 2014).

3.8.1.1. Resident Farmer Member of the Public Scenarios

The first set of dose scenarios applies to both ELLWF PAs and SRS CAs. It assumes that a MOP establishes residence near the waste site and uses contaminated GW or contaminated surface water for personal consumption and to irrigate a garden and pasture where produce and farm animals are raised. Products from the garden and farm animals are also used for personal consumption. General dose exposure pathways for the resident farmer scenario are ingestion, inhalation, external

exposure, and recreational (CA only). Smith et al. (2019) devotes a chapter each in the data package report to the four exposure pathways for the resident farmer. Doses from the four pathways are directly related to the contaminant concentration in water.

3.8.1.1.1. Ingestion Dose Pathways to Resident Farmer Member of the Public

Figure 3-85 displays a schematic diagram of the sources of dose to a MOP through ingestion pathways originating from the use of contaminated GW or surface water. The MOP is assumed to be a resident farmer who uses either well water drawn from contaminated GW or contaminated surface water from the Savannah River for both direct consumption and to raise a garden and farm animals which provide milk and meat that are also consumed. For GW use, the well is typically assumed to be 100 meters down gradient from the boundary of the contamination source (PA only). For surface water use (CA only), the water is assumed to be drawn from POAs that fall into two general categories: (1) POAs in the Savannah River as a source of drinking water, irrigation water and recreation water; (2) POAs at the mouths of SRS surface streams entering the Savannah River as a source of recreation water only.

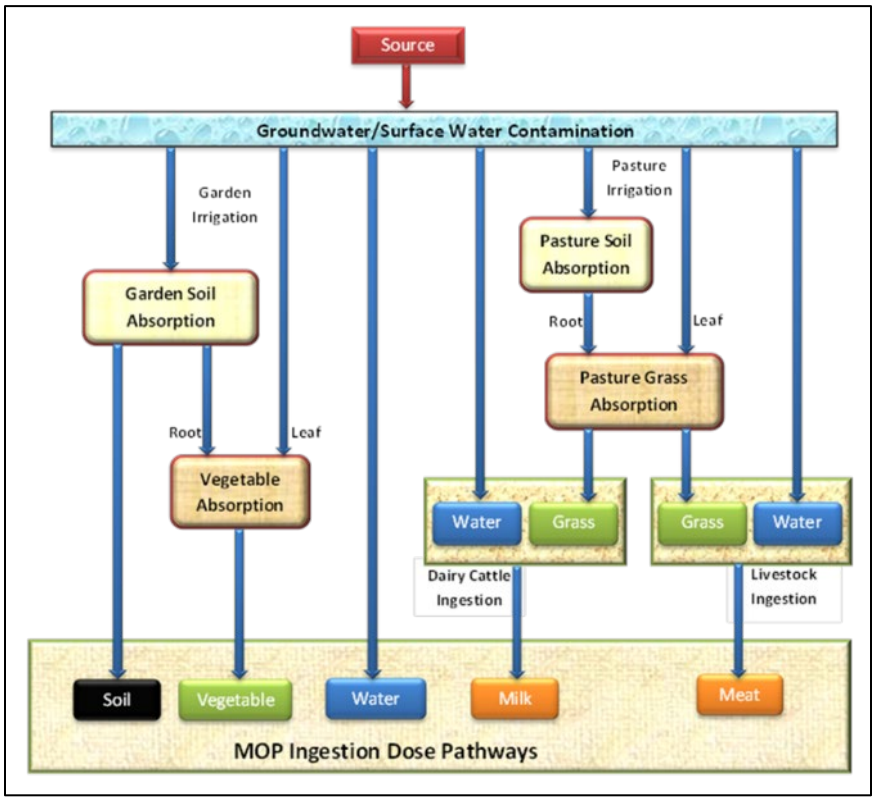

Figure 3-85. Potential Ingestion Dose Pathways to Residential Member of the Public in *Rad-Dose Data Package*

Contaminated water drawn from the Savannah River for use by the MOP is more dilute than contaminated water found at the mouth of SRS surface streams. Therefore, applying the correct radionuclide-contaminated water concentration in dose equations involves knowing the location of the POA from which the water originated. It is assumed that the concentration of contaminants in the GW is known as a function of time and that the stream and/or river dilution factor is known

as well. In general, dilution can vary with time; however, typically a constant annual-average river or stream flow is used.

The following mechanisms of contaminant transfer from water to the human receptor via ingestion are considered in the *Rad-Dose Data Package* models:

1. Direct consumption of contaminated water
2. Consumption of garden produce contaminated by the use of water for irrigation
3. Consumption of milk from dairy cattle that drink contaminated water and consume pasture grass irrigated with contaminated water
4. Consumption of meat from farm animals that drink contaminated water and consume pasture grass irrigated with contaminated water
5. Inadvertent consumption of dust from garden soil contaminated by use of water for irrigation

Section 3.7 describes whether an individual pathway is assumed to occur for purposes of the ELLWF PA and, therefore, whether a quantified dose calculation is required.

Produce or vegetable contamination occurs through two routes. The first is absorption of contaminated water used for garden irrigation through plant leaves. The second is absorption of contaminants from soil through the plant roots where the soil has been contaminated by water through irrigation. Farm animals that provide milk and meat for human consumption are similarly exposed to contaminants by their direct ingestion of the water and by ingestion of plants exposed to contaminated water by irrigation. Like garden produce, pasture grass consumed by the animals is contaminated by absorption through both the leaves and roots from irrigation of the pasture using contaminated water.

It is assumed that the concentration of contaminants in the water is known as a function of time. Ingestion dose to a human receptor depends on the amount of contaminated water, produce, milk, meat, and soil consumed and on the accumulation of contaminants in the ingested same.

3.8.1.1.2. Inhalation Dose Pathways to Resident Farmer Member of the Public

Figure 3-86 presents a schematic diagram of *potential* sources of dose to a MOP from the inhalation of contaminated GW or surface water and inhalation of contaminated soil. The MOP is assumed to be a resident farmer who uses water drawn from the contaminated source to irrigate a garden. For GW, the well is typically assumed to be 100 meters down gradient from the boundary of an ELLWF DU (PA only). For surface water, the water is assumed to be drawn from the mouth of an SRS stream or the Savannah River. The following mechanisms of contaminant transfer from water inhalation to the human receptor are included in the *Rad-Dose Data Package* models, although not all will require a quantified dose calculation for the ELLWF PA:

1. Inhalation of contaminated water during garden irrigation
2. Inhalation of dust that has been contaminated by use of water for garden irrigation
3. Inhalation of contaminated water during showering

Section 3.7 describes whether an individual pathway is assumed to occur for purposes of the ELLWF PA and, therefore, whether a quantified dose calculation is required.

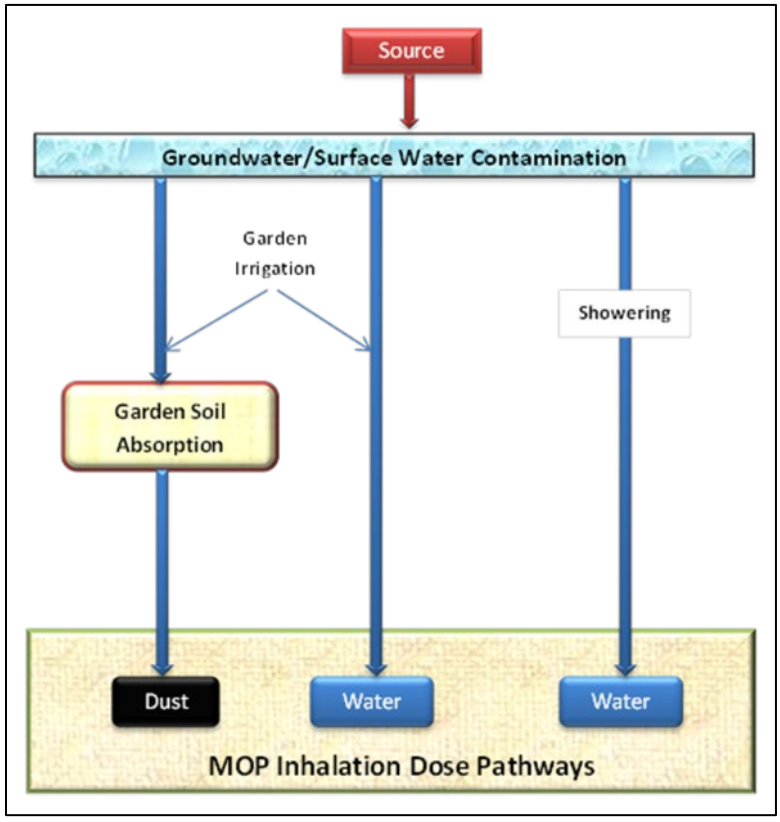

Figure 3-86. Potential Inhalation Dose Pathways to Residential Member of the Public in *Rad-Dose Data Package*

It is assumed that the concentration of contaminants in the water is known as a function of time. Dose to a human receptor depends on the amount of contaminated water inhaled during garden irrigation and showering, if applicable, and on the accumulation of contaminants in inhaled soil. Accumulation of contaminants in the soil was treated when considering ingestion pathways in Section 3.8.1.1.1.

In addition to the three inhalation pathways shown in Figure 3-86, inhalation of contaminated water during swimming and boating could also be included. However, swimming and boating are considered recreational activities that would take place in the Savannah River or mouth of an SRS stream contaminated by GW. As such, they are considered part of the resident farmer recreational exposure pathways included in the CA only and will not be discussed further.

3.8.1.1.3. External Exposure Dose Pathways to Resident Farmer Member of the Public

Figure 3-87 shows a schematic diagram of sources of dose to a MOP from external exposure to contaminated GW or surface water used for irrigation and showering. The MOP is assumed to be a resident farmer who uses water drawn from the contaminated source to irrigate a garden and to shower. The GW source is typically assumed to be a well 100 meters down gradient from the boundary of an ELLWF disposal unit (PA only). The surface water source is assumed to be POAs in the Savannah River or the mouth of an SRS stream contaminated by GW seepage. The following mechanisms for external exposure of the human receptor to contaminants are considered in the *Rad-Dose Data Package* models:

1. Exposure to soil contaminated by water during garden irrigation
2. Exposure to contaminated water during showering

Section 3.7 describes whether an individual pathway is assumed to occur for purposes of the ELLWF PA and, therefore, whether a quantified dose calculation is required.

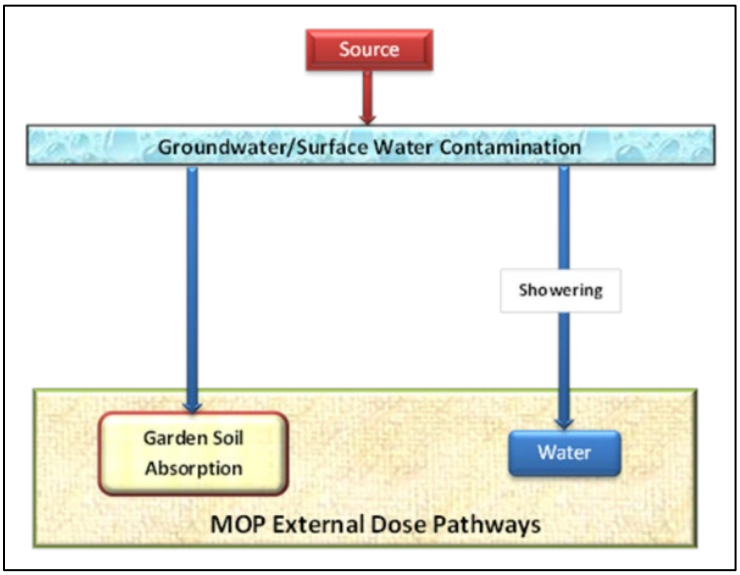

Figure 3-87. Potential External Exposure Dose Pathways to Residential Member of the Public in *Rad-Dose Data Package*

It is assumed that the concentration of contaminants in the water is known as a function of time. External dose to a human receptor depends on the time of exposure and contamination level in water used for showering and on the accumulation of contaminants in garden soil. Accumulation of contaminants in soil was treated when considering ingestion pathways in Section 3.8.1.1.1.

In addition to the two external exposure pathways shown in Figure 3-87, exposure to contaminated water during swimming and boating could also be included. However, swimming and boating are considered recreational activities that would only take place in a stream contaminated by GW. As such, they are considered part of the recreational exposure pathways included in the CA only and will not be discussed further.

3.8.1.2. Inadvertent Human Intruder Scenarios

Additional dose scenarios considered for the ELLWF PA assume that an IHI encroaches on the waste disposal site after loss of IC. General dose exposure pathways considered for the IHI are ingestion, inhalation, and external exposure. Again, Smith et al. (2019) devotes a chapter each in the data package report to the three exposure pathways for the IHI. Doses from all IHI pathways are directly related to the contaminant concentration in the buried waste.

3.8.1.2.1. Ingestion Dose Pathways for Inadvertent Human Intruder

The IHI is exposed to ingestion dose pathways involving exhumed waste (indistinguishable from soil) or waste remaining in the exposed disposal facility on which the IHI's home is located. The IHI scenario does not include the direct ingestion of contaminated GW or the use of contaminated GW for crop irrigation. The three ingestion pathways included in the *Rad-Dose Data Package* models for an IHI are:

1. Ingestion of vegetables grown in contaminated garden soil
2. Ingestion of dust originating from contaminated garden soil
3. Ingestion of dust originating from the waste zone

Pathways 1 and 2 apply to the agriculture and post-drilling scenarios for a chronic IHI. Pathway 3 applies to the basement construction and well drilling scenarios for an acute IHI. Figure 3-88 is a schematic diagram of the sources of dose to an IHI through the three ingestion pathways. Section 3.7 describes whether an individual pathway is assumed to occur for purposes of the ELLWF PA and, therefore, whether a quantified dose calculation is required.

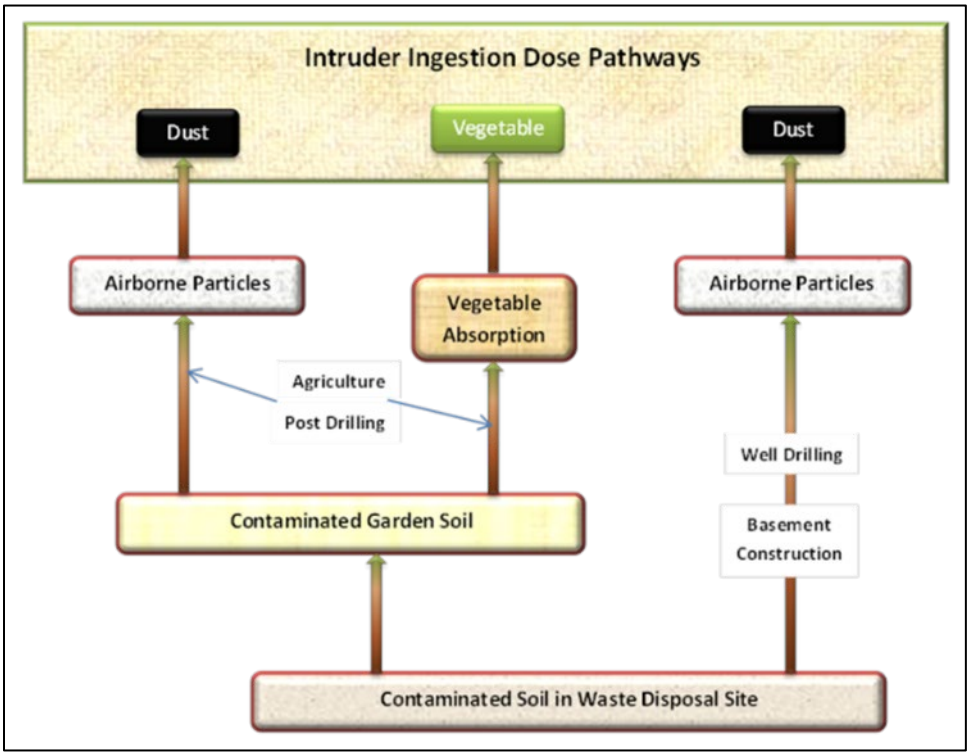

Figure 3-88. Potential Ingestion Dose Pathways to Inadvertent Human Intruder in *Rad-Dose Data Package*

3.8.1.2.2. Inhalation Dose Pathways for the Inadvertent Human Intruder

The IHI is exposed to inhalation dose pathways involving exhumed waste or waste remaining in the exposed disposal facility on which the IHI's home is located. The inhalation pathways included in the *Rad-Dose Data Package* models for an IHI are:

1. Inhalation of dust originating from contaminated garden soil while working in a garden
2. Inhalation of dust originating from contaminated garden soil while residing in a home
3. Inhalation of dust originating from the waste zone

Pathways 1 and 2 apply to the agriculture scenario for a chronic IHI. Pathway 1 also applies to the post-drilling scenario for a chronic IHI. Pathway 3 applies to the basement construction and well drilling scenarios for an acute IHI. Figure 3-89 is a schematic diagram of the sources of dose to an IHI through the inhalation pathways. Section 3.7 describes whether an individual pathway is assumed to occur for purposes of the ELLWF PA and, therefore, whether a quantified dose calculation is required.

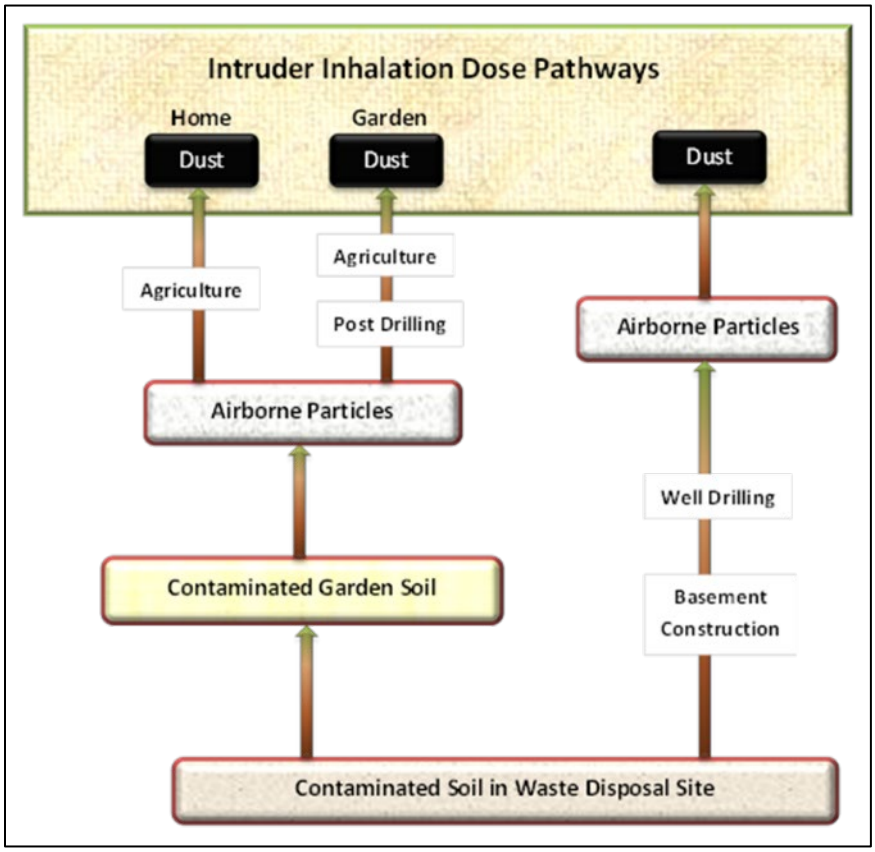

Figure 3-89. Potential Inhalation Dose Pathways to Inadvertent Human Intruder in *Rad-Dose Data Package*

3.8.1.2.3. External Exposure Dose Pathways for Inadvertent Human Intruder

The IHI receives an external dose from direct exposure to contaminated soil. The external exposure pathways included in the *Rad-Dose Data Package* models for an IHI are:

1. Exposure to contaminated soil in a garden
2. Exposure to contaminated soil from the waste zone
3. Exposure while residing in a home located above the waste disposal site

Pathway 1 applies to the agriculture and post-drilling scenarios for a chronic IHI. Pathway 2 applies to the well drilling, basement construction, and discovery scenarios for an acute IHI. Pathway 3 applies to the agriculture and residential scenarios for a chronic IHI. Figure 3-90 is a schematic diagram of the sources of dose to an IHI through the external exposure pathways. While Figure 3-90 shows soil shielding affecting all of the acute dose pathways, soil shielding typically only impacts the discovery scenario. Section 3.7 describes whether an individual pathway is assumed to occur for purposes of the ELLWF PA and, therefore, whether a quantified dose calculation is required.

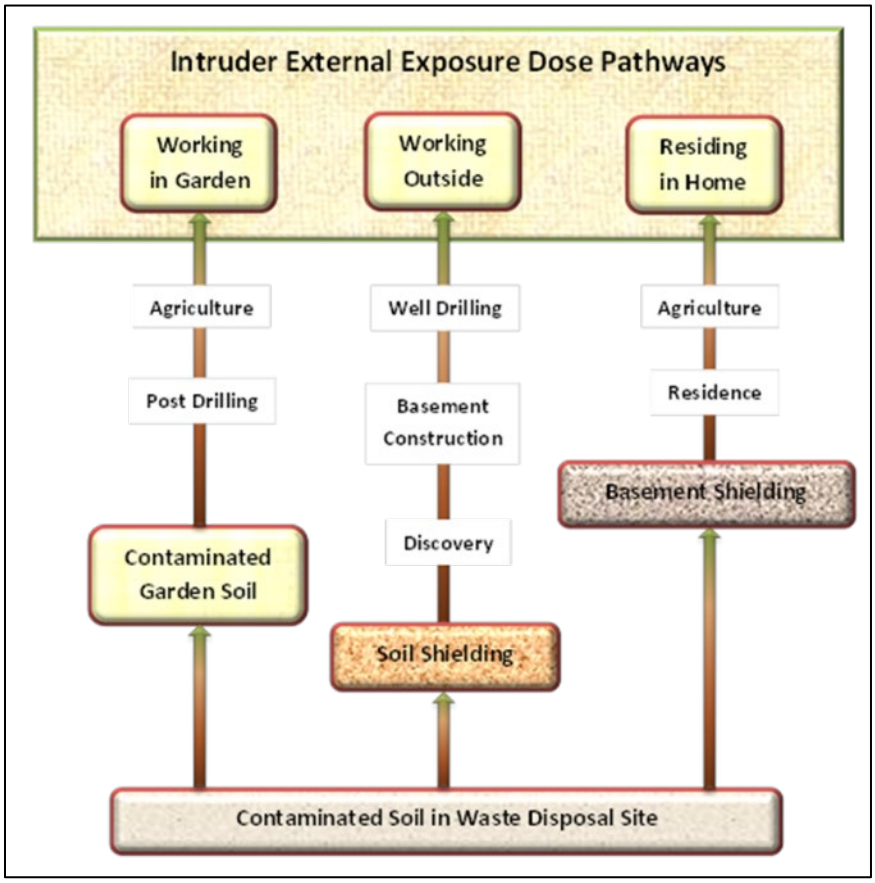

Figure 3-90. Potential External Exposure Dose Pathways to Inadvertent Human Intruder in *Rad-Dose Data Package*

3.8.1.3. Microsoft Excel Database

Chapter 10 of the *Rad-Dose Data Package* report describes the Microsoft Excel database named *Radionuclide, Element and Dose Parameter Data Package* (SRNL, 2019b) that was created to provide a system for maintaining the data required to perform radionuclide transport and dose calculations. The database includes:

- Isotope physical parameters and radioactive decay data needed for both transport and dose calculations
- Isotope-specific dose coefficients and soil shielding factors associated with exposure pathways
- Radionuclide drinking water concentration limits either published by the U.S. EPA or derived from internal dose coefficients to meet GW protection requirements as required by U.S. DOE (2021b)
- Element-specific bio-transfer factors used in dose calculations
- Dose equations and values of physical parameters and human factors used in dose calculations
- Key physical constants used in dose calculations

The *Rad-Dose Data Package* provides a framework not only for storing the best-available data at the time of issue in a single, protected database but also for updating the data as new or better information becomes available. The data package underwent an extensive, independent verification of all numerical values and decay chains. The bases for selection of a Microsoft Excel workbook for the data package were ease of use and ready distribution. The data package is part of an ongoing PA/CA maintenance program to periodically review and update existing databases.

3.8.2. Geochemical Parameters

The *Geochemical Data Package, Ver. 3.1, dated April 27, 2018* (SRNL, 2018) refers to the SRNL-compiled and -maintained Microsoft Excel database of geochemistry data, including sorption coefficients, liquid-phase solubilities, and chemical leach factors, for various materials typically considered in fate and transport analyses of SRS facilities. The data package is referred to as the *GeoChem Data Package* for short. The technical report detailing the development and content of the *GeoChem Data Package* is *Geochemical Data Package for Performance Assessment Calculations Related to the Savannah River Site* by Kaplan (2016b), which builds upon earlier geochemical data packages and reports by Kaplan (2007a), Kaplan (2010), and McDowell-Boyer et al. (2000).

In addition to the recommended parameter values, Kaplan (2016b) describes the geochemical conceptual model for each type of DU, the approach used for selecting the parameter values, the justification for selecting the data, and the assumptions made to assure that the conceptual and numerical geochemical models are reasonably conservative (i.e., the recommended input values are biased to reflect conditions that tend to predict maximum risk to the hypothetical receptor). The data package provides 1,088 input parameters for geochemical parameters describing transport processes for 64 elements (>740 radioisotopes) potentially occurring within eight subsurface disposal facility types/areas at SRS: STs, ETs, LAWV, ILV, NRCDAs, CIG SWFs, Saltstone Disposal Facility, and closed High-Level Liquid Waste Tanks. Six of the eight disposal facility types/areas are relevant to the ELLWF PA. The geochemical parameters included in the data package are the distribution or partition coefficient (K_d value), apparent solubility concentration (k_s value), and the cementitious leachate impact factor. Cementitious leachate impact factors are element-specific values used to modify K_d values to account for the influence of leachate from cement structures on GW chemistry that may alter radionuclide partitioning to subsurface sediment.

3.8.2.1. Scope of GeoChem Data Package

The *GeoChem Data Package* provides geochemical input values for isotopes of the following 64 elements: Ac, Ag, Al, Am, Ar, As, At, Ba, Bi, Bk, C, Ca, Cd, Ce, Cf, Cl, Cm, Co, Cr, Cs, Cu, Es, Eu, F, Fe, Fm, Fr, Gd, H (as ^{3}H), Hg, I, K, Kr, Lu, Mn, Mo, N (as NO_3^- and NO_2^-) Na, Nb, Ni, Np, Pa, Pb, Pd, Po, Pu, Pt, Ra, Rb, Re, Rn, Sb, Se, Sm, Sn, Sr, Tc, Te, Th, Tl, U, Y, Zn, and Zr.

The duration of interest varies among types of calculations, but is commonly 1,000 years, 10,000 years, or the duration required for the maximum dose for PA models. Therefore, if geochemical conditions are expected to change during the periods of interest, appropriate adjustments to the geochemical conceptual and numerical models were made. The tendency for

radionuclides to migrate can be greatly influenced by the geochemical conditions of the subsurface system. The primary conceptual environments considered in the data package that are relevant to the ELLWF PA are:

- Sandy sediment
- Clayey sediment
- Young (Stage I) cement
- Moderately aged (Stage II) cement
- Aged (Stage III) cement
- Young (Stage I) reduced cement
- Moderately aged (Stage II) reduced cement
- Aged (Stage III) reduced cement
- Cementitious-leachate-impacted sandy sediment
- Cementitious-leachate-impacted clayey sediment

For each conceptual environment, 64 K_d values and/or apparent solubility values (k_s) are provided in the *GeoChem Data Package*. For each constituent of concern and conceptual environment, "best," "minimum," and "maximum" estimates of K_d and k_s are provided. The "best" estimates represent the most likely K_d and k_s values for a given conceptual environment. The best-estimate values are based primarily on the literature, SRS site-specific experimental data, or expert judgment.

3.8.2.2. Basis for Use of Empirical K_d Values

The basic philosophy employed to develop and parameterize the geochemical models originated from a broad range of basic and applied research. Basic mechanistic studies and first principles guided the development of the conceptual geochemical models. Empirical studies, preferably with site-specific materials and conditions, provided input estimates to help quantify the conceptual models. Radionuclide partitioning between the aqueous and solid phases is described using the distribution or partition coefficient (K_d value) and the apparent solubility concentration (k_s value). A series of look-up tables were prepared summarizing these parameters which vary with the type of porous media (e.g., sandy sediment, clayey sediment, cementitious material, reducing cementitious material) and, in the case of cementitious materials, the age of the solid and the presence or absence of slag (a strong reducing agent). The look-up tables became the basis for the Microsoft Excel version of the *GeoChem Data Package* (SRNL, 2018).

Contaminant-sediment interactions are complex, and include adsorption, absorption, partitioning into organic matter, complexation, precipitation, and coprecipitation. The magnitude of these interactions for a given contaminant can vary greatly depending on solid-phase composition or porewater chemical composition. Each type of interaction between the contaminant and solid phases has a unique numerical representation. However, the most common approach used in coupled reactive-transport modeling is to incorporate the effect of all of these reactions into a single, operationally defined K_d value. The K_d value is the simplest construct describing contaminant sorption to sediments. K_d (mL g^{-1}) is the ratio of the contaminant concentration sorbed

to the solid phase [C_{solid} (gmol g^{-1})] to the contaminant concentration in the liquid surrounding the solid phase [C_{liquid} (gmol mL^{-1})] as given by:

$$K_d = \frac{C_{solid}}{C_{liquid}} \qquad \text{Eq. (3-38)}$$

Eq. (3-38) assumes that steady state has been achieved and sorption kinetics is not limiting under the assumed modeling conditions. Sorption kinetics is typically not an issue when GW flow rates do not exceed a few centimeters per day, thereby providing long contact times between the aqueous and solid phases. K_d also assumes linear sorption as highlighted in the light blue region of Figure 3-91. As the concentration of a solute on the solid phase increases, the sorption isotherm becomes non-linear, taking on a Freundlich sorption profile (yellow-highlighted region in Figure 3-91). The non-linearity is attributed to the number of available sorption sites diminishing to a point that it becomes less likely for the solute to find an available sorption site. The aqueous phase concentration where this transition occurs varies with solute. Upon adding even more solute to the system, as may occur near a source term, precipitation may occur and solubility controls the release of the solute to the aqueous phase (orange-highlighted region labeled "Precipitation" in Figure 3-91). It is in the solubility-controlled region where k_s applies.

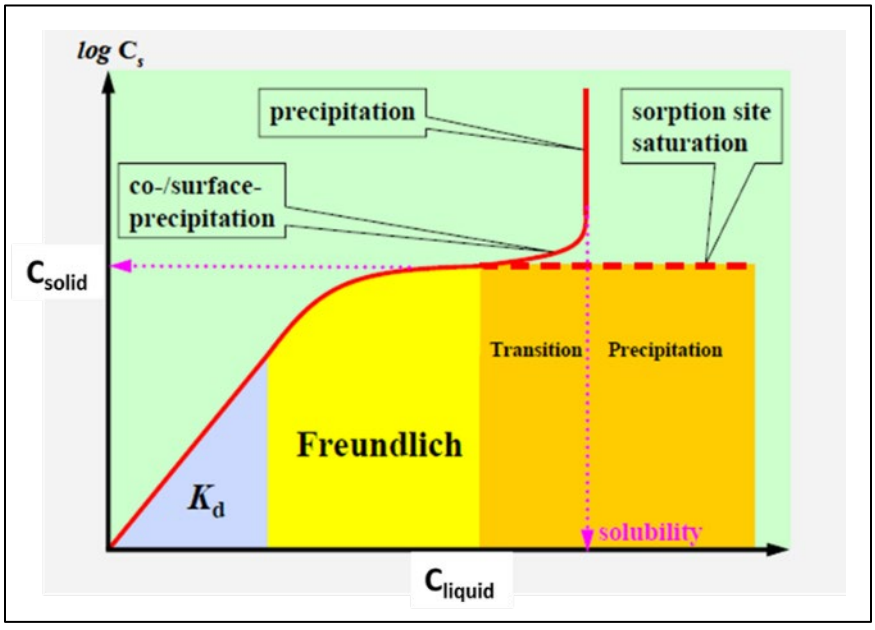

Figure 3-91. Sorption Isotherm (Aqueous Radionuclide Concentration, C_{liquid}, vs. Surface-Bound Radionuclide, C_{solid}) Identifying Linear Range (K_d), Non-Linear Range (Freundlich isotherm), and Apparent Solubility Value (k_s) [after Wang et al. (2009)]

In contaminant transport models, K_d is used to define the retardation factor (R_f, unitless), which is equal to the ratio of the average linear (pore) velocity of water (υ_w, m s^{-1}) to the average linear (pore) velocity of the contaminant (υ_c, m s^{-1}). For water-saturated systems, such as aquifer

systems, K_d is related to R_f by the bulk density (ρ_b, g cm^{-3}) and porosity (η, m^3 m^{-3}) as given by Bouwer (1991) and Valocchi (1985):

$$R_f = \frac{\upsilon_w}{\upsilon_c} = \left(1 + \frac{K_d \rho_b}{\eta}\right) \quad \text{Eq. (3-39)}$$

where the bulk density is expressed as:

$$\rho_b = \rho_p \left(1 - \eta\right) \quad \text{Eq. (3-40)}$$

and ρ_p (g cm^{-3}) represents the particle density of the solid phase. The bulk density and porosity terms in Eq. (3-39) convert the mass-normalized K_d value into a volume-normalized value. Note that for partially saturated sediments, such as in the VZ, the porosity term, η, is replaced by the volumetric water content of the VZ sediments.

An important limitation of the empirical K_d is that it describes sorption under a limited set of aqueous- and solid-phase environmental conditions (i.e., it is operationally defined). Changes in either set of conditions will be expected to alter the K_d value. Still, reasons for selecting the K_d construct for PA modeling include:

1. Most of the existing sorption literature on radionuclide sorption, especially at SRS, can be classified as empirical K_d values.
2. Under the expected low contaminant concentrations in the far field, sorption is expected to be linear (i.e., sorption can be considered independent of contaminant concentration and, therefore, K_d is constant for a given contaminant/geological material/water composition combination under identical geochemical conditions).
3. Generally, mass transfer processes are assumed to be fast enough to reflect near liquid-solid phase equilibria; however, lower K_d values are used for C-14 because of its measured slow approach to equilibrium.
4. K_d can be used directly in all PA transport codes (PORFLOW and GoldSim®).
5. There is presently no thermodynamics-based conceptual model that is robust enough to accurately predict the degree of radionuclide adsorption by natural sediments (see below).

By using site-specific materials, namely sediments or cementitious materials and GW from disposal areas, it is possible to gather relevant data and not rely on extrapolation from other sediment and aqueous systems reported in the literature.

Another aspect of the K_d construct that has been relaxed in the PA contaminant transport calculations is strict adherence to the assumption of reversibility. Laboratory K_d values measured with natural sediments and GW often reflect not only fast, reversible adsorption and exchange reactions, but also absorption, specific or somewhat irreversible adsorption, surface complexation, and varying degrees of (co)precipitation reactions. In fact, desorption experiments in the literature

indicate that true reversibility is the exception rather than the rule (Krupka et al., 1999); desorption often occurs at a slower rate than the (ad)sorption process.

Additional rationalization for the use of empirical K_d values in PA models is provided by Kaplan (2016b).

3.8.2.3. Apparent Solubility Values

In addition to the K_d construct, the apparent solubility value, k_s, (gmol L^{-1} or M) is used to describe radionuclide geochemical behavior, especially within disposal sites and within waste forms (i.e., liquid-phase concentrations become limited as shown in Figure 3-91). The apparent solubility value is used when the concentrations of one or more radionuclides are believed to exceed the solubility of an assumed solubility-controlling mineral phase(s). Identification of controlling mineral phases for SRS PA activities is based on laboratory experiments, calculations, and the literature. Once the solubility-controlling mineral phases are identified, the upper-bound concentration (i.e., conservative value for the GW pathway analysis) for each constituent of concern is calculated using the appropriate background electrolyte composition (GW composition). It is anticipated that when the concentration of each constituent of concern exceeds the solubility concentration value for a given mineral phase, precipitation occurs, and the subsequent radionuclide aqueous concentration is controlled by k_s rather than K_d. At concentrations below the solubility limit, the radionuclide concentration is assumed to be controlled by the K_d construct.

3.8.2.4. Approach to Selection of Geochemical Parameters

Ideally, all input data would be derived from experiments conducted using site-specific materials under the appropriate conditions for the conceptual environment of interest. For example, much of the Clayey Sediment and Sandy Sediment K_d data were, in fact, derived from sorption experiments conducted with site-specific sediments. A recent major effort has been directed at understanding and quantifying radionuclide transport through SRS VZ sediments at longer durations and larger scales than is typically provided through laboratory experiments. These experiments are housed in the Radionuclide Field Lysimeter Experiment (RadFLEx) Test Bed Facility. The RadFLEx facility was initiated in July 2012 and will continue to operate through July 2022. Additional information about the RadFLEx Test Bed Facility is provided by Kaplan (2016b).

Where site-specific data was not available, literature K_d values using non-SRS solid and aqueous phases were used. Careful selection of the literature values was required to ensure that the experimental conditions used to generate the K_d values were appropriate for SRS conditions. For example, literature values were used when choosing "best" K_d values for K, Mn, and Fe sorption in clayey sediment and sandy sediment conceptual environments. Lastly, when site-specific and literature values were not available, expert judgement was used to estimate values based on chemical analogue information. For example, no site-specific sorption data is available for Fr and Rb; however, substantial SRS sediment sorption data for Cs are available. Cs, Fr, and Rb share many similar chemical characteristics, including the fact that all three are Group 1A elements having a valence of 1 and oxidation state of +1. As a result, they form weak complexes with anions and exist in GW primarily as uncomplexed monovalent free ions (Greenwood and Earnshaw,

1998). For these reasons, K_d values for Fr and Rb were assumed to be approximated by and therefore equal to the measured K_d values for Cs in SRS sediments.

In summary, the ranked priority for selecting K_d and k_s values is:

1. Site-specific measured data
2. Literature experimental data
3. Technical judgment based on analogue

Uncertainty in the selected "best" values is bounded by "minimum" and "maximum" estimates based on experimental data reported by Grogan (2008), Grogan et al. (2010), and Kaplan et al. (2008). "Minimum" and "maximum" values are reported in the data package to provide ranges of potential values needed for sensitivity and uncertainty analysis. The experimental data consist of hundreds of K_d measurements for monovalent, divalent, trivalent and tetravalent radionuclides from 27 E-Area subsurface sediments. The data yielded statistical distributions for the sample means (K_d values) and the 95% confidence intervals, which served as the basis for the "minimum" and "maximum" estimates.

3.8.2.5. Sediment Conceptual Environments

The subsurface environments beneath the DUs at SRS are assumed to consist of two primary geological strata based on analysis by Nichols and Butcher (2020) of particle-size distribution data and observations of several E-Area borehole specimens. Nichols and Butcher (2020) described the upper strata as extending about 25 feet below the surface and having a finer texture than the lower strata, which may extend some 90 feet below ground surface depending on the specifics of the site lithology. The upper 25-foot layer was referred to as the UVZ, while the lower 65 feet included both the LVZ and the Aquifer Zone. The water table in E-Area and Z-Area is approximately 50 to 80 feet below the ground surface. An example of the sediment texture and the delineation of the UVZ, LVZ, and Aquifer Zone is presented in Figure 3-92. The unique K_d values for Clayey Sediment and Sandy Sediment in the *GeoChem Data Package* are meant to represent the UVZ and LVZ/Aquifer Zone, respectively.

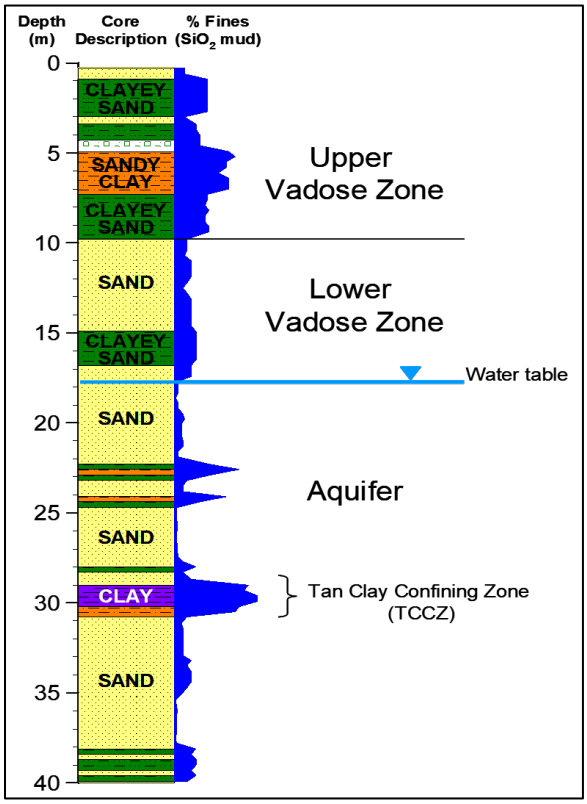

Figure 3-92. Borehole Profile for E-Area Well BGO-3A Demonstrating Tendency for Sediments With More Clayey Texture to Exist in Upper Vadose Zone, Whereas Sediments with Sandier Texture Exist in Lower Vadose Zone and Aquifer Zone (Grogan, 2008; Grogan et al., 2010)

3.8.2.5.1. Clayey Sediment Conceptual Environment

The Clayey Sediment Conceptual Environment represents a subsurface sediment environment with clay and silt content greater than about 25 wt%; mineralogy composed primarily of kaolinite, hydroxy-interlayered vermiculite, quartz, gibbsite, goethite, and hematite (most notable is the very low concentrations of 2:1 clay minerals such as smectites and vermiculites); low organic matter content (<0.01 wt%); pH ~5.5; iron-oxide surface coatings that give it a reddish color.

3.8.2.5.2. Sandy Sediment Conceptual Environment

The Sandy Sediment Conceptual Environment represents a subsurface sediment environment that is like the Clayey Sediment except that the clay and silt content is less than 25 wt%. Most sorption data considered for the *GeoChem Data Package* originated from sandy sediments with clay and silt concentrations appreciably less than 25 wt% (closer to 2 to 8 wt%). The Sandy Sediment Conceptual Environment has a pH of 5.5, very low organic matter content, and the sediment tends to have a yellowish color derived from Fe-oxide coatings (most noticeably, goethite).

3.8.2.5.3. Cementitious Materials Conceptual Environments

The conceptual model describing radionuclide geochemistry in cementitious environments is largely based on work by Bradbury and Sarott (1995) who describe three conceptual environments

(stages) that all cementitious materials progress through as they age (Figure 3-93).[16] The three stages represent the progression that essentially all cementitious materials undergo as they age. The duration of each stage is controlled by how much water passes through them, measured in units of pore volumes or exchange cycles (x-axis of Figure 3-93). The advantage of using Figure 3-93, with the concept of exchange cycles, is that it is generic to a wide range of cementitious material configurations. Once flow models have been established for a specific facility, the exchange cycles can be quantified. Facilities with more concrete will have longer exchange cycles (i.e., more pore volumes) than those with less concrete.

Development of the Bradbury and Sarott (1995) conceptual model was based on laboratory studies as well as on natural analogue and ancient cement/concrete characterization studies. One of the key aqueous parameters used to identify when one stage ends and the next one begins is pH (Figure 3-93). The pH changes are the result of mineralogical transformations that occur as cement ages. The cement solids present in each stage are assumed to have unique sorption properties; therefore, unique K_d and k_s values were assigned to the cement solids in each stage.

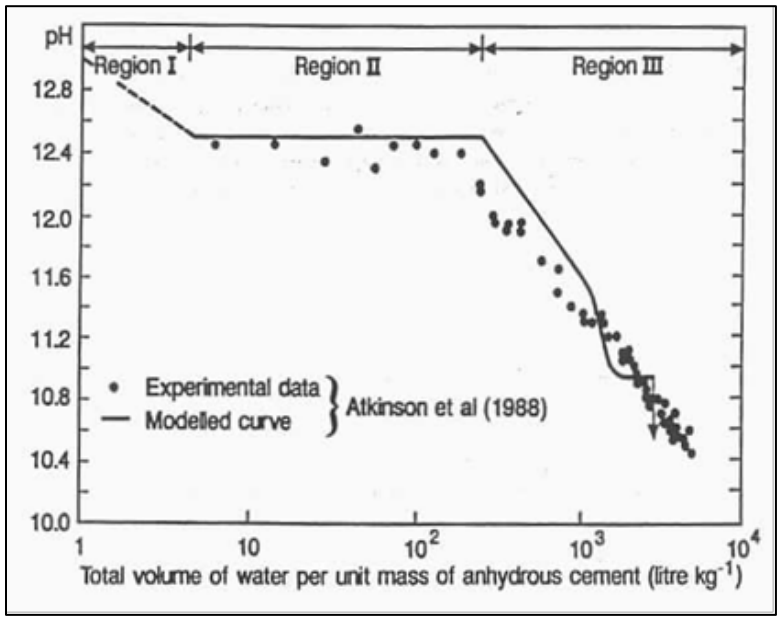

Figure 3-93. Conceptual Model Used by Bradbury and Sarott (1995) Describing Influence of Exchange Cycles (x-axis) on pH and Designated Stages or Regions (Atkinson et al., 1988)

Young Cementitious Materials Conceptual Environment (Stage I)

The Young Cementitious Solids Conceptual Environment (Stage I) occurs immediately after the cementitious material hardens and infiltrating water enters. The cementitious material porewater is characterized as having a high pH (>12.5), high ionic strength, and high concentrations of potassium and sodium. The high concentrations of these monovalent cations result from the dissolution of alkali impurities in the various constituents comprising the solids (e.g., Portland cement, fly ash, aggregate and sometimes slag). Hydration continues during Stage I with the

[16] More recently, a fourth stage has been included (Ochs et al., 2016; Wang et al., 2009) that is experimentally indistinguishable from the cementitious-leachate-impacted sediment environments described below.

formation of calcium-silicate-hydrate gels (CSH, which is a CaO-SiO_2-H_2O amorphous material that hardens and constitutes "cement") and portlandite [$Ca(OH)_2$]. The composition of the cement pore fluid is at equilibrium with portlandite during this time, which accounts for the high pH. Stage I may last from 1 to 100 exchange cycles (Berner, 1992).[17] Assuming a low number of exchange cycles for Stage I will be conservative for some constituents of concern, such as Pb, but will not be conservative for other constituents of concern that form precipitates at high pH (i.e., constituents of concern with a low solubility). Absent a project-specific value, Stage I is assumed to last 50 exchange cycles for SRS-relevant scenarios.

Moderately Aged Cementitious Materials Conceptual Environment (Stage II)

During Stage II, soluble salts of the alkali metals have completely dissolved and washed out of the cement solids. The pH of the cement pore water stabilizes around 12.5, controlled by the solubility of portlandite. CSH gel and portlandite are the major solid phases present. The duration of Stage II depends on how much water percolates through the system as well as the mass of cement present in the concrete structure. Total dissolved calcium is constant at ~20 mM, pH is strongly buffered at pH ~12.5, and the silica concentration is <0.03 mM. Infiltrating water must dissolve all slightly soluble portlandite before the leachate chemistry will change.

Berner (1992) determined that Stage II lasts between 100 and 1,000 exchange cycles. According to Ochs et al. (2016) and adopted here, most radionuclides have higher K_d values and solubility concentration limits in Stage II than in Stage III. Therefore, a shorter Stage II lifespan is conservative. Stage II K_d and k_s values are also generally higher than those for Stage I.[18] Considering the slightly greater dissolution capacity of low-carbonate SRS GW when in contact with cementitious solids, 500 exchange cycles were assumed for Stage II.

Aged Cementitious Materials Conceptual Environment (Stage III)

In Stage III, portlandite has been fully dissolved/reacted and the solubility or reactions of CSH gel with the infiltrating water control the pH of the cement porewater/leachate (Figure 3-93). CSH gel begins to dissolve incongruently, marked by a continual decrease in pH until it reaches the pH of the background sediment (pH 5.5 at SRS). At the beginning of Stage III, CSH gel has a calcium:silicate ratio of about 1.7; by the end of Stage III, only silicate remains (SiO_2) as the solubility control for porewater pH. The ionic strength of the cement leachate during this period is relatively low. Solution calcium concentrations drop from 20 mM to 1-5 mM while silica concentrations increase from <0.03 mM to 2-6 mM. When the number of exchange cycles is very high, other sparingly soluble solids, such as brucite [$Mg(OH)_2$], may buffer the solution pH and dissolved cation concentrations. Berner (1992) suggested that the duration of Stage III ranges from 1,000 to 10,000 exchange cycles. Because SRS GW is low in carbonate, a Stage III duration of

[17] An exchange cycle is a unitless parameter that represents the length of time it takes for a pore volume to pass through a cementitious structure. This parameter can be quickly converted into units of time once the water travel rate through a specific cementitious facility is established.
[18] Notable exceptions include when cation (Sr) or anion (I, Tc, Se) adsorption are expected to be the dominant mode of solid-phase uptake, in which case K_d values in Stage I will be lower than in Stage II because of the high salt concentration in the porewater.

4,000 cycles was selected for SRS PA calculations. A discussion of estimating concrete longevity in the subsurface is given by Kaplan (2010).

Cementitious-Leachate-Impacted Clayey Sediment Environment

Cement porewater contains moderate levels of dissolved solids. When it enters the underlying sediment, porewater chemistry is altered and the mobility of aqueous radionuclides sorbed onto the sediment may be impacted. To demonstrate this point under SRS conditions, thermodynamic simulations were conducted of the porewater chemistry during each of the three idealized stages of cement aging (Denham, 2009). During Stages I, II, and III, portlandite, CSH gel, and calcite, respectively, were assumed to be the dominant solid phases controlling aqueous composition. Denham (2009) notes that the pH and ionic strength during early Stages I and II are much higher than background SRS GW. Such background solutions can increase sorption by promoting precipitation (e.g., UO_2^{2+}) or, in other cases, decrease sorption by promoting competition for sorption sites (e.g., anionic species such as SeO_4^{2-} and SeO_3^{2-}). Kaplan (2010) calculated that hydroxides emanating from cementitious leachate during Stages I and II of concrete degradation (pH 11, ionic strength 20 mM) will likely overwhelm the buffering capacity of SRS subsurface VZ sediments. For example, a 1-m thick cementitious slab overwhelmed the sediment buffering capacity of a 30-meter thick VZ. Once the high-pH front reached the aquifer zone, it would be rapidly diluted and likely have negligible influence on subsequent sorption of the constituents of concern. Kaplan (2016b) provides a more in-depth discussion of the impact of pH, ionic strength, and nuclide speciation on radionuclide mobility in sediments.

The Cementitious-Leachate-Impacted Clayey Sediment Conceptual Environment is defined as a Clayey Sediment Conceptual Environment located between a cementitious waste form and the aquifer. This conceptual environment has a nominal pH of 10.5 and an elevated ionic strength of >20 mM dominated by hydroxide and Ca^{2+} ions. The Cementitious Leachate Impact Factor, $f_{CementLeach}$, is given by Eq. (3-41) and is used to convert traditional K_d values into $K_{d\ CementLeach}$ values that are more representative of a cementitious-impacted sediment:

$$f_{CementLeach} = \frac{K_{d\ CementLeach}}{K_d} \qquad \text{Eq. (3-41)}$$

where $K_{d\ CementLeach}$ and K_d are measured under cementitious-leachate and natural GW conditions, respectively. For purposes of the PA modeling, Eq. (3-41) was rearranged to give:

$$K_{d\ CementLeach} = f_{CementLeach} \times K_d \qquad \text{Eq. (3-42)}$$

It is important to recognize that the $f_{CementLeach}$ is a simplified construct for a complex and dynamic PA environment;[19] a construct that can be made more robust with additional site-specific

[19] Complexity stems from: (1) there are several different types of cementitious materials of interest to PAs (reducing grout, Saltstone, CLSM, traditional concrete, high-strength concrete, etc.); (2) leachate chemistry is expected to change over time; (3) the impact of cementitious leachate on traditional K_d values will vary with soil properties.

measurements. Kaplan (2016b) provides in-depth discussion of site-specific studies undertaken since PA2008 to improve estimates of SRS-relevant $f_{CementLeach}$ values. Values for $f_{CementLeach}$ in the current *GeoChem Data Package* are largely based on the original recommended values reported by Kaplan (2010).

Cementitious-Leachate-Impacted Sandy Sediment Environment

Similar to the Cementitious-Leachate-Impacted Clayey Sediment Environment above, the Cementitious-Leachate-Impacted Sandy Sediment Environment addresses the lower Sandy Sediment Conceptual Environment that exists between cementitious waste forms and the aquifer. Values for $K_{d\ CementLeach}$ are similarly calculated using Eq. (3-42); however, in this case, K_d values for Sandy Sediment are used along with the identical $f_{CementLeach}$ values reported in the *GeoChem Data Package*.

3.8.2.5.4. Reducing Cementitious Materials

Some cementitious materials have blast-furnace slag (BFS) included in their formulations to promote stabilization of certain redox-sensitive radionuclides (e.g., Np, Pu, and Tc) by reductive precipitation, thus decreasing their tendency to leach from the solid waste form. The reductive capacity of the BFS-cementitious material is expected to decrease over time. As the waste form ages and becomes increasingly oxidized, it is expected that the capacity of the waste form to immobilize targeted contaminants will decrease. Kaplan (2016b) provides a summary of recent studies evaluating the effect of reducing cementitious materials on Tc immobilization, a key risk driver in several PAs. Kaplan (2016b) also introduces the Shrinking Core Model which simulates the advancement of an oxidized front resulting from oxidized porewater diffusing into the cement and then chemically consuming (oxidizing) the unspecified reductant in the reducing cementitious material. The reducing cementitious materials are assigned a unique set of K_d and k_s values for each radionuclide, which for the ELLWF PA, are relevant to the LAWV and ILV VZ transport models. In general, less mobile radionuclides lead to less dose exposure at the POAs, which is considered to be a more favorable response.

Young Reducing Cementitious Solids Conceptual Environment (Stage I)

This environment is conceptually identical to that of the Young Cementitious Solids (Stage I) Conceptual Environment (Section 3.8.2.5.3) except for the addition of BFS. The BFS creates a reducing environment that promotes the reduction of several radionuclides, including Pu and Tc. The reduced forms of these radionuclides are less mobile, leading to more favorable K_d and k_s values.

Moderately Aged Reducing Cementitious Solids Conceptual Environment (Stage II)

This environment is conceptually identical to that of the Moderately-Aged Cementitious Solids (Stage II) Conceptual Environment (Section 3.8.2.5.3) except for the addition of BFS. As with the Stage I reduced cementitious solids, the reduced forms of certain redox-active radionuclides of interest are less mobile, leading to more favorable K_d and k_s values.

Aged Reducing Cementitious Solids Conceptual Environment (Stage III)

This environment is conceptually identical to that of the Aged Cementitious Solids (Stage III) Conceptual Environment (Section 3.8.2.5.3) except for the addition of BFS. As with the Stage I and Stage II reduced cementitious solids, the reduced forms of certain redox-active radionuclides of interest are less mobile, leading to more favorable K_d and k_s values.

3.8.2.5.5. Radionuclide Leaching from Waste Materials

Radioactive waste materials are disposed at SRS in several different forms, and once disposed in the subsurface, become the source terms for radionuclides entering the environment. For this reason, the mechanisms by which radionuclides sorb and desorb from these materials are important. Little is known about how radionuclides interact with the large number of buried solid waste phases; therefore, the following simplified assumptions were made. Unless waste-specific data are available, partitioning of a radionuclide to the waste material is assumed to be similar to partitioning of the same radionuclide to the sediment in contact with the waste. For example, the leaching rate of Th associated with lumber disposed in STs is calculated using the reported K_d for Th in Clayey Sediment, which is the solid phase in contact with the lumber.

3.8.2.5.6. Radionuclide Leaching from Special Waste Forms

The extent to which radionuclides desorb from special waste forms can be estimated using K_d and k_s values for sorption (i.e., the use of K_d and k_s values to estimate desorption is simply the reverse of adsorption). A key assumption in the K_d construct is that sorption is fully reversible, meaning that adsorption and desorption occur at the same rate.

Only a limited number of waste-specific K_d and k_s values are available for ELLWF special waste forms. These include measured K_d values for I-129, C-14, and Tc-99 sorption/desorption from SRS activated carbon, anionic resins, and water treatment facility filtercakes reported by Kaplan and Coffey (2002), Kaplan and Iversen (2001), Kaplan and Serkiz (2000), and Kaplan et al. (1999).

3.8.2.6. Geochemical Parameters' Ranges and Distributions

Associated with the "best" K_d and k_s values are parameters that address the expected variability associated with these parameters. The distribution and range of the K_d parameters are important for stochastic modeling. Additionally, the lower 95% confidence interval value also provides a likely minimum, or conservative estimate, for the GW pathway. The range and distribution of K_d values for Am, Cd, Cs, Ce, Co, Hg, Sr, Sn, Tc, and Y were measured in 27 SRS sediments (triplicate measurements resulting in 81 K_d measurements per element and 810 in total) collected from the subsurface VZ and aquifer zone of E-Area (Grogan, 2008; Grogan et al., 2010; Kaplan et al., 2008). The statistical ranges and distributions of these K_d values were reported by Grogan (2008) and Kaplan et al. (2008), while the implication of the distributions and a depiction of the results of the normal and log-normal distributions are presented by Grogan et al. (2010).

The 95th-percentile range and type of distributions assigned to radionuclide K_d values should be assigned based on general rules derived from the measurements by Grogan (2008), some geochemical/geological considerations, and parsimony.

- K_d distributions were most closely log-normal for the entire set of 27 samples taken from an E-Area well borehole.
- The width of the 95% confidence interval for the estimated mean K_d was twice the mean in the Aquifer Zone (16.5 to 30.3 meter depth – Sandy Sediment Environment), equal to the mean for the UVZ (3.3 to 9.8 meter depth – Clayey Sediment Environment), and half the mean for the LVZ (9.8 to 16.5 meter depth – Sandy Sediment Environment).
- The distribution of K_d values was log normal in the UVZ and Aquifer Zone but normal in the LVZ.

Based on these findings, K_d distributions and ranges were estimated for each of the various conceptual environments. No data are presently available to calculate ranges and distributions of K_d values for cementitious environments or for k_s values; therefore, their ranges and distributions were assumed to be similar to the ranges and distributions of K_d values for sandy and clayey sediments.

3.8.2.6.1. Distribution and Ranges for Mean K_d Values in Sandy Sediment Environments

For the Sandy Sediment Conceptual Environments (including the Cementitious-Leachate-Impacted Sandy Sediment Environment) that are dominant in the Aquifer Zone and LVZ, the 95% confidence interval for the mean K_d is assumed to be 1.5 times the mean, which is an approximate, weighted combination of the recommended multiplying factors for the Aquifer Zone and the LVZ. The minimum (*Min*) and maximum (*Max*) K_d values are given by: [20]

$$K_{d\,Min} = K_d - \left(1.5 \times 0.5 \times K_d\right) \cong 0.3K_d \qquad \text{Eq. (3-43)}$$

$$K_{d\,Max} = K_d + \left(1.5 \times 0.5 \times K_d\right) \cong 1.8K_d \qquad \text{Eq. (3-44)}$$

where the 0.5 multiplier in both equations is to account for half the 95% confidence interval width upon which the 1.5 factor is based. Although the sample distributions were assumed to be log-normal (Grogan, 2008; Kaplan et al., 2008), the distribution of the sample mean K_d is assumed to be normal based on the central limit theorem. The functional form chosen conforms to data collected for a wide range of species.

3.8.2.6.2. Distribution and Ranges for Mean K_d Values in Clayey Sediment Environments

For the Clayey Sediment Conceptual Environments (including the Cementitious-Leachate-Impacted Clayey Sediment Environment) that are dominant in the UVZ, the 95% confidence interval for the mean K_d is assumed to be 1.0 times the mean, which corresponds to the value recommended by Grogan (2008) for the UVZ. The minimum (*Min*) and maximum (*Max*) K_d values are given by:

$$K_{d\,Min} = K_d - \left(1.0 \times 0.5 \times K_d\right) \cong 0.5K_d \qquad \text{Eq. (3-45)}$$

$$K_{d\,Max} = K_d + \left(1.0 \times 0.5 \times K_d\right) \cong 1.5K_d \qquad \text{Eq. (3-46)}$$

[20] The values of the multipliers (0.3 and 1.8, respectively) in Eq. (3-43) and Eq. (3-44) were originally reported by Grogan (2008) with one additional significant figure (0.25 and 1.75, respectively).

where the 0.5 multiplier in both equations is to account for half the 95% confidence interval width upon which the 1.0 factor is based.

Although the sample distributions were assumed to be log-normal (Grogan, 2008; Kaplan et al., 2008), the distribution of the sample mean K_d is assumed to be normal based on the central limit theorem. The functional form chosen conforms to data collected for a wide range of species.

3.8.2.6.3. Distribution and Ranges for Mean K_d Values in Cementitious Environments

For cementitious conceptual environments, the range is assumed to be the same as for the Sandy Sediment Conceptual Environments as given by Eq. (3-43) and Eq. (3-44). The distributions are assumed to be log-normal (Almond et al., 2012).

3.8.2.6.4. Distribution and Ranges for Apparent Solubility Values in Cementitious Environments

Apparent solubility values were assumed to have a range of two orders of magnitude and to be log-normally distributed. For example, a constituent of concern with a k_s value of 10^{-9} M would have a $k_s(min)$ of 10^{-10} M and a $k_s(max)$ of 10^{-8} M.

3.8.3. Material and Hydraulic Properties

The *Hydraulic Properties Data Package, Rev. 3, dated December 1, 2020* (SRNL, 2020) refers to the SRNL-compiled and -maintained Microsoft Excel database of material and hydraulic properties estimates for soils, cementitious materials, and waste zones associated with DUs included in the ELLWF PA. The technical report detailing the development and content of the Hydraulic Properties Data Package is *Hydraulic Properties Data Package for the E-Area Soils, Cementitious Materials, and Waste Zones – Update* by Nichols and Butcher (2020), which builds upon previous work by Phifer et al. (2006) in support of PA2008.

Nominal or "best estimate" material and hydraulic property values for use in deterministic and uncertainty quantification and sensitivity analysis (UQSA) models are provided by Nichols and Butcher (2020) and SRNL (2020), along with representations of the material and hydraulic property value uncertainties for use in the UQSA. The properties provided for ELLWF materials include:

- Material properties such as total and effective porosities (η), dry bulk density (ρ_b), and particle density (ρ_p).
- Hydraulic properties such as horizontal and vertical saturated hydraulic conductivities (K_h and K_v, respectively).
- Water retention curves (WRCs) represented by the complete set of van Genuchten (VG) parameters (θ_s, θ_r, α, n, and m). [21] For certain blended mixtures, tabular data are employed directly.
- Saturated effective diffusion coefficients (D_e).

[21] The water retention characteristics of sediments are commonly represented by WRCs based on a closed form equation published by van Genuchten (1980). The VG equation relates water content (θ), and thus water saturation (S), to pressure head (ψ) which can be used with laboratory data to determine the VG parameters for a WRC.

- Unsaturated soil properties for materials employed in the various VZ models including the UVZ, LVZ, CCB, ILV backfill, OSC, and gravel.[22]
- Unsaturated cementitious properties used in models of the LAWV, ILV, CIG trench segments, concrete rubble, etc.
- Saturated aquifer soil properties, including sand and clay material properties and saturated effective diffusion coefficients, used in the aquifer flow models. Aquifer hydraulic conductivities are not explicitly provided in the Hydraulic Properties Data Package (SRNL, 2020). Aquifer sand and clay hydraulic conductivities are estimated using the PEST (Watermark Numerical Computing, 2016) optimization process while calibrating the PORFLOW GSA flow model. The final set of aquifer hydraulic conductivity values are computed during the GSA_2021 flow model recalibration efforts (Section 3.5.2.12).
- Soil and waste zone properties before and after dynamic compaction for STs and ETs.
- Blended waste zone properties where more than one material type (e.g., bulk waste and containerized waste) exists within a single waste zone.

A representation of the uncertainty associated with each property, excluding the WRCs, is provided for each material except for the ELLWF waste zones. The nominal (typically assumed to be best estimate) parameter values and parameter uncertainty representations for each of the ELLWF soils, cementitious materials, and waste zones are based upon the following in priority order:

- Site-specific field data
- Site-specific laboratory data
- Similarity to material with site-specific field or laboratory data
- Literature data

Uncertainty in the property values for total porosity, dry bulk density, and particle density are derived through arithmetic averaging and calculation of the standard error of the mean.[23] Uncertainty in recommended nominal values derived through non-linear averaging processes (K_{sat}) or solely from literature-based values (D_e) is estimated using Monte Carlo (MC) simulation. In MC simulation, numerous realizations are generated by randomly sampling the statistical distributions of input parameters and computing sample statistics from the corresponding output values. For this PA, 10,000 realizations are generated in each MC simulation so that the sample statistics are sufficiently reliable. MC simulations are performed using the GoldSim® software (GoldSim Technology Group, 2018a).

Uncertainty in the sample of small-scale conductivity measurements is addressed using a bootstrapping technique (Efron, 1982). In the bootstrap approach, the data sample is used as a

[22] Pure sand and pure clay are included in the Hydraulic Properties Data Package (SRNL, 2020) but they were not explicitly used in the PORFLOW and GoldSim® models.
[23] Uncertainty in the property values is derived through arithmetic averaging of material property data for n samples to generate a sample mean ($\bar{x}$), sample standard deviation (σ), and standard error of the mean (SE) using the equation $SE = \sigma / \sqrt{n}$.

surrogate for the true underlying population. Sample realizations are generated by randomly resampling the actual sample with replacement. For effective/equivalent K_h and K_v, uncertain inputs to the analysis are the averaging exponents, p_h and p_v, and the sample of small-scale or "point" conductivity measurements.

The tables developed by Nichols and Butcher (2020) and listed below provide nominal parameter values and parameter uncertainty representation for ELLWF soils of interest in this PA.

- Table 3-52 – Recommended Soil Properties for ELLWF PA Models.[24]
- Table 3-53 – UQSA Summary Statistics for Total Porosity. [24]
- Table 3-54 – UQSA Summary Statistics for Bulk Density. [24]
- Table 3-55 – UQSA Summary Statistics for Particle Density. [24]
- Table 3-56 – UQSA Summary Statistics for Saturated Hydraulic Conductivity.[25]
- Table 3-57 – UQSA Summary Statistics for Saturated Effective Diffusion Coefficient.,[26]

Similarly, the tables developed by Nichols and Butcher (2020) and listed below provide nominal parameter values and parameter uncertainty representation for ELLWF cementitious materials of interest in this PA.

- Table 3-58 – Recommended Material Properties for Cementitious Materials in the Various Types of Disposal Units.
- Table 3-59 – Cementitious Material Uncertainty Summary Statistics for Effective Porosity.
- Table 3-60 – Cementitious Material Uncertainty Summary Statistics for Dry Bulk Density.
- Table 3-61 – Cementitious Material Uncertainty Summary Statistics for Particle Density.
- Table 3-62 – Cementitious Material Uncertainty Summary Statistics for Saturated Hydraulic Conductivity.
- Table 3-63 – Cementitious Material Uncertainty Summary Statistics for Saturated Effective Diffusion Coefficient.

Table 3-64 provides the recommended waste zone representation for each of the ELLWF DUs. An explicit uncertainty representation for the ELLWF DU waste zones is not provided because of the absence of reliable data from which to derive such a representation.

[24] The properties are based primarily on available property data for soils in the vicinity of the ELLWF DUs. In some cases, data from Z-Area (Saltstone) at SRS are also incorporated into the evaluation. Data sources are specified in the table columns labeled “Source.”

[25] Table 3-56 summarizes sample statistics derived through MC simulation. Log-normal distributions are observed to be reasonable representations of the MC probability distributions for hydraulic conductivity and the saturated effective diffusion coefficient. The mean values for hydraulic conductivity are very close, if not identical to, the deterministic values reported by Nichols and Butcher (2020; Table 5-7), suggesting that 10,000 MC realizations are sufficient to produce reliable uncertainty statistics.

[26] The molecular diffusion coefficient is assumed to be well known and only tortuosity is randomly varied in MC simulations. Uncertainty in each tortuosity value is represented by a truncated normal distribution with a mean value defined by Table 3-57, a standard deviation of 0.5, and truncation limits at ±1.5 (3σ) about the mean.

Table 3-52. Recommended Soil Properties for E-Area Low-Level Waste Facility Performance Assessment Models (Nichols and Butcher, 2020; Table 5-20)

Material	Saturated Hydraulic Conductivity				Bulk Properties					
	K_h (cm s^{-1})	K_v (cm s^{-1})	K_h/K_v	Source	Saturated Effective Diffusion Coefficient, D_e (cm^2 s^{-1})	Source	Total Porosity (unitless)	Dry Bulk Density (g cm^{-3})	Particle Density (g cm^{-3})	Source
Upper Vadose Zone (Above 264 ft-msl in E-Area)	6.2E-05	8.7E-06	7.1	a	5.3E-06	k	0.385	1.65	2.69	h
Lower Vadose Zone (Below 264 ft-msl in E-Area)	3.3E-04	9.1E-05	3.6	a	5.3E-06	k	0.380	1.66	2.67	h
E-Area Operational Soil Cover Before Dynamic Compaction	1.3E-04	1.3E-04	1.0	d	5.3E-06	k	0.456	1.44	2.65	i
E-Area Operational Soil Cover after Dynamic Compaction	1.6E-05	1.6E-05	1.0	f	4.0E-06	k	0.275	1.92	2.65	i
Controlled Compacted Backfill	7.6E-05	4.1E-05	1.9	c	5.3E-06	k	0.355	1.71	2.65	h
ILV Permeable Backfill	1.4E-03	7.6E-04	1.9	g	8.0E-06	k	0.415	1.56	2.67	g
Sand (<25% Mud)	5.0E-04	2.8E-04	1.8	b	8.0E-06	k	0.383	1.65	2.67	h
Clay-Sand (25-50% Mud)	8.3E-05	2.1E-05	4.0	b	5.3E-06	k	0.374	1.68	2.69	h
Clay (>50% Mud)	2.0E-06	9.5E-07	2.1	b	4.0E-06	k	0.433	1.52	2.68	h
Gravel	1.5E-01	1.5E-01	1.0	e	9.4E-06	k	0.300	1.82	2.60	j
Saturated Zone Soils	--	--	--	o	Sand: 5.3E-06 Clay: 4.0E-06	p	0.25	1.04	1.39	p

Material	Water Retention Curve Parameters					
	θ_s	θ_r	α	n	m	Source
Upper Vadose Zone (Above 264 ft-msl in E-Area)	0.385000	0.102446	0.030177	1.153676	0.133205	l
Lower Vadose Zone (Below 264 ft-msl in E-Area)	0.380000	0.077849	0.167698	1.195226	0.163338	l
E-Area Operational Soil Cover Prior to Dynamic Compaction	0.456000	0.121330	0.040416	1.153656	0.133191	n
E-Area Operational Soil Cover after Dynamic Compaction	0.275000	0.073171	0.018263	1.153659	0.133193	n
Controlled Compacted Backfill	0.355000	0.198349	0.037124	1.463642	0.316773	m
ILV Permeable Backfill	0.415000	0.136697	0.037919	1.724947	0.420272	m
Sand (<25% Mud)	0.383000	0.082137	0.199006	1.241769	0.194697	m
Clay-Sand (25-50% Mud)	0.374000	0.057974	0.035465	1.140621	0.123285	m
Clay (>50% Mud)	0.433000	0.278156	0.009832	1.287965	0.223581	m
Gravel	0.300000	0.021000	0.137676	1.479624	0.324153	m
Saturated Zone Soils	--	--	--	--	--	n/a

Notes:

a Based on 2σ of MegacptN/ATN location and sample; using CPT to define thickness and textural properties; averaging based on textural properties ("clay," "clay-sand," and "sand") and thickness and using combination of arithmetic and geometric averaging (p_v = -0.33 and p_h = 0.59).

b Based on 2σ; uses "most reliable" data (based on comparing bulk density); averaging uses combination of arithmetic and geometric averaging (p_v = -0.33 and p_h = 0.59).

c Uses all samples from ORWBG and Z-Area composite samples; averaging uses combination of arithmetic and geometric averaging (p_v = -0.33 and p_h = 0.59).

d Based on Kozeny-Carman equation, Upper Zone porosity and hydraulic conductivity, assumed bulk density of operational soil cover of 90 pcf, and bulk density of 2.65 g cm^{-3} (calculated porosity of 0.456); the three ETs planned for Plot 8 are assumed to be backfilled with LVZ soils due to the absence of a UVZ in this vicinity; therefore, will need to use the same analysis (Kozeny-Carman equation) described by Nichols and Butcher (2020; Section 5.4.1) for estimating hydraulic conductivity for Plot 8 OSC before dynamic compaction.

e Based on straight arithmetic average of two samples [GL-1 and GL-2 from WSRC-RP-93-894 (Yu et al., 1993)].

f Based on Kozeny-Carman equation, Upper Zone porosity and hydraulic conductivity, assumed bulk density of operational soil cover of 120 pcf, and bulk density of 2.65 g cm^{-3} (calculated porosity of 0.27); the three ETs planned for Plot 8 are assumed to be backfilled with LVZ soils due to the absence of a UVZ in this vicinity; therefore, will need to use the same analysis (Kozeny-Carman equation) described by Nichols and Butcher (2020; Section 5.4.1) for estimating hydraulic conductivity for Plot 8 OSC after dynamic compaction.

g Based on straight arithmetic average of two samples (VL-1 44-46 and VL-1 13-15; samples with < 15% mud) with K_h/K_v = 1.9 (based upon CCB).

h Based on straight arithmetic average of all samples (used most reliable data from hydraulic conductivity standpoint).

i (Phifer and Wilhite, 2001) used as reference for bulk density of operational cover before (90pcf) and after (120pcf) dynamic compaction; particle density based on Hillel (1982).

j Used Freeze and Cherry (1979; Groundwater) and Dutro et al. (1989; AGI Data Sheets) to come up with an estimate of porosity and particle density (calculated bulk density from these values).

k Based on literature values of tortuosity and molecular diffusion coefficients.

l Used CPT to define thickness and textural properties at MegacptN/ATN location; averaged textural property curves ("clay," "clay-sand," and "sand") based on the proportion of each in the upper zone, lower zone, and single zone.

m Averaging of all reliable samples; samples for the CCB come from ORWBG and Z-Area composite samples; gravel samples include GL-1 and GL-2 curves [WSRC-RP-93-894 by Yu et al. (1993)]; ILV permeable backfill includes VL-1 44-46 and VL-1 13-15.

n Used Upper Zone and adjusted suction head based on estimated porosity and estimated hydraulic conductivity (Leverett scaling).

o Refer to Flach and Harris (1997) and Flach et al. (2004).

p Refer to discussion by Nichols and Butcher (2020; Section 5.6, Saturated Zone); porosity, dry bulk density, and particle density values are the “effective” values.

Table 3-53. UQSA Summary Statistics for Total Porosity (unitless) (Nichols and Butcher, 2020; Table 5-17)

Material	Upper Vadose Zone	Lower Vadose Zone	"SAND"	"CLAY-SAND"	"CLAY"	Operational Soil Cover (before DC)[1]	Operational Soil Cover (after DC)[1]	Controlled Compacted Backfill	ILV Permeable Backfill[2]	Gravel[3]
Type of Distribution	Normal	Normal	Normal	Normal	Normal	Normal	Normal	Normal	Normal	Normal
Min (3σ)	0.23	0.26	0.29	0.23	0.31	0.31	0.12	0.24	0.32	0.21
Max (3σ)	0.54	0.50	0.47	0.52	0.56	0.61	0.42	0.47	0.50	0.39
Variance of Sample Mean	2.54E-03	1.69E-03	9.22E-04	2.43E-03	1.78E-03	2.54E-03	2.54E-03	1.40E-03	9.22E-04	9.22E-04
Standard Deviation of Sample Mean	5.04E-02	4.11E-02	3.04E-02	4.93E-02	4.21E-02	5.04E-02	5.04E-02	3.75E-02	3.04E-02	3.04E-02
Mean	0.39	0.38	0.38	0.37	0.43	0.46	0.27	0.35	0.41	0.30
Count	23	21	15	19	7	n/a	n/a	19	n/a	n/a

Table 3-54. UQSA Summary Statistics for Bulk Density (g cm^{-3}) (Nichols and Butcher, 2020; Table 5-17)

Material	Upper Vadose Zone	Lower Vadose Zone	"SAND"	"CLAY-SAND"	"CLAY"	Operational Soil Cover (before DC)[1]	Operational Soil Cover (after DC)[1]	Controlled Compacted Backfill	ILV Permeable Backfill[2]	Gravel[3]
Type of Distribution	Normal	Normal	Normal	Normal	Normal	Normal	Normal	Normal	Normal	Normal
Min (3σ)	1.24	1.35	1.40	1.32	1.16	1.03	1.51	1.42	1.31	1.57
Max (3σ)	2.06	1.97	1.90	2.05	1.89	1.85	2.33	2.00	1.81	2.07
Variance of Sample Mean	1.88E-02	1.04E-02	6.95E-03	1.48E-02	1.48E-02	1.88E-02	1.88E-02	9.43E-03	6.95E-03	6.95E-03
Standard Deviation of Sample Mean	1.37E-01	1.02E-01	8.34E-02	1.22E-01	1.22E-01	1.37E-01	1.37E-01	9.71E-02	8.34E-02	8.34E-02
Mean	1.65	1.66	1.65	1.68	1.52	1.44	1.92	1.71	1.56	1.82
Count	23	21	15	19	7	n/a	n/a	19	n/a	n/a

Notes:

1 No data is available for the operational soil cover; assumed to have same standard deviation as the UVZ; DC=dynamic compaction.

2 Mean value based on two measurements; type of distribution, variance, and standard deviation are assumed to be same as “sand.”

3 Little data are available for the gravel; assumed to have same standard deviation as "sand."

Table 3-55. UQSA Summary Statistics for Particle Density (g cm^{-3}) (Nichols and Butcher, 2020; Table 5-17)

Material	Upper Vadose Zone	Lower Vadose Zone	"SAND"	"CLAY-SAND"	"CLAY"	Operational Soil Cover (before DC)[1]	Operational Soil Cover (after DC)[1]	Controlled Compacted Backfill	ILV Permeable Backfill[2]	Gravel[3]
Type of Distribution	Normal	Normal	Normal	Normal	Normal	Normal	Normal	Normal	Normal	Normal
Min (3σ)	2.61	2.54	2.60	2.56	2.58	2.57	2.57	2.60	2.60	2.53
Max (3σ)	2.77	2.80	2.74	2.81	2.78	2.73	2.73	2.70	2.74	2.67
Variance of Sample Mean	7.43E-04	1.75E-03	5.57E-04	1.74E-03	1.14E-03	7.43E-04	7.43E-04	2.88E-04	5.57E-04	5.57E-04
Standard Deviation of Sample Mean	2.73E-02	4.19E-02	2.36E-02	4.17E-02	3.37E-02	2.73E-02	2.73E-02	1.70E-02	2.36E-02	2.36E-02
Mean	2.69	2.67	2.67	2.69	2.68	2.65	2.65	2.65	2.67	2.60
Count	23	21	15	19	7	n/a	n/a	19	n/a	n/a

Notes:

1 No data is available for the operational soil cover; assumed to have same standard deviation as the UVZ; DC=dynamic compaction.

2 Mean value based on two measurements; type of distribution, variance, and standard deviation are assumed to be same as “sand.”

3 Little data are available for the gravel; assumed to have same standard deviation as "sand."

Table 3-56. UQSA Summary Statistics for Saturated Hydraulic Conductivity (cm s^{-1}) (Nichols and Butcher, 2020; Table 5-18)

Statistical Results from Bootstrapping Technique (Based on Sample Data)										
Parameter	**Upper Vadose Zone**	**Lower Vadose Zone**	**"SAND"**	**"CLAY-SAND"**	**"CLAY"**	**Operational Soil Cover (before DC)[2,3]**	**Operational Soil Cover (after DC)[2,3]**	**Controlled Compacted Backfill**	**ILV Permeable Backfill[4]**	**Gravel[5]**
Log K_h[1]										
Type of Distribution	Normal	Normal	Normal	Normal	Normal	Normal	Normal	Normal	Normal	Normal
Min (3σ)	-5.21	-4.13	-4.00	-5.08	-6.94	-4.49	-5.40	-4.40	-3.27	-1.24
Max (3σ)	-4.01	-3.35	-3.16	-3.88	-5.44	-3.29	-4.20	-3.86	-2.43	-0.40
Variance of Sample Mean	4.00E-02	1.69E-02	1.96E-02	4.00E-02	6.25E-02	4.00E-02	4.00E-02	7.92E-03	1.96E-02	1.96E-02
Standard Deviation of Sample Mean	2.00E-01	1.30E-01	1.40E-01	2.00E-01	2.50E-01	2.00E-01	2.00E-01	8.90E-02	1.40E-01	1.40E-01
Mean[6]	-4.61	-3.74	-3.58	-4.48	-6.19	-3.89	-4.80	-4.13	-2.85	-0.82
	2.5E-05	1.8E-04	2.6E-04	3.3E-05	6.5E-07	1.3E-04	1.6E-05	7.6E-05	1.43E-03	1.5E-01
Count	3	7	15	19	7	n/a	n/a	32	n/a	n/a
Log K_v[1]										
Type of Distribution	Normal	Normal	Normal	Normal	Normal	Normal	Normal	Normal	Normal	Normal
Min (3σ)	-6.36	-5.24	-5.10	-5.78	-7.57	-4.67	-5.58	-4.71	-4.05	-1.75
Max (3σ)	-4.80	-3.80	-3.24	-4.46	-5.71	-3.11	-4.02	-4.05	-2.19	0.11
Variance of Sample Mean	6.76E-02	5.76E-02	9.61E-02	4.84E-02	9.61E-02	6.76E-02	6.76E-02	1.21E-02	9.61E-02	9.61E-02
Standard Deviation of Sample Mean	2.60E-01	2.40E-01	3.10E-01	2.20E-01	3.10E-01	2.60E-01	2.60E-01	1.10E-01	3.10E-01	3.10E-01
Mean[6]	-5.58	-4.52	-4.17	-5.12	-6.64	-3.89	-4.80	-4.38	-3.12	-0.82
	2.6E-06	3.0E-05	6.8E-05	7.6E-06	2.3E-07	1.3E-04	1.6E-05	4.1E-05	7.64E-04	1.5E-01
Count	3	7	15	19	7	n/a	n/a	32	n/a	n/a

Modified Statistics Using Adjusted Saturated Hydraulic Conductivities (Based on +2σ)					
Parameter	**Upper Vadose Zone**	**Lower Vadose Zone**	**"SAND"**	**"CLAY-SAND"**	**"CLAY"**
Log K_h[1]					
Type of Distribution	normal	normal	normal	normal	normal
Min (3σ)	-4.81	-3.87	-3.72	-4.68	-6.45
Max (3σ)	-3.61	-3.09	-2.88	-3.48	-4.95
Variance of Sample Mean	4.00E-02	1.69E-02	1.96E-02	4.00E-02	6.25E-02
Standard Deviation of Sample Mean[7]	2.00E-01	1.30E-01	1.40E-01	2.00E-01	2.50E-01
Recommended Value[8]	-4.21	-3.48	-3.30	-4.08	-5.70
	6.2E-05	3.3E-04	5.0E-04	8.3E-05	2.0E-06
Count	3	7	15	19	7
Log K_v[1]					
Type of Distribution	normal	normal	normal	normal	normal
Min (3σ)	-5.84	-4.76	-4.48	-5.34	-6.95
Max (3σ)	-4.28	-3.32	-2.62	-4.02	-5.09
Variance of Sample Mean	6.76E-02	5.76E-02	9.61E-02	4.84E-02	9.61E-02
Standard Deviation of Sample Mean[7]	2.60E-01	2.40E-01	3.10E-01	2.20E-01	3.10E-01
Recommended Value[8]	-5.06	-4.04	-3.55	-4.68	-6.02
	8.7E-06	9.1E-05	2.8E-04	2.1E-05	9.5E-07
Count	3	7	15	19	7

Notes:

1 K_h and K_v are log normally distributed.

2 No data is available for the operational soil cover; hydraulic conductivity estimated based on UVZ properties; assumed to have same standard deviation as UVZ; DC=dynamic compaction.

3 ET07, ET08, and ET09 planned for Plot 8 are assumed to be backfilled with LVZ soils due to the absence of a UVZ in this vicinity; therefore, will need to use the same analysis (Kozeny-Carman equation) described by Nichols and Butcher (2020; Section 5.4.1) for estimating mean hydraulic conductivity for Plot 8 OSC before and after dynamic compaction applying the modified statistics from Table 3-56; this will result in a different set of summary statistics than for OSC obtained from UVZ material.

4 Mean value based on two measurements; type of distribution, variance, and standard deviation are assumed to be same as “sand.”

5 Few hydraulic conductivity data available; assumed to have same standard deviation as "sand."

6 Top number is the log of the mean; bottom number is the mean.

7 Standard deviation of sample mean based on statistical results from bootstrapping technique (see above tables).

8 Top number is the log of the recommended value; bottom number is the recommended value.

Table 3-57. UQSA Summary Statistics for Saturated Effective Diffusion Coefficient ($cm^2\ s^{-1}$) (Nichols and Butcher, 2020; Table 5-19)

log D_e[1]										
Material	**Upper Zone**	**Lower Zone**	**"SAND"**	**"CLAY-SAND"**	**"CLAY"**	**Operational Soil Cover (before DC)**	**Operational Soil Cover (after DC)**	**Controlled Compacted Backfill**	**ILV Permeable Backfill[2]**	**Gravel**
Type of Distribution	normal	normal	normal	normal	normal	normal	normal	normal	normal	normal
Min (3σ)	-5.49	-5.49	-5.44	-5.49	-5.55	-5.49	-5.55	-5.49	-5.46	-5.39
Max (3σ)	-5.05	-5.05	-4.72	-5.05	-5.23	-5.05	-5.23	-5.05	-4.74	-4.67
Variance of Sample Mean	5.18E-03	5.18E-03	1.44E-02	5.18E-03	2.81E-03	5.18E-03	2.81E-03	5.18E-03	1.44E-02	1.44E-02
Standard Deviation of Sample Mean	0.072	0.072	0.12	0.072	0.053	0.072	0.053	0.072	0.12	0.12
Mean[3]	-5.27	-5.27	-5.08	-5.27	-5.39	-5.27	-5.39	-5.27	-5.10	-5.03
	5.4E-06	5.4E-06	8.3E-06	5.4E-06	4.1E-06	5.4E-06	4.1E-06	5.4E-06	8.0E-06	9.4E-06

Notes:

1 Note that D_e is assumed to be log normally distributed; no data available so assumptions were made based on literature values.

2 Mean value based on two measurements; type of distribution, variance, and standard deviation are assumed to be same as "sand."

3 Top number is the log of the mean; bottom number is the mean.

Table 3-58. Recommended Material Properties for Cementitious Materials in Various Types of Disposal Units (Nichols and Butcher, 2020; Table 6-28)

Property	**Material**					
	CIG Grout[1]		**CLSM [1] (C3)**	**Concrete Mat [2] (C4)**	**Vault Concrete [1] (C5)**	**Vault Crack [4] (G1)**
	Old (C1)	**New (C2)**				
K_{sat}, cm s^{-1}	4.5E-5	9.0E-09	2.2E-06	9.0E-09	1.0E-12	1.5E-01
Porosity, η	0.224	0.233	0.328	0.233	0.158	0.300
Dry bulk density, g cm^{-3}	1.79	1.90	1.78	1.90	2.54	1.82
Particle Density, g cm^{-3}	2.31	2.48	2.65	2.48	3.02	2.60
θ_s	WRC calculated from combination of two materials, see Nichols and Butcher (2020; Section 6.3.3.1)	0.233000	0.328000	0.233000	0.158000	0.300
θ_r		0.000000	0.028399	0.000000	0.000000	0.021000
α		7.555E-06	2.867E-03	7.555E-06	3.701E-06	0.137676
n		1.191467	1.500000	1.191467	1.305542	1.479624
m		0.160698	0.333333	0.160698	0.234034	0.324153
Saturated Effective Diffusion Coefficient [3] D_e, $cm^2\ s^{-1}$	1.9E-6	8.0E-07	4.0E-06	8.0E-07	6.4E-08	9.4E-06

Notes:

1 Site-specific η, ρ_b, and K_{sat} laboratory data are available for the old and new E-Area CIG grout, E-Area CLSM, and E-Area vault concrete (i.e., LAWV and ILV). Typically, average values are used. Particle density is calculated using the porosity and bulk density laboratory data.

2 Site-specific laboratory data are not available for the E-Area CIG reinforced concrete mats. The η, ρ_b, ρ_p, and K_{sat} of the E-Area CIG concrete mats are assumed to be the same as the new E-Area CIG Grout as both materials are placed with standard field construction practices (i.e., minimal consolidation and curing requirements).

3 New E-Area CIG Grout, E-Area CIG concrete mats, and E-Area vault concrete (i.e., LAWV and ILV) are considered fairly typical cementitious materials for which D_e can be reasonably derived from literature values as described in detail by Nichols and Butcher (2020; Section 6.3.4). While old E-Area CIG grout and E-Area CLSM are cementitious materials, it is not considered appropriate to assign these materials D_e values based strictly upon cementitious material literature for reasons given by Nichols and Butcher (2020; Section 6.3.4). Instead, E-Area CLSM is assigned the same D_e as clay (>50% mud), which is 4.0E-06 $cm^2\ s^{-1}$ (Table 3-52). D_e for old E-Area CIG grout is calculated as if it consists of 15% sand with D_e of 8.0E-06 $cm^2\ s^{-1}$ (Table 3-52) and 85% low quality concrete with D_e of 8.0E-07 $cm^2\ s^{-1}$ Nichols and Butcher (2020; Table 6-29). This results in a weighted D_e of 1.9E-06 $cm^2\ s^{-1}$ for old E-Area CIG grout as calculated by Nichols and Butcher (2020; Section 6.3.4).

4 Vault crack assigned the properties of gravel (G1) as defined in Table 3-52.

Table 3-59. Cementitious Material Uncertainty Summary Statistics for Effective Porosity (%) (Nichols and Butcher, 2020; Table 6-33)

Material	**Distribution Type**	**Value (%)**	**Count**	**Standard Deviation of the Mean**	**Variance of the Mean**	**Mean Minimum (3σ)**	**Mean Maximum (3σ)**
Old E-Area CIG Grout (Segments 1 - 8 only)	Normal	22.4	6	0.59	0.36	20.6	24.2
New E-Area CIG Grout (i.e., Segments beyond Segment 8)	Normal	23.3	6	0.13	0.02	22.9	23.7
E-Area CLSM	Normal	32.8	3	0.93	0.81	30.1	35.5
E-Area CIG Concrete Mats [1]	Normal	23.3	-	0.13	0.02	22.9	23.7
E-Area Vault Concrete	Normal	15.8	4	0.64	0.41	13.9	17.7

Notes:

1 No data are available on E-Area CIG concrete mats; therefore, bulk properties for this material are assumed to be the same as new E-Area CIG grout.

Table 3-60. Cementitious Material Uncertainty Summary Statistics for Dry Bulk Density (g cm^{-3}) (Nichols and Butcher, 2020; Table 6-34)

Material	Distribution Type	Value (g cm^{-3})	Count	Standard Deviation of the Mean	Variance of the Mean	Mean Minimum (3σ)	Mean Maximum (3σ)
Old E-Area CIG Grout (Segments 1 - 8 only)	Normal	1.79	10	0.031	9.61E-04	1.70	1.88
New E-Area CIG Grout (i.e., Segments beyond Segment 8)	Normal	1.90	6	0.0095	9.6E-05	1.87	1.93
E-Area CLSM	Normal	1.78	4	0.029	8.41E-04	1.69	1.87
E-Area CIG Concrete Mats [1]	Normal	1.90	-	0.0095	9.6E-05	1.87	1.93
E-Area Vault Concrete	Normal	2.54	6	0.013	1.57E-04	2.50	2.58

Notes:

[1] No data are available on E-Area CIG concrete mats; therefore, bulk properties for this material are assumed to be the same as new E-Area CIG grout.

Table 3-61. Cementitious Material Uncertainty Summary Statistics for Particle Density (g cm^{-3}) (Nichols and Butcher, 2020; Table 6-35)

Material	Distribution Type	Value (g cm^{-3})	Count	Standard Deviation of the Mean	Variance of the Mean	Mean Minimum (3σ)	Mean Maximum (3σ)
Old E-Area CIG Grout (Segments 1 - 8 only)	Normal	2.31	6	0.021	4.41E-04	2.25	2.37
New E-Area CIG Grout (i.e., Segments beyond Segment 8)	Normal	2.48	6	0.011	1.03E-4	2.45	2.51
E-Area CLSM	Normal	2.65	3	0.010	1.00E-04	2.62	2.68
E-Area CIG Concrete Mats [1]	Normal	2.48	-	0.011	1.3E-04	2.45	2.51
E-Area Vault Concrete	Normal	3.02	4	0.031	9.87E-04	2.93	3.11

Notes:

[1] No data are available on E-Area CIG concrete mats; therefore, bulk properties for this material are assumed to be the same as new E-Area CIG grout.

Table 3-62. Cementitious Material Uncertainty Summary Statistics for Saturated Hydraulic Conductivity (cm s^{-1}) (Nichols and Butcher, 2020; Table 6-38)

Material	Distribution Type	Log Normal Value [1] (cm s^{-1})	Count	Log Standard Deviation of the Mean	Log Variance of the Mean	Log Mean Minimum (3σ)	Log Mean Maximum (3σ)
Old E-Area CIG Grout (Segments 1 - 8 only)	Normal [2]	-4.35 (4.5E-05)	8	0.63	3.92E-01	-6.228	-2.472
New E-Area CIG Grout (i.e., Segments beyond Segment 8)	Normal	-8.05 (9.0E-09)	6	0.034	1.0E-03	-8.157	-7.950
E-Area CLSM	Normal	-5.66 (2.2E-06)	3	0.114	1.30E-02	-6.002	-5.318
E-Area CIG Concrete Mats [3]	Normal	-8.05 (9.0E-09)	-	0.034	1.0E-03	-8.157	-7.950
E-Area Vault Concrete	Normal	-12 (1.0E-12)	3	0.074	5.48E-03	-12.222	-11.778

Notes:

[1] Saturated hydraulic conductivity values from Table 3-58 are provided in parentheses; the log of the values is shown first.

[2] Saturated hydraulic conductivity is log normally distributed; therefore, the log of saturated hydraulic conductivity is normally distributed.

[3] No data are available on E-Area CIG concrete mats; therefore, bulk properties for this material are assumed to be the same as new E-Area CIG grout.

Table 3-63. Cementitious Material Uncertainty Summary Statistics for Saturated Effective Diffusion Coefficient ($cm^2\ s^{-1}$) (Nichols and Butcher, 2020; Table 6-40)

Material	Distribution Type	Log Normal Value [1] ($cm\ s^{-1}$)	Count	Log Standard Deviation of the Mean	Log Variance of the Mean	Log Mean Minimum (3σ)	Log Mean Maximum (3σ)
Old E-Area CIG Grout (Segments 1 - 8 only)	Normal [2]	-5.72 (1.9E-06)	-	0.053	2.81E-03	-5.88	-5.56
New E-Area CIG Grout (i.e., Segments beyond Segment 8)	Normal	-6.10 (8.0E-07)	-	0.21	4.54E-02	-6.74	-5.46
E-Area CLSM	Normal	-5.40 (4.0E-06)	-	0.053	2.81E-03	-5.56	-5.24
E-Area CIG Concrete Mats [3]	Normal	-6.10 (8.0E-07)	-	0.21	4.54E-02	-6.74	-5.46
E-Area Vault Concrete	Normal	-7.19 (6.4E-08)	-	0.025	6.25E-04	-7.38	-7.22

Notes:

[1] Saturated effective diffusion coefficients from Table 3-58 are provided in parentheses; the log of the values is shown first.

[2] The saturated effective diffusion coefficient is log normally distributed; therefore, the log of the saturated effective diffusion coefficient is normally distributed.

[3] No data are available on E-Area CIG concrete mats; therefore, bulk properties for this material are assumed to be the same as new E-Area CIG grout.

Table 3-64. Material Properties for Waste Zones in the E-Area Low-Level Waste Facility (Nichols and Butcher, 2020; Table 7-2)

Type	Condition	Thickness (ft)	K_{sat} ($cm\ s^{-1}$)	Porosity, faction	Bulk Density ($g\ cm^{-3}$)	Particle Density ($g\ cm^{-3}$)	Effective Diffusion Coefficient ($cm^2\ s^{-1}$)	θ_s	θ_r	α	n	m
Slit Trench	Before Dynamic Compaction	16	9.4E-05	0.600	1.059	2.65	5.3E-06	The WRC and k_r are calculated using Eq. (4-8) and Eq. (4-11) in Section 4.1.1.1.2				
	After Dynamic Compaction	11.1	1.5E-05	0.277	1.915	2.65	4.0E-06	The WRC and k_r are calculated using Eq. (4-8) and Eq. (4-11) in Section 4.1.1.1.2				
Engineered Trench	Before Dynamic Compaction	16	2.2E-05	0.889	0.293	2.65	5.3E-06	The WRC and k_r are calculated using Eq. (4-8) and Eq. (4-11) in Section 4.1.1.1.2				
	After Dynamic Compaction	2.5	8.7E-06	0.303	1.847	2.65	4.0E-06	The WRC and k_r are calculated using Eq. (4-8) and Eq. (4-11) in Section 4.1.1.1.2				
CIG Trench Segments	Structurally and Hydraulically Intact	14	1.0E-12	0.456	1.44	2.65	5.3E-06	0.456000	0.121330	0.040416	1.153656	0.133191
	Structurally Intact and Hydraulically Degraded	14	1.2E-04	0.456	1.44	2.65	5.3E-06	0.456000	0.121330	0.040416	1.153656	0.133191
	Structurally and Hydraulically Degraded	7	1.2E-04	0.456	1.44	2.65	5.3E-06	0.456000	0.121330	0.040416	1.153656	0.133191
LAWV	Before Collapse	17.3	2.2E-06	0.900 [1]	0.245 [1]	2.45 [1]	4.0E-06	0.328000	0.028399	0.002867	1.500000	0.333333
	After Collapse	2.5	1.2E-04	0.456	1.44	2.65	5.3E-06	0.456000	0.121330	0.040416	1.153656	0.133191
ILV	Before Collapse	25.83	1.0E-02	0.736 [1]	0.612 [1]	2.32 [1]	1.6E-05	0.300000	0.021000	0.137676	1.479624	0.324153
	After Collapse	10	1.2E-04	0.456	1.44	2.65	5.3E-06	0.456000	0.121330	0.040416	1.153656	0.133191
Naval Reactor Components [2]	Hydraulically Intact	8.2 (bolted container) 18 (welded cask)	5.0E-15	0.991	0.025	2.65	1E-13	The WRC and k_r are calculated using Eq. (4-8) and Eq. (4-11) in Section 4.1.1.1.2				
	Hydraulically Degraded	8.2 (bolted container) 18 (welded cask)	2.2E-05	0.889	0.293	2.65	5.3E-6	The WRC and k_r are calculated using Eq. (4-8) and Eq. (4-11) in Section 4.1.1.1.2				

Notes:

[1] Recommended by Phifer et al. (2006) in order to not overestimate the retardation of radionuclides during transport.

[2] Bolted, gasketed containers are treated as generic waste in the PA VZ model, while welded casks are treated as a special waste form. During the time when bolted containers (0 and 750 years) and welded casks (750 years) are considered hydraulically intact, there is essentially no flow and no advective release of contaminants. Therefore, the characteristic curves are essentially irrelevant until a leak develops.

3.8.3.1. Unsaturated Zone Soil Properties

The purpose of the soils evaluation conducted by Nichols and Butcher (2020) is to provide estimates of porosity (η), dry bulk density (ρ_b), particle density (ρ_p), saturated hydraulic conductivity (K_{sat}), WRCs (suction head, saturation, and relative permeability), and the effective diffusion coefficient (D_e) for input to the ELLWF PA models. Parameter estimates are provided for the following materials:

- undisturbed VZ soils
- controlled compacted backfill
- 4-foot OSC (before and after dynamic compaction)
- permeable backfill for the ILV
- generic "gravel"

Material properties for undisturbed VZ soils, CCB, OSC, and permeable backfill for the ILV are derived by compositing properties for individual samples. The method of compositing varies depending on the specific material being represented by the composited results. Each compositing method is described in detail by Nichols and Butcher (2020; Section 5.0).

Existing soils data from the GSA have been gathered from databases, SRS documents, and laboratory reports as outlined by Nichols and Butcher (2020; Section 5.1.2). The primary types of soils data for this evaluation include:

- grain size [sieve analyses] (Nichols and Butcher, 2020; Section 5.1.2.1)
- hydraulic property datasets [laboratory measurements of vertical hydraulic conductivity and water retention] (Nichols and Butcher, 2020; Section 5.1.2.1)
- bulk property measurements [bulk density and porosity] (Nichols and Butcher, 2020; Section 5.1.2.1)
- piezocone penetration test or cone penetration test (CPT) logs (Nichols and Butcher, 2020; Section 5.1.2.2)
- continuous core descriptions/geophysical logs (Nichols and Butcher, 2020; Section 5.1.2.3)

Sampling protocols used by the various labs in conducting these analyses are listed for reference in Table 3-65.

Table 3-65. Test Methods used in Material and Hydraulic Property Analyses (Nichols and Butcher, 2020; Table 5-1)

Parameter	Test Method
Grain Size	ASTM D422/D1140, D2217
Bulk Density	ASTM D4531
Porosity	EM1110-2-1906
Saturated Hydraulic Conductivity	ASTM D5084
Water Retention	ASTM D2325

3.8.3.1.1. Vadose Zone Soils

Table 3-66 provides the approximate number of each data type for E-Area and Z-Area undisturbed VZ soils. Figure 3-94 shows the location of the various data types in E-Area. The number of samples and locations identified for hydraulic property datasets in Table 3-66 reflect the data that were collected. Samples may not have been included in this evaluation if the samples were suspected to be of poor quality (or non-representative). Data quality for undisturbed VZ soil hydraulic properties is discussed by Nichols and Butcher (2020; Section 5.2.2).

Table 3-66. Datasets for E-Area and Z-Area Undisturbed Vadose Zone Soil (Nichols and Butcher, 2020; Table 5-2)

Data Type	E-Area	Z-Area
Grain-size analyses	92 samples (25 locations)	373 samples (39 locations)
Hydraulic & bulk property	64 samples (11 locations)	4 samples (2 locations)
CPT logs	90 locations in vicinity of future and existing DUs	31 locations in vicinity of future and existing vaults
Continuous core descriptions/geophysical logs	8 locations in vicinity of future and existing DUs	7 locations in vicinity of future and existing vaults

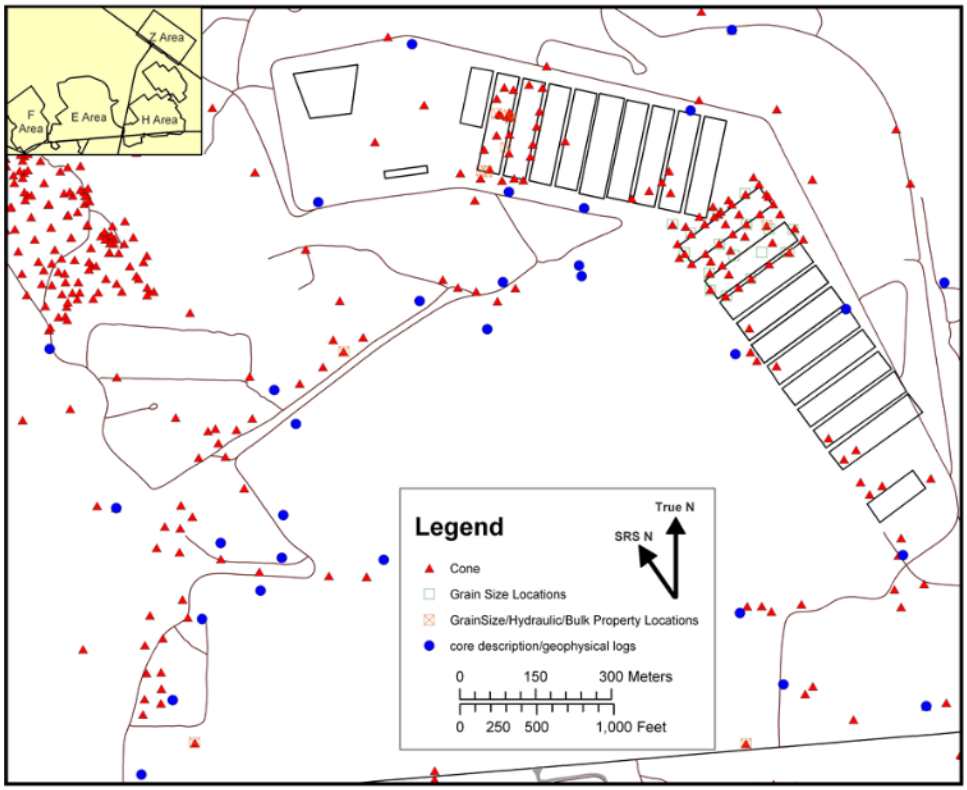

Figure 3-94. Map of E-Area Soils Dataset Locations (Nichols and Butcher, 2020; Figure 5-1)

In addition, Millings et al. (2011) present the results of a 2011 characterization program to collect site-specific data for the VZ beneath the adjacent plots comprising the undeveloped "second 100 acres" in E-Area (see Figure 2-6). The 2011 characterization program consisted of collecting CPT logs (tip resistance, sleeve resistance, friction ratio, pore pressure, and electrical resistivity) and individual soil samples (grain-size distribution, dry bulk density, porosity, saturated hydraulic

conductivity, water retention characteristics, mineralogy, elemental composition, and organic content). Figure 3-95 shows the four characterization locations in Plots 6, 7, 8, and 9 (three inside Plots 7, 8, and 9, and the fourth near the edges of Plots 6 and 8) where the eight soil borings were made and the four geophysical logs, 522 feet of soil core, and 33 Shelby tube samples were collected.

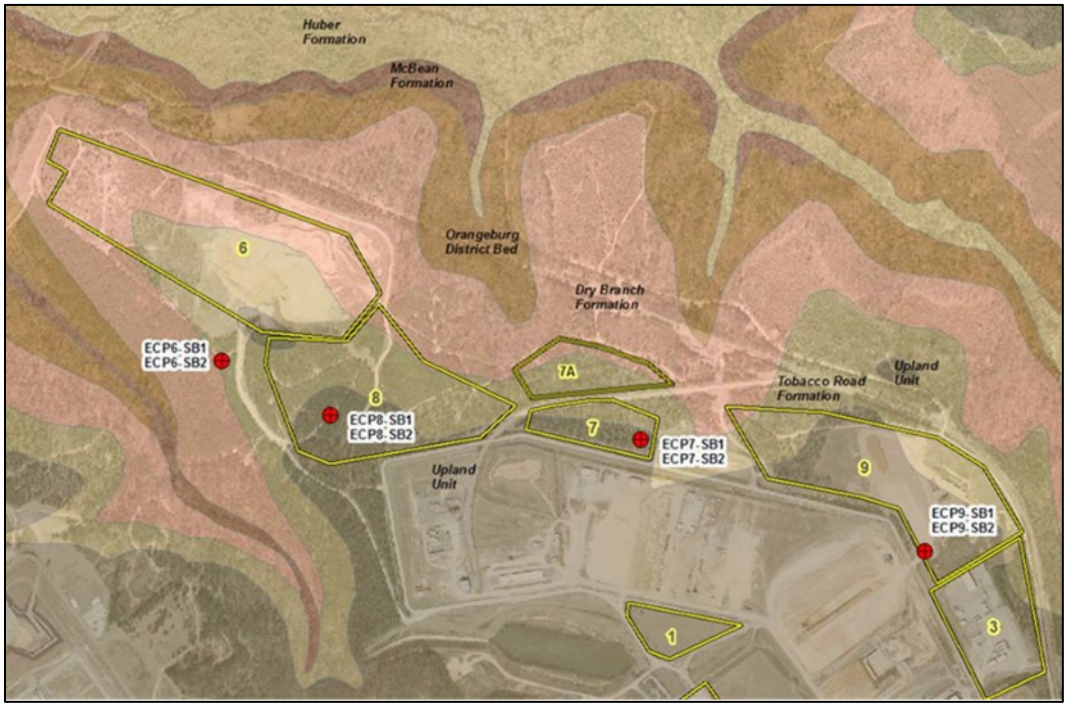

Figure 3-95. Four Characterization Locations Within "Second 100 Acres" of E-Area Including Plot 8 (Nichols and Butcher, 2020; Figure 5-2)

Grain Size

Section 2.1.5.2.6 discusses soil texture and soil classification by grain size for the ELLWF VZ soils. A textural triangle for the VZ soils is presented in Figure 2-18, while Table 2-5 provides a list of USCS classifications and the number of samples from E-Area classified in each category. As described in more detail in Section 2.1.7.3, the VZ is divided into an upper and lower zone based upon textural properties to better represent the hydrologic processes that regulate GW flow. The UVZ consists of Clay and Clay-Sand and the LVZ consists of Clay-Sand and Sand.

Saturated Hydraulic Conductivity

Nichols and Butcher (2020; Section 5.2.2.1) review sample selection and data quality for the saturated hydraulic conductivity measurements of the E-Area and Z-Area samples. Because grain-size analyses are more widely available than the hydraulic property datasets and percent mud is typically considered to have a controlling effect on hydraulic conductivity, the statistical distribution of percent mud helps in determining whether samples analyzed for hydraulic properties are representative of area soils. Percent mud reflects the clay and silt size fraction from grain-size analyses and includes the sediment fraction less than 0.074 mm in size (or 0.062 mm for a few labs). Nichols and Butcher (2020; Figure 5-5) highlight the relationship between percent

mud and vertical saturated hydraulic conductivity for the samples used in this evaluation. As percent mud increases, the vertical saturated hydraulic conductivity decreases. In general, the sample populations of percent mud used by Nichols and Butcher (2020) for this PA are log-normally distributed as evidenced by Nichols and Butcher (2020; Figure 5-6). From the available data, the hydraulic conductivity samples appear representative of all E-Area grain-size samples.

Atlantic Coastal Plain sediment deposits are naturally heterogeneous at multiple scales, and characterization data are invariably sparse. Nichols and Butcher (2020; Section 5.2.2.2) describe four stochastic approaches,[27] as presented by Sánchez-Vila et al. (1995), for interpreting laboratory permeability data[28] and for processing these data to arrive at upscaled[29] horizontal and vertical conductivities that account for spatial variability at the field scale and that adequately describe a homogeneous, but anisotropic, hydraulic conductivity field in numerical flow and transport models. The goal is to reproduce the average flow behavior of the heterogeneous system. The effect of heterogeneity on solute transport, specifically field-scale dispersion, is captured in this PA through appropriate dispersivity settings in a Fickian dispersion model (Gelhar, 1997).

Two of the four stochastic approaches reviewed by Sánchez-Vila et al. (1995) are practical because they provide a mechanism for computing model block conductivity from point values. The Desbarats (1992) approach is particularly appealing because of its simplicity. Desbarats (1992) conjectured that equivalent block conductivities can be formulated as a power-average, which is a reasonable hypothesis considering the successful use of p-norms in defining effective conductivity. Desbarats (1992) empirically determined the appropriate power through numerical experimentation.

Atlantic Coastal Plain sediments are clearly stratified and imply anisotropic correlation scales. Judgement based on knowledge of the depositional environment and visual inspection of outcrops suggests a reasonable ratio of horizontal to vertical correlation lengths for point conductivities is

[27] The stochastic approaches are based on an assumed statistical distribution of small-scale or "point" values of conductivity (K), and a spatial correlation model. Although not without shortcomings, K is often assumed to have a stationary log-normal distribution and a single correlation scale, based on supporting characterization data (Freeze and Cherry, 1979) and partly for analytical convenience. Stationary means that the statistical properties of the medium (mean, variance, spatial correlation) do not change with location within the region of interest. These assumptions are most reasonable in the context of a single facie but can be applied to a formation with further approximation. Sarris and Paleologos (2004) have shown that log-normality is preserved as conductivity is upscaled, which supports the assumption regardless of scale of data observation (support scale).

[28] In this PA, laboratory measurements for vertical hydraulic conductivity are assumed to reflect horizontal hydraulic conductivity for upscaling purposes. This assumption is believed to be valid because the laboratory sample sizes are small and thus the measurements likely reflect a homogeneous hydraulic conductivity. On the other hand, this assumption may be slightly biased if there is significant preferential deposition or weathering of minerals.

[29] Upscaling refers to the process of replacing a heterogeneous conductivity field within a particular finite volume with a single, "equivalent," conductivity value. The equivalent conductivity is defined as the value that reproduces some average behavior of the block, such as mean flow for a given head difference. A closely related problem is that of determining the "effective" conductivity of a heterogeneous media. The distinction is stated by Sánchez-Vila et al. (1995) as, "effective parameters are defined as representative values of the mean behavior through an ensemble of realizations, while equivalent parameters are associated with a certain geometry and defined as spatial averages computed on a single realization. These two definitions should converge to the same value for very large geometries and under the assumption of ergodicity."

$\lambda_h / \lambda_v = 10$. For anisotropic media assuming model block dimensions of $L_h / \lambda_h = L_v / \lambda_v = 3$ and $\lambda_h / \lambda_v = 10$, the optimal averaging exponents were found by Desbarats (1992) through numerical experimentation to be $p_h = 0.59$ and $p_v = -0.33$, where λ_i is the integral scale of heterogeneity for direction *i*, L_i is the model block dimension for direction *i*, subscripts *h* and *v* represent the horizontal and vertical directions, respectively, and p_h and p_v are the averaging exponents associated with the equivalent horizontal and vertical block conductivities, respectively.[30]

Nichols and Butcher (2020; Section 5.2.2.2) provide a detailed evaluation of the four upscaling approaches considered and spell out a stepwise procedure for interpreting small-scale permeability data for each formation. In addition, Nichols and Butcher (2020; Section 5.2.2.2 and Table 5-6) discuss the rationale for choosing optimal averaging exponents of $p_h = 0.59$ and $p_v = -0.33$ for this PA based on an assumed model block size (L/λ) of 3.0. Triangular distributions are used to represent the uncertainty in p_h and p_v (see Table 3-67).

Table 3-67. Descriptive Statistics for Triangular Distributions Describing p_h and p_v (Nichols and Butcher, 2020; Table 5-16)

Statistic	p_h	p_v
Min	0.34	-0.73
Peak	0.59	-0.33
Max	0.84	0.07

Using the described upscaling method, horizontal (K_h) and vertical (K_v) conductivities are calculated for the undisturbed VZ soils. Laboratory data are subdivided according to the following textural properties:

- >50% mud (generalized as "clay")
- 25-50% mud (generalized as "clay-sand")
- <25% mud (generalized as "sand")

K_h, K_v, and K_h/K_v for these textural classes are provided in Table 3-52.

Saturated hydraulic conductivities have also been estimated for the UVZ and LVZ hydrostratigraphic units in E-Area. Grain-size data, visual core descriptions, and CPT logs indicate that the UVZ and LVZ have different textural properties. Figure 3-96 illustrates this difference.

[30] The p-norm is defined by $K_p \overset{def}{=} \left[\frac{1}{N} \sum_i (K_i)^p \right]^{1/p} = \left(\overline{K^p} \right)^{1/p}$ because $K_p = K_g exp\left(\frac{p\sigma^2}{2} \right)$. K_p represents the upscaled horizontal conductivity (K_h) for $p = p_h$ and vertical conductivity (K_v) for $p = p_v$; K_g is the geometric mean of the point conductivity field; σ^2 is the variance of the natural logarithm of point conductivities (ln K_i). The p-norm encompasses the familiar averages of arithmetic ($p = 1$), geometric ($p \to 0$), harmonic ($p = -1$), and any blend in between (Ababou and Wood, 1990).

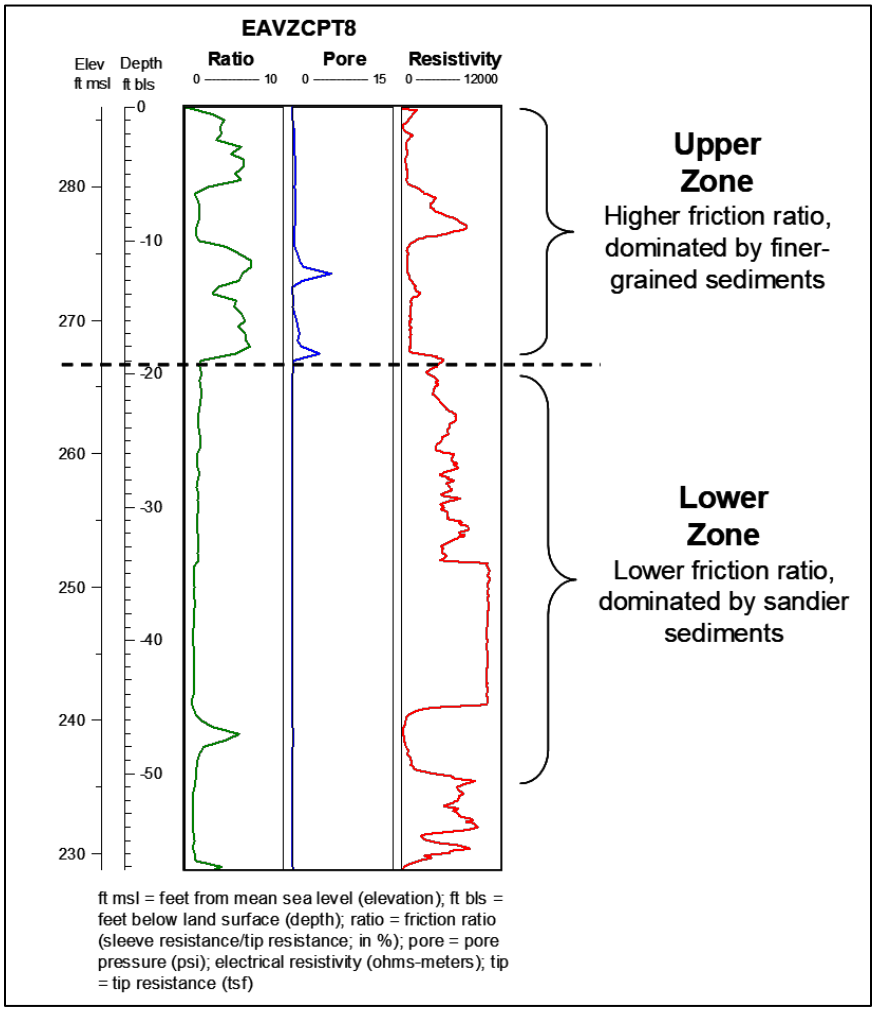

Figure 3-96. Upper and Lower Vadose Zones for E-Area CPT Sample EAVZCPT8 (Nichols and Butcher, 2020; Figure 5-7)

Using CPT logs and grain-size analyses, laboratory K_{sat} data are lumped into an upper zone and a lower zone. The data are then upscaled using the method described above to generate K_h and K_v for the UVZ and LVZ. The results summarized in Table 3-52 highlight that the UVZ has a lower K_h and K_v than the LVZ, reflecting the greater abundance of fine-grained sediments and heterogeneity in the UVZ.

Using available CPT logs, visual core descriptions, and grain-size analyses, the boundaries of the UVZ and LVZ were defined across E-Area (Bagwell and Bennett, 2017). Bagwell and Bennett (2017) identified the top and bottom of the primary hydrogeologic units beneath the center of each of the ELLWF DUs. Figure 3-97 displays a vertical cross-section along the transect line (red) shown in the inset illustrating the various hydrogeologic units beneath each DU. It is important to note that the UVZ is absent in E-Area to the west. In addition, the LVZ crosses below the TCCZ (labeled TCCU in figure), also to the west, due to a declining water table.

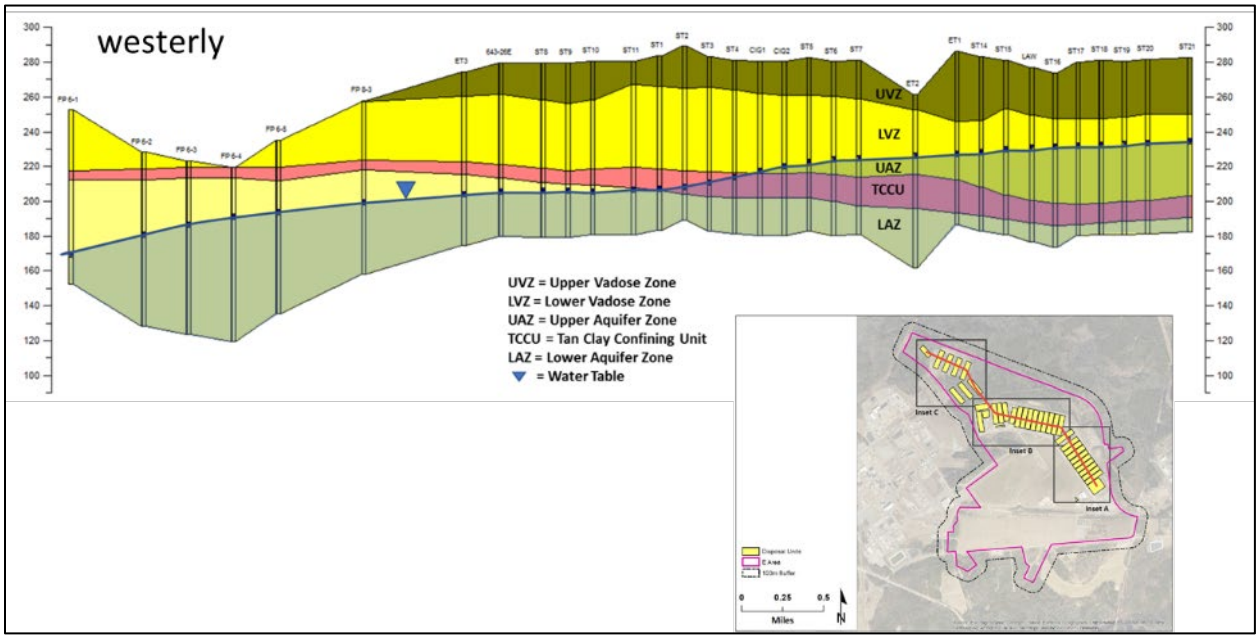

Figure 3-97. Cross-Section of Transect 1 in E-Area (Nichols and Butcher, 2020; Figure 5-9)

Calculated K_h and K_v values using the described approach are within the range of K_h and K_v measured from pump tests for the water table aquifer near TNX and D-Area. Although the measurements reflect the saturated zone, the water table aquifer at TNX and D-Area is like the E-Area VZ. At TNX and D-Area, the water table aquifer is approximately 40 to 60 feet in thickness and consists of a highly layered system of fine sands, silts, and clays. The E-Area VZ has a similar thickness and is likewise comprised of layers of sands, silts, and clays. Data from TNX and D-Area pump tests (Phifer et al., 2000) were used for comparative purposes to confirm that K_h and K_v calculated for this PA are reasonable estimates. See Nichols and Butcher (2020; Table 5-8) for more detail.

Water Retention Curves

The van Genuchten equation (van Genuchten, 1980), which relates water content (θ), and thus water saturation (S), to pressure head (ψ), is used with laboratory data to determine the VG parameters for a water retention curve via Eq. (3-47) and Eq. (3-48).

$$S_e = \left[1 + \left|\alpha\psi\right|^n\right]^{-m} \qquad \text{Eq. (3-47)}$$

$$S_e = \frac{\theta - \theta_r}{\theta_s - \theta_r} \qquad \text{Eq. (3-48)}$$

where:

S_e = effective water saturation ($m^3\ m^{-3}$)
α and n are dimensionless fitting parameters (i.e., shape factors)
ψ = pressure head (m)

m = [1 – 1/n] which is a constraint to yield closed-form permeability expressions
θ = water content (m^3 m^{-3})
θ_s = total porosity (m^3 m^{-3})
θ_r= residual water content (m^3 m^{-3})

First, WRCs for individual VZ samples are developed by performing a least squares regression[31] of suction head vs. water content data for each sample to generate the VG parameters. Suction head was measured at five different water contents for each soil sample. Figure 3-98 displays the results from the least squares regression of six sand samples.

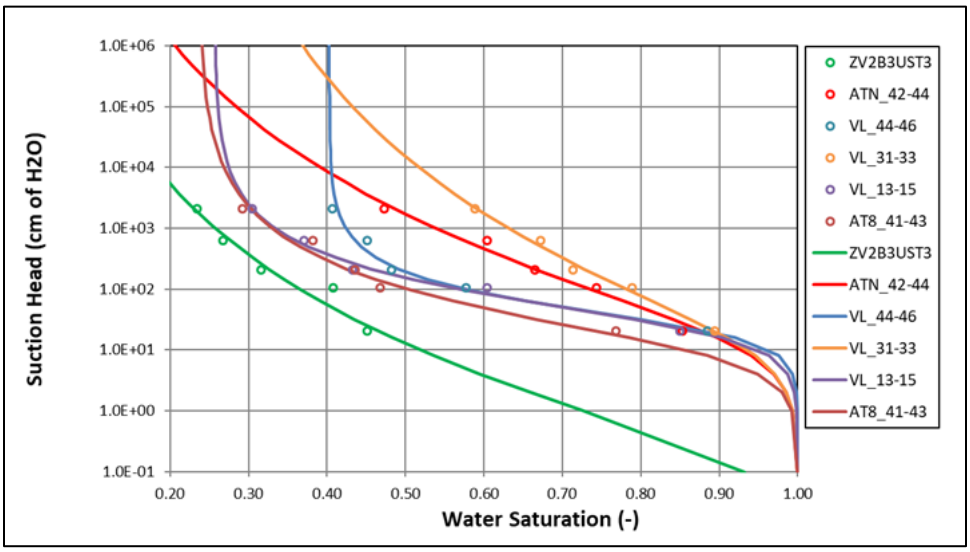

Figure 3-98. Water Retention Data and Water Retention Curves for Vadose Zone Sand Samples (Nichols and Butcher, 2020; Figure 5-10)

Second, WRCs for individual soil samples are grouped by previously identified textural class to produce representative soil types (Nichols and Butcher, 2020; Section 5.2.3). The WRCs in each textural class are then composited to develop a WRC and VG parameters for the representative soil type (i.e., "sand," "clay-sand," and "clay" as listed in Table 3-52). Individual samples are composited in a class by averaging the water saturation (S_i) for each sample (i) at selected suction heads (ψ_j) according to Eq. (3-49).

$$\overline{S_{\psi_j}} = \frac{1}{n}\sum_{i=1}^{n} S_i\left(\psi_j\right) \qquad \text{Eq. (3-49)}$$

where:

S_i = saturation at suction head (ψ_j) for sample i (m^3 m^{-3})
n = number of samples for specific soil type (n = 6 for "sand," 6 for "clay-sand," and 3 for "clay")

[31] An unweighted least-squares fit method was implemented using the SOLVER routine in Microsoft Excel.

Uniform weighting of the composite soil type is employed. Figure 3-99 displays the WRC for individual samples identified as sand and the resulting data set for the representative soil type "sand" WRC.

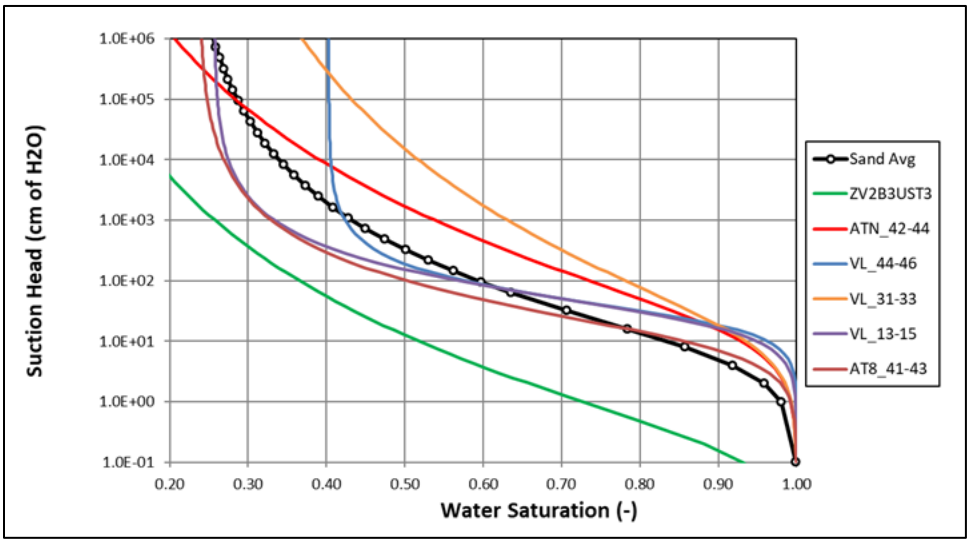

Figure 3-99. Water Retention Curves for Individual Samples Identified as Sand and Resulting Water Retention Curve for Representative Soil Type "Sand" (Nichols and Butcher, 2020; Figure 5-11)

Third, the resulting composited data sets for each of the three representative soil types are fit to Eq. (3-47) and Eq. (3-48) to determine VG parameters using the previously described least squares regression method. Figure 3-100 shows the composite data set and WRC curve for each of the three representative soil types.

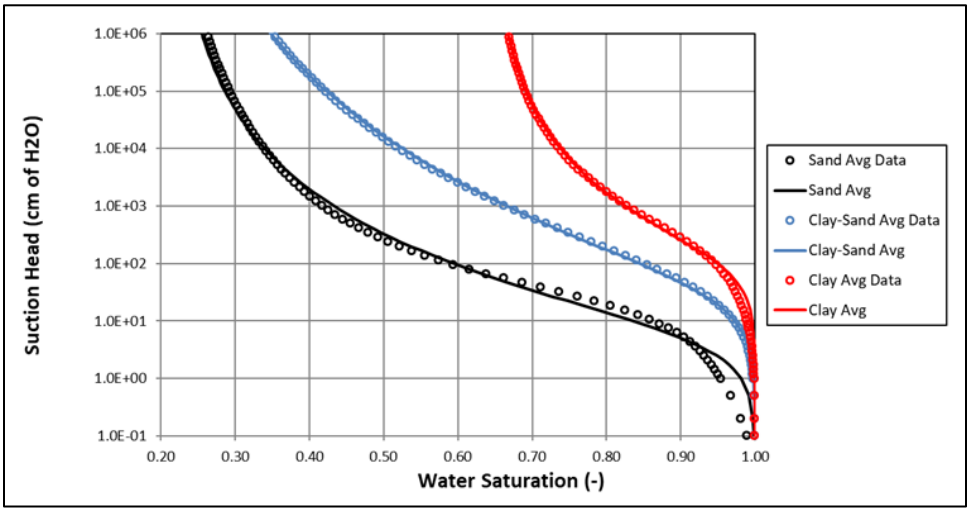

Figure 3-100. Water Retention Curves for Individual Samples Identified as Sand and Resulting Water Retention Curve for Representative Soil Type "Sand" (Nichols and Butcher, 2020; Figure 5-11)

A closed-form equation was published by van Genuchten (1980) to calculate the relative permeability (k_r) of soils.[32] Eq. (3-50) relates k_r to ψ using the VG parameters derived from S,ψ data described above.

$$k_r = S_e^L \left[1 - \left(1 - S_e^{1/m} \right)^m \right]^2 \qquad \text{Eq. (3-50)}$$

Eq. (3-50) is used to generate relative permeability curves for each of the representative soil types. Results are presented in Figure 3-101.

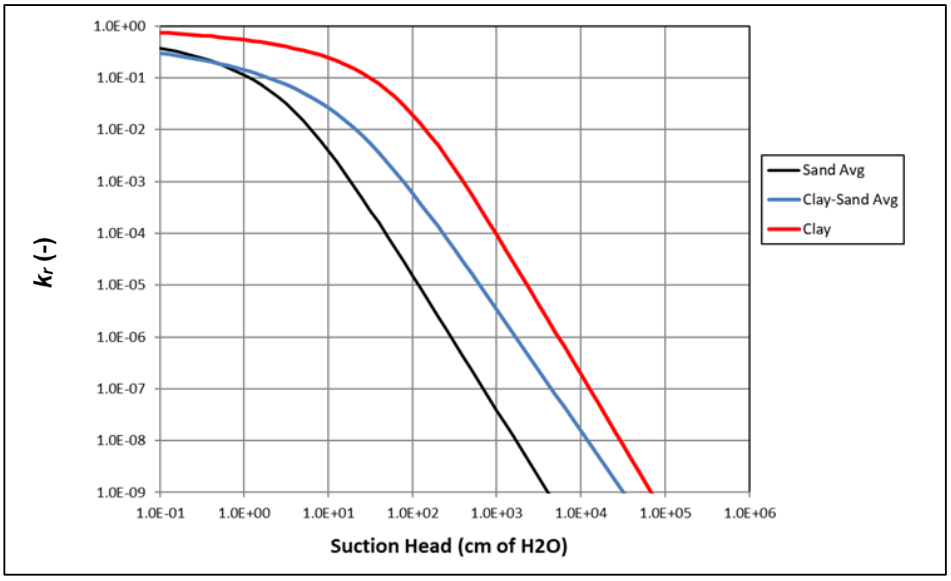

Figure 3-101. Relative Permeability Curves for Representative Soil Types "Clay," "Clay-Sand," and "Sand" (Nichols and Butcher, 2020; Figure 5-13)

For a representative location (e.g., AT-North/Megacptnorth), data are categorized into an UVZ and LVZ. Thicknesses of the representative soil types ("sand," "clay-sand," and "clay") are determined using CPT logs, visual core descriptions, and grain-size analyses. Figure 3-102 shows the representative soil types and layer thicknesses comprising the UVZ and LVZ at this location. Using these thicknesses, a proportion (or percentage) of the textural categories is computed for the upper and lower VZs. For example, the 21.5-foot-thick UVZ consists of approximately 81% "clay-sand" and 19% "clay." The soil moisture profiles for the "clay," "clay-sand," and "sand" are then combined into a single curve based on the proportion of each textural category. The method of using a representative location, textural properties, and layer thicknesses appears to generate curves that are representative of the "average" conditions for the UVZ and LVZ and is less influenced by outlier samples, when compared to averaging data for each zone with no account for thicknesses of the various soil types.

[32] van Genuchten (1980) referred to this term as the relative hydraulic conductivity or K_{rel}. In this PA, the terminology relative permeability is used, which is represented by the variable k_r.

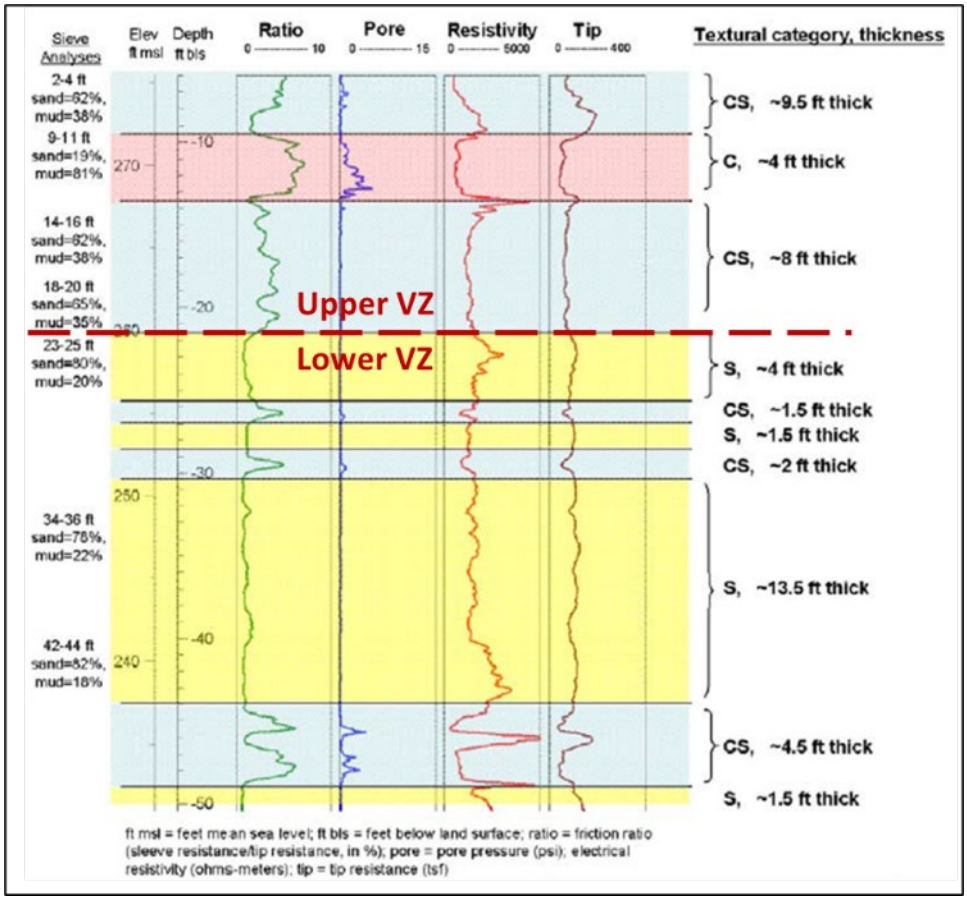

Figure 3-102. Identification of Representative Soil Types and Layer Thicknesses Comprising Upper and Lower Vadose Zones at Location AT-North/Megacptnorth (Nichols and Butcher, 2020; Figure 5-14)

VG parameters are calculated for the UVZ and LVZ by compositing the appropriate representative soil types. The UVZ is represented by 81% "clay-sand" and 19% "clay." WRCs for these two representative soil types are composited to develop a data set for the UVZ using Eq. (3-51). The resulting data set is then analyzed using the previously described method to determine VG parameters for the UVZ.

$$S_{UVZ}\left(\psi_i\right) = 0.81 \times S_{ClSd}\left(\psi_i\right) + 0.19 \times S_{Cl}\left(\psi_i\right) \qquad \text{Eq. (3-51)}$$

The LVZ is represented by 72% "sand" and 28% "clay-sand." WRCs for these two representative soil types are composited to develop a data set for the LVZ using Eq. (3-52). The resulting data set is then analyzed using the previously described method to determine VG parameters for the LVZ.

$$S_{LVZ}\left(\psi_i\right) = 0.72 \times S_{Sd}\left(\psi_i\right) + 0.28 \times S_{ClSd}\left(\psi_i\right) \qquad \text{Eq. (3-52)}$$

Figure 3-103 and Figure 3-104 show the WRC and k_r curves for the UVZ and LVZ, respectively.

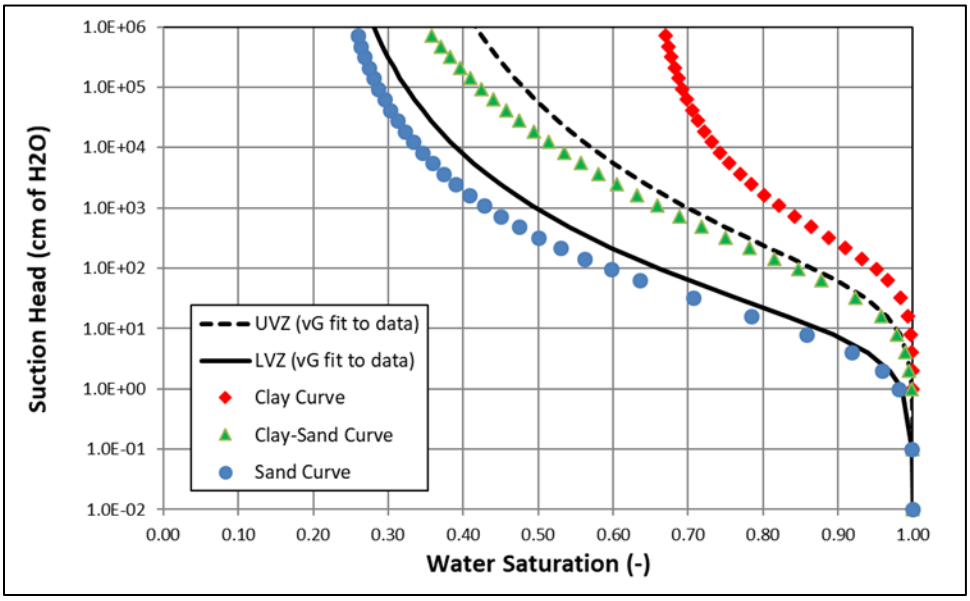

Figure 3-103. Water Retention Curves for Upper and Lower Vadose Zones (Nichols and Butcher, 2020; Figure 5-15)

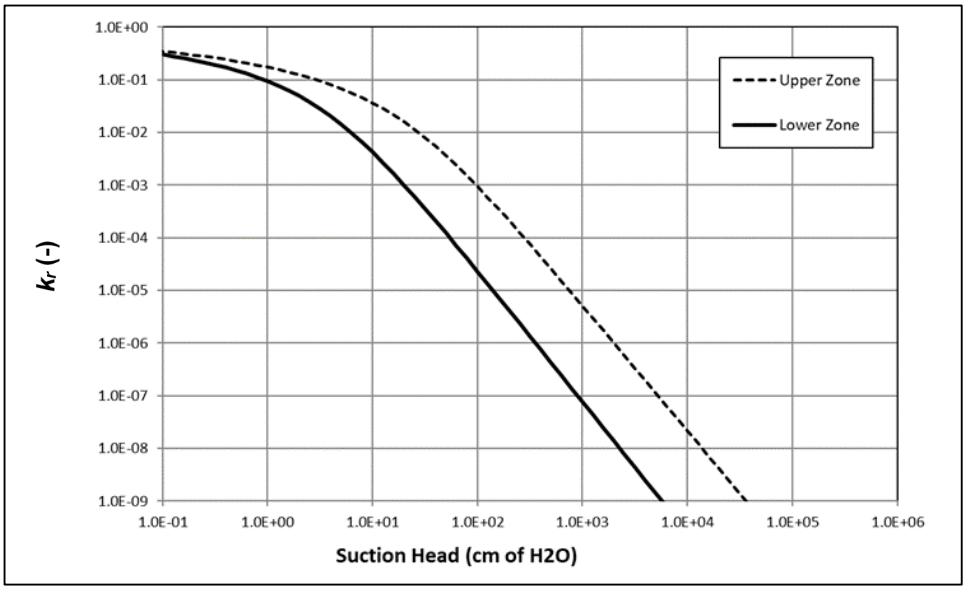

Figure 3-104. Relative Permeability Curves for Upper and Lower Vadose Zones (Nichols and Butcher, 2020; Figure 5-16)

VG parameters for all VZ soil categories (i.e., undisturbed and disturbed soils) are provided in Table 3-52 along with K_{sat}, η, ρ_b, and ρ_p, and D_e for these materials. Derivations of these property values for OSC, CCB, ILV permeable backfill, and gravel are discussed below in Sections 3.8.3.1.2, 3.8.3.1.3, 3.8.3.1.4, and 3.8.3.1.5, respectively.

Porosity, Bulk Density, and Particle Density

Porosity values reflect laboratory measurements of the total volume of pore space in the soil samples. Because samples were collected from the VZ, where flow primarily occurs in the vertical

direction perpendicular to strata, the total porosity is assumed to be roughly equivalent to the effective porosity. Bulk density corresponds to the dry bulk density or the total mass of dry soil per unit volume of material (including pore spaces). Particle density reflects the mass of dry soil particles per unit volume of soil particles (not including pore space). Particle density is calculated using laboratory measurements of porosity and dry bulk density using Eq. (3-53) from Hillel (1982):

$$\rho_p = \frac{\rho_b}{(1-\eta)} \qquad \text{Eq. (3-53)}$$

Total porosity (η), bulk density (ρ_b), and particle density (ρ_p) are calculated for the UVZ and the LVZ. Calculations entail arithmetic averaging of laboratory data. Estimates for the textural property categories (i.e., "clay", "clay-sand," and "sand") include all samples for which corresponding grain-size data are available. All available laboratory data are lumped into either the upper or lower VZ using CPT logs and visual core descriptions and arithmetically averaged. Nichols and Butcher (2020; Table 5-10) provides ranges of the laboratory data along with the calculated averages. Porosity measurements range from 29% to 48%; dry bulk density ranges from 1.37 g cm^{-3} to 1.90 g cm^{-3}; particle density varies from 2.61 g cm^{-3} to 2.81 g cm^{-3}.

Saturated Effective Diffusion Coefficient

D_e is defined as the molecular diffusion coefficient (D_m) divided by the porous medium tortuosity (τ) as calculated by:

$$D_e = \frac{D_m}{\tau} \qquad \text{Eq. (3-54)}$$

Note that D_e does not include the effects of sorption or porosity. D_m is the aqueous diffusion coefficient of a chemical species in open or pure water. Because no measured D_e data are available from the laboratory or literature for soils typical of E-Area and Z-Area, generic literature values for D_m and τ are used to calculate D_e. Nichols and Butcher (2020; Table 5-11) provide D_m values from the literature for several inorganic compounds and ions. Tortuosity is defined by Nichols and Butcher (2020; Eq. 23). Literature values for τ evaluated for this PA are given by Nichols and Butcher (2020; Table 5-12); τ values used to calculate D_e for the UVZ and LVZ soils are summarized by Nichols and Butcher (2020; Table 5-13).

3.8.3.1.2. Operational Soil Cover

Because OSC will be derived from UVZ soils, properties for the UVZ soils can be used to estimate OSC properties before dynamic compaction (OSC1) and after dynamic compaction (OSC2) as described in detail by Nichols and Butcher (2020; Section 5.4).

Saturated Hydraulic Conductivity

Three different methods were evaluated by Nichols and Butcher (2020; Section 5.4.1.1) to estimate the horizontal hydraulic conductivity of OSC1. The chosen method uses the Kozeny-Carman

equation as described by Freeze and Cherry (1979) to relate K_{sat} to mean particle diameter (d_m) and the shape and packing of grains as represented by porosity (η).

$$K_{sat} = \left(\frac{\rho g}{\mu}\right)\left[\frac{\eta^3}{(1-\eta)^2}\right]\left(\frac{d_m{}^2}{180}\right) \qquad \text{Eq. (3-55)}$$

where:

ρ Fluid density (g m^{-3})
g Acceleration due to gravity (m s^{-2})
μ Fluid viscosity (g m^{-1} s^{-1})

It is assumed that the particle size distributions (and d_m) of OSC1 and UVZ are roughly the same because they are the same soil. As a result, K_{sat} for OSC1 is related to K_{sat} for UVZ by:

$$\frac{K_{sat-OSC1}}{K_{sat-UVZ}} = \frac{\left[\frac{\eta_2{}^3}{(1-\eta_2)^2}\right]}{\left[\frac{\eta_1{}^3}{(1-\eta_1)^2}\right]} = \frac{\left[\frac{(0.456)^3}{(1-0.456)^2}\right]}{\left[\frac{(0.385)^3}{(1-0.385)^2}\right]} = 2.123 \qquad \text{Eq. (3-56)}$$

where η (m^3 m^{-3}) for OSC1 and UVZ are provided in Table 3-52. In this PA, $K_{h\text{-}OSC1}$ (horizontal $K_{sat\text{-}OSC1}$) is set equal to 2.123 x 6.2E-05 cm s^{-1} ($K_{h\text{-}UVZ}$) = 1.3E-04 cm s^{-1}.

As documented by Nichols and Butcher (2020; Section 5.4.1.2), Eq. (3-56) is similarly applied to approximate K_h for OSC2 assuming a calculated porosity of 0.275 for OSC2 (see "Porosity, Bulk Density, Particle Density" below) and 0.385 for UVZ soil. For this PA, $K_{h\text{-}OSC2}$ is set equal to 0.261 x 6.2E-05 cm s^{-1} ($K_{h\text{-}UVZ}$) = 1.6E-05 cm s^{-1}.

The vertical hydraulic conductivity (K_v) values for OSC1 and OSC2 both before and after dynamic compaction are set equal to the horizontal hydraulic conductivities as reported in Table 3-52. OSC consists of excavated soil from the UVZ that is stockpiled until later placement over the waste using a bulldozer. These operational techniques are assumed to grossly homogenize UVZ soil, thereby eliminating most large-scale layering and creating loosely packed soils with similar vertical and horizontal hydraulic conductivities.

Water Retention Curves

Estimations of water retention and unsaturated hydraulic conductivity curves for OSC1 and OSC2 entail using Leverett scaling (Bear, 1972) and sample data for UVZ soil as derived by Nichols and Butcher (2020; Section 5.4.2). Leverett scaling consists of adjusting capillary pressure based on permeability. Similarly to Eq. (3-56), a scaling equation is derived relating the unknown suction head (ψ_{OSC}) at a particular saturation in OCS to the corresponding (known) suction head (ψ_{UVZ}) at the same saturation in UVZ soil.

$$\psi_{OSC} = \left[\frac{K_{UVZ}\eta_{OSC}}{K_{OSC}\eta_{UVZ}}\right]^{1/2} \psi_{UVZ} \quad \text{Eq. (3-57)}$$

Using estimates of hydraulic conductivity and porosity for OSC1 and OSC2 and measured values for UVZ soils, water retention curves for OSC1 and OSC2 are estimated using Eq. (3-57) to give:

$$\psi_{OSC1} = 0.747 \times \psi_{UVZ} \quad \text{Eq. (3-58)}$$

$$\psi_{OSC2} = 1.653 \times \psi_{UVZ} \quad \text{Eq. (3-59)}$$

WRCs for OSC1 and OSC2 are provided by Nichols and Butcher (2020; Figure 5-20). At a particular suction head, OSC1 (before dynamic compaction) has a lower water saturation than UVZ soil and OSC2 (after dynamic compaction). k_r versus ψ curves are given by Nichols and Butcher (2020; Figure 5-21). At a given ψ, k_r for OSC1 is lower than the values for UVZ and OSC2. The resulting WRC data sets for OSC1 and OSC2 are fit to the VG equation to determine VG parameters using a least squares regression method described by Nichols and Butcher (2020; Section 5.2.3). The VG parameters are reported in Table 3-52.

Porosity, Bulk Density, Particle Density

The porosities of OSC1 (0.456) and OSC2 (0.275) in Table 3-52 are calculated using Eq. (3-53) assuming bulk densities of 1.442 g cm^{-3} and 1.92 g cm^{-3} (Phifer and Wilhite, 2001), respectively, and a particle density of 2.65 g cm^{-3} (Hillel, 1982).

Saturated Effective Diffusion Coefficient

A D_e value of 5.3E-06 cm^2 s^{-1} is assumed for OSC1, which is the same value assigned to both the UVZ and LVZ soils. OSC2 will likely possess a lower D_e than OSC1 because of an increase in τ resulting from the decreasing pore space and tighter packing of grains caused by dynamic compaction. A D_e equal to 4.0E-06 cm^2 s^{-1} is assigned to OSC2 (Nichols and Butcher, 2020; Section 5.4.4).

3.8.3.1.3. Controlled Compacted Backfill

Samples from the ORWBG and compacted composite samples from Z-Area were used in the evaluation to represent the CCB soil. Table 3-68 provides an approximate number of each data type. Samples collected in 2001 from the ORWBG consist of borrow pit material that was placed on top of the ORWBG to increase runoff. The tested material consists primarily of sandy clay soils and is typical of CCB material. Z-Area samples were collected in May 2005 from two locations at depths of 4, 6, 8, 10, and 12 feet. At each location, the five depth samples were mixed to form a composite sample for analysis. Data quality for CCB hydraulic properties is discussed by Nichols and Butcher (2020; Section 5.3.2)

Table 3-68. Datasets for E-Area and Z-Area Controlled Compacted Backfill Soil (Nichols and Butcher, 2020; Table 5-3)

Data Type	E-Area (2001)	Z-Area (May 2005)
Grain-size analyses	41 samples (27 locations)	2 samples (2 locations)
Hydraulic & bulk property	14 samples (14 locations)	8 samples (2 locations)

Grain Size

Grain-size analyses for the samples representing CCB are reported on a textural triangle by Nichols and Butcher (2020; Figure 5-18). The data include samples from the ORWBG and compacted composite samples from Z-Area. All data cluster together in the sandy clay loam category. Samples evaluated according to the USCS are classified as "SC" (clayey sands or sand-clay mixtures) or "SM" (silty sands, sand-silt mixtures).

Saturated Hydraulic Conductivity

Nichols and Butcher (2020; Section 5.3.2) details the sample reliability screening process for the 32 samples selected for the K_{sat} evaluation. The upscaling method used for VZ soil (Nichols and Butcher, 2020; Section 5.2.2.2) was applied to the data for CCB to include heterogeneity and spatial continuity. Using p_h = +0.59 and p_v = -0.33, the calculated K_h and K_v are 7.6E-5 cm s^{-1} and 4.1E-5 cm s^{-1}, respectively, as reported in Table 3-52.

Water Retention Curves

Water retention data collected on samples from the ORWBG were used to develop VG parameters for CCB employing the same approach described for VZ soils (Section 3.8.3.1.1) by Nichols and Butcher (2020; Section 5.2.3). VG parameters for the CCB are reported in Table 3-52, and WRCs for individual ORWBG samples and the CCB are reported by Nichols and Butcher (2020; Table 5-9 and Figure 5-19, respectively). Samples used in the evaluation are only representative of the CCB because they are not true samples of the future CCB; therefore, soil moisture curves should be considered as rough estimates for the potential properties of CCB.

Porosity, Bulk Density, Particle Density

Only 19 of 32 samples used in the K_{sat} evaluation above included laboratory measurements of η and ρ_b. Using arithmetic averaging, samples representing CCB have an average porosity of 0.355, an average bulk density of 1.71 g cm^{-3}, and a calculated particle density of 2.65 g cm^{-3} as summarized by Nichols and Butcher (2020; Table 5-10) and as reported in Table 3-52.

Saturated Effective Diffusion Coefficient

No laboratory measurements of D_e, D_m, or τ are available for the CCB samples. Because the controlled compacted soil will come from the VZ, a D_e equal to 5.3E-6 cm^2 s^{-1} is assumed (Nichols and Butcher, 2020; Section 5.3.5), which is the same value assigned to UVZ, LVZ, OSC1, and the "clay-sand" category in Table 3-52.

3.8.3.1.4. Intermediate-Level Vault Permeable Backfill

According to engineered drawings, the ILV was constructed using a permeable backfill with <15% mud. The backfill likely came from local borrow pits and, therefore, VZ soils data are used to

estimate the properties of the backfill. Two samples (VL-1, 44-46 ft bls and VL-1, 13-15 ft bls from E-Area) were used by Nichols and Butcher (2020) in the evaluation.

Saturated Hydraulic Conductivity

The arithmetic average of the laboratory measured K_v values for the two VL-1 samples is 7.6E-04 cm s^{-1} as reported in Table 3-52. K_h/K_v for the ILV permeable backfill is set equal to 1.9, the same as for CCB which will undergo similar handling and operational processes during installation. Using this ratio, K_h is calculated to be 1.4E-03 cm s^{-1}.

Water Retention Curves

Water retention data collected on the two VL-1 samples were used to develop VG parameters for the ILV permeable backfill utilizing the approach described by Nichols and Butcher (2020; Section 5.2.3). The VG parameters are reported in Table 3-52.

Porosity, Bulk Density, Particle Density

The laboratory measured porosity and dry bulk density of the two VL-1 samples averaged 0.415 g $cm^{-3}$and 1.56 g cm^{-3}, respectively (Nichols and Butcher, 2020; Section 5.5.3.2). A particle density of 2.67 g cm^{-3} was calculated using Eq. (3-53).

Saturated Effective Diffusion Coefficient

The molecular diffusion coefficient assumed for VZ soils (D_m = 1.6E-05 cm^2 s^{-1}) and the tortuosity assumed for sand (τ = 2) are used in Eq. (3-54) to estimate D_e (8.0E-6 cm^2 s^{-1}) for ILV permeable backfill because no experimental data are available. The tortuosity of sand is assumed because the two VL-1 samples are categorized as "sand" in the initial VZ soils evaluation in the 1980s (Nichols and Butcher, 2020; Section 5.5.4.1).

3.8.3.1.5. Gravel

Soil properties were estimated for a generic G1 "gravel" layer based on literature and reported laboratory results for gravel utilized in the construction of some of the vaults in the area. The reported data (Yu et al., 1993) include water retention and relative permeability for two gravel samples (GL-1 and GL-2).

Saturated Hydraulic Conductivity

The arithmetic average of the laboratory measured K_{sat} values for the two GL samples is 1.5E-01 cm s^{-1}. K_h/K_v for the G1 gravel is assumed to be 1.0; therefore, K_h is equal to K_v as reported in Table 3-52.

Water Retention Curves

Soil moisture data for the two GL gravel samples were used to develop the VG parameters for G1 gravel utilizing the approach described by Nichols and Butcher (2020; Section 5.2.3). The VG parameters are reported in Table 3-52.

Porosity, Bulk Density, Particle Density

Per Nichols and Butcher (2020; Section 5.5.3.2), generic gravel is assigned a porosity of 0.300 based on a review of literature data (Fredlund and Rahardjo, 1993; Freeze and Cherry, 1979) for gravels as well as laboratory data for the GL-1 and GL-2 samples.

Saturated Effective Diffusion Coefficient

The τ for gravel is expected to be lower than the value assumed for the VZ soils ($\tau = 3$). A τ of 1.7 was chosen based on the approach described by Nichols and Butcher (2020; Section 5.5.4.2). Assuming D_m for VZ soils (1.6E-05 $cm^2\ s^{-1}$) and τ equal to 1.7, Eq. (3-54) calculates a D_e equal to 9.4E-6 $cm^2\ s^{-1}$ for gravel as reported in Table 3-52.

3.8.3.2. Saturated Zone Soil Properties

Porosity and saturated hydraulic conductivity for the saturated (aquifer) zone are set within the GSA GW flow model (Flach, 2019). The effective, total, and diffusive porosities are all set equal to 0.25. Flach and Harris (1999) recommend an effective porosity (η_e) equal to 0.25 for all saturated zone soils based on data reported by Aadland et al. (1995; Tables 3 and 7).[33] Aadland et al. (1995) estimate the average porosity of the UTRA and GAU to be about 0.35. Regions of relatively immobile water, ranging from grain-sized "dead-end" pores to macroscale clay intervals, do not effectively participate in contaminant transport. Therefore, an "effective" porosity value, smaller than the total porosity, is commonly used for transport simulations and particle tracing related to contaminant migration. An effective porosity value of 0.25 is assumed uniformly in the GSA model for computing a pore velocity field that may be used later for particle tracing. The assumed porosity value is consistent with the general recommendation by Looney et al. (1987; p. 39). A more in-depth discussion on the rationale for using effective porosity for saturated zone soils versus total porosity for VZ soils is provided by Nichols and Butcher (2020; Section 5.6.2).

Flach (2019) and Section 3.5.2 discuss in detail the assignment of K_{sat} within the GSA GW flow model. For the saturated zone, for which both saturation and relative permeability are equal to one, WRCs are not applicable.

As described by Flach (2019), dry bulk density, particle density, and effective diffusion coefficient of the soil materials are not specifically incorporated into the GSA GW flow model. However, for combined flow and transport modeling as conducted within the PA, these parameters are required, along with K_d (Section 3.8.1.3). The characteristics of the UTRA and GAU are similar to the LVZ

[33] Use of a lower value than total porosity for saturated flow and transport is common modeling practice (Fetter, 1993) and defines the effective area/volume through which porous-medium flow occurs. In the context of numerical field-scale transport simulations, an effective porosity partially addresses the effects of unresolved physical heterogeneity at the sub-grid scale. In the context of sedimentary geologic systems, a computational block contains strata of varying permeability with essentially no flow occurring in a fraction of strata with sufficiently low permeability. Although the vadose and saturated zones exhibit similar physical heterogeneity, total porosity is currently assumed in VZ PA models because of markedly different flow conditions. VZ flow is predominantly perpendicular to strata, rather than parallel to layering in the aquifer. Also, unsaturated conditions in the VZ significantly reduce the permeability contrast between coarse- and fine-grained materials, in comparison to saturated conditions in the aquifer. Both phenomena significantly reduce the extent to which flow can effectively bypass portions of the porous medium.

as described in Section 3.8.3.1.1. As reported in Table 3-52, the LVZ has an average porosity, dry bulk density, and particle density of 0.38, 1.66 g cm^{-3}, and 2.67 g cm^{-3}, respectively.

Because an effective porosity of 0.25, rather than a total porosity of 0.38, has been assigned to these materials, the LVZ particle density of 2.67 g cm^{-3} cannot be assigned to these materials (Bechtel, 2005; Flach, 2012). With porosity in the denominator of the combined equation, Eq. (3-60), employed to calculate the retardation factor (R) in the aquifer flow and transport model, a particle density of 2.67 g cm^{-3} results in artificially greater contaminant retardation within the aquifer:

$$R = 1 + \frac{\rho_p \left(1 - \eta_T\right) K_d}{\eta_T} \qquad \text{Eq. (3-60)}$$

where:

η_T Total porosity [m^3 m^{-3}] (Freeze and Cherry, 1979; Hillel, 1982)

As evidenced by Eq. (3-60), lowering the porosity from η_T = 0.38 to η_e = 0.25, while still maintaining an equivalent R, requires an "effective" particle density (ρ_{pe}) that is less than the assumed particle density (ρ_{pT}) of 2.67 g cm^{-3} for the LVZ. Nichols and Butcher (2020) derived the following equation to calculate ρ_{pe}:

$$\rho_{pe} = \frac{\rho_{pT} \left(1 - \eta_T\right) \eta_e}{\left(1 - \eta_e\right) \eta_T} \qquad \text{Eq. (3-61)}$$

Substitution in Eq. (3-61) yields an "effective" particle density of 1.45 g cm^{-3}.

The "effective" dry bulk density (ρ_{be}) associated with η_e = 0.25 is calculated using Eq. (3-62):

$$\rho_{be} = \rho_{pe} \left(1 - \eta_e\right) \qquad \text{Eq. (3-62)}$$

which yields ρ_{be} = 1.09 g cm^{-3}.

Within the GSA_2018 flow model (Flach, 2019), soils with K_{sat} > 1.0E-07 cm s^{-1} are defined as "sand" and those with K_{sat} < 1.0E-07 cm s^{-1} are defined as "clay" for the purpose of defining transport properties (i.e., K_d and D_e). For consistency with VZ soils (Section 3.8.3.1.1), D_e values in the GSA_2018 model for soils defined as "sand" and "clay" are assigned a D_e of 5.3E-06 cm^2 s^{-1} (LVZ, Table 3-52) and 4.0E-06 cm^2 s^{-1} (Clay, Table 3-52), respectively.

Table 3-69 provides a summary of the material and hydraulic properties for saturated zone soils.

Table 3-69. Material and Hydraulic Properties for Saturated Zone Soils

Saturated Hydraulic Conductivity	WRC Parameters	Effective Porosity (unitless)	Effective Dry Bulk Density (g cm^{-3})	Effective Particle Density (g cm^{-3})	Saturated Effective Diffusion Coefficient (cm^2 s^{-1})
Table 3-21	N/A	0.250	1.09	1.45	Sand: 5.3E-06 Clay: 4.0E-06

3.8.3.3. Cementitious Material Properties

Nichols and Butcher (2020; Sections 6.1 and 6.2) summarize the results of extensive internal and external literature reviews of cementitious material properties relevant to the ELLWF PA. Five cementitious materials are used to represent the various cementitious barriers present in ELLWF DUs as described in Section 2.2. The five materials are identified as old E-Area CIG grout (C1), new E-Area CIG Grout (C2), E-Area CLSM (C3), E-Area CIG Concrete Mat (C4), and E-Area Vault Concrete (C5). Nichols and Butcher (2020; Section 6.3) and Table 3-58 present recommended property values for these five cementitious materials. Table 3-58 also presents the properties for a vault crack, which assumes the properties of gravel (G1) as defined in Table 3-52. The property values assigned to the E-Area cementitious materials are based upon the priority order given in Section 3.8.3.

Limited site-specific field and laboratory data are available for most of the E-Area cementitious materials as outlined by Nichols and Butcher (2020; Section 6.2). Literature data for generic cementitious materials are summarized by Nichols and Butcher (2020; Section 6.1). When available, site-specific field and laboratory data are utilized to provide material property representations for both the material tested and similar materials. When site-specific laboratory data are unavailable, generic external literature data are employed.

Site-specific data for old E-Area CIG Grout (C1) used in CIG trench segments 1 through 8 are provided by Dixon and Phifer (2006) and described by Nichols and Butcher (2020; Section 6.2.3 and Table 6-16). A semi-empirical approach is selected to generate WRCs using surrogate materials to represent the micro- and macro-porosity drainage behavior of this grout material. The composite WRC is a blend of these two materials but does not adhere to a VG formulation.

Site-specific data for the new E-Area CIG grout formulation (C2) are provided by Dixon and Phifer (2007) and described by Nichols and Butcher (2020; Section 6.2.4). WRCs based on a VG formulation (Table 3-58) are fitted to select available data sources where physical properties are employed to establish the saturated water content value.

Site-specific data for E-Area CLSM (C3) is the same data reported by Phifer et al. (2006) as described by Nichols and Butcher (2020; Section 6.2.3). Tabulated values for the WRCs (Table 3-58) have been replaced with a VG formulation. WRCs based on a VG formulation are fitted to select available data sources where physical properties are employed to establish the saturated water content value.

No physical or hydraulic data are available for E-Area CIG concrete mats (C4); therefore, properties for this material are assumed to be the same as for new E-Area CIG Grout (C2) as shown in Table 3-58 and as discussed by Nichols and Butcher (2020; Section 6.3.3.4).

Site specific data for the vault concrete (C5) are available from a study by Phifer (2014), which is described by Nichols and Butcher (2020; Section 6.2.5). WRCs based on a VG formulation (Table 3-58) are fitted to select available data sources where physical properties are employed to establish the saturated water content value.

3.8.3.3.1. Porosity, Bulk Density, and Particle Density

Site-specific porosity and bulk density laboratory data are available for the old and new E-Area CIG grout, E-Area CLSM, and E-Area vault concrete (i.e., LAWV and ILV). Table 3-58 provides the recommended porosity, bulk density, and calculated particle density data for each of the cementitious materials. Typically, average values are used. Site-specific laboratory data are not available for the E-Area CIG reinforced concrete mats. The porosity, bulk density, and particle density of the E-Area CIG concrete mats are assumed to be the same as the new E-Area CIG Grout because both materials are placed with standard field construction practices (i.e., minimal consolidation and curing requirements).

3.8.3.3.2. Saturated Hydraulic Conductivity

Site-specific K_{sat} laboratory data are available for the old and new E-Area CIG grout, E-Area CLSM, and E-Area vault concrete (i.e., LAWV and ILV). Table 3-58 provides recommended K_{sat} values for each of these materials. Site-specific laboratory data are not available for the E-Area CIG concrete mats; therefore, K_{sat} for the E-Area CIG concrete mats is also assumed to be the same as K_{sat} for new E-Area CIG grout (i.e., 2.6E-08 cm s^{-1}) for the same reason stated above for porosity, dry bulk density, and particle density.

3.8.3.3.3. Water Retention Curves (Suction Head, Saturation, and Relative Permeability)

Site-specific WRCs are again available for old and new E-Area CIG grout, E-Area CLSM, and E-Area vault concrete. The WRC for concrete mats is again based on the WRC for new E-Area CIG grout. WRC parameters based on a VG formulation are listed in Table 3-58. The derivation of these parameters is presented by Nichols and Butcher (2020; Section 6.3.3) for each cementitious material.

3.8.3.3.4. Saturated Effective Diffusivity

The new E-Area CIG Grout, E-Area CIG concrete mats, and E-Area vault concrete (i.e., LAWV and ILV) are considered fairly typical cementitious materials for which D_e can be reasonably derived from literature values presented by Nichols and Butcher (2020; Section 6.1.4).

As concluded by Nichols and Butcher (2020; Section 6.1.4), D_e values for typical cementitious materials range from approximately 1.0E-08 to 5.0E-07 cm^2 s^{-1} (Nichols and Butcher, 2020; Tables 6-9, 6-10, and 6-11). This is a relatively narrow range when compared to the range of K_{sat} values for cementitious materials. The data clearly show that D_e decreases with decreasing water-to-cementitious material ratio and with the addition of fly ash, blast furnace slag, and silica

fume. Based upon this information, three categories of cementitious materials (low-quality concrete, ordinary-quality concrete, and high-quality concrete) have been defined as outlined by Nichols and Butcher (2020; Table 6-29) to assign appropriate D_e values to each of the E-Area cementitious materials. Nichols and Butcher (2020; Table 6-29) provide the resulting D_e assignments for each of these materials along with its justification.

While old E-Area CIG grout and E-Area CLSM are cementitious materials, it is not considered appropriate to assign D_e values for these materials based strictly upon the cementitious material literature for the following reasons:

- As outlined by Nichols and Butcher (2020; Sections 6.3.2 and 6.3.3), the porosity of old E-Area CIG grout consists of a small fraction of macropores (~15% of material volume characterized as containing macropores) with a high hydraulic conductivity that result in rapid drainage and a larger fraction of micropores (~85% of material volume characterized as containing micropores) with a relatively low hydraulic conductivity that drain slowly. Therefore, with respect to D_e, the old E-Area CIG grout probably behaves more like a blended material comprised of ~15 vol% sand containing macropores and ~85 vol% cementitious material containing micropores.
- As outlined by Nichols and Butcher (2020; Section 6.3.2), E-Area CLSM has a saturated hydraulic conductivity (average 2.2E-06 cm s^{-1}) like that of clay (>50% mud) as discussed by Nichols and Butcher (2020; Section 5.2.2) and as reported in Table 3-52 (2.0E-06 cm s^{-1}). Additionally, as outlined by Nichols and Butcher (2020; Section 6.3.3.3), E-Area CLSM has significant interconnected porosity, poor cementation at the aggregate-paste boundaries, and heterogeneity which make the CLSM appear to have soil-like properties. Finally, the fly ash used in CLSM is a relatively fine-grained material. Therefore, in terms of D_e, E-Area CLSM probably behaves more like a clayey soil than a cementitious material.

Based upon this reasoning, D_e for old E-Area CIG grout is calculated as though it consists of 15 vol% sand with a D_e of 8.0E-06 $cm^2\ s^{-1}$ (Nichols and Butcher, 2020; see Section 5.2.5 and Table 5-13) and 85 vol% cementitious material with a D_e of 8.0E-07 $cm^2\ s^{-1}$ (Nichols and Butcher, 2020; see Table 6-29 for low-quality concrete). This results in a blended D_e equal to 1.9E-06 $cm^2\ s^{-1}$ for old E-Area CIG grout as shown below:

$$D_e = (0.85)(8.0\text{E-}07\ \ cm^2\ s^{-1}) + (0.15)(8.0\text{E-}06\ cm^2\ s^{-1}) = 1.9\text{E-}06\ \ cm^2\ s^{-1}$$

Additionally, based upon this reasoning, E-Area CLSM is assigned the same D_e as clay (>50% mud) or 4.0E-06 $cm^2\ s^{-1}$ (Nichols and Butcher, 2020; see Section 5.2.5 and Table 5-13).

Table 3-58 and Nichols and Butcher (2020; Table 6-30) list the D_e values assigned to each of the E-Area cementitious materials.

3.8.3.4. Blended Waste Form Properties

The approach to blending material and hydraulic properties is discussed on an individual DU basis in Section 4.1.1.1.2 (containerized waste disposal in STs and ETs, including SWFs), Section 4.1.1.1.3 (hybrid ST), Section 4.5.3.6 (modeling concrete degradation in the LAWV), Section 4.6.3.5 (modeling concrete degradation in the ILV), and Section 4.7.2 (NRCDA waste zone material properties).

3.8.4. Infiltration

The *Infiltration Data Package, Ver. 1.0, dated October 16, 2019* (SRNL, 2019a) refers to the SRNL-compiled and -maintained Microsoft Excel database of infiltration data used to establish the upper-boundary flow conditions for the PORFLOW VZ and GoldSim® system models for the following types of ELLWF DUs: STs, ETs, LAWV, ILV, and NRCDAs. Infiltration rates for CIG trench segments are discussed in Section 3.8.4.3.5. The infiltration data used for STs and ETs are also employed in defining degradation behavior for the various covers over time within the PORFLOW aquifer flow model.

The technical report detailing the development and content of the *Infiltration Data Package* is *Infiltration Data Package for the E-Area Low-Level Waste Facility Performance Assessment* (Dyer, 2019b). Dyer (2019b) provides the input parameters, cap design and material properties assumptions, and modeling results for the HELP infiltration model simulations performed in support of the ELLWF PA. The current infiltration data package and accompanying report build upon the PA2008 infiltration data package (McDowell-Boyer et al., 2011) as well as foundational PA technical reports from the past 15 years (Dyer, 2017b; Dyer, 2017c; 2018a; 2018b; Dyer and Flach, 2017; 2018; Jones and Phifer, 2007; Phifer, 2004a; Phifer and Jones, 2007; Phifer et al., 2007; Shipmon and Dyer, 2017). Three important components comprise the infiltration data package: HELP model input parameter datasheets documenting the closure cap design and material properties assumptions, HELP model input and output filenames and directory structure, and infiltration rates as a function of time for each scenario (intact and subsidence) for each type of DU. Sensitivity and uncertainty analysis guidance and results are also included.

3.8.4.1. Background

The U.S. DOE LFRG review team report for PA2008 (LFRG, 2008) raised a secondary issue regarding the input parameter assumptions and HELP model results for the PA2008 infiltration analysis. The secondary issue and the proposed resolution as summarized by McDowell-Boyer et al. (2011) were:

> *"7.2.3.1: The HELP code that provided the basis of the cap infiltration analyses is well tested, generally accepted, and has been benchmarked against a broad range of codes that perform similar calculations. However, there is no discussion of the HELP modeling results with respect to the results of other analyses. Input parameters for HELP were difficult to find and were found in multiple documents cited in Phifer (2006).*

Proposed Resolution: A discussion of the HELP modeling results with respect to other modeling results for other analyses using available site data and information should be added. These data should be compiled into a single data package in the PA."

In response to the LFRG's secondary issue and proposed resolution, the strategic plan for the next ELLWF PA (Butcher and Phifer, 2016a) outlined a consolidated recommendation for the infiltration data package and new infiltration estimates:

"Produce a separate data package for the ELLWF closure cap and infiltration estimates generated by HELP modeling. Include closure cap material properties (e.g., hydraulic conductivity, porosity, field capacity, and wilting point), site-specific input data (e.g., precipitation, temperature, solar radiation, and evapotranspiration), and closure cap layer data (e.g., erosion, silting, holes in HDPE, geosynthetic clay liner (GCL), chemical degradation, pine tree root intrusion, etc.). As part of this data package, produce infiltration estimates for intact, degraded, and subsided-cap conditions based on the new closure cap conceptual design (profile, plot plan, and cross-sections) as inputs to the upper boundary conditions for PORFLOW models. This will include development of subsided infiltration estimates for individual disposal unit types, as applicable. This work should be performed prior to the time of execution of the next PA revision."

The current ELLWF PA infiltration data package, coupled with the extensive work leading up to it, addresses the issues raised by the LFRG in 2008.

3.8.4.2. HELP Model and Alternatives

Section 3.9.4 describes the SRNL-recompiled version of HELP Ver. 3.07 used in PA2022 and summarizes SRNL's rigorous evaluations of the HELP model against five alternative computer codes that use Richards' equation for variably-saturated flow. Dyer (2019c) concluded that the HELP model remains the preferred choice over other commercial and public-domain hydrologic models for the ELLWF PA. The origin and generation of the weather data input files employed in the HELP model simulations are explained below.

The HELP model requires the input of evapotranspiration, precipitation, temperature, and solar radiation data. Four input options are available for each type of weather data (Schroeder et al., 1994a; Schroeder et al., 1994b):

1. Historical records for specific cities (HELP model default)
2. Synthetic data generated using the statistical characteristics of historical data for specific cities.
3. Synthetic data generated utilizing mean monthly precipitation and temperature data for the specific location of interest
4. Manual data entry

The default historical weather databases (Option 1) included with the HELP model (Ver. 3.07 and SRNL-recompiled Ver. 4.0) are quite limited with respect to the period covered and the number of cities available. A complete set of historical weather data for either SRS or Augusta, GA is

unavailable in the HELP model. Alternatively, the HELP model will generate up to 100 years of synthetic weather data for many more cities than are included in the default historical weather databases (Option 2). For example, synthetic weather data can be generated for Augusta, GA, but not SRS. A third option is to utilize actual monthly precipitation and temperature data from SRS to modify the synthetic data generated for Augusta, GA. Lastly, manual data entry (Option 4) is time consuming to implement because it requires the availability of daily precipitation, temperature, and solar radiation data as well as placement of the data in a fixed format acceptable to HELP. Option 3 was chosen as the best option for the ELLWF PA.

One hundred years of synthetic daily precipitation, temperature, and solar radiation data were generated using HELP's synthetic weather data generator for Augusta, GA as modified with SRS-specific mean monthly precipitation and temperature data. SRS collects meteorological data from a network of nine weather stations. SRS precipitation data has been collected primarily at the SRNL (773-A) weather station between 1952 and 1995 and at the Central Climatology site (CLM) since 1995. The closest weather station to the ELLWF and the FTF is the 200-F weather station, where precipitation data has been collected from a manual rain gauge daily (with some exceptions) since 1961. The primary source of SRS temperature data is the SRNL (773-A) weather station from 1968 to 1995 and the CLM from 1995 to present. Temperature data is not collected at the 200-F weather station.

SRS monthly precipitation and temperature data from the combined SRNL/CLM weather stations and precipitation data from the 200-F weather station were obtained from the SRNL Atmospheric Technologies Center website (https://weather.srs.gov/weather/). To be consistent with the HELP model simulations for the FTF closure cap design, mean monthly precipitation data from the 200-F weather station and mean monthly temperature data from the combined SRNL/CLM weather stations were used in the HELP model simulations for the ELLWF. Phifer et al. (2007) describe in detail how missing precipitation data from the 200-F weather station were addressed.

Table 3-70 provides monthly precipitation totals for the years 1961 to 2006 from the 200-F weather station as reported by Phifer et al. (2007). The mean monthly precipitation rate for this 46-year period is shown on the last line of the table.

Table 3-70. Monthly Precipitation Data (Inches) for 200-F Weather Station (Dyer, 2019b; Appendix A)

Year	Jan	Feb	March	April	May	June	July	August	Sept	October	Nov	Dec
1961	3.55	5.53	7.57	7.23	4.21	2.00	2.94	8.55	0.56	0.02	1.80	6.20
1962	4.35	5.28	6.46	3.85	2.61	1.97	1.74	4.36	4.03	1.87	3.31	2.40
1963	6.05	3.59	3.15	3.18	2.37	7.04	2.00	1.54	5.05	0.00	3.24	4.11
1964	7.67	5.69	5.40	5.81	3.56	5.18	10.99	10.87	5.19	6.44	0.77	4.17
1965	2.12	6.24	8.13	2.45	1.70	4.28	9.63	1.75	2.11	3.00	2.18	1.31
1966	6.82	5.42	4.39	3.26	4.87	3.82	3.88	5.17	4.68	1.37	1.18	3.21
1967	3.56	3.71	7.54	2.60	4.56	2.13	6.28	7.31	1.02	0.53	2.37	2.83
1968	3.92	0.97	1.92	1.83	2.91	4.32	4.93	3.14	1.88	3.03	4.14	2.84
1969	1.85	2.13	3.43	4.20	3.41	4.36	1.99	5.43	5.96	1.96	0.34	3.83
1970	2.78	2.62	7.65	1.33	4.99	3.09	2.87	3.20	0.69	4.29	1.83	5.06
1971	5.01	3.97	8.70	2.85	2.03	6.73	11.52	9.40	2.33	4.91	2.16	3.03
1972	7.93	3.66	2.78	0.47	3.75	5.84	2.68	6.88	1.28	0.76	3.62	4.73
1973	5.31	4.82	6.48	4.97	5.17	8.52	4.50	5.83	3.22	1.22	0.35	4.69
1974	2.68	6.60	2.91	2.63	3.86	4.97	4.00	6.98	3.24	0.01	2.05	4.12
1975	5.45	6.19	5.97	3.98	5.48	3.24	7.65	3.95	7.86	1.00	4.43	4.00
1976	4.22	1.50	3.95	2.22	10.86	6.40	3.28	2.41	5.40	5.54	3.89	4.82
1977	3.86	2.20	7.90	1.02	2.61	3.79	4.02	8.43	4.66	5.44	2.07	5.14
1978	8.44	1.45	3.07	4.85	3.33	1.94	4.13	2.72	3.74	0.20	3.54	2.17
1979	3.41	9.31	3.95	5.37	7.44	1.55	7.55	9.14	7.77	1.38	7.34	2.29
1980	4.29	2.33	11.44	2.31	3.57	3.30	0.99	2.86	7.38	1.95	2.21	1.96
1981	0.93	3.91	3.87	2.71	4.51	5.05	4.39	5.92	0.85	2.88	0.91	8.45
1982	4.73	3.86	1.95	4.90	2.37	4.07	10.53	6.45	5.02	3.61	2.06	4.58
1983	4.00	8.06	5.49	4.71	3.00	2.77	3.71	6.21	3.52	2.21	4.98	3.66
1984	3.53	5.34	6.05	7.11	10.73	1.82	6.46	3.52	1.06	0.40	0.97	1.16
1985	2.98	6.36	1.06	0.83	3.49	4.88	9.82	2.90	0.90	3.77	7.51	2.74
1986	1.18	3.05	2.75	0.96	3.47	2.60	2.61	8.59	0.80	3.05	5.76	4.94
1987	6.79	7.50	4.35	0.75	1.86	5.02	5.68	4.20	2.91	0.32	2.28	1.37
1988	3.74	1.03	2.48	4.88	0.97	6.67	2.24	2.98	4.79	3.50	1.92	1.66
1989	1.24	2.91	4.83	5.89	3.36	5.82	9.51	0.39	4.84	5.51	3.65	3.35
1990	2.91	1.84	1.88	0.94	2.16	3.87	7.65	10.65	0.50	17.84	1.25	2.55
1991	6.73	1.80	7.86	5.43	3.93	3.35	14.4	9.79	2.05	0.80	1.47	3.19
1992	3.63	5.32	2.93	2.74	1.54	8.28	5.18	8.70	2.42	6.21	8.57	2.96
1993	8.90	5.09	8.48	1.37	1.56	6.03	2.87	3.48	6.56	0.61	2.29	1.79
1994	4.81	3.38	6.68	0.98	1.20	4.80	5.54	5.29	1.48	10.5	2.56	4.91
1995	5.97	7.50	0.83	0.93	2.10	12.73	4.27	6.69	5.42	2.31	2.13	3.90
1996	3.08	2.08	6.81	1.69	2.40	4.59	5.55	10.58	3.14	2.09	1.46	2.97
1997	4.20	5.56	2.32	3.88	2.42	6.77	7.02	2.33	5.80	5.54	5.49	7.57
1998	8.42	6.59	6.48	5.97	3.63	3.74	4.79	3.63	8.30	0.78	0.76	1.90
1999	5.82	2.60	3.04	1.34	2.55	8.67	4.70	2.87	5.66	2.24	0.65	1.35
2000	5.80	1.06	3.06	2.08	2.27	6.02	2.90	5.84	6.47	0.02	3.86	2.02
2001	3.21	3.55	6.88	1.44	4.00	6.29	5.30	1.78	5.70	0.04	0.97	0.68
2002	2.07	2.13	3.50	2.19	1.54	2.75	4.76	6.02	3.87	3.34	5.64	4.20
2003	1.62	5.97	8.10	9.67	6.60	7.28	5.86	3.09	2.32	3.10	1.30	2.27
2004	4.63	6.81	0.99	1.69	2.47	8.49	3.01	4.21	10.54	3.32	4.11	3.81
2005	2.88	3.96	6.57	1.35	3.82	7.78	5.09	6.00	0.20	4.80	2.42	6.33
2006	3.47	3.37	2.45	3.22	1.53	7.73	5.88	1.49	2.34	2.53	3.25	5.12
Monthly Average Precip.	4.36	4.21	4.88	3.18	3.54	5.05	5.38	5.29	3.82	2.96	2.85	3.53

Notes to Table 3-70

All precipitation data is from the 200-F Weather Station, except as noted below:

- 200-F Weather Station precipitation data is unavailable in the SRS ATG Climate Data database on the following days: 3/30/1967, 3/31/1967, 4/1/1967 through 4/18/1967, 11/4/1968, 10/31/1970, 1/24/1971, 11/27/1971, and 10/31/1998.
- The monthly data highlighted in grey represents months where some daily precipitation data is missing from the 200-F weather station database (i.e., possible underreporting). For these seven instances, if the monthly precipitation total for the combined SRNL/CLM weather stations exceeded the value reported by the 200-F weather station, the monthly total for the combined SRNL/CLM weather stations was used instead.
    - March 1967: Monthly 200-F precipitation total of 5.29 inches was replaced with the monthly combined SRNL/CLM total of 7.54 inches.
    - April 1967: Monthly 200-F precipitation total of 2.58 inches was replaced with the monthly combined SRNL/CLM total of 2.6 inches.
    - November 1968: Monthly 200-F precipitation total of 2.89 inches was replaced with the monthly combined SRNL/CLM total of 4.14 inches.
    - October 1970: Monthly 200-F precipitation total of 4.29 inches was retained.
    - January 1971: Monthly 200-F precipitation total of 4.47 inches was replaced with the monthly combined SRNL/CLM total of 5.01 inches.
    - November 1971: Monthly 200-F precipitation total of 1.75 inches was replaced with the monthly combined SRNL/CLM total of 2.16 inches.
    - October 1998: Monthly 200-F precipitation total of 0.78 inches was retained.

Table 3-71 provides monthly temperature data for the years 1968 through 2006 obtained from the combined SRNL/CLM weather stations. The mean monthly temperature for this 39-year period is shown on the last line of the table.

Evapotranspiration data, which is considered constant from year to year, was based on HELP model default data for Augusta, GA. The evaporative zone depth is the maximum depth to which the HELP model will allow evapotranspiration to occur. Except where noted, an evaporative zone "fair" depth of 22 inches was chosen based on guidance from the HELP manual (Schroeder et al., 1994b). Twenty-two inches is considered a conservative maximum evaporative-zone depth due to anticipated capillarity associated with the surficial soil types (i.e., topsoil and upper backfill) and the anticipated root depths. The maximum leaf area index (LAI) is a measure of the maximum active biomass that the HELP model allows to be present. The actual LAI utilized by the HELP model is modified from the maximum based upon daily temperature, daily solar radiation, and the beginning and ending dates of the growing season. Except where noted, a maximum LAI equal to 3.5 (good stand of grass) was chosen based on guidance from the HELP manual (Schroeder et al., 1994b).

The methodology used by the HELP model to calculate the evapotranspiration rate is described in detail by Schroeder et al. (1994b). The methodology takes into consideration daily solar radiation, daily temperature, humidity, wind speed, vegetation type, LAI, growing season, surface and soil water content, maximum evaporative depth, soil water transport, and soil capillarity. The vegetative cover for the ELLWF final closure cap is initially assumed to be Bahia grass before pine-tree intrusion 160 years after cap installation.

Table 3-71. Monthly Temperature Data (°F) for SRNL/CLM Weather Station (Dyer, 2019b; Appendix A)

Year	Jan	Feb	Mar	Apr	May	June	July	Aug	Sept	Oct	Nov	Dec
1968	43.5	43.4	57.1	66.5	71.3	80	83.1	82.8	77	67	55.4	45.9
1969	46.5	46.6	51.5	64.5	70.5	80.3	83.3	77.6	72.8	66.1	52.1	45.4
1970	39	47.2	55.9	66.8	74.2	79	81.1	80.8	78.6	67	51.6	49.3
1971	44.6	46.4	49.5	63.4	70.7	81.3	80.7	80.4	75.2	70.2	55.5	56.9
1972	51.7	45.6	57.6	67.4	72.4	75.3	79.7	80.6	77.2	64.8	54.4	53.2
1973	46.1	45.9	60.7	61.9	70.5	77.7	79.1	74.5	70.5	62.4	59	50.3
1974	59.6	50.8	62.2	66.2	75.3	77.5	81.5	80.9	75.3	64.5	56.6	49
1975	51.4	53.2	55.8	63.9	75.6	79.1	79.7	82.4	75.7	68.7	59.3	48.5
1976	44.2	55.7	61.5	64.8	68.9	75.6	80.4	78	73.1	60.1	48.7	44.8
1977	35.3	47.1	60	66.9	73.3	80.6	83.6	80.6	77.9	62.1	58.2	46.7
1978	39.3	41.3	54.2	65.7	70.9	79.7	82.1	81.2	77.1	65.6	60.7	49.6
1979	42.1	44.6	57.5	64.5	71.3	75.1	79.6	80.5	73.4	64.8	57.4	47.4
1980	45.9	44.3	52.6	63.5	71.2	78.3	83.8	82.5	79.2	62.7	52.8	46
1981	40.4	48.5	53	67	68.6	81.3	81.3	76.3	74	62.1	54.4	43.2
1982	43	50	58.9	62.4	75.7	78.8	80.9	80.1	75	66.2	58.7	54.8
1983	43.3	48	55.3	59.4	66.8	76.7	84.3	83.9	74.8	67.2	56.4	45.8
1984	45	51.7	56.5	62.6	71.9	80.1	80.1	80.8	74	73.4	53.4	56.9
1985	42.9	49.5	60.2	67.5	74.5	80.8	81.1	79.7	75.7	70.8	65.5	45.4
1986	45.4	54.6	57.9	66.4	74.4	82.7	86.9	80.1	78.4	67.1	61.3	49.3
1987	46.2	48.6	56.5	62.3	74.5	79.9	82.8	83.8	76.6	60.7	59.1	52.9
1988	42.3	47.8	56.8	64.2	70.4	76.8	81.6	81.4	75.4	61.2	58	49.1
1989	52.2	52	58.3	64.2	70.6	79.8	81.4	80.9	75.3	67.3	52.4	44.2
1990	54.9	57.5	60	64	72.9	80.5	83.7	83.8	79	69.4	59.9	54.6
1991	47.9	54.1	60.3	69.2	76.9	79.5	83.6	81.2	77.4	68.1	55.4	54
1992	49.5	54.1	57.2	65	71.2	78.9	83.7	80.7	76.9	65	57.1	48
1993	51.7	47.8	53.2	58.9	69.7	78.2	83.6	80	75.2	62.8	55.2	43.6
1994	41.5	50.1	60.2	68	71.2	82.3	81.8	81.2	77.4	67.2	62.3	53.3
1995	45.5	49.9	58.6	65.9	73.5	75	79.9	79	71.8	65.9	50.8	43.8
1996	44.6	50.1	50.6	61.6	72.9	76.5	79.3	76	72.7	62.1	51.6	48.8
1997	48.2	52.9	63.3	61.2	68.5	74	80.2	79	75	64.1	51.6	47
1998	49.7	51.1	53.6	62.7	74.6	82.1	82.6	80.3	75.8	66.9	60.5	53.6
1999	51.9	51.6	53.4	67.2	69.7	76.6	80.7	82.9	73.8	64.3	58.1	48.6
2000	44.4	50.2	58.5	60.7	75.1	78	79.9	77.6	71.7	62.5	53.1	38.2
2001	43.8	52.4	53	63.9	71.3	75.3	77.7	78.8	71.2	62.2	60	52.4
2002	47.3	48	57.6	68.1	70.2	77.5	80.5	78.4	75.4	66.7	51.7	44.5
2003	42	47.5	57.6	61.6	70.6	75.2	77.3	77.7	71.9	63.7	58.2	42.9
2004	43.7	45.2	58.5	63.4	74	77.7	80.1	77.3	73.2	66.2	56.1	45.8
2005	47.9	49	53.1	60.9	68	75.4	79.4	78.8	77	64.7	56.1	44.3
2006	50.8	47.3	55.3	66.3	70.1	76.2	80.3	80.5	72.9	62.4	53.6	50.6
Mean	**46.0**	**49.3**	**56.8**	**64.4**	**71.9**	**78.3**	**81.3**	**80.1**	**75.1**	**65.3**	**56.2**	**48.4**

The following four weather data input files were generated using the HELP model's synthetic weather generator and were utilized in all HELP model runs, except where noted:

- Augusta, GA synthetic precipitation modified with SRS-specific average monthly precipitation data over 100 years (file name: FPREC.D4)
- Augusta, GA synthetic temperature modified with SRS-specific average monthly temperature data over 100 years (file name: FTEMP.D7)
- Augusta, GA synthetic solar radiation data over 100 years (file name: FSOLAR.D13)
- Augusta, GA evapotranspiration data (file name: FEVAP.D11)

Due to their size, the precipitation, temperature, and solar radiation data files are not reproduced here but are available electronically.

Figure 3-105 displays the HELP model evapotranspiration input file FEVAP.D11 used in the infiltration simulations, except where noted. Figure 3-106 shows the modified HELP model evapotranspiration input file ICEVAP.D11 used in the infiltration simulations for the IC (interim cover) case for STs and ETs. For the IC case, the LAI is assumed to equal zero (bare ground to represent HDPE geomembrane) and the evaporative zone depth is assumed to be 0.0001 inches (essentially zero; however, a small nonzero value must be assumed to enable model convergence).

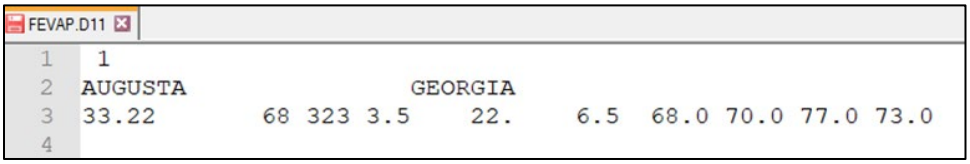

Figure 3-105. FEVAP.D11 File Used in E-Area Low-Level Waste Facility Performance Assessment HELP Model Simulations (except where noted)

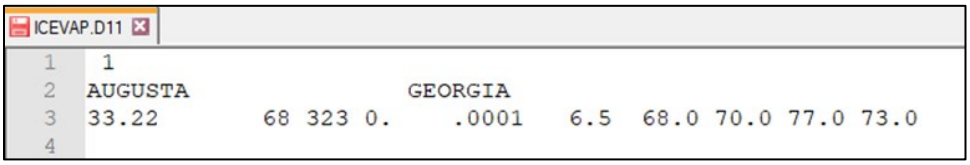

Figure 3-106. ICEVAP.D11 File Used in HELP Model Simulations of Institutional Control Period

Figure 3-107 presents the modified HELP model evapotranspiration input file VCOLEVAP.D11 used in the simulations of roof collapse for the LAWV, ILV and the CIG trench segments. An LAI equal to 1.0 for a poor stand of grass and an evaporative zone depth of 16 inches were assumed. Figure 3-108 displays the modified HELP model evapotranspiration input file ROOFEVAP.D11 used in the simulations of the operational and IC periods for the on-vault intact concrete roof cases for the LAWV and ILV. An LAI equal to zero for bare ground and an evaporative zone depth of 10 inches were assumed.

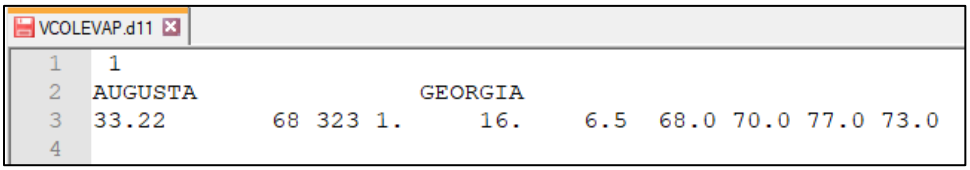

Figure 3-107. VCOLEVAP.D11 File Used in HELP Model Simulations of Concrete Roof Collapse Cases for Low-Activity Waste Vault, Intermediate-Level Vault, and Components-in-Grout Trench Segments

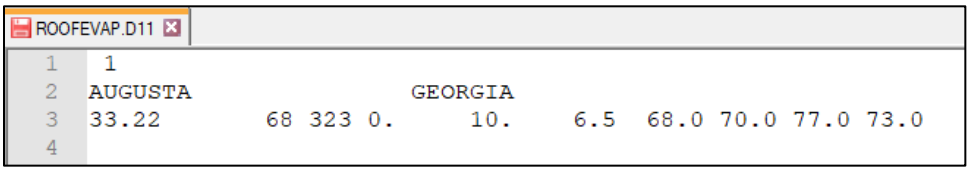

Figure 3-108. ROOFEVAP.D11 File Used in HELP Model Simulations of Intact Concrete Roof Cases for Low-Activity Waste Vault and Intermediate-Level Vault

3.8.4.3. Slit and Engineered Trenches

Details associated with surface infiltration rates are provided in the following subsections.

3.8.4.3.1. Planned Closure

ELLWF closure is planned in stages to accommodate ongoing operations for many more years, minimize infiltration into the underlying waste zone, and optimize future waste stabilization measures. Three stages of closure are envisioned: operational, interim, and final closure.

Operational closure encompasses those closure actions taken immediately or within a few years of filling a trench unit. During the operational period for STs and ETs (i.e., earlier than relative Year 0 in the infiltration calculations when the trench is still accepting waste and is less than 100% full), the infiltration estimates assume the placement of a minimum 4-foot-thick, clean soil cover over the filled portions of the ST and grading to provide positive drainage (i.e., no surface water run-on from adjacent areas). When a trench unit is full and no longer accepting waste, operational closure occurs. As described in detail by Phifer et al. (2009), operational closure of a ST entails adding 4 feet of soil as a foundation layer followed by installation of a surface operational stormwater runoff cover integrated with a drainage system to optimize stormwater runoff and removal and to minimize infiltration into the underlying buried waste. The stormwater runoff cover currently installed over each of the first five STs is an HDPE geomembrane, which is also assumed to be used for future closure. On the other hand, an ET receives no additional cover, beyond the 4-foot-thick soil cover, until sometime later when a similar polymeric geomembrane material will be applied at interim closure to optimize stormwater runoff. As a result, ETs will experience a longer period with only the operational soil cover present.

Interim closure begins a nominal 100-year period of IC when close to 100% of E-Area is filled with waste. As outlined in Table 2-14, interim closure is currently assumed to commence on September 30, 2040, for all STs and ETs that are completely filled by that date, and September 30, 2065, for all trenches that remain open beyond 2040. The SRS Nuclear Materials Management Plan FY 2016-2030 (SRS, 2016) currently assumes that Environmental Management operations cease in the year 2065. Infiltration rates in the data package are presented as a function of a relative year, rather than an absolute year, and assume an IC period of 100 years duration. For simplification, relative Year 0 corresponds to calendar Year 2065, and marks the beginning of the IC period. Relative Year 100 corresponds to calendar Year 2165, which is defined as the date of final closure when installation of the final multilayer soil-geomembrane closure cap occurs. For trench units where interim closure begins in 2040, the IC period will instead last 125 years, beginning in relative Year −25.

Before the start of interim closure in either 2040 or 2065, a surface interim stormwater runoff cover(s) will be placed over the closed ST and ET units. As outlined by Phifer et al. (2009), the HDPE cover(s) will be integrated with the ELLWF stormwater drainage system to expedite excess stormwater runoff removal. The operational stormwater runoff covers in place at that time may transition into the interim runoff cover if their continued performance and serviceability are demonstrated. Otherwise, an alternative cover(s) may be introduced to serve as a more durable interim runoff cover. In either case, surface stormwater covers are assumed to be maintained at

intact conditions until final closure in calendar Year 2165 (relative Year 100) when installation of the final multilayer soil-geomembrane cover occurs.

The final stage of closure occurs at relative Year 100 in the infiltration calculations. Final closure consists of waste-layer stabilization measures (e.g., dynamic compaction) followed by installation of a multilayered soil-geomembrane cover. The stabilization measures taken are assumed to sufficiently consolidate the underlying waste layer and eliminate subsidence except in the presence of "non-crushable" containers as described in Section 3.8.4.3.3. The next section describes infiltration through an intact final closure cap in the absence of non-crushable containers.

3.8.4.3.2. Intact Infiltration Scenario

Dyer (2017b) used the HELP model to analyze ten intact infiltration model scenarios based on the FTF closure cap design (Phifer et al., 2007) that bracket the minimum and maximum slope and slope-length design conditions (2% to 4% slope and 150-foot to 600-foot slope length) for the planned ELLWF final closure cap. Figure 3-109 highlights that a single bounding case of 2% slope and 585-foot slope length represents an upper bound on infiltration rates for the ten intact infiltration scenarios. Building upon this analysis and as detailed in Section 3.8.4.3.4 below, Shipmon and Dyer (2017) used the HELP model to perform a detailed sensitivity analysis of rainfall infiltration through the planned intact ELLWF final closure cap. The purpose of the evaluation was to identify the cap design and material property parameters that most significantly impact intact infiltration rates over a 10,000-year simulation period. Results showed that saturated hydraulic conductivity (K_{sat}) for select cap layers, precipitation rate, surface vegetation type, and geomembrane layer defect density are dominant factors affecting the intact infiltration rate. Dyer (2018a) further considered the impacts of vegetative cover type, geomembrane layer defects, and pine tree intrusion on infiltration rates using the HELP model for five closure-cap scenarios: FTF Bahia grass (Phifer et al., 2007), ELLWF Bahia grass with the PA2008 timeline for pine tree intrusion, ELLWF Bahia grass using a more aggressive timeline for pine tree intrusion, ELLWF unmanaged bamboo cover, and ELLWF managed bamboo cover. Dyer (2018a) affirmed again that the Bahia grass case with 2% slope and 585-foot slope length represents a reasonable upper bound on intact infiltration rates for the ELLWF final closure cap design shown in Figure 2-35 and Figure 2-41. It is important to note that an upper bound on infiltration rate is a conservative assumption for some radionuclides but not all.

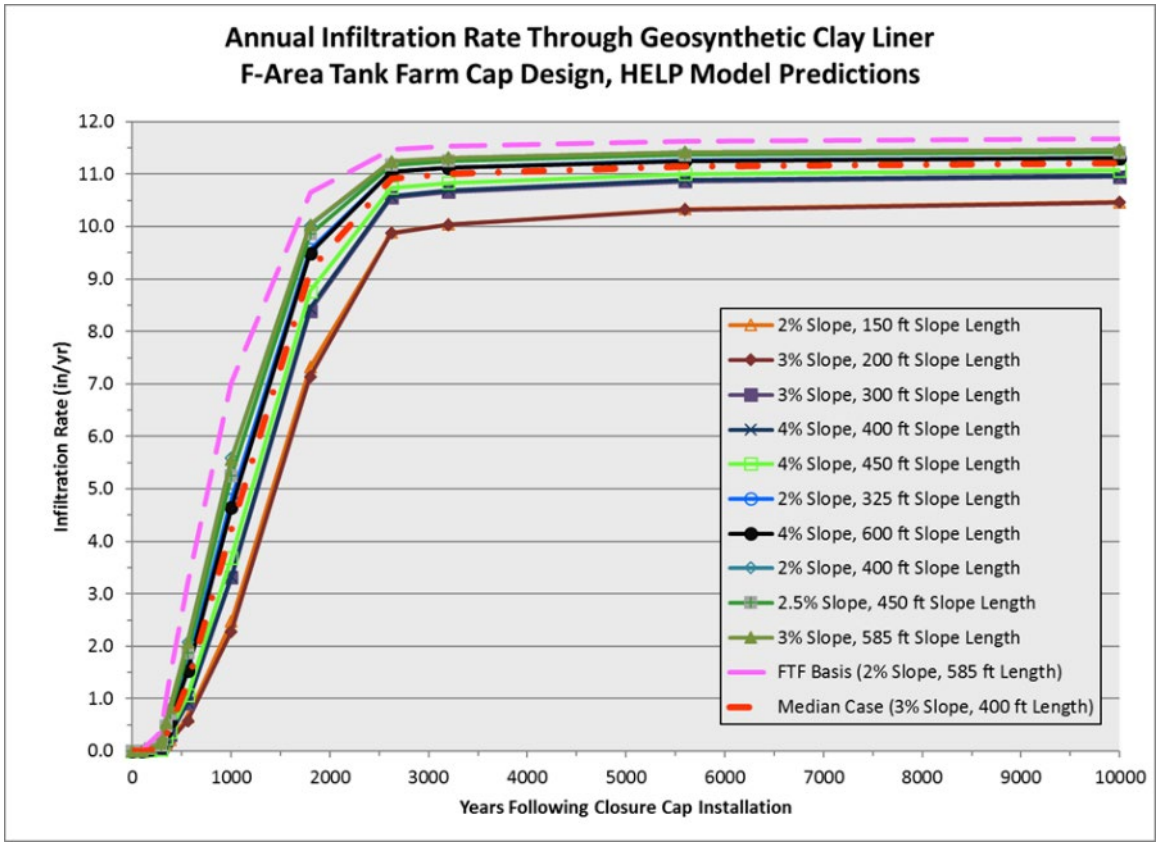

Figure 3-109. Infiltration Rate (inches/year) as Function of Percent Slope and Slope Length (Dyer, 2017b; Figure 2-1)

As described in Section 2.2.2.3 and delineated in Table 2-17, the ELLWF final closure cap will include the following ten layers from top to bottom:

- Topsoil (6 inches)
- Upper backfill layer (30 inches)
- Erosion barrier (12 inches)
- Geotextile filter fabric (100 mil)
- LDL (12 inches)
- Geotextile filter fabric (100 mil)
- HDPE geomembrane (60 mil)
- GCL (200 mil)
- Blended soil-bentonite layer (12 inches)
- Foundation layer (varying thickness)

The minimum foundation layer thickness is one foot for the STs and ETs and assumes the presence of a preexisting minimum 4-foot-thick operational soil cover. The middle backfill layer in the original FTF cap design is not included in the ELLWF final closure cap design to ensure that the average cap thickness above the LAWV and ILV satisfies differential settlement and maximum seismic load considerations.

The use of a single intact infiltration case reduces the number of more computationally intensive VZ and aquifer zone PORFLOW simulations for both the intact- and subsided-cap scenarios. SRNL-recompiled Ver. 4.0 of the HELP model (Dixon, 2017) was utilized to generate the desired intact infiltration rate time profile (i.e., the final closure cap degradation curve) based on the same (or slight modifications thereof) cap design and degradation parameters employed for the FTF infiltration calculations (Phifer et al., 2007). The simulation period of interest for the ELLWF final closure cap is 100 to 10,100 years, where relative Year 100 is the installation date of the final closure cap. The actual compliance period for the PA is 1,000 years following final closure (i.e., relative Year 1,100); however, infiltration estimates are extended to 10,000 years (i.e., relative Year 10,100) to ensure steady-state infiltration conditions are captured in support of transport calculations employed to capture concentration peaks. Dyer and Flach (2018) and Phifer et al. (2007) describe in greater detail the formulation and execution of the HELP model for the intact infiltration case, including degradation assumptions for the barrier and lateral drainage layers.

HELP Ver. 4.0 model files for the ELLWF intact infiltration case (2% slope, 585-foot slope length, 100 to 10,100 years, Bahia grass) were stored in the parent directory C:\Help4.0 in three subdirectories:[34]

- C:\Help4.0\Hweather stores input parameters for evapotranspiration calculations (FEVAP.D11) as well as HELP-model-generated weather input files containing 100 years of daily precipitation (FPREC.D4), temperature (FTEMP.D7), and solar radiation (FSOLAR.D13) data. Section 3.8.4.2 provides additional background information on weather data input for the HELP model.
- C:\Help4.0\STET_INTACT contains the input and output files for each intact-infiltration time step (stored in separate subdirectories labeled C:\Help4.0\STET_INTACT\ST00 for Year 100 through C:\Help4.0\STET_INTACT\ST13 for Year 10,100).
- C:\Help4.0\Source contains the executable Fortran files for the HELP model.

Dyer (2019b; Appendix B, Figure B-1) presents a diagram of the file hierarchy.

All 14 intact infiltration timesteps were executed simultaneously by double-clicking the HELP.bat Windows batch file stored in the subdirectory C:\Help4.0\STET_INTACT. Overall summary files labeled ST.OUT, ST_DRAINAGE.OUT, ST_PERC.OUT, and ST_RUNOFF.OUT were created by double-clicking the Python-based model cat_FC.py stored in the subdirectory C:\Help4.0\STET_INTACT. Output files for each individual time-step were stored in C:\Help4.0\STET_INTACT\STxx\Output, where xx ranges from 00 to 13.

Table 3-72 lists technical reports relevant to the calculation of intact infiltration rates for the ELLWF.

[34] The as-written batch execution files embedded in the HELP directories for this data package require the HELP model to be executed from the C: drive. If executed from another directory or drive, then the Python script and the .bat files in the parent directory and each of the subdirectories for each case will need to be edited for the new directory pathway.

Table 3-72. Technical Reports Relevant to the Calculation of Infiltration Rates for the Bounding Intact Case for Slit and Engineered Trenches (Dyer, 2019b; Table 2-1)

Report Number	Authors/Year	Title	Relevance
SRNL-STI-2017-00104, Rev. 0	Dixon (2017)	HELP 4.0 Documentation Updates for Software and Data	HELP model adaptations to run on Windows 10
SRNL-STI-2017-00678, Rev. 0	Dyer (2017b)	Conceptual Modeling Framework for E-Area PA HELP Infiltration Model Simulations	Basis for percent slope and slope length assumptions
SRNL-STI-2018-00141, Rev. 0	Dyer (2018a)	Impact of Different Vegetative Cover Scenarios on Infiltration Rates for the E-Area PA Intact Case	Basis for Bahia grass vegetative cover
SRNL-STI-2018-00121, Rev. 0	Dyer (2018b)	Method for Including Uncertainty in Infiltration Rates in the E-Area PA System Model	Basis for upper bounding case
SRNL-STI-2018-00327, Rev. 0	Dyer and Flach (2018)	Infiltration Time Profiles for E-Area LLWF Intact and Subsidence Scenarios[1]	Intact infiltration rates and HELP model assumptions
SRNL-STI-2017-00506, Rev. 0	Shipmon and Dyer (2017)	Analysis of Factors that Influence Infiltration Rates using the HELP Model	Basis for upper bounding case
WSRC-STI-2007-00184, Rev. 2	Phifer et al. (2007)	FTF Closure Cap Concept and Infiltration Estimates	Cap degradation narrative, cap design, and HELP model assumptions
SRNL-RP-2009-00075, Rev. 0	Phifer et al. (2009)	Closure Plan for the E-Area Low-Level Waste Facility	Operational and interim covers

Notes:

[1] The intact infiltration rates reported in SRNL-STI-2018-00327, Rev. 0 were based on the FTF closure cap design which includes a middle backfill layer. The planned closure cap design for the ELLWF no longer includes a middle backfill layer, which was removed to ensure that the average cap thickness above the LAWV and ILV satisfies differential settlement and maximum seismic load considerations. As a result, the calculated intact infiltration rates decreased slightly.

Dyer (2019b; Appendix B, Table B-1 through Table B-16) provides the HELP model input parameter data sheets for each time step in the intact infiltration degradation curve. An input data sheet for an example HELP model simulation case is displayed in Figure 3-110.

All input parameters required by the HELP model, including assumed hydraulic properties for each of the closure cap layers, are included on the input data sheet for each simulation case (see Figure 3-110; note that empty fields are not omissions but are irrelevant parameters for a given modeling case). Table 3-73 and Figure 3-111 provide the infiltration rates for the bounding intact case for a 10,000-year period. Figure 3-112 is a log-log version of Figure 3-111 and is provided to highlight the much lower estimated infiltration rates during the first few hundred years. Included in Table 3-73 are the HELP model input (xx.D10), output (xx.OUT), and weather input data (xx.D4, xx.D7, xx.D11, xx.D13) filenames corresponding to each time step. Reported infiltration rates from the HELP model are temporally (annually) and spatially (585-foot total slope length) averaged.

Input Parameter (HELP Model Query)	Generic Input Parameter Value
Landfill area =	0.2686 acres
Percent of area where runoff is possible =	100%
Do you want to specify initial moisture storage? (Y/N)	Y
Amount of water or snow on surface =	0 inches
CN Input Parameter (HELP Model Query)	CN Input Parameter Value
Slope =	2 %
Slope length =	585 ft
Soil Texture =	4 (HELP model default soil texture)
Vegetation =	4 (i.e., a good stand of grass)
HELP Model Computed Curve Number = 46.2	

Layer	Layer Number	Layer Type
Topsoil	1	1 (vertical percolation layer)
Upper Backfill	2	1 (vertical percolation layer)
Erosion Barrier	3	1 (vertical percolation layer)
Lateral Drainage Layer	4	2 (lateral drainage layer)
HDPE Geomembrane	5	4 (geomembrane liner)
GCL	6	3 (barrier soil liner)
Foundation Layer (1E-06)	7	1 (vertical percolation layer)
Foundation Layer (1E-03)	8	1 (vertical percolation layer)

Layer #	Layer Type	Layer Thickness (in)	Soil Texture No.	Total Porosity (Vol/Vol)	Field Capacity (Vol/Vol)	Wilting Point (Vol/Vol)	Initial Moisture [2] (Vol/Vol)
1	1	5.90		0.396	0.109	0.047	0.109
2	1	30		0.35	0.252	0.181	0.252
3	1	12		0.15	0.1	0.07	0.1
4	2	12		0.414	0.052	0.024	0.052
5	4	0.06					
6	3	0.2		0.75	0.747	0.4	0.75
7	1	12		0.35	0.252	0.181	0.252
8	1	72		0.457	0.131	0.058	0.131

Layer #	Layer Type	Sat. Hyd. Conductivity (cm/sec)	Drainage Length (ft)	Drain Slope (%)	Leachate Recirc. (%)	Recirc. to Layer (#)	Subsurface Inflow (in/yr)
1	1	3.1E-03					
2	1	4.1E-05					
3	1	1.3E-04					
4	2	3.86E-02	585	2			
5	4	2.0E-13					
6	3	5.0E-08					
7	1	1.0E-06					
8	1	1.0E-03					

Layer #	Layer Type	Geomembrane Pinhole Density (#/acre)	Geomembrane Instal. Defects (#/acre)	Geomembrane Placement Quality	Geotextile Transmissivity (cm^2/sec)
5	4	1	96	2	

Figure 3-110. HELP Model Input Data for Year 300 (ST03.D10) for Intact Case (Dyer, 2019b; Appendix B, Table B-6)

Table 3-73. Bounding Intact Infiltration Rates for Slit and Engineered Trenches and Associated HELP Model Input and Output Files (Dyer, 2019b; Table 2-2)

Relative Year[1]	Cover Type	HELP Model Input, Output, and Weather Files[2]	PC Directory Location for Execution	Infiltration Rate (inches/year)
-30 to 0	Operational (4 feet soil)	ST_OpCover.D10 ST_OpCover.OUT	C:\Help4.0\SLIT_OpCover\ ST_OpCover	15.78
0 to 100	Interim (HDPE)	ST_IC.D10 ST_IC.OUT ICEVAP.D11[2]	C:\Help4.0\SLIT_IC\ST_IC	0.1
100	Closure Cap	ST00.D10 ST00.OUT	C:\Help4.0\STET_INTACT\ST00	0.0008
180	Closure Cap	ST01.D10 ST01.OUT	C:\Help4.0\STET_INTACT\ST01	0.007
290	Closure Cap	ST02.D10 ST02.OUT	C:\Help4.0\STET_INTACT\ST02	0.16
300	Closure Cap	ST03.D10 ST03.OUT	C:\Help4.0\STET_INTACT\ST03	0.18
340	Closure Cap	ST04.D10 ST04.OUT	C:\Help4.0\STET_INTACT\ST04	0.30
380	Closure Cap	ST05.D10 ST05.OUT	C:\Help4.0\STET_INTACT\ST05	0.38
480	Closure Cap	ST06.D10 ST06.OUT	C:\Help4.0\STET_INTACT\ST06	1.39
660	Closure Cap	ST07.D10 ST07.OUT	C:\Help4.0\STET_INTACT\ST07	3.23
1,100	Closure Cap	ST08.D10 ST08.OUT	C:\Help4.0\STET_INTACT\ST08	6.82
1,900	Closure Cap	ST09.D10 ST09.OUT	C:\Help4.0\STET_INTACT\ST09	10.24
2,723	Closure Cap	ST10.D10 ST10.OUT	C:\Help4.0\STET_INTACT\ST10	11.10
3,300	Closure Cap	ST11.D10 ST11.OUT	C:\Help4.0\STET_INTACT\ST11	11.18
5,700	Closure Cap	ST12.D10 ST12.OUT	C:\Help4.0\STET_INTACT\ST12	11.30
10,100+	Closure Cap	ST13.D10 ST13.OUT	C:\Help4.0\STET_INTACT\ST13	11.35

Notes:

[1] Year 0: Beginning of IC period. Interim runoff cover is installed and maintained for next 100 years (i.e., any subsidence is repaired). Infiltration rate for interim cover is assumed to equal 0.1 inches/year. Year 100: End of IC period; installation date of final closure cap.

[2] HELP Weather files are FPREC.D4, FTEMP.D7, FEVAP.D11, and FSOLAR.D13 except where noted in the table.

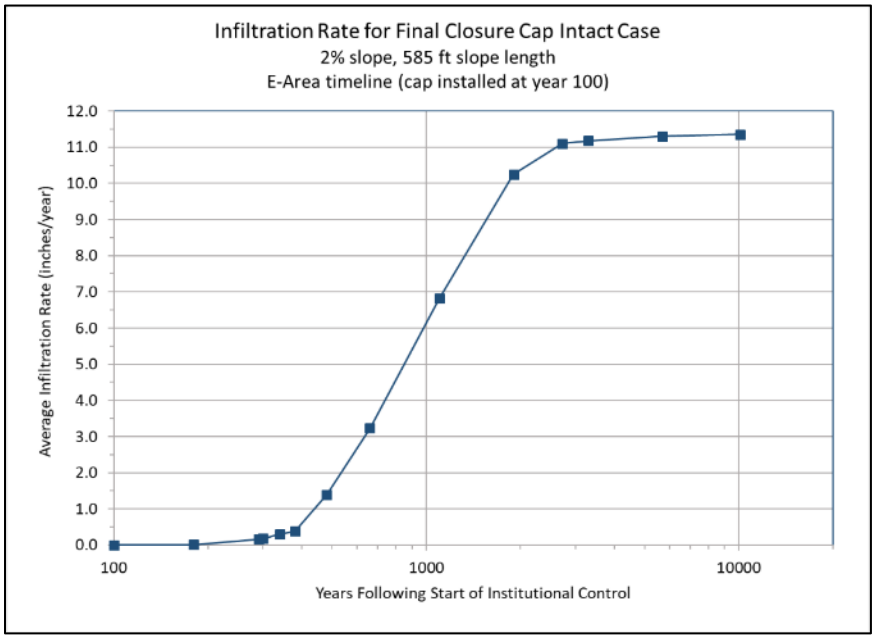

Figure 3-111. Linear-Log Plot of Infiltration Rate vs. Time for Bounding Intact Case for Slit and Engineered Trenches (Dyer, 2019b; Figure 2-3)

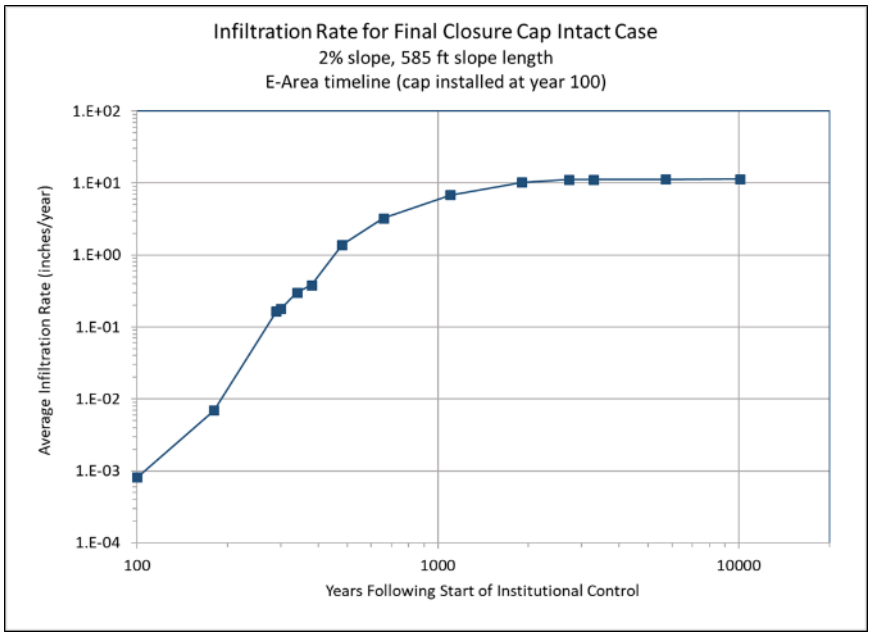

Figure 3-112. Log-Log Plot of Infiltration Rate vs. Time for Bounding Intact Case for Slit and Engineered Trenches (Dyer, 2019b; Figure 2-4)

3.8.4.3.3. Subsidence Infiltration Scenarios

Non-crushable packages are defined as containers and equipment that do not collapse during previous waste stabilization measures, including dynamic compaction, but that fail catastrophically immediately upon installation of the final multilayer soil-geomembrane closure cap. The collapse is assumed to result in localized failures that create subsidence areas (or holes) in the closure cap surface. Subsidence refers specifically to the non-crushable containers that fail

catastrophically; therefore, percent subsidence is synonymous with percent non-crushable packages. Excluded from the list of "non-crushable packages" are ETF vessels, heat exchangers, and reactor vessels that remain structurally intact for thousands of years and will not fail.

Two different approaches were developed for incorporating the effect of localized cap subsidence on infiltration rates in the PORFLOW flow and transport model simulations: (1) spatial and slope-length averaging of infiltration rates based on a Monte Carlo probabilistic model to establish the upper inflow boundary condition for the PORFLOW VZ model simulations; and (2) weighted blending of radionuclide fluxes to the water table using the results of less than a dozen PORFLOW VZ simulations representative of specific subsidence cases determined from reviewing historical ST and ET inventory data for non-crushable packages.

Spatially Averaged and Slope-Length-Weighted Averaged Infiltration Rates

(Dyer and Flach, 2017); Dyer and Flach (2018) describe a Python-based probabilistic model that employs Monte Carlo sampling to calculate a spatially averaged infiltration rate for each subsidence case based on infiltration rates generated by the HELP model for the intact case. Percent subsidence can range from 0% to 100%. Spatial averaging of infiltration rates is implemented in the model by averaging across both the user-specified length (slope length) and width (100,000 Monte Carlo realizations or cap slices) of the cap surface. Slope-length-weighted averaging is a post-processing step that occurs outside the probabilistic model using Microsoft Excel. For closure-cap transects with two sides of unequal slope length, the probabilistic model was executed twice (once for each slope length) at each percent subsidence of interest. A single slope-length-weighted, spatially averaged infiltration-rate time profile for each percent-subsidence case was then calculated using the probabilistic model output for the two slope lengths.

Dyer and Flach (2017) found that two cases (150-foot slope length at 2% slope and 585-foot slope length at 2% slope) represented the lower and upper bounds, respectively, for the ten intact infiltration cases which bracket the minimum and maximum slope and slope-length design conditions (2% to 4% slope and 150-foot to 600-foot slope length) for the planned ELLWF final closure cap. The same two bounding intact cases also served as the basis for the slope-length-weighted averaging calculations for the subsidence cases.

A key component of the probabilistic model is the generation of statistical distributions of an upslope-intact-area to subsided-area ratio ($Area_{UAi}/Area_{SAi}$) for closure cap subsidence scenarios that differ in assumed percent subsidence, compartment size, and the total number of intact plus subsided compartments. Mean values for $Area_{UAi}/Area_{SAi}$ can be utilized to calculate the mass flux of water that will drain into a subsided compartment or hole. Mass inflows to a hole include the mean run-on (LDL plus surface runoff) from the area of the intact closure cap located upslope of the hole as well as the net influx of precipitation (average annual rainfall minus evapotranspiration) from directly above the hole. Eq. (3-63), which is embedded within the probabilistic model, gives the approximate total mass flux of water, I_{hole}, that is assumed to drain into a subsided compartment of the ELLWF final closure cap:

$$I_{hole}\left(inches/year\right)=16.5+\left(Area_{UAi}/Area_{SAi}\right)\left(16.5-I_{\text{int}\,act}\right) \qquad \text{Eq. (3-63)}$$

where $I_{\text{int}\,act}$ is the intact infiltration rate (inches/year) at time, *t*, and 16.5 inches/year is an approximation based on HELP model simulations of average annual rainfall (49.14 inches/year) minus evapotranspiration (32.64 inches/year) for the SRS. Eq. (3-63) is a reasonable upper-bound approximation of the total mass inflow of water into a subsided area of the cap and avoids the need to execute the HELP model at every time step for each different subsidence scenario.

The probabilistic infiltration model consists of two files: SubsideAverage_rev6.py (Python source code) and runPython_rev6D.bat (Windows batch file). The Windows batch file contains the required input parameters and model/output filenames for each simulation case and can be set up to generate multiple infiltration-rate time profiles in one model execution step. Fourteen timesteps were included for each infiltration-rate time profile; however, the number of timesteps can be changed as needed. Dyer (2019b; Appendix C) provides the batch input file (runPython_rev6D.bat) including definitions of the required input parameters (i.e., Python source code file, output file prefix, compartment size, total number of compartments, percent subsidence, average annual rainfall minus average evapotranspiration rate from HELP, intact infiltration rate from HELP, and the number of realizations).

Table 3-74 summarizes the percent subsidence[35] assumptions for individual STs and ETs. The bases for these assumptions are:

- For trench units with less than or equal to 2% non-crushable items, hole (or compartment) size is set at 10 feet in the infiltration model simulations. As discussed by Dyer and Flach (2017), a minimum hole size of 10 feet is considered reasonable based on typical non-crushable container dimensions. For trench units with more than 2% non-crushable items, a larger hole size may be more realistic and warranted. For example, 6% non-crushable items spread across a 500-foot slope length equates to a total subsided length of 30 feet. In this situation, the infiltration model could assume three 10-foot holes, two 15-foot holes, or one 30-foot hole.
- 2% subsidence is assumed universally for all future trench units (including those to be constructed in Plot 8).
- 2% subsidence is also assumed for partially filled, currently operating (open) trench units with a non-crushable content to date of less than 2%. These trench units will be capped at 2% non-crushable packages.
- For closed trench units, percent subsidence is based on the actual recorded area of non-crushable packages, which will be greater than 2% for ST03 and ST04.

There are no open trench units with greater than 2% non-crushable packages.

[35] Percent subsidence values reported in the infiltration data package are based on the total footprint area of the disposal unit, not the area of the waste zone alone. This is an important distinction for STs where the waste footprint is roughly 64% of the total DU footprint.

Table 3-74. Subsidence Assumptions for Slit and Engineered Trench Units (Dyer, 2019b; Table 2-3)

Trench ID	Original Name	Percent Filled[1] (1/31/18)	Total Disposal Unit Footprint Area[2] (ft^2)	Actual Trench Waste Area[2] (ft^2)	Non-Crush Area[3] (ft^2)	Calculated Percent Non-Crushable Packages [4]	Assumed Percent Subsidence
ET01	Engineered Trench #1	100%	96,840	96,840	0	0.00%	0%
ET02[5]	Engineered Trench #2	76.8%	104,592	104,592	34	0.04%	2%
ET03[6]	Engineered Trench #3	53.4%	80,848	80,848	0	0.00%	0%
ET04	Engineered Trench #4	Future	103,320			2%	2%
ET05	Slit Trench 15	Future	102,992			2%	2%
ET06	Slit Trench 16	Future	101,705			2%	2%
ET07	Plot 8 West Unit	Future	96,000			2%	2%
ET08	Plot 8 Center Unit	Future	96,000			2%	2%
ET09	Plot 8 East Unit	Future	96,000			2%	2%
ST01	Slit Trench 1	100%	103,430	65,000	0	0.00%	0%
ST02	Slit Trench 2	100%	103,336	65,000	2,046	1.98%	2%
ST03	Slit Trench 3	100%	102,992	65,000	5,019	4.87%	4.9%
ST04	Slit Trench 4	100%	102,992	65,000	3,710	3.60%	3.6%
ST05	Slit Trench 5	100%	102,992	65,000	557	0.54%	0.54%
ST06[5]	Slit Trench 6	90.6%	102,992	65,000	1,866	2.00%	2%
ST07[5]	Slit Trench 7	66.4%	102,992	65,000	435	0.64%	2%
ST08[5]	Slit Trench 8	95.0%	102,992	65,000	13	0.013%	2%
ST09[5]	Slit Trench 9	87.7%	102,992	65,000	0	0.00%	2%
ST10	Slit Trench 10	Future	93,572			2%	2%
ST11	Slit Trench 11	Future	80,278			2%	2%
ST14[5]	Slit Trench 14	65.9%	102,989	65,000	383	0.59%	2%
ST17	Slit Trench 17	Future	101,705			2%	2%
ST18	Slit Trench 18	Future	101,705			2%	2%
ST19	Slit Trench 19	Future	101,705			2%	2%
ST20	Slit Trench 20	Future	101,705			2%	2%
ST21	Slit Trench 21 North	Future	84,780			2%	2%
ST22	Slit Trench 21 South	Future	70,650			2%	2%
ST23[7]	CIG Trench 1 (CIG-1)	~20% as CIG	102,992			Prorated 2% [8]	Prorated 2% [8]
ST24[7]	CIG Trench 2 (CIG-2)	Future	102,992			2%	2%

Notes:

1 From SWE January 2018 LLW review memo (SRNS-N4222-2018-00002, Stewart to Mooneyhan, 02/01/2018). Orange highlighting (100%) indicates that the unit is closed. Gold highlighting identifies units that are still open. Green highlighting indicates future trench units.

2 Calculated areas for ET units based on as-built corner coordinates of trench base summarized by Hamm (2019). ST areas based on nominal five trench segments each 20 feet wide by 650 feet long.

3 From 02/01/2018 Waste Inventory Tracking System (WITS) report.

4 Percent non-crushable values are based on total footprint area of the DU, not area of the waste zone alone. Percent non-crushable packages for closed units equals: (non-crushable area x 100%) / total footprint area. Percent non-crushable packages for partially filled units equals: (non-crushable area x 100%) / (total footprint area x fraction filled) to normalize the non-crushable area to 100% filled. Percent non-crushable packages is assumed to be 2% for all future trench units. Excluded from the list of non-crushable packages are ETF vessels, heat exchangers, and reactor vessels that remain structurally intact for thousands of years and will not fail.

5 Allow for 2% non-crushable packages as conservative assumption in setting limits for open trenches with less than 2% non-crushable packages to date (exception is ET03).

6 ET03 has a current restriction of 0% non-crushable packages based on an earlier Unreviewed Disposal Question Evaluation. ET03 will almost certainly be filled by 2022.

7 The remaining portion of ST23 (formerly CIG01) will be used as a ST for remainder of its life. ST24 (formerly CIG02) will now be used as a future ST.

8 2% subsidence is assumed for the remaining ~80% of ST23 that will function as a future ST.

Table 3-75 lists technical reports relevant to the calculation of subsidence infiltration rates for the ELLWF. Dyer (2019b; Appendix C) contains the batch input file (runPython_rev6D.bat) and simulation results (Table C-1 through Table C-4) for the eight ST and ET subsidence cases: 0.54%, 2%, 3.6%, and 4.9% subsidence for waste-zone-only slope lengths of 545 feet (585-foot slope length minus 40-foot overhang) and 110 feet (150-foot slope length minus 40-foot overhang) each. The 40-foot cap overhangs are not included in the probabilistic model simulations because no waste is buried beneath them.

Table 3-75. Technical Reports Relevant to the Calculation of Infiltration Rates for Slit and Engineered Trench Subsidence Cases (Dyer, 2019b; Table 2-4)

Report Number	Authors/Year	Title	Relevance
SRNL-STI-2017-00729, Rev. 0	Dyer and Flach (2017)	E-Area LLWF Vadose Zone Model: Probabilistic Model for Estimating Subsided-Area Infiltration Rates	Genesis of the probabilistic model for subsidence infiltration calculations
SRNL-STI-2018-00327, Rev. 0	Dyer and Flach (2018)	Infiltration Time Profiles for E-Area LLWF Intact and Subsidence Scenarios	Current probabilistic model for subsidence infiltration rates

Table 3-76, Figure 3-113, and Figure 3-114 present slope-length-weighted, spatially averaged infiltration rates as a function of relative time for the intact and 0.54%, 2%, 3.6%, and 4.9% subsidence cases for the ELLWF closure cap design.

Table 3-76. Spatially Averaged Infiltration Rates for Subsidence Cases Based on 2%-Slope, 585-Foot-Slope-Length Intact Case (Dyer, 2019b; Table 2-5)

Relative Year	Intact Infiltration Rate (inches/year)	Slope-Length-Weighted, Spatially Averaged Infiltration Rate (inches/year)			
		0.54% Subsidence (ST05)	2.0% Subsidence (ST02, ST06-11, ST14, ST17-24, ET02, ET04-09)	3.6% Subsidence (ST04)	4.9% Subsidence (ST03)
0	0.1	N/A	N/A	N/A	N/A
100	0.0008	1.99	5.82	8.47	9.90
180	0.0070	1.99	5.83	8.49	9.87
290	0.16	2.10	5.92	8.56	9.96
300	0.18	2.13	5.92	8.55	9.96
340	0.30	2.24	6.05	8.61	10.00
380	0.38	2.32	6.06	8.65	10.04
480	1.39	3.20	6.74	9.15	10.44
660	3.23	4.82	7.93	10.03	11.17
1,100	6.82	7.97	10.25	11.79	12.61
1,900	10.24	11.00	12.45	13.46	13.98
2,723	11.10	11.74	13.01	13.87	14.34
3,300	11.18	11.82	13.06	13.90	14.37
5,700	11.30	11.92	13.15	13.97	14.41
10,100	11.35	11.97	13.18	13.99	14.43

Year 0: Beginning of IC period. Interim runoff cover is installed and maintained for next 100 years (i.e., any subsidence is repaired). Infiltration rate for interim cover is estimated to equal 0.1 inches/year.

Year 100: End of IC period; installation date of final closure cap.

For PORFLOW VZ simulations of closure cap transects with two sides of unequal slope length, the probabilistic model was executed twice (once each for waste-zone-only slope lengths of 545 feet and 110 feet) a t each percent subsidence of interest. A single slope-length-weighted, spatially averaged infiltration-rate time profile for each percent-subsidence case was then calculated using the model output for the two different slope lengths.

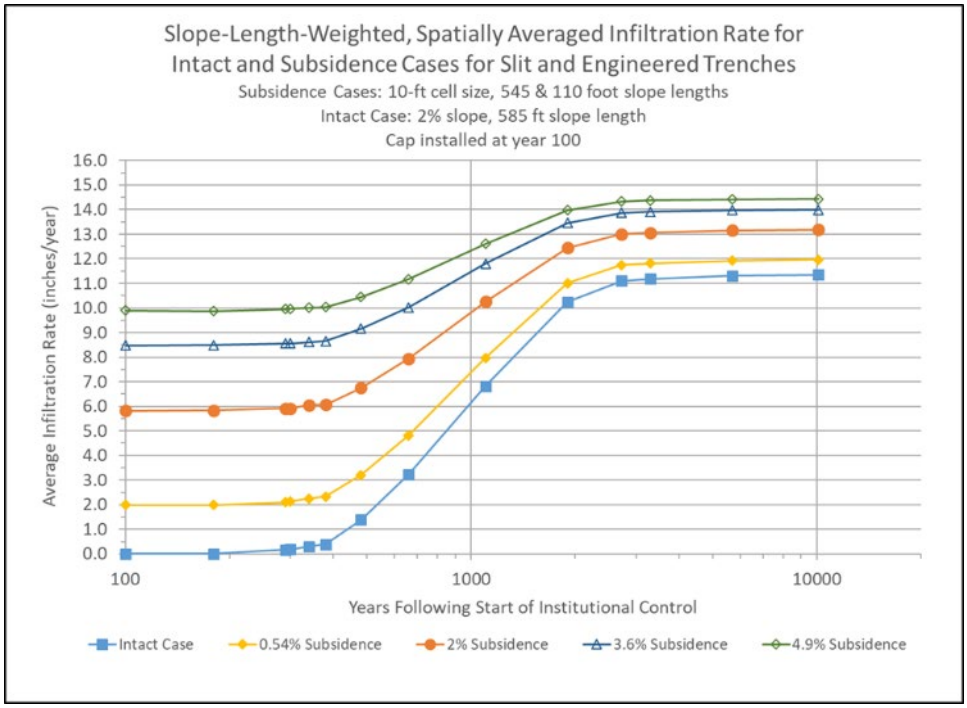

Figure 3-113. Linear-Log Plot of Slope-Length-Weighted, Spatially Averaged Infiltration Rates Versus Time for Slit and Engineered Trench Subsidence Cases (Dyer, 2019b; Figure 2-5)

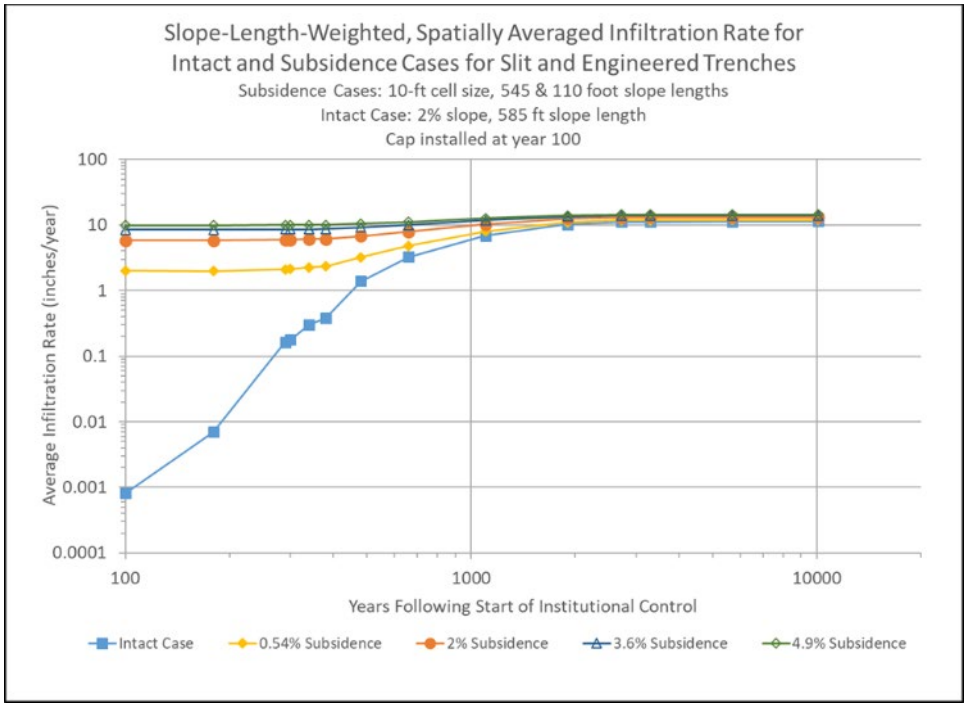

Figure 3-114. Log-Log Plot of Slope-Length-Weighted, Spatially Averaged Infiltration Rates Versus Time for Slit and Engineered Trench Subsidence Cases (Dyer, 2019b; Figure 2-6)

The intact infiltration-rate profile is based on an upper bound case of 2% slope and 585-foot slope length as described above. The reported infiltration rates for the four subsidence cases are slope-length-weighted spatial averages for slope lengths of 545 feet and 110 feet (i.e., portion of

the total cap length that overlies the waste footprint). More specifically, for PORFLOW VZ simulations of closure-cap transects with two sides of unequal slope length, the probabilistic model was executed twice (once for each slope length) at each percent subsidence of interest. A single slope-length-weighted, spatially averaged infiltration-rate time profile for each percent-subsidence case was then calculated using the model output for the two different slope lengths. A Microsoft Excel spreadsheet was used for slope-length averaging. Table 3-77 provides the input and output filenames and storage directory for the probabilistic subsidence model executed cases. The Python script can be executed from any PC directory or subdirectory.

Table 3-77. Probabilistic Subsidence Model Input and Output Files for Slit and Engineered Trenches (Dyer, 2019b; Table 2-6)

Description	Filename	Storage Directory on Server
Python model	SubsidedAverage_rev6.py	\Infiltration_Python
Batch input file	runPython_rev6D.bat	\Infiltration_Python
Output Files		
0.54% subsidence (ST05)	Case_0.54_Per_550ft.out Case_0.54_Per_550ft.sum Case_0.54_Per_550ft.tab Case_0.54_Per_110ft.out Case_0.54_Per_110ft.sum Case_0.54_Per_110ft.tab	\Infiltration_Python
2% subsidence (ST02, ST6-11, ST14, ST17-24, ET02, ET04-09)	Case_2_Per_550ft.out Case_2_Per_550ft.sum Case_2_Per_550ft.tab Case_2_Per_110ft.out Case_2_Per_110ft.sum Case_2_Per_110ft.tab	\Infiltration_Python
3.6% subsidence (ST04)	Case_3.6_Per_550ft.out Case_3.6_Per_550ft.sum Case_3.6_Per_550ft.tab Case_3.6_Per_110ft.out Case_3.6_Per_110ft.sum Case_3.6_Per_110ft.tab	\Infiltration_Python
4.9% subsidence (ST03)	Case_4.9_Per_550ft.out Case_4.9_Per_550ft.sum Case_4.9_Per_550ft.tab Case_4.9_Per_110ft.out Case_4.9_Per_110ft.sum Case_4.9_Per_110ft.tab	\Infiltration_Python

Weighted Averaging of Radionuclide Fluxes for Specific Subsidence Cases

An alternative approach for addressing subsidence and its impact on infiltration in STs and ETs is to blend radionuclide fluxes for specific deterministic PORFLOW subsidence cases at the water table rather than to blend infiltration rates based on a probabilistic infiltration model as was presented above. During the process of developing the PORFLOW VZ models, it became apparent that this alternative approach was preferable because flux through the VZ is nonlinear with respect

to infiltration at the upper boundary. Implementation of the blending of fluxes approach for STs and ETs, which builds upon the foundational work presented in the section above, is described in Section 4.1.3.7.

Danielson (2019b) separately developed a Monte Carlo rectangle packing algorithm for generating most probable spatial distributions of non-crushable packages based on the historical ELLWF inventory data for STs and ETs. The Python-based algorithm provides a reasonable, logistical filling pattern that would likely result from normal Solid Waste Management disposal operations. The heat maps for several test cases indicated that the most probable spatial locations for non-crushable packages within a 157-foot-wide ET are along the outside edges. In contrast, Monte Carlo packing simulations for a 20-foot-wide ST geometry showed that the non-crushable filling pattern is essentially insensitive to any modifications of the waste inventory distribution.

As suggested by Danielson (2019b), the Monte Carlo rectangle packing algorithm can be implemented in tandem with post-processing of profiles for radionuclide flux to the water table for subsidence geometries that were selected based on additional data that includes the package placement date of each non-crushable package. Such data, when coupled with the opening and closing dates for each DU, will provide more insight on the location of the non-crushable packages and whether they are isolated or clustered. Once specific subsidence geometries are selected and groundwater radionuclide transport simulations are performed in PORFLOW for each deterministic case, the probability heat maps from the Monte Carlo rectangle packing algorithm can be consulted to generate weighting factors for blending flux to the water table. In this approach, the upper boundary condition for the VZ simulations in PORFLOW will be based instead on the actual intact infiltration rates from Table 3-73 and hole- and case-specific infiltration rates as calculated using Eq. (3-63), rather than using the slope-length-weighted, spatially averaged infiltration rates from Section 3.8.4.3.3.

3.8.4.3.4. Method for Quantifying Uncertainty in Infiltration Rates

Dyer (2018b) developed a method for generating uncertainty distributions for intact infiltration cases for inclusion in the GoldSim® probabilistic system model. The method combines sensitivity analysis of cover system infiltration rate using the HELP model with nonlinear regression of the resulting infiltration rate versus time profiles using Minitab® 17 to obtain a bounding set of log-logistic growth curves for pessimistic, best estimate, and optimistic cases. Specific recommendations were to:

- Conduct HELP model simulations of intact infiltration scenarios for both best-estimate and sensitivity-analysis cases to generate a reasonable and defensible distribution of infiltration rate versus time profiles.
- Identify three HELP infiltration profiles that represent the most pessimistic, best estimate, and most optimistic cases.
- Use Minitab® 17 or equivalent statistical software to fit the above three infiltration profiles to a four-parameter log-logistic growth curve.

- Add two additional cases (more pessimistic and more optimistic) via manual adjustment of the four fitting parameters to arrive at a set of five log-logistic growth curves that represents the uncertainty distribution for the closure-cap scenario of interest.

HELP Model Sensitivity Analysis

Shipmon and Dyer (2017) used the HELP model to conduct a sensitivity analysis of rainfall infiltration through the proposed intact ELLWF closure cap. The objective of the analysis was to identify the cap design and material property parameters that most significantly impact intact infiltration rates over a 10,000-year simulation period. The results of the sensitivity analysis showed that saturated hydraulic conductivity (K_{sat}) for select cap layers, precipitation rate, surface vegetation type, and geomembrane layer defect density are dominant factors affecting intact infiltration rate. Interestingly, calculated intact infiltration rates were substantially influenced by changes in the saturated hydraulic conductivity of the Upper Foundation and Lateral Drainage layers. For example, an order-of-magnitude decrease in K_{sat} for the Upper Foundation layer lowered the maximum infiltration rate from a base-case 11 inches per year to only 2 inches per year, while an order-of-magnitude increase in K_{sat} led to an increase in infiltration rate from 11 to 15 inches per year.

Figure 3-115 (linear-linear plot) and Figure 3-116 (log-log plot) present the intact infiltration rate versus time curves for the following sensitivity parameters evaluated by Shipmon and Dyer (2017):

- Closure cap slope (2% minimum, 3% base case, 5% maximum)
- Closure cap slope length (150-foot minimum, 400-foot base case, 600-foot maximum)
- Surface vegetation type, which affects evapotranspiration (bare ground, base-case grass, pine trees)
- Surface run-off factor (lesser run-off: CN=30; base-case run-off: CN=50; greater run-off: CN=70, where CN is the Soil Conservation Service curve number) [36]
- Mean (μ) monthly precipitation (μ - 0.5σ, μ, μ + 0.5σ)
- Linear rate of increase (X) in number of geomembrane defects (0.5X, base-case X, 2X)
- Saturated hydraulic conductivity (K_{sat}) of upper foundation layer (0.5K_{sat}, base-case K_{sat}, 2K_{sat})
- Saturated hydraulic conductivity of LDL (0.5K_{sat}, base-case K_{sat}, 2K_{sat})

Shipmon and Dyer (2017) provide a much more detailed description of the parameter values used in the HELP model simulations for each sensitivity case.

[36] The Soil Conservation Service curve number (CN) is calculated internally within the HELP model and accounts for the effect of surface soil texture and vegetation type on surface runoff. A higher value for CN is indicative of increased runoff and, hence, a decrease in the infiltration rate.

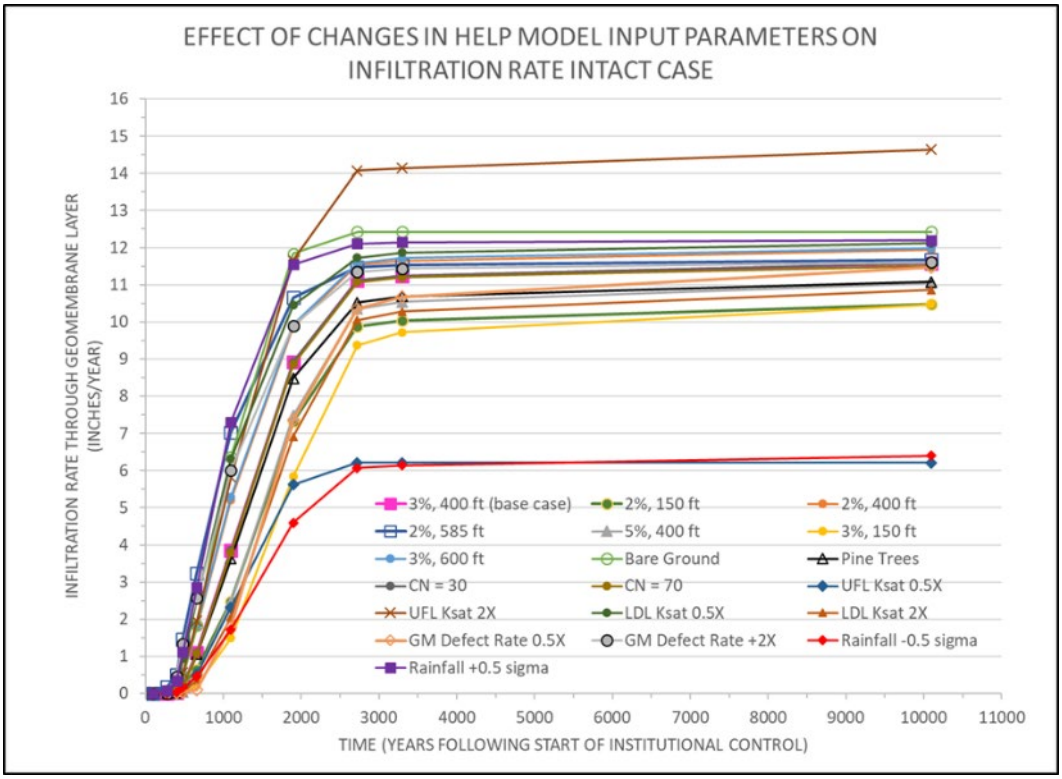

Figure 3-115. Effect of Changes in HELP Input Parameters on Intact Infiltration Rates (Dyer, 2019b; Figure 2-7, linear-linear plot)

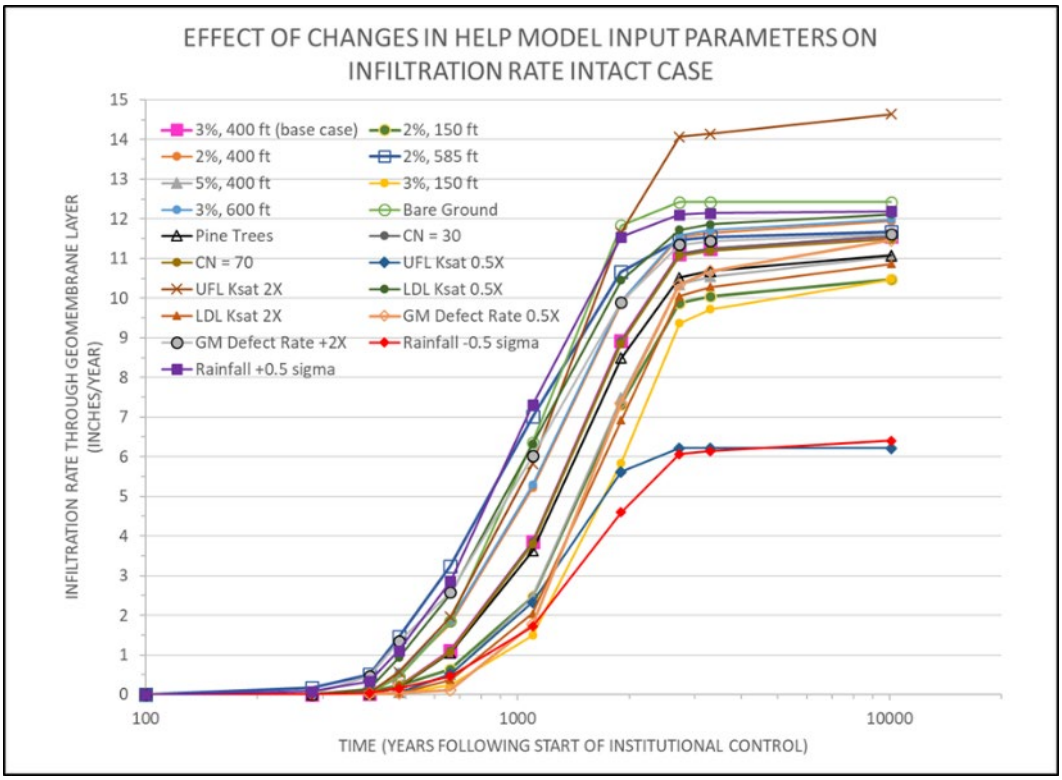

Figure 3-116. Effect of Changes in HELP Input Parameters on Intact Infiltration Rates (Dyer, 2019b; Figure 2-8, log-log plot)

Impact of Vegetative Cover and Timing of Pine Tree Intrusion

The impact of geomembrane layer defects and pine tree intrusion on infiltration rate was evaluated by Dyer (2018a) using HELP Ver. 4.0 (Dixon, 2017) for five closure-cap scenarios: (1) FTF Bahia grass (Phifer et al., 2007); (2) E-Area Bahia grass using the PA2008 timeline for pine tree intrusion (Phifer et al., 2007);[37] (3) E-Area Bahia grass using a revised timeline for pine tree intrusion given by Skibo (2018); (4) E-Area unmanaged bamboo cover (Skibo, 2018); (5) E-Area managed bamboo cover (Skibo, 2018). Conclusions were:

- HELP model simulations for the five closure-cap scenarios above reinforced that the FTF Bahia grass case with 2% slope and 585-foot slope length is a reasonable upper bound for ELLWF infiltration rates.
- The main difference between the FTF Bahia grass and the ELLWF cases was a shift in the E-Area intact infiltration rate profiles by up to 100 years (Figure 3-117 and Figure 3-118) due to a corresponding shift in the defect profiles for the geomembrane layer (Figure 3-119). The shift arises because the ELLWF final closure cap will not be installed until the end of the 100-year IC period, whereas the FTF closure cap will be installed at the start of IC. The impact of the 100-year offset on intact infiltration rates is most significant during the first 600 to 700 years after the start of IC.
- The difference in intact infiltration rates between the E-Area bamboo and Bahia grass cases appears during a narrow window from 160 to 300 years (shaded region in Figure 3-120), after the start of IC when pine tree intrusion occurs. The benefit of a bamboo versus Bahia grass vegetative cover is small compared to infiltration changes occurring over thousands of years due to cap degradation. However, this difference is potentially of significance for DUs with no or minimal non-crushable waste, for which the intact cap scenario controls disposal limits. Radionuclides potentially most affected will be ones whose mass flux at the water table peaks during this period.
- An assumed 35-year extended maintenance period beyond the end of IC to remove pine tree seedlings (Skibo Bamboo Managed case) does not appear to offer significant reductions in intact infiltration rate over an extended period.

[37] This is essentially the intact infiltration case used in the current ELLWF PA except for the inclusion of the middle backfill layer. The middle backfill layer in the original FTF cap design (Phifer et al., 2007) is not included in the current proposed ELLWF cap design to ensure that the average cap thickness above the LAWV and ILV satisfies differential settlement and maximum seismic load considerations.

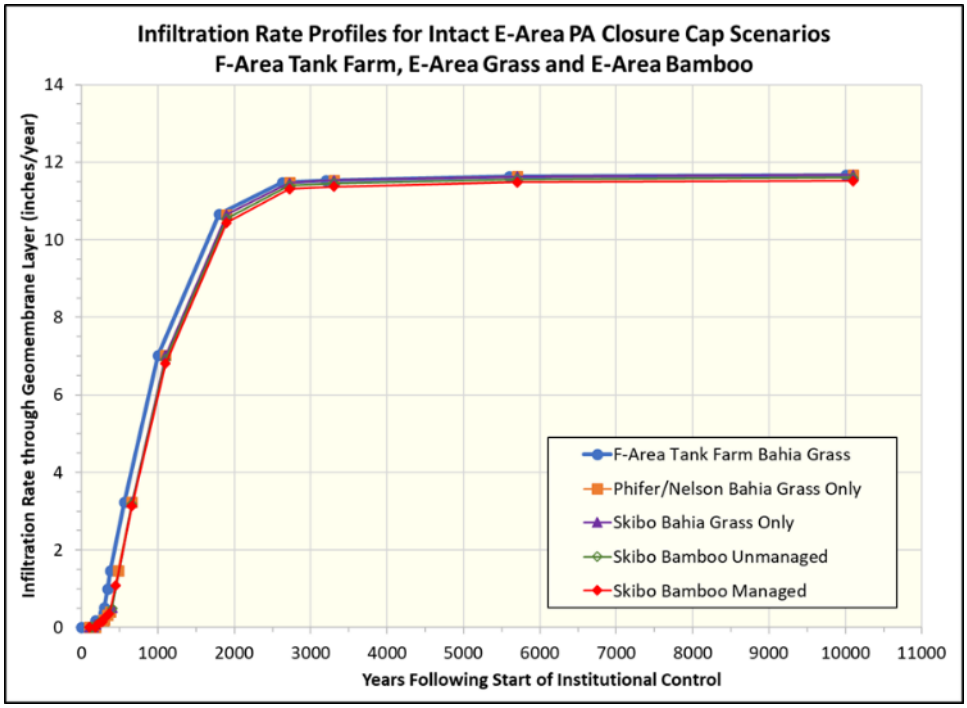

Figure 3-117. Comparison of Infiltration Rate Profiles for F-Area Tank Farm Bahia Grass and E-Area Bahia Grass and Bamboo Scenarios [linear-linear scale, 0 to 10,000 years] (Dyer, 2018a; Figure 1)

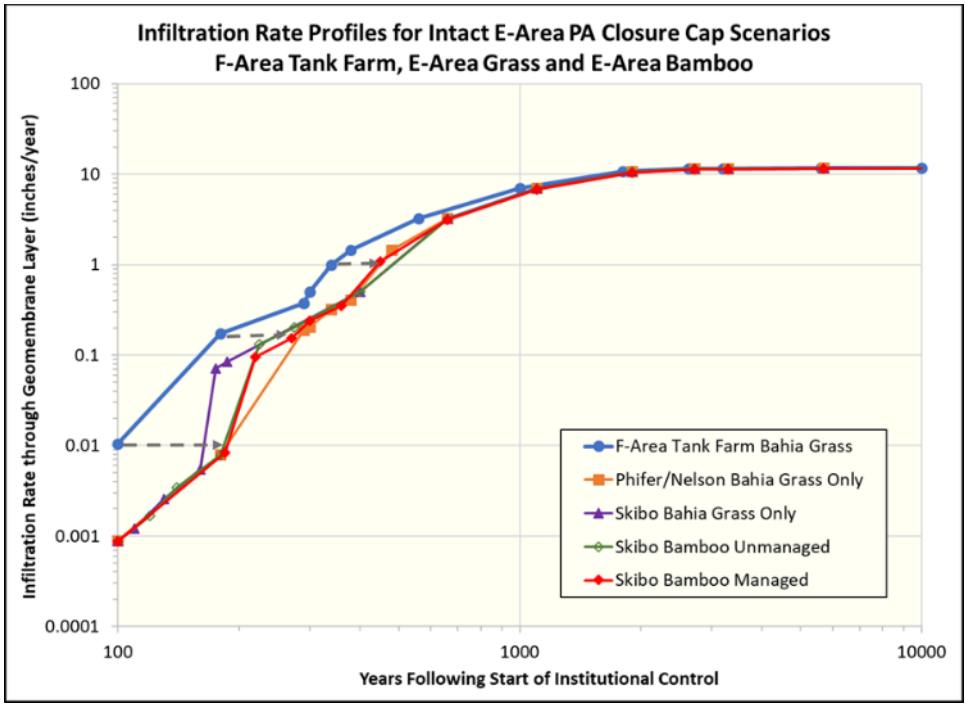

Figure 3-118. Comparison of Infiltration Rate Profiles for F-Area Tank Farm Bahia Grass and E-Area Bahia Grass and Bamboo Scenarios [log-log scale, 100 to 10,000 years] (Dyer, 2018a; Figure 2)

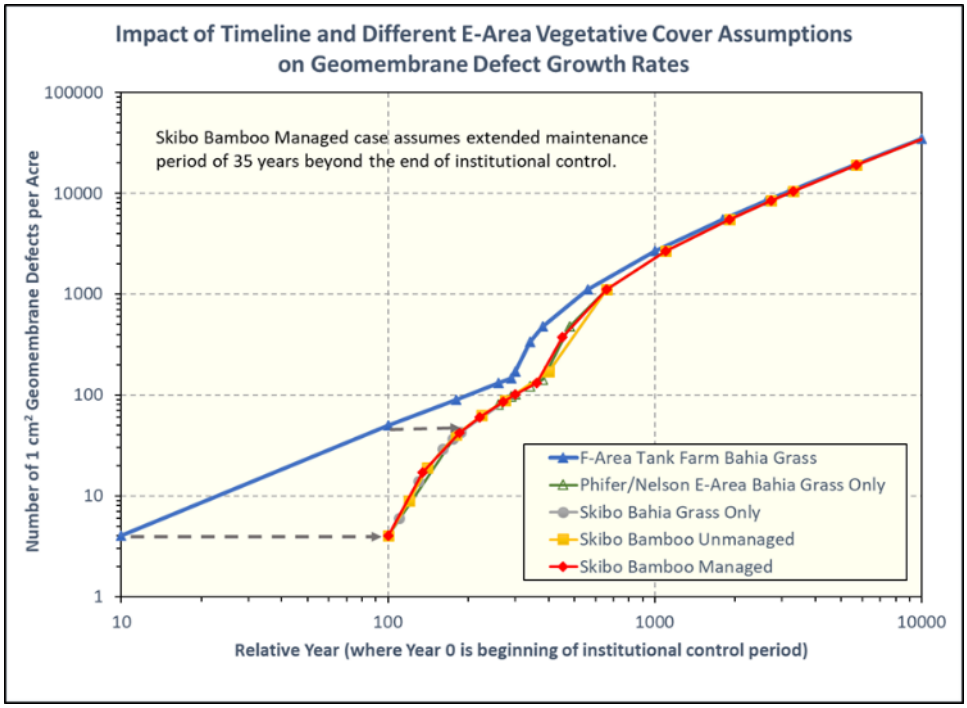

Figure 3-119. Comparison of Geomembrane Defect Growth Rates for F-Area Tank Farm Bahia Grass and E-Area Bahia Grass and Bamboo Scenarios [10 to 10,000 years] (Dyer, 2018a; Figure 3)

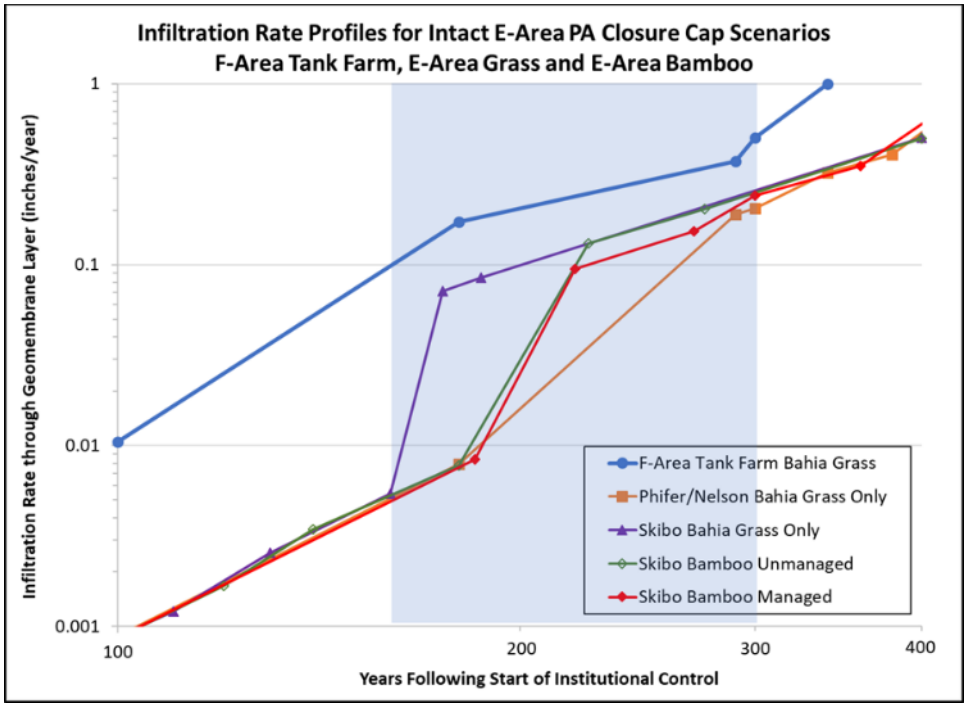

Figure 3-120. Comparison of Infiltration Rate Profiles for F-Area Tank Farm Bahia Grass and E-Area Bahia Grass and Bamboo Scenarios [log-log scale, 100 to 400 years] (Dyer, 2018a; Figure 5)

Table 3-78 compares the number of geomembrane layer defects assumed in the HELP Ver. 4.0 model simulations for the five closure-cap scenarios. In the HELP model, the number of defects is defined as the number of 1 square centimeter holes. The assumptions and calculation bases used to arrive at the number of defects and the pine tree intrusion rate for the FTF Bahia grass case are described in detail by Phifer et al. (2007; Appendix I, see lower table on pg. 329 for the number of defects assumed in the FTF case versus time). The same FTF assumptions for the rate of pine tree intrusion and the rate of increase in the number of geomembrane defects are also used in the Phifer/Nelson E-Area Bahia grass scenario (essentially the intact infiltration case used in this PA); however, the actual number of defects for each model simulation time step was adjusted to account for the 100-year shift in the DU timeline due to the delayed installation date for the final closure cap. The Skibo E-Area Bahia grass and bamboo scenarios also use Phifer et al. (2007) as a basis for the rate of increase in geomembrane defects, but Skibo (2018) as the basis for the different pine tree intrusion timelines. Similarly, the number of geomembrane defects for each model simulation time step was adjusted to account for the different Skibo E-Area grass and bamboo timelines. The time-adjusted defect numbers were linearly interpolated using the FTF defect numbers and interpolation equation reported by Phifer et al. (2007; Appendix I, see table on pg. 325). For the E-Area cases, the interpolated time (Yr_x) used in the linear interpolation equation was “relative year minus 100” to account for the later cap installation date. For example, the number of defects at relative Year 180 for the E-Area cases is based on the FTF defect number at relative Year 80. The initial number of “installation defects” assumed at time zero for the FTF and time 100 years for the E-Area cases is four as shown in Table 3-78.

Table 3-78. HELP Model Geomembrane Defect Assumptions for Vegetative Cover Sensitivity Analysis (Dyer, 2018a; Table 1)

Facility Event	Relative Year	F-Area Tank Farm (# defects)[1]	Relative Year	E-Area Phifer/Nelson Grass Only (# defects)[1]	Relative Year	E-Area Skibo Grass Only (# defects)[1]	Relative Year	E-Area Skibo Bamboo Unmanaged (#defects)[1]	Relative Year	E-Area Skibo Bamboo Managed (# defects)[1]
Start of Institutional Control	0	4	0		0		0		0	
Interim Cap Installed	N/A		0		0		0		0	
Establish 600-foot Bahiagrass Buffer	0		0		0		0		0	
Final Cap Installed	0		100	4	100	4	100	4	100	4
Bamboo Planted as Final Vegetative Cover	N/A		N/A		N/A		100		100	
End of Active Cap Maintenance	100	50	100		100		100		135	17
	180	90	180	40						
Initial Pine Tree Encroachment	260	131	260	80	110	6	120	9	185	42
Tap Roots Reach Geomembrane	290	146	290	96	160		180		270	85
Pine Trees Cover 1/3 Cap	300	170	300	101	130	14	140	19	220	60
Pine Trees Cover 2/3 Cap	340	334	340	121	160	29	180	40	300	101
Pine Trees Cover 100% Cap	380	479	380	141	175	37	225	63	360	131
Mature Pine Tree Stand with 100-year Turnover	380		380		187	43	275	88	450	373
			480	479	400	170	400	170		
	560	1,115	660	1,115	660	1,115	660	1,115	660	1,115
	1,000	2,669	1,100	2,669	1,100	2,669	1,100	2,669	1,100	2,669
	1,800	5,496	1,900	5,496	1,900	5,496	1,900	5,496	1,900	5,496
Silting-In of Lateral Drainage Layer Complete	2,623	8,403	2,723	8,403	2,723	8,403	2,723	8,403	2,723	8,403
	3,200	10,442	3,300	10,442	3,300	10,442	3,300	10,442	3,300	10,442
	5,600	18,921	5,700	18,921	5,700	18,921	5,700	18,921	5,700	18,921
	10,000	34,466	10,100	34,466	10,100	34,466	10,100	34,466	10,100	34,466

Notes:

[1] Number of 1 cm^2 holes in geomembrane layer.

Values highlighted in gold: Pine tree roots reach geomembrane or pine trees cover 1/3 cap, whichever comes later.

The number of defects for the FTF case are given by Phifer et al. (2007; Appendix I, pg. 329, lower table).

The number of defects for the four E-Area cases are also derived from the FTF case but are adjusted to account for the four different E-Area grass and bamboo timelines shown in the table above. The time-adjusted defect numbers are calculated via linear interpolation of values reported by Phifer et al. (2007; Appendix I, tables on pp. 325 and 329).

Log-Logistic Growth Curve

A four-parameter log-logistic growth curve or Fisk distribution is commonly used by hydrologists to represent stream flow and precipitation, which are both characterized by a rate that increases initially and then decreases with time. The functional form of a four-parameter log-logistic growth curve is given by:

$$Infiltration\ Rate\left(inches\ /\ year\right) = \theta_1 + \left(\frac{\theta_2 - \theta_1}{1 + e^{\left(\theta_4 * \ln\left(t/\theta_3\right)\right)}}\right) \qquad \text{Eq. (3-64)}$$

where t equals time in years, and θ_1, θ_2, θ_3, and θ_4 are the four fitting parameters. Figure 3-121 shows a generalized depiction of a log-logistic growth curve. The log-logistic growth curve is also quite effective at capturing the sigmoidal shape of the infiltration rate versus time curves generated by the HELP model as part of the final closure cap degradation analysis.

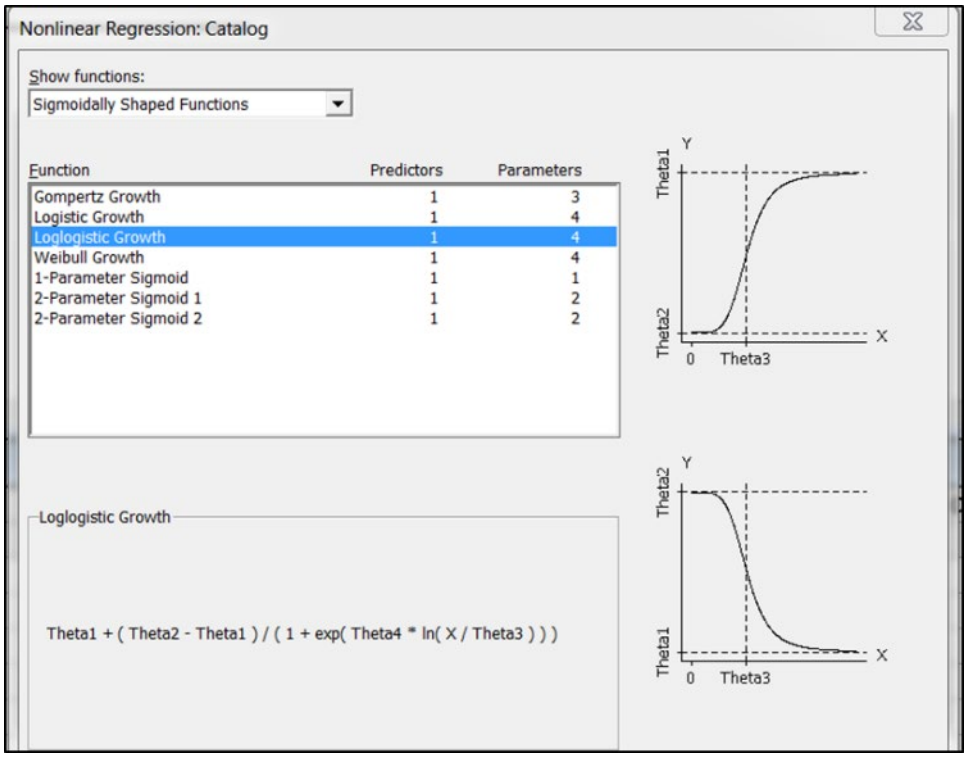

Figure 3-121. Log-Logistic Growth Curve from Minitab® 17 Nonlinear Regression Catalog (Dyer, 2019b; Figure 2-9)

The cover system degradation analysis considers loss of permeability in the LDL due to "silting in;" erosion of surface layer(s); subsidence of the cap due to waste compaction; and degradation of the HDPE geomembrane and GCL due to oxidation, tears, and tree-root penetration over 10,000 years.

The goal was to build upon the sensitivity analysis results above and generate a set of five log-logistic growth curves that represents a reasonable and defensible uncertainty distribution for the intact infiltration case of interest. The set of five log-logistic curves seeks to capture the most

pessimistic, more pessimistic, best estimate, more optimistic, and most optimistic infiltration rates over the 1,000-year compliance period. By way of example, visual inspection of Figure 3-116 indicates that the cases below represent a reasonable uncertainty distribution for the intact scenario during the first 1,000 years following closure cap installation:

- Most pessimistic: 2% slope, 585-foot slope length
- Best estimate: 3% slope and 400-foot slope length
- Most optimistic: 3% slope, 150-foot slope length

The method used to arrive at an uncertainty distribution for the intact infiltration case has two steps:

- Nonlinear regression of HELP model infiltration data for the most pessimistic, best estimate, and most optimistic cases in Figure 3-116 using Minitab® 17 to generate the log-logistic growth curves (Figure 3-122, Figure 3-123, and Figure 3-124) and associated regression parameters (Table 3-79). Note that the nonlinear regressions were performed assuming a timeline where relative Year 0 is the installation date of the final closure cap rather than the start of the 100-year IC period.
- Manual adjustment of the theta parameters, using the values listed in Table 3-79 for the most pessimistic, best estimate, and most optimistic cases as guidance, to arrive at log-logistic growth curves for the more pessimistic and more optimistic cases shaded in light blue.

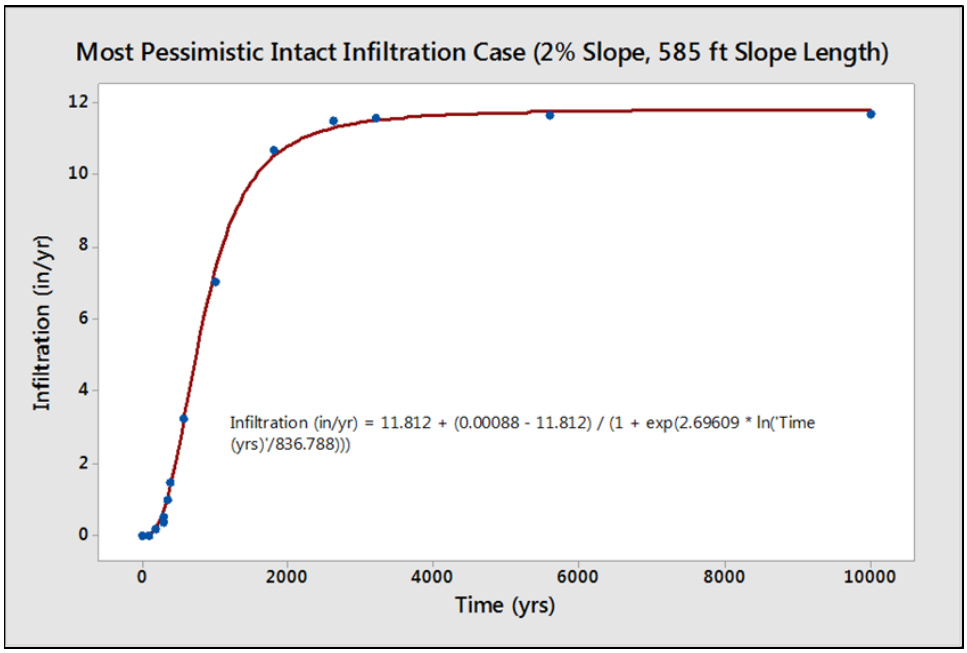

Figure 3-122. Log-Logistic Fit of HELP Model Results for 2% Slope and 585-foot Slope Length Where Year 0 is Installation Date of Final Closure Cap (Dyer, 2019b; Figure 2-10)

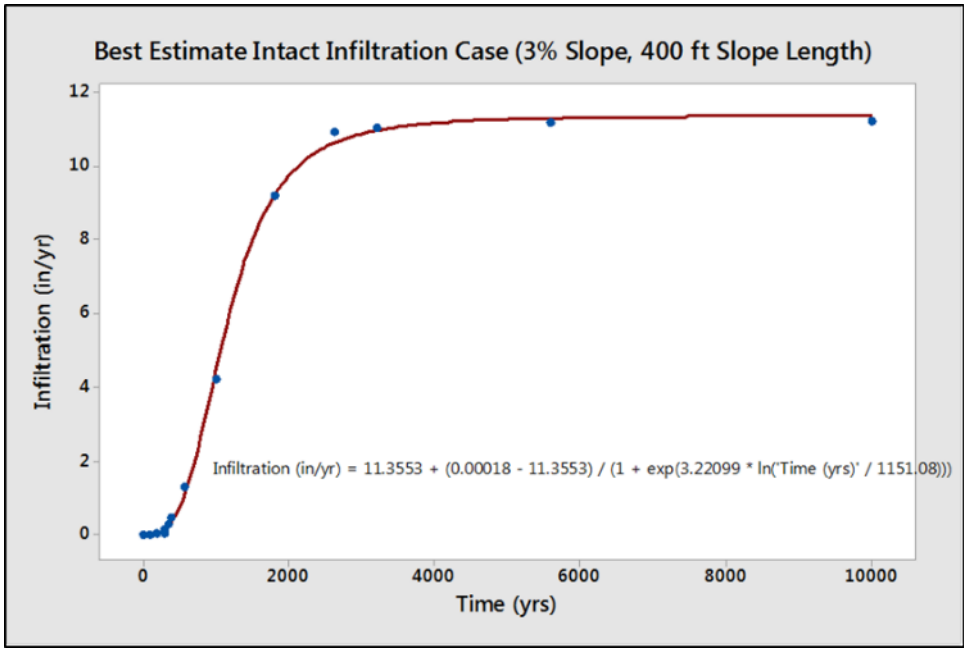

Figure 3-123. Log-Logistic Fit of HELP Model Results for 3% Slope and 400-foot Slope Length Where Year 0 is Installation Date of Final Closure Cap (Dyer, 2019b; Figure 2-11)

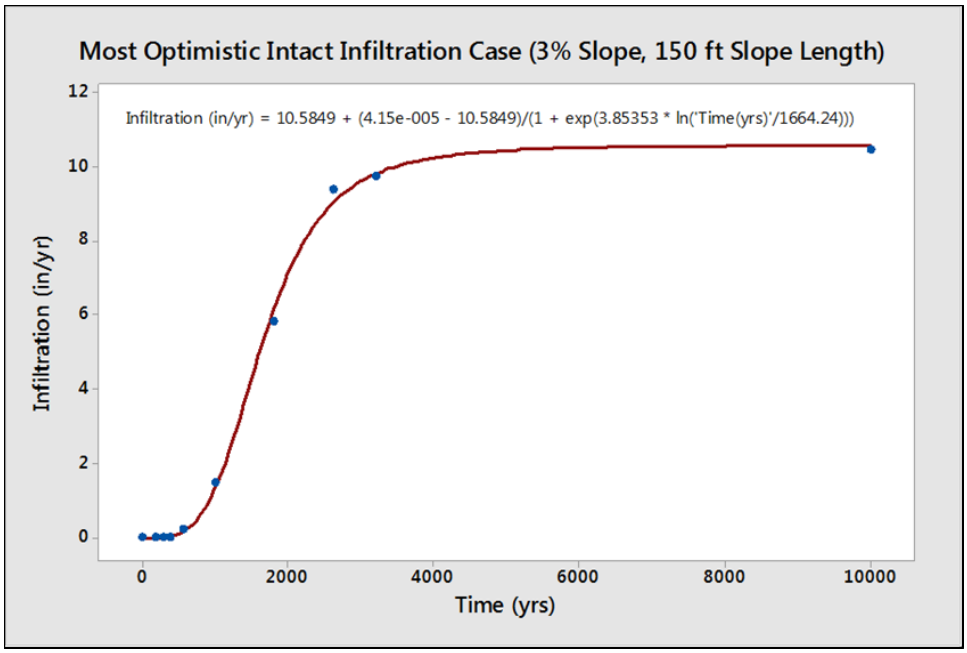

Figure 3-124. Log-Logistic Fit of HELP Model Results for 3% Slope and 150-foot Slope Length Where Year 0 is Installation Date of Final Closure Cap (Dyer, 2019b; Figure 2-12)

Table 3-79. Best-Fit Log-Logistic Growth Curve Parameters and Predicted Infiltration Rates for Final Closure Cap Intact Uncertainty Cases (Dyer, 2019b; Table 2-7)

	Theta Parameters for Log-Logistic Growth Curve				
	Most Pessimistic	More Pessimistic	Best Estimate	More Optimistic	Most Optimistic
θ_1	11.812	11.542547	11.3553	11.039436	10.5849
θ_2	0.00088	0.000467	0.00018	0.0001232	4.15E-05
θ_3	836.788	1022.22028	1151.08	1361.4756	1664.24
θ_4	2.69609	3.005781	3.22099	3.4803314	3.85353
Time	**Infiltration Rate (inches/year)**				
	Most Pessimistic	More Pessimistic	Best Estimate	More Optimistic	Most Optimistic
0	0.00088	0.000467	0.00018	0.0001232	4.15E-05
100	0.0392	0.0111	0.004517	0.00137	0.0002498
180	0.1855	0.0625	0.0289	0.0098	0.0020
290	0.6425	0.2563	0.1325	0.0506	0.0126
300	0.7002	0.2831	0.1476	0.0569	0.0144
340	0.9582	0.4076	0.2194	0.0877	0.0233
380	1.2573	0.5614	0.3112	0.1286	0.0356
560	2.9887	1.6253	1.0155	0.4797	0.1569
1000	7.2983	5.5810	4.4128	2.8114	1.3036
1800	10.4829	9.7608	9.1804	8.0088	6.0861
2623	11.2932	10.9009	10.6080	10.0171	9.0221
3200	11.5028	11.1805	10.9488	10.5029	9.7962
5600	11.7422	11.4734	11.2862	10.9596	10.4872
10000	11.7973	11.5304	11.3446	11.0288	10.5744

Notes:

Regression parameters for the more pessimistic and more optimistic cases are located -41% and +41% of the distance between the best estimate and the most optimistic and most pessimistic cases, respectively, as shown in Figure 3-125. Time zero is the start of IC, which lasts 100 years. The final closure cap is installed at relative Year 100.

The method assumes (1) a log-triangular uncertainty distribution for infiltration rate (I), i.e., log I has a triangular distribution, (2) the triangular distribution for log I is symmetric, and (3) a modified 1-D Latin hypercube sampling (LHS) technique with five samples. In traditional 1-D LHS, the cumulative distribution function (CDF) is divided into an equal number of partitioned regions (N); one sample point is then randomly selected from each of the N partitioned regions. For the modified LHS technique proposed here, the five samples are not randomly selected from each CDF partition but are instead positioned at the midpoint of each equally sized partitioned region as shown in Figure 3-125. The five nonrandom samples correspond to the following uncertainty cases: most optimistic (CDF = 0.1), more optimistic (CDF = 0.3), best estimate (CDF = 0.5), more pessimistic (CDF = 0.7), and most pessimistic (CDF = 0.9). In Figure 3-125, variable x represents one of the four theta fitting parameters (θ_1, θ_2, θ_3, and θ_4) in Eq. (3-64), whose value is equal to zero for the best estimate case and is normalized to -1 and +1 for the most optimistic and most pessimistic cases, respectively. The more optimistic and more pessimistic cases are situated at -0.41 and +0.41, respectively, which is -41% and +41% of the distance between the best estimate and the most optimistic and most pessimistic cases, respectively.

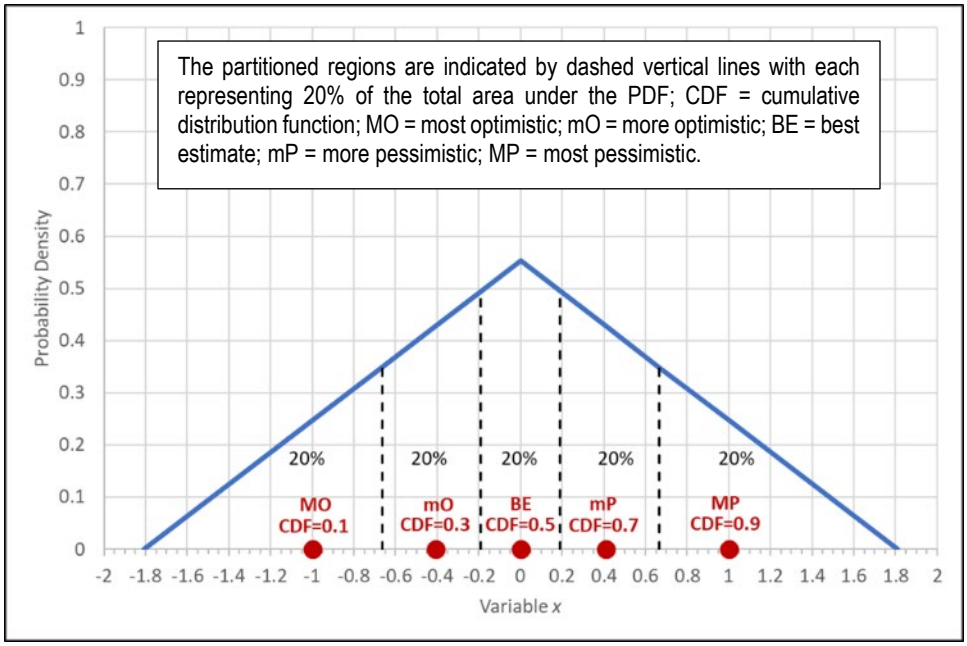

Figure 3-125. Representative Symmetric Probability Density Function for Modified One-Dimensional Latin Hypercube Sampling Technique With Five Non-Random Samples (Dyer, 2019b; Figure 2-13)

Figure 3-126 and Figure 3-127 are linear-linear and log-log plots, respectively, displaying the five log-logistic growth curves for the intact infiltration case included in Table 3-79. This set of five infiltration-rate-versus-time profiles depicts the reasonable and defensible uncertainty distribution for the intact closure-cap scenario considered by Shipmon and Dyer (2017).

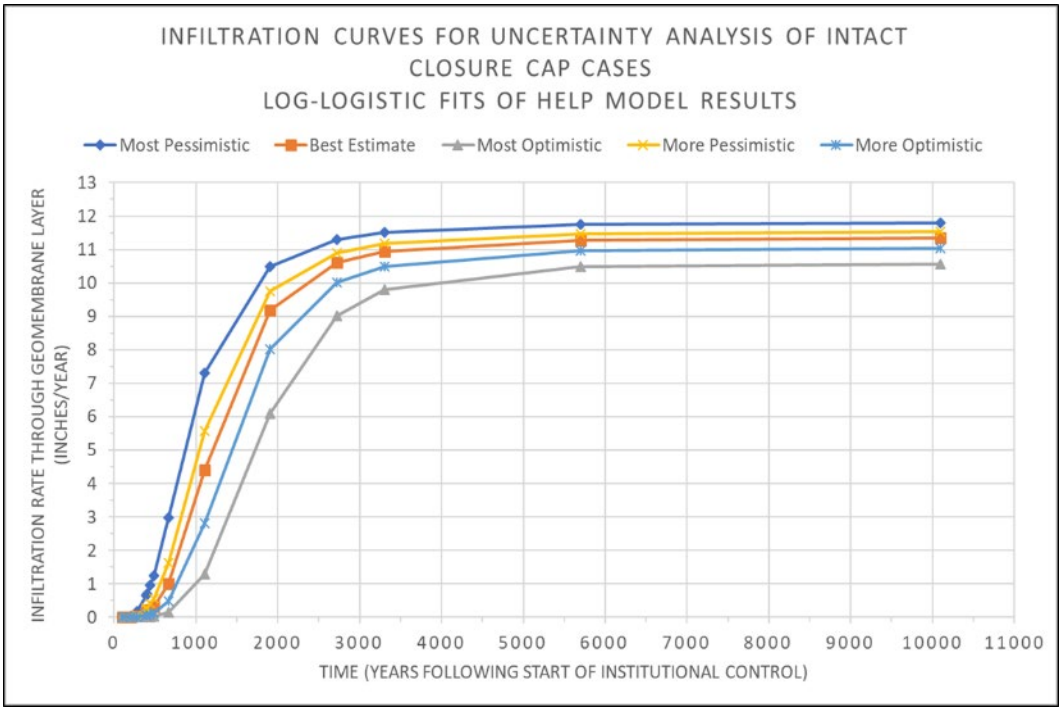

Figure 3-126. Proposed Intact Infiltration Rate Profiles for Uncertainty Analysis (Dyer, 2019b; Figure 2-14; linear-linear plot)

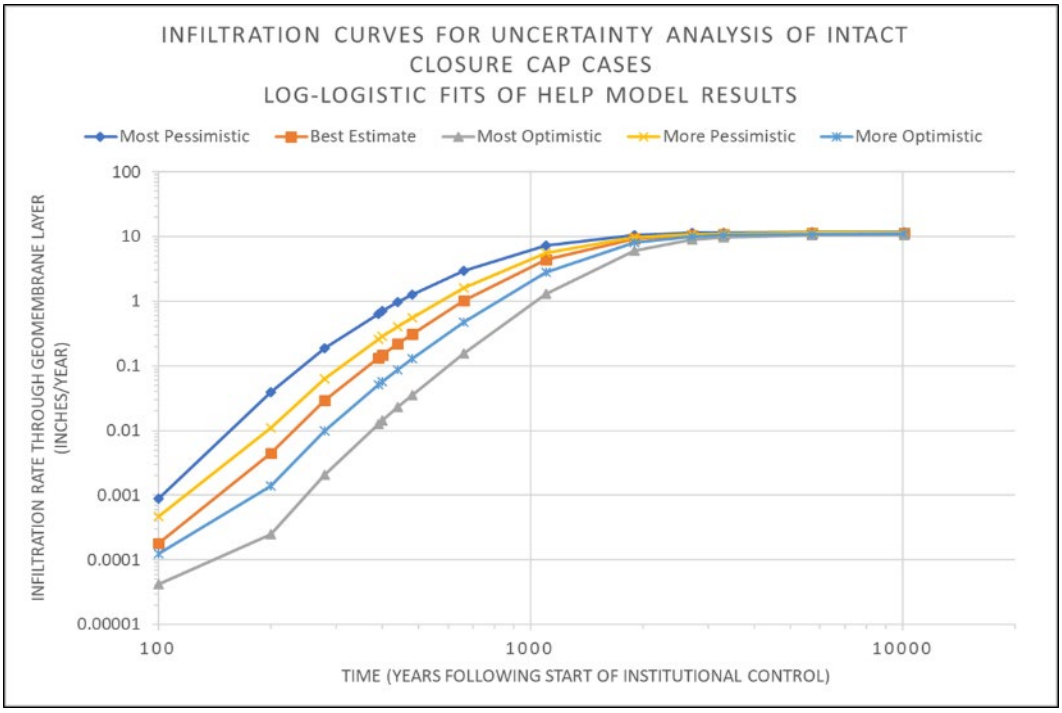

Figure 3-127. Proposed Intact Infiltration Rate Profiles for Uncertainty Analysis (Dyer, 2019b; Figure 2-15; log-log plot)

Similar sets comprised of five infiltration curves each were generated for the 0.54%, 2%, 3.6%, and 4.9% subsidence scenarios using the Python-based probabilistic subsidence model together with the five intact infiltration rate uncertainty distributions from Table 3-79. The slope-length- weighted, spatially averaged infiltration rate uncertainty distributions for the four subsidence scenarios are summarized in Table 3-80, Table 3-81, Table 3-82, Table 3-83, and Table 3-84 for the most optimistic, more optimistic, best estimate, more pessimistic, and most pessimistic cases, respectively.[38] Figure 3-128, Figure 3-129, Figure 3-130, and Figure 3-131 plot the same subsided-case infiltration data sorted by percent subsidence. As percent subsidence increases, the impact of uncertainty in the intact infiltration rates on the uncertainty in the subsidence infiltration rates decreases (i.e., the infiltration rate profiles for the five uncertainty cases become more tightly grouped).

[38] Year 0: Beginning of IC period; interim runoff cover is installed and maintained for next 100 years (i.e., any subsidence is repaired); infiltration rate for interim cover is estimated to be 0.1 inches/year. Year 100: End of IC; installation date of final closure cap. For PORFLOW VZ simulations of closure-cap transects with two sides of unequal slope length, the probabilistic model was executed twice (once for each waste-zone-only slope lengths of 545 feet and 110 feet) at each percent subsidence of interest. A single slope-length-weighted, spatially averaged infiltration-rate time profile for each percent-subsidence case was then calculated using the model output for the two different slope lengths.

Table 3-80. Infiltration Rates for Most Optimistic Probabilistic Subsidence Cases for Slit and Engineered Trenches (Dyer, 2019b; Table 2-8)

Relative Year	Slope-Length-Weighted, Spatially Averaged Infiltration Rate (inches/year)			
	0.54% Subsidence (ST05)	2.0% Subsidence (ST02, ST06-11, ST14, ST17-24, ET02, ET04-09)	3.6% Subsidence (ST04)	4.9% Subsidence (ST03)
0	N/A	N/A	N/A	N/A
100	1.98	5.85	8.48	9.89
180	1.98	5.82	8.45	9.90
290	1.97	5.86	8.46	9.90
300	1.97	5.84	8.47	9.88
340	2.00	5.84	8.47	9.90
380	1.99	5.84	8.47	9.87
480	2.00	5.84	8.47	9.89
660	2.11	5.95	8.53	9.97
1,100	3.14	6.68	9.12	10.41
1,900	7.34	9.77	11.45	12.34
2,723	9.91	11.68	12.86	13.50
3,300	10.60	12.16	13.24	13.82
5,700	11.21	12.62	13.57	14.09
10,100	11.28	12.67	13.62	14.13

Table 3-81. Infiltration Rates for More Optimistic Probabilistic Subsidence Cases for Slit and Engineered Trenches (Dyer, 2019b; Table 2-9)

Relative Year	Slope-Length-Weighted, Spatially Averaged Infiltration Rate (inches/year)			
	0.54% Subsidence (ST05)	2.0% Subsidence (ST02, ST06-11, ST14, ST17-24, ET02, ET04-09)	3.6% Subsidence (ST04)	4.9% Subsidence (ST03)
0	N/A	N/A	N/A	N/A
100	1.98	5.87	8.47	9.89
180	1.98	5.83	8.49	9.86
290	1.97	5.85	8.49	9.89
300	2.03	5.88	8.49	9.92
340	2.04	5.85	8.48	9.91
380	2.05	5.92	8.51	9.90
480	2.09	5.93	8.54	9.92
660	2.41	6.16	8.73	10.09
1,100	4.44	7.63	9.85	11.01
1,900	9.03	11.02	12.36	13.10
2,723	10.80	12.31	13.34	13.90
3,300	11.21	12.63	13.57	14.10
5,700	11.63	12.92	13.80	14.28
10,100	11.68	12.97	13.83	14.31

Table 3-82. Infiltration Rates for Best Estimate Probabilistic Subsidence Cases for Slit and Engineered Trenches (Dyer, 2019b; Table 2-10)

Relative Year	Slope-Length-Weighted, Spatially Averaged Infiltration Rate (inches/year)			
	0.54% Subsidence (ST05)	2.0% Subsidence (ST02, ST06-11, ST14, ST17-24, ET02, ET04-09)	3.6% Subsidence (ST04)	4.9% Subsidence (ST03)
0	N/A	N/A	N/A	N/A
100	1.97	5.84	8.47	9.90
180	1.99	5.85	8.48	9.90
290	2.00	5.85	8.49	9.90
300	2.10	5.91	8.53	9.93
340	2.11	5.91	8.54	9.95
380	2.18	5.97	8.56	9.97
480	2.26	6.04	8.64	10.00
660	2.87	6.48	8.98	10.29
1,100	5.87	8.68	10.61	11.67
1,900	10.06	11.76	12.94	13.57
2,723	11.31	12.68	13.64	14.13
3,300	11.62	12.91	13.79	14.27
5,700	11.90	13.13	13.96	14.41
10,100	11.96	13.17	13.99	14.43

Table 3-83. Infiltration Rates for More Pessimistic Probabilistic Subsidence Cases for Slit and Engineered Trenches (Dyer, 2019b; Table 2-11)

Relative Year	Slope-Length-Weighted, Spatially Averaged Infiltration Rate (inches/year)			
	0.54% Subsidence (ST05)	2.0% Subsidence (ST02, ST06-11, ST14, ST17-24, ET02, ET04-09)	3.6% Subsidence (ST04)	4.9% Subsidence (ST03)
0	N/A	N/A	N/A	N/A
100	1.99	5.84	8.46	9.87
180	1.96	5.83	8.45	9.87
290	2.03	5.87	8.48	9.91
300	2.20	5.98	8.58	9.99
340	2.23	6.00	8.60	10.00
380	2.32	6.12	8.67	10.06
480	2.47	6.21	8.75	10.12
660	3.41	6.90	9.25	10.54
1,100	6.87	9.46	11.19	12.13
1,900	10.57	12.15	13.22	13.80
2,723	11.57	12.88	13.78	14.26
3,300	11.82	13.06	13.91	14.37
5,700	12.07	13.25	14.05	14.49
10,100	12.12	13.29	14.09	14.51

Table 3-84. Infiltration Rates for Most Pessimistic Probabilistic Subsidence Cases for Slit and Engineered Trenches (Dyer, 2019b; Table 2-12)

Relative Year	Slope-Length-Weighted, Spatially Averaged Infiltration Rate (inches/year)			
	0.54% Subsidence (ST05)	2.0% Subsidence (ST02, ST06-11, ST14, ST17-24, ET02, ET04-09)	3.6% Subsidence (ST04)	4.9% Subsidence (ST03)
0	N/A	N/A	N/A	N/A
100	1.97	5.84	8.49	9.88
180	2.04	5.83	8.49	9.93
290	2.15	5.93	8.57	9.96
300	2.54	6.24	8.78	10.14
340	2.60	6.30	8.79	10.16
380	2.80	6.45	8.95	10.28
480	3.10	6.64	9.09	10.42
660	4.61	7.77	9.94	11.10
1,100	8.40	10.56	12.01	12.82
1,900	11.21	12.60	13.57	14.09
2,723	11.91	13.14	13.97	14.41
3,300	12.10	13.27	14.07	14.49
5,700	12.31	13.43	14.19	14.59
10,100	12.36	13.46	14.21	14.61

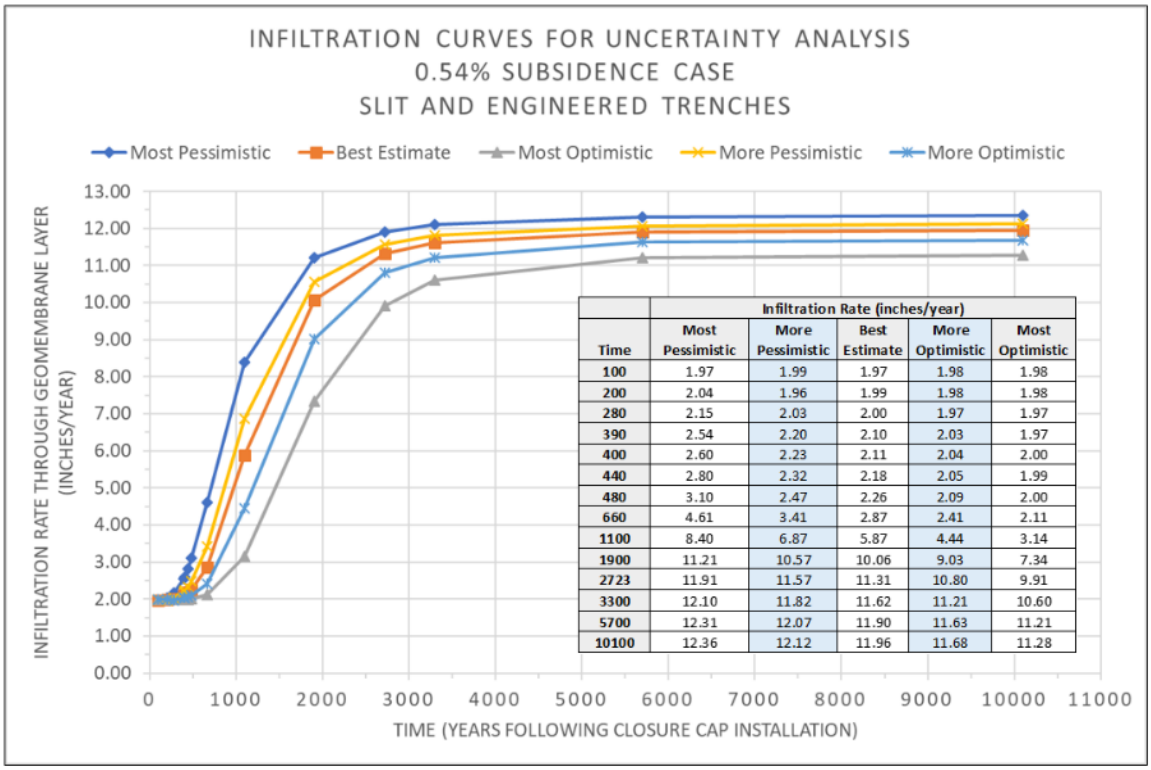

Figure 3-128. Probabilistic Infiltration Rate Profiles for 0.54% Subsidence Case for Slit and Engineered Trenches (Dyer, 2019b; Figure 2-16)

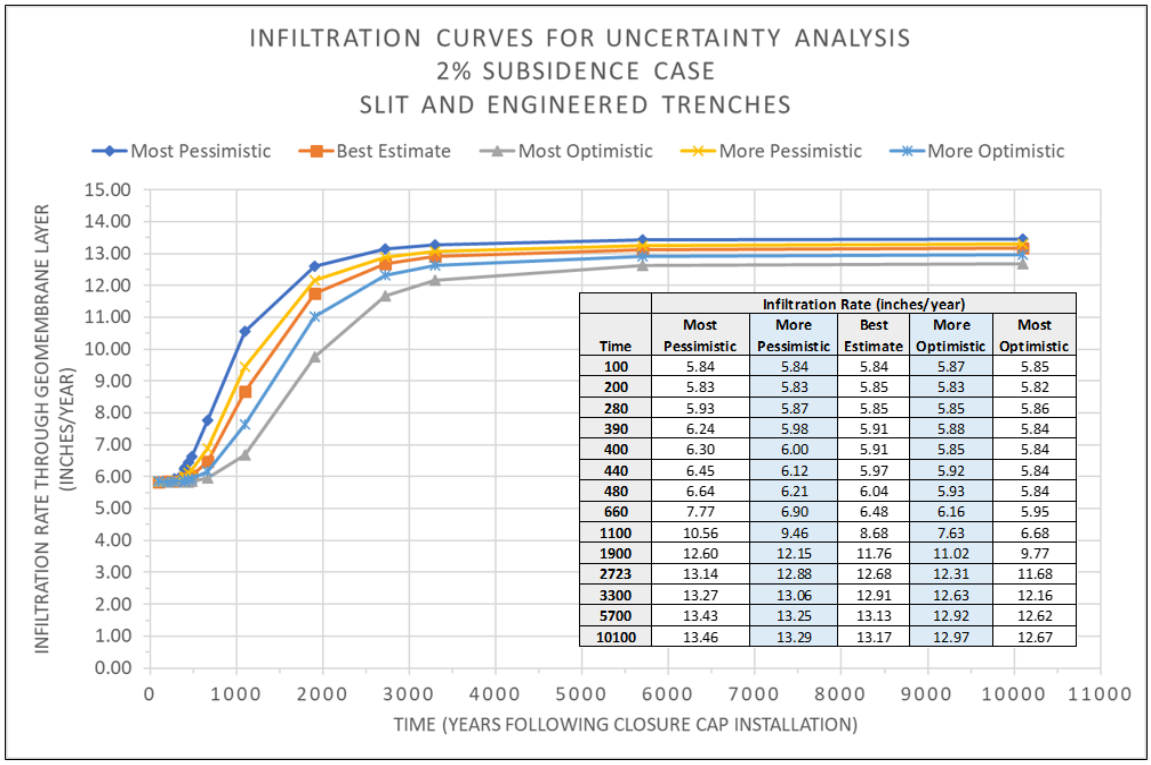

	Infiltration Rate (inches/year)				
Time	Most Pessimistic	More Pessimistic	Best Estimate	More Optimistic	Most Optimistic
100	5.84	5.84	5.84	5.87	5.85
200	5.83	5.83	5.85	5.83	5.82
280	5.93	5.87	5.85	5.85	5.86
390	6.24	5.98	5.91	5.88	5.84
400	6.30	6.00	5.91	5.85	5.84
440	6.45	6.12	5.97	5.92	5.84
480	6.64	6.21	6.04	5.93	5.84
660	7.77	6.90	6.48	6.16	5.95
1100	10.56	9.46	8.68	7.63	6.68
1900	12.60	12.15	11.76	11.02	9.77
2723	13.14	12.88	12.68	12.31	11.68
3300	13.27	13.06	12.91	12.63	12.16
5700	13.43	13.25	13.13	12.92	12.62
10100	13.46	13.29	13.17	12.97	12.67

Figure 3-129. Probabilistic Infiltration Rate Profiles for 2% Subsidence Case for Slit and Engineered Trenches (Dyer, 2019b; Figure 2-17)

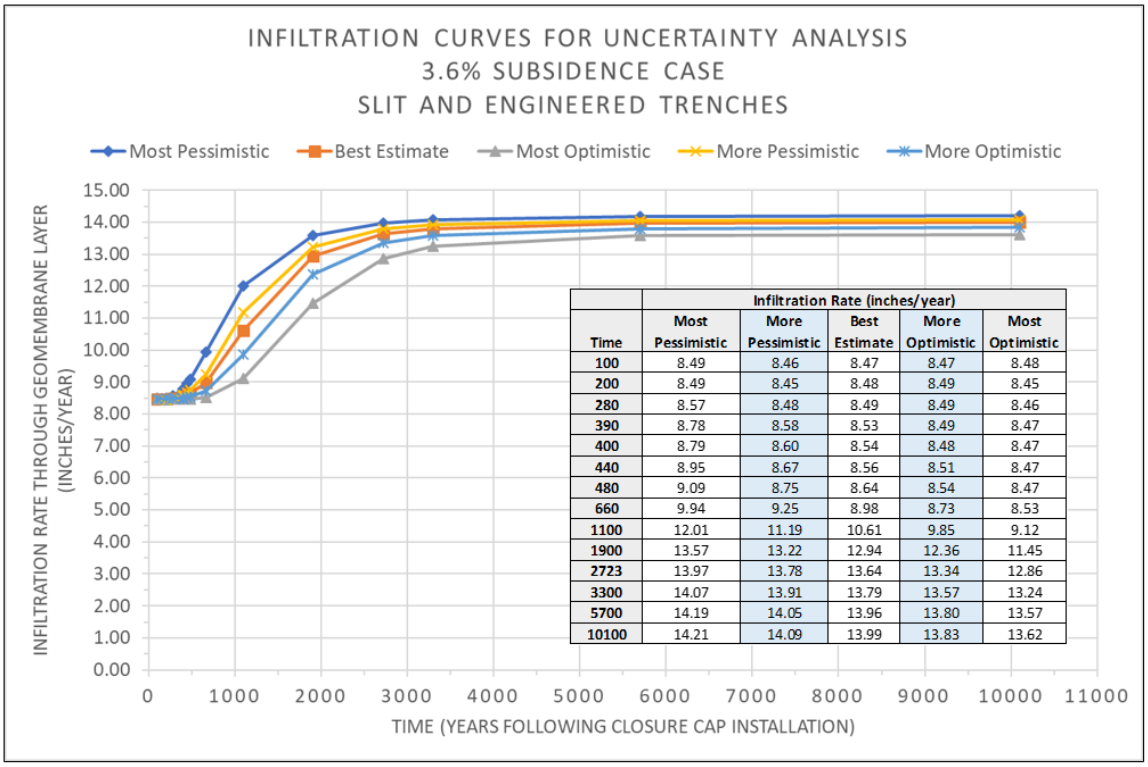

	Infiltration Rate (inches/year)				
Time	Most Pessimistic	More Pessimistic	Best Estimate	More Optimistic	Most Optimistic
100	8.49	8.46	8.47	8.47	8.48
200	8.49	8.45	8.48	8.49	8.45
280	8.57	8.48	8.49	8.49	8.46
390	8.78	8.58	8.53	8.49	8.47
400	8.79	8.60	8.54	8.48	8.47
440	8.95	8.67	8.56	8.51	8.47
480	9.09	8.75	8.64	8.54	8.47
660	9.94	9.25	8.98	8.73	8.53
1100	12.01	11.19	10.61	9.85	9.12
1900	13.57	13.22	12.94	12.36	11.45
2723	13.97	13.78	13.64	13.34	12.86
3300	14.07	13.91	13.79	13.57	13.24
5700	14.19	14.05	13.96	13.80	13.57
10100	14.21	14.09	13.99	13.83	13.62

Figure 3-130. Probabilistic Infiltration Rate Profiles for 3.6% Subsidence Case for Slit and Engineered Trenches (Dyer, 2019b; Figure 2-18)

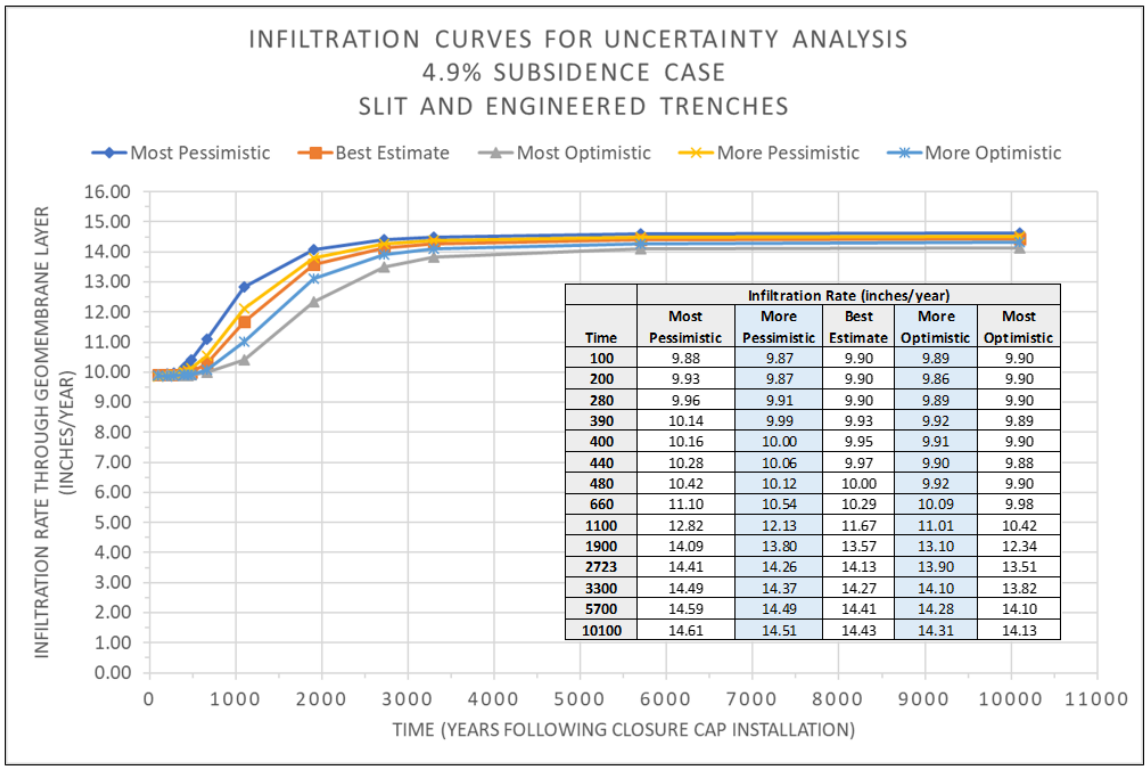

	Infiltration Rate (inches/year)				
Time	Most Pessimistic	More Pessimistic	Best Estimate	More Optimistic	Most Optimistic
100	9.88	9.87	9.90	9.89	9.90
200	9.93	9.87	9.90	9.86	9.90
280	9.96	9.91	9.90	9.89	9.90
390	10.14	9.99	9.93	9.92	9.89
400	10.16	10.00	9.95	9.91	9.90
440	10.28	10.06	9.97	9.90	9.88
480	10.42	10.12	10.00	9.92	9.90
660	11.10	10.54	10.29	10.09	9.98
1100	12.82	12.13	11.67	11.01	10.42
1900	14.09	13.80	13.57	13.10	12.34
2723	14.41	14.26	14.13	13.90	13.51
3300	14.49	14.37	14.27	14.10	13.82
5700	14.59	14.49	14.41	14.28	14.10
10100	14.61	14.51	14.43	14.31	14.13

Figure 3-131. Probabilistic Infiltration Rate Profiles for 4.9% Subsidence Case for Slit and Engineered Trenches (Dyer, 2019b; Figure 2-19)

3.8.4.3.5. Components-in-Grout Trench Segment Special Waste Form

Two CIG trench DUs (CIG01 and CIG02) were originally proposed for the ELLWF as shown in Figure 3-132; however, there are currently no forecasted needs for CIG waste disposal through the end of ELLWF operations. A total of nine grouted CIG trench segments occupies only a portion of CIG01. Consequently, the remaining unused portion of CIG01 and the entire areal footprint of CIG02 will be repurposed as Slit Trenches and renamed ST23 and ST24, respectively (Hamm, 2019).

Figure 3-132. Location of Original Components-in-Grout Trenches Repurposed as ST23 and ST24

The nine existing CIG trench segments (CIG-1 through CIG-9) will be treated in the upcoming PA revision as CIG SWFs having unique subsidence assumptions within the overall ST23 footprint. The nine below-grade earthen trench segments contain grout-encapsulated waste components that provide greater waste isolation than STs and ETs. The grouting operation was conducted to achieve a minimum 12-inch grout thickness below, between, and above components as well as the surrounding undisturbed soil and soil cover for complete encapsulation. Infiltration boundary conditions for the CIG-1 through CIG-9 are presented as part of the discussion of simple SWFs in Section 4.2.1.2.

The unused trench segments in ST23 and all five trench segments in ST24 will be treated the same as other STs from an infiltration perspective (2% slope, 585-foot slope length bounding intact case, and 2% subsidence based only on the area of the ST23 total footprint utilized as a ST).

3.8.4.4. Low-Activity Waste Vault

Details associated with surface infiltration rates are provided in the following subsections.

3.8.4.4.1. Planned Closure

Operational closure of the LAWV will occur in stages whereby individual cells will be closed as they are filled with stacks of containerized waste and the entire vault will be closed after it is full. Closure actions consist of sealing vault openings and sumps. No additional closure actions beyond operational closure are anticipated for the LAWV during the 100-year IC period (i.e., interim closure).

Final closure of the LAWV will take place during final closure of the entire ELLWF. It will involve installation of a common multilayer soil-geomembrane closure cap over all E-Area DUs that is integrated with a drainage system to collect and convey surface runoff and subsurface lateral drainage to nearby sediment basins. The crest lines of the closure cap will be approximately centered over the long and short axes of the LAWV and sloped a minimum 1.3% away from the apex to minimize the overburden loads on the vault and maximize runoff and lateral drainage from the overlying closure cap.

Following installation of the final closure cap but before LAWV structural failure after an assumed 2,800 years (Carey, 2005), the final closure cap, along with the structurally intact concrete vault, will minimize infiltration into the vault. During this period, the hydraulic properties of the closure cap are assumed to degrade, resulting in increased infiltration through the closure cap over time (Dyer, 2019b). In addition, cracks are assumed to develop in the roof slab upon placement of the closure cap load, resulting in increased infiltration through the vault roof (Jones and Phifer, 2007).

3.8.4.4.2. Low-Activity Waste Vault Infiltration Scenario

The LAWV is positioned parallel to and between the future ET05 and ET06 (originally ST15 and ST16) footprints (Figure 2-30). The same Bahia grass case with 2% slope and 585-foot slope length assumed for STs and ETs will also represent an upper bound on intact infiltration rates for the portions of the closure cap over the LAWV as indicated in Figure 2-70. The layers comprising the final closure cap over the LAWV are identical to those listed in Section 3.8.4.3.2 for STs and

ETs; however, the earthen foundation layer thickness above the LAWV will be minimal (Figure 2-70) because the waste below is encased in a concrete vault enclosure with a concrete roof. As depicted in Figure 2-68, the vault consists of 24-inch thick, cast-in-place, reinforced, interior and exterior concrete walls structurally mated to a continuous 30-inch-thick footer and a 16-inch-thick concrete roof fabricated from 3.5-inch-thick precast deck panels overlaid by a 12.5-inch-thick cast-in-place, reinforced concrete slab. At operational closure, openings will be sealed with reinforced concrete, a bonded-in-place layer of fiberboard insulation and a layer of waterproof membrane roofing will be placed on top of the roof slab, and a gutter/downspout system will be added to drain the roof. In addition, the average closure cap thickness above the LAWV will be maintained at 9 feet or less to satisfy differential settlement and maximum seismic load considerations.

SRNL-recompiled Ver. 4.0 of the HELP model (Dixon, 2017) was employed to generate the desired intact infiltration rate time profiles for both on-vault and off-vault locations as described by Jones and Phifer (2007) and McDowell-Boyer et al. (2011). On-vault locations refer to those areas overlying the vault roof; off-vault locations refer to the areas adjacent to the vault sides which were modeled to determine whether subsurface drainage from the roof would sufficiently move through the lowermost backfill (Jones and Phifer, 2007). The infiltration profiles assume collapse of the LAWV roof 2,805 years after final closure and are based on the same degradation scenario for the final closure cap that was assumed for STs and ETs. In contrast to the 4-foot-thick soil operational cover and HDPE interim cover for STs and ETs, infiltration simulations for the operational and IC periods for the LAWV on-vault scenario are based on a 12.5-inch-thick concrete roof of low permeability.

The simulation period for the LAWV was relative Year 100 to relative Year 10,100, where relative Year 100 is the installation date of the final closure cap. The actual compliance period for the PA is 1,000 years following final closure (i.e., relative Year 1,100); however, infiltration estimates were extended to relative Year 10,100 to capture roof collapse at relative Year 2,905 and to be consistent with the simulation period for STs and ETs. Dyer and Flach (2018) and Phifer et al. (2007) describe in greater detail the formulation and execution of the HELP model for the intact closure cap infiltration cases, including degradation assumptions for the barrier and lateral drainage layers.

During the operational and IC periods, water entrance into the LAWV is minimized through the vault subdrain system, the minimum 24-inch thick concrete walls, and the 16-inch thick concrete slab roof with bonded-in-place fiberboard insulation covered by a layer of waterproof membrane roofing (Jones and Phifer, 2007). Any water that enters the vault is intercepted by the individual cell floor collection systems. This results in essentially zero infiltration through the waste during the operational and IC periods. Infiltration through the permanent reinforced concrete roof slab was modeled in HELP assuming the waterproof membrane roofing was not in place.

Upon structural failure of the LAWV roof at relative Year 2,905, the conservative assumption is that the roof collapses into the vault and the overlying closure cap subsides. Closure cap subsidence results in the cap losing its runoff and drainage layer functionality together with a decrease in

evapotranspiration in the subsided area. Increased infiltration will occur through the portion of the closure cap overlying the collapsed LAWV (Jones and Phifer, 2007). Jones and Phifer (2007) calculated the subsidence potential to be approximately 21 feet.

HELP Ver. 4.0 model files for the on-vault and off-vault infiltration cases were stored in the parent directory C:\Help4.0 in three separate subdirectories:[39]

- C:\Help4.0\Hweather stores input parameters for evapotranspiration calculations (ROOFEVAP.D11, FEVAP.D11, VCOLEVAP.D11) as well as HELP-model-generated weather input files containing 100 years of daily precipitation data (FPREC.D4), daily temperature data (FTEMP.D7), and daily solar radiation data (FSOLAR.D13). Section 3.8.4.2 provides additional background information on weather data input for the HELP model.
- C:\Help4.0\LAW contains the input and output files for each on-vault time step that are stored in separate subdirectories labeled C:\Help4.0\LAW\LAWRF (roof only), C:\Help4.0\LAW\LAW00 (Year 100 cap) through C:\Help4.0\LAW\LAW11 (Year 2,905 cap), and C:\Help4.0\LAW \LAWCLPSE (roof collapse and beyond).
- C:\Help4.0\LAWOFF contains the input and output files for each off-vault time step that are stored in separate subdirectories labeled C:\Help4.0\LAWOFF\LAWOP (operational period, soil only), C:\Help4.0\LAWOFF\LAWIC (IC period, soil only), C:\Help4.0\LAWOFF\LAW00 (Year 100 cap) through C:\Help4.0\LAWOFF\LAW11 (Year 2,905 cap), and C:\Help4.0\LAWOFF\LAWCLPSE (roof collapse and beyond).
- C:\Help4.0\Source contains the executable Fortran files for the HELP model.

Dyer (2019b; Appendix D, Figure D-1) presents a diagram of the file hierarchy.

All infiltration timesteps were executed together by double-clicking the HELP.bat Windows batch file stored in the subdirectories C:\Help4.0\LAW and C:\Help4.0\LAWOFF. Overall summary files labeled LAW.OUT, LAW_DRAINAGE.OUT, LAW_PERC.OUT, and LAW_RUNOFF.OUT were created by double-clicking the Python-based model cat_FC.py stored in the subdirectories C:\Help4.0\LAW and C:\Help4.0\LAWOFF. Output files for each on-vault case were stored in C:\Help4.0\LAW\LAWxx\Output, where xx is RF, 00 through 11, or CLPSE. Output files for each individual off-vault case were stored in C:\Help4.0\LAWOFF\LAWxx\Output, where xx is OP, IC, 00 through 11, or CLPSE.

HELP model simulations for the on-vault scenario treat the 12-inch thick lower backfill layer just above the vault roof as a lateral drainage layer with a conservative 2% slope and 62-foot slope length (north side roof) based on analyses completed by Jones and Phifer (2007). Designating the lower backfill as a drainage layer with backfill hydraulic properties allows water to drain from the

[39] The as-written batch execution files embedded in the HELP directories for this data package require the HELP model to be executed from the C: drive. If executed from another directory or drive, then the Python script and the .bat files in the parent directory and each of the subdirectories for each case will need to be edited for the new directory pathway.

roof and avoids the buildup of hydraulic head. The concrete roof slab is treated in the HELP model as a barrier soil liner with an estimated saturated hydraulic conductivity equal to 1.0E-12 cm s^{-1}.

Jones and Phifer (2007) describe in detail the conceptual model for the off-vault simulations of the LAWV using the HELP model. The off-vault simulation region of interest is the soil backfill adjacent to and within 10 feet of the north and south sides (long axis) of the LAWV. The purpose of the off-vault simulations is to confirm that subsurface drainage (runoff) from the concrete vault roof will adequately drain through the lowermost backfill layers adjacent to the vault walls. An off-vault width of 10 feet represents one half of the approximately 20-foot distance between the LAWV and the neighboring Slit Trenches. The differences in model setup between the on-vault and off-vault simulations (based on relative Year 100 nondegraded closure cap case) are:

- On-Vault Layers 8 and 9 (24-inch Foundation Layer (1.0E-03) and 12-inch Lower Drainage Layer) in the on-vault simulations are combined for the off-vault simulations into a single 36-inch vertical-percolation foundation layer (Off-Vault Layer 8) with identical material and hydraulic properties.
- On-Vault Layer 10 (Concrete Roof Slab) in the on-vault simulations is changed for the off-vault simulations to a 12.5-inch-thick barrier soil liner (Off-Vault Layer 9) with the same material and hydraulic properties as the 36-inch-thick Foundation Layer (1.0E-03) above.
- A 298-inch-thick vertical percolation layer with same properties as Foundation Layer (1.0E-03) above is added to represent backfill material extending from the bottom of Off-Vault Layer 9 to the vault's construction grade. The total thickness of the layer is the rounded sum of the vault's wall height to the bottom of the roof edge (24.5 feet, Figure 2-68 cross-section A-A') and the thickness of the roof's precast deck panels (3.5 inches = 16-inch total roof thickness less 12.5-inch concrete slab).
- Drainage off the concrete roof (On-Vault Layer 9) in the on-vault simulations is added as a subsurface inflow (run-on) to Layer 8 in the time-equivalent off-vault simulations. Due to the difference in surficial drainage area and to conserve mass, the subsurface drainage flux (inches per year) must be multiplied by the roof-to-off-vault width ratio (62 feet ÷ 10 feet = 6.2) to obtain the subsurface inflow flux for the off-vault simulations. Dyer (2019b; Appendix D, Table D-1) provides a tabular summary of the subsurface inflow inputs to Off-Vault Layer 8 for the off-vault simulations.

Table 3-85 lists technical reports relevant to the calculation of infiltration rates for the LAWV. Dyer (2019b; Appendix D) provides the HELP model input parameter data sheets for each time step for both the on-vault and off-vault cases. Table 3-86 and Table 3-87 summarize the infiltration rates for the LAWV on-vault and off-vault cases, respectively, from the operational period through roof collapse at relative Year 2,905 and beyond. Included in Table 3-86 and Table 3-87 are the HELP model input (xx.D10), output (xx.OUT), and weather input data (xx.D4, xx.D7, xx.D11, xx.D13) filenames corresponding to each time step. Reported infiltration rates from the HELP model are temporally (annually) and spatially (585-foot total slope length) averaged.

Table 3-85. Technical Reports Relevant to Calculation of Infiltration Rates for Low-Activity Waste Vault (Dyer, 2019b; Table 3-1)

Report Number	Authors/Year	Title	Relevance
SRNL-STI-2017-00104, Rev. 0	Dixon (2017)	HELP 4.0 Documentation Updates for Software and Data	HELP model adaptations to run on Windows 10
WSRC-TR-2005-00405, Rev. 0	Jones and Phifer (2007)	E-Area Low-Activity Waste Vault Subsidence Potential and Closure Cap Performance.	Conceptual approach for calculating infiltration rates for the LAWV
SRNL-STI-2010-00618, Rev. 0	McDowell-Boyer et al. (2011)	Data Package for HELP Models used in the E-Area Low-Level Waste Facility Performance Assessment	Infiltration rates used in PA2008 for the LAWV
SRNL-RP-2009-00075, Rev. 0	Phifer et al. (2009)	Closure Plan for the E-Area Low-Level Waste Facility	Operational and interim closure covers

Table 3-86. Infiltration Rates and HELP Model Input and Output Files for Low-Activity Waste Vault: On-Vault Case (Dyer, 2019b; Table 3-2)

Relative Year[1]	Period	HELP Model Input, Output, and Weather Files[2]	PC Directory Location for Execution	Infiltration Rate Reported for Layer[3]	On-Vault Infiltration Rate (inches/year)
-40 to 0	Operational	LAWRF.D10, LAWRF.OUT, ROOFEVAP.D11 [2]	C:\Help4.0\LAW\LAWRF	Concrete Roof	0.0
0 to 100	Institutional Control	LAWRF.D10, LAWRF.OUT, ROOFEVAP.D11 [2]	C:\Help4.0\LAW\LAWRF	Concrete Roof	0.0
100	Closure Cap	LAW00.D10, LAW00.OUT	C:\Help4.0\LAW\LAW00	Geomembrane	0.00081
180	Closure Cap	LAW01.D10, LAW01.OUT	C:\Help4.0\LAW\LAW01	Geomembrane	0.007
290	Closure Cap	LAW02.D10, LAW02.OUT	C:\Help4.0\LAW\LAW02	Geomembrane	0.16
300	Closure Cap	LAW03.D10, LAW03.OUT	C:\Help4.0\LAW\LAW03	Geomembrane	0.18
340	Closure Cap	LAW04.D10, LAW04.OUT	C:\Help4.0\LAW\LAW04	Geomembrane	0.30
380	Closure Cap	LAW05.D10, LAW05.OUT	C:\Help4.0\LAW\LAW05	Geomembrane	0.38
480	Closure Cap	LAW06.D10, LAW06.OUT	C:\Help4.0\LAW\LAW06	Geomembrane	1.39
660	Closure Cap	LAW07.D10, LAW07.OUT	C:\Help4.0\LAW\LAW07	Geomembrane	3.23
1,100	Closure Cap	LAW08.D10, LAW08.OUT	C:\Help4.0\LAW\LAW08	Geomembrane	6.82
1,900	Closure Cap	LAW09.D10, LAW09.OUT	C:\Help4.0\LAW\LAW09	Geomembrane	10.24
2,723	Closure Cap	LAW10.D10, LAW10.OUT	C:\Help4.0\LAW\LAW10	Geomembrane	11.10
2,905	Closure Cap	LAW11.D10, LAW11.OUT	C:\Help4.0\LAW\LAW11	Geomembrane	11.13
2,905+	Roof Collapse	LAWCLPSE.D10, LAWCLPSE.OUT, VCOLEVAP.D11 [2]	C:\Help4.0\LAW\LAWCLPSE	Collapsed Cap	18.89

Notes:

1 Year 0: Beginning of IC period. Year 100: End of IC period; installation date of final closure cap.

2 HELP Weather files are FPREC.D4, FTEMP.D7, FEVAP.D11, and FSOLAR.D13 except where noted in the table.

3 On-vault infiltration rates for the geomembrane layer represent the volumetric flux of water that will percolate vertically downward to the sloped concrete roof and drain horizontally to the roof edges. In HELP model simulations of the intact closure cap, the predicted percolation rate through the concrete slab roof is essentially zero. As a result, 100% of the water that percolates through the geomembrane layer above the LAWV will drain to the roof edges and becomes an inflow (subsurface run-on) for the off-vault infiltration simulations. When setting the upper boundary condition for the PORFLOW VZ simulations, it is important to consider the conservation of mass because the "Soil Next to Vault Roof" off-vault infiltration rates reported in Table 3-87 include the on-vault geomembrane drainage flux.

Table 3-87. Infiltration Rates and HELP Model Input and Output Files for Low-Activity Waste Vault: Off-Vault Case (Dyer, 2019b; Table 3-3)

Relative Year[1]	Period	HELP Model Input, Output, and Weather Files[2]	PC Directory Location for Execution	Infiltration Rate Reported for Layer[3]	On-Vault Infiltration Rate (inches/year)
-40 to 0	Operational	LAWOP.D10, LAWOP.OUT, VCOLEVAP.D11 [2]	C:\Help4.0\LAWOFF\LAWOP	Off-Vault Ground Surface	16.17
0 to 100	Institutional Control	LAWIC.D10, LAWIC.OUT, VCOLEVAP.D11 [2]	C:\Help4.0\LAWOFF\LAWIC	Off-Vault Ground Surface	16.17
100	Closure Cap	LAW00.D10, LAW00.OUT	C:\Help4.0\LAWOFF\LAW00	Geomembrane	0.00081
				Soil Next to Vault Roof	0.00571
180	Closure Cap	LAW01.D10, LAW01.OUT	C:\Help4.0\LAWOFF\LAW01	Geomembrane	0.0070
				Soil Next to Vault Roof	0.047
290	Closure Cap	LAW02.D10, LAW02.OUT	C:\Help4.0\LAWOFF\LAW02	Geomembrane	0.16
				Soil Next to Vault Roof	1.12
300	Closure Cap	LAW03.D10, LAW03.OUT	C:\Help4.0\LAWOFF\LAW03	Geomembrane	0.18
				Soil Next to Vault Roof	1.21
340	Closure Cap	LAW04.D10, LAW04.OUT	C:\Help4.0\LAWOFF\LAW04	Geomembrane	0.30
				Soil Next to Vault Roof	2.09
380	Closure Cap	LAW05.D10, LAW05.OUT	C:\Help4.0\LAWOFF\LAW05	Geomembrane	0.38
				Soil Next to Vault Roof	2.65
480	Closure Cap	LAW06.D10, LAW06.OUT	C:\Help4.0\LAWOFF\LAW06	Geomembrane	1.39
				Soil Next to Vault Roof	9.87
660	Closure Cap	LAW07.D10, LAW07.OUT	C:\Help4.0\LAWOFF\LAW07	Geomembrane	3.23
				Soil Next to Vault Roof	23.09
1,100	Closure Cap	LAW08.D10, LAW08.OUT	C:\Help4.0\LAWOFF\LAW08	Geomembrane	6.82
				Soil Next to Vault Roof	48.80
1,900	Closure Cap	LAW09.D10, LAW09.OUT	C:\Help4.0\LAWOFF\LAW09	Geomembrane	10.24
				Soil Next to Vault Roof	73.37
2,723	Closure Cap	LAW10.D10, LAW10.OUT	C:\Help4.0\LAWOFF\LAW10	Geomembrane	11.10
				Soil Next to Vault Roof	79.49
2,905	Closure Cap	LAW11.D10, LAW11.OUT	C:\Help4.0\LAWOFF\LAW11	Geomembrane	11.13
				Soil Next to Vault Roof	79.72
2,905+	Roof Collapse	LAWCLPSE.D10, LAWCLPSE.OUT	C:\Help4.0\LAWOFF\LAWCLPSE	Geomembrane	11.13
				Soil Next to Vault Roof	11.11 [4]

Notes:

1 Year 0: Beginning of IC period. Year 100: End of IC period; installation date of final closure cap.

2 HELP Weather files are FPREC.D4, FTEMP.D7, FEVAP.D11, and FSOLAR.D13 except where noted in the table.

3 For the off-vault case, vertical infiltration rates are reported at two elevations: the cap geomembrane layer above and the soil backfill layer below at the same elevation as the outside edge of the sloped concrete roof. When setting the upper boundary condition for the PORFLOW VZ simulations, it is important to consider the conservation of mass because the "Soil Next to Vault Roof" off-vault infiltration rates reported above include the on-vault "Geomembrane" drainage flux. In addition, HELP model simulations of the intact closure cap predict that the percolation rate through the concrete slab roof is essentially zero. If PORFLOW simulations of the LAWV assume nonzero leakage through cracks in the concrete roof, then the "Soil Next to Vault Roof" infiltration rates at each time step will need to be lowered by (62 feet ÷ 10 feet) x (concrete slab leakage flux in inches/year).

4 The off-vault infiltration rate through the backfill soil adjacent to the vault roof decreases significantly after roof collapse because there is no longer any on-vault lateral drainage (subsurface run-on) from the sloped concrete roof.

3.8.4.5. Intermediate-Level Vault

Details associated with surface infiltration rates are provided in the following subsections.

3.8.4.5.1. Planned Closure

Operational closure of the ILV will occur in stages as described in detail in Section 2.2.6. When individually filled, the ILT module (consisting of two cells) and the ILNT module (consisting of seven cells) will be operationally closed via installation of separate, permanent, reinforced-concrete roof slabs with overlying bonded-in-place fiberboard insulation and waterproof membrane roofing over the entirety of each module. The temporary rain covers and shielding tees are no longer required after installation of the permanent roof slab. No additional closure actions beyond operational closure are anticipated for the ILV during the 100-year IC period.

Final closure of the ILV will take place during final closure of the entire ELLWF, which will occur at the end of the 100-year IC period. Final closure will consist of installation of a multilayer soil-geomembrane closure cap installed over all the DUs as well as a run-off drainage system. The closure cap will have a 2% slope perpendicular to the long axis of the ILV to minimize the overburden loads on the vault and maximize runoff and lateral drainage from the overlying closure cap. In addition, the average closure cap thickness above the ILV will be maintained at 9 feet or less to satisfy differential settlement and maximum seismic load considerations.

Following installation of the final closure cap, but before structural failure of the vault after an assumed 7,000 years, the final closure cap and the structurally intact concrete vault will minimize infiltration into the vault. During this period, the hydraulic properties of the closure cap are assumed to degrade, resulting in increased infiltration through the closure cap over time (Dyer, 2019b). In addition, cracks are assumed to develop in the roof slab upon placement of the closure cap load, resulting in increased infiltration through the vault roof (Jones and Phifer, 2007).

3.8.4.5.2. Intermediate-Level Vault Infiltration Scenario

The ILV is located to the south of ST08 and ST09 as shown in Figure 2-71. Based on its size and location (Figure 2-75 and Figure 2-76), the intact infiltration model of the proposed ILV final closure cap design assumed a Bahia grass vegetative cover, 2% slope, and 250-foot maximum slope length. The layers comprising the final closure cap over the ILV are identical to those listed in Section 3.8.4.3.2 for ST and ETs; however, the earthen foundation layer thickness above the ILV will be minimal (Figure 2-76) because the waste below is encased in a concrete vault enclosure with a concrete roof. A thickness of 27 inches (minimum roof slab thickness shown in Figure 2-75) was assumed for the concrete slab roof layer in the HELP model simulations.

SRNL-recompiled Ver. 4.0 of the HELP model (Dixon, 2017) was used to generate the desired infiltration rate time profiles for both on-vault and off-vault locations in a manner similar to what was reported by McDowell-Boyer et al. (2011) for PA2008. On-vault locations refer to those areas overlying the vault roof; off-vault locations refer to the 10-foot wide area adjacent to the downslope (northern) side of the vault which was modeled to determine whether subsurface drainage from the roof would sufficiently move through the lowermost backfill (Jones and Phifer,

2007). The infiltration profiles assume collapse of the ILV roof 7,000 years[40] after final closure and are based on the same degradation scenario for the final closure cap that was assumed for ST and ETs. In contrast to the 4-foot-thick soil operational cover and HDPE interim cover for STs and ETs, infiltration simulations for the operational and IC periods for the ILV on-vault scenario are based on a 27-inch-thick concrete roof of low permeability.

The simulation period for the ILV was relative Year 100 to relative Year 10,100, where relative Year 100 is the installation date of the final closure cap. The actual compliance period for the PA is 1,000 years following final closure (i.e., relative Year 1,100); however, infiltration estimates were extended to relative Year 10,100 to capture roof collapse at relative Year 7,100 and to be consistent with the simulation period for STs and ETs. Dyer and Flach (2018) and Phifer et al. (2007) describe in greater detail the formulation and execution of the HELP model for the intact closure cap infiltration cases, including degradation assumptions for the barrier and lateral drainage layers.

During the operational and IC periods, water entrance into the ILV is minimized through the vault subdrain system, the minimum 24-inch-thick concrete walls, and sloped roof cover (i.e., temporary sloped metal rain cover with roofing membrane over each cell during the operational period or a minimum 27-inch-thick concrete slab roof with bonded-in-place fiberboard insulation covered by a layer of waterproof membrane roofing during IC). Any water that enters the vault is intercepted by the individual cell floor collection systems. This results in essentially zero infiltration through the waste during the operational and IC periods. Infiltration through the permanent reinforced concrete roof slab was modeled in HELP assuming the waterproof membrane roofing was not in place.

McDowell-Boyer et al. (2011) conservatively assumed that upon structural failure at relative Year 7,100, the ILV roof will collapse into the interior of the vault followed by subsidence of the overlying final closure cover. Subsidence of the closure cover results in the loss of its runoff and drainage layer functionality together with a decrease in evapotranspiration in the subsided area. In addition, because of its positioning under the ELLWF closure cap relative to other DUs, surface run-off and lateral drainage from the upslope intact closure cap will drain into the subsided ILV area. Dyer (2019b; Appendix E, Table E-18 footnote) explains how the subsurface run-on flux was calculated. Increased infiltration will occur through the portion of the subsided closure cap overlying the collapsed ILV. PA2022 assumes a subsidence potential of 17 feet for the ILV.

HELP Ver. 4.0 model files for the on-vault and off-vault infiltration cases were stored in the parent directory C:\Help4.0 in three separate subdirectories:[41]

[40] To align with the timing of the HELP model simulation cases and to remain pessimistically bounding, the PORFLOW model of the ILV assumes that roof collapse occurs after 5,770 years rather than 7,000 years. See Section 4.6.3.4 for a detailed explanation.

[41] The as-written batch execution files embedded in the HELP directories for this data package require the HELP model to be executed from the C: drive. If executed from another directory or drive, then the Python script and the .bat files in the parent directory and each of the subdirectories for each case will need to be edited for the new directory pathway.

- C:\Help4.0\Hweather stores input parameters for evapotranspiration calculations (ROOFEVAP.D11, FEVAP.D11, VCOLEVAP.D11) as well as HELP-model-generated weather input files containing 100 years of daily precipitation data (FPREC.D4), daily temperature data (FTEMP.D7), and daily solar radiation data (FSOLAR.D13). Section 3.8.4.2 provides additional background information on weather data input for the HELP model.
- C:\Help4.0\ILV contains input and output files for each on-vault time step stored in separate subdirectories labeled C:\Help4.0\ILV\ILVRF (roof only), C:\Help4.0\ILV\ILV00 (Year 100 cap) through C:\Help4.0\ILV\ILV14 (Year 7,100 cap), and C:\Help4.0\ILV\ILVCLPSE (roof collapse and beyond).
- C:\Help4.0\ILVOFF contains the input and output files for each off-vault time step that are stored in separate subdirectories labeled C:\Help4.0\ILVOFF\ILVOP (operational period, soil only), C:\Help4.0\ILVOFF\ILVIC (IC period, soil only), C:\Help4.0\ILVOFF\ILV00 (Year 100 cap) through C:\Help4.0\ILVOFF\ILV14 (Year 7,100 cap), and C:\Help4.0\ILVOFF\ILVCLPSE (roof collapse and beyond).
- C:\Help4.0\Source contains the executable Fortran files for the HELP model.

U.S. DOE, 2017Dyer (2019b; Appendix E, Figure E-1) presents a diagram of the file hierarchy.

All infiltration timesteps were executed together by double-clicking the HELP.bat Windows batch file stored in the subdirectories C:\Help4.0\ILV and C:\Help4.0\ILVOFF. Overall summary files labeled ILV.OUT, ILV_DRAINAGE.OUT, ILV_PERC.OUT, and ILV_RUNOFF.OUT were created by double-clicking the Python-based model cat_FC.py stored in the subdirectories C:\Help4.0\ILV and C:\Help4.0\ILVOFF. Output files for each on-vault case were stored in C:\Help4.0\ILV\ILVxx\Output, where xx is RF, 00 through 14, or CLPSE. Output files for each individual off-vault case were stored in C:\Help4.0\ ILVOFF\ILVxx\Output, where xx is OP, IC, 00 through 14, or CLPSE.

HELP model simulations for the on-vault scenario treat the 12-inch thick lower backfill layer just above the vault roof as a lateral drainage layer with 2% slope and 49.5-foot slope length (Figure 2-75 and Figure 2-76) as was similarly done for the LAWV by Jones and Phifer (2007). Designating the lower backfill as a drainage layer with backfill hydraulic properties allows water to drain from the roof and avoids the buildup of hydraulic head. The concrete roof slab is treated in the HELP model as a barrier soil liner with an estimated saturated hydraulic conductivity equal to 1.0E-12 cm s^{-1}.

The off-vault simulations of the ILV using the HELP model were executed using the same conceptual model as described by Jones and Phifer (2007) for the LAWV. The off-vault simulation region of interest is the soil backfill adjacent to and within 10 feet of the north side (long axis) of the ILV. The purpose of the off-vault simulations is to confirm that subsurface drainage (runoff) from the concrete vault roof will adequately drain through the lowermost backfill layers adjacent to the vault wall. The differences in model setup between the on-vault and off-vault simulations are (based on relative Year 100 nondegraded closure cap case):

- On-Vault Layer 8 (12-inch Lower Drainage Layer) in the on-vault simulations is treated in the off-vault simulations as a 12-inch vertical-percolation backfill foundation layer (Off-Vault Layer 8) with identical material and hydraulic properties.
- On-Vault Layer 9 (Concrete Roof Slab) in the on-vault simulations is changed for the off-vault simulations to a 27-inch-thick barrier soil liner (Off-Vault Layer 9) with the same material and hydraulic properties as the 12-inch-thick Foundation Layer (1.0E-03) above.
- A 312-inch-thick vertical percolation layer with same properties as Foundation Layer (1.0E-03) above is added to represent backfill material extending from the bottom of Off-Vault Layer 9 to the vault's construction grade. The layer thickness (26 feet) equals the vault's northside wall height to the bottom of the roof edge for the ILT modules (Figure 2-75).
- Drainage off the concrete roof (On-Vault Layer 9) in the on-vault simulations is added as a subsurface inflow (run-on) to Layer 8 in the time-equivalent off-vault simulations. Due to the difference in surficial drainage area and to conserve mass, the subsurface drainage flux (inches per year) must be multiplied by the roof-to-off-vault width ratio (49.5 feet/10 feet = 4.95) to obtain the subsurface inflow flux for the off-vault simulations. Dyer (2019b; Appendix E, Table E-1) includes a tabular summary of the subsurface inflow inputs to Off-Vault Layer 8 for the off-vault simulations.

Table 3-88 lists technical reports relevant to the calculation of infiltration rates for the ILV. Dyer (2019b; Appendix E) provides the HELP model input parameter data sheets for each time step for both the on-vault and off-vault cases. Table 3-89 and Table 3-90 summarize the infiltration rates for the ILV on-vault and off-vault cases, respectively, from the operational period through roof collapse at relative Year 7,100 and beyond.

Included in Table 3-89 and Table 3-90 are the HELP model input (xx.D10), output (xx.OUT), and weather input data (xx.D4, xx.D7, xx.D11, xx.D13) filenames corresponding to each time step. Reported infiltration rates from the HELP model are temporally (annually) and spatially (250-foot total slope length) averaged.

Table 3-88. Technical Reports Relevant to Calculation of Infiltration Rates for Intermediate-Level Vault (Dyer, 2019b; Table 4-1)

Report Number	Authors/Year	Title	Relevance
SRNL-STI-2017-00104, Rev. 0	Dixon (2017)	HELP 4.0 Documentation Updates for Software and Data	HELP model adaptations to run on Windows 10
WSRC-TR-2005-00405, Rev. 0	Jones and Phifer (2007)	E-Area Low-Activity Waste Vault Subsidence Potential and Closure Cap Performance.	Conceptual approach for calculating infiltration rates for the ILV
SRNL-STI-2010-00618, Rev. 0	McDowell-Boyer et al. (2011)	Data Package for HELP Models used in the E-Area Low-Level Waste Facility Performance Assessment	Infiltration rates used in PA2008 for the ILV
SRNL-RP-2009-00075, Rev. 0	Phifer et al. (2009)	Closure Plan for the E-Area Low-Level Waste Facility	Operational and interim closure covers

Table 3-89. Infiltration Rates and HELP Model Input and Output Files for Intermediate-Level Vault: On-Vault Case (Dyer, 2019b; Table 4-2)

Relative Year[1]	Period	HELP Model Input, Output, and Weather Files[2]	PC Directory Location for Execution	Infiltration Rate Reported for Layer[3]	On-Vault Infiltration Rate (inches/year)
-40 to 0	Operational	ILVRF.D10, ILVRF.OUT, ROOFEVAP.D11 [2]	C:\Help4.0\ILV\ILVRF	Removable Metal Roof	0.0
0 to 100	Institutional Control	ILVRF.D10, ILVRF.OUT, ROOFEVAP.D11 [2]	C:\Help4.0\ILV\ILVRF	Concrete Roof	0.0
100	Closure Cap	ILV00.D10, ILV00.OUT	C:\Help4.0\ILV\ILV00	Geomembrane	0.00015
180	Closure Cap	ILV01.D10, ILV01.OUT	C:\Help4.0\ILV\ILV01	Geomembrane	0.0009
290	Closure Cap	ILV02.D10, ILV02.OUT	C:\Help4.0\ILV\ILV02	Geomembrane	0.02
300	Closure Cap	ILV03.D10, ILV03.OUT	C:\Help4.0\ILV\ILV03	Geomembrane	0.022
340	Closure Cap	ILV04.D10, ILV04.OUT	C:\Help4.0\ILV\ILV04	Geomembrane	0.08
380	Closure Cap	ILV05.D10, ILV05.OUT	C:\Help4.0\ILV\ILV05	Geomembrane	0.10
480	Closure Cap	ILV06.D10, ILV06.OUT	C:\Help4.0\ILV\ILV06	Geomembrane	0.41
660	Closure Cap	ILV07.D10, ILV07.OUT	C:\Help4.0\ILV\ILV07	Geomembrane	1.18
1,100	Closure Cap	ILV08.D10, ILV08.OUT	C:\Help4.0\ILV\ILV08	Geomembrane	3.86
1,900	Closure Cap	ILV09.D10, ILV09.OUT	C:\Help4.0\ILV\ILV09	Geomembrane	8.68
2,723	Closure Cap	ILV10.D10, ILV10.OUT	C:\Help4.0\ILV\ILV10	Geomembrane	10.60
2,905	Closure Cap	ILV11.D10, ILV11.OUT	C:\Help4.0\ILV\ILV11	Geomembrane	10.64
3,300	Closure Cap	ILV12.D10, ILV12.OUT	C:\Help4.0\ILV\ILV12	Geomembrane	10.71
5,700	Closure Cap	ILV13.D10, ILV13.OUT	C:\Help4.0\ILV\ILV13	Geomembrane	10.89
7,100	Closure Cap	ILV14.D10, ILV14.OUT	C:\Help4.0\ILV\ILV14	Geomembrane	10.94
7,100+	Roof Collapse	ILVCLPSE.D10, ILVCLPSE.OUT, VCOLEVAP.D11 [2]	C:\Help4.0\ILV\ILVCLPSE	Collapsed Cap	36.85

[1] Year 0: Beginning of IC period. Year 100: End of IC period; installation date of final closure cap.

[2] HELP Weather files are FPREC.D4, FTEMP.D7, FEVAP.D11, and FSOLAR.D13 except where noted in the table.

[3] On-vault infiltration rates for the geomembrane layer represent the volumetric flux of water that will percolate vertically downward to the sloped concrete roof and drain horizontally to the northern roof edge. In HELP model simulations of the intact closure cap, the predicted percolation rate through the concrete slab roof is essentially zero. As a result, 100% of the water that percolates through the geomembrane layer above the ILV will drain to the northern roof edge and becomes an inflow (subsurface run-on) for the off-vault infiltration simulations. When setting the upper boundary condition for the PORFLOW VZ simulations, it is important to consider the conservation of mass because the "Soil Next to Vault Roof" off-vault infiltration rates reported in Table 3-90 include the on-vault geomembrane drainage flux.

Table 3-90. Infiltration Rates and HELP Model Input and Output Files for Intermediate-Level Vault: Off-Vault Case (Dyer, 2019b; Table 4-3)

Relative Year[1]	Period	HELP Model Input, Output, and Weather Files[2]	PC Directory Location for Execution	Infiltration Rate Reported for Layer[3]	Off-Vault Infiltration Rate (inches/year)
-40 to 0	Operational	ILVOP.D10, ILVOP.OUT, VCOLEVAP.D11 [2]	C:\Help4.0\ILVOFF\ILVOP	Off-Vault Ground Surface	16.17
0 to 100	Institutional Control	ILVIC.D10, ILVIC.OUT, VCOLEVAP.D11 [2]	C:\Help4.0\ILVOFF\ILVIC	Off-Vault Ground Surface	16.17
100	Closure Cap	ILV00.D10, ILV00.OUT	C:\Help4.0\ILVOFF\ILV00	Geomembrane	0.00015
				Soil Next to Vault Roof	0.00085
180	Closure Cap	ILV01.D10, ILV01.OUT	C:\Help4.0\ILVOFF\ILV01	Geomembrane	0.0009
				Soil Next to Vault Roof	0.0053
290	Closure Cap	ILV02.D10, ILV02.OUT	C:\Help4.0\ILVOFF\ILV02	Geomembrane	0.02
				Soil Next to Vault Roof	0.11
300	Closure Cap	ILV03.D10, ILV03.OUT	C:\Help4.0\ILVOFF\ILV03	Geomembrane	0.02
				Soil Next to Vault Roof	0.12
340	Closure Cap	ILV04.D10, ILV04.OUT	C:\Help4.0\ILVOFF\ILV04	Geomembrane	0.08
				Soil Next to Vault Roof	0.48
380	Closure Cap	ILV05.D10, ILV05.OUT	C:\Help4.0\ILVOFF\ILV05	Geomembrane	0.10
				Soil Next to Vault Roof	0.59
480	Closure Cap	ILV06.D10, ILV06.OUT	C:\Help4.0\ILVOFF\ILV06	Geomembrane	0.41
				Soil Next to Vault Roof	2.38
660	Closure Cap	ILV07.D10, ILV07.OUT	C:\Help4.0\ILVOFF\ILV07	Geomembrane	1.18
				Soil Next to Vault Roof	6.96
1,100	Closure Cap	ILV08.D10, ILV08.OUT	C:\Help4.0\ILVOFF\ILV08	Geomembrane	3.86
				Soil Next to Vault Roof	22.86
1,900	Closure Cap	ILV09.D10, ILV09.OUT	C:\Help4.0\ILVOFF\ILV09	Geomembrane	8.68
				Soil Next to Vault Roof	51.52
2,723	Closure Cap	ILV10.D10, ILV10.OUT	C:\Help4.0\ILVOFF\ILV10	Geomembrane	10.60
				Soil Next to Vault Roof	62.91
2,905	Closure Cap	ILV11.D10, ILV11.OUT	C:\Help4.0\ILVOFF\ILV11	Geomembrane	10.64
				Soil Next to Vault Roof	63.16
3,300	Closure Cap	ILV12.D10, ILV12.OUT	C:\Help4.0\ILVOFF\ILV12	Geomembrane	10.71
				Soil Next to Vault Roof	63.59
5,700	Closure Cap	ILV13.D10, ILV13.OUT	C:\Help4.0\ILVOFF\ILV13	Geomembrane	10.89
				Soil Next to Vault Roof	64.66
7,100	Closure Cap	ILV14.D10, ILV14.OUT	C:\Help4.0\ILVOFF\ILV14	Geomembrane	10.94
				Soil Next to Vault Roof	64.93
7,100+	Roof Collapse	ILVCLPSE.D10, ILVCLPSE.OUT	C:\Help4.0\ILVOFF\ILVCLPSE	Geomembrane	10.94
				Soil Next to Vault Roof	10.93 [4]

Notes:

1 Year 0: Beginning of IC period. Year 100: End of IC period; installation date of final closure cap.

2 HELP Weather files are FPREC.D4, FTEMP.D7, FEVAP.D11, and FSOLAR.D13 except where noted in the table.

3 For the off-vault case, vertical infiltration rates are reported at two elevations: the cap geomembrane layer above and the soil backfill layer below at the same elevation as the outside edge of the sloped concrete roof. When setting the upper boundary condition for the PORFLOW VZ simulations, it is important to consider the conservation of mass because the “Soil Next to Vault Roof” off-vault infiltration rates reported above include the on-vault “Geomembrane” drainage flux. In addition, HELP model simulations of the intact closure cap predict that the percolation rate through the concrete slab roof is essentially zero. If PORFLOW simulations of the LAWV assume nonzero leakage through cracks in the concrete roof, then the “Soil Next to Vault Roof” infiltration rates at each time step will need to be lowered by (62 feet ÷ 10 feet) x (concrete slab leakage flux in inches/year).

4 The off-vault infiltration rate through the backfill soil adjacent to the vault roof decreases significantly after roof collapse because there is no longer any on-vault lateral drainage (subsurface run-on) from the sloped concrete roof.

3.8.4.6. Naval Reactor Component Disposal Areas

As introduced in Section 2.2.7, reactor components from the U.S. Navy have been disposed in two areas associated with the ELLWF: the currently operating at-grade gravel disposal pad (NR26E) located inside the original 100-acre ELLWF, and the operationally closed at-grade gravel disposal pad (NR07E) located in the old burial ground adjacent to the ELLWF. Figure 2-78 shows the layout of the two NRCDAs relative to other ELLWF DUs.

NR waste consists of (1) highly radioactive components within thick-walled, welded, carbon-steel casks and (2) auxiliary equipment at low-activity levels within thinner-walled, bolted, gasket-sealed, steel containers. No additional operational closure or interim closure beyond simply placing containers on the NRCDA pads is necessary due to the water- and air-tight nature of the casks and bolted containers. However, if radiation shielding is required for personnel protection during the operational or IC period, the casks may be surrounded with a structurally suitable material that will be capable of supporting the final closure cap without resulting in differential subsidence at the time the cap is installed.

Final closure of the NRCDAs will take place during final closure of the entire ELLWF at the end of the 100-year IC period. Before final closure, the space around, between, and over the casks will be filled with a structurally suitable material that will support the final closure cap without resulting in differential subsidence. Dynamic compaction of the NRCDAs will not be conducted. Final closure will consist of installation of an integrated multilayer soil-geomembrane closure cap designed to minimize moisture contact with the waste and to provide an IHI deterrent.

Because the NRCDA casks and containers will be assumed to maintain their structural integrity throughout the operational, IC, and final closure cap periods, an intact infiltration scenario will always apply (i.e., no cap subsidence). The NR26E pad will be covered by the main ELLWF final closure cap. The slope and maximum slope length above the NR26E pad are 2% and approximately 200 feet, respectively. The NR07E pad will require an individual final closure cap as discussed in Section 2.2.2.9.4 and shown schematically in Figure 2-55. Like the main closure cap design, specifications for the NR07E closure cap will include a slope ranging from 2% to 5% and a maximum slope length of 585 feet. The actual slope length will be substantially shorter.

For simplicity and consistency, the upper-bound intact infiltration scenario for ST and ETs (Section 3.8.4.3.2) will be used for the NRCDA pads as well. The only difference in infiltration rates for the NRCDAs versus ST and ETs occurs during the IC period because an HDPE interim cover will not be placed over the structural fill surrounding the NRCDAs. Table 3-91 summarizes the infiltration rates for the NRCDAs from the operational period through Year 10,100 and beyond.

Table 3-91. Intact Infiltration Rates and HELP Input and Output Files for Naval Reactor Component Disposal Areas (Dyer, 2019b; Table 6-2)

Relative Year[1]	Cover Type	HELP Model Input, Output, and Weather Files[2]	PC Directory Location for Execution	Infiltration Rate (inches/year)
-30 to 0	Structural Soil Fill	ST_OpCover.D10, ST_OpCover.OUT	C:\Help4.0\SLIT_OpCover\ST_OpCover	15.78
0 to 100	Structural Soil Fill	ST_OpCover.D10, ST_OpCover.OUT	C:\Help4.0\SLIT_OpCover\ST_OpCover	15.78
100	Closure Cap	ST00.D10, ST00.OUT	C:\Help4.0\STET_INTACT\ST00	0.0008
180	Closure Cap	ST01.D10, ST01.OUT	C:\Help4.0\STET_INTACT\ST01	0.007
290	Closure Cap	ST02.D10, ST02.OUT	C:\Help4.0\STET_INTACT\ST02	0.16
300	Closure Cap	ST03.D10, ST03.OUT	C:\Help4.0\STET_INTACT\ST03	0.18
340	Closure Cap	ST04.D10, ST04.OUT	C:\Help4.0\STET_INTACT\ST04	0.30
380	Closure Cap	ST05.D10, ST05.OUT	C:\Help4.0\STET_INTACT\ST05	0.38
480	Closure Cap	ST06.D10, ST06.OUT	C:\Help4.0\STET_INTACT\ST06	1.39
660	Closure Cap	ST07.D10, ST07.OUT	C:\Help4.0\STET_INTACT\ST07	3.23
1,100	Closure Cap	ST08.D10, ST08.OUT	C:\Help4.0\STET_INTACT\ST08	6.82
1,900	Closure Cap	ST09.D10, ST09.OUT	C:\Help4.0\STET_INTACT\ST09	10.24
2,723	Closure Cap	ST10.D10, ST10.OUT	C:\Help4.0\STET_INTACT\ST10	11.10
3,300	Closure Cap	ST11.D10, ST11.OUT	C:\Help4.0\STET_INTACT\ST11	11.18
5,700	Closure Cap	ST12.D10, ST12.OUT	C:\Help4.0\STET_INTACT\ST12	11.30
10,100	Closure Cap	ST13.D10, ST13.OUT	C:\Help4.0\STET_INTACT\ST13	11.35

Notes:

[1] Year 0: Beginning of IC period. Year 100: End of IC period; installation date of final closure cap. An HDPE cover is not used during the IC period for NRCDAs. Instead, a soil structural fill is placed around and over the disposal pads for radiation shielding.

[2] HELP Weather files are FPREC.D4, FTEMP.D7, FEVAP.D11, and FSOLAR.D13 except where noted in the table.

3.8.5. Hydrostratigraphic Surfaces

The *Hydrostratigraphic Surfaces Data Package* refers to the SRNL-compiled and -maintained Microsoft Excel database of hydrostratigraphic data for E-Area at SRS entitled "Change Control Rev1 and Rev0 dataset (Appendix 5 to SRNL-STI-2017-00301).xlsx," dated 11/03/2017 (SRNL, 2017). The technical report detailing the development and content of the *Hydrostratigraphic Surfaces Data Package* is "Elevation of Water Table and Various Stratigraphic Surfaces Beneath E-Area Low Level Waste Disposal Facility" by Bagwell and Bennett (2017). The data source for the Microsoft Excel database is Appendix 5 in the report by Bagwell and Bennett (2017).

Meanwhile, "General Separations Area (GSA) Groundwater Flow Model Update: Hydrostratigraphic Data" by Bagwell et al. (2017) documents the activity to update and calibrate the GSA GW flow model utilizing the most up-to-date hydrogeologic data from the 2017 *Hydrostratigraphic Surfaces Data Package*. As described in more detail in Section 3.5.2, the hydrogeologic data in the existing GSA flow model were reviewed, new borehole data were interpreted, and a new larger dataset was created to support the model. This activity improved the resolution of the GSA flow model by adding more than 200 new borehole control points and more than 600 new hydrostratigraphic interpretations ("picks") to the model dataset.

Bagwell and Bennett (2017) developed four subsurface elevation models for the ELLWF:

1. Water table
2. Lower Aquifer Zone (LAZ) of the Upper Three Runs Aquifer (UTRA)
3. Tan Clay Confining Zone (TCCZ)
4. Tobacco Road Sand (TRS); interpreted as the boundary between UVZ and LVZ

From each model, elevation data were extracted at the vertices and centroids of individual ELLWF DUs. At these same vertices and centroids, ground surface elevations were extracted from the SRS LiDAR[42] raster (collected 2009). At each vertex and centroid, the elevations of the four subsurface locations were subtracted from the ground elevation to yield depth measurements. The model area is defined by a 100-meter spatial buffer around the ELLWF (Figure 1-2); this area includes multiple existing and future individual DUs (Figure 2-30).

3.8.5.1. Subsurface Zones of Interest

Beneath E-Area, the relationship between the water table and various stratigraphic units is locally complex and is affected by sediment properties (hydraulic conductivity), by seasonal and long-term precipitation (recharge), and by proximity to Upper Three Runs Creek to the north of the model area. Figure 3-21 illustrates this complexity, as well as the subsurface units – water table, LAZ, TCCZ, and TRS – for which elevation models were prepared.

3.8.5.2. Modeling, Extraction, and Mathematical Processes

All existing control points (elevations) for the four subsurface units of interest were assembled into discrete datasets. The water table dataset included mean water levels from 99 monitoring wells during the period 2004-2014 (Hiergesell et al., 2015); to this dataset, 20 additional control points along Upper Three Runs Creek and its tributaries (all gaining streams) were added to improve spatial resolution in the northern part of the model area. Control points for the LAZ, TCCZ, and TRS included 716 stratigraphic "picks" (interpretations) based on core descriptions and borehole geophysical logs (Bagwell et al., 2017; Smits et al., 1997; SRS GDMS, 2017). The number of controls points for each subsurface was: LAZ = 218; TCCZ = 233; TRS = 265.

Control points were loaded into *ArcMap 10.4* and individual elevation models (interpolation rasters) were constructed using the *Exponential with Nugget* algorithm available with the *ArcToolbox/Spatial Analyst/Interpolation/Kriging* tool. Figure 3-133 through Figure 3-136 show the elevation models and control points for the water table, LAZ, TCCZ, and TRS, respectively. Appendices 1, 2, 3, and 4 in the *Hydrostratigraphic Surfaces Data Package* report (Bagwell and Bennett, 2017) include the control points for the water table, LAZ, TCCZ, and TRS models, respectively; model settings, variograms, etc. are included with each appendix in the data package report.

[42] LiDAR, which stands for Light Detection and Ranging, is a remote sensing method that uses light in the form of a pulsed laser to measure ranges (variable distances) to the Earth.

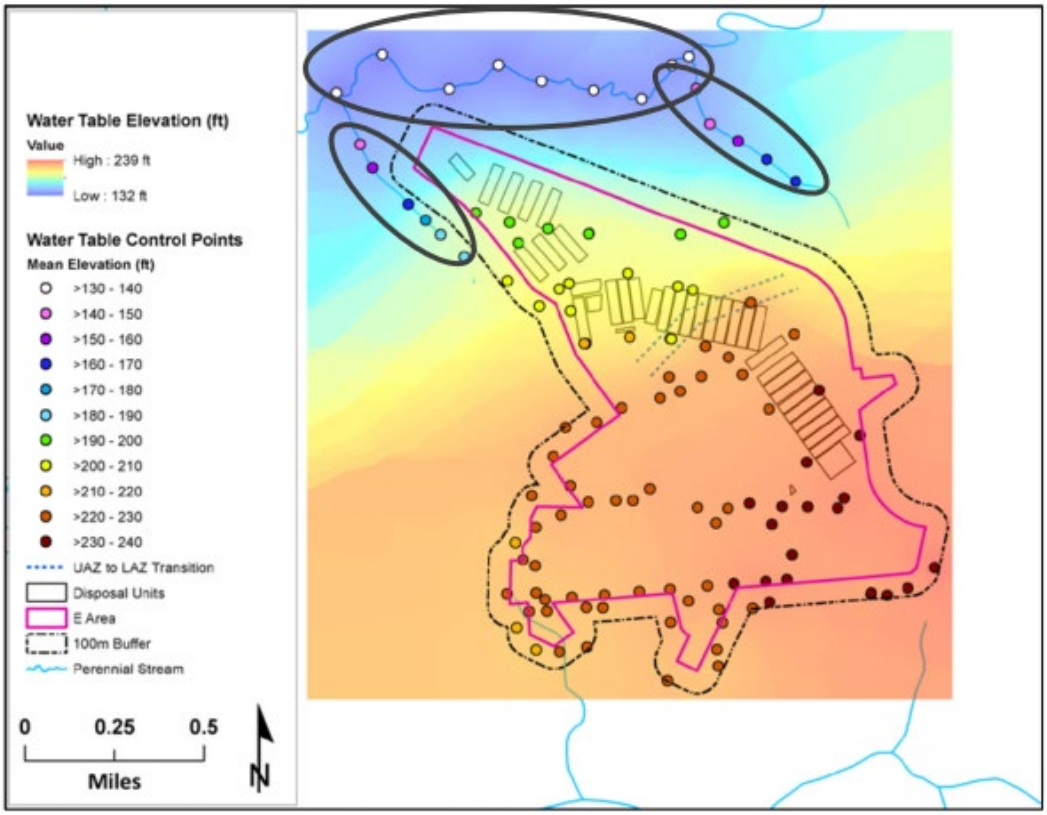

Figure 3-133. Elevation Model and Control Points for Water Table (Large Ovals Indicate Control Points Added Along Perennial Streams)

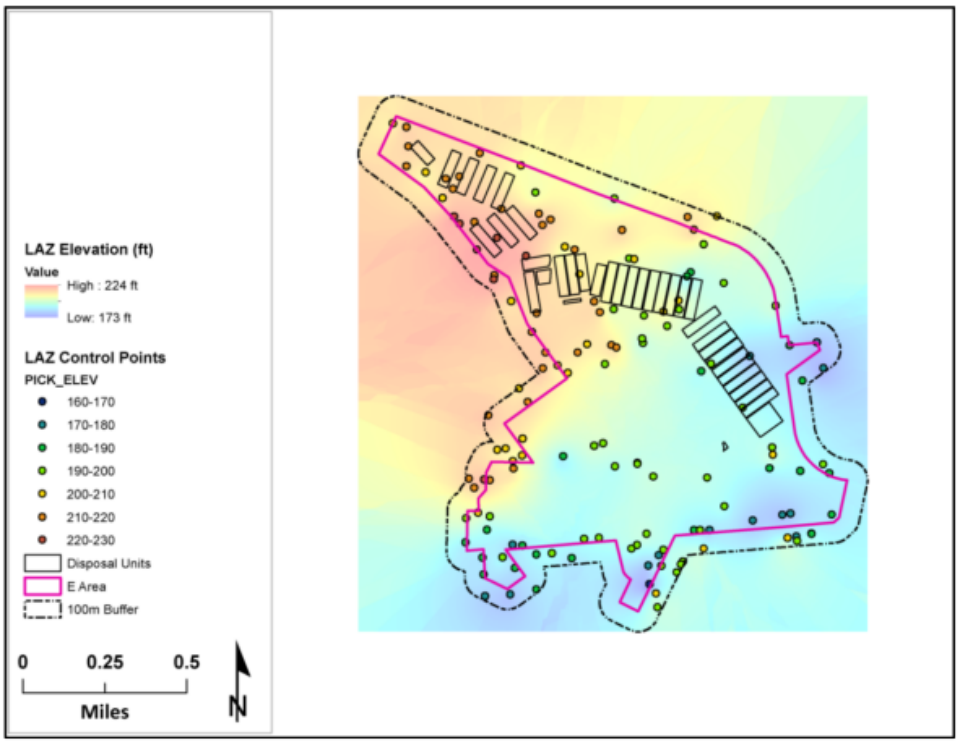

Figure 3-134. Elevation Model and Control Points for Lower Aquifer Zone

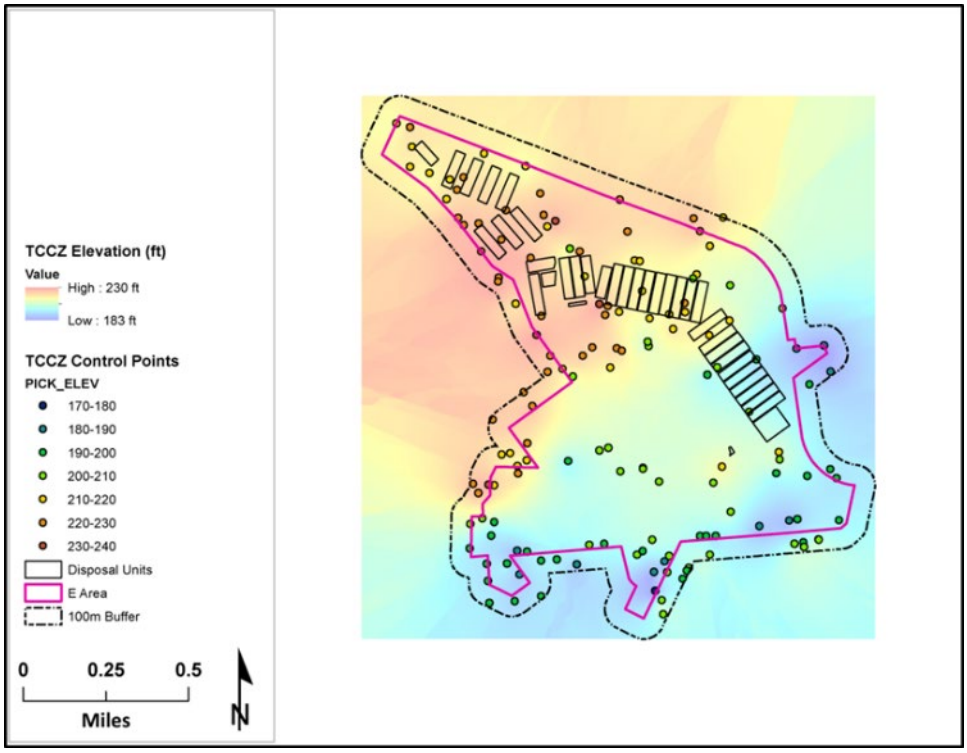

Figure 3-135. Elevation Model and Control Points for Tan Clay Confining Zone

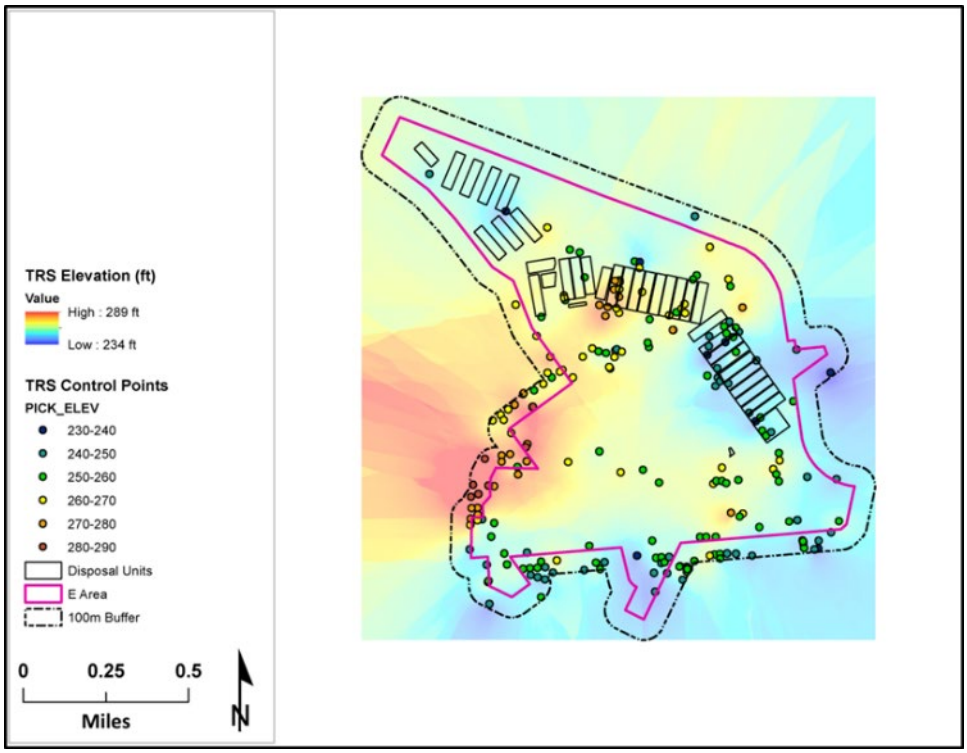

Figure 3-136. Elevation Model and Control Points for Tobacco Road Sand

Applying the *ArcToolbox/Spatial Analyst/Extraction/Extract Values to Points* tool to each of the four elevation models, the elevation values at the vertices and centroids of the 37 DUs were extracted. Figure 3-137 illustrates the modeling and extraction processes. At each vertex and centroid, the elevations of the four subsurfaces were subtracted from the ground elevation (SRS LiDAR) to yield depth measurements. Appendix 5 in the *Hydrostratigraphic Surfaces Data Package* report (Bagwell and Bennett, 2017) presents the results of the extractions and subtractions.

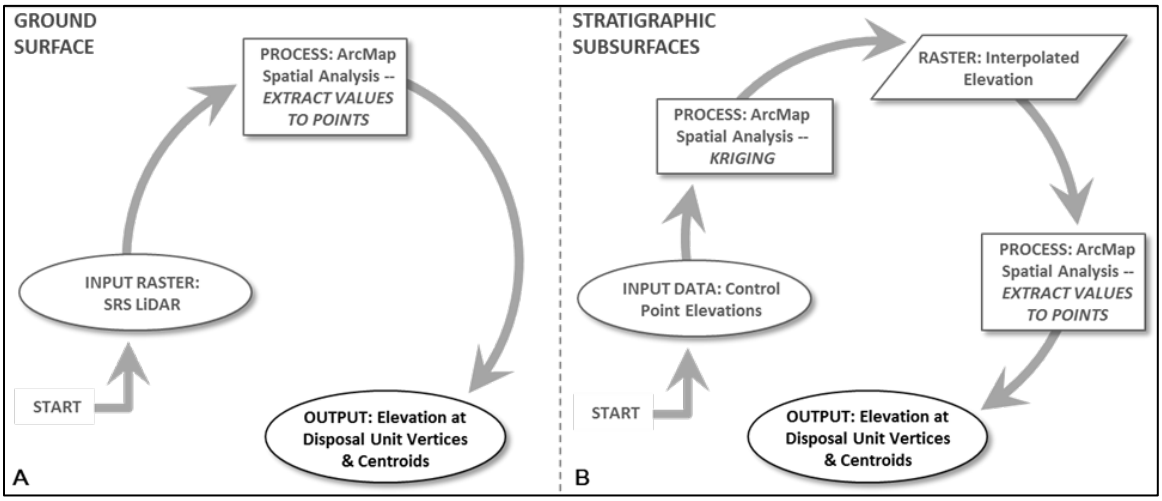

Figure 3-137. Process for Determining Elevations of (A) Ground Surface and (B) Stratigraphic Subsurfaces (Water Table, LAZ, TCCZ, and TRS) at Vertices and Centroids of Disposal Units

3.8.5.3. Observations and Notes on Elevation Models

The utility of interpolation rasters depends on – and is limited by – the number, density, and accuracy of control points, and on the method and settings of interpolation. In the case of geologic elevation models, understanding these limitations is especially important.

3.8.5.4. Tobacco Road Sand

Additional spatial analysis of the TRS elevation raster illustrates a noteworthy caveat on its use, specifically its prediction beyond the actual outcrop extent. Figure 3-138A shows the geographic extent of the TRS raster, encompassing a rectangular region that includes the entire model area.[43] Figure 3-138B shows the effect of truncating the TRS raster to the SRS LiDAR (ground elevation) raster, effectively removing all regions where the TRS has been eroded. The legitimacy of this truncation can be confirmed by comparing the truncated TRS raster with the outcrop geology map (SCGS, 2008). Figure 3-139 illustrates the general agreement between the mapped outcrop extent of the TRS (and overlying formations) and the truncated TRS raster.

[43] The data illustrated in Figure 3-138A correspond to the data in column "TRS elevation (ft) from kriged dataset" in Appendix 5 of the *Hydrostratigraphic Surfaces Data Package* report (Bagwell and Bennett, 2017).

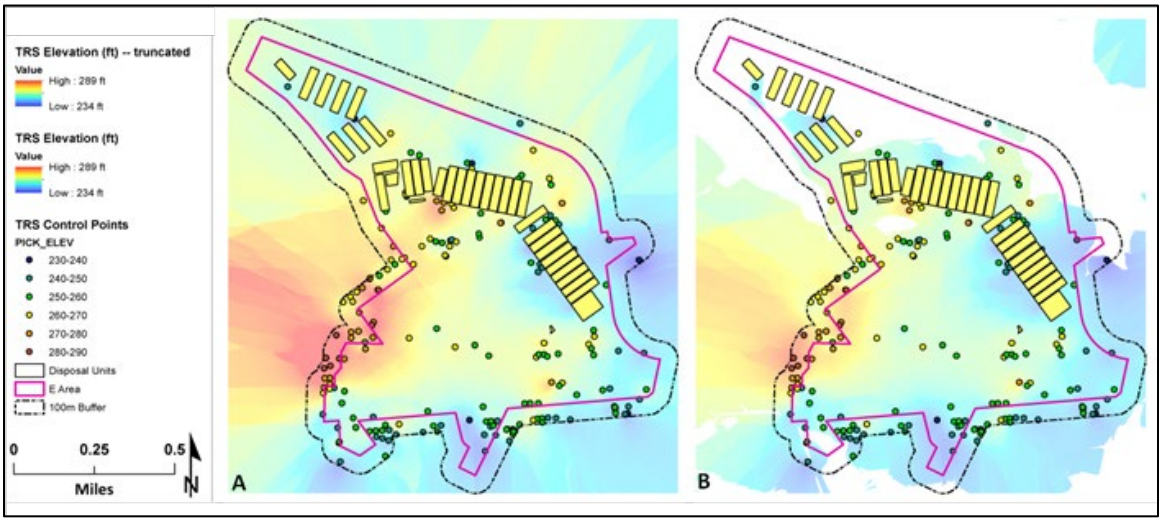

Figure 3-138. Elevation Model for Tobacco Road Sand Without (A) and With (B) Truncation to Ground Surface

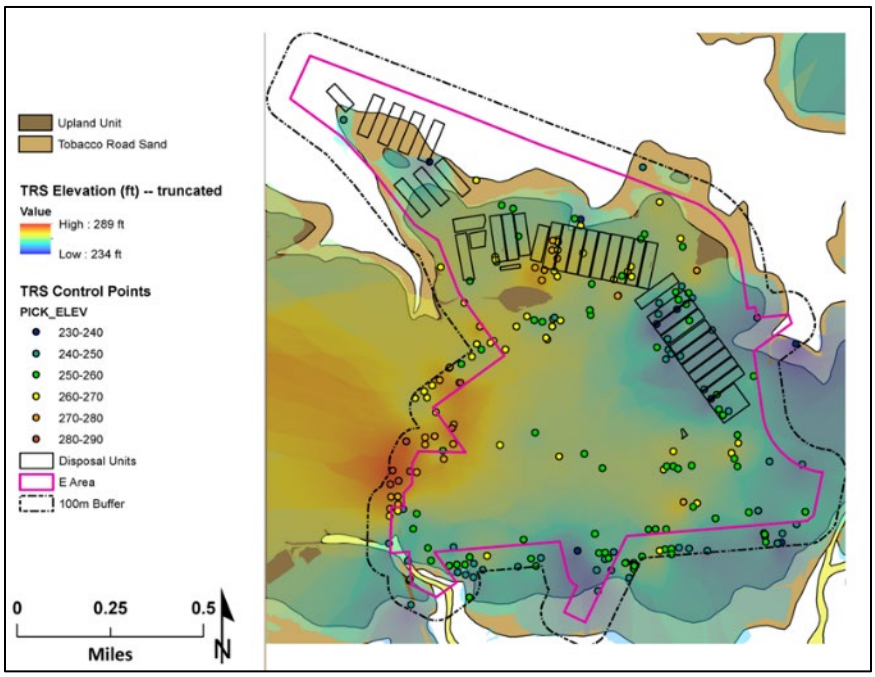

Figure 3-139. Tobacco Road Sand – Truncated Elevation Model Compared With Mapped Outcrop Extent

3.9. MODELING TOOLS

A variety of commercial, public-domain, and SRNL-developed computational models are employed in the PA to perform both deterministic and stochastic calculations for closure cap infiltration, vadose- and saturated-zone flow and transport, gas-phase diffusion and air transport, radiological dose, and model parameter sensitivity and uncertainty for the purpose of demonstrating compliance with POs and risk evaluations. This section provides a brief description of each of the major modeling tools. The relevant SQAPs and software classification documents (SWCDs) are described in Chapter 10.

3.9.1. PORFLOW

PORFLOW is a commercial software package developed by Analytic & Computational Research, Inc. (ACRi, 2018). It is a comprehensive mathematical model for simulating multiphase fluid flow, heat transfer, and mass transport in variably saturated porous and fractured media. PORFLOW can simulate transient or steady-state problems in Cartesian or cylindrical geometry. The porous medium may be anisotropic and heterogeneous and may contain discrete fractures or boreholes within the porous matrix. The theoretical models within the code provide a unified treatment of concepts relevant to fluid flow and transport.

PORFLOW is used widely at SRS with applications related to solid waste disposal (e.g., Saltstone Disposal Facility, ELLWF), high-level waste tank closures, and D&D. The results of the PORFLOW simulations form a basis of support for analyses that are used to ensure compliance with DOE Orders and environmental regulations. The main features of PORFLOW that are relevant to PA modeling include variably saturated flow and transport of parent and progeny radionuclides. The current version of the software used for the ELLWF PA is PORFLOW Ver. 6.43.0. PORFLOW has been employed at SRNL for more than two decades and several of the key PORFLOW commands and features were created by ACRi under SRNL's direction. Examples include the STAT command used in locating and storing maximum concentrations at and beyond the POA and the four-parameter aquifer dispersion model extracted from the SRNL-developed FACT code (Hamm and Aleman, 2000).

PORFLOW software used for GW and contaminant transport analyses in the ELLWF PA is classified as Level C (Butcher, 2013b) that can operate on either Microsoft Windows or Linux. The SQAP and associated software test plan were prepared by Hang (2007) and Hang (2012), respectively. According to Hang (2012), SRNL created a set of PORFLOW verification test cases that are relevant to PA modeling at SRS. The test cases comprise problems that include variably saturated GW flow and transport of parent and progeny radionuclides in the vadose and aquifer zones underlying the SRS. The PORFLOW Testing and Verification Document by Whiteside (2020) for Version 6.43.0 provides detailed discussions of the test cases and how they were compared to closed-form analytical solutions as well as to results from other well-recognized computer programs.

Several pre- and post-processing applications are used in support of PORFLOW model development and simulations. They include:

- **MESH3D Ver. 3.1** (Butcher, 2018b; Danielson, 2017): The aquifer transport analysis is based on the advective mass flux and saturation fields produced by the GSA regional GW flow model. Although the GSA flow field can be used directly for PORFLOW aquifer transport simulations, typical practice at SRNL is to use flow information defined on a localized grid of smaller extent but higher resolution using the Aquifer Model Refinement Tool, MESH3D. MESH3D Ver. 3.1 extracts a subregion of the GSA coarse mesh and subdivides the coarse mesh to produce a higher-resolution grid. MESH3D Ver 3.1 also transfers advective mass flux , velocity, and saturation data from the original GSA grid to the refined mesh through an interpolation process.

- **MESH2D Ver. 2** (Butcher, 2017b; Hang, 2017b): Mesh2D is a Fortran 90 program developed by SRNL (Flach, 2017b) to generate 2-D structured grids of the form [*x(i),y(i,j)*], where [*x,y*] are grid coordinates identified by indices (*i,j*). The *x(i)* coordinates alone can be used to specify a 1-D grid. The software has been used to support SRS PAs and SAs and is a component of the Cementitious Barriers Partnership Software Toolbox.
- **PEST Ver. 13.6** (Butcher, 2016; Whiteside, 2016b): PEST (Parameter ESTimation), developed by Watermark Numerical Computing, expedites the process of model calibration wherein values for model parameters are back-calculated by matching model outputs to measurements of system state. "Parameters" used within a model can represent the properties of the materials in which the processes simulated by the model take place, the stresses which initiate and support those processes, or both. PEST uses a model control file to input parameter values to a model (e.g., PORFLOW), run the model, parse the output, compare the results to previous runs, and continue running the model until the parameter values stabilize or the limit to the number of model runs is reached. PEST operates in a model-independent manner. For example, it interacts with a PORFLOW model through PORFLOW's own input and output files.
- **PlotConc Ver. 1** (Butcher, 2017e; Hang, 2017c): PlotConc is a Fortran 90 program developed by SRNL to extract concentrations from a PORFLOW archive file for a 2-D transport simulation and create a Tecplot data file to support PA- and SA-related work.
- **PlotConc3d Ver. 1** (Butcher, 2017c; Hang, 2017d): PlotConc3d is a Fortran 90 program developed by SRNL to extract concentrations from a PORFLOW archive file for a 3-D structured-grid transport simulation and create a Tecplot data file to support PA- and SA-related work.
- **PlotConc3dU Ver. 1** (Butcher, 2017d; Hang, 2017e): PlotConc3dU is a Fortran 90 program developed by SRNL to extract concentrations from a PORFLOW archive file for a 3-D unstructured-grid transport simulation and create a Tecplot data file to support PA- and SA-related work.
- **PlotFlux Ver. 1** (Butcher, 2018c; Hang, 2018b): PlotFlux is a Fortran 90 program developed by SRNL to extract information from a PORFLOW flux file and create PORFLOW and Tecplot data files.
- **PlotFlow2d Ver. 1** (Butcher, 2017f; Hang, 2017f): PlotFlow2d is a Fortran 90 program developed by SRNL to extract information from a PORFLOW archive file for a 2-D structured-grid flow simulation and create a Tecplot data file to support PA- and SA-related work.
- **PlotFlow3dS Ver. 1** (Hang, 2021a; 2021b): PlotFlow3dS is a Fortran 90 program developed by SRNL to extract information from a PORFLOW archive file for a 3-D structured-grid flow simulation and create a Tecplot data file to support PA- and SA-related work.
- **PlotHist Ver. 1** (Butcher, 2018d; Hang, 2018c): PlotHist is a Fortran 90 program developed by SRNL to extract information from a PORFLOW history file and create a Tecplot data file to support PA- and SA-related work.

- **PlotStat Ver. 1** (Butcher, 2018e; Hang, 2018d): PlotStat is a Fortran 90 program developed by SRNL to extract information from a PORFLOW statistics file and create Tecplot data file to support PA- and SA-related work.
- **MakeWhole Ver. 1** (Butcher, 2018a; Hang, 2018a): MakeWhole is a Fortran 90 program designed to insert "Include" file contents into the main data file to support PA- and SA-related work. “Include” is a command used to include a file at run time in the main data stream.
- **avgVal Ver. 1** (Butcher, 2017a; Hang, 2017a): avgVal is a Fortran 90 program developed by SRNL to find the average value of a piecewise linear function over an interval to support PA- and SA-related work.
- **GoldSimFlows Ver. 2** (Butcher, 2013a; Flach and Butcher, 2013): GoldSimFlows is a Fortran 90 program developed by SRNL to extract flow field data from a series of steady-state 2-D PORFLOW simulations for selected regions in the model domain and writes the data to a tab-delimited spreadsheet-type file.

3.9.2. GoldSim® Monte Carlo Simulation Software

GoldSim® is a graphical, object-oriented, Windows-based commercial software package for conducting dynamic, probabilistic simulations of complex systems to facilitate decision-making (GoldSim Technology Group, 2018a). The software can also function in a deterministic mode as might be needed in PAs for dose-receptor calculations or deterministic sensitivity analyses. GoldSim® functions as a "visual spreadsheet” by allowing the user to visually create and manipulate data and equations in large, complex models comprised of different input, function, stock and delay, and linking objects or *elements*. Depending on how the selected elements in the model relate to each other, GoldSim® automatically indicates their influences and interdependencies by visually connecting them in an appropriate way. GoldSim® also sets up and solves the equations represented by the elements and their interdependencies. The following features make GoldSim® an attractive tool for PA work (GoldSim Technology Group, 2018a):

- A system model can be constructed in a hierarchical, modular manner, allowing the model to evolve and for detail to be added as system knowledge grows. Graphics, explanatory text, notes, and hyperlinks can be included to document design bases, assumptions, data sources, and model revisions for current and future users.
- The uncertainty inherent in processes, parameters, and future events in natural and engineered systems can be addressed quantitatively in a computationally efficient manner.
- Dimensional consistency is ensured throughout the model; all unit conversions are handled internally using the extensive internal database of units and conversion factors. Custom units can also be defined by the user.
- External programs or spreadsheets, such as physical and geochemical properties databases, can be dynamically linked to the GoldSim® system model. In addition, customized modules (program extensions) can be added, including the GoldSim® Contaminant Transport Module (GoldSim Technology Group, 2018b) which is used in the ELLWF PA System Model.

- Lastly, the software has the capability to manipulate arrays, "localize" parts of a model, and assign version numbers to models undergoing frequent modifications.

While the main GoldSim® model framework is quite generic, the Contaminant Transport Module is specifically designed to model the release of mass from specified sources as well as the transport of mass through multiple transport pathways within an environmental system (e.g., aquifer, stream, lake, atmosphere, soil pore space). Output from the Contaminant Transport Module includes predicted masses and mass transfer rates at specific locations within the system as well as predicted concentrations within environmental media (e.g., air, water, soil) throughout the system (GoldSim Technology Group, 2018b). Simulated transport mechanisms include advection via fluids and solids, diffusion through fluids, diffusion across interfaces (e.g., air-water), and advection and diffusion of contaminated suspended particles in fluids. In addition, solubility constraints, contaminant partitioning, chemical reactions, and decay processes, all of which are required for ELLWF PA simulations, can be included in the system model.

For this PA, GoldSim® Ver. 12.1.4 #235 (October 22, 2019) (GoldSim Technology Group, 2018a) is employed for two purposes:

1. **Trench System Model:** The GoldSim® Trench System Model (Section 3.5.4) simulates the release and mass transport of current and future radiological inventory disposed in STs and ETs,[44] and was developed to perform the sensitivity and uncertainty analyses required by DOE M 435.1-1, Chg. 3 (U.S. DOE, 2021b). The simplified Trench System Model is calibrated to the corresponding 3-D PORFLOW flow and transport models for selected STs and ETs to ensure confidence in the stochastic results.
2. **Atmospheric Release Model:** The ARM (Section 3.6.1) is designed to conduct the air and radon pathways analyses for all types of DUs for the ELLWF PA. The 1-D GoldSim® model evaluates the flux of gaseous radionuclides as they volatilize from ELLWF DU waste zones, diffuse across the water-air interface into the partially water-saturated, air-filled soil pores surrounding the waste, and emanate at the land surface.

A general user's manual for the GoldSim® software is provided by GoldSim Technology Group (2018a). A separate user's guide is available for the Contaminant Transport Module (GoldSim Technology Group, 2018b). GoldSim® is classified as Quality Assurance "Level C" software on the basis that it is commercially available software used to comply with regulatory laws, environmental permits or regulations and/or commitments to compliance (Wohlwend, 2021a). The SQAP was prepared by Wohlwend (2021b). Verification testing for GoldSim® Ver. 12.1.4 #235 (October 22, 2019) was performed as outlined in the SQAP.

[44] Sensitivity analyses for the LAWV, ILV, and NRCDAs are performed using the PORFLOW VZ and aquifer models developed for these DUs due to the added complexities associated with the concrete and steel barriers.

3.9.3. Savannah River National Laboratory Dose Toolkit

The SRNL Dose Toolkit was developed by Aleman (2019) to calculate GW and IHI disposal limits and GW and IHI (PA) and surface water (CA) dose impacts for PAs, CAs, UDQEs, UCAQEs and SAs. The Toolkit consists of three Fortran programs (*PreDose* module, *PreDose Maximum Concentration* module, and *SRNL PA/CA Limits and Doses Tool*) that serve as modules/tools to implement the latest dose methodology and data contained in "Dose Calculation Methodology and Data for Solid Waste Performance Assessment and Composite Analysis at the Savannah River Site" by Smith et al. (2019). First, GW modeling calculations are performed by PORFLOW to establish VZ and aquifer zone flow fields. Second, contaminant transport calculations are completed using PORFLOW (or GoldSim®) for both the VZ and aquifer zone to generate concentration history profiles for each parent and short-chain progeny radionuclide at and beyond the 100-meter POA boundary. Third, the *PreDose* module takes the concentration history profiles from PORFLOW (or GoldSim®) and expands the short-chain radionuclide decay chain results to produce full decay chain results based on the assumption of secular equilibrium. The *PreDose* output is written as binary files (e.g., Am-241.bin) for each existing/future inventory and PORFLOW VZ case scenario analyzed. Fourth, the *PreDose* module output is input to the *SRNL PreDose Maximum Concentration* module to generate composite 'worst-case' full-chain concentration history profiles for each existing/future inventory scenario. Fifth, the 'worst-case' binary files are input to the *SRNL PA/CA Limits and Doses Tool* which generates a series of binary concentration and dose files for each GW pathway where contributions from each full-chain progeny have been rolled up to the parent nuclide (e.g., Am-241-GWPA.his). The *.his files are on a "per Ci of parent buried" basis.

A user's guide for the SRNL Dose Toolkit is provided by Aleman (2019). The SRNL Dose Toolkit is classified as QA "Level C" software on the basis that it is used to comply with regulatory laws, environmental permits or regulations, and/or commitments to compliance (Aleman, 2021b). The SQAP was prepared by Aleman (2021a). Verification testing for the SRNL Dose Toolkit was performed as outlined in the SQAP.

3.9.3.1. PreDose Module

The *PreDose* module post-processes simulated concentration time series for select parent nuclides with short-chain or full-chain progeny for the PA GW and IHI screening and tiered limits and doses approach. The output of this module is input to the *PreDose Maximum Concentration* module or the *PA/CA Limits and Doses Tool*.

- **Tier 1** screening based on the method outlined in NCRP-123 (NCRP, 1996) using full chains for all 1252 radionuclides listed in the *SRNL Radionuclide, Element and Dose Parameter Data Package* (SRNL, 2019b) and site-specific K_d values. This new screening tool does not exist in this module.
- **Tier 2** is a bounding CA approach (1-D VZ and aquifer zone flow and transport) to compute concentrations at the 100-meter POA boundary for each parent nuclide with short-chain progeny remaining after Tier 1 screening. This approach can be used in a PA, if needed, to further screen out additional radionuclides before the detailed analysis (Tier 3 and 4).

- **Tier 3** analyzes generic waste forms (Tier 2 screened parents with no engineered barriers) modeled using PORFLOW 2-D VZ and 3-D aquifer flow and transport models. Each PORFLOW aquifer transport simulation computes a maximum element (STAT) or multiple element (HISTORY) concentration time series for parent radionuclides and short-chain progeny at or beyond the POA boundary.
- **Tier 4** analyzes special waste forms (same parent list and calculation procedure as Tier 3 but waste release is controlled by encapsulation or special waste form properties).

An additional option analyzes generic or special waste forms modeled using GoldSim® VZ and aquifer transport models. Deterministic or Monte Carlo GoldSim® transport simulations compute maximum aquifer concentration time series for parent nuclides and short-chain progeny at each POA boundary. Monte Carlo realizations of GoldSim® transport simulations provide maximum aquifer concentration time series at user-defined percentile ranks (e.g., 5%, 25%, 50%, 75%, 95%).

The PORFLOW parent and short-chain progeny concentrations are typically in units of gmol/ft^3 or gmol/ft^3 per one gmole of parent buried for existing or future inventory, respectively. The short-chain concentrations are converted into short-chain activities (pCi L^{-1} or pCi m^{-3}) which, for future inventories, are normalized to the equivalent activity of the parent. The short-chain is then expanded into a full-chain to compute activities for nuclides not included in PORFLOW transport simulations. The activities are computed assuming secular equilibrium with appropriate branching fractions. Figure 3-140 shows the Am-241 full-chain concentration time series generated by *PreDose* for Case01 in ST15. The four short-chain radionuclides ($t_{1/2}$ > 5 years) analyzed by PORFLOW were Am-241, Np-237, U-233 and Th-229. Pa-233 is in secular equilibrium with Np-237. Ra-225 through Pb-209 are in secular equilibrium with Th-229.

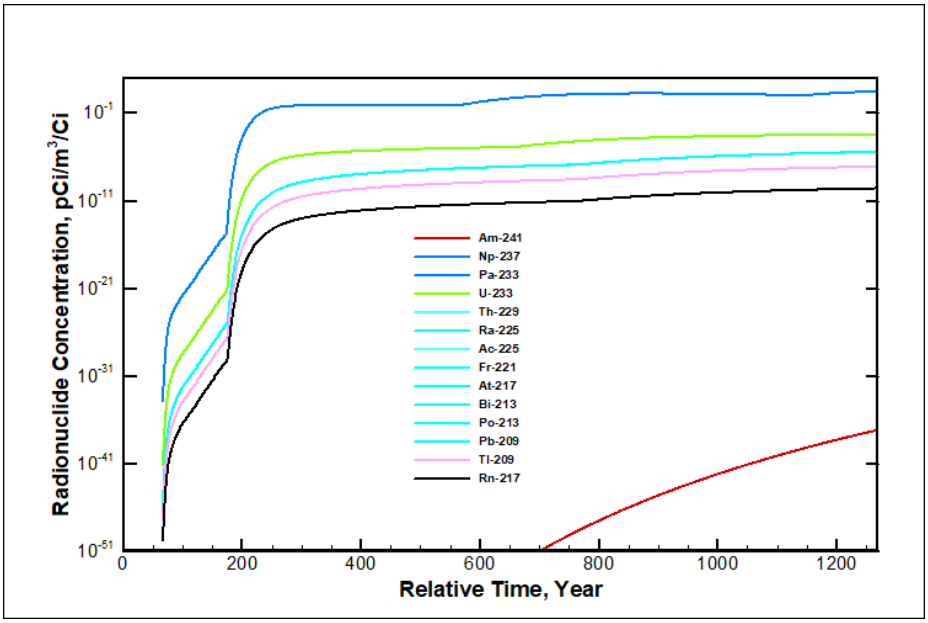

Figure 3-140. Am-241 Full-Chain Concentration Time Series from *PreDose* for Case01 in ST15

3.9.3.2. PreDose Maximum Concentration Module

The *PreDose Maximum Concentration* module determines the maximum concentration at each point in time for each parent nuclide and its full-chain progeny in a DU from a series of *PreDose* files. Each series of *PreDose* files is derived from PORFLOW (or GoldSim®) flow and transport simulations where various VZ scenarios (i.e., Case01) were analyzed. The *PreDose* files contain full-chain radionuclide time series concentrations post-processed from a single- or multiple-element PORFLOW concentration output. Figure 3-141 displays the Ni-59 concentration time series for ST15 derived from three PORFLOW cases (i.e., Case01 has an intact cover; Case11a and Case11b have differing subsidence locations) analyzed as well as the maximum concentration values (dash-dotted) for the entire simulation period. The output from this module is ASCII or binary *PreDose* concentration time series files used as input to the *PA/CA Limits and Doses Tool*.

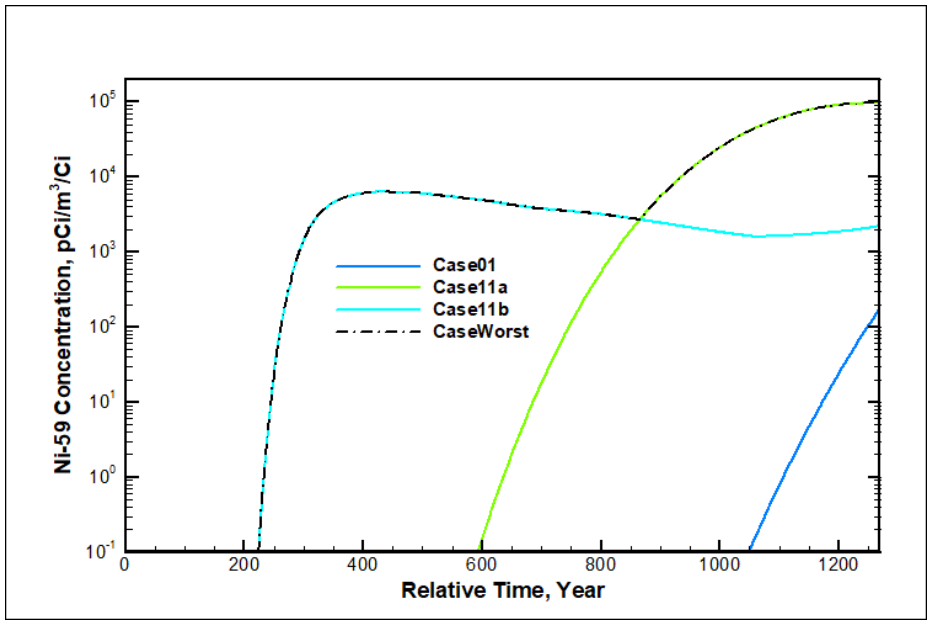

Figure 3-141. Ni-59 Concentration Time Series in ST15 from Three PORFLOW Cases Analyzed

3.9.3.3. PA/CA Limits and Doses Tool

The *PA/CA Limits and Doses Tool* was developed to implement the dose calculations and parameters described in "Dose Calculation Methodology and Data for Solid Waste Performance Assessment and Composite Analysis at the Savannah River Site" by Smith et al. (2019). The *PA/CA Limits and Doses Tool* calculates (1) doses and disposal limits for a resident farmer (i.e., the GW only all-pathways receptor) and an IHI for PA; (2) resident and recreational doses for CA; (3) PA disposal limits based on U.S. EPA GW protection standards.

The first set of dose scenarios assumes that a member of the public establishes residence near the waste site and uses contaminated GW or contaminated surface water for personal consumption and to irrigate a garden and pasture where produce and farm animals are raised. Products from the garden and farm animals are used for personal consumption. This scenario applies to both ELLWF PA and SRS CA studies. General dose exposure pathways for the resident farmer scenario include:

- Ingestion pathways (Drinking Water, Garden Vegetables, Meat, Milk, and Garden Soil)
- Inhalation pathways (Garden Soil, Irrigation Water, and Shower Water)
- External exposure pathways (Garden Soil and Shower Water)
- Recreational pathways for CA only (Dermal Absorption of tritium, Fish ingestion, Swimming Water inhalation and external exposure, Boating Water external exposure, and Shore Soil external exposure)

Additional dose scenarios considered for ELLWF PA assume that an IHI encroaches on the waste disposal site after loss of IC. General dose exposure pathways considered for the IHI are:

- Ingestion pathways
- Inhalation pathways
- External exposure pathways

Doses for all IHI pathways are directly related to contaminant concentration in the buried waste.

Data required to perform radionuclide dose calculations are exported as ASCII files from Microsoft Excel files generated from the *SRNL Radionuclide, Element and Dose Parameters Data Package* (SRNL, 2019b) and the *Geochemical Data Package, Ver. 3.1, dated April 27, 2018* (SRNL, 2018).

Output options from the *PA/CA Limits and Doses Tool* are:

- **Conc_Doses_from_STAT** gives preliminary inventory limits and concentrations/doses.
- **Conc_Doses_from_HIST** provides a series of binary concentration and dose files for each GW pathway where contributions from each full chain progeny have been rolled up to the parent nuclide (input to *ELLWF Dose Investigation Tool*).

3.9.4. HELP Model

The HELP model is a quasi-two-dimensional hydrologic model for conducting landfill water balance calculations. The model requires the input of weather, soil, and closure cap design data, and provides quantitative estimates of surface runoff, evapotranspiration, lateral drainage, vertical percolation (i.e., infiltration), hydraulic head build-up, and water storage for the evaluation of different landfill designs. The HELP model was used to perform all intact case infiltration calculations for the ELLWF PA.

United States Army Corps of Engineers (USACE) personnel at the Waterways Experiment Station in Vicksburg, MS developed the HELP model under an interagency agreement (DW21931425) with the U.S. EPA. As such, the HELP model is a U.S. EPA-approved model for conducting water balance analyses of landfills and other land disposal systems. HELP model Ver. 3.07 (released November 1, 1997) is the most recent official-release public-domain version of the model available for download at https://www.epa.gov/land-research/hydrologic-evaluation-landfill-performance-help-model. U.S. EPA and the USACE provide the following documentation for the HELP model:

- A user's guide (Schroeder et al., 1994b) that gives instructions on setting up and executing the HELP model.
- Engineering documentation (Schroeder et al., 1994a) that provides information on the FORTRAN source code, hardware necessary to operate the code, data generation methodologies available for use, and methods of solution.
- Verification test reports comparing the model's drainage layer estimates to the results of large-scale physical models (Schroeder and Peyton, 1987b) and water balance estimates to "field data from a total of 20 landfill cells at 7 sites in the United States" (Schroeder and Peyton, 1987a).

3.9.4.1. SRNL-Recompiled Version of HELP Model

The graphical user interface for HELP Ver. 3.07 is incompatible with Windows 7 or later. As a result, the user must execute HELP Ver. 3.07 using Windows XP or from within a virtual Windows XP environment. HELP Ver. 4.0 (Dixon, 2017) is an SRNL-recompiled version of HELP Ver. 3.07 that is compatible with 64-bit Windows 7/10 operating systems. HELP Ver. 3.07 was recompiled using the open source compiler GFORTRAN (GNU Compiler Collection, GNU Project). Dixon (2017) documents the details of the code recompilation as well as the successful completion of verification testing of the recompiled code in accordance with the HELP Model SQAP [Q-SQA-A-00005, Rev. 1 by Phifer (2006)]. HELP Ver. 4.0 is classified as QA "Level C" software on the basis that it is used to comply with regulatory laws, environmental permits or regulations, and/or commitments to compliance (Phifer, 2007). HELP Ver. 4.0 was used to perform all infiltration calculations for the ELLWF PA.

3.9.4.2. Alternatives to HELP Model

Whiteside et al. (2009) completed a literature review and basic infiltration model simulations to evaluate the HELP model against five alternative computer codes that use Richards' equation for variably saturated flow. Of the five alternative codes reviewed (LEACHM, UNSAT-H, SVFlux, HYDRUS-2D3D, and VADOSE/W), only HYDRUS-2D3D and VADOSE/W were recommended for further evaluation. The evaluation involved a side-by-side comparison of infiltration rates through a one-layer soil column with 2% slope from right to left as predicted by HELP, HYDRUS-2D3D, and VADOSE/W. While the authors recommended use of HYDRUS-2D3D over VADOSE/W, they were inconclusive about replacing the HELP model with HYDRUS-2D3D pending more rigorous simulations of the proposed multilayer closure cap design.

Dyer (2019c) carefully evaluated the hydrologic model and design and performance recommendations for the planned SDF closure cap at SRS as described by Benson and Benavides (2018) and Benson (2018). In addition, Dyer (2019c) revisited the infiltration model evaluation by Whiteside et al. (2009) and subsequently conducted an independent evaluation of the HYDRUS-1D code to more definitively assess its capabilities to perform the wide variety of intact and subsidence infiltration model simulations across multiple types of DUs as required for the ELLWF PA. Dyer (2019c) concluded that the HELP model remains the preferred choice over other commercial and public-domain hydrologic models for the ELLWF PA for a variety of practical reasons:

- Benson and Benavides (2018) chose to couple the 1-D WinUNSAT-H model based on Richards' equation with Giroud's equations (Giroud, 1997; Giroud and Houlihan, 1995; Giroud et al., 2004; Giroud et al., 2000) to simulate the multilayer SDF cover system because WinUNSAT-H cannot simulate flow through lateral drainage and barrier layers. WinUNSAT-H was used to model water flow in the earthen layers above the LDL, while the Giroud equations calculated drainage-layer flow and percolation through the composite barrier layer (i.e., geomembrane/GCL/finely textured foundation layer). Like the SDF, the ELLWF is also located in a wetter climate and its final closure cap design will include a composite barrier providing the predominant resistance to flow at its base. As a result, any improvement in accuracy gained by switching to an infiltration model of the unsaturated zone based on Richards' equation is largely offset in a wet climate by the need to couple WinUNSAT-H or HYDRUS-2D3D with a separate model for the drainage and barrier layers.
- In addition, the HELP model bases its predictions of leakage rate through holes in the geomembrane barrier layer on the same set of Giroud's semi-empirical equations referenced above. The HELP model selects from a set of empirical leakage rate equations developed originally by Giroud and Bonaparte (1989) that are chosen based on two user-specified input parameters: placement quality of the geomembrane and saturated hydraulic conductivity of the flow-controlling GCL below the geomembrane. If a placement quality of "good" is assumed, Giroud's equations as implemented by Benson and Benavides (2018) for the SDF cap predict a leakage rate through the barrier layer that is in close agreement with the leakage rate predicted by the HELP model for the same cap design. The leakage rate is quite sensitive to the placement quality assumption.
- The cap degradation and subsidence narratives for the ELLWF closure cap demand a flexible, robust infiltration model that readily converges over a wide range of assumed cap and material design properties and conditions. Despite its limitations, the HELP model excels over models that use Richards' equation for variably saturated flow including WinUNSAT-H, HYDRUS-1D, and HYDRUS-2D3D. For example, the coupled WinUNSAT-H/Giroud equation model used by Benson and Benavides (2018) gave unrealistic predictions for leakage rate through the composite barrier as the number of assumed defects in the geomembrane layer exceeded about 1,000 holes per hectare.
- Benson and Benavides (2018) showed that the erosion layer in the SDF and ELLWF closure cap designs will create a hydraulic choke that maintains nearly saturated conditions in the earthen layers below. Therefore, an assumption of unit gradient vertical flow below the erosion layer is reasonable and consistent with the use of a unit vertical hydraulic gradient in the HELP model which diminishes the importance of using an infiltration model based on Richards' equation in a wetter climate such as the SRS.
- The HELP model contains an internal weather generator that creates synthetic daily weather data for long-term simulations (e.g., 100 years) using historical monthly average precipitation, temperature, and solar radiation data. WinUNSAT-H and the HYDRUS software do not include a synthetic weather generator which makes data entry more cumbersome and limited to the availability of historical daily data.

- Sensitivity studies by Shipmon and Dyer (2017) using the HELP model identified primary drivers of the predicted infiltration rate for the FTF closure cap design. The primary drivers, which are all cap degradation model assumptions, include the degradation rate of the geomembrane liner (number of holes per unit area vs. time), the silting-in rate of the LDL, the rate of pine tree intrusion and associated root penetration through the GCL, and the size and location of subsided areas due to non-crushable containers disposed in STs and ETs. These primary drivers change the infiltration rate by more than four orders of magnitude over a 10,000-year period. In contrast, Dyer (2019c) concluded that the choice of one hydrologic model over another is only a secondary driver of predicted infiltration rates (i.e., differences between WinUNSAT-H, HYDRUS-1D, and HELP model predictions for the same scenario are less than an order of magnitude).

In summary, HELP was designed specifically for simulating multilayer closure cap systems, and it remains the best option for modeling such systems in a wet climate where a unit hydraulic gradient is a reasonable assumption. HELP, which is a mass balance model, is also better suited for PA work where flexibility in model construction and ease of model convergence are important. Existing hydrologic models based on Richards' equation, on the other hand, are not specifically designed for multilayer landfill cover systems, are more difficult to converge, and often must be coupled with a second model for the drainage and composite barrier layers. WinUNSAT-H and the HYDRUS software are more necessary for evapotranspiration cover designs that are common in an arid environment.

3.9.5. CAP88-PC

CAP88-PC Ver. 4.1 is a set of computer programs, databases, and associated utility programs developed by the U.S. EPA (U.S. EPA, 2020) for estimating dose and risk from radionuclide emissions to air. CAP88-PC is the personal computer version of the original CAP88 mainframe software. The CAP88-PC software was developed by the U.S. EPA and has been used to demonstrate compliance with 40 CFR 61 National Emissions Standards for Hazardous Air Pollutants, Subpart H (U.S. EPA, 2006). CAP88-PC employs a modified Gaussian plume equation to estimate the average dispersion of radionuclides released from up to six emitting sources. The sources may be either elevated stacks or uniform area sources, such as a pile of uranium mill tailings. Plume rise is calculated assuming either a fixed, momentum, or buoyant-driven plume. Assessments are done for a circular grid of distances and directions for a radius of up to 50 miles around the facility (U.S. EPA, 2020).

For the ELLWF PA, CAP88-PC estimates the annual dose to human receptors based on atmospheric plume data generated from gas-phase radionuclide diffusion data for each DU simulated in the GoldSim® ARM. CAP88-PC models the total effective dose to a receptor at specified locations in 16 compass point directions by first estimating the relative average air concentration (χ/Q) of the released radionuclides and then applying the appropriate exposure parameters and dose coefficients to estimate pathway-specific doses (Dixon and Jannik, 2021). To estimate the χ/Qs, CAP88-PC accesses a site-specific, five-year meteorological database (Bell, 2020a) that includes wind speed, wind direction, temperature, dew point, and horizontal and

vertical turbulence intensities. The resultant relative air concentrations are used to estimate total effective dose for ingestion, inhalation, plume shine (air immersion), and ground shine exposure pathways for the MEI (Dixon and Jannik, 2021).

A user's guide for CAP88-PC Ver 4.1 is available. (U.S. EPA, 2020). CAP88-PC Ver. 4.1 was verified by running test cases as outlined in the SQAP for Environmental Dosimetry (Jannik, 2018). The results of the verification process are documented by Stagich (2020). The software classification for CAP88-PC is Level B (Stagich, 2021).

3.9.6. Closure Analysis Toolkit

A stochastically based closure analysis is chosen to demonstrate overall ELLWF compliance with POs. The use of a stochastic approach to address compliance aspects in the ELLWF has been employed in the past. The Closure Analysis Toolkit explicitly addresses POs for all four dose pathways (i.e., GW, IHI, air, and radon) throughout each pathway's compliance period for every ELLWF DU. Given the inherent uncertainties associated with inventories and their projection to calendar year 2065, a stochastic-based approach to closure analysis is warranted. Section 9.1.2 and Appendix I, Section I.3, respectively, describe the closure analysis approach and Closure Analysis Toolkit in detail.

The Closure Analysis Toolkit is treated as an "engineering calculation" in lieu of developing a SQAP for several reasons:

- The model is used as a one-time calculation for this PA closure analysis only.
- Results of the closure analysis do not impact any CWTS inventory disposal limits to be employed in this PA.
- The model is only performing an overall post-assessment.

3.9.7. RETC for Windows

RETC Ver. 6.02 is a public-domain computer program for analyzing the soil-water retention and hydraulic conductivity functions of unsaturated soils. These hydraulic properties are key parameters in any quantitative description of water flow into and through the unsaturated zone of soils. The program uses the parametric models developed by Brooks and Corey (1964) and van Genuchten (1978; 1980) to represent the soil-water retention curve, and the theoretical pore-size distribution models developed by Burdine (1953) and Mualem (1976; 1986) to predict the unsaturated hydraulic conductivity function from observed soil-water retention data. The user's manual (van Genuchten et al., 1991) provides a detailed discussion of the different analytical expressions used for quantifying the soil-water retention and hydraulic conductivity functions, as well as a brief review of the nonlinear least-squares parameter optimization method used for estimating the unknown coefficients in the hydraulic models. RETC Ver 6.02 was used in support of the *Hydraulic Properties Data Package* (Nichols and Butcher, 2020) for the ELLWF PA. RETC was used in some cases to predict hydraulic conductivities from observed soil-water retention data assuming that one observed conductivity value (not necessarily at saturation) was available. The program also allowed the user to fit analytical functions simultaneously to observed water retention

and hydraulic conductivity data. The software classification for RETC Ver. 6.02 is Level C (Dixon, 2014). The SQAP was prepared by Jones (2007). Verification testing for RETC Ver. 6.02 was performed as outlined in the SQAP.

3.10. REFERENCES

Aadland, R. K., Gellici, J. A., and Thayer, P. A. (1995). "Hydrogeologic Framework of West-Central South Carolina." Rep. No. 5. PIT-MISC-0112. Water Resources Division, South Carolina Department of Natural Resources, Columbia, SC.

Ababou, R., and Wood, E. F. (1990). Comment on "Effective Groundwater Model Parameter Values: Influence of Spatial Variability of Hydraulic Conductivity, Leakance, and Recharge" by JJ Gómez-Hernández and SM Gorelick. *Water Resources Research* **26**(8), 1843-1846.

Abt, S. R., and Johnson, T. L. (1991). Riprap Design for Overtopping Flow. *Journal of Hydraulic Engineering* **117**(8), 959-972.

ACRi (2000). "PORFLOW User's Manual; Version 4.00, Rev. 4." Analytical & Computational Research, Inc., Bel Air, CA.

ACRi (2018). "PORFLOW User's Manual, Keyword Commands Version 6.42.9, Revision 0." Analytical & Computational Research, Inc., Los Angeles, CA. April 23, 2018.

Aleman, S., and Flach, G. (2010). "Acceptance Testing for PORFLOW version 6.30.1 (S. Aleman and G. Flach to B. T. Butcher)." SRNL-L6200-2010-00016. Savannah River National Laboratory, Aiken, SC. September 1, 2010.

Aleman, S. E. (2007). "PORFLOW Testing and Verification Document." WSRC-STI-2007-00150, Rev. 0. Savannah River National Laboratory, Aiken, SC.

Aleman, S. E. (2019). "Savannah River National Laboratory Dose Toolkit." SRNL-TR-2019-00337, Rev. 0. Savannah River National Laboratory, Aiken, SC.

Aleman, S. E. (2021a). "Software Quality Assurance Plan for the SRNL Dose Toolkit, Ver. 1.0." Q-SQP-A-00021, Rev. 0. Savannah River National Laboratory, Aiken, SC.

Aleman, S. E. (2021b). "SRNL Dose Toolkit Software Classification Document." Q-SWCD-A-00047, Rev. 0. Savannah River National Laboratory, Aiken, SC. August 2021.

Aleman, S. E., Hamm, L. L., Flach, G. P., and Jones, W. F. (1999). "Subsurface Flow and Contaminant Transport Documentation and User's Guide." WSRC-TR-95-0223, Rev. 1. Westinghouse Savannah River Company, Aiken, SC. April 1999.

Almond, P. M., Kaplan, D. I., and Shine, E. P. (2012). "Variability of Kd Values in Cementitious Materials and Sediments." SRNL-STI-2011-00672, Rev. 0. Savannah River National Laboratory, Aiken, SC.

Anderson, M. P., and Woessner, W. W. (1992). "Applied Groundwater Modeling: Simulation of Flow and Advective Transport," Academic Press, San Diego, CA.

Atkinson, A., Everett, N., and Guppy, R. (1988). "Evolution of pH in a Radwaste Repository: Internal Reactions Between Concrete Constituents." AERE-R-12939. Materials Development Division, UKAEA Harwell Laboratory, Harwell, Oxfordshire, UK.

Bagwell, L. A., and Bennett, P. L. (2017). "Elevation of Water Table and Various Stratigraphic Surfaces Beneath E-Area Low Level Waste Disposal Facility." SRNL-STI-2017-00301, Rev. 1. Savannah River National Laboratory, Aiken, SC.

Bagwell, L. A., Bennett, P. L., and Flach, G. P. (2017). "General Separations Area (GSA) Groundwater Flow Model Update: Hydrostratigraphic Data." SRNL-STI-2016-00516. Savannah River National Laboratory, Aiken, SC.

Bagwell, L. A., and Flach, G. P. (2016). "General Separations Area (GSA) Groundwater Flow Model Update: Program and Execution Plan." SRNL-STI-2016-00261, Rev. 0. Savannah River National Laboratory, Aiken, SC.

Bear, J. (1972). "Dynamics of Fluids in Porous Media," Dover Publications, New York.

Bechtel, S. (2005). "Saturated Zone Flow and Transport Model Abstraction." MDL-NBS-HS-000021, Rev. 3. Bechtel SAIC Company, LLC, Las Vegas, NV.

Bell, E. S. (2020a). "Creation of CAP88 and MAXDOSE Meteorological Datasets (2014-2018) for Regulatory Dose Assessment." SRNL-STI-2020-00259, Rev. 0. Savannah River National Laboratory, Aiken, SC. July 2020.

Benson, C. H. (1999). Final Covers for Waste Containment Systems: A North American Perspective. *In* "XVII Conference of Geotechnics of Torino: Control and Management of Subsoil Pollutants," Torino, Italy, November 23-25, 1999.

Benson, C. H. (2018). "Lessons Learned from Hydrologic Modeling of the Saltstone Cap." *For* Webinar presentation made to the Performance Assessment Community of Practice. University of Virginia/CRESP, Charlottesville, VA. September 27, 2018.

Benson, C. H., and Benavides, J. M. (2018). "Predicting Long-Term Percolation From the SDF Closure Cap." SRRA107772-000009 (UVA Report No. GENV-18-05). University of Virgina School of Engineering, Charlottesville, VA. April 23, 2018.

Berner, U. R. (1992). Evolution of Pore Water Chemistry during Degradation of Cement in a Radioactive Waste Repository Environment. *Waste Management* **12**(2-3), 201-219.

Bethke, C. M. (2005). The Geochemist's Workbench®. Ver. 6.0. University of Illinois, Urbana, IL.

Bonaparte, R., Daniel, D. E., and Koerner, R. M. (2002). "Assessment and Recommendations for Improving the Performance of Waste Containment Systems." EPA/600/R-02/099. U.S. Environmental Protection Agency, Office of Research and Development, Cincinnati, OH. December 2002.

Bouwer, H. (1991). Simple Derivation of the Retardation Equation and Application to Preferential Flow and Macrodispersion. *Groundwater* **29**(1), 41-46.

Bradbury, M. H., and Sarott, F.-A. (1995). "Sorption Databases for the Cementitious Near-Field of a L/ILW Repository for Performance Assessment " PSI 95-06. Paul Scherrer Institute, Villigen Switzerland. March 1995.

Brooks, R. H., and Corey, A. T. (1964). Hydraulic Properties of Porous Media. *In* "Hydrology Papers No. 3". Colorado State University, Fort Collins, CO.

Burdine, N. T. (1953). Relative Permeability Calculations from Pore Size Distribution Data. *Journal of Petroleum Technology* **5**(3), 71-78.

Butcher, B. T. (2013a). "GoldSimFlows Software Classification Document." B-SWCD-A-00641, Rev. 0. Savannah River National Laboratory, Aiken, SC. June 4, 2013.

Butcher, B. T. (2013b). "PORFLOW Software Classification Document." G-SWCD-A-00063, Rev. 3. Savannah River National Laboratory, Aiken, SC. September 19, 2013.

Butcher, B. T. (2016). "PEST Software Classification Document." Q-SWCD-A-00035, Rev. 0. Savannah River National Laboratory, Aiken, SC. June 6, 2016.

Butcher, B. T. (2017a). "avgVal Software Classification Document." Q-SWCD-A-00036, Rev. 0. Savannah River National Laboratory, Aiken, SC. October 30, 2017.

Butcher, B. T. (2017b). "MESH2D Software Classification Document." B-SWCD-A-00615, Rev. 2. Savannah River National Laboratory, Aiken, SC. October 17, 2017.

Butcher, B. T. (2017c). "PlotConc3d Software Classification Document." Q-SWCD-A-00038, Rev. 0. Savannah River National Laboratory, Aiken, SC. November 14, 2017.

Butcher, B. T. (2017d). "PlotConc3dU Software Classification Document." Q-SWCD-A-00039, Rev. 0. Savannah River National Laboratory, Aiken, SC. November 28, 2017.

Butcher, B. T. (2017e). "PlotConc Software Classification Document." Q-SWCD-A-00037, Rev. 0. Savannah River National Laboratory, Aiken, SC. October 30, 2017.

Butcher, B. T. (2017f). "PlotFlow2d Software Classification Document." Q-SWCD-A-00040, Rev. 0. Savannah River National Laboratory, Aiken, SC. December 18, 2017.

Butcher, B. T. (2018a). "MakeWhole Software Classification Document." Q-SWCD-A-00045, Rev. 0. Savannah River National Laboratory, Aiken, SC. February 9, 2018.

Butcher, B. T. (2018b). "MESH3D Software Classification Document." B-SWCD-A-00582, Rev. 2. Savannah River National Laboratory, Aiken, SC. April 25, 2018.

Butcher, B. T. (2018c). "PlotFlux Software Classification Document." Q-SWCD-A-00041, Rev. 0. Savannah River National Laboratory, Aiken, SC. January 22, 2018.

Butcher, B. T. (2018d). "PlotHist Software Classification Document." Q-SWCD-A-00042, Rev. 0. Savannah River National Laboratory, Aiken, SC. January 30, 2018.

Butcher, B. T. (2018e). "PlotStat Software Classification Document." Q-SWCD-A-00043, Rev. 0. Savannah River National Laboratory, Aiken, SC. February 5, 2018.

Butcher, B. T., and Phifer, M. A. (2016a). "Strategic Plan for Next E-Area Low-Level Waste Facility Performance Assessment." SRNL-STI-2015-00620, Rev. 0. Savannah River National Laboratory, Aiken, SC. February 2016.

Butcher, B. T., and Phifer, M. A. (2016b). "Strategic Plan for Next E-Area Low-Level Waste Facility Performance Assessment: Appendix 1.0 Topical Presentations and Team Deliberations." SRNL-STI-2015-00620, Rev. 0. Savannah River National Laboratory, Aiken, SC. February 2016.

Cahill, J. M. (1982). "Hydrology of the Low-Level Radioactive-Solid-Waste Burial Site and Vicinity near Barnwell, South Carolina." Open-File Report 82-863. U. S. Geological Survey, Columbia, SC.

Carey, S. (2005). "Low Activity Waste (LAW) Vault Structural Degradation Prediction." T-CLC-E-00018, Rev. 1. Westinghouse Savannah River Company, Aiken, SC. October 27, 2005.

Clarke, J. S., and West, C. T. (1998). "Simulation of Ground-Water Flow and Stream-Aquifer Relations in the Vicinity of the Savannah River Site, Georgia and South Carolina, Predevelopment through 1992." Water-Resources Investigations Report 98-4062. United States Geological Survey, Denver, CO.

Cook, J. R., and Hunt, P. D. (1994). "Radiological Performance Assessment for the E-Area Vaults Disposal Facility." WSRC-RP-94-218, Rev. 0. Westinghouse Savannah River Company, Aiken, SC. April 15, 1994.

Danielson, T. (2017). "Software Quality Assurance Plan for Aquifer Model Refinement Tool (MESH3D)." Q-SQP-G-00003, Rev. 2. Savannah River National Laboratory, Aiken, SC.

Danielson, T. L. (2019b). "A Monte Carlo Rectangle Packing Algorithm for Identifying Likely Spatial Distributions of Final Closure Cap Subsidence in the E-Area Low-Level Waste Facility." SRNL-STI-2019-00440, Rev. 0. Savannah River National Laboratory, Aiken, SC.

Danielson, T. L. (2019c). "PORFLOW Implementation of Vadose Zone Conceptual Model for Slit and Engineered Trenches in the E-Area Low Level Waste Facility Performance Assessment." SRNL-STI-2019-00193. Savannah River National Laboratory, Aiken, SC.

de Marsily, G. (1986). "Quantitative Hydrogeology," Academic Press, Orlando, FL.

Denham, M. E. (2009). "Conceptual Model of Waste Release from the Contaminated Zone of Closed Radioactive Waste Tanks." WSRC-STI-2007-00544, Rev. 1. Savannah River National Laboratory, Aiken, SC. October 2009.

Dennehy, K. F., and McMahon, P. B. (1989). Water Movement in the Unsaturated Zone at a Low-Level Radioactive-Waste Burial Site Near Barnwell, South Carolina. *In* "U.S. Geological Survey Water-Supply Paper 2345" (U.S. Geological Survey, ed.). United States Government Printing Office,, Denver, Colorado.

Desbarats, A. J. (1992). Spatial Averaging of Hydraulic Conductivity in Three-Dimensional Heterogeneous Porous Media. *Mathematical Geology* **24**(3), 249-267.

Dixon, K. L. (2014). "RETC Software Classification Document." G-SWCD-G-00040, Rev. 3. Savannah River National Laboratory, Aiken, SC. March 4, 2014.

Dixon, K. L. (2017). "HELP 4.0 Documentation and Software QA." SRNL-STI-2017-00104, Rev. 0. Savannah River National Laboratory, Aiken, SC.

Dixon, K. L., and Jannik, G. T. (2021). "Air Pathway Dose Modeling for the E-Area Low-Level Waste Facility." SRNL-STI-2016-00512, Rev. 3. Savannah River National Laboratory, Aiken, SC. August 2021.

Dixon, K. L., and Minter, K. M. (2017). "Air Pathway Dose Modeling for the E-Area Low-Level Waste Facility." SRNL-STI-2016-00512, Rev. 1. Savannah River National Laboratory, Aiken, SC.

Dixon, K. L., and Phifer, M. A. (2006). "Hydraulic and Physcial Properties of Cementitious Materials Used at the Component-in-Grout Waste Trenches and the Intermediate Level Vault." WSRC-STI-2006-00199, Rev. 0. Savannah River National Laboratory, Aiken, SC.

Dixon, K. L., and Phifer, M. A. (2007). "Cementitious Material Selection for Future Component-In-Grout Waste Disposals." WSRC-STI-2007-00207, Rev. 0. Savannah River National Laboratory, Aiken, SC.

DOE-ID (2019). "Performance Assessment for the INTEC Calcined Solids Storage Facility at the INL Site (Draft)." DOE/ID-12008, Rev. B. Idaho Falls, ID. September 2019.

DOE LFRG (2008). "DOE Low-Level Waste Disposal Facility Federal Review Group, Review Team Report for the E-Area Low-Level Waste Facility, DOE 435.1 Performance Assessment at the Savannah River Site." U.S. Department of Energy, Aiken, SC. February 4, 2008.

Doherty, J. E., and Hunt, R. J. (2010). "Approaches to Highly Parameterized Inversion: A Guide to Using PEST for Groundwater-Model Calibration." Scientific Investigations Report 2010–5169. U.S. Geological Survey, Reston, VA.

Dutro, J. T., Dietrich, R. V., and Foose, R. M. (1989). AGI Data Sheets for Geology in the Field, Laboratory, and Office. American Geological Institute, Alexandria, VA.

Dyer, J. A. (2017b). "Conceptual Modeling Framework for E-Area PA HELP Infiltration Model Simulations." SRNL-STI-2017-00678. Savannah River National Laboratory, Aiken, SC.

Dyer, J. A. (2017c). "E-Area Low-Level Waste Facility Vadose Zone Model: Confirmation of Water Mass Balance for Subsidence Scenarios." Rep. No. 10.2172/1411194. SRNL-STI-2017-00728. Savannah River National Laboratory, Aiken, SC.

Dyer, J. A. (2017d). "Recommended Henry's Law Constants for Non-Groundwater Pathways Models in GoldSim." SRNL-STI-2017-00331. Savannah River National Laboratory, Aiken, SC.

Dyer, J. A. (2018a). "Impact of Different Vegetative Cover Scenarios on Infiltration Rates for the E-Area PA Intact Case." SRNL-STI-2018-00141, Rev. 0. Savannah River National Laboratory, Aiken, SC.

Dyer, J. A. (2018b). "Method for Including Uncertainty in Infiltration Rates in the E-Area PA System Model." SRNL-STI-2018-00121, Rev. 0. Savannah River National Laboratory, Aiken, SC.

Dyer, J. A. (2019b). "Infiltration Data Package for the E-Area Low-Level Waste Facility Performance Assessment." SRNL-STI-2019-00363, Rev. 0. Savannah River National Laboratory, Aiken, SC. November 2019.

Dyer, J. A. (2019c). "Justification for Use of the HELP Model to Estimate Infiltration Rates for the E-Area Low-Level Waste Facility Performance Assessment." SRNL-STI-2019-00362, Rev. 0. Savannah River National Laboratory, Aiken, SC.

Dyer, J. A., and Flach, G. P. (2017). "E-Area LLWF Vadose Zone Model: Probabilistic Model for Estimating Subsided-Area Infiltration Rates." SRNL-STI-2017-00729, Rev. 0. Savannah River National Laboratory, Aiken, SC.

Dyer, J. A., and Flach, G. P. (2018). "Infiltration Time Profiles for E-Area LLWF Intact and Subsidence Scenarios." SRNL-STI-2018-00327, Rev. 0. Savannah River National Laboratory, Aiken, SC.

Eckerman, K. F., and Leggett, R. W. (2013). "User Guide to DCFPAK 3.0." Oak Ridge National Laboratory, Oak Ridge, TN.

Eckerman, K. F., and Ryman, J. C. (1993). "External Exposure to Radionuclides in Air, Water, and Soil." Federal Guidance Report No. 12 (EPA-402-R-93-081). Prepared for U.S. Environmental Protection Agency by Oak Ridge National Laboratory, Washington, DC. September 1993.

Efron, B. (1982). The Jackknife, the Bootstrap and Other Resampling Plans. *In* "CBMS-NSF Regional Conference Series in Applied Mathematics." Society for Industrial and Applied Mathematics, Monograph 38, Philadelphia, PA.

Egloffstein, T. A. (2001). Natural Bentonites—Influence of the Ion Exchange and Partial Desiccation on Permeability and Self-Healing Capacity of Bentonites used in GCLs. *Geotextiles and Geomembranes* **19**(7), 427-444.

Fetter, C. W. (1993). "Contaminant Hydrogeology," MacMillan Publishing, New York.

Flach, G. P. (2004). "Groundwater Flow Model of the General Separations Area Using PORFLOW (U)." WSRC-TR-2004-00106, Rev. 0. Westinghouse Savannah River Company, Aiken, SC.

Flach, G. P. (2012). Effective Porosity Implies Effective Bulk Density in Sorbing Solute Transport. *Ground Water* **50**(5), 657-658.

Flach, G. P. (2015a). "Code Selection for General Separations Area Flow Simulation and Model Calibration." SRNL-STI-2015-00061, Rev. 0. Savannah River National Laboratory, Aiken, SC.

Flach, G. P. (2015b). "Velocity Field Calculation For Non-Orthogonal Numerical Grids." SRNL-STI-2015-00115, Rev. 0. Savannah River National Laboratory, Aiken, SC.

Flach, G. P. (2017b). "Mesh2d Grid Generator Design and Use." SRNL-STI-2012-00005, Rev. 1. Savannah River National Laboratory, Aiken, SC. October 2017.

Flach, G. P. (2018). "Recommended Aquifer Grid Resolution for E-Area PA Revision Transport Simulations." SRNL-STI-2018-00012, Rev. 0. Savannah River National Laboratory, Aiken, SC.

Flach, G. P. (2019). "Updated Groundwater Flow Simulations of the Savannah River Site General Separations Area." SRNL-STI-2018-00643, Rev. 0. Savannah River National Laboratory, Aiken, SC.

Flach, G. P., Bagwell, L. A., and Bennett, P. L. (2017). "Groundwater Flow Simulation of the Savannah River Site General Separations Area." SRNL-STI-2017-00008, Rev. 1. ; Savannah River Site (SRS), Aiken, SC (United States).

Flach, G. P., and Butcher, B. T. (2013). "Software Quality Assurance Plan for PORFLOW Flow-Field Extraction Tool (GoldSimFlows)." Q-SQP-A-00008, Rev. 0. Savannah River National Laboratory, Aiken, SC.

Flach, G. P., Collard, L. B., Phifer, M. A., Crapse, K. P., Dixon, K. L., Koffman, L. D., and Wilhite, E. L. (2005). "Preliminary Closure Analysis for Slit Trenches #1 and #2." WSRC-TR-2005-00093. Westinghouse Savannah River Company, Aiken, SC.

Flach, G. P., Crisman, S. A., and Molz, F. J. (2004). Comparison of Single-Domain and Dual-Domain Subsurface Transport Models. *Ground Water* **42**(6), 815-828.

Flach, G. P., Hamm, L. L., Harris, M. K., Thayer, P. A., Haselow, J. S., and Smits, A. D. (1996). "Groundwater Flow and Tritium Migration from the SRS Old Burial Ground to Fourmile Branch (U)." WSRC-TR-96-0037. Westinghouse Savannah River Company, Aiken, SC. April 1996.

Flach, G. P., and Harris, M. K. (1997). "Corrective Measures Study Modeling Results for the Southwest Plume - Burial Ground Complex/Mixed Waste Management Facility (U)." WSRC-TR-96-0411. Westinghouse Savannah River Company, Aiken, SC. January 1997.

Flach, G. P., and Harris, M. K. (1999). "Integrated Hydrogeological Model of the General Separations Area (U), Volume 2: Groundwater Flow Model (U)." WSRC-TR-96-0399, Rev. 1. Westinghouse Savannah River Company, Aiken, SC.

Flach, G. P., Harris, M. K., Hiergesell, R. A., Smits, A. D., and Hawkins, K. L. (1999). "Regional Groundwater Flow Model for C, K, L, and P Reactor Areas, Savannah River Site, Aiken, South Carolina (U)." WSRC-TR-99-00248, Rev. 0. Westinghouse Savannah River Company, Aiken, SC.

Flach, G. P., Kaplan, D. I., Nichols, R. L., Seitz, R. R., and Serne, R. J. (2016). "Solid Secondary Waste Data Package Supporting Hanford Integrated Disposal Facility Performance Assessment." SRNL-STI-2016-00175, Rev. 0. Savannah River National Laboratory, Aiken, SC. May 2016.

Fredlund, D. G., and Rahardjo, H. (1993). "Soil Mechanics for Unsaturated Soils," John Wiley & Sons, New York, NY.

Freeze, R. A., and Cherry, J. A. (1979). "Groundwater," Prentice-Hall, Inc., Englewood Cliffs, NJ.

Gelhar, L. W. (1997). Perspectives on Field-Scale Application of Stochastic Subsurface Hydrology. *In* "Subsurface Flow and Transport: A Stochastic Approach" (G. Dagan and S. P. Neuman, eds.), pp. 157-176. Cambridge University Press, New York.

Gelhar, L. W., Welty, C., and Rehfeldt, K. R. (1992). A Critical Review of Data on Field-Scale Dispersion in Aquifers. *Water Resour. Res* **28**(7), 1955-1974.

Giroud, J. P. (1997). Equations for Calculating the Rate of Liquid Migration Through Composite Liners Due to Geomembrane Defects. *Geosynthetics International* **4**(3-4), 335-348.

Giroud, J. P., and Bonaparte, R. (1989). Leakage through Liners Constructed with Geomembranes—Part I. Geomembrane Liners. *Geotextiles and Geomembranes* **8**(1), 27-67.

Giroud, J. P., and Houlihan, M. F. (1995). Design of Leachate Collection Layers. *In* "Proceedings of the Fifth International Landfill Symposium," Vol. 2, pp. 613-640.

Giroud, J. P., Zhao, A., Tomlinson, H. M., and Zornberg, J. G. (2004). Liquid Flow Equations for Drainage Systems Composed of Two Layers including a Geocomposite. *Geosynthetics International* **11**(1), 43-58.

Giroud, J. P., Zornberg, J. G., and Zhao, A. (2000). Hydraulic Design of Geosynthetic and Granular Liquid Collection Layers. *Geosynthetics International* **7**(4-6), 285-380.

Goldman, S. J., Jackson, K., and Bursztynsky, T. A. (1986). "Erosion and Sediment Control Handbook," McGraw-Hill Publishing Company, New York.

GoldSim Technology Group (2018a). GoldSim User's Guide. Ver. 12.1. Retrieved June, 2018 from https://www.goldsim.com/Web/Customers/Education/Documentation/. GoldSim Technology Group LLC, Seattle, WA.

GoldSim Technology Group (2018b). GoldSim Version 12.1 Contaminant Transport Module User's Guide. Ver. 7.1. Retrieved June, 2018 from https://www.goldsim.com/Web/Customers/Education/Documentation/. GoldSim Technology Group LLC, Seattle, WA.

Greenwood, N. N., and Earnshaw, A. (1998). "Chemistry of the Elements," Butterworth Heinemann, Oxford, UK.

Grogan, K. P. (2008). Spatial Variability of Radionuclide Distribution Coefficients at the Savannah River Site and the Subsurface Transport Implications, Clemson University, Clemson, SC.

Grogan, K. P., Fjeld, R. A., Kaplan, D., DeVol, T. A., and Coates, J. T. (2010). Distributions of Radionuclide Sorption Coefficients (Kd) in Sub-Surface Sediments and the Implications for Transport Calculations. *Journal of Environmental Radioactivity* **101**(10), 847-853.

Hamm, L. L. (2019). "Confirmation of Disposal Unit Footprints for Use in E-Area Performance Assessment Revision." SRNL-STI-2019-00205, Rev. 0. Savannah River National Laboratory, Aiken, SC.

Hamm, L. L., and Aleman, S. E. (2000). "FACT (Version 2.0) - Subsurface Flow and Contaminant Transport Documentation and User's Guide." WSRC-TR-99-00282, Rev. 0. Westinghouse Savannah River Company, Aiken, SC.

Hamm, L. L., Aleman, S. E., and Danielson, T. L. (2019). "Preliminary Assessment for Continued Use of Plume Interaction Factors and Other Options for Revised Performance Assessment Methodology." SRNL-STI-2019-00149, Rev. 0. Savannah River National Laboratory, Aiken, SC. March 7, 2019.

Hamm, L. L., Collard, L. B., Aleman, S. E., Gorensek, M. B., and Butcher, B. T. (2012). "Special Analysis for Slit Trench Disposal of the Reactor Process Heat Exchangers." SRNL-STI-2012-00321, Rev. 0. Savannah River National Laboratory, Aiken, SC.

Hamm, L. L., and Smith, F. G. (2010). "Special Analysis for Slit Trench Disposal of the Heavy Water Components Test Reactor." SRNL-STI-2010-00574, Rev. 0. Savannah River National Laboratory, Aiken, SC.

Hang, T. (2007). "PORFLOW Software Quality Assurance Plan." G-SQP-A-00012, Rev. 0. Westinghouse Savannah River Company, Aiken, SC.

Hang, T. (2012). "PORFLOW Software Test Plan." G-STP-A-00009, Rev. 1. Savannah River National Laboratory, Aiken, SC. August 2012.

Hang, T. (2017a). "Software Quality Assurance Plan for avgVal." Q-SQP-A-00009, Rev. 0. Savannah River National Laboratory, Aiken, SC.

Hang, T. (2017b). "Software Quality Assurance Plan for MESH2D." G-SQP-G-00015, Rev. 1. Savannah River National Laboratory, Aiken, SC.

Hang, T. (2017c). "Software Quality Assurance Plan for PlotConc." Q-SQP-A-00010, Rev. 0. Savannah River National Laboratory, Aiken, SC.

Hang, T. (2017d). "Software Quality Assurance Plan for PlotConc3d." Q-SQP-A-00011, Rev. 0. Savannah River National Laboratory, Aiken, SC.

Hang, T. (2017e). "Software Quality Assurance Plan for PlotConc3dU." Q-SQP-A-00012, Rev. 0. Savannah River National Laboratory, Aiken, SC.

Hang, T. (2017f). "Software Quality Assurance Plan for PlotFlow2d." Q-SQP-A-00013, Rev. 0. Savannah River National Laboratory, Aiken, SC.

Hang, T. (2018a). "Software Quality Assurance Plan for MakeWhole." Q-SQP-A-00017, Rev. 0. Savannah River National Laboratory, Aiken, SC.

Hang, T. (2018b). "Software Quality Assurance Plan for PlotFlux." Q-SQP-A-00014, Rev. 0. Savannah River National Laboratory, Aiken, SC.

Hang, T. (2018c). "Software Quality Assurance Plan for PlotHist." Q-SQP-A-00015, Rev. 0. Savannah River National Laboratory, Aiken, SC.

Hang, T. (2018d). "Software Quality Assurance Plan for PlotStat." Q-SQP-A-00016, Rev. 0. Savannah River National Laboratory, Aiken, SC.

Hang, T. (2019a). "GSA Aquifer Cutouts for E-Area PA Revision Transport Simulations." SRNL-STI-2019-00736, Rev. 0. Savannah River National Laboratory, Aiken, SC.

Hang, T. (2021a). "PlotFlow3dS Software Classification Document." Q-SWCD-A-00046, Rev. 1. Savannah River National Laboratory, Aiken, SC. December 2021.

Hang, T. (2021b). "Software Quality Assurance Plan for PlotFlow3dS, Ver. 1.0." Q-SQP-A-00020, Rev. 0. Savannah River National Laboratory, Aiken, SC. December 2021.

Hiergesell, R. A., and Taylor, G. A. (2011). "Special Analysis: Air Pathway Modeling of E-Area Low-Level Waste Facility." SRNL-STI-2011-00327, Rev. 0. Savannah River National Laboratory, Aiken, SC.

Hiergesell, R. A., and Taylor, G. A. (2015). "General Separations Areas (GSA) Groundwater Level Measurement Analysis." SRNL-STI-2015-00034, Rev. 0. Savannah River National Laboratory, Aiken, SC.

Hiergesell, R. A., Taylor, G. A., Phifer, M. A., Whiteside, T. S., and Flach, G. P. (2015). "General Separations Areas (GSA) Groundwater Model Calibration Targets." SRNL-STI-2015-00351, Rev. 0. Savannah River National Laboratory, Aiken, SC.

Hillel, D. (1982). "Introduction to Soil Physics," Academic Press, Inc., San Diego, CA.

Hsuan, Y. G., and Koerner, R. M. (1998). Antioxidant Depletion Lifetime in High Density Polyethylene Geomembranes. *Journal of Geotechnical and Geoenvironmental Engineering* **124**(6), 532-541.

Hubbard, J. E. (1986). "An Update on the SRP Burial Ground Area Water Balance and Hydrology." DPST-85-958. E. I. du Pont de Nemours and Company, Savannah River Plant, Aiken, SC. January 9, 1986.

Hubbard, J. E., and Emslie, R. H. (1984). "Water Budget for SRP Burial Ground Area." DPST-83-742. E. I. du Pont de Nemours and Company, Savannah River Plant, Aiken, SC. March 19, 1984.

Hubbard, J. E., and Englehardt, M. (1987). "Calculation of Groundwater Recharge at the Old SRP Burial Ground Using the CREAMS Model (1961-1986)." DPST-83-742. State University of New York, Brockport, NY (prepared for E. I. du Pont de Nemours and Company, Savannah River Site).

IAEA (2004). "Safety Assessment Methodologies for Near Surface Disposal Facilities, Results of a Coordinated Research Project, Volume 1: Review and Enhancement of Safety Assessment Approaches and Tools." IAEA-ISAM-1. International Atomic Energy Agency, Vienna, Austria. July 2004.

ICRP (2008). Nuclear Decay Data for Dosimetric Calculations. ICRP Publication 107. *Ann. ICRP* **38**(3).

Jannik, G. T. (2014). "Facility Area Coordinates and Grade Elevations for the Savannah River Site (U)." SRNL-L4310-2014-00027. Savannah River National Laboratory, Aiken, SC. August 21, 2014.

Jannik, G. T. (2018). "Software Quality Assurance Plan for Environmental Dosimetry." Q-SQP-A-00002, Rev. 5. Savannah River National Laboratory, Aiken, SC.

Jannik, G. T., and Stagich, B. H. (2017). "Land and Water Use Characteristics and Human Health Input Parameters for use in Environmental Dosimetry and Risk Assessments at the Savannah River Site - 2017 Update." SRNL-STI-2016-00456, Rev. 1. Savannah River Site, Aiken, SC. May 2017.

Jannik, G. T., and Stagich, B. H. (2017). "Land and Water Use Characteristics and Human Health Input Parameters for use in Environmental Dosimetry and Risk Assessments at the Savannah River Site - 2017 Update." SRNL-STI-2016-00456. Savannah River Site, Aiken, SC. May 2017.

Jannik, G. T., and Trimor, P. P. (2017). "MAXDOSE-SR and POPDOSE-SR: Routine-Release Atmospheric Dose Models used at SRS." SRNL-STI-2013-00722, Rev. 1. Savannah River National Laboratory, Aiken, SC. July 2017.

Jo, H. Y., Benson, C. H., Shackelford, C. D., Lee, J.-M., and Edil, T. B. (2005). Long-Term Hydraulic Conductivity of a Geosynthetic Clay Liner Permeated with Inorganic Salt Solutions. *Journal of Geotechnical and Geoenvironmental Engineering* **131**(4), 405-417.

Johnson, T. L. (2002). "Design of Erosion Protection for Long-Term Stabilization." NUREG-1623. U.S. Nuclear Regulatory Commission, Office of Nuclear Material Safety and Safeguards, Washington, DC. September 2002.

Jones, W. E. (2007). "Software Quality Assurance Plan for the RETC (RETention Curve) Computer Code." Q-SQP-A-00006, Rev. 0. Westinghouse Savannah River Company, Aiken, SC.

Jones, W. E., Millings, M. R., and Rambo, B. H. (2010). "Hydrogeologic Data Summary in Support of the H-Area Tank Farm Performance Assessment." SRNL-STI-2010-00148, Rev. 0. Savannah River National Laboratory, Aiken, SC. February 2010.

Jones, W. E., and Phifer, M. A. (2007). "E-Area Low-Activity Waste Vault Subsidence Potential and Closure Cap Performance (U)." WSRC-TR-2005-00405. Washington Savannah River Company, Aiken, SC.

Kaplan, D. I. (2005). "Estimate of Gaseous 14C Concentrations Emanating from the Intermediate-Level Vault Disposal Facility (U)." WSRC-TR-2005-00222, Rev. 0. Westinghouse Savannah River Company, Aiken, SC.

Kaplan, D. I. (2007a). "Geochemical Data Package for Performance Assessment Calculations Related to the Savannah River Site." WSRC-TR-2006-00004, Rev. 1. Washington Savannah River Company, Aiken, SC. September 30, 2007.

Kaplan, D. I. (2010). "Geochemical Data Package for Performance Assessment Calculations Related to the Savannah River Site." SRNL-STI-2009-00473, Rev. 0. Savannah River National Laboratory, Aiken, SC.

Kaplan, D. I. (2016b). "Geochemical Data Package for Performance Assessment Calculations Related to the Savannah River Site." SRNL-STI-2009-00473, Rev. 1. Savannah River National Laboratory, Aiken, SC.

Kaplan, D. I., and Coffey, C. (2002). "Distribution Coefficients (Kd Values) for Waste Resins Generated from the K & L Disassembly Basin Facilities." WSRC-TR-2002-00349, Rev. 0. Westinghouse Savannah River Company, Aiken, SC. August 9, 2002.

Kaplan, D. I., and Iversen, G. (2001). "Free-Moisture Content and ^{129}I-Kd Values of Filtercake Material Generated from the F-Area Groundwater Treatment Unit." WSRC-TR-2001-00253, Rev. 0. Westinghouse Savannah River Company, Aiken, SC. August 17, 2001.

Kaplan, D. I., Roberts, K., Shine, E. P., Grogan, K. P., Fjeld, R. A., and Seaman, J. C. (2008). "Range and Distribution of Technetium Kd Values in the SRS Subsurface Environment." SRNS-STI-2008-00286, Rev. 1. Savannah River National Laboratory, Aiken, SC. October 28, 2008.

Kaplan, D. I., and Serkiz, S. M. (2000). "^{129}Iodine Desorption from Resin, Activated Carbon, and Filtercake Waste Generated from the F- and H-Area Water Treatment Units." WSRC-TR-2000-00308, Rev. 0. Westinghouse Savannah River Company, Aiken, SC. October 26, 2000.

Kaplan, D. I., Serkiz, S. M., and Bell, N. C. (1999). "I-129 Desorption from SRS Water Treatment Media from the Effluent Treatment Facility and the F-Area Groundwater Treatment Facility." WSRC-TR-99-00270. Westinghouse Savannah River Company, Aiken, SC. August 24, 1999.

Koerner, R. M. (1998). "Designing with Geosynthetics," 4th/Ed. Prentice Hall, Upper Saddle River, NJ.

Koerner, R. M., and Hsuan, Y. G. (2003). Lifetime Prediction of Polymeric Geomembranes Used in New Dam Construction and Dam Rehabilitation. *In* "Proceedings of the Association of State Dam Safety Officials Conference," Lake Harmony, PA, June 4-6, 2003.

Krupka, K. M., Kaplan, D. I., Whelan, G., Serne, R. J., and Mattigod, S. V. (1999). "Understanding Variation in Partition Coefficient, K_d, Values. Volume II: Review of Geochemistry and Available K_d Values for Cadmium, Cesium, Chromium, Lead, Plutonium, Radon, Strontium, Thorium, Tritium (^{3}H), and Uranium." EPA-402-R-99-004B. Office of Air and Radiation, Office of Solid Waste and Emergency Response, U.S. Environmental Protection Agency, Washington, DC. August 1999.

Kubilius, W. P., and Joyce, W. D. (2018). "Optimization of the Groundwater Monitoring Program at the E-Area Low-Level Waste Facility (ELLWF)." SRNS-RP-2018-01123, Rev. 0. Savannah River National Laboratory, Aiken, SC. December 2018.

Lee, P. L. (2006). "Air Pathway Dose Modeling for the E-Area Low Level Waste Facility at the Savannah River Site." WSRC-STI-2006-00262, Rev. 0. Savannah River National Laboratory, Washington Savannah River Company, Aiken, SC. October 31, 2006.

LFRG (2008). "Review Team Report for the E-Area Low-Level Waste Facility DOE 435.1 Performance Assessment at the Savannah River Site." Department of Energy Low-Level Waste Disposal Facility Federal Review Group Review Team. February 4, 2008.

Li, J., You, K., Zhan, H., and Huang, G. (2012). Analytical Solution to Subsurface Air Pressure in a Three-Layer Unsaturated Zone with Atmospheric Pressure Changes. *Transport in Porous Media* **93**(3), 461-474.

Lin, L. C., and Benson, C. H. (2000). Effect of Wet-Dry Cycling on Swelling and Hydraulic Conductivity of GCLs. *Journal of Geotechnical and Geoenvironmental Engineering* **126**(1), 40-49.

Looney, B. B., Grant, M. W., and King, C. M. (1987). "Estimation of Geochemical Parameters for Assessing Subsurface Transport at the Savannah River Plant." DPST-85-904. Savannah River Laboratory, Aiken, SC. March 1987.

Lowry, W., Dunn, S. D., and Neeper, D. (1996). Barometric Pumping with a Twist: VOC Containment and Remediation without Boreholes. *In* "Industry Partnerships to Deploy Environmental Technology, October 22-24, 1996, Morgantown, WV." Science and Engineering Associates, Inc., Santa Fe, NM.

McDowell-Boyer, L., Phifer, M. A., and Cook, J. R. (2011). "Data Package for HELP Models used in the E-Area Low-Level Waste Facility Performance Assessment." SRNL-STI-2010-00618, Rev. 0. Savannah River National Laboratory, Aiken, SC.

McDowell-Boyer, L., Yu, A. D., Cook, J. R., Kocher, D. C., Wilhite, E. L., Holmes-Burns, H., and Young, K. E. (2000). "Radiological Performance Assessment for the E-Area Low-Level Waste Facility." WSRC-RP-94-218, Rev. 1. Westinghouse Savannah River Company, Aiken, SC.

McKenzie, D. H., Cadwell, L. L., Kennedy, W. E., Jr., Prohammer, L. A., and Simmons, M. A. (1986). "Relevance of Biotic Pathways to the Long-Term Regulation of Nuclear Waste Disposal, Phase II, Final Report." NUREG/CR-2675, PNL-4241. Pacific Northwest Laboratory, Richland, WA. November 1986.

Mehta, S., Kozak, M. W., Hasan, N., Khaleel, R., Morgans, D. L., McMahon, W. J., Sun, B., Bergeron, M. P., Field, J. G., Singleton, K. M., and Connelly, M. P. (2016). "Performance Assessment of Waste Management Area C, Hanford Site, Washington." RPP-ENV-58782, Rev. 0. Washington River Protection Solutions, Richland, WA. September 2016.

Millings, M., Bagwell, L., Amidon, M., and Dixon, K. (2011). "Sediment Properties: E Area Completion Project." SRNL-STI-2011-00095, Rev. 0. Savannah River National Laboratory, Aiken, SC.

Mualem, Y. (1976). A New Model for Predicting the Hydraulic Conductivity of Unsaturated Porous Media. *Water Resour. Res.* **12**(3), 513-522.

Mualem, Y. (1986). Hydraulic Conductivity of Unsaturated Soils: Prediction and Formulas. *In* "Methods of Soil Analysis: Part 1, Physical and Mineralogical Methods" (A. Klute, ed.), Vol. 5, pp. 799-823. American Society of Agronomy, Madison, WI.

Mueller, W., and Jakob, I. (2003). Oxidative Resistance of High-Density Polyethylene Geomembranes. *Polymer Degradation and Stability* **79**(1), 161-172.

NCRP (1996). "Screening Models for Releases of Radionuclides to Atmosphere, Surface Water and Ground." NCRP Report No. 123 I and II. National Council on Radiation Protection and Measurements, Bethesda, MD. Jan. 22, 1996.

NDAA (2014). "Ronald W. Reagan National Defense Authorization Act for Fiscal Year 2005." Section 3116, Defense Site Acceleration Completion, Public Law 108-375, October 28, 2004.

NEA (2012). "Methods for Safety Assessment of Geological Disposal Facilities for Radioactive Waste – Outcomes of the MeSA Initiative." NEA No. 6923. Organization for Economic Cooperation and Development – Nuclear Energy Agency, Paris, France.

Needham, A., Gallagher, E., Peggs, I., Howe, G., and Norris, J. (2004). "The Likely Medium to Long-Term Generation of Defects in Geomembrane Liners." R&D Technical Report P1-500/1/TR. Environment Agency, Bristol, England.

Neeper, D. A. (2002). Investigation of the Vadose Zone using Barometric Pressure Cycles. *Journal of Contaminant Hydrology* **54**(1-2), 59-80.

Nichols, R. L., and Butcher, B. T. (2020). "Hydraulic Properties Data Package for the E-Area Soils, Cementitious Materials, and Waste Zones - Update." SRNL-STI-2019-00355, Rev. 1. Savannah River National Laboratory, Aiken, SC.

Nimmo, J. R., Deason, J. A., Izbicki, J. A., and Martin, P. (2002). Evaluation of Unsaturated Zone Water Fluxes in Heterogeneous Alluvium at a Mojave Basin Site. *Water Resources Research* **38**(10), 33-1 to 33-13.

Ochs, M., Mallants, D., and Wang, L. (2016). "Radionuclide and Metal Sorption on Cement and Concrete," Springer, Heidelberg, Switzerland.

Parizek, R. R., and Root, R. W. (1986). "Development of a Ground-Water Velocity Model for the Radioactive Waste Management Facility Savannah River Plant, South Carolina." Prepared for E. I. du Pont de Nemours and Company, Savannah River Plant, DuPont Rpt. No. DPST-86-658. The Pennsylvania State University, University Park, PA. June 1986.

Peregoy, W. (2006a). "Structural Evaluation of Component-in-Grout Trenches." T-CLC-E-00026, Rev. 0. Washington Savannah River Company, Aiken, SC.

Peregoy, W. (2006b). "Structural Evaluation of Intermediate Level Waste Storage Vaults for Long-Term Behavior." T-CLC-E-00024, Rev. 0. Washington Savannah River Company, Aiken, SC. June 27, 2006.

Phifer, M. A. (2003a). "Saltstone Disposal Facility Mechanically Stabilized Earth Vault Closure Cap Degradation Base Case: Institutional Control To Pine Forest Scenario." WSRC-TR-2003-00523. Westinghouse Savannah River Company, Aiken, SC.

Phifer, M. A. (2004a). "Preliminary E-Area Trench Closure Cap Closure Sequence, Infiltration, and Waste Thickness (U)." WSRC-TR-2004-00119, Rev. 0. Westinghouse Savannah River Company, Aiken, SC.

Phifer, M. A. (2006). "Software Quality Assurance Plan for the Hydrologic Evaluation of Landfill Performance (HELP) Model." Q-SQA-A-00005, Rev. 0. Savannah River National Laboratory, Aiken, SC.

Phifer, M. A. (2007). "HELP Software Classification Document." K-SWCD-A-00001, Rev. 2. Savannah River National Laboratory, Aiken, SC. October, 17, 2007.

Phifer, M. A. (2014). "E-Area Vault Concrete Material Property And Vault Durability/Degradation Projection Recommendations." SRNL-STI-2013-00706, Rev. 0. Savannah River National Laboratory, Aiken, SC.

Phifer, M. A., Crapse, K. P., Millings, M. R., and Serrato, M. G. (2009). "Closure Plan for the E-Area Low-Level Waste Facility." SRNL-RP-2009-00075, Rev. 0. Savannah River National Laboratory, Aiken, SC.

Phifer, M. A., and Jones, W. E. (2007). "CIG-1 Segments 1 through 8 Infiltration Estimates." Washington Savannah River Company LLC, Aiken, SC. November 2007.

Phifer, M. A., Jones, W. E., Nelson, E. A., Denham, M. E., Lewis, M. R., and Shine, E. P. (2007). "FTF Closure Cap Concept and Infiltration Estimates." WSRC-STI-2007-00184, Rev. 2. Savannah River National Laboratory, Washington Savannah River Company, Aiken, SC.

Phifer, M. A., Millings, M. R., and Flach, G. P. (2006). "Hydraulic Property Data Package for the E-Area and Z-Area Vadose Zone Soils, Cementitious Materials, and Waste Zones." WSRC-STI-2006-00198, Rev. 0. Washington Savannah River Company, Aiken, SC.

Phifer, M. A., and Nelson, E. A. (2003). "Saltstone Disposal Facility Closure Cap Configuration and Degredation Base Case: Institutional Control to Pine Forest Scenario (U)." WSRC-TR-2003-00436, Rev. 0. Westinghouse Savannah River Company, Aiken, SC. September 22, 2003.

Phifer, M. A., Sappington, F. C., and Jones, W. E. (2000). "DCB-8C Step and Constant Rate Pump Tests D-Area Unconfined Aquifer Hydraulic Parameter Estimation." SRT-EST-2000-00226. Westinghouse Savannah River Company, Aiken, SC. July 18, 2000.

Phifer, M. A., and Wilhite, E. L. (2001). "Waste Subsidence Potential versus Supercompaction." WSRC-RP-2001-00613. Westinghouse Savannah River Company, Aiken, SC.

Rengard, K. G., Foster, G. R., Weesies, G. A., McCool, D. K., and Yoder, D. C. (1997). "Predicting Soil Erosion by Water: A Guide to Conservation Planning with the Revised Universal Soil Loss Equation (RUSLE)," Agriculture Handbook No. 703, U.S. Department of Agriculture, Tucson, AZ.

Rogers, V. C., and Nielson, K. K. (1991). Correlations for Predicting Air Permeabilities and 222Rn Diffusion Coefficients of Soils. *Health Physics* **61**(2), 225-230.

Rosenberger, K. (2007). "Potential Dose to F-Tank Farm Closure Cap Geomembrane (K. Rosenberger to M. A. Phifer)." SRS-REG-2007-00001. Washington Savannah River Company, Aiken, SC. June 1, 2007.

SAIC (2000). "Analysis of FY99 Aquifer Testing at the F-Area Seepage Basins Hazardous Waste Management Facility." WSRC-RP-99-4202, Rev. 0. Scientific Applications International Corporation, Aiken, SC. January 2000.

Sánchez-Vila, X., Girardi, J. P., and Carrera, J. (1995). A Synthesis of Approaches to Upscaling of Hydraulic Conductivities. *Water Resources Research* **31**(4), 867-882.

Sangam, H., and Rowe, R. (2002). Effects of Exposure Conditions on the Depletion of Antioxidants from High-Density Polyethylene (HDPE) Geomembranes. *Canadian Geotechnical Journal* **39**(6), 1221-1230.

Sarris, T. S., and Paleologos, E. K. (2004). Numerical Investigation of the Anisotropic Hydraulic Conductivity Behavior in Heterogeneous Porous Media. *Stochastic Environmental Research and Risk Assessment* **18**(3), 188-197.

Savannah River Remediation (2009). "Performance Assessment for the Saltstone Disposal Facility at the Savannah River Site." LWO-RIP-2009-00011. Savannah River Remediation LLC, Aiken, SC. March 2009.

Savannah River Remediation (2012). "Performance Assessment for the H-Area Tank Farm at the Savannah River Site." SRR-CWDA-2010-00128. Savannah River Remediation LLC, Aiken, SC. November 2012.

Savannah River Remediation (2014). "Dose Calculation Methodology for Liquid Waste Performance Assessments at the Savannah River Site." SRR-CWDA-2013-00058, Rev. 1. Savannah River Remediation LLC, Aiken, SC. July 2014.

Savannah River Remediation (2020). "Performance Assessment for the Saltstone Disposal Facility at the Savannah River Site." SRR-CWDA-2019-00001, Rev. 0. Savannah River Remediation LLC, Aiken, SC. March 2020.

SCGS (2008). "7.5 Minute Geologic Quadrangle Data." Retrieved Spring/Summer, 2017 from https://www.dnr.sc.gov/geology/digital-data.html. South Carolina Geological Survey, Columbia, SC.

Schroeder, P. R., Dozier, T. S., Zappi, P. A., McEnroe, B. M., Sjostrom, J. W., and Peyton, R. L. (1994a). "The Hydrologic Evaluation of Landfill Performance (HELP) Engineering Documentation for Version 3." EPA/600/R-94/168b. Office of Research and Development, United States Environmental Protection Agency (EPA), Cincinnati, Ohio. September 1994.

Schroeder, P. R., Lloyd, C. M., Zappi, P. A., and Aziz, N. M. (1994b). "The Hydrologic Evaluation of Landfill Performance (HELP) Model User's Guide for Version 3." EPA/600/R-94/168a. Office of Research and Development, United States Environmental Protection Agency (EPA), Cincinnati, Ohio. September 1994.

Schroeder, P. R., and Peyton, R. L. (1987a). "Verification of the Hydrologic Evaluation of Landfill Performance (HELP) Model Using Field Data." EPA/600/2-87/050. Office of Research and Development, United States Environmental Protection Agency (EPA), Cincinnati, Ohio. July 1987.

Schroeder, P. R., and Peyton, R. L. (1987b). "Verification of the Lateral Drainage Component of the HELP Model Using Physical Models." EPA/600/2-87/049. Office of Research and Development, United States Environmental Protection Agency (EPA), Cincinnati, Ohio. July 1987.

Seitz, R. R. (2020). "Safety Functions and Features, Events and Processes for the E-Area Performance Assessment." SRNL-STI-2020-00039, Rev. 0. Savannah River National Laboratory, Aiken, SC.

Shine, E. P. (2007). "F-Area Tank Farm Closure Cap Probability Model of Pine Tree Tap Root Penetrations of HDPE Geomembrane (U)." WSRC-TR-2007-00369, Rev. 0. Savannah River National Laboratory, Aiken, SC. September 11, 2007.

Shipmon, J. C., and Dyer, J. A. (2017). "Analysis of Factors that Influence Infiltration Rates using the HELP Model." SRNL-STI-2017-00506, Rev. 0. Savannah River National Laboratory, Aiken, SC.

Sink, D. F. (2016c). "FY16 SWMF Low Level Waste Plan and Disposal Strategies." SRNS-RP-2016-00162, Rev. 0. Savannah River Nuclear Solutions, Aiken, SC. April 2016.

Skibo, A. Z. (2018). "SRNL Bamboo (Phyllostachys Species) Planting Site Assessment, Savannah River Site." SRNL-STI-2017-00638, Rev. 0. Savannah River National Laboratory, Aiken, SC.

Smith, F. G., III, Butcher, B. T., Hamm, L. L., and Kubilius, W. P. (2019). "Dose Calculation Methodology and Data for Solid Waste Performance Assessment and Composite Analysis at the Savannah River Site." SRNL-STI-2015-00056, Revision 1. Savannah River National Laboratory, Aiken, SC. August 2019.

Smits, A. D., Harris, M. K., Hawkins, K. L., and Flach, G. P. (1997). "Integrated Hydrogeological Model of the General Separations Area, Volume 1: Hydrogeologic Framework." WSRC-TR-96-0399, Rev. 0. Westinghouse Savannah River Company, Aiken, SC.

SRNL (2010). "Savannah River DOE 435.1 Composite Analysis." SRNL-STI-2009-00512, Rev. 0. Savannah River National Laboratory, Aiken, SC. June 10, 2010.

SRNL (2017). "The Hydrostratigraphic Surfaces Data Package [Change Control Rev1 and Rev0 dataset (Appendix 5 to SRNL-STI-2017-00301).xlsx]." Rev. 1. Retrieved August, 2020 from \\godzilla-01\hpc_project\projwork50\QA\Data\ELLWF\SubsurfaceElevDepth. *Last Updated* November 3, 2017. SRNL High Performance Computing File Server Network, Savannah River National Laboratory, Aiken, SC.

SRNL (2018). "The Geochemical Data Package (GeochemPackage_Ver3.1_4-27-18_FINAL.xls)." Version 3.1. Retrieved December, 2018 from \\godzilla-01\hpc_project\projwork50\QA\Data\ELLWF\Rad-Dose. *Last Updated* April 27, 2018. SRNL High Performance Computing File Server Network, Savannah River National Laboratory, Aiken, SC.

SRNL (2019a). "The Infiltration Data Package (Infiltration-Data-Package_Ver1.0_10-16-2019_DRAFT.xlsx)." Version 1.0. Retrieved August, 2020 from \\godzilla-01\hpc_project\projwork50\QA\Data\ELLWF\Infiltration. *Last Updated* October 25, 2019. SRNL High Performance Computing File Server Network, Savannah River National Laboratory, Aiken, SC.

SRNL (2019b). "RadDosePackage_Version-2.0_CLEAN_8-13-19_FINAL.xlsx." Version 2.0. Retrieved August, 2019 from \\godzilla-01\hpc_project\projwork50\QA\Data\ELLWF\Rad-Dose\Current\ Rev1Report_Ver2.0-Database. SRNL High Performance Computing File Server Network, Savannah River National Laboratory, Aiken, SC.

SRNL (2020). "The Hydraulic Properties Data Package (HydraulicProperties_Rev3_12-01-2020.xlsm)." Rev. 3. Retrieved December, 2020 from \\godzilla-01\hpc_project\projwork50\QA\Data\ELLWF\Material\Current. *Last Updated* December 1, 2020. SRNL High Performance Computing File Server Network, Savannah River National Laboratory, Aiken, SC.

SRNS (2017a). "Annual Corrective Action Report for the F-Area Hazardous Waste Management Facility, the H-Area Hazardous Waste Management Facility, and the Mixed Waste Management Facility (U)." SRNS-RP-2017-00134, Volume I. Savannah River Site, Aiken, SC. April 2017.

SRS (2016). "Savannah River Site Nuclear Materials Management Plan FY 2016-2030." SRNL-RP-2016-00362, Rev. 0. Savannah River National Laboratory, Aiken, SC. June 23, 2016.

SRS GDMS (2017). "Savannah River Site Geological Data Management System." Retrieved Spring/Summer, 2017 from http://sqlsan1/reports$srs1_p/Pages/Report.aspx?ItemPath=/GDMS/GDMS-Web/SearchResultsReport.

Stagich, B., and Jannik, T. (2020). "Exposure Pathways and Scenarios for the E-Area Low-Level Waste Facility Performance Assessment." SRNL-STI-2020-00007, Rev. 0. Savannah River National Laboratory, Aiken, SC.

Stagich, B. H. (2020). "CAP88-PC Version 4.1 Verification (Technical Memo: B. H. Stagich to Environmental Dosimetry Files)." SRNL-L3200-2020-00028, Rev. 0. Savannah River National Laboratory, Aiken, SC. March 17, 2020.

Stagich, B. H. (2021). "Clean Air Act Assessment Package 1988 PC Version/CAP88 PC, Software Ver. 4.1." Q-SWCD-A-00010, Rev. 6. Savannah River National Laboratory, Aiken, SC. September 30, 2021.

Stagich, B. H., Jannik, G. T., LaBone, E., and Dixon, K. L. (2021). "Radiological Impact of 2020 Operations at the Savannah River Site." SRNL-STI-2021-00284, Rev. 0. Savannah River National Laboratory, Aiken, SC.

Stone, D. K., and Jannik, G. T. (2013). "Site Specific Reference Person Parameters and Derived Concentration Standards for the Savannah River Site." SRNL-STI-2013-00115. Savannah River Site, Aiken, SC. March 2013.

Stricker, V. A. (1983). "Base Flow of Streams in the Outcrop Area of Southeastern Sand Aquifer: South Carolina, Georgia, Alabama, and Mississippi." Water Resources Investigations Report 83-4106. United States Geological Survey, Denver, CO.

SWM (2021). "Savannah River Site Solid Waste Management Facility Documented Safety Analysis." WSRC-SA-22, Rev. 31. Savannah River Site, Aiken, SC. July 2021.

Tecplot (2021). "Tecplot 360 EX User's Manual." Tecplot, Inc., Bellevue, WA.

Tian, K., Benson, C. H., Tinjum, J. M., and Edil, T. B. (2017). Antioxidant Depletion and Service Life Prediction for HDPE Geomembranes Exposed to Low-Level Radioactive Waste Leachate. *Journal of Geotechnical and Geoenvironmental Engineering* **143**(6), 04017011.

U.S. DOE (2007). "Format and Content Guide for U.S. Department of Energy Low-Level Waste Disposal Facility Performance Assessments and Composite Analyses." U.S. Department of Energy, Washington, DC. May 2007.

U.S. DOE (2011a). "DOE Standard: Derived Concentration Technical Standard." DOE-STD-1196-2011. U. S. Department of Energy, Washington, DC. April 2011.

U.S. DOE (2017). "Disposal Authorization Statement and Tank Closure Documentation." DOE-STD-5002-2017. U.S. Department of Energy, Washington, DC.

U.S. DOE (2020b). Radiation Protection of the Public and the Environment. DOE O 458.1 Chg 4. U. S. Department of Energy, Washington, DC. September 15, 2020.

U.S. DOE (2021b). "Radioactive Waste Management Manual." DOE M 435.1-1, Chg 3: 1-11-2021. U. S. Department of Energy, Washington, DC. January 11, 2021.

U.S. EPA (2006). National Emissions Standards for Hazardous Air Pollutants, Subpart H (Title 40 CFR Part 61). 54 FR 51695, Dec. 15, 1989, as amended at 65 FR 62156, Oct. 17, 2000; 67 FR 57166, Sept. 9, 2002. United States Environmental Protection Agency, Washington, DC.

U.S. EPA (2020). "CAP88-PC Version 4.1 User Guide." United States Environmental Protection Agency, Office of Radiation and Indoor Air, Washington, DC.

Valocchi, A. J. (1985). Validity of the Local Chemical Equilibrium Assumption for Describing Sorbing Solute Transport through Homogeneous Soils. *Water Resour. Res.* **21**(6), 808-820.

van Genuchten, M. T. (1978). "Calculating the Unsaturated Hydraulic Conductivity with a New Closed-Form Analytical Model." Research Report No. 78-WR-08. Department of Civil Engineering, Princeton University, Princeton, NJ.

van Genuchten, M. T. (1980). A Closed-Form Equation for Predicting the Hydraulic Conductivity of Unsaturated Soils. *Soil Science Society of America Journal* **44**(5), 892-898.

van Genuchten, M. T., Leij, F. J., and Yates, S. R. (1991). "The RETC Code for Quantifying the Hydraulic Functions of Unsaturated Soils." EPA/600/2-91/065. Robert S. Kerr Environmental Research Laboratory, Office of Research and Development, U.S. Environmental Protection Agency, Ada, OK. December 1991.

Wang, L., Martens, E., Jacques, D., Decanniere, P., Berry, J., and Mallants, D. (2009). "Review of Sorption Values for the Cementitious Near Field of a Near Surface Radioactive Waste Disposal Facility." NIRAS-MP5-03/NIROND-TR-2008-23E. ONDRAF/NIRAS, Mol, Brussels.

Watermark Numerical Computing (2016). "PEST, Model-Independent Parameter Estimation, User Manual Part I: PEST, SENSAN and Global Optimisers," 6th/Ed.

Whiteside, T., Hang, T., and Flach, G. P. (2009). "Evaluation of HELP Model Replacement Codes." SRNL-STI-2009-00572, Rev. 0. Savannah River National Laboratory, Aiken, SC.

Whiteside, T. S. (2016a). "PORFLOW 6.42.3 Testing and Verification Document." SRNL-STI-2016-00724, Rev. 0. Savannah River National Laboratory, Aiken, SC. December 2016.

Whiteside, T. S. (2016b). "Software Quality Assurance Plan for PEST." Q-SQP-G-00004, Rev. 0. Savannah River National Laboratory, Aiken, SC.

Whiteside, T. S. (2017b). "PORFLOW 6.42.4 Testing and Verification Document." SRNL-STI-2017-00167, Rev. 0. Savannah River National Laboratory, Aiken, SC. March 2017.

Whiteside, T. S. (2020). "PORFLOW 6.43.0 Testing and Verification Document." SRNL-STI-2020-00219, Rev. 0. Savannah River National Laboratory, Aiken, SC. June 2020.

Wike, L. D., Martin, F. D., Nelson, E. A., Halverson, N. V., Mayer, J. J., Paller, M. H., Riley, R. S., Serrato, M. G., and Specht, W. L. (2006). "SRS Ecology: Environmental Information Document." WSRC-TR-2005-00201. Washington Savannah River Company, Aiken, SC. March 2006.

Wilson, L. G. (1980). "Monitoring in the Vadose Zone: A Review of Technical Elements and Methods." EPA-600/7-80-134. Environmental Monitoring Systems Laboratory, U.S. Environmental Protection Agency, Las Vegas, NV. June 1980.

Witt, K. J., and Siegmund, M. (2001). Laboratory Testing of GCL under Changing Humidity. *In* "Proceedings of the 8th International Waste Management and Landfill Symposium, Sardinia Second Conference, Euro Waste," Sardinia, Italy.

Wohlwend, J. L. (2017). "Atmospheric Release Model for the E-Area Low-Level Waste Facility: Updates and Modifications." SRNL-STI-2017-00592. Savannah River National Laboratory, Aiken, SC.

Wohlwend, J. L. (2018). "Updated General Separations Areas (GSA) Groundwater Model Calibration Targets." SRNL-STI-2018-00336, Rev. 0. Savannah River National Laboratory, Aiken, SC.

Wohlwend, J. L. (2020). "E-Area Low-Level Waste Facility GoldSim System Model." SRNL-STI-2020-00079, Rev. 0. Savannah River National Laboratory, Aiken, SC. April 2020.

Wohlwend, J. L. (2021a). "GoldSim Software Classification Document." Q-SWCD-A-00002, Rev. 3. Savannah River National Laboratory, Aiken, SC.

Wohlwend, J. L. (2021b). "Software Quality Assurance Plan for GoldSim." G-SQA-A-00011, Rev. 1. Savannah River National Laboratory, Aiken, SC.

Wohlwend, J. L., and Aleman, S. E. (2020). "GoldSim E-Area Low-Level Waste Facility Vadose Zone Model Benchmarking." SRNL-STI-2020-00372, Rev. 0. Savannah River National Laboratory, Aiken, SC. October 2020.

Wohlwend, J. L., and Butcher, B. T. (2018). "Proposed NRCDA Groundwater Pathway Conceptual Model." SRNL-STI-2018-00633, Rev. 0. Savannah River National Laboratory, Aiken, SC.

Wohlwend, J. L., and Hamm, L. L. (2020). "GoldSim E-Area Low-Level Waste Facility Aquifer Zone Model Calibration Methodology." SRNL-STI-2020-00346, Rev. 0. Savannah River National Laboratory, Aiken, SC. October 2020.

WSRC (1992). "Radiological Performance Assessment for the Z-Area Disposal Facility." WSRC-RP-92-1360, Rev. 0. Westinghouse Savannah River Company, Aiken, SC. December 18, 1992.

WSRC (2000). "White Paper for In Situ pH Adjustment, F-Area Seepage Basins." WSRC-RP-2000-4169. Westinghouse Savannah River Company, Aiken, SC. November 2000.

WSRC (2008). "E-Area Low-Level Waste Facility DOE 435.1 Performance Assessment." WSRC-STI-2007-00306, Rev. 0. Washington Savannah River Company, Savannah River Site, Aiken, SC.

Young, M. H., and Pohlmann, K. F. (2001). "Analysis of Vadose Zone Monitoring System: Computer Simulation of Water Flux: E-Area Disposal Trenches." Task Order GA0074 (KG43360-0). Division of Hydrologic Sciences, Desert Research Institute, Las Vegas, NV. August 2001.

Young, M. H., and Pohlmann, K. F. (2003). "Analysis of Vadose Zone Monitoring System: Computer Simulation of Water Flux under Conditions of Variable Vegetative Cover: E-Area Disposal Trenches." Publication No. 41188. Division of Hydrologic Sciences, Desert Research Institute, Las Vegas, NV. August 2001.

Yu, A. D., Langton, C. A., and Serrato, M. G. (1993). "Physical Properties Measurement Program." WSRC-RP-93-894. Westinghouse Savannah River Company, Aiken, SC. June 30, 1993.

Yu, C., Zielen, A. J., Cheng, J. J., LePoire, D. J., Gnanapragasam, E., Kamboj, S., Arnish, J., Wallo Iii, A., Williams, W. A., and Peterson, H. (2001). "Users Manual for RESRAD Version 6." Environmental Assessment Division, Argonne National Laboratory, Chicago, IL. July 2001.